Vol. 65 ▪ No. 8 ▪ August 2024

JNM

The Journal of Nuclear Medicine

FEATURED ARTICLE Performance Characteristics of the NeuroEXPLORER, a Next-Generation Human Brain PET/CT Imager. Hongdi Li et al. See page 1320.

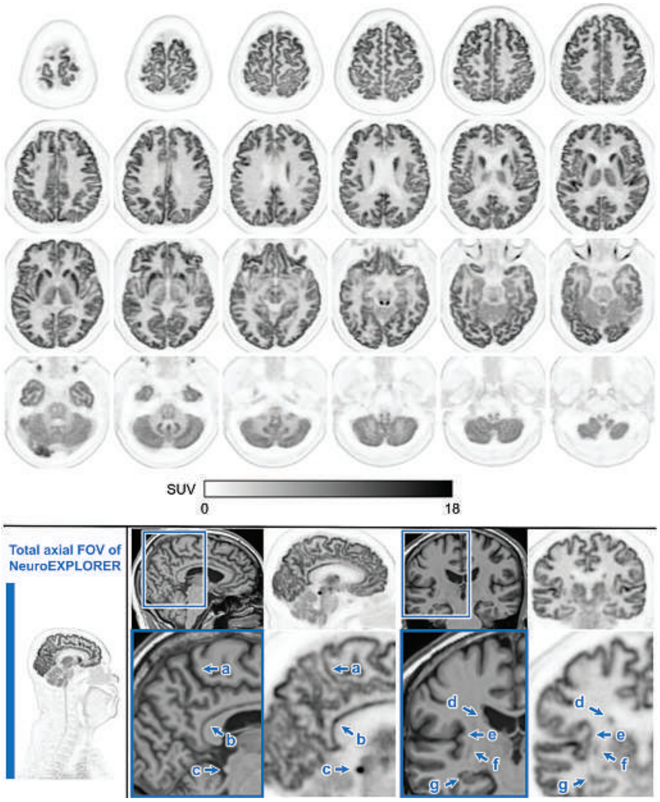

Targeting the neurotensin receptor-1: Modification of tracer pharmacokinetic properties to improve effectiveness in theranostic pairs. German O. Fonseca Cabrera et al. See page 1250.

SNMMI SOCIETY OF NUCLEAR MEDICINE & MOLECULAR IMAGING

UNITED IMAGING

Innovative PET/CT Technology

Paving the Way for the Future of Molecular Imaging

In 2018, United Imaging revolutionized the field of PET/CT imaging by launching the world's first total-body PET/CT uEXPLORER.® This ultra-high-resolution digital PET/CT boasts a remarkable 194 cm axial PET field of view (FOV), enabling the entire body to be scanned in a single bed position, thus changing the way whole-body PET/CT imaging has traditionally been performed and enables low dose, long delay, or fast scan times for total-body imaging.

The uEXPLORER is unmatched in its total-body coverage and unprecedented sensitivity, enabling the dynamic changes to radiotracer distribution to be captured with ultra-high resolution. This innovative technology is taking healthcare applications and scientific research to the next level.

Drawing on insights from the development of total-body systems, United Imaging has unveiled uExcel UDP, a next-generation digital detector. This cutting-edge PET detector is currently available on the uMI Panorama™ family of systems, with long axial FOV ranging from 35 cm to 148 cm. The uExcel UDP improves timing resolution, reduces partial volume effects, and provides high sensitivity. These benefits are particularly valuable in oncology for comprehensive cancer staging, treatment planning for theranostics, and restaging.

Leveraging cutting-edge technologies and a firm commitment to excellence, United Imaging is actively shaping the future landscape of molecular imaging with its forward-thinking approaches and state-of-the-art solutions. We invite you to join us in this exciting journey of innovation and discovery.

uEXPLORER

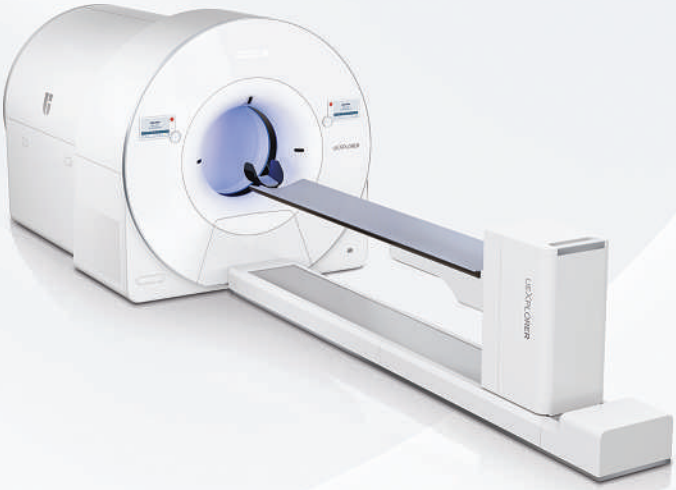

uMI Panorama Family

uMI Panorama

uMI Panorama GS

© 2024 United Imaging Healthcare Co., Ltd. All rights reserved.
9370 Kirby Drive, Houston, Texas 77054

www.united-imaging.com

IC-US-240118-1326

Scan QR code for more information

JNM

Volume 65 • Number 8 • August 2024

DISCUSSIONS WITH LEADERS

THE STATE OF THE ART

ISSUES AND CONTROVERSIES

ONCOLOGY

Clinical

THERANOSTICS

Clinical

Basic

RADIOBIOLOGY/DOSIMETRY

Clinical

CARDIOVASCULAR

Clinical

NEUROLOGY

Clinical

Basic

MOLECULAR IMAGING

Basic

AI/ADVANCED IMAGE ANALYSIS

Basic

PHYSICS AND INSTRUMENTATION

Clinical

THE ILLUSTRATED POST

LETTERS TO THE EDITOR

DEPARTMENT

JNM The Journal of
NUCLEAR MEDICINE

The Official Publication of **SNMMI**

MISSION STATEMENT: *The Journal of Nuclear Medicine* advances the knowledge and practice of molecular imaging and therapy and nuclear medicine to improve patient care through publication of original basic science and clinical research.

JNM (ISSN 0161-5505 [print]; ISSN 2159-662X [online]) is published monthly by SNMMI, 1850 Samuel Morse Drive, Reston, VA 20190-5316. Periodicals postage is paid at Herndon, VA, and additional mailing offices. Postmaster, send address changes to *The Journal of Nuclear Medicine,* 1850 Samuel Morse Drive, Reston, VA 20190-5316. The costs of publication of all nonsolicited articles in *JNM* were defrayed in part by the payment of page charges. Therefore, and solely to indicate this fact, these articles are hereby designated “advertisements” in accordance with 18 USC section 1734.

DISCLOSURE OF COMMERCIAL INTEREST: Johannes Czernin, MD, editor-in-chief of *The Journal of Nuclear Medicine,* has indicated that he is a founder of Sofie Biosciences and holds equity in the company and in intellectual property invented by him, patented by the University of California, and licensed to Sofie Biosciences. He is also a founder and board member of Trethera Therapeutics and holds equity in the company and in intellectual property invented by him, patented by the University of California, and licensed to Trethera Therapeutics. He also serves on the scientific advisory boards of RayzeBio and Aktis Oncology. No other potential conflicts of interest were reported. Manuscripts submitted to *JNM* with potential conflicts are handled by a guest editor.

EDITORIAL COMMUNICATIONS should be sent to: Editor-in-Chief, Johannes Czernin, MD, *JNM* Office, SNMMI, 1850 Samuel Morse Drive, Reston, VA 20190-5316. Phone: (703) 326-1185; Fax: (703) 708-9018. To submit a manuscript, go to https://submit-jnm.snmjournals.org.

BUSINESS COMMUNICATIONS concerning permission requests should be sent to the publisher, SNMMI, 1850 Samuel Morse Drive, Reston, VA 20190-5316; (703) 708-9000; home page address: jnm.snmjournals.org. Subscription requests and address changes should be sent to Membership Department, SNMMI at the address above. Notify the Society of change of address and telephone number at least 30 days before date of issue by sending both the old and new addresses. Claims for copies lost in the mail are allowed within 90 days of the date of issue. Claims are not allowed for issues lost as a result of insufficient notice of change of address. For information on advertising, contact Team SNMMI (Kevin Dunn, Rich Devanna, and Charlie Meitner; (201) 767-4170; fax: (201) 767-8065; TeamSNMMI@cunnasso.com). Advertisements are subject to editorial approval and are restricted to products or services pertinent to nuclear medicine. Closing date is the first of the month preceding the date of issue.

INDIVIDUAL SUBSCRIPTION RATES for the 2024 calendar year are $665 within the United States and Canada; $714 elsewhere. Make checks payable to the SNMMI. CPC IPM Sales Agreement No. 1415158. Sales of individual back copies from 1999 through the current issue are available for $60 at http://www.snmmi.org/subscribe (subscriptions@snmmi.org; fax: (703) 667-5134). Individual articles are available for sale online at http://jnm.snmjournals.org.

JNM | The Journal of Nuclear Medicine | Editorial Board

EDITOR-IN-CHIEF
Johannes Czernin, MD
University of California at Los Angeles
Los Angeles, California

IMMEDIATE PAST EDITOR
Dominique Delbeke, MD, PhD
Vanderbilt University Medical Center
Nashville, Tennessee

ASSOCIATE EDITORS, CONTINUING EDUCATION
Hossein Jadvar, MD, PhD, MPH, MBA, MSL, FACNM, FSNMMI
University of Southern California
Los Angeles, California
Lale Kostakoglu, MD, MPH
University of Virginia Health System
Charlottesville, Virginia

ASSOCIATE EDITORS
Ramsey Derek Badawi, PhD
UC Davis Medical Center
Sacramento, California
Henryk Barthel, MD, PhD
Leipzig University
Leipzig, Germany
Frank M. Bengel, MD
Hannover Medical School
Hannover, Germany
Lisa Bodei, MD, PhD
Memorial Sloan Kettering Cancer Center
New York, New York
Irene Buvat, PhD
Université Paris Sud
Orsay, France
Jérémie Calais, MD
University of California at Los Angeles
Los Angeles, California
Sharmila Dorbala, MBBS
Brigham and Women's Hospital
Lexington, Massachusetts
Alexander E. Drzezga, MD
University Hospital of Cologne
Cologne, Germany
Jan Grimm, MD, PhD
Memorial Sloan Kettering Cancer Center
New York, New York
Ken Herrmann, MD, MBA
Universitätsklinikum Essen
Essen, Germany
Thomas A. Hope, MD
University of California, San Francisco
San Francisco, California
Jason S. Lewis, PhD
Memorial Sloan Kettering Cancer Center
New York, New York
David A. Mankoff, MD, PhD
University of Pennsylvania
Philadelphia, Pennsylvania
Heiko Schöder, MD
Memorial Sloan Kettering Cancer Center
New York, New York
Wolfgang Weber, MD
Technical University of Munich
München, Germany

SERIES EDITOR, FOCUS ON MI
Carolyn J. Anderson, PhD
University of Missouri
Columbia, Missouri

SERIES EDITOR, HOT TOPICS
Heinrich R. Schelbert, MD, PhD
University of California at Los Angeles
Los Angeles, California

CONSULTING EDITORS
Nancy Knight, PhD
University of Maryland School of Medicine
Baltimore, Maryland
Barry A. Siegel, MD
Mallinckrodt Institute of Radiology
St. Louis, Missouri
Arnold M. Strashun, MD
SUNY Downstate Medical Center
Scarsdale, New York
H. William Strauss, MD
Memorial Sloan Kettering Cancer Center
New York, New York

ASSOCIATE EDITORS (INTERNATIONAL)
Gerald Antoch, MD
Dusseldorf, Germany
Richard P. Baum, MD, PhD
Bad Berka, Germany
Ambros J. Beer, MD
Ulm, Germany
François Bénard, MD, FRCPC
Vancouver, Canada
Thomas Beyer, PhD
Vienna, Austria
Andreas K. Buck, MD, PhD
Würzburg, Germany
Ignasi Carrió, MD
Barcelona, Spain
June-Key Chung, MD
Seoul, Korea
Matthias Eiber, MD
Munich, Germany
Louise M. Emmett, MBChB, FRACP, MD
Sydney, Australia
Stefano Fanti, MD
Bologna, Italy
Wolfgang Peter Fendler, MD
Munich, Germany
Markus Hacker, MD
Wien, Austria
Rodney J. Hicks, MD, FRACP
Melbourne, Australia
Michael S. Hofman, MBBS, FRACP
Melbourne, Australia
Ora Israel, MD
Haifa, Israel
Andreas Kjaer, MD, PhD, DMSc
Copenhagen, Denmark
Adriaan A. Lammertsma, PhD
Amsterdam, The Netherlands
Michael Lassman, PhD
Würzburg, Germany
Helmut R. Mäcke, PhD
Freiburg, Germany
Wim J.G. Oyen, MD, PhD
Milan, Italy
John O. Prior, MD, PhD
Lausanne, Switzerland
Osman Ratib, MD, PhD
Geneva, Switzerland
Mike Sathekge, MBChB, MMed, PhD
Pretoria, South Africa
Markus Schwaiger, MD
München, Germany
Andrew M. Scott, MD
Heidelberg, Australia
Nagara Tamaki, MD, PhD
Kyoto, Japan
Jia-He Tian, PhD
Beijing, China
Mei Tian, MD, PhD
Hangzhou, China

EDITORIAL CONSULTANTS
Martin S. Allen-Auerbach, MD
Los Angeles, California
Magnus Dahlbom, PhD
Los Angeles, California
Andrew Quon, MD
Los Angeles, California
Christiaan Schiepers, MD, PhD
Los Angeles, California
Daniel H. Silverman, MD, PhD
Los Angeles, California
Roger Slavik, PhD
Winterthur, Switzerland

EDITORIAL BOARD
Diane S. Abou, PhD
St. Louis, Missouri
Hojjat Ahmadzadehfar, MD
Dortmund, Germany
Valentina Ambrosini, MD, PhD
Bologna, Italy
Norbert Avril, MD
Cleveland, Ohio
Shadfar Bahri
Los Angeles, California
Jacques Barbet, PhD
Saint-Herbalin, France
Bradley Jay Beattie, PhD
New York, New York
Freek J. Beekman, PhD
Delft, The Netherlands
Matthias Richard Benz, MD
Los Angeles, California
Elie Besserer-Offroy, PhD, FACSc
Los Angeles, California
Pradeep Bhambhvani, MD
Birmingham, Alabama
Angelika Bischof-Delaloye, MD
Lausanne, Switzerland
Ronald Boellaard, PhD
Groningen, The Netherlands
Nicolaas Bohnen, MD
Ann Arbor, Michigan
Wesley E. Bolch, PhD
Gainesville, Florida
Elias H. Botvinick, MD
San Francisco, California
Winfried Brenner, MD, PhD
Berlin, Germany
Richard C. Brunken, MD
Cleveland, Ohio
Ralph Buchert, PhD
Hamburg, Germany
Alfred Buck, MD
Menzingen, Switzerland
Denis B. Buxton, PhD
Bethesda, Maryland
Weibo Cai, PhD
Madison, Wisconsin
Federico Caobelli, MD
Basel, Switzerland
Giuseppe Carlucci, PhD
Los Angeles, California
Richard E. Carson, PhD
New Haven, Connecticut
Paolo Castellucci, MD
Bologna, Italy
Franscesco Ceci, MD, PhD
Turin, Italy
Juliano J. Cerci
Curitiba, Brazil
Delphine Chen, MD
Seattle, Washington
Xiaoyuan Chen, PhD
Singapore
Simon R. Cherry
Davis, California
Arturo Chiti, MD
Rozzano, Italy
Peter M. Clark, PhD
Los Angeles, California
Christian Cohade, MD
Montreal, Canada
Ekaterina (Kate) Dadachova, PhD
Saskatoon, Canada
Issa J. Dahabreh, MD
Boston, Massachusetts
Heike Elisabeth Daldrup-Link, MD, PhD
Stanford, California
Farrokh Dehdashti, MD
St. Louis, Missouri
Robert C. Delgado-Bolton, MD, PhD
Logroño, Spain
Thorsten Derlin, MD
Hannover, Germany
Elisabeth G.E. de Vries, PhD
Groningen, The Netherlands
Marcelo F. Di Carli, MD
Boston, Massachusetts
David W. Dick, PhD
Iowa City, Iowa
Vasken Dilsizian, MD
Baltimore, Maryland
Jacob Dubroff, MD, PhD
Philadelphia, Pennsylvania
Janet F. Eary, MD
Bethesda, Maryland
W. Barry Edwards, PhD
Columbia, Missouri
David Eidelberg, MD
Manhasset, New York
Georges El Fakhri, PhD
Boston, Massachusetts
Peter J. Ell, MD
London, United Kingdom
Keigo Endo, MD
Nantan, Japan
Einat Even-Sapir, MD, PhD
Tel Aviv, Israel
Frederic H. Fahey, DSc
Boston, Massachusetts

EDITORIAL BOARD, continued
Melpomeni Fani, PhD, MSc
Basel, Switzerland
Andrea Farolfi, MD
Bologna, Italy
James W. Fletcher, MD
Indianapolis, Indiana
Amy M. Fowler, MD, PhD
Madison, Wisconsin
Kirk A. Frey, MD, PhD
Ann Arbor, Michigan
Andrei Gafita
Los Angeles, California
Victor H. Gerbaudo, PhD, MSHCA
Boston, Massachusetts
Frederik L. Giesel, MD, PhD, MBA
Düsseldorf, Germany
Karolien Goffin, MD, PhD
Leuven, Belgium
Serge Goldman, MD, PhD
Brussels, Belgium
Stanley J. Goldsmith, MD
New York, New York
Martin Gotthardt, MD, PhD
Nijmegen, The Netherlands
Michael Graham, MD, PhD
Iowa City, Iowa
David Groheux, MD, PhD
Paris, France
Uwe A. Haberkorn, MD
Heidelberg, Germany
Mathieu Hatt, PhD, HDR
Brest, France
Wolf-Dieter Heiss, MD
Cologne, Germany
Karl Herholz, MD
Manchester, United Kingdom
Thomas F. Heston, MD
Las Vegas, Nevada
John M. Hoffman, MD
Salt Lake City, Utah
Carl K. Hoh, MD
San Diego, California
Jason P. Holland, DPhil
Zurich, Switzerland
Roland Hustinx, MD, PhD
Liege, Belgium
Andrei H. Iagaru, MD
Stanford, California
Masanori Ichise, MD
Chiba, Japan
Amir Iravani, MD
Seattle, Washington
Heather A. Jacene, MD
Boston, Massachusetts
Francois Jamar, MD, PhD
Brussels, Belgium
Jae Min Jeong, PhD
Seoul, Korea
John A. Katzenellenbogen, PhD
Urbana, Illinois
Zohar Keidar, MD, PhD
Haifa, Israel
Kimberly A. Kelly, PhD
Charlottesville, Virginia
Laura M. Kenny, MD, PhD
London, United Kingdom
Fabian Kiessling, MD
Aachen, Germany
E. Edmund Kim, MD, MS
Orange, California
Francoise Kraeber-Bodéré, MD, PhD
Nantes, France
Clemens Kratochwil, MD
Heidelberg, Germany
Kenneth A. Krohn, PhD
Portland, Oregon
Brenda F. Kurland, PhD
Pittsburgh, Pennsylvania
Constantin Lapa, MD
Augsburg, Germany
Suzanne E. Lapi, PhD
Birmingham, Alabama
Steven M. Larson, MD
New York, New York
Dong Soo Lee, MD, PhD
Seoul, Korea
Jae Sung Lee, PhD
Seoul, Korea
Jeffrey Leyton, PhD
Sherbrooke, Canada
Xiang-Guo Li, PhD
Turku, Finland
Hannah M. Linden, MD
Seattle, Washington
Martin A. Lodge, PhD
Baltimore, Maryland
Katharina Lückerath, PhD
Los Angeles, California
Susanne Lütje, MD, PhD
Bonn, Germany
Umar Mahmood, MD, PhD
Boston, Massachusetts
H. Charles Manning, PhD
Nashville, Tennessee
Giuliano Mariani, MD
Pisa, Italy
Chester A. Mathis, PhD
Pittsburgh, Pennsylvania
Alan H. Maurer, MD
Philadelphia, Pennsylvania
Jonathan McConathy, MD, PhD
Birmingham, Alabama
Alexander J.B. McEwan, MD
Edmonton, Canada
Yusuf Menda, MD
Iowa City, Iowa
Philipp T. Meyer, MD, PhD
Freiburg, Germany
Matthias Miederer, MD
Mainz, Germany
Jasna Mihailovic, MD, PhD
Sremska Kamenica, Serbia
Erik Mittra, MD, PhD
Portland, Oregon
Christine E. Mona, PhD
Los Angeles, California
Dae Hyuk Moon, MD
Seoul, Korea
Jennifer Murphy, PhD
Los Angeles, California
Helen Nadel, MD, FRCPC
Stanford, California
Matthias Nahrendorf, MD, PhD
Boston, Massachusetts
Yuji Nakamoto, MD, PhD
Kyoto, Japan
David A. Nathanson, PhD
Los Angeles, California
Nghi C. Nguyen, MD, PhD
Dallas, Texas
Sridhar Nimmagadda, PhD
Baltimore, Maryland
Egbert U. Nitzsche, MD
Aarau, Switzerland
Daniela E. Oprea-Lager, MD, PhD
Amsterdam, The Netherlands
Medhat M. Osman, MD, PhD
Saint Louis, Missouri
Christopher J. Palestro, MD
New Hyde Park, New York
Miguel Hernandez Pampaloni, MD, PhD
San Francisco, California
Neeta Pandit-Taskar, MD
New York, New York
Ashwin Singh Parihar, MBBS, MD
Saint Louis, Missouri
Michael E. Phelps, PhD
Los Angeles, California
Gerold Porenta, MD, PhD
Vienna, Austria
Sophie Poty, PhD
Montpellier, France
Edwin (Chuck) Pratt, PhD, MS Eng
New York, New York
Daniel A. Pryma, MD
Philadelphia, Pennsylvania
Valery Radchenko, PhD
Vancouver, Canada
Caius G. Radu, MD
Los Angeles, California
Isabel Rauscher, MD
Munich, Germany
Nick S. Reed, MBBS
Glasgow, United Kingdom
Mark Rijpkema, PhD
Nijmegen, The Netherlands
Steven P. Rowe, MD, PhD
Baltimore, Maryland
Mehran Sadeghi, MD
West Haven, Connecticut
Orazio Schillaci, MD
Rome, Italy
Charles Ross Schmidtlein, PhD
New York, New York
David M. Schuster, MD
Atlanta, Georgia
Travis Shaffer, PhD
Stanford, California
Sai Kiran Sharma, PhD
New York, New York
Anthony F. Shields, MD, PhD
Detroit, Michigan
Barry L. Shulkin, MD, MBA
Memphis, Tennessee
Yu Shyr, PhD
Nashville, Tennessee
Albert J. Sinusas, MD
New Haven, Connecticut
Riemer H.J.A. Slart, MD, PhD
Groningen, The Netherlands
Piotr Slomka, PhD, FACC
Los Angeles, California
Simon John Christoph Soerensen, MD
Stanford, California
Ida Sonni, MD
Los Angeles, California
Michael G. Stabin, PhD
Richland, Washington
Lisa J. States, MD
Philadelphia, Pennsylvania
Sven-Erik Strand, PhD
Lund, Sweden
Rathan M. Subramaniam, MD, PhD, MPH
Dunedin, New Zealand
John Sunderland, PhD
Iowa City, Iowa
Suleman Surti, PhD
Philadelphia, Pennsylvania
Julie Sutcliffe, PhD
Sacramento, California
David Taieb, MD, PhD
Marseille, France
Laura H. Tang, MD, PhD
New York, New York
Ukihide Tateishi, MD, PhD
Tokyo, Japan
James T. Thackeray, PhD
Hannover, Germany
Mathew L. Thakur, PhD
Philadelphia, Pennsylvania
Alexander Thiel, MD
Montreal, Canada
Daniel L.J. Thorek, PhD
St. Louis, Missouri
David W. Townsend, PhD
Singapore
Timothy Turkington, PhD
Durham, North Carolina
Gary A. Ulaner, MD, PhD
Irvine, California
David Ulmert, MD, PhD
Los Angeles, California
Lena M. Unterrainer, MD, MHBA
Munich, Germany
Christopher H. van Dyck, MD
New Haven, Connecticut
Douglas Van Nostrand, MD
Washington, District of Columbia
Patrick Veit-Haibach, MD
Toronto, Canada
Nerissa Viola-Villegas, PhD
Detroit, Michigan
John R. Votaw, PhD
Atlanta, Georgia
Richard L. Wahl, MD
St. Louis, Missouri
Anne Marie Wallace, MD
La Jolla, California
Martin A. Walter, MD
Geneva, Switzerland
Rudolf A. Werner, MD
Wuerzburg, Germany
Andreas G. Wibmer, MD
New York, New York
Anna M. Wu, PhD
Duarte, California
Randy Yeh, MD
New York, New York
Hyewon (Helen) Youn, PhD
Seoul, Korea
Pat B. Zanzonico, PhD
New York, New York
Brian M. Zeglis, PhD
New York, New York
Robert Zeiser, MD
Freiburg, Germany
Hong Zhang, MD, PhD
Hangzhou, China
Hongming Zhuang, MD, PhD
Philadelphia, Pennsylvania
Sibylle I. Ziegler, PhD
Munich, Germany

ASSISTANT TO THE EDITOR
Joshua N. Wachtel
Los Angeles, California

THIS MONTH IN JNM

Discussions with leaders: Heinrich Schelbert, a pioneer in assessment of cardiac function and a past *JNM* editor-in-chief, talks with Heiko Schoder and Johannes Czernin about his long career in nuclear medicine. . . . . ***Page 1163***

Effects of ^{177}Lu dose conversion method: Brosch-Lenz and members of the SNMMI ^{177}Lu dosimetry challenge continue their evaluation of sources contributing to variability in dosimetry workflow and calculation of absorbed dose. . . . . ***Page 1166***

Ending the LNT model: Doss explores factors contributing to the persistence of the linear no-threshold model and offers a suggestion for resolving this contentious and long-standing issue. . . . . ***Page 1173***

Radioembolization of NENs: Watanabe and colleagues report on the potential of multicompartment dosimetry in ^{90}Y glass microsphere radioembolization of neuroendocrine neoplasms, observing higher response rates and longer progression-free survival with higher doses. . . . . ***Page 1175***

Posttreatment PET/CT in HNSCC: Clement and colleagues evaluate the diagnostic performance of ^{18}F-FDG PET/CT in detecting subclinical recurrence over a 5-y period after treatment for head and neck squamous cell carcinoma. . . . . ***Page 1181***

^{68}Ga-FAPI46 in mesothelioma: Kessler and colleagues characterize the association of histopathologic FAP expression and ^{68}Ga-FAPI46 PET uptake in malignant mesothelioma and compare resulting sensitivity, specificity, positive/negative predictive values, and detection rates with those of ^{18}F-FDG PET/CT and contrast-enhanced CT. . . . . ***Page 1188***

PET/CT and prognosis in anal cancer: Combet-Curt and colleagues document the predictive value of ^{18}F-FDG PET/CT in terms of recurrence-free, colostomy-free, and overall survival after radiation therapy of squamous cell carcinoma of the anus, including baseline and posttherapeutic imaging. . . . . ***Page 1194***

PRECISE-MDT study: Bauckneht and colleagues assess the impact of different imaging modalities on guidance of metastasis-directed therapy and resulting effects on oncologic outcomes within a large, multiinstitutional cohort of patients with oligorecurrent prostate cancer. . . ***Page 1202***

PSMA PET with HOXB13 profiling: Angappulige and colleagues investigate whether SUVs on PSMA PET correlate with expression of Homeobox 13, an oncogenic transcription factor that promotes resistance to androgen receptor–targeted therapies in prostate cancer. . . . . ***Page 1210***

FAP in glioblastoma and gliosarcoma: Oster and colleagues explore the clinical relevance of FAP expression in gliosarcoma and glioblastoma and the diagnostic and therapeutic implications of the ways in which this expression correlates with ^{68}Ga-FAP inhibitor–46 PET uptake.. . ***Page 1217***

SIRT AD and spatial liver function: Lu and colleagues identify correlations between ^{90}Y PET absorbed dose voxel maps and nontumoral changes in regional liver function derived from dynamic MRI before and after selective internal radiation therapy. . . . . ***Page 1224***

VIOLET trial protocol: Buteau and colleagues report on a planned phase I/II trial to determine whether [^{161}Tb]Tb-PSMA-I&T can deliver effective radiation to sites of metastatic prostate cancer with an acceptable safety profile. . . . . ***Page 1231***

[^{18}F-Flotufolastat PET/CT reader agreement: Kuo and colleagues document inter- and intrareader reproducibility of ^{18}F-flotufolastat PET/CT scans from 2 phase 3 studies in patients with newly diagnosed and recurrent prostate cancer. . . . ***Page 1239***

Biomarker for ^{177}Lu-DOTATATE–induced leukopenia: Steinhelfer and colleagues identify spleen volume reduction as a reliable and independent predictor of long-term leukopenia risk after peptide receptor radionuclide therapy. . . . . ***Page 1244***

Radiopharmaceuticals targeting NTSR-1: Fonseca Cabrera and colleagues use multiamine macrocyclic moieties as linkers or chelators in theranostic tracers targeting the neurotensin receptor-1, with a goal of achieving elevated tumor uptake, minimal background interference, and prolonged tumor retention. . . . . ***Page 1250***

FAP-targeted radiopharmaceutical therapy: Mukkamala and colleagues detail the design, development, and preclinical evaluation of a new FAP-targeted radioligand incorporating optimal features of 3 previous therapies and offering high tumor–to–healthy-tissue ratios. . . . . . . ***Page 1257***

Metaanalysis of [^{177}Lu]Lu-PSMA dosimetry: Ells and colleagues conduct a systematic review and metaanalysis comparing dosimetry methods for the most frequently used [^{177}Lu]Lu-PSMA radiopharmaceutical therapy compounds. . . . . . . ***Page 1264***

STP [^{177}Lu]Lu-PSMA dosimetry: Resch and colleagues compare different single-time-point approaches in radionuclide therapy dosimetry using multiple-time-point protocols as references and call for greater standardization to facilitate reliable STP dosimetry. . . . . ***Page 1272***

Myocardial somatostatin PET uptake: Larive and colleagues research factors associated with detection of myocardial uptake on somatostatin PET scans recorded for oncology indications and differential PET criteria that characterize myocardial uptake in acute myocarditis patients. . . . . ***Page 1279***

[^{18}F]MFBG LAFOV PET/CT in neuroblastoma: Borgwardt and colleagues detail experience with a long-axial-field-of-view PET/CT system and this new tracer in children with neuroblastoma, noting shorter scan times, higher sensitivity, and avoidance of general anesthesia or sedation. . . . . ***Page 1286***

Noninvasive imaging of olfaction: Adilbay and colleagues describe preclinical and human tissue studies on the use of Tsp1a-IR800$_P$, a novel fluorescent probe, as a tool to diagnose loss of smell by selectively targeting Na$_V$1.7 expression in olfactory epithelium. . . . . ***Page 1293***

Bimodal guidance in hepatobiliary surgery: Rietbergen and colleagues summarize development and preclinical studies with ^{99m}Tc-*h*HEPATO-Cy5, a bimodal tracer that facilitates both fluorescence guidance and radioguidance in surgical resection of deep hepatic lesions. . . . . ***Page 1301***

"Explainable" radiomics: Captier and colleagues introduce a model- and modality-agnostic tool that explains predictions of multiregion radiomic models by highlighting the contribution of each individual region. . . . . ***Page 1307***

HMC algorithm for uMI Panorama: Kang and colleagues validate Neurofocus, a head motion–correction algorithm for the uMI Panorama PET/CT system, using a data-driven, statistics-based approach. . . . . ***Page 1313***

NeuroEXPLORER performance: Li and colleagues provide the physical characteristics, performance evaluation, and first human images with the NeuroEXPLORER, a dedicated brain PET imager with high spatial resolution, high sensitivity, and a 3D camera for markerless continuous motion tracking. . . . . ***Page 1320***

Off-target effects of enzalutamide: Bauckneht and colleagues compare brain metabolism in patients with metastatic castration-resistant prostate cancer with and without enzalutamide treatment. . . . . ***Page 1327***

False-positive FAPI PET after therapy: Ludwig and colleagues offer an illustrative case study in a patient with lingering [^{68}Ga]Ga-FAPI uptake in postchemotherapy fibronecrotic tissue and urge caution in interpretation of posttherapy residual lesions.. . . . . ***Page 1328***

Illuminating Cardiac Function

Heinz Schelbert Talks with Heiko Schöder and Johannes Czernin About a Pioneering Career in Nuclear Cardiology

Heinrich Schelbert[1], Heiko Schöder[2], and Johannes Czernin[1]

[1]David Geffen School of Medicine at UCLA, Los Angeles, California; and [2]Memorial Sloan Kettering Cancer Center, New York, New York

Heiko Schöder, MD, MBA, chief of the Molecular Imaging and Therapy Service in the Department of Radiology at Memorial Sloan Kettering Cancer Center and professor of radiology at Weill Cornell Medical College (both in New York, NY), and Johannes Czernin, MD, editor-in-chief of *The Journal of Nuclear Medicine* (*JNM*) and a professor at the David Geffen School of Medicine at the University of California Los Angeles (UCLA), spoke with Heinrich (Heinz) Schelbert, MD, PhD, about his groundbreaking career in nuclear cardiology. Dr. Schelbert is a Distinguished Professor Emeritus of Pharmacology and Radiologic Sciences and former chief of the Nuclear Medicine Service at UCLA.

Dr. Schelbert received his medical degree and doctorate from the University of Würzburg School of Medicine and completed his residency at Fitzgerald Mercy Catholic Medical Center of Southeastern Pennsylvania in Philadelphia. In 1976 he joined the active and innovative early PET program at UCLA, with a personal focus on cardiac applications of the new technology. Among his many major research achievements has been the development and validation of noninvasive radionuclide imaging techniques for investigating cardiovascular function and their application to the study of functional and metabolic consequences of coronary artery disease. He is credited with identifying specific patterns of blood flow and metabolism in chronically dysfunctional myocardium that are predictive of potential reversibility and with development and validation of PET-based techniques for measuring regional myocardial blood flow in absolute units using ^{13}N-ammonia.

From 2004 to 2011, Dr. Schelbert served as editor-in-chief of *JNM*, successfully modernizing the journal while continuing long traditions of broad inclusiveness and high editorial standards. During his editorship, the journal's manuscript submission and review transitioned from a paper-based to an electronic process. He oversaw the redesign of the journal and introduced online prepublication of manuscripts and the availability of complete past issues in an improved online database, with consistently high annual impact factors.

Throughout his career, Dr. Schelbert has been recognized with numerous scientific, educational, and service awards and honors, including the Georg Charles de Hevesy Nuclear Pioneer Award for distinguished contributions to nuclear medicine by SNMMI and the Georg von Hevesy Prize (twice) from the World Federation of Nuclear Medicine and Biology. In 2012, he received the Distinguished Lifetime Achievement Award from the American College of Cardiology, which called him "a giant in the field of cardiology," adding that "with a plethora of seminal achievements as a pioneer in the development and application of PET and other nuclear cardiovascular technologies, he is a rare researcher who can truly claim the honor of witnessing the direct application of his experimental research to clinical care and improved patient outcomes during his lifetime."

Heinrich R. Schelbert, MD, PhD (Courtesy of Mei Tian, Hangzhou, China)

Dr. Czernin: *Dr. Schöder and I were both students of cardiovascular imaging in your group in the 1990s and late 1980s, respectively. You have been a leader in cardiovascular imaging for a long time. Your initial training was in Germany, but your career took off in the United States. What prompted your move here?*

Dr. Schelbert: After finishing medical school and a 1-year internship in Germany, I wanted to see how medicine was practiced in other countries. I ended up in the United States in a community hospital outside of Philadelphia through an internship program for foreign medical school graduates. After that I trained in internal medicine, which was very intense but also very good. A German cardiologist in Philadelphia, Otto F. Müller, MD, made cardiology exciting and attracted me to the field. I soon began to read electrocardiograms and was fascinated by the amount of information that could be derived from ECGs. I also became involved in echocardiography, which began to enter clinical cardiology at that time.

Before returning home, I wanted to learn something in cardiology that would be unique in Germany. The leading cardiology group in the United States was headed by Eugene Braunwald and John Ross, Jr., at the NIH. I applied, was accepted, and after the group had—unexpectedly for me—moved to San Diego, I started there in the fall of 1968. My research tasks were to find ways to improve contractile function in infarcted myocardium and, in another project, to explore the possibility of myocardial perfusion imaging with radiolabeled microspheres administered into the coronary circulation.

While I was in San Diego in 1975, UCLA had established a new PET research program and had recruited David E. Kuhl, MD, who had developed the first SPECT device at the University of Pennsylvania, and Michael Phelps, PhD, who had built the first PET device in St. Louis, MO, together with Edward Hoffman, PhD, and Henry Huang, DSc. At that time, PET was applied mostly in neurology but very little in cardiology. The UCLA group invited me to come to explore the use of PET for cardiac applications.

Dr. Czernin: *Can you talk about the environment, atmosphere, and spirit of this group at the time? Was this team both running the nuclear medicine clinic and doing research?*

Dr. Schelbert: I was of course very excited to join this unique group of young, aggressive, and highly resourceful investigators at UCLA. There was a tremendous level of comradery and excitement to explore what seemed like an unlimited potential of this new

---

DOI: 10.2967/jnumed.124.268302

technology for studying human biology. The research group did not run the nuclear medicine clinic; we had clinical appointment in nuclear medicine. The amount of time spent in research or clinical service depended on the amount of research support we had generated.

Dr. Schöder: *How did you settle on* ^{13}*N-ammonia as a blood flow tracer? Was that simply because it was available, or had you already realized that this might be the best perfusion tracer to answer your questions?*

Dr. Schelbert: Yes, because it was available. ^{13}N-ammonia was used for brain imaging at that time. I thought, let's try it for the heart. I explored this in canine experiments and found that it produced high-quality flow images. We then worked out the tissue kinetics of ^{13}N-ammonia, with the goal of quantifying myocardial blood flow.

Dr. Schöder: *When and how did you translate the technique to humans?*

Dr. Schelbert: The ^{13}N-ammonia images we obtained in dogs were of superb diagnostic quality. We then explored effects of coronary stenoses on myocardial perfusion images in chronically instrumented dogs, which Lance Gould brought from the University of Wahington in Seattle to UCLA. Once we had received IRB approval, we validated the technique against coronary angiography in humans and confirmed its high sensitivity and specificity.

Dr. Schöder: *You also extensively studied cardiac metabolism. What was the hypothesis there?*

Dr. Schelbert: At that time, Lionel Opie had demonstrated that mild reductions in coronary flow produced an increase in glucose utilization in the affected myocardium. We wondered whether this observation could be demonstrated noninvasively with ^{18}F-FDG and ^{13}N-ammonia. And indeed, we saw an increase in ^{18}F-FDG uptake in the region of diminished myocardial blood flow downstream of an experimental coronary stenosis.

We asked whether a similar flow–metabolism pattern existed in humans and could be shown with PET. We studied a patient with chest pain at rest as a sign of acute ischemia. In fact, we found a perfusion defect downstream of a left anterior descending artery stenosis that was associated with an intense increase in ^{18}F-FDG activity; in other words, we saw a blood flow–metabolism mismatch that we had already seen in dogs with experimentally induced acute ischemia. I said, "If that's acute ischemia, then let's study a patient without clinical signs of ischemia. We should not see a mismatch pattern!" We expected to now find a matching flow–metabolism defect, but what we saw was another mismatch.

Dr. Czernin: *When you initially came out with these data and the associated publications, there was a lot of skepticism from the cardiac SPECT community.*

Dr. Schelbert: People didn't know what to do with quantitative myocardial blood flows. Also, PET was perceived as a direct competitor of SPECT perfusion imaging. The viability issue was different; it had direct clinical implications and thus was accepted.

Dr. Schöder: *You created a large and leading cardiovascular research program. How did you recruit postdoctoral fellows from all over the world?*

Dr. Schelbert: Word got around that PET was useful not only in brain imaging but also in cardiology. That, of course, attracted many young people. I received applications from Europe (Germany, Austria, Italy, The Netherlands. Denmark, Sweden, and others) and from Asia. Our postdoctoral fellows were all highly qualified and truly interested in and committed to research. More than 50 postdoctoral fellows attended our research program.

Dr. Czernin: *There is now a resurgence of clinical PET with the expected commercial availability of* ^{18}*F-flurpiridaz. How do you see the future of PET myocardial perfusion imaging?*

Dr. Schelbert: You asked an interesting and important question, because the number of stress/rest perfusion imaging studies over the past 10 years has and continues to decline. This may be for several reasons; one is the use of appropriateness criteria. Another is referral of high-risk patients directly to invasive coronary angiography. Also, reimbursement for nuclear perfusion imaging studies has declined.

Most importantly, the clinical presentation of coronary artery disease has been changing from obstructive disease with acute events to a more diffuse nonobstructive disease associated with fewer acute events but a rise in heart failure hospitalizations. Quantitative myocardial blood flows will remain important in these changing scenarios of nonobstructive disease because the myocardial flow reserve as the ratio of hyperemic to baseline flows provides important diagnostic and prognostic information and will continue to be important for risk stratification, especially in patients without perfusion defects.

Dr. Schöder: *What do you think was the influence of the rubidium generator, which obviated the need for a cyclotron for cardiac PET imaging—an advantage or disadvantage overall?*

Dr. Schelbert: Unlike the cyclotron, the generator system is available all the time, and you can use it as many times as you want. The diagnostic quality of rubidium perfusion images is not as good as that of ^{13}N-ammonia, but they are diagnostically adequate. The ready availability of the rubidium generator has been a major driver of the clinical use of PET perfusion imaging.

"When I looked at what was happening in the field—the exciting imaging technologies and radiotracers, such as those targeting prostate-specific membrane antigen—it became clear to me that the future was and is bright for nuclear medicine."

Dr. Schöder: *What is the future of molecular imaging as it relates to cardiac imaging and also to the general development of new probes?*

Dr. Schelbert: I think quantitative flow measurements will stay with us because they're important. Other conditions that are likely to benefit from new and emerging molecular probes include myocardial inflammation and nonischemic cardiomyopathies. This will be especially important in patients with heart failure with preserved ejection fraction and in patients with inflammatory disorders of the myocardium.

Dr. Schöder: *Let's talk about* JNM *for a moment. You had a highly successful run as editor-in-chief. What prompted you to apply for the editorship?*

Dr. Schelbert: I saw an opportunity to become editor. So, I applied; I thought this was an interesting challenge, which I wanted to take on!

Dr. Schöder: *You had a vision, and obviously you changed the journal and improved the quality. How did that happen?*

Dr. Schelbert: In applying for the editorship, I presented a plan for what needed to be changed or innovated. At that time, the number of manuscript submissions to *JNM* had markedly declined. The whole review system was a mess, and I proposed what I would change and improve. I also addressed content and introduced several new series or types of publications that I thought would be of interest to the *JNM* readership and that I believe became quite successful.

Dr. Schöder: *We are in the era of artificial intelligence (AI) and very different means of communication. What do you think is the future of a traditional journal such as* JNM*?*

Dr. Schelbert: I have no doubt that traditional journals such as *JNM* will continue to exist. Yet, there will be more brief communications and letters to the editors for quickly communicating research findings. Paper publication will disappear; everything will be online. I do believe that social media will play a greater role although I am concerned about the superficiality of reports and communications. And I do think that AI will have a role, not so much in the scientific content or its assessment but rather for quality control as well plagiarism and data fabrication. Although more science will be disseminated through social media (we see that at *JNM*), I think the basic time-tested more rigorous format of research papers, with introduction, rationale, methods, results, and discussion, will stay with us, at least for the most important manuscripts.

Dr. Czernin: *If the data are correct and the author wants to use an AI tool, for example, to write the paper so that it's stylistically sound and better, would you object to that?*

Dr. Schelbert: If it is limited to style and grammar, it is OK.

Dr. Czernin: *Many groups have graphic designers who provide figures, and the figures are usually of much higher quality than those the authors themselves could create. Isn't that comparable to having a* manuscript *written by AI?*

Dr. Schelbert: I don't know the answer to that. I agree that AI could create figures that are much better in quality; if we allow those we're sort of on the border. I can't quite tell where the border is between creating figures and writing text. It's a difficult area.

Dr. Schöder: *What will be the role for investigator-initiated versus industry-driven research, where we are basically executing whatever a company is pushing for? Can investigator-driven research survive in this era of company pressure?*

Dr. Schelbert: Investigator-driven research will persist. The NIH and other funding agencies reward new ideas and the development of new concepts. I always wonder about the big trials that are company-sponsored, but those large trials are important. When you look at cardiology—at coronary artery or inflammatory disease, for example—you can answer effectiveness questions on new drugs only through large trials. So, they are necessary.

Dr. Czernin: *You did translational and translatable research long before these terms existed. What do you see as your most successfully translated and impactful research?*

Dr. Schelbert: I think it is the assessment for myocardial viability. The concept of chronically increased myocardial glucose utilization was a new one. No one really knew at that time whether chronic ischemia existed (and it still isn't ischemia). "I would not touch chronic ischemia with a 10-foot pole," a colleague said when I asked him about chronic ischemia. Today it seems more like an adaptive change in myocardial substrate metabolism, perhaps "a recapitulation of the fetal metabolic program," as it has been referred to, in the adult heart.

Dr. Czernin: *We still do quite a few viability studies, so this has staying power. Obviously, there's a clinical need.*

Dr. Schelbert: No matter what some clinical trials have concluded, I believe viability assessments will persist. This is what I hear from colleagues in nuclear medicine and nuclear cardiology and what I see happening at UCLA at present. Our own initial experience with viability imaging was derived from patients with end-stage coronary artery disease considered for surgical revascularization vis-à-vis cardiac transplantation. It is, I believe, in this very challenging clinical situation that viability testing was used at the time we started out and still does contribute to the clinical decision-making process.

Dr. Schöder: *Tell us a little about your interests outside of medicine. How did you balance these interests with your highly successful career? What did your work/life balance look like?*

Dr. Schelbert: Often when you're very busy you do not have time for those things you really like to do. My hobbies are classical music and, of course, reading, mostly history. At times we're all extremely busy writing grant applications or pursuing new ideas. But after some time, I always go back to spending more time with music or reading. I do believe you need to set aside time to do what you really like and to "rebalance" yourself.

Dr. Czernin: *At the time when people (including me) had doomsday predictions for nuclear medicine, you kept telling me that we should not promote such defeatist attitudes and that the specialty would survive and actually grow. You were right. What made you so optimistic for the future of nuclear medicine?*

Dr. Schelbert: When I looked at what was happening in the field—the exciting imaging technologies and radiotracers, such as those targeting prostate-specific membrane antigen—it became clear to me that the future was and is bright for nuclear medicine. Just seeing these many opportunities made me very optimistic. I remember the time when CT arrived, prompting many to believe that nuclear brain imaging was out (that was with CT and MRI), and yet today we do even more brain imaging than before.

Dr. Schöder: *My wife asked me to ask whether you would you do it all over again? Or what would you do differently?*

Dr. Schelbert: Yes, I would do it all over again. The question, however, is, *could* I do it again? Could I repeat it? Probably not, because life brings a series of opportunities, and those opportunities are not the same and change with time. Another thing is whether one grabs those opportunities when they appear. I was very lucky. Looking back, I would say: yes, I would repeat it, but I'm not sure that it is repeatable.

Dr. Czernin: *What kind of advice do you have for the younger generation, the colleagues who enter the field of nuclear medicine or medicine?*

Dr. Schelbert: I think the most important element is attracting young people to our field and stimulating our younger colleagues. This requires presenting the field as exciting and with a future that motivates them to research, emphasizing that it's important to find new things. So, I would go that way. Based on my own experience, that's what I would do.

Dr. Czernin: *As a follow-up to an initial question, who was your most important mentor?*

Dr. Schelbert: My initial mentor was Otto F. Müller, the German cardiologist in Philadelphia, whom I mentioned earlier. He made cardiology exciting and brought me into it. Other mentors who affected my professional life were Eugene Braunwald, who introduced me to the research side, and Franz Loogen, the chief of cardiology when I trained in clinical cardiology in Düsseldorf, Germany, who taught me the human side of medicine. There is also Sherman Mellinkoff, the dean of the UCLA Medical School when I joined UCLA, whom I deeply admired for his intellect, honesty, curiosity, kindness, and integrity.

Dr. Czernin: *Thank you very much, Heinz, for all your accomplishments and contributions and for the time spent with us and our readers.*

An International Study of Factors Affecting Variability of Dosimetry Calculations, Part 3: Contribution from Calculating Absorbed Dose from Time-Integrated Activity

Julia Brosch-Lenz[1], Sara Kurkowska[2,3], Eric Frey[4,5], Yuni K. Dewaraja[6], John Sunderland*[7], and Carlos Uribe*[3,8,9]

[1]Department of Nuclear Medicine, Rechts der Isar Medical Center, Technical University of Munich, Munich, Germany; [2]Department of Nuclear Medicine, Pomeranian Medical University, Szczecin, Poland; [3]Department of Integrative Oncology, BC Cancer Research Institute, Vancouver, British Columbia, Canada; [4]Rapid, LLC, Baltimore, Maryland; [5]Department of Radiology, Johns Hopkins University, Baltimore, Maryland; [6]Department of Radiology, University of Michigan, Ann Arbor, Michigan; [7]Department of Radiology, University of Iowa, Iowa City, Iowa; [8]Molecular Imaging and Therapy, BC Cancer, Vancouver, British Columbia, Canada; and [9]Department of Radiology, University of British Columbia, Vancouver, British Columbia, Canada

Image-based dosimetry-guided radiopharmaceutical therapy has the potential to personalize treatment by limiting toxicity to organs at risk and maximizing the therapeutic effect. The ^{177}Lu dosimetry challenge of the Society of Nuclear Medicine and Molecular Imaging consisted of 5 tasks assessing the variability in the dosimetry workflow. The fifth task investigated the variability associated with the last step, dose conversion, of the dosimetry workflow on which this study is based. **Methods:** Reference variability was assessed by 2 medical physicists using different software, methods, and all possible combinations of input segmentation formats and time points as provided in the challenge. General descriptive statistics for absorbed dose values from the global submissions from participants were calculated, and variability was measured using the quartile coefficient of dispersion. **Results:** For the liver, which included lesions with high uptake, variabilities of up to 36% were found. The baseline analysis showed a variability of 29% in absorbed dose results for the liver from datasets where lesions included and excluded were grouped, indicating that variation in how lesions in normal liver were treated was a significant source of variability. For other organs and lesions, variability was within 7%, independently of software used except for the local deposition method. **Conclusion:** The choice of dosimetry method or software had a small contribution to the overall variability of dose estimates.

Key Words: radiopharmaceutical therapy; dosimetry; variability; standardization; dosimetry challenge

J Nucl Med 2024; 65:1166–1172
DOI: 10.2967/jnumed.123.267293

The field of radiopharmaceutical therapy is rapidly evolving, and the possible roles for dosimetry in pre- and posttherapeutic treatment planning and verification are being recognized (*1,2*). Patient-specific image-based dosimetry-guided radiopharmaceutical therapies have the potential to limit damage to organs at risk and maximize the therapeutic effect. The ^{177}Lu dosimetry challenge of the Society of Nuclear Medicine and Molecular Imaging (SNMMI) is designed to quantitatively isolate and assess the variability contributed by each of the major steps in the determination of absorbed dose (AD) by asking participants to perform 5 tasks: region-of-interest segmentation, decay correction, curve fitting, time integration, and conversion of time-integrated activities (TIAs) to ADs. In the fifth task, both organ and lesion segmentations, as well as 3-dimensional (3D) TIA images, were provided for 2 ^{177}Lu-DOTATATE SPECT/CT datasets. By separating out the variability associated with segmentation, decay correction, curve fitting, and integration methods, one can determine the remaining variability that was contributed by the actual AD calculation method.

Different dosimetry methods with varying complexity and accuracy exist (*3–5*). MIRD pamphlets 11 and 17 (*3,4*) provide general guidelines for calculating ADs at the organ or voxel level, and the European Association of Nuclear Medicine recently published a guideline for dosimetry for ^{177}Lu (*6*). However, accurately characterizing dose–effect relationships for both organs and tumors is critical before effective clinical implementation of personalized dose prescriptions is possible. Generation of accepted dose–effect relationships will, in turn, be entirely dependent on the accuracy and comparability of AD estimates. Different steps within the dosimetry workflow will impact the final AD estimate to varying extents.

The aim of this part of the study was to understand the variability in ADs associated with the last step of the dosimetry workflow and to make recommendations related to the application of S values both at the voxel level and at the organ level.

MATERIALS AND METHODS

Challenge Design

The challenge design and data curation are described in our first 2 installments of this series (*7,8*). In brief, anonymized data from 2 patients undergoing ^{177}Lu-DOTATATE therapy were made available publicly to participants through the Deep Blue Data repository of the University of Michigan (*9*). Sharing of patient images and data was approved by the University of Michigan Institutional Review Board, and both patients gave written informed consent. Each patient was imaged 4 times after administration over 1 wk. In task 5, participants

---

Received Dec. 17, 2023; revision accepted May 21, 2024.

For correspondence or reprints, contact Carlos Uribe (curibe@bccrc.ca).

*Contributed equally to this work.

were given access to the image data; volume-of-interest (VOI) files for kidney, liver, spleen, and lesions; and a 3D image of the TIA. Applying the VOIs to the TIA image gives organ TIAs without the variability associated with segmentation, curve fitting, and integration. Participants were asked to estimate the AD to both organs and tumors from the organ and tumor TIAs, respectively. Participants submitted their results on preformatted spreadsheets that requested details regarding their methods and intermediate results for the various steps across the different tasks. All submitted data spreadsheets for task 5 were concatenated into a single data frame collected using the Python data analysis library (Pandas, version 1.3.5) with columns corresponding to the specific variables.

Analysis of Submissions

Submissions were grouped and categorized on the basis of user-reported values and a written description of their methodology, when provided. The categories analyzed included dosimetry method, software used, and voxel S value source. Commercial software (CS) names were pseudonymized. Further data curation was performed following the findings of our previous publication (*8*).

Assessment of Variability: Baseline Data

The variability analysis was performed stepwise to establish a baseline variability in a controlled environment, to investigate the impact of the use of Radiotherapy Structure Sets (RTstructs) versus masks for the VOIs (the 2 formats used to provide segmentation to participants) and then to assess the variability in ADs from the participants.

Two medical physicists (MPs) independently performed dosimetry using the data provided in task 5 using several dosimetry software and methods that were available to both. Organ-level dosimetry using organ S values (OSVs) was tested with OLINDA (version 2.2.3) (*11*), IDAC-Dose (version 2.1) (*11*), and MIRDcalc (*12*). Tumors were treated as isolated spheres with unit density (OLINDA) or choice of density (IDAC-Dose and MIRDcalc). For the kidneys, the TIA was input to the software for the left, right, and total kidneys separately with their corresponding masses for the mass correction of the S values. S values are derived using human anthropomorphic phantoms and can be adjusted by multiplying by the phantom organ mass and dividing by the actual organ mass of an individual patient. 3D dosimetry using voxel S values (VSVs) was tested using ^{177}Lu kernels for soft tissue that were simulated using 10^8 primaries in GATE (version 9.2, based on GEANT4 11.0) followed by CT-based density weighting per voxel (*13*). Density weighting is an attempt to correct for tissue heterogeneities and uses a voxelwise density image derived from the patient's CT image that is multiplied by the 3D VSV dose image. Lastly, individual patient Monte Carlo (MC) simulations using GATE were performed (*14,15*). ADs were compared per organ and per lesion between the different investigated dosimetry approaches by each of the 2 MPs and between the submitted data of task 5.

The segmentation of organs for the SNMMI ^{177}Lu dosimetry challenge was performed for each imaging time point separately, and small differences could be found across the 4 SPECT/CT studies. The challenge inadvertently introduced variability through the provision of VOIs in both RTstruct and binary-mask formats (*8*), leading to slightly different VOIs because the 2 formats are interpreted differently by various software. Specifically, RTstruct files contain coordinates of the vertices of polygonal VOIs and thus allow definition at the subvoxel level in a way that depends on the implementation and settings of the software used to apply VOIs to the images. On the other hand, binary masks are digitized representations that unambiguously define the voxels included in the VOI. Both were provided since not all software supports both methods. To investigate the contribution of the different VOI formats to the variability of the calculated AD, one MP applied all possible combinations of RTstructs and masks at all time points to the provided TIA image of patient A and calculated the resulting ADs using IDAC-Dose (version 2.1) to understand and report the impact of VOI formats on observed AD variabilities.

Assessment of Variability: Participant Data

For the data from participants, general descriptive statistics (mean, SD, quartiles) of AD were calculated for liver, spleen, kidneys, 2 prespecified soft-tissue tumors in patient A, and 4 prespecified tumors in patient B. The quartile coefficient of dispersion (QCD) was calculated as the ratio of the difference and sum of the 75th and 25th quartiles. The QCD was used to assess the variability of AD results between methods and software (*8*). The QCD was chosen in this analysis since it is less sensitive to data outlies than is the coefficient of variation. The QCD multiplied by 1.4826 is equal to the coefficient of variation for a normal distribution. A statistical analysis compared the median of the 2 distributions of ADs from voxel- and organ-level dosimetry, and separately between commercial and non-CS, using the Mann–Whitney *U* test.

RESULTS

Assessment of Variability: Baseline Data

The first part of our analysis addressed the question of how different dosimetry methods affect variability when the same person or similarly trained persons (2 MPs) perform dosimetry on the same input data. Figure 1 shows the results for the ADs calculated using different OSVs, voxelized S value kernels, and full MC simulation when the procedure was performed by the 2 MPs. Only small variations were found between the 2 MPS and among the 5 investigated dosimetry approaches and software. The percentage difference in ADs reported by the 2 MPs were between −1% and +2% for the organs and between −2% and +1% for the lesions (Figs. 1C and 1D). These variations are attributed to the way each MP rounded values.

The impact on variability from using either the provided VOIs as RTstructs or masks on the TIA image of task 5 was assessed for patient A by one MP. Furthermore, the impact on the AD estimates was investigated when no mass scaling was used. Since the liver of patient A contained lesions, we investigated the effect in the ADs when lesions were included or excluded as part of the liver when performing the calculation.

We noted that there were 18 combinations of how ADs could be calculated with the provided data. Use of the 2 VOI formats (i.e., mask and RTstruct) for each of the 4 time points, with and without mass scaling, provided the first 16 cases. The last two used

NOTEWORTHY

- What is the contribution of the dose conversion step to the total variability in AD estimates in radiopharmaceutical therapy when different methods and software are used at different centers?
- The contribution of the dose conversion step to the total variability in AD was found to be smaller than 7% for organs and lesions. Only healthy normal-organ tissue should be counted in the volume for dose calculation when lesions are present within an organ.
- The analysis of task 5 of the SNMMI ^{177}Lu dosimetry challenge data has demonstrated that neither dosimetry method nor software had a larger impact on variability than other factors. The information on sources of variability is important for reducing variability in dose estimates and thus improving the utility of routine dosimetry and dosimetry-based personalization of radiopharmaceutical therapies.

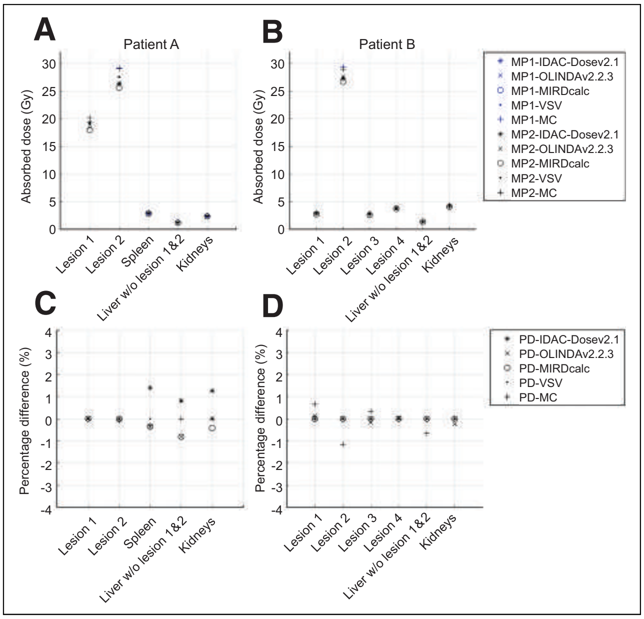

FIGURE 1. (A and B) Dosimetry results for patients A (A) and B (B), when performed by 2 MPs using same dosimetry methods. (C and D) Percentage difference in ADs between 2 MPs for patients A (C) and B (D). PD = percentage difference.

the organ mass averaged through the 4 time points for each of the 2 VOI formats. Supplemental Figure 1 shows the differences in VOI volume over the scan time point and VOI format (supplemental materials are available at http://jnm.snmjournals.org). The AD results per organ for all 18 combinations are given in Supplemental Figure 2. The largest ranges in ADs were found for the liver, when all results of scenarios that removed lesions from the healthy liver tissue AD calculation and those that included them were combined. The range of ADs for all organs, including the different scenarios for how the liver was handled, are shown in Figure 2. Differences of 0.9–1.5 Gy were observed for the liver for all scenarios combined, as well as for spleen and total kidney.

Figure 3 provides the QCDs for all 18 results of Figure 2, when performed by one MP. The largest QCD, 29%, was found when all liver results were combined—independently of whether the liver lesions were removed. For all other organs, the QCDs ranged between 5% and 7%, indicating that VOI format (i.e., mask vs. RTstruct), selection of the time point to use for VOI definition, and application or omission of mass scaling of S values result in AD differences of up to 7%.

Assessment of Variability: Participant Data

After the data curation, there were a total of 25 submissions per patient from 23 institutions. Table 1 provides an overview of the different dosimetry methods and software used by the participants as indicated in their submissions. There were 15 non-CS and 10 CS solutions. Overall, 13 submissions used organ-level approaches (10 OSV methods plus 3 organ-level local deposition methods), whereas 12 submissions performed voxel-level dosimetry (9 VSV methods, plus 2 MC methods and 1 voxel-level local deposition method).

The box plots in Figures 4 and 5 represent the ADs reported for the different dosimetry methods and software, respectively, for each of the VOIs provided to participants. Overall, the local deposition method showed the largest variability in ADs (Fig. 4), as

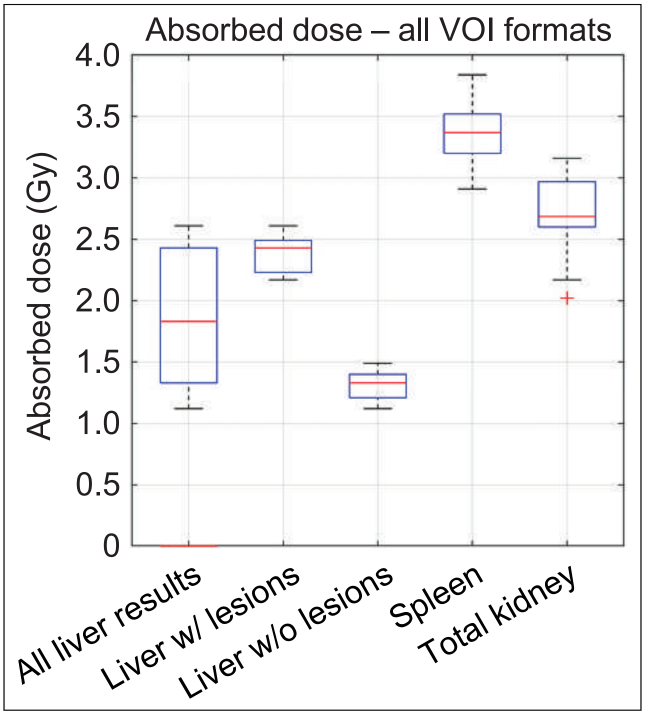

FIGURE 2. Range of ADs per organ for all possible combinations of VOI formats and scan time point used for patient A. "All Liver Results" illustrates range of liver AD results when results from both scenarios—with and without lesions included inside liver—were combined.

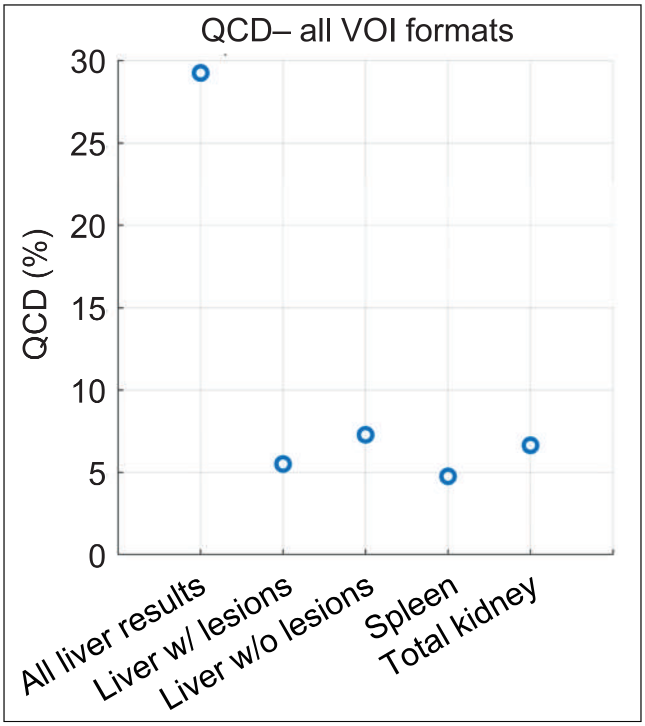

FIGURE 3. QCD for all possible 18 combinations of VOI formats and time points, with or without mass scaling, or using average mass for mass scaling, used to yield ADs in Figure 2. Furthermore, combination of all liver results—with and without lesions included—are given in "All Liver Results."

TABLE 1
Number of Submissions per Patient for Each Dosimetry Method and Software

Parameter	Submissions (*n*)
Dosimetry method	
OSV	10
VSV	9
Local deposition (organ and voxel level)	4
MC simulation	2
Dosimetry software	
Noncommercial	15
CS 1	4
CS 2	3
CS 3	2
CS 4	1

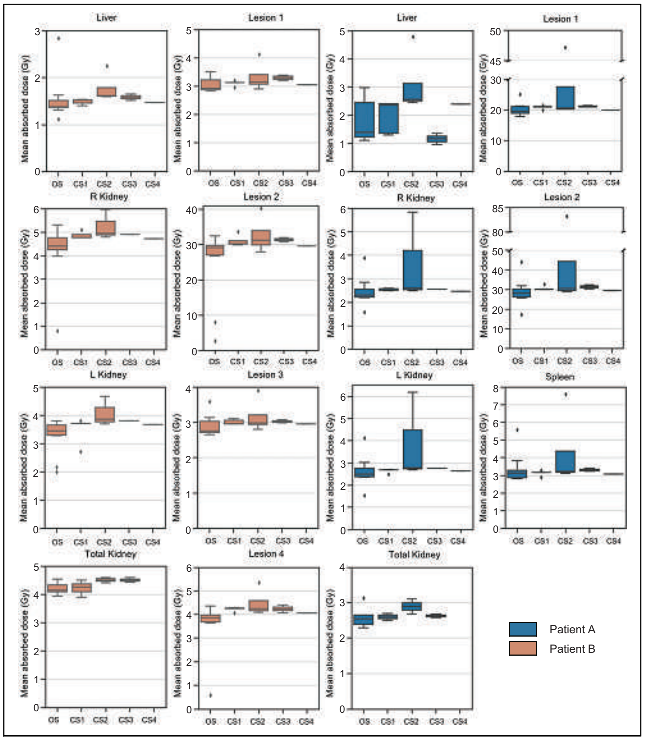

FIGURE 5. Mean AD per region using different available software solutions for all regions of patients A and B. OS = open-source/freely available and well-validated dosimetry non-CS, including in-house solutions.

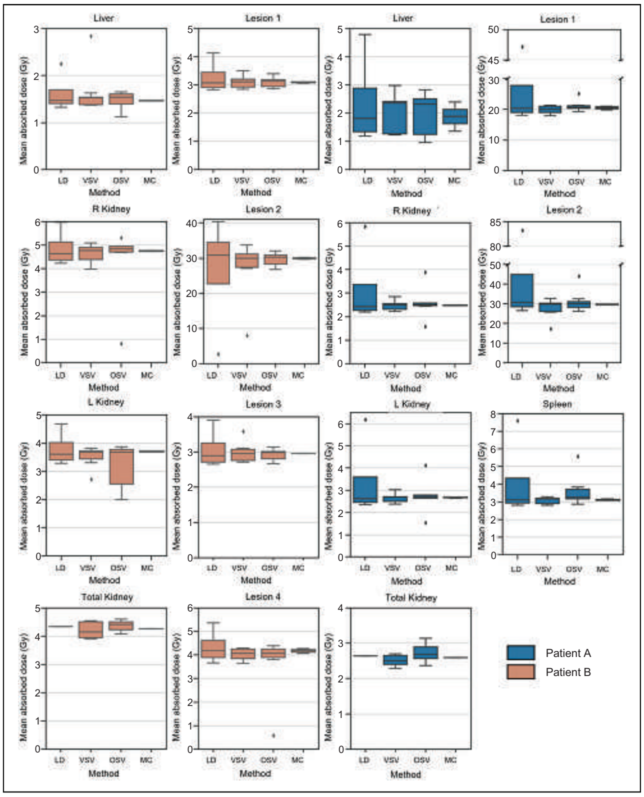

FIGURE 4. Mean AD per region for different methods that were used for calculation. Number of submissions that included each method is provided in Table 1. LD = local deposition; MC = MC dosimetry simulations; OSV = organ S value; VSV = voxel S value–based dosimetry.

illustrated by the biggest dispersion of the box plots. The MC method, with only 2 submissions, showed the smallest range in the box plot. The comparable larger range in ADs for healthy organs using the OSV method may be related to whether mass scaling of the OSV was applied. The different commercial dosimetry software yielded comparable ADs as illustrated by the comparable medians and dispersion of the ADs in the box plot in Figure 5, respectively, independently of the method, except for CS 2, which provides organ-level (using OSVs) and voxel-level (using local deposition method) dosimetry, leading to the larger range of ADs. The non-CS showed a higher variability as indicated by the second largest range of the box plot in Figure 5. This can be attributed to the use of multiple different dosimetry methods when in-house solutions are used. In the baseline analysis, we included well-known freely available and validated dosimetry software, including IDAC-Dose and MIRDcalc.

The results of the statistical analysis between voxel- and organ-level dosimetry are given in Table 2. For this test, all submissions performing 3D dosimetry (i.e., voxel level; $n = 12$) were grouped, and all organ-level submissions ($n = 13$) were grouped and compared against each other. Statistically significant differences ($P \leq 0.05$) were found for spleen (patient A) and right and left kidneys (both patients). No statistically significant differences were found for lesions, liver, and total kidney.

The results of the statistical analysis between CS and non-CS (in-house solutions, well validated software, and open-source software) are given in Table 3. For this test, all submissions using CS ($n = 10$) were grouped, and all open-source software submissions ($n = 15$) were grouped and compared against each other. Statistically significant differences ($P \leq 0.05$) were found for most lesions of both patients and the normal organs of patient B except for the total kidney. No statistically significant differences were found for the normal organs of patient A, total kidney, and lesions 1 and 3 of patient B.

Figures 6 and 7 show the QCD results between the dosimetry methods and software. The largest QCDs, up to 36%, were found for the liver for most dosimetry methods and software; the smallest QCDs, only 1% (except for liver, with 14%), were found for the MC dosimetry method, with only 2 submissions, followed by

TABLE 2

P Value Results of Mann–Whitney *U* Test Between Voxel- and Organ-Level Dosimetry

Patient	Liver	Spleen	R kidney	L kidney	Total kidney	Lesion 1	Lesion 2	Lesion 3	Lesion 4
A	0.29	<0.01*	0.04*	0.01*	0.30	0.07	0.08		
B	0.30		0.01*	0.05*	0.28	0.15	0.18	0.38	0.18

---

*Statistically significant difference ($P \leq 0.05$).

VSVs for healthy organs with QCDs of up to 7% (liver ≤ 31%) and the S value approach for lesions with QCDs below 5%. Among dosimetry software, CS 2 and the non-CS approaches showed the largest QCDs, 25% (liver, 11%) and 7% (liver, 34%), respectively, although different dosimetry methods were used.

DISCUSSION

This analysis focused on task 5 of the SNMMI ^{177}Lu dosimetry challenge based on 2 ^{177}Lu-DOTATATE patient datasets with the aim of acquiring a better understanding of the variability and the sources of this variability in the last step of the dosimetry workflow, conversion of TIAs to ADs. We evaluated the use of OSVs, VSVs, local deposition method, and MC simulations.

We assessed the baseline variability in AD when performed by 2 independent MPs using the same set of dosimetry methods and software. When the same corrections were applied such as mass scaling and density weighting, the differences in ADs between methods and software were low, ranging from −1% to +2% for healthy organs and from −2% to +1% for the lesions (Fig. 1). This demonstrates that consistent ADs between different experts can be obtained independently of software and method when mass scaling and similar VOIs (*6,13*) are used. Note that this analysis was limited to soft-tissue structures, for which the impact of tissue heterogeneity is likely to be small. We did not evaluate tissue such as lungs, bone, and (particularly) spongiosa regions relevant for bone marrow dosimetry.

A separate analysis investigated the effect on AD variability of different formats for provision of VOIs—that is, RTstruct and binary masks, selection of VOI time point, and use or nonuse of mass scaling on OSVs. The analysis was performed only for healthy organs of patient A. The lesions were not assessed, since the VOIs were defined by a radiologist on the CT of a single time point and then copied to subsequent time points, whereas for healthy organs, CT-based segmentation was performed at each scan time point.

Overall, the up to 7% variability as assessed by QCD for kidneys and spleen was due to the 2 VOI formats, the different VOIs per scan time point, and the fact that S value mass scaling was not used in all cases (Fig. 2). The largest dispersion in ADs was found for the liver, where different scenarios with and without inclusion of the liver lesions in the liver TIA were assessed (Fig. 2). For the liver, a QCD of 29% was found when all AD data were combined—that is, AD data derived from including and excluding lesions in the overall liver VOI. The findings for the liver from the baseline variability analysis were also observed in data from participants, where QCDs of up to 36% were found for most dosimetry methods and software, which can likely be attributed to averaging of lesion dose with healthy liver dose (Figs. 6 and 7). The provided VOIs in tasks 4 and 5 of the challenge did not automatically remove the lesion uptake from the liver. A region was given for the whole liver and for individual lesions, and the participants needed to decide whether and how to remove the lesions in the liver. These findings indicate a strong need for a standardization on treatment of lesion uptake in normal tissues, especially for small organs, where the effect is assumed to be larger.

There was some variability resulting from the fact that some participants used RTstruct VOIs whereas others used binary masks. The binary masks were generated from the RTstruct VOIs and had no ambiguity about the SPECT voxels to be included. However, the application of RTstructs, which are based on polygonal contours, to SPECT images to sum voxel values has some ambiguity in terms of which fraction of voxels at the edges of the VOI should be included. How this is done is an area that would seem to be a good target for standardization to remove this source of variability.

Furthermore, VOIs for the same organ can be different for the different imaging time points depending on how they are defined. It would be beneficial for the field if recommendations could be provided as to whether individual VOIs should be obtained for each separate time point or whether only one segmentation should be performed and transferred to other time points (assuming good registration).

Finally, we observed that some of the variability in ADs is caused by use or nonuse of mass scaling for OSVs. Mass scaling is essential in obtaining accurate dose values for OSVs by adapting standard-phantom S values to patient-specific organ masses and should always be performed. If VOIs are generated for each time point, we recommend using a mass of the organ that is the average of the different VOIs.

For the analysis of the submissions from participants, the local deposition method showed the largest dispersion in ADs

TABLE 3

P value Results of Mann–Whitney *U* Test Between CS and Non-CS

Patient	Liver	Spleen	R kidney	L kidney	Total kidney	Lesion 1	Lesion 2	Lesion 3	Lesion 4
A	0.14	0.18	0.08	0.12	0.20	0.03*	0.01*		
B	0.01*		0.03*	0.02*	0.19	0.07	0.05*	0.06	<0.01*

---

*Statistically significant difference ($P \leq 0.05$).

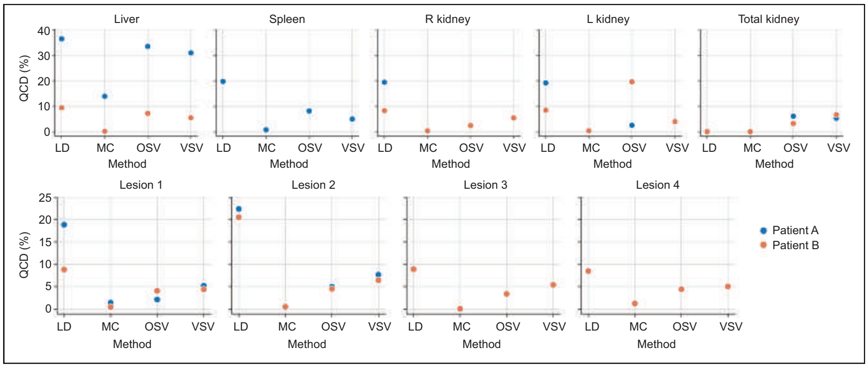

FIGURE 6. QCD per organ for different dosimetry methods. LD = local deposition; MC = MC dosimetry simulations.

(QCD ≤ 36%) (Fig. 6). It is likely that this finding is due to different values of the mean energies of the ^{177}Lu β-emissions used by participants (e.g., 134 vs. 147 keV (*6*) or not specified). This clearly requires standardization and should include the energy of the Auger electrons that are also emitted by ^{177}Lu. Smaller variability in ADs was found for the VSV method (Fig. 4). The remaining dispersion in values could potentially be attributed to the use of different sources of VSVs, the application of density weighting, or—to a lesser extent given that here we are dealing with soft tissue—whether different VSVs were used for different tissue types. Two submissions used MC simulations with different MC codes, and the results were comparable.

The common approach of OSVs showed comparable results to the VSV approach (Fig. 4). It is not surprising that the OSV approach yielded the second smallest variability for the lesions, since this approach treats lesions as isolated spheres (*10–12*) and spheric S values seem to be well standardized. However, differences between ADs of lesions obtained with OSVs and voxel-level approaches exist because the former accounts for cross dose as well as tumor heterogeneity.

The use of commercial dosimetry software yielded comparable results (Fig. 5), with QCDs smaller than 3% except for the liver (Fig. 7). However, QCDs of CS 2 were larger, up to 25%, suggesting that the end user choose between organ- and voxel-level dosimetry in this software package, limiting the interpretation of the results for this CS. Because of the lack of further details provided by the participants, we were unable to distinguish between organ- and voxel-level dosimetry using this software. The use of non-CS (in-house solutions or freely available) showed a larger range in ADs (Fig. 5). However, this group was quite diverse in terms of the codes, methods, and level of validation. Despite this approach, these methods still provided QCDs smaller than 7% (Fig. 6, except for liver), indicating that the choice of dosimetry method or software might not be the largest source of variability in the dosimetry workflow. Many of the freely available software are extensively validated against the literature (*11,12*).

Comparing voxel-level versus organ-level dosimetry approaches, we found statistically significant differences among the ADs for healthy organs, whereas the differences among lesion ADs were not statistically significant (Table 2). These findings are surprising, since one would expect differences in AD for lesions when 3D methods are chosen that are capable of accounting for cross dose, whereas organ-level approaches rely on isolated spheres as representation for lesions. In contrast, there were statistically significant differences for the spleen and kidneys, even though cross dose is included in the organ-level calculation. However, these results must be treated with caution because of the small number of submissions ($n = 25$) per patient and because not all submissions included results for left kidney, right kidney, and total kidney. For the comparison of CS and non-CS, statistically significant differences in ADs were found for most lesions of both patients and the normal organs of patient B except for the total kidney. No statistically significant differences were found for normal organs of patient A or for total kidney and lesions 1 and 3 of patient B. This indicates that the dosimetry software itself may not introduce statistically significant differences in AD for all patients and organs and lesions.

Generally, we can say that the overall variability as assessed by the QCD was below 7% for all dosimetry methods, software, and regions except for the liver in patient A (Figs. 6 and 7), CS 2, and the local deposition method. These findings are in concordance with previous work that addressed the differences in ADs using different methods and software (*16–19*).

The small number of submissions and the fact that only 2 patient cases were provided during the challenge are limitations of our study. Furthermore, the organs and lesions included in the challenge were limited to soft-tissue structures, where differences in dosimetry methods can have a smaller impact than in heterogeneous tissue. We are aware that not all possible relevant patient characteristics were covered by these 2 cases. The issue of providing VOIs in RTstruct and mask format across the multiple imaging time points is another source of variability that is specific to this challenge. This resulted in differences in ADs of up to ±20% for the different organs. We believe that this underlines the need for standardization of VOI formats and segmentation in general to avoid such differences in volumes and therefore masses.

This analysis has shown that participants made several choices within the dosimetry workflow that increased the variability of the AD results. We believe that standardization can reduce the variability of dose calculations. We therefore recommend adoption of the following best practices.

(1) For MIRD-style, organ-level dosimetry, mass scaling is essential to account for

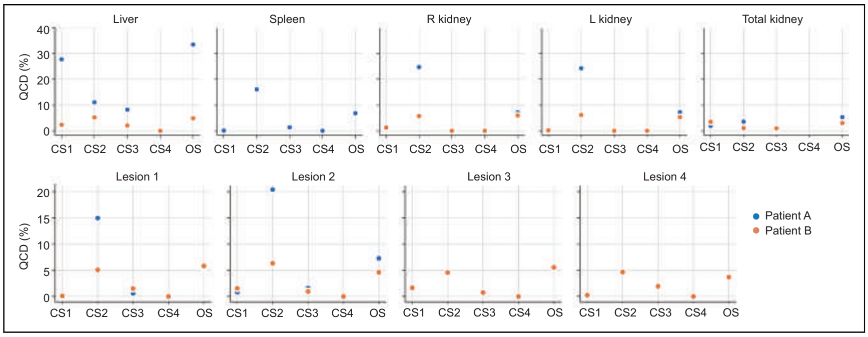

FIGURE 7. QCD per organ for different dosimetry software. OS = open-source/freely available dosimetry software, including in-house solutions and well-validated software.

differences between the patient's organ mass and the mass of the stylized phantoms from which S values are precalculated.

(2) For voxelized approaches other than MC dosimetry simulation, voxel density based on registered and resampled CT images should be used to take into account patient-specific tissue heterogeneities.

(3) We found variabilities in ADs of up to 36% for the liver depending on whether lesions were included or excluded from the VOIs. For ^{177}Lu, the AD from the liver excluding lesions is likely to be a better predictor of organ toxicity than if the lesions are included. We thus recommend standardization that excludes lesions present in the organ from VOIs used to estimate AD to healthy tissues using the OSV approach. 3D dosimetry methods can account for cross irradiation of lesions to healthy tissue, and VOIs for healthy tissue should consequently exclude the lesion VOI to extract mean ADs from 3D dose images.

(4) Local energy deposition methods showed high variability because different mean energies for the ^{177}Lu electron emissions were used. We recommend using a mean energy of 147.1 keV Bq^{-1} s^{-1} as specified in several guidelines (*6,20*).

(5) We observed significant variability when applying VOIs given as binary masks versus polygonal contours (as RTstruct). This could be related to differences in how polygonal masks defined at a higher resolution (e.g., using CT images) are applied to SPECT images with larger voxels and on how subvoxel contours are in general compared against binary masks. Standardization of the VOI format is needed for the application in dosimetry.

(6) It is imperative not just to report ADs but to also include a detailed description of the methods used such that if discrepancies between reported values are present, those differences can be understood and harmonization of results pursued.

(7) Widely used software, both CS and freely available, resulted in ADs that were comparable to each other. One explanation is that this software is better validated. There was greater variability in results calculated using less widely used software. Use of software that is well validated is thus highly recommended.

CONCLUSION

The analysis of task 5 of the SNMMI ^{177}Lu dosimetry challenge data based on ^{177}Lu-DOTATATE patients has demonstrated that the contribution to variability from the dosimetry methods and software used are small and that other possible factors such as segmentation and curve fitting and integration have a higher impact. The contribution of the dose conversion step to the total variability in AD was found to be smaller than 7% for lesions and organs not containing lesions. We have made some recommendations that, if adopted widely by the community, can further reduce variability in AD results.

DISCLOSURE

This work was partly supported by the SNMMI Value Initiative. Yuni Dewaraja acknowledges funding from grant R01CA240706 awarded by the National Cancer Institute for the patient studies and the resources made available by the University of Michigan Deep Blue Data Repository for data sharing. Eric Frey is a cofounder and part-owner of Rapid, LLC, receives royalty income from GE Healthcare, and acknowledges support from grants R44CA213782 and R01CA240779 awarded by the National Cancer Institute. Carlos Uribe acknowledges funding from Natural Science and Engineer Research Council (NSERC) discovery grant RGPIN-2021-02965. No other potential conflict of interest relevant to this article was reported.

ACKNOWLEDGMENTS

We express our deepest gratitude to Bonnie Clarke, the director of research and discovery at the SNMMI. The challenge and the analysis would not have been possible without her excellent support. Special thanks are extended to all the participants: Alessandro Desy, Arda Könik, Ashok Tiwari, Carlos Montes Fuentes, Eric Brunner, Greta Mok, Ivan Yeung, Joe Grudzinski, Johan Blakkisrud, Joshua Scheuermann, Julia Brosch-Lenz, Lorena Sandoval, Natalie Cole, Nathaly Barbosa, Nuria Carrasco, Paulo Ferreira, Price Jackson, Rachele Danieli, Richard Laforest, Shalini Subramanian, Su Bin Kim, Valentina Ferri, and Vikram Adhikarla.

REFERENCES

1. Danieli R, Milano A, Gallo S, et al. Personalized dosimetry in targeted radiation therapy: a look to methods, tools and critical aspects. *J Pers Med.* 2022;12:205.
2. Garin E, Tselikas L, Guiu B, et al. Personalised versus standard dosimetry approach of selective internal radiation therapy in patients with locally advanced hepatocellular carcinoma (DOSISPHERE-01): a randomised, multicentre, open-label phase 2 trial. *Lancet Gastroenterol Hepatol.* 2021;6:17–29.
3. Snyder WS, Ford MR, Warner GG, Watson SB. *MIRD Pamphlet No. 11.* Society of Nuclear Medicine and Molecular Imaging. 1975:92–93.
4. Bolch WE, Bouchet LG, Robertson JS, et al. MIRD pamphlet no. 17: the dosimetry of nonuniform activity distributions—radionuclide S values at the voxel level. *J Nucl Med.* 1999;40:11S–36S.
5. Sarrut D, Bardiès M, Boussion N, et al. A review of the use and potential of the GATE Monte Carlo simulation code for radiation therapy and dosimetry applications. *Med Phys.* 2014;41:064301.
6. Sjögreen Gleisner K, Chouin N, Gabina PM, et al. EANM dosimetry committee recommendations for dosimetry of ^{177}Lu-labelled somatostatin-receptor- and PSMA-targeting ligands. *Eur J Nucl Med Mol Imaging.* 2022;49:1778–1809.
7. Uribe C, Peterson A, Van B, et al. An international study of factors affecting variability of dosimetry calculations, part 1: design and early results of the SNMMI dosimetry challenge. *J Nucl Med.* 2021;62:36S–47S.
8. Brosch-Lenz J, Ke S, Wang H, et al. An international study of factors affecting variability of dosimetry calculations, part 2: overall variabilities in absorbed dose. *J Nucl Med.* 2023;64:1109–1116.
9. Lu-177 DOTATATE anonymized patient datasets: Lu-177 SPECT time integrated activity maps. Deep Blue Data website. https://deepblue.lib.umich.edu/data/concern/data_sets/gb19f607x. Published August 23, 2021. Modified November 18, 2022. Accessed May 29, 2024.
10. Stabin M, Farmer A. OLINDA/EXM 2.0: the new generation dosimetry modeling code [abstract]. *J Nucl Med.* 2012;53(suppl 1):585.
11. Andersson M, Johansson L, Eckerman K, Mattsson S. IDAC-Dose 2.1, an internal dosimetry program for diagnostic nuclear medicine based on the ICRP adult reference voxel phantoms. *EJNMMI Res.* 2017;7:88.
12. Kesner AL, Carter LM, Ramos JCO, et al. MIRD pamphlet no. 28, part 1: MIRDcalc—a software tool for medical internal radiation dosimetry. *J Nucl Med.* 2023; 64:1117–1124.
13. Brosch-Lenz J, Uribe C, Gosewisch A, et al. Influence of dosimetry method on bone lesion absorbed dose estimates in PSMA therapy: application to mCRPC patients receiving Lu-177-PSMA-I&T. *EJNMMI Phys.* 2021;8:26.
14. Papadimitroulas P. Dosimetry applications in GATE Monte Carlo toolkit. *Phys Med.* 2017;41:136–140.
15. Sarrut D, Baudier T, Borys D, et al. The OpenGATE ecosystem for Monte Carlo simulation in medical physics. *Phys Med Biol.* 2022;67:184001.
16. Mora-Ramirez E, Santoro L, Cassol E, et al. Comparison of commercial dosimetric software platforms in patients treated with ^{177}Lu-DOTATATE for peptide receptor radionuclide therapy. *Med Phys.* 2020;47:4602–4615.
17. Grimes J, Celler A. Comparison of internal dose estimates obtained using organ-level, voxel S value, and Monte Carlo techniques. *Med Phys.* 2014;41:092501.
18. Kim KM, Lee MS, Suh MS, Cheon GJ, Lee JS. Voxel-based internal dosimetry for ^{177}Lu-labeled radiopharmaceutical therapy using deep residual learning. *Nucl Med Mol Imaging.* 2023;57:94–102.
19. Dewaraja YK, Mirando DM, Peterson AB, et al. A pipeline for automated voxel dosimetry: application in patients with multi-SPECT/CT imaging after ^{177}Lu-peptide receptor radionuclide therapy. *J Nucl Med.* 2022;63:1665–1672.
20. XCOM: photon cross section database. NIST website. http://physics.nist.gov/xcom. Updated November 2010. Accessed May 29, 2024.

Facilitating the End of the Linear No-Threshold Model Era

Mohan Doss

Diagnostic Imaging, Fox Chase Cancer Center, Philadelphia, Pennsylvania

The linear no-threshold (LNT) model, which asserts that any level of ionizing radiation increases cancer risk, has been the basis of global radiation protection policies since the 1950s. Despite ongoing endorsements, a growing body of evidence challenges the LNT model, suggesting instead that low-level radiation exposure might reduce cancer risk, a concept known as radiation hormesis. This editorial examines the persistence of the LNT model despite evidence favoring radiation hormesis and proposes a solution: a public, online debate between proponents of the LNT model and advocates of radiation hormesis. This debate, organized by a government agency like Medicare, would be transparent and thorough, potentially leading to a shift in radiation protection policies. Acceptance of radiation hormesis could significantly reduce cancer mortality rates and streamline radiation safety regulations, fostering medical innovation and economic growth.

Key Words: cancer; LNT model; NCRP; radiation hormesis; radiation safety

J Nucl Med 2024; 65:1173–1174
DOI: 10.2967/jnumed.124.267868

The linear no-threshold (LNT) model, which posits that even minimal exposure to ionizing radiation increases cancer risk, has been the cornerstone of global radiation protection policies since the 1950s, driven largely by recommendations from advisory bodies such as the National Council on Radiation Protection and Measurements (*1*). Despite repeated endorsements from such bodies, including the latest one by the National Council on Radiation Protection and Measurements in its commentary 27 (*2*), my critical examination of the evidence presented revealed a lack of support for the LNT model (*3*). Conversely, a body of evidence (*4–10*) supports an alternative perspective known as radiation hormesis (*11*), suggesting that low-level radiation exposure might actually decrease cancer risk. I had hoped that review of such evidence would prompt a reevaluation of the LNT model by advisory bodies, signaling the end of the LNT model era (*3*). However, after more than 5 y since the publication of my article (*3*), and despite numerous other publications questioning the adoption and validity of the LNT model (*12,13*), its widespread recommendation (*14*) and application (*15*) persist. In this editorial, I will explore the factors contributing to the persistence of the LNT model era and offer a suggestion for resolving this contentious issue.

In a burgeoning scientific field, researchers naturally propose and explore various hypotheses, even contradictory ones. However, as time elapses and a significant body of evidence accrues, it becomes untenable for scientists to continue supporting conflicting hypotheses. The scientific community's role is to scrutinize these hypotheses rigorously, discarding those that fail to align with accumulating evidence. This process is especially crucial when hypotheses carry significant public health implications. It is paramount for the scientific community to identify the correct hypothesis to guide public policy, because adhering to erroneous hypotheses can result in substantial harm.

Consider the long-standing use of the LNT model by the global community since the 1950s. If evidence confirms the validity of radiation hormesis—an opposing concept to the LNT model—indicating that low-dose radiation exposure actually reduces cancer risk, the implications are profound. Data suggesting a notable decrease in cancer risk, ranging from 20% to 40%, after exposure to low-dose radiation (*16*) underscore the potential major impact.

Had the scientific community not adhered to the LNT model but instead explored radiation hormesis in clinical trials when it was proposed in the 1980s by Luckey (*17,18*), adoption of radiation hormesis might have led to reduction in cancer deaths by around 20%. This would have translated to preventing nearly 2 million cancer deaths in 2022 alone, given the staggering global toll of 9.7 million cancer deaths that year (*19*). Thus, the decision of advisory bodies to persist with the LNT model, despite published evidence supporting radiation hormesis, may have contributed to millions of preventable cancer deaths over recent decades.

The tendency of advisory bodies to overlook or discount evidence for radiation hormesis raises questions about their decision-making processes. When I brought to the attention of the authors of the National Council on Radiation Protection and Measurements commentary the substantial evidence supporting radiation hormesis (*20*), their response (*21*) was concerning. They argued that much of the evidence I cited was not robust because it involved "comparisons of risks between study cohorts and the general population" and that "occupational cohorts tend to be selected for good health compared with the wide range of health status in the general population." However, this critique does not hold up under scrutiny. None of the studies I referenced involved comparisons of occupational cohorts with the general population. Instead, these studies examined cancer rates among cancer patients (*4,5*), radiologists (*6*), tuberculosis patients (*7*), and residents of apartment buildings compared with the general population (*8,9*). Therefore, the authors' criticism lacks validity.

The persistent refusal of advisory bodies to acknowledge evidence supporting radiation hormesis raises questions about potential conflicts of interest that these organizations may have. Acceptance of radiation hormesis would show that they have been wrong for decades because of their consistent support for the LNT model, tarnishing their reputation and diminishing their credibility, influence, and funding. Do these factors influence the reluctance of advisory bodies to recognize the validity of radiation hormesis? This issue merits investigation by an impartial government agency to ensure transparency and accountability.

Received May 9, 2024; revision accepted Jun. 5, 2024.

For correspondence or reprints, contact Mohan Doss (mohan.doss@fccc.edu).

The prolonged impasse between the LNT model and radiation hormesis stems from the refusal of the LNT proponents to acknowledge the validity of evidence supporting radiation hormesis, often instead offering unfounded criticisms. To address this deadlock, I propose a solution: a public, online debate between supporters of the LNT model and advocates of radiation hormesis should be organized by a government agency, such as Medicare, which spent over $1 trillion on cancer treatments in 2023 (*22*). When announcing the debate, it should be made clear that if one side fails to participate, it would be considered the losing side.

In this debate, each side would present its most compelling evidence. This would be followed by rebuttals from the opposing side and responses from the first side. These back-and-forth rebuttals and responses would continue until each piece of evidence is assessed as being valid or invalid. All the arguments and counterarguments would be conducted transparently in the public domain, ensuring that interested parties can access the reasoning and evidence presented and call out any invalid arguments. Once completed, this transparent process would enable rejection of invalid evidence and establishment of the ground truth on the contentious issue, paving the way for evidence-based decision-making in radiation protection policies. If the debate concludes with validation of the LNT model and rejection of radiation hormesis, the status quo for radiation protection policies would continue. On the other hand, if it results in validation of the concept of radiation hormesis, the debate would lead to the adoption and application of the radiation hormesis concept to prevent cancer and could significantly reduce Medicare's cancer treatment expenses.

If the scientific community accepts radiation hormesis and rejects the LNT model after such a debate, society stands to gain numerous benefits. Embracing radiation hormesis would pave the way for extensive research and application of low-dose radiation in cancer prevention and treatment, potentially resulting in a significant reduction by 20% or more in cancer mortality rates. Additionally, the efficacy of low-dose radiation in treating various noncancerous diseases (*23*) would be further explored and used in medical practice.

Rejecting the LNT model would also lead to a reduction in radiation safety regulations, simplifying operations in radiation-related fields such as nuclear power and nuclear medicine. This would also alleviate concerns among patients and parents regarding radiation exposure from medical imaging procedures. Although there would be a decrease in jobs related to radiation safety, the emergence of new job opportunities in supporting applications of low-dose radiation in medicine would more than offset this decline. Overall, the adoption of radiation hormesis promises to usher in a new era of medical innovation and improved patient care while fostering economic growth in related industries.

It is my fervent hope that the proposed online debate takes place soon, validates the evidence for radiation hormesis, and leads to the end of the LNT model era so that society can benefit fully from the many applications of radiation.

DISCLOSURE

The views and opinions expressed herein are those of the author and do not necessarily reflect those of his employer. This research was funded in part through the NIH/NCI Cancer Center support grant P30 CA006927. No other potential conflict of interest relevant to this article was reported.

REFERENCES

1. Sinclair WK. Radiation protection: the NCRP guidelines and some considerations for the future. *Yale J Biol Med.* 1981;54:471–484.
2. *NCRP Commentary No. 27: Implications of Recent Epidemiologic Studies for the Linear-Nonthreshold Model and Radiation Protection.* National Council on Radiation Protection and Measurements; 2018:140.
3. Doss M. Are we approaching the end of the LNT model era? *J Nucl Med.* 2018;59:1786–1793.
4. Tubiana M, Diallo I, Chavaudra J, et al. A new method of assessing the dose-carcinogenic effect relationship in patients exposed to ionizing radiation. A concise presentation of preliminary data. *Health Phys.* 2011;100:296–299.
5. Sakamoto K. Fundamental and clinical studies on cancer control with total and upper half body irradiation. *J Jpn Soc Ther Rad Onc.* 1997;9:161–175.
6. Berrington A, Darby SC, Weiss HA, Doll R. 100 years of observation on British radiologists: mortality from cancer and other causes 1897-1997. *Br J Radiol.* 2001;74:507–519.
7. Davis FG, Boice JD Jr, Hrubec Z, Monson RR. Cancer mortality in a radiation-exposed cohort of Massachusetts tuberculosis patients. *Cancer Res.* 1989;49:6130–6136.
8. Hwang SL, Guo HR, Hsieh WA, et al. Cancer risks in a population with prolonged low dose-rate gamma-radiation exposure in radiocontaminated buildings, 1983-2002. *Int J Radiat Biol.* 2006;82:849–858.
9. Doss M. Comment on '30 years follow-up and increased risks of breast cancer and leukaemia after long-term low-dose-rate radiation exposure.' *Br J Cancer.* 2018;118:e9.
10. Sponsler R, Cameron JR. Nuclear shipyard worker study (1980-1988): a large cohort exposed to low-dose-rate gamma radiation. *Int J Low Radiat.* 2005;1:463–478.
11. Macklis RM, Beresford B. Radiation hormesis. *J Nucl Med.* 1991;32:350–359.
12. Calabrese EJ. Cancer risk assessment, its wretched history and what it means for public health. *J Occup Environ Hyg.* 2024;21:220–238.
13. Siegel JA, Pennington CW, Sacks B, Welsh JS. The birth of the illegitimate linear no-threshold model: an invalid paradigm for estimating risk following low-dose radiation exposure. *Am J Clin Oncol.* 2018;41:173–177.
14. Laurier D, Billarand Y, Klokov D, Leuraud K. The scientific basis for the use of the linear no-threshold (LNT) model at low doses and dose rates in radiological protection. *J Radiol Prot.* 2023;43:024003.
15. Siegel JA, Sacks B, Greenspan BS. NRC rejects petitions to end reliance on LNT model. *J Nucl Med.* 2021;62(11):17N–22N.
16. Doss M. Changing the paradigm of cancer screening, prevention, and treatment. *Dose Response.* 2016;14:1559325816680539.
17. Luckey TD. *Hormesis with Ionizing Radiation.* CRC Press; 1980.
18. Luckey TD. *Radiation Hormesis.* CRC Press; 1991.
19. Bray F, Laversanne M, Sung H, et al. Global cancer statistics 2022: GLOBOCAN estimates of incidence and mortality worldwide for 36 cancers in 185 countries. *CA Cancer J Clin.* 2024;74:229–263.
20. Doss M. Comment on 'Implications of recent epidemiologic studies for the linear nonthreshold model and radiation protection'. *J Radiol Prot.* 2019;39:650–654.
21. Shore RE, Beck HL, Boice JD, et al. Reply to comment on 'Implications of recent epidemiologic studies for the linear nonthreshold model and radiation protection'. *J Radiol Prot.* 2019;39:655–659.
22. *Cancer in Medicare: An American Cancer Society Cancer Action Network Chartbook.* American Cancer Society Cancer Action Network; 2024:37.
23. Cuttler JM. Application of low doses of ionizing radiation in medical therapies. *Dose Response.* 2020;18:1559325819895739.

Dose–Response Relationship in Patients with Liver Metastases from Neuroendocrine Neoplasms Undergoing Radioembolization with ^{90}Y Glass Microspheres

Masao Watanabe[1,2], Stephan Leyser[1,2], Jens Theysohn[2,3], Benedikt Schaarschmidt[2,3], Johannes Ludwig[4], Wolfgang P. Fendler[1,2], Alexandros Moraitis[1,2], Harald Lahner[5], Annie Mathew[5], Ken Herrmann[1,2], and Manuel Weber[1,2]

[1]Department of Nuclear Medicine, University Clinic Essen, Essen, Germany; [2]University of Duisburg–Essen and German Cancer Consortium–University Hospital, Essen, Germany; [3]Institute of Diagnostic and Interventional Radiology and Neuroradiology, University Clinic Essen, Essen, Germany; [4]Department of Radiology and Nuclear Medicine, University Medical Center Mannheim, Heidelberg University, Mannheim, Germany; and [5]Department of Endocrinology, Diabetes, and Metabolism and Division of Laboratory Research, University Clinic Essen, Essen, Germany

The benefit of multicompartment dosimetry in the radioembolization of neuroendocrine neoplasms is not firmly established. We retrospectively assessed its potential with patient outcome. **Methods:** Forty-three patients were eligible. The association of mean absorbed dose (MAD) for tumors and treatment response was tested per lesion with a receiver operating characteristic curve analysis, and the association of MAD with progression-free survival (PFS) and overall survival was tested per patient using uni- and multivariate Cox regression analyses. **Results:** The area under the curve for treatment response based on MAD was 0.79 (cutoff, 196.6 Gy; $P < 0.0001$). For global PFS, grade (grade 2 vs. 1: hazard ratio [HR], 2.51; $P = 0.042$; grade 3 vs. 1: HR, 62.44; $P < 0.001$), tumor origin (HR, 6.58; $P < 0.001$), and MAD (HR, 0.998; $P = 0.003$) were significant. For overall survival, no prognostic parameters were significant. **Conclusion:** In line with prior publications, a MAD of more than 200 Gy seemed to favor treatment response. MAD was also associated with PFS and may be of interest for radioembolization planning for neuroendocrine neoplasm patients.

Key Words: radioembolization; neuroendocrine neoplasm; multicompartment dosimetry

J Nucl Med 2024; 65:1175–1180
DOI: 10.2967/jnumed.124.267774

Neuroendocrine neoplasms (NENs) are metastatic at initial diagnosis in up to 85% of patients with pancreatic NENs and 90% of those with small-intestine NENs, with the liver being the organ mainly affected (*1*), which negatively impacts survival and potentially leads to hormonal excess due to a lack of hepatic first-pass effect (*2*).

Radioembolization is an effective and safe treatment for primary liver tumors (e.g., hepatocellular carcinoma) and for liver metastases secondary to, for example, colorectal carcinoma or NENs (*2–5*). For the latter, radioembolization is mentioned as a treatment option, especially in the context of large lesions, hormonally active tumors, and somatostatin-receptor–negative tumors (*1,2,6*).

In many previous trials on radioembolization in NENs, activity was routinely calculated by use of single-compartment dosimetry, that is, based on average values to the perfused target tissue (*2*). However, in recent years, a benefit with regard to progression-free survival (PFS) and overall survival (OS) could be shown in hepatocellular carcinoma patients when using multicompartment modeling, that is, optimizing doses to the tumor and nontumor tissue by separately assessing average doses to these 2 compartments (*7*). Therefore, this approach is also recommended in the new European Association of Nuclear Medicine guidelines on treating liver tumors (*5*). The doses to each compartment are derived from pretherapeutic ^{99m}Tc-macroaggregated albumin (MAA) SPECT (*5*), which has been shown to be an imperfect but moderately reliable surrogate for ^{90}Y microsphere dose distribution.

For NENs, evidence on the association of multicompartment dosimetry and patient outcome is scarce (*8,9*). In addition, safety doses for nontumor liver tissue have not been established.

We therefore aimed to assess the association of dosimetry parameters derived from multicompartment dosimetry on the one hand and patient outcome on the other hand in patients with NENs by performing a retrospective analysis of patients treated in our institution.

MATERIALS AND METHODS

Patients

From June 2007 to April 2022, 99 consecutive patients were retrieved from our radioembolization database, of whom 43 could be enrolled for this retrospective study. The patient enrollment process is summarized in Figure 1, and the patient characteristics are summarized in Table 1.

To be included, patients had to have undergone radioembolization for the treatment of hepatic metastases secondary to NENs with no other organs being affected, or with extrahepatic spread being judged as prognostically irrelevant, or with hormone-associated symptoms being insufficiently controlled pharmacologically. The exclusion criteria were incomplete treatment records on radioembolization including ^{99m}Tc-MAA SPECT/CT and contrast-enhanced CT or enhanced MRI, untreated liver lesions after radioembolization, and unavailable information on the Ki-67 index of the tumor or PFS.

All analyses were performed in accordance with the principles laid out in the Declaration of Helsinki and its later amendments and approved by the institutional review board of the Medical Faculty of the University

---

Received Mar. 13, 2024; revision accepted May 30, 2024.

For correspondence or reprints, contact Masao Watanabe (d7he4ng@gmail.com).

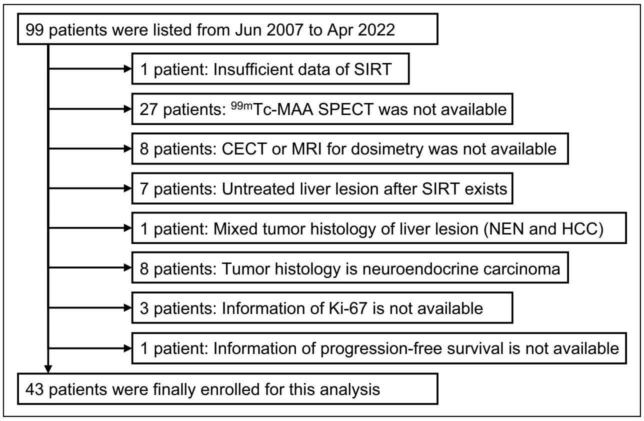

FIGURE 1. Consort diagram of patient enrollment. CECT = contrast-enhanced CT; HCC = hepatocellular carcinoma; SIRT = selective internal radiation therapy.

Duisburg–Essen (approval 13-5325BO). All patients gave written informed consent for the analysis of available data.

Image Acquisition and Treatment Algorithm

A median of 150.0 MBq (range, 147.0–163.0 MBq) of ^{99m}Tc-MAA was administered into the hepatic target vessels, and image acquisition started within 2 h. Details regarding the acquisition protocol, image reconstruction, and interpretation have been published previously (*10*). Treatment activity was calculated using unicompartment dosimetry, mostly aiming at a mean absorbed dose (MAD) to the perfused target volume of between 80 and 150 Gy (*5*).

Dosimetry Procedure

Post hoc multicompartment dosimetry was performed by a board-certified nuclear medicine physician and radiologist using Simplicit90Y (Mirada Medical).

After manual coregistration of contrast-enhanced CT or MRI and ^{99m}Tc-MAA SPECT/CT images, segmentation of whole-liver volume, perfused target volumes, tumor tissue, and nontumor liver tissue was performed both manually and automatically or semiautomatically by use of the tools "Liver Segmentation" and "Region with % of Max." Segmentation of the whole liver volume was performed automatically, whereas tumor lesions were segmented on ^{99m}Tc-MAA SPECT using visually determined thresholds, since optimal coregistration with the diagnostic CT or MRI was severely impeded in many patients because of multifocal disease.

Most but not all tumors displayed a high tumor–to–normal-tissue ratio; in these cases, a percentage-based threshold was placed around the tumor to delineate the hypervascular part. In line with a round-robin study (*11*), this threshold was chosen individually for each patient, since fixed thresholds may induce systematic errors in the volumetric assessment of lesions with different uptake levels. In the remainder, that is, tumors with very low tumor–to–normal-tissue ratios, the delineation was performed manually.

On the basis of prior publications, we measured the MAD for tumor on a per-lesion and per-patient basis (*9*).

To evaluate prognostic factors for liver toxicity after radioembolization, we calculated the MAD to the whole nontumor liver tissue using multicompartment dosimetry (*10*).

Evaluation of Tumor Response to Selective Internal Radiation Therapy

We evaluated baseline and the first follow-up contrast-enhanced CT images using the criteria of Choi et al. (*12*), in consideration of prior publications demonstrating its suitability for response assessment in NEN patients (*13*). Up to 10 lesions per patient were selected, and the anatomic location of each tumor across contrast-enhanced CT and ^{99m}Tc-MAA SPECT/CT was precisely recorded, with a preference for bigger and well-marginated lesions to avoid individual patient bias. To avoid the partial-volume effect, lesions smaller than 2 cm were excluded from lesion-based analyses (*14*). Eight patients did not have lesions 2 cm or larger, and the follow-up enhanced CT was not available in 7 patients. Finally, 28 patients were eligible for this response evaluation. Lesions were classified into the categories of complete remission (CR), partial response (PR), stable disease (SD), and progressive disease (PD). We also categorized the lesions as responding (CR + PR) or nonresponding (SD + PD) (*12*). In the 28 patients eligible for lesion-based response analysis, the median interval between the baseline imaging and radioembolization, between radioembolization and the first follow-up imaging, and between baseline imaging and the first follow-up imaging was 2 mo (range, 1–5 mo), 4 mo (range, 1–6 mo), and 6 mo (range, 2–9 mo), respectively.

Follow-up

All patients were followed up for OS and PFS (using RECIST 1.1) until August 2023. All patients underwent cross-sectional imaging as part of the follow-up imaging. The imaging interval was based on the treating physician's decision, typically every 3 mo, rarely (e.g., in slowly growing tumors) less frequently.

In addition, 29 patients could be followed up using aspartate aminotransferase, alanine aminotransferase, total bilirubin measurements, and albumin for at least 12 mo. Adverse events were graded using the Common Terminology Criteria for Adverse Events (CTCAE) version 5. Relevant liver toxicity was defined as a binary metric by the occurrence of grade 3+ toxicity in aspartate aminotransferase, alanine aminotransferase, bilirubin, and albumin levels, based on prior publications identifying it as a particularly suitable marker for liver toxicity after radioembolization (*9*).

Statistical Analysis

We used the Mann–Whitney *U* test to compare MAD among lesions with CR, PR, SD, and PD. To determine the model fit and a cutoff between responding and nonresponding lesions, we performed a receiver operating characteristic curve analysis with the Youden index, as well as the hepatic response per patient. We calculated the sensitivity, specificity, positive predictive value, negative predictive value, and accuracy for the lesion-based response and the patient-based hepatic response.

A proportional-hazards regression analysis (Cox analysis) was performed for hepatic PFS, global PFS, and OS using MAD per patient; grade 1 (G1), grade 2 (G2), and grade 3 (G3); and tumor origin (pancreatic vs. other origins). Prognostic factors with *P* values of less than 0.05 in the univariate analysis entered the multivariate analysis.

To investigate the difference in hepatic response and MAD per patient with regard to NEN grading, we performed the χ^2 (Cochran–Armitage) test for trend and the Kruskal–Wallis test, respectively.

For these analyses, we used Prism version 8 (GraphPad Software) and MedCalc version 22.014 (MedCalc Software). A *P* value of less than 0.05 was regarded as statistically significant.

RESULTS

Patients

Of 99 initially available patients, 36 were excluded because of insufficient data (e.g.,^{99m}Tc-MAA SPECT/CT or contrast-enhanced CT or MRI) for dosimetry. Seven patients had untreated liver lesions after radioembolization, and 9 patients were excluded because of the tumor histology (NEN and hepatocellular carcinoma, *n* = 1; neuroendocrine carcinoma, *n* = 8). Four patients did not have enough clinical data for the survival analysis. Finally, 43 patients were eligible for our study.

TABLE 1
Patient Characteristics (n = 43)

Clinical variable	Value
Age (y)	Median, 60; range, 35–77
Male/female (*n*)	24/19
Origin of tumor: pancreas/gastrointestinal/unknown	11/30/2
NEN grade: 1/2/3	14/26/3
Endocrine syndrome: positive/negative (*n*)	12/31
Liver cirrhosis: positive/negative (*n*)	1/42
Extrahepatic lesions: positive/negative (*n*)	19/24
Number of involved regions: 1/2/3/4 (*n*)*	12/4/2/1
Lymph node/thyroid gland/lung (*n*)	14/1/3
Adrenal gland/peritoneum/ovary/bone (*n*)	1/5/2/4
Partial-liver/whole-liver SIRT (*n*)	6†/37
Sessions for whole-liver SIRT: 1/2 (*n*)	29/8
Treated volume (mL)	Median, 1,735.4; range, 828.6–6,377.3
Treated fraction (%)	Median, 100; range, 61.4–100
Administered dose (GBq)	Median, 3.9; range, 2.1–22.0
MIRD dose (Gy)	Median, 107.1; range, 44.8–164.3
MAD (Gy)	Median, 219.5; range, 48.1–1014.6
Perfused volume normal-tissue AD (Gy)	Median, 96.2; range, 13.7–181.0
Whole-liver normal-tissue AD (Gy)	Median, 95.3; range, 13.6–181.1
Lung shunt fraction (%)	Median, 2.9; range, 0.7–29.0
PV thrombosis: Vp1–Vp3/Vp4/negative (*n*)	1/0/42
Prior therapy (*n*)	40
Number of therapies: 0/1/2/3/4/5 (*n*)‡	3/9/11/11/4/5
Tumor resection: primary/liver metastasis (*n*)	34/8
TACE/RFA/radiotherapy (*n*)	5/3/1
Somatostatin/PRRT/systemic therapy (*n*)	29/12/13
After SIRT (*n*)	38
Number of therapies: 0/1/2/3/4/5 (*n*)‡	5/17/14/4/2/1
Tumor resection: primary/liver metastasis (*n*)	1/2
TACE/RFA/radiotherapy (*n*)	2/0/0
Somatostatin/PRRT/systemic therapy (*n*)	28/16/18
Additional SIRT (≥6 mo later) (*n*)	3

*Number of involved regions per patient.

†Four and 2 patients underwent radioembolization for right lobe and right lobe plus medial segment, respectively.

‡Number of therapies per patient.

SIRT = selective internal radiation therapy; AD = absorbed dose; PV = portal vein; TACE = transarterial chemoembolization; RFA = radiofrequency ablation. PRRT = peptide receptor radionuclide therapy; systemic therapy = mammalian target of rapamycin inhibitor or chemotherapy.

Of 37 patients (37/43, 86.0%) who underwent whole-liver radioembolization, 29 (78.4%) underwent single-session radioembolization and 8 (21.6%) underwent sequential treatment 4–6 wk apart. In the remaining 6 patients who underwent single-session partial-liver radioembolization (right liver in 4 patients, right liver including segment 4 in the remainder), the median fraction of treated liver volume was 73.0% (range, 61.4%–93.0%). In 43 of a total of 51 treatment sessions, the microspheres were used within 7 d after calibration; in the remainder, after more than 7 d. The median duration between calibration and radioembolization was 4 d (range, 2–11 d).

Lesion-Based Tumor Response Analysis

Of 28 eligible patients for the response evaluation, 21 (75.0%) responded (CR + PR) in the follow-up imaging. The median hepatic PFS, global PFS, and OS of the eligible subcohort for the response analysis were 11 mo (range, 1–73 mo), 10.5 mo (range, 1–73 mo), and 28 mo (range, 2–115 mo), respectively.

In 28 eligible patients who had liver lesions 2 cm or larger, 126 lesions were available for lesion-based analyses. There were 85 responding and 41 nonresponding lesions; 14 of the latter progressed despite treatment.

Median values for responding versus nonresponding lesions were 237.6 Gy (range, 52.7–1178.0 Gy) and 120.2 Gy (range, 29.9–424.9 Gy) for MAD (area under the curve, 0.79; cutoff, 196.6 Gy; $P < 0.0001$). The sensitivity, specificity, positive predictive value, negative predictive value, and accuracy were 64.7% (55/85), 85.4% (35/41), 90.2% (55/61), 53.8% (35/65), and 71.4% (90/126), respectively.

Median values for patient-based hepatic response versus lack thereof were 268.7 Gy (range, 52.7–1,014.6 Gy) and 148.1 Gy (range, 78.8–284.6 Gy) for MAD (area under the curve, 0.78; cutoff, 175.0 Gy; $P = 0.003$). The sensitivity, specificity, positive predictive value, negative predictive value, and accuracy were 66.7% (14/21), 71.2% (5/7), 87.5% (14/16), 41.7% (5/12), and 67.9% (19/28), respectively.

The results including Mann–Whitney test and receiver operating characteristic analyses are summarized in Figures 2 and 3.

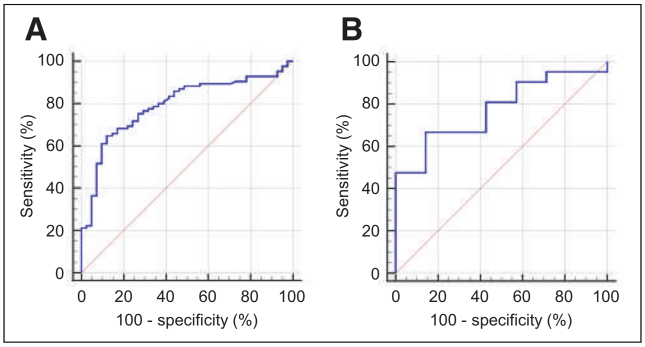

FIGURE 3. Receiver operating characteristic comparison of tumor response to radioembolization in terms of MAD for tumors to classify responder group vs. nonresponder group per lesion (A, 126 lesions) and per patient (B, 28 patients).

Survival Analysis

The median follow-up period was 34 mo (range, 2–151 mo). During this period, 35 of 43 (81.4%) patients died, 33 patients (76.7%) experienced global disease progression, and 24 patients (55.8%) experienced hepatic disease progression. The median hepatic PFS, global PFS, and OS of the entire cohort was 15 mo (range, 1–151 mo), 12 mo (range, 1–151 mo), and 34 mo (range, 2–151 mo), respectively.

The median MAD in all enrolled patients was 219.5 Gy (range, 48.1–1014.6 Gy).

In the univariate analysis for hepatic PFS, NEN grade (G2 vs. G1: hazard ratio [HR], 4.02; 95% CI of HR, 1.31–12.32; $P = 0.015$) and tumor origin (HR, 2.66; 95% CI of HR, 1.05–6.76; $P = 0.040$) were significant prognostic factors, whereas MAD was not. In the multivariate analysis, grade (G2 vs. G1: HR, 3.90; 95% CI of HR, 1.26–12.07; $P = 0.018$) and tumor origin (HR, 2.65; 95% CI of HR, 1.01–6.93; $P = 0.048$) were significant prognostic factors for shorter hepatic PFS. The results are shown in Table 2.

In the univariate analysis for global PFS, grade (G2 vs. G1: HR, 2.49; 95% CI of HR, 1.04–5.96; $P = 0.040$; G3 vs. G1: HR, 36.53; 95% CI of HR, 6.71–198.93; $P < 0.001$), tumor origin (HR, 2.47; 95% CI of HR, 1.14–5.33; $P = 0.021$), and MAD (HR, 0.998; 95% CI of HR, 0.997–1.000; $P = 0.0498$) were significant prognostic factors. In the multivariate analysis, grade (G2 vs. G1: HR, 2.51; 95% CI of HR, 1.04–6.09; $P = 0.042$; G3 vs. G1: HR, 62.44; 95% CI of HR, 9.96–391.48; $P < 0.001$), tumor origin (HR, 6.58; 95% CI of HR, 2.50–17.36; $P < 0.001$), and MAD (HR, 0.998; 95% CI of HR, 0.996–0.999; $P = 0.003$) were significant. These results are summarized in Table 2.

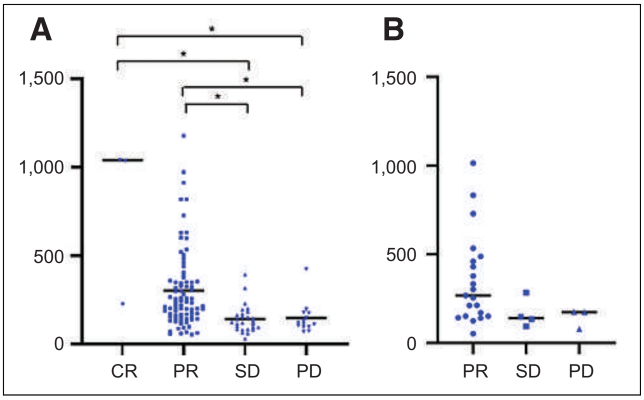

FIGURE 2. Lesion-based (A) and patient-based (B) comparisons of MAD for tumors among groups with CR, PR, SD, and PD. Horizontal line embedded in scatterplot is median value of each group. No CR response per patient was observed. There were no significant differences among PR, SD, and PD groups per patient. *$P < 0.01$; each value was compared using Mann–Whitney test.

In the univariate Cox analysis for OS, grade (G3 vs. G1: HR, 3.88; 95% CI of HR, 1.03–14.63; $P = 0.045$) and MAD (HR, 0.998; 95% CI of HR, 0.996–1.000; $P = 0.049$) were significant prognostic factors. In the multivariate analysis for OS, no prognostic factors were significant. These results are summarized in Table 2.

Differences in hepatic response and MAD per patient with regard to NEN grading were not statistically significant ($P > 0.99$ and $P = 0.078$, respectively).

Liver Toxicity After Radioembolization

Laboratory data were fully available for 29 patients for 12 mo after the radioembolization. During this interval, CTCAE grade 0, 1, 2, and 3+ liver toxicity was observed in 3, 23, 2, and 1 cases, respectively, based on elevated aspartate aminotransferase; in 10, 17, 1, and 1 cases, respectively, based on elevated alanine aminotransferase; in 17, 4, 7, and 1 cases, respectively, based on hyperbilirubinemia; and in 28, 0, 0, and 1 cases, respectively, based on hypoalbuminemia.

One patient experienced CTCAE grade 3+ hyperbilirubinemia and hypoalbuminemia within 6 mo after partial-liver radioembolization, and another patient experienced CTCAE grade 3+ elevated aspartate aminotransferase and alanine aminotransferase within 6 mo after whole-liver radioembolization. The nontumor liver tissue doses and the perfused normal-liver absorbed doses were 107.7 and 125.2 Gy in the former patient and 181.1 and 181.0 Gy in the other, respectively. Treatment after radioembolization consisted of somatostatin analogs in both patients, with 1 patient additionally receiving temozolomide 6–12 mo after radioembolization.

DISCUSSION

Our study showed a significant association between treatment response and absorbed doses in NEN patients treated with radioembolization. After excluding lesions smaller than 2 cm to reduce partial-volume effects, we could show that higher absorbed doses increased the likelihood of treatment response, with an MAD of 196.6 Gy per lesion and 175.0 Gy per patient being the most accurate predictor of treatment response. This threshold is in line with previously published target doses (*9*) and may serve for orientation in radioembolization planning in NENs; with the optimal cutoff

TABLE 2

Uni- and Multivariate Cox Proportional Hazards Regression Analyses for Hepatic and Global PFS and OS

		Univariate		Multivariate	
Survival type	Grade	HR	*P*	HR	*P*
Hepatic PFS	NEN grade				
	Grade 2 vs. 1	4.02 (1.31–12.32)	0.015	3.90 (1.26–12.07)	0.018
	Grade 3 vs. 1	3.74 (0.67–20.97)	0.13	4.43 (0.78–25.35)	0.094
	Tumor origin	2.66 (1.05–6.76)	0.040	2.65 (1.01–6.93)	0.048
	MAD	0.999 (0.997–1.001)	0.29		
Global PFS	NEN grade				
	Grade 2 vs. 1	2.49 (1.04–5.96)	0.040	2.51 (1.04–6.09)	0.042
	Grade 3 vs. 1	36.53 (6.71–198.93)	<0.001	62.44 (9.96–391.48)	<0.001
	Tumor origin	2.47 (1.14–5.33)	0.021	6.58 (2.50–17.36)	<0.001
	MAD	0.998 (0.997–1.000)	0.0498	0.998 (0.996–0.999)	0.003
OS	NEN grade				
	Grade 2 vs. 1	1.82 (0.85–3.86)	0.12	1.81 (0.84–3.87)	0.13
	Grade 3 vs. 1	3.88 (1.03–14.63)	0.045	3.15 (0.82–12.12)	0.095
	Tumor origin	1.93 (0.88–4.22)	0.099		
	MAD	0.998 (0.996–1.000)	0.049	0.998 (0.997–1.0002)	0.072

Data are for 43 patients and for 24, 33, and 35 events for hepatic PFS, global PFS, and OS, respectively. Data in parentheses are 95% CIs. Prognostic parameters with $P < 0.05$ in univariate analysis entered multivariate analysis.

for MAD (196.6 Gy) in our study, a response was noted in 55 of 61 (90.2%) lesions and 14 of 16 (87.5%) patients.

Higher tumor doses on a per-patient basis were also associated with longer global PFS despite not being a significant prognostic factor for hepatic PFS and OS. A possible explanation for this discrepancy lies in the considerable heterogeneity in our cohort, which included well-, intermediate-, and poorly differentiated NENs. As the degree of differentiation has been shown to be a significant predictor of both hepatic and global PFS in our cohort, this likely constitutes a confounding variable alongside other factors not accounted for in the multivariate analysis. In addition, patients may experience a significant overall reduction in hepatic tumor burden after radioembolization while still meeting the criteria for hepatic disease progression, for example, due to the occurrence of new lesions, thus potentially influencing results.

To our knowledge, so far only 2 other publications have assessed the association between tumor-absorbed dose and patient outcome in NEN patients (*8,9*) using multicompartment dosimetry. Ebbers et al. investigated the dose–response relationship after radioembolization with ^{90}Y glass microspheres using multicompartment dosimetry (*9*). For prediction of treatment response, they determined an optimal cutoff of 135 Gy for MAD, whereas 200 Gy predicted response with a higher specificity (*9*). Importantly, Ebbers et al. used ^{90}Y PET/CT for multicompartment dosimetry, which allows for an optimized assessment of the dose–response relationship, as it takes into account the doses administered during radioembolization, whereas pretherapeutic dose calculations by use of ^{99m}Tc-MAA have been shown to be inaccurate in a considerable fraction of patients (*9*). On the other hand, at least in the context of ^{90}Y microspheres, ^{99m}Tc-MAA is the only modality that enables pretherapeutic assessment of absorbed doses, thereby influencing dosing strategies more profoundly. In addition, because of the hypervascular nature of most NEN tumors, it seems likely that ^{99m}Tc-MAA can accurately predict posttreatment dose distribution, making the pretherapeutic dosimetry fairly reliable (*8*).

In our cohort, only 2 patients experienced CTCAE grade 3+ liver toxicity within 6 mo after radioembolization, with relatively high doses to the nontumor liver tissue and the perfused normal liver. As neither patient underwent hepatotoxic treatment within 6 mo after radioembolization, the hepatotoxicity was possibly caused by high absorbed doses to healthy liver tissue. Ebbers et al. reported grade 3+ liver toxicity in 3 of 30 patients in their cohort (*9*). A significant relationship between the absorbed dose in nontumor liver tissue and any biochemical toxicity of grade 3+ in logistic regression analysis could not be established (*9*). In addition, there are growing concerns among practitioners that radioembolization can lead to durable chronic hepatotoxicity and sometimes can be severely toxic (*15*). Currie et al. demonstrated that 4 of 28 patients (14%) experienced solely radioembolization-induced chronic hepatic toxicity, occurring at a median of 2.3 y (range, 6 mo to 5 y) after radioembolization (*15*). In the future, more studies with a longer follow-up duration may be warranted.

One limitation of our study was its retrospective nature. Other limitations were the heterogeneity of the population and follow-up imaging, lack of safety data due to the low number of events, and insufficient statistical power due to the low sample size. Furthermore, the follow-up of 12 mo may be insufficient to fully capture late-onset hepatotoxicity, previously described in the literature (*15*). As most patients were treated within the first week after calibration, our results may not be applicable to treatments performed in the second week after calibration. Also, not all patients were enrolled in the evaluation of tumor response because some patients did not have tumors 2 cm or larger. Finally, ^{99m}Tc-MAA SPECT/CT was used for dosimetry; although this currently is the most accurate approach for pretherapeutic dose assessment, it may not always accurately reflect intratherapeutic dose distribution.

CONCLUSION

The results of our study indicate a higher response rate and longer global PFS in NEN patients in whom higher tumor doses could be achieved, implying that a higher tumor-absorbed dose may be critical to achieve a treatment response.

DISCLOSURE

Masao Watanabe has a postdoctoral fellowship from Humboldt Foundation. Benedikt Schaarschmidt received a research grant from PharmaCept for an ongoing investigator-initiated study not related to this paper. Wolfgang Fendler reports fees from SOFIE Biosciences (research funding), Janssen (consultant, speaker), Calyx (consultant, image review), Bayer (consultant, speaker, research funding), Novartis (speaker, consultant), Telix (speaker), GE Healthcare (speaker), Eczacıbaşı Monrol (speaker), and Abx (speaker), outside the submitted work. Ken Herrmann reports personal fees from Bayer, SIRTEX, Adacap, Curium, Endocyte, IPSEN, Siemens Healthineers, GE Healthcare, Amgen, Novartis, ymabs, Aktis Oncology, Theragnostics, and Pharma 15; personal fees and other fees from Sofie Biosciences; nonfinancial support from ABX; and grants and personal fees from BTG, outside the submitted work. Manuel Weber reports personal fees from Boston Scientific, Terumo, Advanced Accelerator Applications, IPSEN, and Eli Lilly, outside the submitted work. No other potential conflict of interest relevant to this article was reported.

KEY POINTS

QUESTION: Are tumor doses derived from multicompartment dosimetry predictive of treatment response, PFS, OS, and liver failure in patients with NEN undergoing radioembolization?

PERTINENT FINDINGS: Higher absorbed tumor doses are associated with treatment response and global PFS but not with hepatic PFS and OS. Higher mean doses to the nontumor liver tissue may carry an increased risk of liver decompensation.

IMPLICATIONS FOR PATIENT CARE: Dosimetric parameters derived from multicompartment dosimetry may be helpful to maximize treatment efficacy and safety in NEN patients undergoing radioembolization.

REFERENCES

1. Pavel M, Öberg K, Falconi M, et al. Gastroenteropancreatic neuroendocrine neoplasms: ESMO clinical practice guidelines for diagnosis, treatment and follow-up. *Ann Oncol.* 2020;31:844–860.
2. Lewandowski RJ, Toskich BB, Brown DB, El-Haddad G, Padia SA. Role of radioembolization in metastatic neuroendocrine tumors. *Cardiovasc Intervent Radiol.* 2022;45:1590–1598.
3. Schaarschmidt BM, Wildgruber M, Kloeckner R, et al. ^{90}Y radioembolization in the treatment of neuroendocrine neoplasms: results of an international multicenter retrospective study. *J Nucl Med.* 2022;63:679–685.
4. Salem R, Padia SA, Lam M, et al. Clinical, dosimetric, and reporting considerations for Y-90 glass microspheres in hepatocellular carcinoma: updated 2022 recommendations from an international multidisciplinary working group. *Eur J Nucl Med Mol Imaging.* 2023;50:328–343.
5. Weber M, Lam M, Chiesa C, et al. EANM procedure guideline for the treatment of liver cancer and liver metastases with intra-arterial radioactive compounds. *Eur J Nucl Med Mol Imaging.* 2022;49:1682–1699.
6. Ramdhani K, Bratt AJAT. The evolving role of radioembolization in the treatment of neuroendocrine liver metastases. *Cancers (Basel).* 2022;14:3415.
7. Garin E, Tselikas L, Guiu B, et al. Personalized versus standard dosimetry approach of selective internal radiation therapy in patients with locally advanced hepatocellular carcinoma (DOSISPHERE-01): a randomised, multicentre, open-label phase 2 trial. *Lancet Gastroenterol Hepatol.* 2021;6:17–29.
8. Chansanti O, Jahangiri Y, Matsui Y, et al. Tumor dose response in yttrium-90 resin microsphere embolization for neuroendocrine liver metastases: a tumor-specific analysis with dose estimation using SPECT-CT. *J Vasc Interv Radiol.* 2017;28:1528–1535.
9. Ebbers SC, Roekel CV, Braat MNGJA, Barentsz MW, Lam MGEH, Braat AJAT. Dose-response relationships after yttrium-90-radioembolization with glass microspheres in patients with neuroendocrine tumor liver metastases. *Eur J Nucl Med Mol Imaging.* 2022;49:1700–1710.
10. Watanabe M, Grafe H, Theysohn J, et al. Voxel-based dosimetry predicts hepatotoxicity in hepatocellular carcinoma patients undergoing radioembolization with ^{90}Y glass microspheres. *J Nucl Med.* 2023;64:1102–1108.
11. Lam M, Garin E, Palard-Novello X, et al. Direct comparison and reproducibility of two segmentation methods for multicompartment dosimetry: round robin study on radioembolization treatment planning in hepatocellular carcinoma. *Eur J Nucl Med Mol Imaging.* 2023;51:245–257.
12. Choi H, Charnsangavej C, Faria SC, et al. Correlation of computed tomography and positron emission tomography in patients with metastatic gastrointestinal stromal tumor treated at a single institution with imatinib mesylate: proposal of new computed tomography response criteria. *J Clin Oncol.* 2007;25:1753–1759.
13. Solis-Hernandez MP, Valle AFD, Carmona-Bayonas A, et al. Evaluating radiological response in pancreatic neuroendocrine tumours treated with sunitinib: comparison of Choi versus RECIST criteria (CRIPNET_GETNE1504 study). *Br J Cancer.* 2019;121:537–544.
14. Garin E, Rolland Y, Laffont S, Edeline J. Clinical impact of ^{99m}Tc-MAA SPECT/CT-based dosimetry in the radioembolization of liver malignancies with ^{90}Y-loaded microspheres. *Eur J Nucl Med Mol Imaging.* 2016;43:559–575.
15. Currie BM, Nadolski G, Mondschein J, et al. Chronic hepatotoxicity in patientswith metastatic neuroendocrine tumor: transarterial chemoembolization versus transarterial radioembolization. *J Vasc Interv Radiol.* 2020;31:1627–1635.

Diagnostic Performance of ^{18}F-FDG PET/CT According to Delay After Treatment to Detect Subclinical Recurrence of Head and Neck Squamous Cell Carcinoma

Camille Clement[1], Jean-Christophe Leclère[1,2], Clémentine Maheo[1,2], Romain Le Pennec[3,4], Gregoire Le Gal[5], Olivier Delcroix[3], Philippe Robin[2], Jean Rousset[6], Valentin Tissot[7], Aziliz Gueguen[1], Maryne Allio[1], Vincent Bourbonne[8], Ulrike Schick[8], Remi Marianowski[1,2], Pierre-Yves Salaun[3,4], and Ronan Abgral[3,4]

[1]Head and Neck Surgery Department, CHU of Brest, Brest, France; [2]LIEN, University of Brest, Brest, France; [3]Nuclear Medicine Department, CHU of Brest, Brest, France; [4]UMR INSERM, 1304 GETBO, University of Brest, Brest, France; [5]Clinical Investigation Center, CIC 1412, CHU of Brest, Brest, France; [6]Radiology Department, Military Hospital of Brest, Brest, France; [7]Radiology Department, CHU of Brest, Brest, France; and [8]Radiotherapy Department, CHU of Brest, Brest, France

Head and neck squamous cell carcinoma (HNSCC) remains a malignancy with high rates of locoregional recurrence and poor prognosis for recurrent cases. Early detection of subclinical lesions is challenging but critical for effective patient management. Imaging surveillance after treatment, particularly ^{18}F-FDG PET/CT, has shown promise in the diagnosis of HNSCC recurrence. The aim was to evaluate the diagnostic performance of ^{18}F-FDG PET/CT according to delay after treatment in detecting subclinical recurrence (SCR) in HNSCC patients. **Methods:** In this retrospective study, all ^{18}F-FDG PET/CT scans were performed at a single center. All adults with histologically proven HNSCC who were treated with curative intent between January 1, 2006, and December 31, 2021, were included. They had a normal clinical examination before each scan. Patients who underwent an intensive follow-up strategy after treatment had ^{18}F-FDG PET/CT with an intravenous contrast agent at 3–6 mo and annually thereafter for 5 y. The primary endpoint was diagnostic performance (positive and negative predictive values, sensitivity, specificity, and accuracy). **Results:** In total, 2,566 ^{18}F-FDG PET/CT scans were performed among 852 patients, with an average of 3 scans per patient. The overall diagnostic performance measures were as follows: positive predictive value (88%), negative predictive value (98%), sensitivity (98%), specificity (89%), and accuracy (93%). There were no significant differences in diagnostic performance over time. The scans detected 126 cases of SCR (14.8%) and 118 cases of metachronous cancer (13.8%). The incidence of SCR decreased over time, with the highest detection rate in the first 2 y after treatment. Positive predictive value improved over time, reaching 90% for the digital Vision 600 system (third period) compared with 76% for the analog Gemini GXLi system (first period, $P < 0.001$). Multivariate analysis identified advanced stage, high body mass index, and initial PET/CT upstaging as predictive factors for detection of SCR. **Conclusion:** Our study demonstrates that ^{18}F-FDG PET/CT has high diagnostic performance in detecting SCR during follow-up after treatment of HNSCC, especially in the first 2 y. Advanced tumor stage, initial PET/CT upstaging, and high body mass index were associated with a higher likelihood of SCR detection. The routine use of ^{18}F-FDG PET/CT during follow-up seems justified for patients with HNSCC.

Key Words: HNSCC; PET/CT; performance

J Nucl Med 2024; 65:1181–1187
DOI: 10.2967/jnumed.124.267391

Head and neck squamous cell carcinoma (HNSCC) is the sixth most common malignancy worldwide, with approximately 800,000 new cases annually (*1*). Despite recent advances in curative-intent treatments, locoregional recurrence occurs in approximately 40%–50% of patients with advanced-stage disease, mostly within the first 2 y after treatment (*2*). Furthermore, the prognosis for patients with recurrent HNSCC remains poor, with a median survival of less than 1 y (*3*). However, a metanalysis of 1,080 patients with recurrent HNSCC demonstrated the benefit of salvage surgery by improving their median 5-y survival to 39% (*4*). These findings highlight that early detection of small subclinical lesions remains a major challenge to guide clinicians in patient management.

According to the guidelines, standard follow-up is based mainly on iterative clinical examinations and less on imaging (*5,6*). In this context, imaging surveillance after treatment may have a role to play in the diagnosis of HNSCC subclinical recurrence (SCR).

^{18}F-FDG PET/CT is recommended for HNSCC after treatment to resolve doubt if recurrence is clinically suspected and to look for distant metastasis if recurrence is confirmed (*6,7*). Although several studies have already demonstrated its high performance in diagnosing disease SCR during routine patient follow-up (*8–10*), ^{18}F-FDG PET/CT is still optional and concerns only patients with locally advanced disease at diagnosis. Its usefulness remains controversial (*11*), mainly because the cost-effectiveness ratio is debated (*12,13*), the prognostic impact has rarely been studied, and there is no consensus on the frequency and duration of the imaging schedule.

A metanalysis of 7 studies and 907 patients found a global detection rate of 14.2% for HNSCC SCR using ^{18}F-FDG PET/CT, with pooled sensitivity and specificity of 89% and 92% (*14*), respectively; however, results were not subanalyzed by delay after treatment. Only data from 2 prospective series provide estimates of detection rates at 6 mo (18.9%) and 1 y (32.9%) after treatment (*8,9*), and a multicenter randomized prospective trial is ongoing to assess the value of performing imaging every 6 mo for 3 y (*15*).

The aim of this study was to evaluate the diagnostic performance of ^{18}F-FDG PET/CT according to delay after treatment for

---

Received Jan. 31, 2024; revision accepted May 13, 2024.

For correspondence or reprints, contact Jean-Christophe Leclère (leclere.jean-christophe@hotmail.fr).

the detection of SCR in a large retrospective single-center cohort of HNSCC patients.

MATERIALS AND METHODS

Population

Our retrospective study included 852 adult patients with newly diagnosed HNSCC who received curative treatment between 2006 and 2021 (Fig. 1). All patients underwent ^{18}F-FDG PET/CT scans 3–6 mo after completion of treatment and annually for 5 y thereafter, replacing annual chest CT. They were required to have a normal clinical examination before each scan. Patient demographics, treatment information, and follow-up data were collected from electronic medical records.

The primary objective of our study was to evaluate the diagnostic performance of ^{18}F-FDG PET/CT in detecting SCR of HNSCC according to delay after treatment. The secondary objectives were to analyze its efficacy according to disease stage, treatment modality, and PET system used and to search for predictive factors for the detection of SCR using ^{18}F-FDG PET/CT.

The study was approved by the Institutional Ethics Committee (29BRC22.0040), and all patients gave written informed consent. The study complied with the French General Data Protection Regulation.

Follow-up

All patients follow-ups consisted of a conventional work-up according to guidelines (*6*), including clinical examinations every 2 mo during the first year, every 3 mo during the second year, every 4 mo during the third year, every 6 mo during the fourth and fifth years, and then annually. As recommended, ^{18}F-FDG PET/CT was performed 3 mo after radiotherapy for patients with node-positive disease to assess the necessity of neck dissection (*16*). All imaging studies were reviewed and interpreted by a panel of experienced nuclear medicine physicians. SCR was defined as lesions detected on ^{18}F-FDG PET/CT that were not clinically or radiographically apparent at the time of imaging. A qualitative criterion was used to identify recurrence, that is, any nonphysiologic uptake above the surrounding background noise (Fig. 2). Because of the rapidly progressive nature of this type of cancer, if a lesion was detected by ^{18}F-FDG PET/CT within 3 mo of the examination, the result was considered false-negative. However, if the lesion was detected more than 3 mo later, it was considered undetectable and the result was classified as true-negative. Suspected recurrence or synchronous cancer was confirmed by histologic sampling or, if not possible, by morphologic or metabolic progression on subsequent imaging within 3 mo.

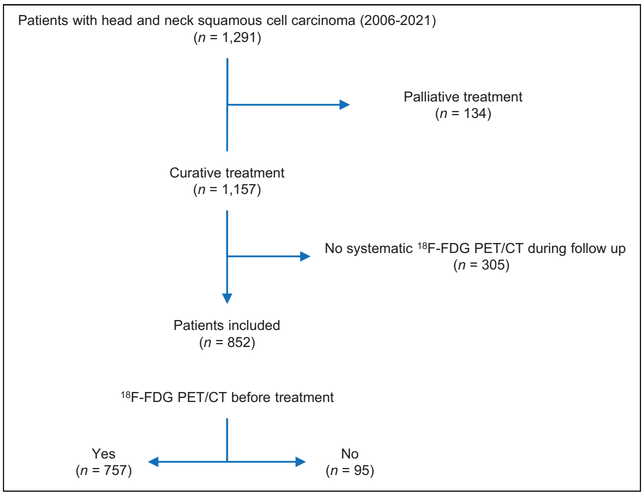

FIGURE 1. Flowchart.

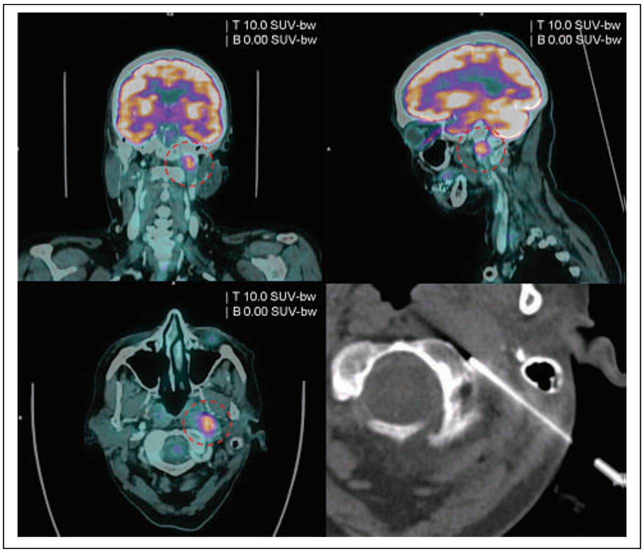

FIGURE 2. ^{18}F-FDG PET/CT performed 18 mo after surgical treatment of T2N0M0 left tonsillar squamous cell carcinoma showing, in coronal (top left), sagittal (top right), and axial (lower left) views, recurrence of squamous cell carcinoma (circle). This was confirmed by CT-guided biopsy (lower right). B = background; SUV-bw = body-weight SUV; T = tumor.

^{18}F-FDG PET/CT Imaging

The examinations were performed on several consecutive PET/CT hybrid scans as follows: from 2006 to 2012 on an analog Gemini GXLi (Philips Healthcare) system, from 2012 to 2018 on an analog Biograph-mCT (Siemens) system, and from 2019 to 2021 on a digital Vision 600 (Siemens) system. PET/CT imaging was performed 1 h after an intravenous injection of 3–5 MBq/kg of ^{18}F-FDG (IBA Molecular Imaging). The detailed parameters of the PET/CT imaging are available in the supplemental materials (supplemental materials are available at http://jnm.snmjournals.org).

Statistical Analysis

Statistical analysis was performed using SPSS software (version 25.0; IBM). Descriptive statistics were used to summarize the demographic and clinical characteristics of the patient cohort.

The overall diagnostic performance of ^{18}F-FDG PET/CT was evaluated using sensitivity, specificity, positive predictive value (PPV), negative predictive value (NPV), and accuracy. Subanalyses were performed in subgroups as follows: interval after treatment (3–6, 7–12, 13–24, 25–36, and ≥37 mo), treatment modality (surgery only and with radiotherapy), disease stage (early stage I/II and advanced stage III/IV), and PET system (first period [P1] Gemini, 2006–2011; second period [P2] Biograph, 2012–2017; and third period [P3] Vision, 2018–2022),

For univariate analysis, a Mann–Whitney test was used for continuous variables and a Fisher exact test for categoric variables. Predictive factors found to be associated with subclinical detection were then entered into a multivariable logistic regression model. A *P* value of less than 0.05 was considered statistically significant.

RESULTS

Patient Characteristics

Among the 852 patients included, 2,566 ^{18}F-FDG PET/CT scans were performed, with an average of 3 scans per patient. Clinical characteristics are shown in Table 1.

TABLE 1
Patient Characteristics (n = 852)

Characteristic	n	%
Male	695	82
Median age ± σ (y)	62	8
Cancer history	161	19
HNSCC history	58	7
Smoking > 10 pack-years	797	94
Alcohol > 3 drinks/d	327	38
Primary location		
Oral cavity	198	23
Oropharynx	292	34
HPV+ oropharynx	56	19
HPV− oropharynx	236	81
Larynx	205	24
Hypopharynx	132	15
CUP	25	3
Initial ^{18}F-FDG PET/CT	757	89
Stage		
Early	209	25
I	124	15
II	85	10
Advanced	633	74
III	133	16
IV	500	59
Treatment		
Surgery	394	46
Alone	213	25
Plus RT	91	11
Plus CRT	90	10
RT	458	54
Alone	151	18
Plus chemotherapy	307	36
Median year of treatment	2016	
Median follow-up (mo)	31	28

HPV = human papilloma virus; CUP = carcinoma unknown primary; RT = radiotherapy; CRT = chemoradiotherapy.

Patients were predominantly men (695/852, 82%), with a median age of 62 y (range, 32–94 y). Of the included patients, 161 (19%) had a previous history of cancer and 58 (7%) had HNSCC from another primary site. The most common tumor site was the oropharynx (292/852, 34%). With regard to the distribution of the main curative treatments, slightly more patients received initial radiotherapy than surgery (458/852 vs. 394/852, respectively).

Diagnostic Performance of PET for SCR

Of the 852 patients, 26% (221/852) had a recurrence of head and neck cancer, of which 57% (126/221) were detected by ^{18}F-FDG PET/CT. The overall detection rate of SCR by ^{18}F-FDG PET/CT was 14.7% (126/852). It was 4.8% (40/830) at 3–6 mo, 10.3% (45/435) at 7–12 mo, 3.5% at 13–24 mo (21/596), 2.6% at 25–36 mo (9/343), and 3.1% at more than 37 mo (11/358).

The overall diagnostic performance of ^{18}F-FDG PET/CT for SCR (n = 126) was 88%, 98%, 98%, 89%, and 93% for PPV, NPV, sensitivity, specificity, and accuracy, respectively. For the subgroup of 95 patients without pretherapeutic ^{18}F-FDG PET/CT imaging, the diagnostic accuracy of the first follow-up ^{18}F-FDG PET/CT scan (92%, 98%, 97%, 95%, and 93% for PPV, NPV, sensitivity, specificity, and accuracy, respectively) was quite similar to that of patients with pretherapeutic ^{18}F-FDG PET/CT imaging.

Per Interval After Treatment. The diagnostic performance of ^{18}F-FDG PET/CT at different time intervals after curative treatment is summarized in Table 2.

Excluding cancers detected at the initial work-up, ^{18}F-FDG PET/CT identified 118 metachronous cancers in 13% (113/852) of patients. Of these, 5 patients developed 2 metachronous cancers during follow-up. The most common sites were the lung (54%, 61/113), colon or rectum (11%, 12/113), head and neck (10%, 11/113), and esophagus (8%, 9/113).

The incidence of SCR decreased over time, with 67% (85/126) detected in the first year and 84% (106/126) detected in the first 2 y. Curative treatment of recurrences detected during follow-up increased over time, from 42% before 13 mo to 83% after 13 mo. Overall, 56% (70/126) of patients who had SCR during follow-up received curative treatment.

The incidence of asymptomatic metachronous cancers was slightly higher in the first year but tended to remain stable over time, around 20 per year. Similarly, the rate of curative treatment increased only slightly over time, from 81% to 96%.

Per PET System. There was an improvement in PPV over time, from 76% to 84% and then 90% from P1 (Gemini) to P2 (Biograph) and then P3 (Vision, $P < 0.001$); all results are shown in Supplemental Table 1. In particular, there was improvement in the characterization of tumor recurrence from P1 to P2–P3, from 76% to 90% ($P < 0.001$). For nodal status, there was an increase from 90% to 93% and then 97% from P1 to P2 and then P3 ($P = 0.004$), and for synchronous cancer detection, there was an increase from 60% to 70% and then 90% from P1 to P2 and then P3 ($P < 0.001$). The results for NPV and sensitivity were similar over time, with excellent values ranging from 98% to 100%. Specificity decreased from 88% to 81% and then increased to 93% from P1 to P2 and then P3 ($P = 0.008$). Accuracy increased from P3 to reach the best overall value of 95%.

Per Disease Stage. There was no significant difference in diagnostic performance according to initial disease stage (Supplemental Table 2). PPV ranged from 84% to 87%, NPV and sensitivity ranged from 99% to 100%, specificity ranged from 88% to 89%, and accuracy remained constant at 93%.

Per Initial Treatment Modality. There was no significant difference in diagnostic performance, according to initial treatment modality (Supplemental Table 3). PPV ranged from 85% to 86%, NPV and sensitivity ranged from 99% to 100%, specificity ranged from 88% to 89%, and accuracy remained constant at 93%.

Predictive Factors for SCR

The analysis of predictive factors for SCR is detailed in Table 3.

In univariate analysis, several factors predicted the detection of recurrence by systematic ^{18}F-FDG PET/CT: body mass index of less than 22 (odds ratio [OR], 0.738; 95% CI, 0.579–0.941; $P = 0.010$), advanced stage (III or IV; OR, 1.904; 95% CI, 1.282–2.826; $P = 0.002$), upstaging by ^{18}F-FDG PET/CT (PETup) at the

TABLE 2
Overall Diagnostic Performance of ^{18}F-FDG PET/CT and by Time Interval After Treatment

	^{18}F-FDG PET/CT					Subclinical recurrence		Metachronous cancer	
Parameter	PPV (%)	NPV (%)	Se (%)	Sp (%)	Acc (%)	*n*	Cur. treatment	*n*	Cur. treatment
Range									
3–6 mo, *n* = 830	88	98	98	88	93	40	16 (40)		28 (82)
7–12 mo, *n* = 435	84	99	99	85	91	45	20 (44)	16	13 (81)
13–24 mo, *n* = 596	91	99	98	93	95	21	17 (81)	25	21 (84)
25–36 mo, *n* = 343	90	98	97	95	95	9	7 (78)	20	19 (95)
≥37 mo, *n* = 358	84	98	97	86	91	11	10 (91)	23	22 (96)
Anatomic site									
All, *n* = 2,566	88	98	98	89	93	126	70 (56)	118	103 (87)
All T	88	100	99	96	96				
All N	94	100	99	99	99				
All lung M	95	100	99	99	99				
All other M	97	100	95	100	100				
All metachronous cancer	79	100	97	97	97				

Se = sensitivity; Sp = specificity; Acc = accuracy; T = tumor; N = node; M = metastasis; Cur. treatment = curative treatment.
Cur. treatment data are number, with percentage in parentheses.

initial assessment (OR, 1.481; 95% CI, 1.141–1.922; *P* = 0.005), and oral primary site (OR, 2.002; 95% CI, 1.233–3.253; *P* = 0.006) or oropharynx primary site (OR, 1.292; 95% CI, 1.06–1.575; *P* = 0.016). In multivariate analysis, 3 factors (advanced stage, body mass index < 22, and PETup) remained significantly associated with the detection of SCR (OR, 2.810; 95% CI, 1.061–7.440; *P* = 0.038; OR, 0.277; 95% CI, 0.116–0.658; *P* = 0.004; and OR, 25.582; 95% CI, 7.939–82.34; *P* < 0.001, respectively).

TABLE 3
Analysis of Predictive Factors for ^{18}F-FDG PET/CT Recurrence Detection in Patients with Proven SCR

	Univariate analysis			Multivariate analysis		
Risk factor	*P*	OR	95% CI	*P*	OR	95% CI
Age < 62 y old	1	0.989	0.755			
Male	0.70	1.142	0.614–2.124			
Smoking > 10 pack-years	0.26	0.957	0.896–1.022			
Alcohol > 3 drinks/d	0.30	1.207	0.881–1.654			
HNSCC history	0.51	1.196	0.748–1.915			
Body mass index < 22	0.010	0.738	0.579–0.941	0.004	0.277	0.116–0.658
Primary location						
Oral cavity	0.006	2.002	1.233–3.253	0.879	1.179	0.142–9.775
Oropharynx	0.016	1.292	1.06–1.575	0.258	3.366	0.412–27.522
Larynx	0.41	0.927	0.78–1.103			
Hypopharynx	0.11	1.093	0.995–1.2			
CUP	0.68	0.984	0.933–1.038		1	
Synchronous cancer	1	1.004	0.938–1.075			
Initial PETup	0.005	1.481	1.141–1.922	0.001	25.582	7.939–82.34
Advanced stage III/IV	0.002	1.904	1.282–2.826	0.038	2.810	1.061–7.440
Initial treatment*	0.013	1.493	1.107–2.013	0.319	0.627	0.251–1.569

*Surgery.
CUP = carcinoma unknown primary.

DISCUSSION

Our study showed that ^{18}F-FDG PET/CT was highly effective in detecting 126 SCRs and 118 metachronous cancers during systematic surveillance of 852 HNSCC patients, corresponding to an occult event rate of 9.5% (244/2,566 scans). To our knowledge, this is the largest study evaluating the diagnostic performance of ^{18}F-FDG PET/CT in this indication. We found good results, with PPV, NPV, sensitivity, specificity, and accuracy estimated at 88%, 98%, 98%, 89%, and 93%, respectively. These findings are consistent with several previous series investigating the usefulness of ^{18}F-FDG PET/CT for the detection of SCR, with sensitivity of 88%–100%, specificity of 43%–95%, PPV of 51%–89%, NPV of 91%–100%, and accuracy of 81%–97%, regardless of anatomic site (tumor, node, or metastasis) or the delay after treatment (*8,9,17–21*).

In addition, the rate of curative treatment for SCR is higher than reported in the literature (23%–46%) (*22–26*). It has been known for several years that early management of recurrence can improve quality of care and overall survival (*23,27*). Recently, a cohort study of HNSCC patients demonstrated a probable protective role of imaging-based follow-up with ^{18}F-FDG PET/CT (hazard ratio, 0.29) (*28*). A single-center retrospective case-control study of 782 patients with ^{18}F-FDG PET/CT imaging showed similar results (OR, 0.71) (*29*). Considering these elements, and given the excellent performance of ^{18}F-FDG PET/CT, its use in routine settings seems justified.

We chose to include only patients with a normal clinical examination at least 3 mo after completion of treatment for 2 reasons. First, it is difficult to distinguish true SCR from residual disease after treatment. Second, it is well known that there is an increased risk of false-positives because of inflammatory changes occurring less than 3 mo after treatment, especially with radiotherapy (*30*). In a retrospective study, Risør et al. (*31*) showed that the diagnostic accuracy of ^{18}F-FDG PET/CT in the follow-up of 279 HNSCC patients improved mainly between the 0- to 3-mo and the 3- to 6-mo intervals after treatment, with a significant decrease in equivocal results (26.3% and 8.4%, respectively; $P = 0.03$). In our series, the diagnostic accuracy of ^{18}F-FDG PET/CT in follow-up after treatment was stable (91%–95%), regardless of the time interval after 3 mo (*32*).

In our study, the incidence of disease recurrence decreased over time (67% in the first year and 84% in the first 2 y), corresponding to a detection rate of SCR by ^{18}F-FDG PET/CT of 4.8% at 3–6 mo, 10.3% at 7–12 mo, and 3.5% at 13–24 mo (21/596). These findings are also consistent with the literature. Ho et al. (*33*) highlighted that PET/CT detection rates in clinically occult patients were 9% (15/175) at 12 mo and 4% (3/77) at 24 mo. Furthermore, in a retrospective study of 388 patients who underwent ^{18}F-FDG PET/CT every 3 mo, Beswick et al. (*34*) concluded that ^{18}F-FDG PET/CT is not useful after 2 y, because 95% of recurrences occur within this period. However, we found a slightly higher incidence of asymptomatic metachronous cancers in the first year, which then stabilized over time at a rate of 4.5% per year. This is in agreement with the retrospective study of 302 patients by Léon et al. (*32*), which showed a relatively constant incidence of metachronous cancers of 4% per year over a 10-y follow-up period.

With regard to our analysis per PET system, we found improvement in diagnostic performance, especially in terms of PPV from P1 (Gemini) to P2 (Biograph) and P3 (Vision, $P < 0.001$) and in terms of accuracy, with a best overall value calculated at 95% ($P = 0.014$). This makes sense because the advances in PET technology (i.e., point spread function + time-of-flight image reconstruction from P1 to P2 and digital detector implementation from P2 to P3) over the last decade have allowed improvement in lesion detectability (*35–38*), as well as increased physician expertise. Using P1 versus P2, in a study comparing the ordered-subset expectation maximization algorithm with or without the point spread function and time of flight, Akamatsu et al. (*39*) showed that the combination of point spread function and time of flight increased $\text{SUV}_{\max}$ by 43.3% in 41 lymph node metastases and improved detection of small lesions. Using P2 versus P3, Delcroix et al. (*40*) showed in a series of 98 patients significant improvement in image quality (noise and sharpness) and lesion detectability with the digital PET/CT dataset compared with the analoglike one.

Our study found no significant difference in performance based on initial treatment type or disease stage. The changes associated with the type of initial treatment suggest that rearrangements in tissues treated by surgery or radiotherapy do not affect this metabolic imaging. Although recurrences are less frequent and rearrangements are less significant in early stages, this does not alter the performance of PET/CT during follow-up.

In our series, multivariate analysis identified PETup at initial work-up (OR, 25.58; $P < 0.001$) and advanced stage disease III or IV (OR, 2.810; $P = 0.038$) as independent prognostic factors for subclinical events after treatment detected by ^{18}F-FDG PET/CT, regardless of the initial stage. To date, ^{18}F-FDG PET/CT is recommended only for HNSCC in advanced III or IV staging before treatment for distant extension (*7*). Nevertheless, several studies have shown its usefulness for restaging as an adjunct to conventional work-up at any stage (*41–43*). In a retrospective study of 477 HNSCC patients, Leclère et al. (*42*) found that ^{18}F-FDG allowed PETup of disease after conventional work-up from stage I or II to advanced stage III or IV in 42 of 130 patients (32.3%). They showed that these changes were mainly related to lymph node status (38.2%) and significantly affected 3-y overall survival compared with patients whose conventional work-up and ^{18}FDG PET/CT results were concordant (54.8 vs. 82.6%, $P = 0.001$). These findings highlight the importance of functional imaging in the initial assessment of head and neck cancer, because it allows greater accuracy in determining lymph node involvement. In a metanalysis of 32 studies including 1,236 patients, Kyzas et al. (*44*) showed sensitivity of 79% and specificity of 86% for ^{18}F-FDG PET/CT in the diagnosis of lymph node extension in HNSCC. They also reported better sensitivity (82% vs. 74%) and specificity (82% vs. 76%) of PET than of CT in 16 studies and better specificity (85% vs. 80%) for equivalent sensitivity of PET than of MRI in 9 studies. Advanced stages are associated with a higher risk of recurrence, particularly in the lymph nodes (*45*). The improved diagnostic performance of ^{18}F-FDG PET/CT over CT alone in the initial assessment of lymph node extension—the region most prone to recurrence—supports the use of PET/CT during follow-up to maximize the likelihood of detecting SCR. In a recent review, You et al. (*46*) highlighted that ^{18}F-FDG PET/CT is a valuable tool for detecting nodal recurrences that may be missed by routine clinical examination or conventional imaging, with implications for patient management. In addition, a body mass index of less than 22 was found to be a protective factor for SCR of cancer in our results (OR, 0.277; $P = 0.004$). This tendency likely results from the increased feasibility of detecting recurrent squamous cell carcinoma in the neck by clinical palpation because of the reduced volume of adipose tissue. In addition, in patients with a body mass index of at least 22, the lower contrast because of fat may also limit the sensitivity or specificity of ^{18}F-FDG PET/CT.

Our study had several limitations. First, its retrospective single-center design requires validation by multicenter randomized prospective studies to limit selection bias. Such a trial is under way to evaluate the value of PET-based follow-up up to 3 y after treatment (*15*). Second, our population included a high proportion of advanced stage disease (74%), which may have artificially increased the incidence of SCR or metachronous disease compared with an unselected population. Nevertheless, this was a real-life study, so this rate is consistent with the available data in our region over the last 20 y. Third, some patients (only 11%) did not undergo pretherapeutic ^{18}F-FDG PET/CT, which may have led to an underdiagnosis of asymptomatic synchronous cancers and thus slightly increased our rate of subsequent metachronous cancers. Fourth, data on human papilloma virus status were missing for two thirds of the patients, because this was not recommended in the early years of the inclusion period. Fifth, ^{18}F-FDG PET/CT imaging was performed with iodinated contrast agents unless contraindicated, a practice that may not be widespread in all centers. The use of contrast agents has been shown to improve the differentiation between anatomic structures and pathologic abnormalities, thus improving the diagnostic accuracy of PET/CT scans (*47–49*). This may explain the sensitivities and specificities observed in this study. Sixth, 56 patients were positive for human papilloma virus. The performance of ^{18}F-FDG PET/CT is better in patients with cancers related to human papilloma virus (*50*), probably in part because the risk of recurrence is lower. Finally, during the long inclusion period (13 y), there has been a remarkable evolution in treatment methods and medical imaging techniques. This time interval may also have affected the PET analysis, depending on the learning curves of the nuclear medicine physicians.

CONCLUSION

In a large cohort of 852 asymptomatic patients, we have shown that ^{18}F-FDG PET/CT has high diagnostic performance in detecting subclinical HNSCC recurrence, as well as metachronous cancers throughout follow-up after treatment. Several factors may predict the likelihood of a positive result, including advanced tumor stage (III or IV), PETup at initial work-up, and tumor location outside the oral cavity. Considering these performance results and recent studies showing the protective role of imaging-based follow-up, the routine use of ^{18}F-FDG PET/CT during follow-up seems justified for patients with HNSCC.

DISCLOSURE

No potential conflict of interest relevant to this article was reported.

KEY POINTS

QUESTION: What is the diagnostic performance of ^{18}F-FDG PET/CT during follow-up in clinically asymptomatic patients treated for HNSCC?

PERTINENT FINDINGS: In this retrospective study that included 852 adults, 2,566 ^{18}F-FDG PET/CT scans were conducted. The overall diagnostic performance measures were as follows: PPV of 88%, NPV of 98%, sensitivity of 98%, specificity of 89%, and accuracy of 93%.

IMPLICATIONS FOR PATIENT CARE: ^{18}FDG PET/CT had excellent performance when used for the follow-up of asymptomatic patients treated for HNSCC.

REFERENCES

1. Siegel RL, Miller KD, Jemal A. Cancer statistics, 2016. *CA Cancer J Clin.* 2016;66:7–30.
2. Global Burden of Disease Cancer Collaboration. Global, regional, and national cancer incidence, mortality, years of life lost, years lived with disability, and disability-adjusted life-years for 32 cancer groups, 1990 to 2015: a systematic analysis for the global burden of disease study. *JAMA Oncol.* 2017;3:524–548.
3. Vermorken JB, Remenar E, van Herpen C, et al. Cisplatin, fluorouracil, and docetaxel in unresectable head and neck cancer. *N Engl J Med.* 2007;357:1695–1704.
4. Goodwin WJ. Salvage surgery for patients with recurrent squamous cell carcinoma of the upper aerodigestive tract: when do the ends justify the means? *Laryngoscope.* 2000;110:1–18.
5. Simo R, Homer J, Clarke P, et al. Follow-up after treatment for head and neck cancer: United Kingdom national multidisciplinary guidelines. *J Laryngol Otol.* 2016;130(suppl 2):S208–S211.
6. NCCN guidelines: head and neck cancers. National Comprehensive Cancer Network website. https://www.nccn.org/guidelines/guidelines-detail?category=1&id=1437.
7. Salaün P-Y, Abgral R, Malard O, et al. Good clinical practice recommendations for the use of PET/CT in oncology. *Eur J Nucl Med Mol Imaging.* 2020;47:28–50.
8. Abgral R, Querellou S, Potard G, et al. Does ^{18}F-FDG PET/CT improve the detection of posttreatment recurrence of head and neck squamous cell carcinoma in patients negative for disease on clinical follow-up? *J Nucl Med.* 2009;50:24–29.
9. Robin P, Abgral R, Valette G, et al. Diagnostic performance of FDG PET/CT to detect subclinical HNSCC recurrence 6 months after the end of treatment. *Eur J Nucl Med Mol Imaging.* 2015;42:72–78.
10. Van Hoe S, Hermans R. Post-treatment surveillance imaging in head and neck cancer: a systematic review. *Insights Imaging.* 2024;15:32.
11. Szturz P, Van Laer C, Simon C, Van Gestel D, Bourhis J, Vermorken JB. Follow-up of head and neck cancer survivors: tipping the balance of intensity. *Front Oncol.* 2020;10:688.
12. Nocon CC, Kennedy A, Jaffe J, Pruitt J, Kuchta K, Bhayani MK. Costs associated with imaging surveillance after treatment for head and neck cancer. *JAMA Otolaryngol Head Neck Surg.* 2021;147:632–637.
13. Mehanna H, Wong W-L, McConkey CC, et al. PET-CT surveillance versus neck dissection in advanced head and neck cancer. *N Engl J Med.* 2016;374:1444–1454.
14. Sheikhbahaei S, Taghipour M, Ahmad R, et al. Diagnostic accuracy of follow-up FDG PET or PET/CT in patients with head and neck cancer after definitive treatment: a systematic review and meta-analysis. *AJR.* 2015;205:629–639.
15. Multicentric comparative study between a conventional and an intensive follow up strategy after treatment of a head and neck squamous cell carcinoma (SURVEIL-L'ORL). ClinicalTrials.gov website. https://clinicaltrials.gov/study/NCT03519048. Updated March 26, 2024. Accessed June 26, 2024.
16. Machiels J-P, René Leemans C, Golusinski W, et al. Squamous cell carcinoma of the oral cavity, larynx, oropharynx and hypopharynx: EHNS-ESMO-ESTRO clinical practice guidelines for diagnosis, treatment and follow-up. *Ann Oncol.* 2020;31:1462–1475.
17. Wong RJ, Lin DT, Schöder H, et al. Diagnostic and prognostic value of [^{18}F]fluorodeoxyglucose positron emission tomography for recurrent head and neck squamous cell carcinoma. *J Clin Oncol.* 2002;20:4199–4208.
18. Kubota K, Yokoyama J, Yamaguchi K, et al. FDG-PET delayed imaging for the detection of head and neck cancer recurrence after radio-chemotherapy: comparison with MRI/CT. *Eur J Nucl Med Mol Imaging.* 2004;31:590–595.
19. Salaun PY, Abgral R, Querellou S, et al. Does ^{18}fluoro-fluorodeoxyglucose positron emission tomography improve recurrence detection in patients treated for head and neck squamous cell carcinoma with negative clinical follow-up? *Head Neck.* 2007;29:1115–1120.
20. Krabbe CA, Pruim J, van der Laan BFAM, Rödiger LA, Roodenburg JLN. FDG-PET and detection of distant metastases and simultaneous tumors in head and neck squamous cell carcinoma: a comparison with chest radiography and chest CT. *Oral Oncol.* 2009;45:234–240.
21. Lapela M, Grénman R, Kurki T, et al. Head and neck cancer: detection of recurrence with PET and 2-[F-18]fluoro-2-deoxy-D-glucose. *Radiology.* 1995;197:205–211.
22. Esteller E, Vega MC, López M, Quer M, León X. Salvage surgery after locoregional failure in head and neck carcinoma patients treated with chemoradiotherapy. *Eur Arch Otorhinolaryngol.* 2011;268:295–301.
23. Zafereo ME, Hanasono MM, Rosenthal DI, et al. The role of salvage surgery in patients with recurrent squamous cell carcinoma of the oropharynx. *Cancer.* 2009;115:5723–5733.
24. Taguchi T, Nishimura G, Takahashi M, et al. Treatment results and prognostic factors for advanced squamous cell carcinoma of the head and neck treated with salvage surgery after concurrent chemoradiotherapy. *Int J Clin Oncol.* 2016;21:869–874.

25. Putten L, Bree R, Doornaert PA, et al. Salvage surgery in post-chemoradiation laryngeal and hypopharyngeal carcinoma: outcome and review. *Acta Otorhinolaryngol Ital.* 2015;35:162–172.
26. Temam S, Pape E, Janot F, et al. Salvage surgery after failure of very accelerated radiotherapy in advanced head-and-neck squamous cell carcinoma. *Int J Radiat Oncol Biol Phys.* 2005;62:1078–1083.
27. Wong LY, Wei WI, Lam LK, Yuen APW. Salvage of recurrent head and neck squamous cell carcinoma after primary curative surgery. *Head Neck.* 2003;25:953–959.
28. Anzai Y, Chang C-P, Rowe K, et al. Surveillance imaging with PET/CT and CT and/or MRI for head and neck cancer and mortality: a population-based study. *Radiology.* 2023;307:e212915.
29. Leclère J-C, Clément C, Le Pennec R, et al. An intensive ^{18}F-fludeoxyglucose-positron emission tomography with computed tomography-based strategy of follow-up in patients treated for head and neck squamous cell carcinoma who are clinically asymptomatic. *JAMA Netw Open.* 2023;6:e2326654.
30. Gupta T, Master Z, Kannan S, et al. Diagnostic performance of post-treatment FDG PET or FDG PET/CT imaging in head and neck cancer: a systematic review and meta-analysis. *Eur J Nucl Med Mol Imaging.* 2011;38:2083–2095.
31. Risør LM, Loft A, Berthelsen AK, et al. FDG-PET/CT in the surveillance of head and neck cancer following radiotherapy. *Eur Arch Otorhinolaryngol.* 2020;277:539–547.
32. León X, Quer M, Diez S, Orús C, López-Pousa A, Burgués J. Second neoplasm in patients with head and neck cancer. *Head Neck.* 1999;21:204–210.
33. Ho AS, Tsao GJ, Chen FW, et al. Impact of positron emission tomography/computed tomography surveillance at 12 and 24 months for detecting head and neck cancer recurrence. *Cancer.* 2013;119:1349–1356.
34. Beswick DM, Gooding WE, Johnson JT, Branstetter BF. Temporal patterns of head and neck squamous cell carcinoma recurrence with positron-emission tomography/computed tomography monitoring. *Laryngoscope.* 2012;122:1512–1517.
35. El Fakhri G, Surti S, Trott CM, Scheuermann J, Karp JS. Improvement in lesion detection with whole-body oncologic time-of-flight PET. *J Nucl Med.* 2011;52:347–353.
36. Surti S, Scheuermann J, El Fakhri G, et al. Impact of time-of-flight PET on whole-body oncologic studies: a human observer lesion detection and localization study. *J Nucl Med.* 2011;52:712–719.
37. van Sluis J, Boellaard R, Somasundaram A, et al. Image quality and semiquantitative measurements on the Biograph Vision PET/CT system: initial experiences and comparison with the Biograph mCT. *J Nucl Med.* 2020;61:129–135.
38. van Sluis J, Boellaard R, Dierckx RAJO, Stormezand GN, Glaudemans AWJM, Noordzij W. Image quality and activity optimization in oncologic ^{18}F-FDG PET using the digital Biograph Vision PET/CT system. *J Nucl Med.* 2020;61:764–771.
39. Akamatsu G, Mitsumoto K, Ishikawa K, et al. Benefits of point-spread function and time of flight for PET/CT image quality in relation to the body mass index and injected dose. *Clin Nucl Med.* 2013;38:407–412.
40. Delcroix O, Bourhis D, Keromnes N, et al. Assessment of image quality and lesion detectability with digital PET/CT system. *Front Med (Lausanne).* 2021;8:629096.
41. Cacicedo J, Fernandez I, Del Hoyo O, et al. Should PET/CT be implemented in the routine imaging work-up of locally advanced head and neck squamous cell carcinoma? A prospective analysis. *Eur J Nucl Med Mol Imaging.* 2015;42:1378–1389.
42. Leclère J-C, Delcroix O, Rousset J, et al. Integration of ^{18}FDG PET/CT in the initial work-up to stage head and neck cancer: prognostic significance and impact on therapeutic decision making. *Front Med (Lausanne).* 2020;7:273.
43. Rohde M, Nielsen AL, Pareek M, et al. A PET/CT-based strategy is a stronger predictor of survival than a standard imaging strategy in patients with head and neck squamous cell carcinoma. *J Nucl Med.* 2018;59:575–581.
44. Kyzas PA, Evangelou E, Denaxa-Kyza D, Ioannidis JPA. ^{18}F-fluorodeoxyglucose positron emission tomography to evaluate cervical node metastases in patients with head and neck squamous cell carcinoma: a meta-analysis. *J Natl Cancer Inst.* 2008;100:712–720.
45. Bulbul MG, Genovese TJ, Hagan K, Rege S, Qureshi A, Varvares MA. Salvage surgery for recurrent squamous cell carcinoma of the head and neck: systematic review and meta-analysis. *Head Neck.* 2022;44:275–285.
46. You H, Subramaniam RM. PET/computed tomography: post-therapy follow-up in head and neck cancer. *PET Clin.* 2022;17:319–326.
47. Antoch G, Freudenberg LS, Beyer T, Bockisch A, Debatin JF. To enhance or not to enhance? ^{18}F-FDG and CT contrast agents in dual-modality ^{18}F-FDG PET/CT. *J Nucl Med.* 2004;45(suppl 1):S56–S65.
48. Haerle SK, Strobel K, Ahmad N, Soltermann A, Schmid DT, Stoeckli SJ. Contrast-enhanced ^{18}F-FDG-PET/CT for the assessment of necrotic lymph node metastases. *Head Neck.* 2011;33:324–329.
49. Suenaga Y, Kitajima K, Ishihara T, et al. FDG-PET/contrast-enhanced CT as a post-treatment tool in head and neck squamous cell carcinoma: comparison with FDG-PET/non-contrast-enhanced CT and contrast-enhanced CT. *Eur Radiol.* 2016;26:1018–1030.
50. Awan MJ, Lavertu P, Zender C, et al. Post-treatment PET/CT and p16 status for predicting treatment outcomes in locally advanced head and neck cancer after definitive radiation. *Eur J Nucl Med Mol Imaging.* 2017;44:988–997.

Fibroblast Activation Protein–Directed Imaging Outperforms ^{18}F-FDG PET/CT in Malignant Mesothelioma: A Prospective, Single-Center, Observational Trial

Lukas Kessler[1–3], Felix Schwaning[1,3], Martin Metzenmacher[3,4], Kim Pabst[1,3], Jens Siveke[4–7], Marija Trajkovic-Arsic[5–7], Benedikt Schaarschmidt[2], Marcel Wiesweg[3,4], Clemens Aigner[8,9], Till Plönes[7,8,10,11], Kaid Darwiche[12], Servet Bölükbas[8], Martin Stuschke[13], Lale Umutlu[2], Michael Nader[1,3], Dirk Theegarten[14], Rainer Hamacher[3,4], Wilfried E.E. Eberhardt[3,15], Martin Schuler[3,4], Ken Herrmann[1,3], Wolfgang P. Fendler[1,3], and Hubertus Hautzel[1,3]

[1]Department of Nuclear Medicine, West German Cancer Center, University Hospital Essen, University of Duisburg–Essen, Essen, Germany; [2]Institute of Diagnostic and Interventional Radiology and Neuroradiology, West German Cancer Center, University Hospital Essen, University of Duisburg–Essen, Essen, Germany; [3]German Cancer Consortium, Partner Site Essen, Essen, Germany; [4]Department of Medical Oncology, West German Cancer Center, University Hospital Essen, University of Duisburg–Essen, Essen, Germany; [5]Bridge Institute of Experimental Tumor Therapy, West German Cancer Center, University Hospital Essen, Essen, Germany; [6]Division of Solid Tumor Translational Oncology, German Cancer Consortium, Partner Site Essen, Essen, Germany; [7]German Cancer Research Center, Heidelberg, Germany; [8]Department of Thoracic Surgery and Thoracic Endoscopy, West German Cancer Center, University Hospital Essen, University of Duisburg–Essen, Essen, Germany; [9]Department of Thoracic Surgery, Medical University of Vienna, Vienna, Austria; [10]Division of Thoracic Surgery, Department of Visceral, Thoracic, and Vascular Surgery, University Hospital Carl Gustav Carus, Technische Universität Dresden, Dresden, Germany; [11]National Center for Tumor Diseases, Dresden, Germany; Faculty of Medicine and University Hospital Carl Gustav Carus, Technische Universität Dresden, Dresden, Germany; and Helmholtz-Zentrum Dresden–Rossendorf, Dresden, Germany; [12]Department of Pulmonary Medicine, Section of Interventional Pulmonology, West German Cancer Center, University Hospital Essen, University of Duisburg–Essen, Essen, Germany; [13]Department of Radiotherapy, West German Cancer Center, University Hospital Essen, University of Duisburg–Essen, Essen, Germany; [14]Institute of Pathology, University Hospital Essen, University of Duisburg–Essen, Essen, Germany; and [15]Division of Thoracic Oncology, West German Cancer Center, University Hospital Essen, University of Duisburg–Essen, Essen, Germany

The fibroblast activation protein (FAP) is highly expressed in tumor and stromal cells of mesothelioma and thus is an interesting imaging and therapeutic target. Previous data on PET imaging with radiolabeled FAP inhibitors (FAPIs) suggest high potential for superior tumor detection. Here, we report the data of a large malignant pleural mesothelioma cohort within a ^{68}Ga-FAPI46 PET observational trial (NCT04571086). **Methods:** Of 43 eligible patients with suspected or proven malignant mesothelioma, 41 could be included in the data analysis of the ^{68}Ga-FAPI46 PET observational trial. All patients underwent ^{68}Ga-FAPI46 PET/CT, contrast-enhanced CT, and ^{18}F-FDG PET/CT. The primary study endpoint was the association of ^{68}Ga-FAPI46 PET uptake intensity and histopathologic FAP expression. Furthermore, secondary endpoints were detection rate and sensitivity, specificity, and positive and negative predictive values as compared with ^{18}F-FDG PET/CT. Datasets were interpreted by 2 masked readers. **Results:** The primary endpoint was met, and the association between ^{68}Ga-FAPI46 SUV_{max} or SUV_{peak} and histopathologic FAP expression was significant (SUV_{max}: $r = 0.49$, $P = 0.037$; SUV_{peak}: $r = 0.51$, $P = 0.030$).^{68}Ga-FAPI46 and ^{18}F-FDG showed similar sensitivity by histopathologic validation on a per-patient (100.0% vs. 97.3%) and per region (98.0% vs. 95.9%) basis. Per-region analysis revealed higher ^{68}Ga-FAPI46 than ^{18}F-FDG specificity (81.1% vs. 36.8%) and positive predictive value (87.5% vs. 66.2%). **Conclusion:** We confirm an association of ^{68}Ga-FAPI46 uptake and histopathologic FAP expression in mesothelioma patients. Additionally, we report high sensitivity and superior specificity and positive predictive value for ^{68}Ga-FAPI46 versus ^{18}F-FDG.

Key Words: mesothelioma; cancer imaging; FAPI; fibroblast activation protein; thoracic cancer

J Nucl Med 2024; 65:1188–1193
DOI: 10.2967/jnumed.124.267473

Malignant mesothelioma is a relatively rare solid malignancy of soft tissue, most frequently affecting the pleura, and is associated with poor survival (*1*). Because of late detection, mesotheliomas are often diagnosed in unresectable, advanced stages, emphasizing the need for accurate imaging methods to identify suspected lesions (*2*). In recent years, the fibroblast activation protein (FAP) has become an interesting target for novel molecular probes because of its high expression in tumor cells of mesenchymal origin and in carcinoma-associated fibroblasts in stromal tissue of various solid tumors (*3,4*). Carcinoma-associated fibroblasts influence tumor cells by producing mediators and can promote tumor angiogenesis, migration, and proliferation (*5*), and FAP overexpression in solid tumors has been linked with poor outcome and is distinctively overexpressed in tumor tissue compared with normal tissue (*4*). Especially, mesothelioma has been shown to highly express FAP on tumor tissue in all histopathologic subtypes (*3*). Therefore, FAP-targeted therapies are of interest for future

---

Received Jan. 21, 2024; revision accepted May 22, 2024.

For correspondence or reprints, contact Lukas Kessler (lukas.kessler@uk-essen.de).

treatments, and experimental and phase I clinical trials for anti-FAP CAR T-cell therapy have already been evaluated (*6,7*). In terms of diagnostic approaches, imaging is still focused on radiologic examinations such as contrast-enhanced CT (Ce-CT), MRI, and ^{18}F-FDG PET, but novel FAP-targeted radiotracers have shown promising tumor uptake in mesothelioma patients (*8–10*).

In 2018, novel FAP-targeted radiotracers were introduced for diagnostic and therapeutic purposes and showed promising diagnostic value for multiple entities, including mesenchymal cancers such as malignant pleural mesothelioma, but have not been investigated in depth (*11,12*).

We initiated a prospective, single-center, observational FAP inhibitor (FAPI) PET trial to investigate the association of histopathologic FAP expression and ^{68}Ga-FAPI46 PET uptake intensity in various tumor entities (*13*). We further aimed to analyze the ^{68}Ga-FAPI46 PET/CT sensitivity, specificity, positive and negative predictive values, and detection rates of this new methodology in comparison to established imaging modalities (^{18}F-FDG PET/CT and Ce-CT).

MATERIALS AND METHODS

Study Design and Patients

This was a subgroup analysis of an ongoing ^{68}Ga-FAPI46 PET observational trial (NCT04571086), and the detailed study protocol has been published before (*14,15*).

Briefly, adult patients scheduled for ^{68}Ga-FAPI46 PET/CT for staging or restaging of proven or suspected mesothelioma as part of clinical workup or routine were enrolled and underwent follow-up prospectively for at least 6 mo after enrollment. In that period, available histopathology specimens, images (CT, MRI, PET/CT, etc.), change-of-management questionnaires, and other clinical data were collected and then analyzed. Correlation of ^{68}Ga-FAPI46 uptake intensity and histopathologic FAP expression was defined as the primary endpoint (Spearman correlation for ordinal data). Secondary endpoints were detection rate and sensitivity, specificity, positive predictive value (PPV), negative predictive value (NPV), and accuracy confirmed by histopathology per patient and per region or by a composite reference standard (pathology and imaging-based lesion follow-up).

The study was initiated, planned, conducted, analyzed, and published by the Department of Nuclear Medicine of University Hospital Essen. No financial support was received from commercial entities. All reported investigations were conducted in accordance with the Declaration of Helsinki and with national regulations. This observational trial was registered on clinicaltrails.gov (NCT04571086) and approved by the local Ethics Committee (permits 19-8991-BO and 20-9485-BO). All patients provided their informed consent.

Figure 1 illustrates the patient flow and the inclusion and exclusion of patients and respective cohorts for the respective endpoints (Fig. 1).

Imaging and Image Analysis

PET scans were performed in the craniocaudal direction on a Vereos (Philips), Biograph mCT (Siemens Healthineers), or Biograph mCT VISION (Siemens Healthineers) device. All ^{68}Ga-FAPI46 PET scans were performed as PET/CT (including low-dose CT). The mean injected activity of ^{68}Ga-FAPI46 was 124 ± 32 MBq, and that of ^{18}F-FDG was 260 ± 71 MBq. ^{68}Ga-FAPI46 PET/CT images were acquired approximately 10–60 min (mean, 24 ± 19 min) after injection, and ^{18}F-FDG PET/CT images were acquired approximately 60 min (mean 74 ± 19 min) after injection. Diagnostic Ce-CT (standard protocol: 80–100 mA, 120 kV with iodinated contrast medium), and ^{18}F-FDG PET/CT images were available for all enrolled patients and were included in the image analysis if performed within 2 wk of ^{68}Ga-FAPI46 PET/CT and no relevant therapeutic changes occurred in that time frame (e.g., surgery, chemotherapy, or radiation).

For image analysis, tumor regions were defined as local (pleura), locoregional lymph nodes, and metastatic lesions, as previously published (*14*). For each scan, the number of lesions per region and per patient and the size and uptake of the lesion with the highest uptake were recorded. Any focal uptake higher than the surrounding background and not physiologic was considered suggestive of malignancy. SUVs (i.e., SUV_{max} and SUV_{peak}) were measured with a region-growing algorithm with a threshold of 40% of the maximal uptake (Syngo.via software; Siemens Healthcare) for the lesion with the highest uptake in the respective tumor region. Images were reported independently by 2 masked expert readers (experience with >500 ^{68}Ga-FAPI46 PET/CT scans, >1,000 ^{18}F-FDG PET/CT scans, and >2,000 Ce-CT scans). Readers were aware of previous surgeries. Divergent findings were discussed and reported in a separate consensus session between readers.

Lesion Detection and Validation

The detection rate was defined as the number and proportion of patients with PET-positive results overall, per region, and per patient, independently of the reference standard or validation (*16*). On CT imaging, lesions were defined according to RECIST 1.1 and mRECIST 1.1 for pleural mesothelioma (e.g., organ lesions > 10 mm; lymph nodes > 15 mm in the short-axis dimension).

Patients were subjected to histopathologic examination and, when feasible, FAP immunohistochemistry for subsequent evaluation. Lesions and tumor regions were validated either by available histopathology from surgeries or biopsies (e.g., endobronchial ultrasound–guided transbronchial fine-needle aspiration) within a 4-wk period of ^{68}Ga-FAPI46 PET or a composite reference standard that combined histopathology and available imaging follow-up (e.g., time point

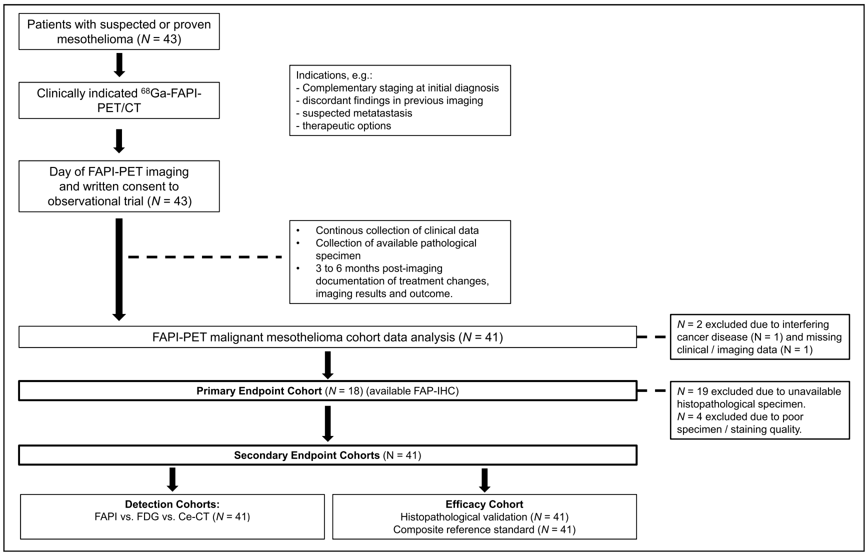

FIGURE 1. Enrollment flowchart. IHC = immunohistochemistry.

response, progression, or cross validation). Validation was performed by local investigators, adhering to the study protocol criteria and relying on images and reports. Lesions were validated for ^{68}Ga-FAPI46 PET/CT and ^{18}F-FDG PET/CT separately.

Immunohistochemistry

Available histopathologic specimen were stained with standard hematoxylin and eosin and for FAP immunohistochemistry and evaluated as previously described (*14,17*). In short, immunohistochemistry samples were visually and semiquantitatively scored as 0 (negative), 1 (1%–10% FAP-positive cells), 2 (11%–50% FAP-positive cells), or 3 (>50% FAP-positive cells).

Statistical Analysis

PET uptake and tissue FAP expression were compared by Pearson correlation for continuous data and Spearman correlation for ordinal data. In addition, uptake and expression data were compared descriptively for each score, uptake, or expression range. Sensitivity, specificity, PPV, NPV, and accuracy on a per-patient and per-region basis for ^{68}Ga-FAPI46 PET and ^{18}F-FDG PET detection of tumor location as confirmed by histopathology, biopsy, or the composite reference standard were calculated and reported along with the corresponding 2-sided 95% CIs. To compare the frequency of detected lesions, contingency testing using the Fisher exact test or χ^2 test was used. The CIs were constructed using the Wilson score method. Uptake measurements of tumor regions were tested for statistical differences using the nonparametric Mann–Whitney *U* test. All statistical analyses were performed using SSPS software (version 28.0; IBM) or Prism (version 9.1.1; GraphPad Software).

RESULTS

Patient Characteristics

From April 2020 till August 2023, 43 patients with suspected or proven malignant mesothelioma were enrolled in the ^{68}Ga-FAPI46 PET observational trial, of whom 41 were included in the analysis (2 were excluded because of additional cancer disease or missing clinical data) (Fig. 1). For all patients, ^{18}F-FDG PET/CT and Ce-CT were available within 14 d of ^{68}Ga-FAPI46 PET/CT. In no patient was a therapeutic change made in the interval between ^{68}Ga-FAPI46, ^{18}F-FDG, and Ce-CT. Table 1 details the clinical characteristics of the included patients. No adverse events were reported.

TABLE 1
Patient Characteristics ($n = 41$)

Characteristic	Data
Age (y)	
Mean ± SD	71.8 ± 8.6
Median	73.0
Range	49.0–87.0
Sex	
Male	34 (82.9%)
Female	7 (17.1%)
Diagnosis	
Malignant pleural mesothelioma	35 (85.4%)
Malignant peritoneal mesothelioma	2 (4.9%)
Benign	4 (9.7%)
Histologic subtype mesothelioma	
Epitheloid	27 (72.9%)
Biphasic	4 (10.8%)
Sarcomatoid	4 (10.8%)
Pleomorphic	2 (5.4%)
UICC stage, initial	
IA	2 (4.8%)
IB	14 (34.1%)
II	5 (12.2%)
III	1 (2.4%)
IV	10 (24.4%)
Not applicable/missing	9 (22.0%)
Cancer risk factors	
Asbestosis/metal working	24 (58.5%)
Smoking	14 (34.1%)

UICC = Union for International Cancer Control.
Data are number, except for age.

Primary Endpoint: Correlation of ^{68}Ga-FAPI46 PET Uptake with FAP Expression

Histopathologic specimens of 22 patients were available for FAP immunohistopathology, of which 18 were of adequate quality for histopathologic evaluation and scoring. No negative immunohistochemistry was reported in this cohort (score 1, $n = 3$; score 2, $n = 9$; and score 3, $n = 6$); representative immunohistochemistry images are depicted in Figure 2A. ^{68}Ga-FAPI46 SUV$_{max}$ and SUV$_{peak}$ showed a moderate, significant linear relationship with the established immunohistochemical scoring system ($n = 18$) (SUV$_{max}$: $r = 0.49$, $P = 0.04$; SUV$_{peak}$: $r = 0.51$, $P = 0.03$) (Fig. 2B). ^{68}Ga-FAPI46 and ^{18}F-FDG showed comparably high uptake for all tumor regions (e.g., local SUV$_{max}$: 14.6 ± 8.8 for ^{68}Ga-FAPI46 vs. 12.4 ± 7.4 for ^{18}F-FDG), with a significant difference only in SUV$_{peak}$ for local tumor (^{68}Ga-FAPI46, 10.9 ± 6.3; ^{18}F-FDG SUV$_{peak}$, 8.1 ± 4.9; $P = 0.02$) (Supplemental Table 1; supplemental materials are available at http://jnm.snmjournals.org).

Secondary Endpoints: Diagnostic Performance

On a per-patient basis, validation by histopathology was possible in all 41 (100%) patients. Lesions were validated in 87 regions by histopathology and in 137 regions by the composite reference standard. The detailed diagnostic performance and CI on a per-patient and per-region basis are shown in Table 2. ^{68}Ga-FAPI46 and ^{18}F-FDG showed similar sensitivity by histopathologic validation on a per-patient (100.0% vs. 97.3%) and per-region (98.0% vs. 95.9%) basis. But per-region analysis revealed a distinct difference in diagnostic performance between ^{68}Ga-FAPI46 and ^{18}F-FDG, with higher specificity (81.1% vs. 36.8%) and PPV (87.5% vs. 66.2%) for ^{68}Ga-FAPI46 by histopathologic validation. Further validation by the composite reference standard showed excellent performance for ^{68}Ga-FAPI46 on a per-region basis in all 4 parameters (sensitivity, 96.6%; specificity, 90.3%; PPV, 90.0%; and NPV, 97.1%) compared with ^{18}F-FDG (sensitivity, 92.2%; specificity, 57.5%; PPV, 65.6%; and NPV, 89.4%). Regardless of the type of validation, ^{68}Ga-FAPI46 showed better diagnostic accuracy than ^{18}F-FDG (Table 2) and especially higher specificity and PPVs. This result is explained by more false-positive regions (^{68}Ga-FAPI46, $n = 7$, vs. ^{18}F-FDG, $n = 31$) and false-negative regions (^{68}Ga-FAPI46, $n = 2$, vs. ^{18}F-FDG, $n = 5$) for ^{18}F-FDG.

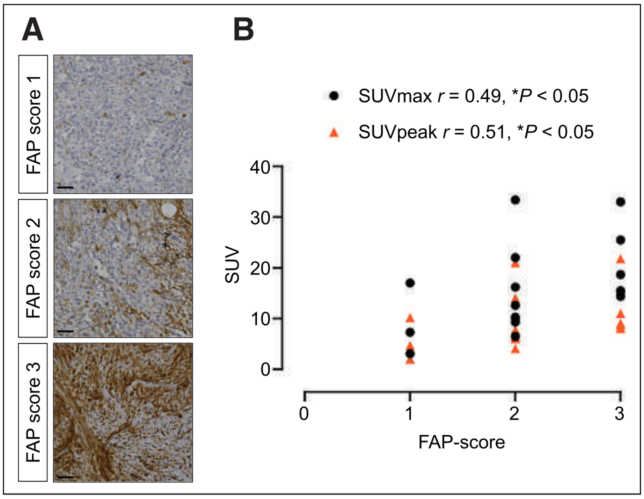

FIGURE 2. Primary endpoint. (A) DAB immunohistochemical staining of FAP-α in pleural mesothelioma specimen and respective positive scores. No negative sample was reported in this cohort. (B) Spearman correlation shows moderate association between ^{68}Ga-FAPI46 PET uptake intensity and FAP immunohistochemistry score for available malignant pleural mesothelioma specimen (n = 18) (SUV$_{\text{max}}$: $r = 0.49$, $P = 0.037$; SUV$_{\text{peak}}$: $r = 0.51$, $P = 0.030$).

Detection Rate

Detection rates for ^{68}Ga-FAPI46 versus ^{18}F-FDG versus Ce-CT ($n = 41$) are summarized in Table 3. Overall, 252 lesions were detected by any modalities combined. ^{18}F-FDG PET/CT had a significantly higher lesion detection rate than ^{68}Ga-FAPI46 and Ce-CT (^{18}F-FDG [$n = 219$], 86.8%, vs. ^{68}Ga-FAPI46 [$n = 144$], 57.1%, vs. Ce-CT [$n = 128$], 50.8%; $P < 0.0001$). No significant difference in detection was observed on a per-patient ($P = 0.3$) or per-region ($P = 0.06$) basis. But especially in the local nodal region, more PET-positive results were reported for ^{18}F-FDG (^{18}F-FDG [$n = 27$], 65.9%, vs. ^{68}Ga-FAPI46 [$n = 13$], 31.7%, vs. Ce-CT [$n = 21$], 51.2%) but with a large proportion of false-positive results for ^{18}F-FDG (i.e., ^{18}F-FDG, 31/137 false-positive results; ^{68}Ga-FAPI46, 7/137 false-positive results). Figure 3 shows a case example of discordant imaging findings, with false-positive mediastinal lymph nodes on ^{18}F-FDG. Endobronchial ultrasound–guided transbronchial fine-needle aspiration ruled out metastatic lymph nodes and diagnosed nodal anthracosis.

DISCUSSION

We established this single-center, prospective, observational trial to investigate the diagnostic value of novel FAP-targeted radioligands and to explore the relationship between ^{68}Ga-FAPI46 uptake and FAP expression levels. Furthermore, we report on the diagnostic performance of ^{68}Ga-FAPI46 in a large group of mesothelioma patients for, what is to our knowledge, the first time.

In line with findings for other tumor entities, we found a moderate association of ^{68}Ga-FAPI46 uptake with immunohistochemical FAP expression, proving our hypothesis that ^{68}Ga-FAPI46 PET is a noninvasive tool for FAP measurement in malignant mesothelioma. Measuring FAP expression is a prerequisite for FAP-targeted treatment, and our results therefore indicate that ^{68}Ga-FAPI46 PET is a suitable tool for noninvasive measurement. Theranostic approaches with ^{68}Ga- and ^{177}Lu-/^{90}Y-FAPI have not, to our knowledge, been investigated in mesothelioma patients but could

TABLE 2
Diagnostic Performance of ^{68}Ga-FAPI46 PET and ^{18}F-FDG PET Compared with Confirmed Reference Validation

Basis	Modality	Reference	Sensitivity	Specificity	PPV	NPV	Accuracy
Per patient	^{68}Ga-FAPI46	Histopathology	100.0 (90.6–100.0)	25.0 (1.3–69.9)	92.5 (80.1–97.4)	100.0 (5.2–100.0)	92.7 (80.1–98.5)
	^{18}F-FDG	Histopathology	97.3 (86.2–99.9)	50.0 (8.9–91.1)	94.7 (82.7–99.1)	66.7 (11.9–98.3)	92.3 (79.1–98.4)
Per region	^{68}Ga-FAPI46	Histopathology	98.0 (89.5–99.9)	81.1 (65.8–90.5)	87.5 (76.4–93.8)	96.8 (83.8–99.8)	90.8 (82.7–96.0)
		Composite standard	96.9 (89.5–99.5)	90.3 (81.3–95.2)	90.0 (81.0–95.1)	97.1 (89.8–99.5)	93.4 (87.9–97.0)
	^{18}F-FDG	Histopathology	95.9 (86.3–99.3)	36.8 (23.4–52.7)	66.2 (54.6–76.1)	87.5 (64.0–97.8)	70.11 (59.4–79.5)

Data in parentheses are 95% CI.

TABLE 3
Detection Rates Compared for ^{68}Ga-FAPI46 vs. Ce-CT vs. ^{18}F-FDG

	PET-positive results or CT lesions			
Parameter	^{68}Ga-FAPI46	Ce-CT	^{18}F-FDG	P (χ^2)
Total lesions (n = 252)	144 (57.1)	128 (50.8)	219 (86.8)	0.0001
Per-patient basis (n = 41)	40 (97.6)	39 (95.1)	39 (95.1)	0.3
Per-region basis (n = 123)	69 (71.9)	79 (82.3)	87 (90.6)	0.06
Primary	40 (97.6)	39 (95.1)	38 (92.7)	
Local nodal	13 (31.7)	21 (51.2)	27 (65.9)	
Metastatic	16 (39.0)	19 (46.3)	22 (53.7)	

Data are number, with percentage in parentheses.

enable novel cancer treatment strategies targeting both tumor cells and the microenvironment simultaneously in other mesenchymal tumor entities (*18,19*).

However, the degree of correlation of immunohistochemical FAP expression and ^{68}Ga-FAPI46 PET signal may be constrained by factors such as specimen heterogeneity and the limited sample size in this study. Consequently, our findings must be interpreted with caution. Aside from that, we demonstrated ^{68}Ga-FAPI46 PET/CT to have high diagnostic performance by histopathologic and composite reference validation. Sensitivity was similar for ^{68}Ga-FAPI46 and ^{18}F-FDG PET. However, ^{68}Ga-FAPI46 showed substantially higher specificity and PPV than did ^{18}F-FDG (e.g., sensitivity of 90.3% vs. 57.5% and PPV of 90.0% vs. 65.6%). Possible reasons for this discrepancy are reactive lymph nodes, anthracosis, or inflammation, which results in false-positive findings on ^{18}F-FDG PET/CT (*20*). These are known general pitfalls in ^{18}F-FDG PET, with, however, high relevance in patients with mesothelioma, who often have other underlying inflammatory disease such as asbestosis or other pneumoconiosis (*21,22*). Independently of validation and reference standard, ^{18}F-FDG had higher detection rates with an overall mediocre specificity, PPV, and NPV, which reflects these findings. In this setting, ^{68}Ga-FAPI46 PET/CT provides better discrimination between unspecific or reactive processes and actual tumor manifestations. Chronic inflammation accompanying fibrotic or granulomatous changes might demonstrate increased FAPI accumulation (*20,23,24*). However, in the context of malignant mesothelioma, inflammation-induced microscopic fibrotic changes in lymph nodes might be too subtle to produce relevant FAPI uptake.

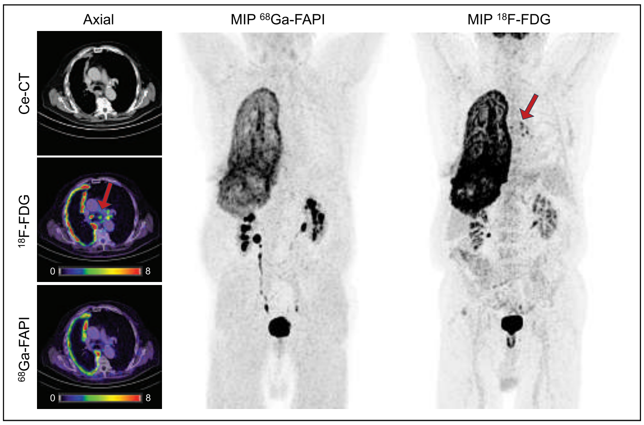

FIGURE 3. Male patient with suspected pleural mesothelioma before surgical biopsy. Ce-CT shows pleural mass and nodular thickening of left pleura with no morphologic signs of local nodal involvement (lymph nodes < 10 mm). ^{18}F-FDG shows high circular uptake in pleura (SUV_{max}, 11.4) and additionally positive lymph nodes (SUV_{max}, 5.5) in levels 4 R/L, 5, 7, and 10 L (red arrows), whereas ^{68}Ga-FAPI46 shows only high uptake in pleura (SUV_{max}, 8.7). Thoracic lymph node levels are determined by International Associate for the Study of Lung Cancer. R = right; L = left. Endobronchial ultrasound–guided transbronchial fine-needle aspiration ruled out metastatic diseases of respective lymph node levels and revealed nodal anthracosis. MIP = maximum-intensity projection.

Because of the variety of common histopathologic subtypes of mesothelioma, different tracers might prove beneficial for selected subtypes. Studies suggest lower ^{18}F-FDG uptake in epitheloid and nonpleomorphic mesothelioma, but differences in diagnostic performance have not been established so far. A recent study suggested a significantly higher SUV_{max} for ^{68}Ga-FAPI than for ^{18}F-FDG—a finding that could only partially be verified in our cohort (*25*). Still, there are no reliable data comparing imaging tracers by subtype, a comparison that appears challenging because of the rarity of some subtypes.

This trial was limited by its observational, single-center character and by a recruited cohort that reflects a real-life patient population rather than a controlled and randomized study population. Accordingly, some patients were pretreated, and specimens for histopathologic evaluation could not be acquired in all cases. Furthermore, a minority of patients underwent follow-up imaging or treatment elsewhere. Nonetheless, the ^{68}Ga-FAPI46 PET data show robust high diagnostic performance as compared with histopathologic and composite reference validation. Although Ce-CT remains the proposed standard imaging method, the superior diagnostic efficacy of ^{18}F-FDG for mesothelioma led us to select it as the primary comparator for ^{68}Ga-FAPI46 (*26*). In this cohort, we investigated the detection rates of only Ce-CT and ^{68}Ga-FAPI46, but future investigations should also assess the advantages over conventional imaging methods.

CONCLUSION

This prospective observational study demonstrated an association between target FAP expression levels and ^{68}Ga-FAPI46 uptake. ^{68}Ga-FAPI46 PET for mesothelioma imaging revealed specificity and PPV higher than—as well as sensitivity similar to—that of ^{18}F-FDG PET. ^{68}Ga-FAPI46 PET is a valuable diagnostic tool in patients with mesothelioma. The therapeutic potential of radiolabeled FAPIs should be investigated in the future.

DISCLOSURE

Hubertus Hautzel receives personal fees from Roche and Urenco and other fees from Pari, Roche, and Urenco outside the submitted work. Wolfgang Fendler reports fees from SOFIE Biosciences (research funding), Janssen (consultant, speaker), Calyx (consultant, image review), Bayer (consultant, speaker, research funding), Novartis (speaker, consultant), Telix (speaker), GE Healthcare (speaker), Eczacıbaşı Monrol (speaker), Abx (speaker), Amgen (speaker), and Urotrials (speaker) outside the submitted work. Kim Pabst received fees from Bayer (research funding) and Novartis (speakers' bureau) and travel fees from IPSEN and has received a Clinician Scientist Stipend from the University Medicine Essen Clinician Scientist Academy (UMEA) sponsored by the faculty of medicine and Deutsche Forschungsgemeinschaft (DFG) outside the submitted work. Benedikt Schaarschmidt has received a research grant from the Deutsche Forschungsgemeinschaft for an ongoing investigator-initiated study not related to this work, as well as research grants from PharmaCept and the Else Kröner-Fresenius Foundation for a past investigator-initiated study not related to this work. Benedikt Schaarschmidt has received speaker fees from AstraZeneca and a travel grant from Bayer AG. Ken Herrmann reports personal fees from Bayer, personal fees and other fees from SOFIE Biosciences, personal fees from SIRTEX, nonfinancial support from ABX, personal fees from Adacap, personal fees from Curium, personal fees from Endocyte, grants and personal fees from BTG, personal fees from IPSEN, personal fees from Siemens Healthineers, personal fees from GE Healthcare, personal fees from Amgen, personal fees from Novartis, personal fees from ymabs, personal fees from Aktis Oncology, personal fees from Theragnostics, personal fees from Pharma15, personal fees from Debiopharm, personal fees from AstraZeneca, and personal fees from Janssen. Jens Siveke receives honoraria as a consultant or for continuing medical education presentations from AstraZeneca, Bayer, Boehringer Ingelheim, Bristol-Myers Squibb, Immunocore, MSD, Novartis, Roche/Genentech, and Servier. His institution receives research funding from Abalos Therapeutics, Boehringer Ingelheim, Bristol-Myers Squibb, Celgene, Eisbach Bio, and Roche/Genentech; he holds ownership and serves on the board of directors of Pharma15, all outside the submitted work. No other potential conflict of interest relevant to this article was reported.

KEY POINTS

QUESTION: Is there an association between FAPI uptake intensity and FAP expression in malignant mesothelioma, and what is the diagnostic performance of FAPI PET in mesothelioma patients?

PERTINENT FINDINGS: The SUV_{max} and SUV_{peak} of ^{68}Ga-FAPI46 were significantly associated with immunohistochemical FAP expression, and the overall diagnostic performance of ^{68}Ga-FAPI46 PET compared well with that of ^{18}F-FDG.

IMPLICATIONS FOR PATIENT CARE: We established the diagnostic utility of ^{68}Ga-FAPI46 PET in patients with malignant mesothelioma, with implications for FAP-targeted therapies.

REFERENCES

1. Neumann V, Löseke S, Nowak D, Herth FJF, Tannapfel A. Malignant pleural mesothelioma: incidence, etiology, diagnosis, treatment, and occupational health. *Dtsch Arztebl Int.* 2013;110:319–326.
2. Taralli S, Giancipoli RG, Caldarella C, et al. The prognostic value of 18f-fdg pet imaging at staging in patients with malignant pleural mesothelioma: A literature review. *J Clin Med.* 2021;11:33.
3. Schuberth PC, Hagedorn C, Jensen SM, et al. Treatment of malignant pleural mesothelioma by fibroblast activation protein-specific re-directed T cells. *J Transl Med.* 2013;11:187.
4. Liu F, Qi L, Liu B, et al. Fibroblast activation protein overexpression and clinical implications in solid tumors: A meta-analysis. *PLoS One.* 2015;10:e0116683.
5. Koczorowska MM, Tholen S, Bucher F, et al. Fibroblast activation protein-α, a stromal cell surface protease, shapes key features of cancer associated fibroblasts through proteome and degradome alterations. *Mol Oncol.* 2016;10:40–58.
6. Bughda R, Dimou P, D'Souza RR, Klampatsa A. Fibroblast Activation Protein (FAP)-Targeted CAR-T Cells: Launching an Attack on Tumor Stroma. *ImmunoTargets Ther.* 2021;10:313–323.
7. Klampatsa A, Albelda SM. Current Advances in CAR T Cell Therapy for Malignant Mesothelioma. *J Cell Immunol.* 2020;2:192–200.
8. Bianco A, Valente T, De Rimini ML, Sica G, Fiorelli A. Clinical diagnosis of malignant pleural mesothelioma. *J Thorac Dis.* 2018;10:S253–S261.
9. Schaarschmidt BM, Sawicki LM, Gomez B, et al. Malignant pleural mesothelioma: initial experience in integrated (18)F-FDG PET/MR imaging. *Clin Imaging.* 2016; 40:956–960.
10. Gündoğan C, Güzel Y, Kömek H, Etem H, Kaplan İ. ^{68}Ga-FAPI-04 PET/CT Versus ^{18}F-FDG PET/CT in Malignant Peritoneal Mesothelioma. *Clin Nucl Med.* 2022;47:e113–e115.
11. Lindner T, Loktev A, Altmann A, et al. Development of Quinoline-Based Theranostic Ligands for the Targeting of Fibroblast Activation Protein. *J Nucl Med.* 2018;59:1415–1422.
12. Loktev A, Lindner T, Mier W, et al. A Tumor-Imaging Method Targeting Cancer-Associated Fibroblasts. *J Nucl Med.* 2018;59:1423–1429.
13. Giesel FL, Kratochwil C, Lindner T, et al. 68 Ga-FAPI PET/CT: Biodistribution and Preliminary Dosimetry Estimate of 2 DOTA-Containing FAP-Targeting Agents in Patients with Various Cancers. *J Nucl Med.* 2019;60:386–392.
14. Kessler L, Ferdinandus J, Hirmas N, et al. 68 Ga-FAPI as a Diagnostic Tool in Sarcoma: Data from the 68 Ga-FAPI PET Prospective Observational Trial. *J Nucl Med.* 2022;63:89–95.
15. Pabst KM, Trajkovic-Arsic M, Cheung PFY, et al. Superior Tumor Detection for ^{68} Ga-FAPI-46 Versus ^{18} F-FDG PET/CT and Conventional CT in Patients with Cholangiocarcinoma. *J Nucl Med.* 2023;64:1049–1055.
16. Fendler WP, Calais J, Allen-Auerbach M, et al. ^{68}Ga-PSMA-11 PET/CT interobserver agreement for prostate cancer assessments: An international multicenter prospective study. *J Nucl Med.* 2017;58:1617–1623.
17. Henry LR, Lee HO, Lee JS, et al. Clinical implications of fibroblast activation protein in patients with colon cancer. *Clin Cancer Res.* 2007;13:1736–1741.
18. Fendler WP, Pabst KM, Kessler L, et al. Safety and Efficacy of ^{90}Y-FAPI-46 Radioligand Therapy in Patients with Advanced Sarcoma and Other Cancer Entities. *Clin Cancer Res.* 2022;28:4346–4353.
19. Ferdinandus J, Kessler L, Hirmas N, et al. Equivalent tumor detection for early and late FAPI-46 PET acquisition. *Eur J Nucl Med Mol Imaging.* 2021;48: 3221–3227.
20. Wang Y, Yang X, Tian M, Lv H, Liu H. Orbital Granulomatous Inflammation Mimicking Malignancy on ^{68}Ga-FAPI PET/CT. *Clin Nucl Med.* 2022;47:380–381.
21. Hewitt RJ, Wright C, Adeboyeku D, et al. Primary nodal anthracosis identified by EBUS-TBNA as a cause of FDG PET/CT positive mediastinal lymphadenopathy. *Respir Med Case Rep.* 2013;10:48–52.
22. Lee J, Kim YK, Seo YY, et al. Clinical Characteristics of False-Positive Lymph Node on Chest CT or PET-CT Confirmed by Endobronchial Ultrasound-Guided Transbronchial Needle Aspiration in Lung Cancer. *Tuberc Respir Dis (Seoul).* 2018;81:339–346.
23. Liu W, Gong W, Yang X, Xu T, Chen Y. Increased FAPI Activity in Pulmonary Tuberculosis. *Clin Nucl Med.* 2023;48:188–189.
24. Meetschen M, Sandach P, Darwiche K, et al. Rabbit fever: granulomatous inflammation by Francisella tularensis mimics lung cancer in dual tracer 18FDG and ^{68}Ga-FAPI PET/CT. *Eur J Nucl Med Mol Imaging.* 2023;50:2567–2569.
25. Güzel Y, Kömek H, Can C, et al. Comparison of the role of 18 F-fluorodeoxyglucose PET/computed tomography and 68 Ga-labeled FAP inhibitor-04 PET/CT in patients with malignant mesothelioma. *Nucl Med Commun.* 2023;44:631–639.
26. Nowak AK, Armato SG, Ceresoli GL, Yildirim H, Francis RJ. Imaging in pleural mesothelioma: A review of Imaging Research Presented at the 9th International Meeting of the International Mesothelioma Interest Group. *Lung Cancer.* 2010;70: 1–6.

Prognostic Value of ^{18}F-FDG PET/CT Assessment After Radiotherapy of Squamous Cell Carcinoma of the Anus in Patients from the National Multicentric Cohort FFCD-ANABASE

Virginie Combet-Curt[1], Chloé Buchalet[2], Karine Le Malicot[3], Claire Lemanski[2], Emmanuel Deshayes[4], Nathalie Bonichon-Lamichhane[5], Astrid Lièvre[6], Florence Huguet[7], Ghoufrane Tlili[8], and Véronique Vendrely[1]

[1]Radiotherapy, CHU Bordeaux, Bordeaux, France; [2]Radiotherapy, ICM–Montpellier, Montpellier, France; [3]Biostatistics, University of Burgundy, FFCD, Dijon, France; [4]Nuclear Medicine, ICM–Montpellier, Montpellier, France; [5]Radiotherapy, Clinique Bordeaux Tivoli-Ducos, Bordeaux, France; [6]Hepatogastroenterology Department, CHU Rennes, Rennes, France; [7]Radiotherapy, Hôpital Tenon AP-HP, Paris, France; and [8]Nuclear Medicine, CHU Bordeaux, Bordeaux, France

This study aimed to evaluate the prognostic value of ^{18}F-FDG PET/CT qualitative assessment in terms of recurrence-free survival (RFS), colostomy-free survival (CFS), and overall survival (OS) after radiation therapy (RT) of squamous cell carcinoma of the anus (SCCA). Secondary objectives were to evaluate the prognostic value of baseline and posttherapeutic quantitative ^{18}F-FDG PET/CT parameters in terms of RFS, CFS, and OS. **Methods:** We included all consecutive patients from the French multicentric cohort FFCD-ANABASE who had undergone ^{18}F-FDG PET/CT at baseline and 4–6 mo after RT or chemoradiotherapy for a localized SCCA. Qualitative assessments separated patients with complete metabolic response (CMR) and non-CMR. Quantitative parameters were measured on baseline and posttreatment ^{18}F-FDG PET/CT. RFS, CFS, and OS were analyzed using the Kaplan–Meier method. Associations among qualitative assessments, quantitative parameters, and RFS, CFS, and OS were analyzed using univariate and multivariate Cox regression. **Results:** Among 1,015 patients treated between January 2015 and April 2020, 388 patients (300 women and 88 men) from 36 centers had undergone ^{18}F-FDG PET/CT at diagnosis and after treatment. The median age was 65 y (range, 32–90 y); 147 patients (37.9%) had an early-stage tumor and 241 patients (62.1%) had a locally advanced-stage tumor; 59 patients (15.2%) received RT, and 329 (84.8%) received chemoradiotherapy. The median follow-up was 35.5 mo (95% CI, 32.8–36.6 mo). Patients with CMR had better 3-y RFS, CFS, and OS, at 84.2% (95% CI, 77.8%–88.9%), 84.7% (95% CI, 77.2%–89.3%), and 88.6% (95% CI, 82.5%–92.7%), respectively, than did non-CMR patients, at 42.1% (95% CI, 33.4%–50.6%), 47.9% (95% CI, 38.1%–56.8%), and 63.5 (95% CI, 53.2%–72.1%), respectively ($P < 0.0001$). Quantitative parameters were available for 154 patients from 3 centers. The following parameters were statistically significantly associated with 3-y RFS: baseline SUV_{max} (primitive tumor [T]) (hazard ratio [HR], 1.05 [95% CI, 1.01–1.1; $P = 0.018$]), SUV_{peak} (T) (HR, 1.09 [95% CI, 1.02–1.15; $P = 0.007$]), MTV 41% (T) (HR, 1.02 [95% CI, 1–1.03; $P = 0.023$]), MTV 41% (lymph node [N]) (HR, 1.06 [95% CI, 1.03–1.1; $P < 0.001$]), MTV 41% (T + N) (HR, 1.02 [95% CI, 1–1.03; $P = 0.005$]), and posttreatment SUV_{max} (HR, 1.21 [95% CI, 1.09–1.34; $P < 0.001$]). **Conclusion:** Treatment response assessed by ^{18}F-FDG PET/CT after RT for SCCA has a significant prognostic value. ^{18}F-FDG PET/CT could be useful for adapting follow-up, especially for patients with locally advanced-stage tumors. Quantitative parameters could permit identification of patients with a worse prognosis but should be evaluated in further trials.

Key Words: anal cancer; squamous cell carcinoma of the anus; chemoradiotherapy; ^{18}F-FDG PET/CT; PET

J Nucl Med 2024; 65:1194–1201
DOI: 10.2967/jnumed.124.267626

Squamous cell carcinoma of the anus (SCCA) is considered a rare tumor, accounting for about 2,000 new cases per year in France (*1*). Its incidence is rising, but the age at diagnosis is decreasing, allowing for an earlier diagnosis, mostly at a localized stage. Only 5% of cases are diagnosed at a metastatic stage (*2*).

The standard of care for patients with localized disease is radiation therapy (RT) associated with chemotherapy, including mitomycin C and 5-fluorouracil with curative intent (*3*). Surgery is a salvage treatment in cases of locoregional relapse.

^{18}F-FDG PET/CT is recommended for the initial staging of SCCA in the French guidelines (*4*,*5*) and is considered an option by the European Society of Medical Oncology (*6*). Indeed, prospective and retrospective studies have shown good performance for ^{18}F-FDG PET/CT, especially in lymph node staging (*7*,*8*), modifying the TNM classification in 15%–40% of cases (*9*,*10*). Thus, identifying pathologic lymph nodes can modify the RT plan and can be useful for target volume delineation (*11*,*12*). Moreover, some metabolic parameters measured by baseline ^{18}F-FDG PET/CT, such as metabolic tumor volume (MTV) or total lesion glycolysis (TLG), could have prognostic value (*13–16*). Studying these parameters could allow identification of patients with a high risk of relapse or treatment failure. During follow-up after treatment, the role of ^{18}F-FDG PET/CT is not clearly defined. ^{18}F-FDG PET/CT is recommended when relapse is suspected (*4*) but could also be useful to assess treatment response.

This study aimed to evaluate the prognostic value of ^{18}F-FDG PET/CT assessment in terms of recurrence-free survival (RFS), colostomy-free survival (CFS), and overall survival (OS) after RT of SCCA. We studied the prognostic value of qualitative response on ^{18}F-FDG PET/CT performed 4–6 mo after RT or chemoradiotherapy,

---

Received Feb. 20, 2024; revision accepted May 28, 2024.

For correspondence or reprints, contact Virginie Combet-Curt (virginie.combet-curt@chu-bordeaux.fr).

and we identified prognostic factors among quantitative parameters measured on ^{18}F-FDG PET/CT.

MATERIALS AND METHODS

Patients treated for SCCA between January 2015 and April 2020 were included in the cohort for French Federation of Digestive Oncology (FFCD)-ANABASE, which is a prospective multicentric observational study conducted by the FFCD. This study aimed to evaluate clinical practice, treatments, and oncologic outcomes for SCCA in France, and the main results have been published (*17*). The ethics committee (CCTIRS-15.698) and the Commission National de l'Informatique et des Libertés (authorization 915622) approved this retrospective study, and the requirement to obtain written informed consent was waived. All patients received written information and provided oral informed consent.

Among the patients included in the FFCD-ANABASE cohort, we focused in this study on those who had undergone ^{18}F-FDG PET/CT at baseline and again at 4–6 mo after the end of RT or chemoradiotherapy. The main objectives were to evaluate the prognostic value of ^{18}F-FDG PET/CT qualitative response to treatment in terms of RFS, CFS, and OS. Secondary objectives were to identify prognostic factors among quantitative parameters measured on baseline and posttreatment ^{18}F-FDG PET/CT in terms of RFS, CFS, and OS.

Image Acquisition and Interpretation

The following data were collected prospectively and entered into the database by the physicians of each center: SUV_{max} and presence of significant ^{18}F-FDG uptake for baseline ^{18}F-FDG PET/CT, and SUV_{max} and global qualitative evaluation for posttreatment ^{18}F-FDG PET/CT.

A complete metabolic response (CMR) was defined as the visual absence of residual ^{18}F-FDG uptake or the presence of nonpathologic minimal residual uptake (left at the discretion of each nuclear medicine physician). A partial metabolic response was defined as any persistent pathologic uptake in the lesions visible on the baseline image. Stability was defined as findings similar to those on the baseline scan. Progressive disease was defined as an increase in uptake because of tumor growth or new pathologic uptake because of the development of a new site of disease.

Moreover, we decided to further analyze the ^{18}F-FDG PET/CT data of patients from 3 large inclusion centers accredited by European Association Research Ltd., which is an accreditation program developed in collaboration with the European Organization for Research and Treatment of Cancer with the aim of providing a common standard for harmonizing the acquisition and interpretation of PET/CT.

Quantitative ^{18}F-FDG PET/CT parameters were collected retrospectively by 2 pairs of physicians (an RT resident and a nuclear medicine senior) by reviewing the native ^{18}F-FDG PET/CT images. These parameters were measured using a volume of interest placed by the physicians over the primary tumor and each involved lymph node. SUV_{max} and SUV_{peak} were, respectively, defined as the maximum voxel intensity and the average SUV within a 1 cm^3 volume of interest centered on the hottest area of the tumor or lymph node. Metabolic tumor volume (MTV) 41% was defined as the hypermetabolic tissue volume with a cutoff greater than 41% of SUV_{max}. SUV_{mean} was defined as the mean of SUV of all voxels within the MTV.

The following data were collected on baseline ^{18}F-FDG PET/CT (where T indicates primitive tumor and N indicates lymph nodes): SUV_{max} (T), SUV_{peak} (T), SUV_{mean} (T), and MTV 41% (T). Total lesion glycolysis (TLG) (T) was calculated (SUV_{mean} [T] × MTV 41% [T]). MTV 41% (N) and SUV_{mean} (N) were collected for zero to 10 lymph nodes. TLG (N) was calculated for each lymph node (SUV_{mean} [N] × MTV 41% [N]). Sums were realized to obtain MTV 41% ([total] N), TLG ([total] N), MTV 41% (T + N), and TLG (T + N).

A quantitative evaluation was realized on posttreatment ^{18}F-FDG PET/CT with a measure of posttreatment SUV_{max}, allowing calculation of change in SUV_{max} ([pretreatment SUV_{max} − posttreatment SUV_{max}]/pretreatment SUV_{max} × 100).

Statistical Analysis

RFS was defined as the time between the start of treatment and the first recurrence or death (from any cause). CFS was defined as the time between the start of treatment and the first colostomy or death (from any cause). Alive patients without recurrence or colostomy were censored at the date of the last follow-up. OS was defined as the time between the start of treatment and death (from any cause). Alive patients were censored at the date of the last follow-up.

Descriptive analyses were performed for each ^{18}F-FDG PET/CT parameter. RFS, CFS, and OS were analyzed using the Kaplan–Meier method and described using medians with 2-sided 95% CIs. Log-rank tests were used to compare rates and event-time distributions with a 95% CI. Univariate and multivariate analyses were done to evaluate the association between qualitative response to treatment on ^{18}F-FDG PET/CT; other parameters linked to ^{18}F-FDG PET/CT and clinical parameters; and RFS, CFS, and OS using Cox proportional hazards regression reporting hazard ratios (HRs) and 95% CI. A receiver operating characteristic curve was used to determine a discriminative threshold value of posttreatment SUV_{max} in terms of RFS, CFS, and OS.

RESULTS

Patient Characteristics

Among 1,015 patients who received first-line RT or chemoradiotherapy for nonmetastatic SCCA between January 2015 and April 2020, 388 from 36 centers underwent ^{18}F-FDG PET/CT at baseline and 4–6 mo after treatment (Fig. 1). There were 88 (22.7%) men and 300 (77.3%) women. The median age was 64 y (range, 32–90 y). Patient and tumor characteristics are presented in Table 1.

Fifty-nine patients (15.2%) received RT, and 329 (84.8%) received chemoradiotherapy, with concurrent mitomycin-5-fluorouracil for 286 patients (86.9%) and cisplatin-5-fluorouracil for 14 patients (4.3%). The median RT dose was 60 Gy on the tumor volume and 45 Gy on the pelvis. Among patients previously described, 154 patients from 3 main recruiter centers had a secondary analysis with quantitative evaluation of baseline and posttreatment ^{18}F-FDG PET/CT.

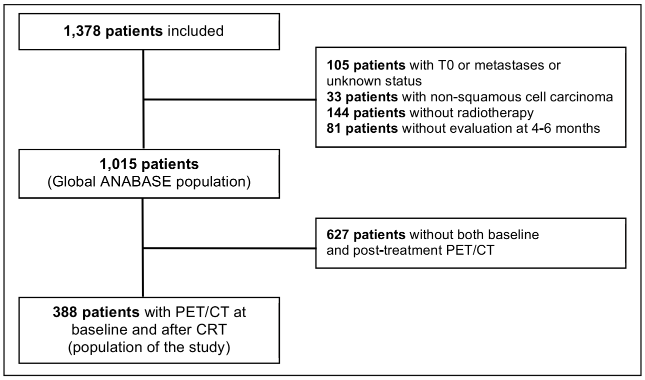

FIGURE 1. Flowchart. CRT = chemoradiotherapy.

TABLE 1
Patient and Tumor Characteristics

Characteristic	Category	Data
Sex (*n* = 388)	Male	88 (22.7)
	Female	300 (77.3)
Age (y) (*n* = 388)		65 (32–90)
OMS status (*n* = 383)	0	258 (67.4)
	1	112 (29.2)
	2	9 (2.3)
	3	4 (1)
	4	0 (0)
Smoking (*n* = 336)	Yes	189 (56.3)
	No	147 (43.8)
HIV status (*n* = 385)	Positive	33 (8.6)
	Negative	178 (42.6)
	Unknown	174 (45.2)
Tumor size (cm) (*n* = 372)		4.16 (0.5–15.5)
T-stage (*n* = 388)	T1	42 (10.8)
	T2	203 (52.3)
	T3	82 (21.1)
	T4	61 (15.7)
N-stage (*n* = 388)	N0	177 (45.6)
	N1	211 (54.4)
Stage (*n* = 388)	Early: T1–2, N0	147 (37.9)
	Locally advanced: T3–4 or N1	241 (62.1)
P16 staining* (*n* = 384)	Positive	225 (58.6)
	Negative	12 (3.1)
	Unknown	147 (38.3)
Baseline imaging (*n* = 388)		
CT	Yes	212 (54.6)
	No	176 (45.4)
MRI	Yes	260 (67)
	No	128 (33)
Echoendoscopy	Yes	111 (28.6)
	No	277 (71.4)

OMS = Organisation Mondiale de la Santé.
Qualitative data are number and percentage; continuous data are median and range.

Outcomes

Median follow-up was 35.5 mo (95% CI, 32.8–36.6). The 3-y RFS, CFS, and OS for the whole population were 68.0% (95% CI, 62.5–72.9), 70.5% (95% CI, 64.8–75.5), and 79.2% (95% CI, 73.8–83.7), respectively. Among the 242 patients with CMR, 213 (88%) were free of recurrence at 3 y. Among the 146 patients with non-CMR, 77 (52.7%) had a recurrence at 3 y.

The 3-y RFS was 84.2% (95% CI, 77.8–88.9) for patients with CMR, compared with 42.1% (95% CI, 33.4–50.6) for patients without CMR ($P < 0.0001$) (Fig. 2). Similarly, the 3-y CFS was 84.7% (95% CI, 78.2–89.3) for patients with CMR and 47.9% (95% CI, 38.1–56.8) for patients without CMR ($P < 0.0001$) (Fig. 3). The 3-y OS was 88.6% (95% CI, 82.5–92.7) for patients with CMR and 63.5 (95% CI, 53.2–72.1) for patients without CMR ($P < 0.0001$) (Fig. 4).

Qualitative response to treatment on ^{18}F-FDG PET/CT was statistically significantly associated with better RFS, CFS, and OS on both univariate and multivariate analysis (Table 2). A descriptive analysis of quantitative ^{18}F-FDG PET/CT parameters analyzed on 154 patients is presented in Table 3.

The results of univariate analysis between ^{18}F-FDG PET/CT parameters and RFS, CFS, and OS are presented in Table 4. An

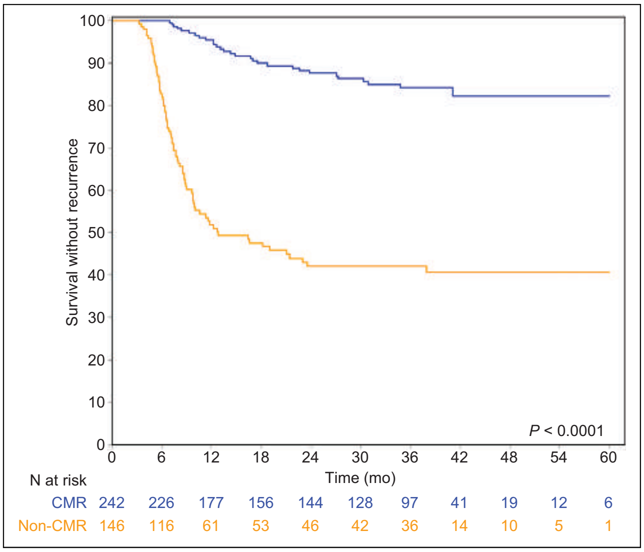

FIGURE 2. RFS curves of CMR patients and non-CMR patients.

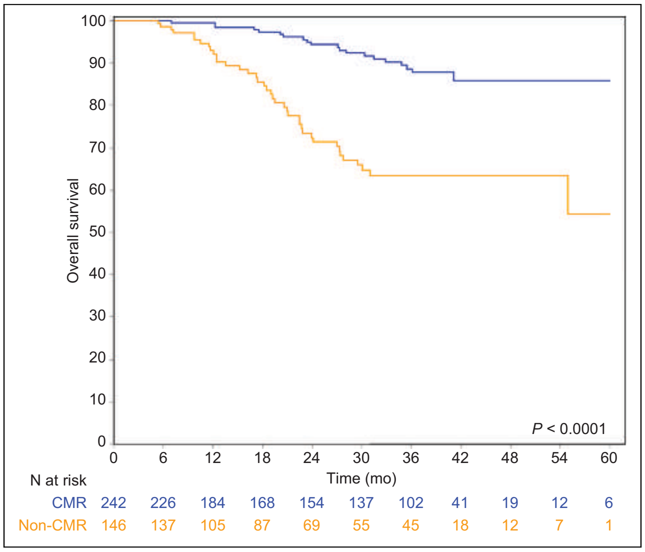

FIGURE 4. OS curves of CMR patients and non-CMR patients.

increase of 1 unit of baseline SUV_{max} (T), SUV_{peak} (T), MTV 41% (T), MTV 41% (N), MTV 41% (T + N), and posttreatment SUV_{max} was significantly associated with a poor RFS, CFS, and OS. There was no statistically significant prognostic impact of TLG and change in SUV_{max}.

By using a receiver operating characteristic curve, we found that a threshold of 5 for posttreatment SUV_{max} separates patients into prognostic groups. The recurrence rate was 35% for patients with a posttreatment SUV_{max} of more than 5 and 18.4% for patients with a posttreatment SUV_{max} 5 or less (HR, 0.44 [95% CI, 0.22–0.87]; $P = 0.018$). Similarly, the colostomy rate was 35% for patients with a posttreatment SUV_{max} of more than 5 and 14.68% for patients with a posttreatment SUV_{max} of 5 or less (HR, 0.30 [95% CI, 0.14–0.61]; $P = 0.001$). OS did not significantly differ between these 2 groups (HR, 0.47 [95% CI, 0.2–1.08]; $P = 0.075$).

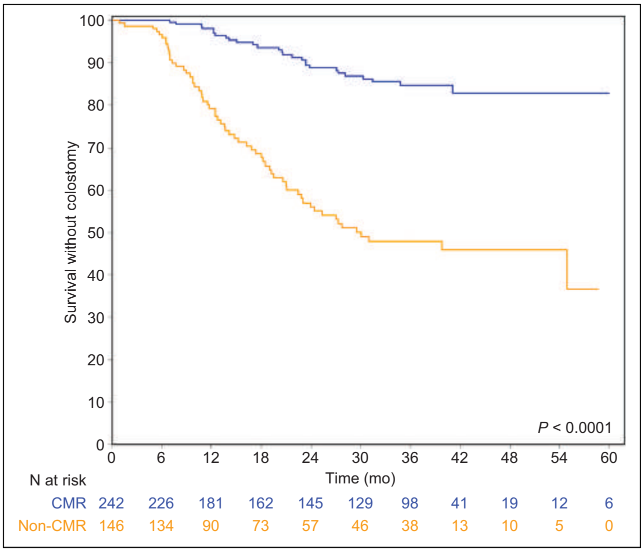

FIGURE 3. CFS curves of CMR patients and non-CMR patients.

DISCUSSION

The purpose of this study was to determine the prognostic value of posttreatment ^{18}F-FDG PET/CT in patients treated with RT or chemoradiotherapy for nonmetastatic SCCA. To our knowledge, our study, with a population of 388 patients, is one of the largest that aimed to assess the predictive value of ^{18}F-FDG PET/CT response to treatment. We confirmed the significant prognostic value of ^{18}F-FDG PET/CT qualitative response to treatment in terms of RFS, CFS, and OS.

Several studies have previously examined the value of treatment response assessed by ^{18}F-FDG PET/CT and showed that a CMR is highly associated with better progression-free survival, OS (*18*,*19*), and cause-specific survival (*20*). Interestingly, metabolic response to treatment has even been found to be a more significant predictor factor of progression-free survival than pretreatment tumor size (based on physical examination) and nodal status in a study of 53 patients (*21*). Finally, it has also been shown that posttreatment ^{18}F-FDG PET/CT has a high negative predictive value and could be used to rule out residual or recurrent disease (*22*).

Regarding quantitative ^{18}F-FDG PET/CT parameters, we identified several significant prognostic factors: MTV, pretreatment SUV_{peak} and SUV_{max}, and posttreatment SUV_{max}. These results are consistent with literature regarding MTV, assessed in 6 different studies (*13*–*16*,*23*,*24*), but also regarding pretreatment SUV_{peak} and posttreatment SUV_{max}, which have not been frequently assessed (*16*,*25*). Literature regarding pretreatment SUV_{max} showed more conflicting results, with a study of 77 patients showing its prognostic value (*26*) but also studies showing negative results (*13*,*23*,*24*,*27*).

By using thresholds to separate patients into prognostic groups, we found that a posttreatment SUV_{max} of 5 or less was predictive of better RFS. A posttreatment SUV_{max} of less than 6.1 has already been shown to be associated with reduced local recurrence and increased OS (*25*). In the literature, an MTV 35% threshold at 40 cm^3 was shown to be the best cutoff to discriminate a low from a high risk of recurrence (*15*).

In this study, we have shown ^{18}F-FDG PET/CT to have major prognostic value regarding qualitative treatment response. Even if

TABLE 2
Association Between ^{18}F-FDG PET/CT Qualitative Treatment Response and RFS, CFS, and OS

	Event		HR	
Response	*n*	%	Univariate analysis	Multivariate analysis*
RFS				
CMR	29/242	11.98	Reference	Reference
PMR	27/91	29.67	2.85 (1.69–4.82), $P < 0.001$	2.64 (1.51–4.62), $P = 0.001$
Stability	7/12	58.33	6.80 (2.97–15.54), $P < 0.001$	5.97 (2.42–14.68), $P < 0.001$
Progression	43/43	100	68.09 (37.69–122.99), $P < 0.001$	56.46 (29.62–107.61), $P < 0.001$
CFS				
CMR	27/242	11.16	Reference	Reference
PMR	28/91	30.77	3.13 (1.84–5.31), $P < 0.001$	3.03 (1.73–5.32), $P < 0.001$
Stability	6/12	50.00	6.12 (2.52–14.87), $P < 0.001$	5.71 (2.09–15.63), $P = 0.001$
Progression	28/43	65.12	11.23 (6.53–19.31), $P < 0.001$	7.69 (4.18–14.14), $P < 0.001$
OS				
CMR	20/242	8.26	Reference	Reference
PMR	13/91	14.29	1.83 (0.91–3.68), $P = 0.090$	1.49 (0.73–3.06), $P = 0.278$
Stability	4/12	33.33	5.41 (1.84–15.9), $P = 0.002$	3.53 (1.11–11.8622), $P = 0.032$
Progression	22/43	51.16	11.27 (6.06–20.96), $P < 0.001$	8.03 (4.18–15.4), $P < 0.001$

*Analysis with sex, OMS status, tumor stage.
PMR = partial metabolic response.
Data in parentheses are 95% CIs.

qualitative evaluation is subjective and is physician-dependent, this study still proves its reliability. Moreover, this study included patients from 36 centers in France with as many physicians, showing reproducibility and confidence in this evaluation.

Finally, we have shown that posttreatment SUV$_{max}$ was significantly associated with RFS, CFS, and OS. It is the main parameter used in ^{18}F-FDG PET/CT interpretation and analysis and is easy to measure.

Our study had some limitations. Patients were included from 36 centers, potentially leading to heterogeneity in patient management and ^{18}F-FDG PET/CT assessment. The 36 centers could have different ^{18}F-FDG PET/CT equipment. Assessment of CMR was left to the discretion of the nuclear medicine physician of each center. We selected patients with ^{18}F-FDG PET/CT at baseline and 4–6 mo after treatment, but all centers did not have the same follow-up policy after RT or chemoradiotherapy of SCCA. ^{18}F-FDG PET/CT could have been done systematically 4–6 mo after treatment or only when relapse was suspected. Concerning the quantitative parameter study, ^{18}F-FDG PET/CT was performed at 3 different centers, and different PET/CT scanners can have variable quantification of ^{18}F-FDG uptake. Moreover, the images were reviewed retrospectively by 2 physicians, and the analysis was univariate.

Currently, ^{18}F-FDG PET/CT is recommended in cases of relapse or suspicion of treatment failure (*4*). By showing the major prognostic value of treatment response as assessed by ^{18}F-FDG PET/CT, this study encourages a systematic evaluation by ^{18}F-FDG PET/CT. We know that patients with early-stage tumors (T1–2, N0) and patients with locally advanced-stage tumors (T3–4 or N+) have different prognoses. Disease-free survival at 3 y is around 85% for patients with early-stage SCCA but 66% for patients with locally advanced SCCA (*17*,*28*). The 3-y CFS and OS are 86% and 92%, respectively, in the early-stage group compared with 67% and 78% in the locally advanced group (*17*). Present research about SCCA focuses on more personalized treatment and management according to tumoral stages. Modalities of evaluation and follow-up after treatment could be adapted too. Patients with early-stage tumors have a low risk of local or metastatic relapse. Most relapses are local and can be detected by clinical evaluation. Surveillance can rely on clinical examination, which seems to be reliable, whereas ^{18}F-FDG PET/CT could be useful in suspected recurrence. On the other hand, patients with locally advanced-stage tumors still present a poor prognosis with a high risk of local and distant recurrence. Moreover, locally advanced tumors frequently involve adjacent organs or deep lymph nodes that cannot be accurately assessed by physical evaluation.

During follow-up, an evaluation by thoracoabdominopelvic CT is recommended once a year during the first 3 y according to the French and European guidelines (*4*,*6*). Pelvic MRI is recommended before salvage surgery (*4*). Despite past studies showing its value, ^{18}F-FDG PET/CT is currently not included in guidelines for systematic follow-up of patients. By confirming its importance in this large-scale study, we suggest that ^{18}F-FDG PET/CT could be recommended at 4–6 mo after the end of chemoradiotherapy for patients with locally advanced-stage tumors. Modalities of follow-up could be adapted according to the response on ^{18}F-FDG PET/CT, since it is known that a CMR is highly predictive of a good outcome.

TABLE 3
Descriptive Analysis of ^{18}F-FDG PET/CT Parameters

Parameter	Category	Data
Baseline ^{18}F-FDG PET/CT (total n = 154)		
SUV$_{max}$ (T)	n	150
	Mean	13.95 (SD, 6.00)
	Median	12.87
	Q1–Q3	10.08–16.35
	Min–max	3.22–41.36
SUV$_{peak}$ (T)	n	130
	Mean	10.89 (SD, 5.14)
	Median	9.94
	Q1–Q3	7.41–13.70
	Min–max	2.36–28.35
SUV$_{mean}$ (T)	n	132
	Mean	8.72 (SD, 5.98)
	Median	7.67
	Q1–Q3	5.86–9.99
	min–max	1.85–61.07
MTV 41% (T) (cm^3)	n	131
	Mean	15.57 (SD, 19.42)
	Median	8.63
	Q1–Q3	4.06–17.29
	Min–max	1.83–115.80
TLG (T) (g)	n	131
	Mean	143.68 (SD, 222.56)
	Median	54.33
	Q1–Q3	24.95–157.79
	Min–max	3.00–1,453.29
MTV 41% (N) (cm^3)	n	134
	Mean	3.07 (SD, 5.94)
	Median	0.00
	Q1–Q3	0.00–4.00
	Min–max	0.00–38.00
TLG (N) (g)	n	134
	Mean	15.69 (SD, 48.05)
	Median	0.00
	Q1–Q3	0.00–11.00
	Min–max	0.00–352.00
MTV 41% (T + N) (cm^3)	n	134
	Mean	18.11 (SD, 21.55)
	Median	10.00
	Q1–Q3	4.11–21.90
	Min–max	0.93–125.29
TLG (T + N) (g)	n	134
	Mean	156.16 (SD, 229.53)
	Median	60.70
	Q1–Q3	27.00–183.00
	Min–max	2.14–1,471.65

(*continued*)

TABLE 3
Descriptive Analysis of ^{18}F-FDG PET/CT Parameters (cont.)

Parameter	Category	Data
Posttreatment ^{18}F-FDG PET/CT (total $n = 154$)		
SUV_{max}	n	149
	Mean	4.77 (SD, 2.46)
	Median	3.94
	Q1–Q3	3.30–5.20
	Min–max	2.06–16.40
Change in SUV_{max} (%)	n	150
	Mean	62.07 (SD, 25.91)
	Median	69.75
	Q1–Q3	53.14–78.39
	Min–max	−60.00–100.00

Min–max = minimum to maximum; Q1–Q3 = first quartile to third quartile.

CONCLUSION

Metabolic treatment response assessed by ^{18}F-FDG PET/CT after RT or chemoradiotherapy for nonmetastatic SCCA has significant prognostic value in terms of RFS, CFS, and OS. ^{18}F-FDG PET/CT could be useful to assess treatment response and adapt follow-up, especially for patients with locally advanced-stage tumors. Quantitative parameters measured on ^{18}F-FDG PET/CT could permit identification of patients with the worst prognosis but should be evaluated in further trials.

TABLE 4
Association Between ^{18}F-FDG PET/CT Parameters and OS, RFS, and CFS (Univariate Analysis)

		HR		
Parameter	Category	OS	RFS	CFS
Baseline ^{18}F-FDG PET/CT	SUV_{max} (T)	1.06 (1–1.12), $P = 0.038$	1.05 (1.01–1.1), $P = 0.018$	1.06 (1.01–1.11), $P = 0.019$
	SUV_{peak} (T)	1.09 (1.01–1.17), $P = 0.022$	1.09 (1.02–1.15), $P = 0.007$	1.09 (1.02–1.16), $P = 0.010$
	SUV_{mean} (T)	1.02 (0.97–1.07), $P = 0.385$	1.02 (0.98–1.06), $P = 0.333$	1.02 (0.98–1.06), $P = 0.342$
	MTV 41% (T)	1.03 (1.01–1.05), $P = 0.001$	1.02 (1–1.03), $P = 0.023$	1.02 (1.01–1.04), $P = 0.002$
	TLG (T)	1.00 (1–1), $P < 0.001$	1.00 (1–1), $P = 0.009$	1.00 (1–1), $P = 0.001$
	MTV 41% (N)	1.06 (1.02–1.1), $P = 0.002$	1.06 (1.03–1.1), $P < 0.001$	1.06 (1.02–1.1), $P = 0.001$
	MTV 41% (T + N)	1.03 (1.01–1.04), $P < 0.001$	1.02 (1–1.03), $P = 0.005$	1.02 (1.01–1.04), $P = 0.001$
	TLG (N)	1.01 (1–1.01), $P = 0.025$	1.01 (1–1.01), $P = 0.001$	1.01 (1–1.01), $P = 0.029$
	TLG (T + N)	1.00 (1–1), $P < 0.001$	1.00 (1–1), $P = 0.004$	1.00 (1–1), $P < 0.001$
Posttreatment ^{18}F-FDG PET/CT	SUV_{max}	1.30 (1.14–1.49), $P < 0.001$	1.21 (1.09–1.34), $P < 0.001$	1.32 (1.19–1.48), $P < 0.001$
Both	Change in SUV_{max}	1.00 (0.98–1.02), $P = 0.889$	1.00 (0.99–1.02), $P = 0.888$	1.00 (0.98–1.01), $P = 0.487$

Data in parentheses are 95% CIs.

DISCLOSURE

Financial support was received from FFCD. No other potential conflict of interest relevant to this article was reported.

KEY POINTS

QUESTION: Could PET/CT be useful in assessing treatment response after RT of SCCA?

PERTINENT FINDINGS: This prospective cohort study showed PET/CT to have statistically significant prognostic value in assessing treatment response in terms of RFS, CFS, and OS.

IMPLICATIONS FOR PATIENT CARE: PET/CT could be useful to assess treatment response and to adapt follow-up, especially for patients with locally advanced-stage tumors.

REFERENCES

1. Defossez G, Le Guyader-Peyrou S, Uhry Z, et al. *National Estimates of Cancer Incidence and Mortality in Metropolitan France Between 1990 and 2018.* Vol 1. French Public Health Service; 2019:372.
2. Bilimoria KY, Bentrem DJ, Rock CE, Stewart AK, Ko CY, Halverson A. Outcomes and prognostic factors for squamous-cell carcinoma of the anal canal: analysis of patients from the National Cancer Data Base. *Dis Colon Rectum.* 2009;52:624–631.
3. Gunderson LL, Winter KA, Ajani JA, et al. Long-term update of US GI intergroup RTOG 98-11 phase III trial for anal carcinoma: survival, relapse, and colostomy failure with concurrent chemoradiation involving fluorouracil/mitomycin versus fluorouracil/cisplatin. *J Clin Oncol.* 2012;30:4344–4351.
4. Moureau-Zabotto L, Vendrely V, Abramowitz L, et al. Anal cancer: French Intergroup Clinical Practice Guidelines for diagnosis, treatment and follow-up (SNFGE, FFCD, GERCOR, UNICANCER, SFCD, SFED, SFRO, SNFCP). *Dig Liver Dis.* 2017;49:831–840.
5. Salaün PY, Abgral R, Malard O, et al. Update of the recommendations of good clinical practice for the use of PET in oncology [in French]. *Bull Cancer.* 2019;106:262–274.
6. Rao S, Guren MG, Khan K, et al. Anal cancer: ESMO clinical practice guidelines for diagnosis, treatment and follow-up. *Ann Oncol.* 2021;32:1087–1100.
7. Caldarella C, Annunziata S, Treglia G, Sadeghi R, Ayati N, Giovanella L. Diagnostic performance of positron emission tomography/computed tomography using fluorine-18 fluorodeoxyglucose in detecting locoregional nodal involvement in patients with anal canal cancer: a systematic review and meta-analysis. *ScientificWorldJournal.* 2014;2014:196068.
8. Cotter SE, Grigsby PW, Siegel BA, et al. FDG-PET/CT in the evaluation of anal carcinoma. *Int J Radiat Oncol Biol Phys.* 2006;65:720–725.
9. Jones M, Hruby G, Solomon M, Rutherford N, Martin J. The role of FDG-PET in the initial staging and response assessment of anal cancer: a systematic review and meta-analysis. *Ann Surg Oncol.* 2015;22:3574–3581.
10. Sveistrup J, Loft A, Berthelsen AK, Henriksen BM, Nielsen MB, Engelholm SA. Positron emission tomography/computed tomography in the staging and treatment of anal cancer. *Int J Radiat Oncol Biol Phys.* 2012;83:134–141.
11. Krengli M, Milia ME, Turri L, et al. FDG-PET/CT imaging for staging and target volume delineation in conformal radiotherapy of anal carcinoma. *Radiat Oncol.* 2010;5:10.
12. Mahmud A, Poon R, Jonker D. PET imaging in anal canal cancer: a systematic review and meta-analysis. *Br J Radiol.* 2017;90:20170370.
13. Bazan JG, Koong AC, Kapp DS, et al. Metabolic tumor volume predicts disease progression and survival in patients with squamous cell carcinoma of the anal canal. *J Nucl Med.* 2013;54:27–32.
14. Mohammadkhani Shali S, Schmitt V, Behrendt FF, et al. Metabolic tumour volume of anal carcinoma on ^{18}FDG PET/CT before combined radiochemotherapy is the only independant determinant of recurrence free survival. *Eur J Radiol.* 2016;85:1390–1394.
15. Le Thiec M, Testard A, Ferrer L, et al. Prognostic impact of pretherapeutic FDG-PET in localized anal cancer. *Cancers (Basel).* 2020;12:1512.
16. Leccisotti L, Manfrida S, Barone R, et al. The prognostic role of FDG PET/CT before combined radio-chemotherapy in anal cancer patients. *Ann Nucl Med.* 2020;34:65–73.
17. Vendrely V, Lemanski C, Pommier P, et al. Treatment, outcome, and prognostic factors in non-metastatic anal cancer: the French nationwide cohort study FFCD-ANABASE. *Radiother Oncol.* 2023;183:109542.
18. Day FL, Link E, Ngan S, et al. FDG-PET metabolic response predicts outcomes in anal cancer managed with chemoradiotherapy. *Br J Cancer.* 2011;105:498–504.
19. Goldman KE, White EC, Rao AR, Kaptein JS, Lien WW. Post-treatment FDG-PET-CT response is predictive of tumor progression and survival in anal carcinoma. *Pract Radiat Oncol.* 2016;6:e149–e154.
20. Houard C, Pinaquy JB, Mesguich C, et al. Role of ^{18} F-FDG PET/CT in posttreatment evaluation of anal carcinoma. *J Nucl Med.* 2017;58:1414–1420.
21. Schwarz JK, Siegel BA, Dehdashti F, Myerson RJ, Fleshman JW, Grigsby PW. Tumor response and survival predicted by post-therapy FDG-PET/CT in anal cancer. *Int J Radiat Oncol Biol Phys.* 2008;71:180–186.
22. Teagle AR, Gilbert DC, Jones JR, Burkill GJ, McKinna F, Dizdarevic S. Negative ^{18}F-FDG-PET-CT may exclude residual or recurrent disease in anal cancer. *Nucl Med Commun.* 2016;37:1038–1045.
23. Gauthé M, Richard-Molard M, Fayard J, Alberini JL, Cacheux W, Lièvre A. Prognostic impact of tumour burden assessed by metabolic tumour volume on FDG PET/CT in anal canal cancer. *Eur J Nucl Med Mol Imaging.* 2017;44:63–70.
24. Filippi L, Fontana A, Spinelli GP, Rossi L, Bagni O. Role of ^{18}F-FDG PET-derived parameters for predicting complete response to chemoradiotherapy in squamous cell anal carcinoma. *Nucl Med Commun.* 2020;41:1089–1094.
25. Cardenas ML, Spencer CR, Markovina S, et al. Quantitative FDG-PET/CT predicts local recurrence and survival for squamous cell carcinoma of the anus. *Adv Radiat Oncol.* 2017;2:281–287.
26. Kidd EA, Dehdashti F, Siegel BA, Grigsby PW. Anal cancer maximum F-18 fluorodeoxyglucose uptake on positron emission tomography is correlated with prognosis. *Radiother Oncol.* 2010;95:288–291.
27. Deantonio L, Milia ME, Cena T, et al. Anal cancer FDG-PET standard uptake value: correlation with tumor characteristics, treatment response and survival. *Radiol Med (Torino).* 2016;121:54–59.
28. Martin D, Schreckenbach T, Ziegler P, et al. Evaluation of prognostic factors after primary chemoradiotherapy of anal cancer: a multicenter study of the German Cancer Consortium-Radiation Oncology Group (DKTK-ROG). *Radiother Oncol.* 2022;167:233–238.

Diverse Imaging Methods May Influence Long-Term Oncologic Outcomes in Oligorecurrent Prostate Cancer Patients Treated with Metastasis-Directed Therapy (the PRECISE-MDT Study)

Matteo Bauckneht[1,2], Francesco Lanfranchi[2], Domenico Albano[3,4], Luca Triggiani[4,5], Flavia Linguanti[6,7], Luca Urso[8], Rosario Mazzola[9], Alessio Rizzo[10], Elisa D'Angelo[11], Francesco Dondi[3,4], Eneida Mataj[4,5], Gloria Pedersoli[4,5], Elisabetta Maria Abenavoli[6], Luca Vaggelli[6], Beatrice Detti[12], Naima Ortolan[8], Antonio Malorgio[13], Alessia Guarneri[14], Federico Garrou[15], Matilde Fiorini[9], Serena Grimaldi[15], Pietro Ghedini[16], Giuseppe Carlo Iorio[17], Antonella Iudicello[16], Guido Rovera[15], Giuseppe Fornarini[18], Diego Bongiovanni[17], Michela Marcenaro[19], Filippo Maria Pazienza[15], Giorgia Timon[19], Matteo Salgarello[20], Manuela Racca[10], Mirco Bartolomei[8], Stefano Panareo[16], Umberto Ricardi[17], Francesco Bertagna[3,4], Filippo Alongi[4,9], Salvina Barra[19], Silvia Morbelli[15], Gianmario Sambuceti[1,2], and Liliana Belgioia[2,19]

[1]Nuclear Medicine, IRCCS Ospedale Policlinico San Martino, Genova, Italy; [2]Department of Health Sciences, University of Genova, Genova, Italy; [3]Nuclear Medicine, ASST Spedali Civili di Brescia, Brescia, Italy; [4]University of Brescia, Brescia, Italy; [5]Radiation Oncology, ASST Spedali Civili di Brescia, Brescia, Italy; [6]Nuclear Medicine, Careggi University Hospital, Florence, Italy; [7]Nuclear Medicine, Ospedale San Donato, Arezzo, Italy; [8]Nuclear Medicine, Oncological Medical and Specialist Department, University Hospital of Ferrara, Ferrara, Italy; [9]Advanced Radiation Oncology, IRCCS Sacro Cuore Don Calabria Hospital, Cancer Care Center, Negrar, Italy; [10]Nuclear Medicine, Candiolo Cancer Institute, FPO–IRCCS, Turin, Italy; [11]Radiation Oncology, University Hospital of Modena, Modena, Italy; [12]Radiation Oncology, Careggi University Hospital, Florence, Italy; [13]Radiotherapy, University Hospital of Ferrara, Ferrara, Italy; [14]Radiation Oncology, Candiolo Cancer Institute, FPO–IRCCS, Turin, Italy; [15]Nuclear Medicine, AOU Città della Salute e della Scienza di Torino, University of Turin, Turin, Italy; [16]Nuclear Medicine, Oncology, and Haematology Department, University Hospital of Modena, Modena, Italy; [17]Radiation Oncology, Department of Oncology, University of Turin, Turin, Italy; [18]Medical Oncology 1, IRCCS Ospedale Policlinico San Martino, Genova, Italy; [19]Radiotherapy, IRCCS Ospedale Policlinico San Martino, Genova, Italy; and [20]Nuclear Medicine, IRCCS Ospedale Sacro Cuore Don Calabria, Negrar, Italy

Metastasis-directed therapy (MDT) has been tested in clinical trials as a treatment option for oligorecurrent prostate cancer (PCa). However, there is an ongoing debate regarding the impact of using different imaging techniques interchangeably for defining lesions and guiding MDT within clinical trials. **Methods:** We retrospectively identified oligorecurrent PCa patients who had 5 or fewer nodal, bone, or visceral metastases detected by choline or prostate-specific membrane antigen (PSMA) PET/CT and who underwent MDT stereotactic body radiotherapy with or without systemic therapy in 8 tertiary-level cancer centers. Imaging-guided MDT was assessed as progression-free survival (PFS), time to systemic treatment change due to polymetastatic conversion (PFS2), and overall survival predictor. Propensity score matching was performed to account for clinical differences between groups. **Results:** Of 402 patients, 232 (57.7%) and 170 (42.3%) underwent MDT guided by [^{18}F]fluorocholine and PSMA PET/CT, respectively. After propensity score matching, patients treated with PSMA PET/CT–guided MDT demonstrated longer PFS (hazard ratio [HR], 0.49 [95% CI, 0.36–0.67]; $P < 0.0001$), PFS2 (HR, 0.42 [95% CI, 0.28–0.63]; $P < 0.0001$), and overall survival (HR, 0.39 [95% CI, 0.15–0.99]; $P < 0.05$) than those treated with choline PET/CT–guided MDT. Additionally, we matched patients who underwent [^{68}Ga]Ga-PSMA-11 versus [^{18}F]F-PSMA-1007 PET/CT, observing longer PFS and PFS2 in the former subgroup (PFS: HR, 0.51 [95% CI, 0.26–1.00]; $P < 0.05$; PFS2: HR, 0.24 [95% CI, 0.09–0.60]; $P < 0.05$). **Conclusion:** Diverse imaging methods may influence outcomes in oligorecurrent PCa patients undergoing MDT. However, prospective, head-to-head studies, ideally incorporating a randomized design, are necessary to provide definitive evidence and facilitate the practical application of these findings.

Key Words: oligorecurrent prostate cancer; metastasis-directed therapy; choline; prostate-specific membrane antigen; PET

J Nucl Med 2024; 65:1202–1209
DOI: 10.2967/jnumed.124.267586

Primary treatment for advanced prostate cancer (PCa) involves androgen deprivation therapy (ADT) (*1*). However, the effectiveness of ADT is limited and often accompanied by significant side effects (*2,3*). Consequently, when metastases are limited in number and location, metastasis-directed therapies (MDTs) using stereotactic body radiotherapy become valuable options, potentially delaying ADT initiation and treatment-related adverse events.

MDT has demonstrated potential in this space in 2 phase II trials (*4–6*). However, the consistency of these data is debated (*7*)

Received Feb. 9, 2024; revision accepted May 9, 2024.

For correspondence or reprints, contact Matteo Bauckneht (matteo.bauckneht@unige.it).

because imaging technologies were used interchangeably for defining oligometastatic lesions and guiding MDT (*4,5*). In this framework, although for many years $[^{18}\text{F}]$fluorocholine and $[^{11}\text{C}]$C-choline PET/CT have been recommended for PCa restaging, prostate-specific membrane antigen (PSMA)–targeted tracers have recently emerged as more sensitive (*1*). It is reasonable to expect that more precise disease identification through advanced imaging could increase the proportion of patients receiving comprehensive MDT, potentially leading to improved oncologic outcomes. However, prospective randomized clinical trials evaluating the benefits of treating oligometastases identified by different imaging approaches are still lacking.

Simultaneously, there is increasing debate about which PSMA radiotracer should be preferred. Although $[^{68}\text{Ga}]$Ga-PSMA-11 is among the most extensively studied PSMA-targeted ligands, the emergence of several other PSMA ligands, including $[^{18}\text{F}]$F-PSMA-1007, has diversified the options available. Recent reports, however, suggest that the higher incidence of unspecific bone uptake associated with $[^{18}\text{F}]$F-PSMA-1007 might result in false-positive findings, potentially compromising its accuracy (*8,9*).

Considering these aspects, our study was designed to assess the impact of different imaging modalities on guidance of MDT and their effects on oncologic outcomes within a multiinstitutional, real-world cohort of patients with oligorecurrent PCa.

MATERIALS AND METHODS

Study Population and Data Collection

We retrospectively analyzed oligorecurrent hormone-sensitive PCa or castration-resistant PCa (CRPC) patients who underwent imaging-guided MDT across 8 Italian tertiary-level cancer centers between July 2012 and May 2023. The inclusion criteria were a histologically confirmed diagnosis of PCa, detection of pelvic or extraregional nodal relapse (M1a) or of bone or visceral metastases (M1b or M1c, respectively) by either choline or PSMA PET/CT, identification of up to 5 metastases by imaging before MDT, treatment with stereotactic body radiotherapy (with or without systemic therapy), and a minimum of 6 mo of clinical follow-up after MDT. The study adhered to the guidelines of the Declaration of Helsinki and was approved by the local ethical committee (registration number 5/2023–DB id 12914). All subjects gave written informed consent.

Imaging-Guided MDT and Follow-up

PET/CT scans were performed following current guidelines (*1,10*). Because of the study's retrospective design, PET/CT studies were acquired on different scanners, as detailed in Supplemental Table 1 (supplemental materials are available at http://jnm.snmjournals.org). Patients were managed according to current international guidelines (*11*). After MDT, patients underwent short-term clinical follow-up according to each institutional protocol, with clinical evaluation and a prostate-specific antigen (PSA) blood test every 3–6 mo. Restaging with PET/CT was performed in cases of biochemical progression after MDT. Further MDT was proposed if patients showed oligoprogression after MDT (with $<$5 new lesions detected outside the irradiated field). Systemic treatments were administered in cases of polymetastatic disease progression, defined as the appearance of more than 5 metastases. Patients with disease progression were followed up for survival status as part of the long-term follow-up.

Statistical Analysis

Continuous data are expressed as the mean ± SD. Categoric variables were compared using the χ^2 test, and continuous variables were analyzed using a 1-way ANOVA. When appropriate, post hoc analyses were performed with the Bonferroni method to adjust for multiple comparisons. Statistical significance was set at a P value of less than 0.05. To compare treatment groups, we calculated a propensity score using multivariable logistic models, including the type of PET tracer used as the independent variable and factors widely reported to influence outcomes as dependent variables. These variables included age at MDT, International Society of Urological Pathology grade group at baseline, CRPC status, PSA level at the time of MDT, concurrent systemic treatment at the time of MDT, and number of metastases. The resulting propensity score aimed to balance these covariates across treatment groups, thereby reducing selection bias and enabling a more accurate comparison of outcomes. Propensity matching was then applied to create comparable cohorts on a one-to-one basis based on nearest-neighbor matching with a calibration of 0.01. This procedure matches participants from one group to participants from the other group according to the absolute difference between their propensity scores, which must result in the smallest difference to establish a match. Propensity score matching was performed between patients who underwent choline versus PSMA PET/CT–guided MDT and between patients who underwent $[^{68}\text{Ga}]$Ga-PSMA-11 versus $[^{18}\text{F}]$F-PSMA-1007 PET/CT. Progression-free survival (PFS) was defined as a composite endpoint, as described previously (*5,6*). Briefly, it included any of the following criteria: a rise in PSA level of at least 2 ng/dL and 25% above the nadir; radiologic progression; clinical progression; initiation of ADT for any reason; or mortality (*5,6*). PFS2 was defined as the interval between imaging time and the systemic treatment change due to polymetastatic conversion. Overall survival (OS) was measured from the initial imaging time to the date of death from any cause. PFS, PFS2, and OS are expressed in months. The Kaplan–Meier method, using the log-rank test, was used to explore differences in PFS, PFS2, and OS among the matched cohorts. A sensitivity analysis using the inverse probability of treatment weighting (*12*) was applied to confirm the results. A dedicated temporal analysis, conducted via univariate Cox regression, was undertaken to assess the impact of the year of MDT on the study's endpoints, ensuring our findings' temporal integrity. Statistical analysis was conducted using SPSS software version 26 (IBM) and MedCalc version 19.4 (MedCalc Software).

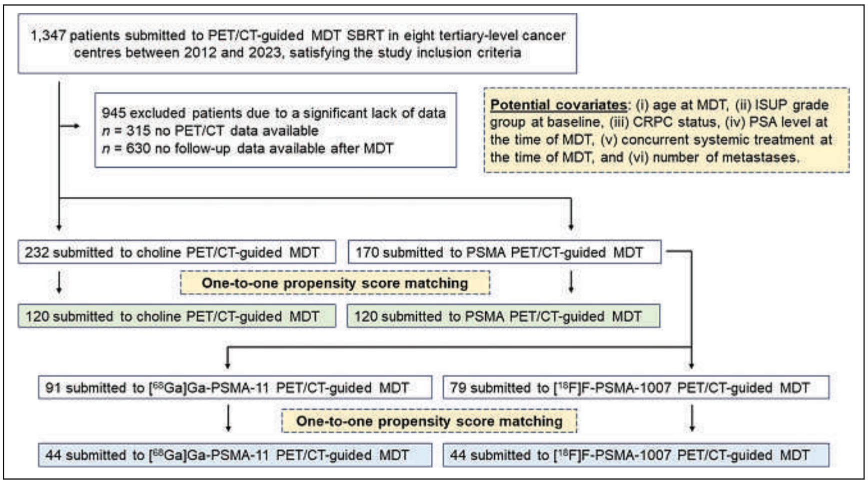

FIGURE 1. Study design and flowchart of patient selection and matching. ISUP = International Society of Urological Pathology; SBRT = stereotactic body radiotherapy.

RESULTS

Patients' Clinical Characteristics and Imaging Findings

We retrospectively selected 402 patients, as detailed in Figure 1. Their clinical characteristics, imaging findings, and MDT parameters are summarized in Table 1. CRPC status was available for 75 patients (18.6%). In most cases (97.8%), patients had 3 or fewer metastases at the pre-MDT imaging. Nodes and bones represented the most frequent metastatic sites. Of 402 patients, 232 (57.7%) and 170 (42.3%) underwent MDT guided by choline and PSMA PET/CT, respectively. All patients who underwent choline PET/CT

TABLE 1
Clinical, Imaging, and Treatment Characteristics of Patients

Parameter	Data
Preimaging clinical characteristics	
Age (y)	72.60 ± 6.81
Initial AJCC stage	
I	16 (3.98%)
II	91 (22.64%)
III	241 (59.95%)
IV	54 (13.43%)
ISUP grade	
1	62 (15.53%)
2	87 (21.58%)
3	102 (25.26%)
4	59 (14.74%)
5	92 (22.89%)
Primary treatment	
Surgery	322 (80.05%)
Radiotherapy (±ADT)	70 (17.46%)
Medical therapy	10 (2.49%)
CRPC at time of MDT	75 (18.66%)
PSA at time of MDT (ng/mL)	3.21 ± 4.47
Imaging findings	
Imaging-guided MDT	
[^{18}F]fluorocholine PET/CT	232 (57.71%)
PSMA PET/CT	170 (42.29%)
Number of metastatic lesions	
1	278 (69.15%)
2	88 (21.89%)
3	27 (6.72%)
4	6 (1.49%)
5	3 (0.75%)
Site of metastases	
Lymph node	283 (70.40%)
Bone	117 (29.10%)
Visceral	2 (0.50%)
MDT parameters and clinical follow-up	
MDT total dose (per lesion)	33.28 ± 4.85
MDT BED (per lesion)	117.67 ± 26.03
Concurrent systemic treatment in addition to MDT	167 (41.54%)
PSA nadir after MDT (ng/mL)	2.07 ± 7.32

AJCC = American Joint Committee on Cancer; ISUP = International Society of Urological Pathology; BED = biologically effective dose.

Qualitative data are number and percentage; continuous data are mean ± SD (*n* = 402).

(*n* = 232) were scanned with [^{18}F]fluorocholine, whereas patients who underwent PSMA PET/CT (*n* = 170) were scanned with either [^{68}Ga]Ga-PSMA-11 (*n* = 91, 53.5%) or [^{18}F]F-PSMA-1007 (*n* = 79, 46.5%).

Clinical Outcome After MDT According to Imaging Modality

After propensity score matching, a cohort of 120 patients who underwent choline PET/CT–guided MDT was compared with an equal cohort of 120 patients who underwent PSMA PET/CT–guided MDT. A well-calibrated and discriminative balance between these matched cohorts was documented by the lack of significant differences in any variables across the 2 groups (Table 2). After MDT, patients were clinically and biochemically followed up for a median of 31 mo (95% CI, 28.3–36.2 mo). The median PFS was 17.9 mo (95% CI, 15.2–76.1 mo). Of the 163 (67.9%) patients who experienced progression after MDT, progressors were significantly fewer

TABLE 2

Clinical, Imaging, and Treatment Characteristics of Patients After Propensity Score Matching

Parameter	Overall (*n* = 240)	[^{18}F]fluorocholine-guided MDT (*n* = 120)	PSMA-guided MDT (*n* = 120)	*P*
Preimaging clinical characteristics				
Age (y)	72.07 ± 6.55	71.71 ± 6.87	72.43 ± 6.23	0.397
Initial AJCC stage				
I	10 (4.17%)	5 (4.17%)	5 (4.17%)	1.000
II	59 (24.58%)	26 (21.67%)	33 (27.50%)	0.295
III	142 (59.17%)	72 (60.00%)	70 (58.33%)	0.792
IV	29 (12.08%)	17 (14.17%)	12 (10.00%)	0.322
ISUP grade				
1	31 (12.92%)	17 (14.17%)	14 (11.67%)	0.565
2	65 (27.08%)	32 (26.67%)	33 (27.50%)	0.885
3	55 (22.92%)	25 (20.83%)	30 (25.00%)	0.443
4	39 (16.25%)	18 (15.00%)	21 (17.5%)	0.600
5	50 (20.83%)	28 (23.33%)	22 (18.33%)	0.341
Primary treatment				
Surgery	200 (83.33%)	95 (79.00%)	105 (87.50%)	0.079
Radiotherapy (±ADT)	36 (15.01%)	22 (18.50%)	14 (11.67%)	0.140
Medical therapy	4 (1.66%)	3 (2.50%)	1 (0.83%)	0.313
CRPC at time of MDT	40 (16.67%)	17 (14.17%)	23 (19.17%)	0.254
PSA at time of MDT (ng/mL)	2.66 ± 3.56	2.93 ± 2.44	2.39 ± 1.99	0.243
Imaging findings				
Number of metastatic lesions				
1	183 (76.25%)	91 (75.83%)	92 (76.67%)	0.879
2	38 (15.83%)	17 (14.17%)	21 (17.50%)	0.481
3–5	19 (7.92%)	12 (10.00%)	7 (5.83%)	0.232
Site of metastases				
Lymph node	169 (70.42%)	90 (75.00%)	79 (65.83%)	0.120
Bone	70 (29.17%)	30 (25.00%)	40 (33.33%)	0.157
Visceral	1 (0.42%)	0 (0.00%)	1 (0.84%)	0.315
MDT parameters and clinical follow-up				
MDT total dose (per lesion)	33.42 ± 4.68	33.35 ± 4.17	33.49 ± 5.17	0.824
MDT BED (per lesion)	119.90 ± 26.48	124.60 ± 33.53	116.62 ± 19.97	0.207
Concurrent systemic treatment in addition to MDT	100 (40.83%)	43 (35.80%)	57 (47.50%)	0.067
PSA nadir after MDT (ng/mL)	1.95 ± 7.93	2.67 ± 11.28	1.32 ± 2.48	0.218
Propensity score matching	0.54 ± 0.13	0.54 ± 0.13	0.54 ± 0.13	0.987

AJCC = American Joint Committee on Cancer; ISUP = International Society of Urological Pathology; BED = biologically effective dose.

Qualitative data are number and percentage; continuous data are mean ± SD.

in the PSMA PET/CT subgroup (59/120, 49.2%) than in the choline subgroup (104/120, 86.7%; $P < 0.001$). Coherently, we observed a significantly longer median PFS in patients undergoing PSMA PET/CT–guided MDT than in those undergoing choline PET/CT–guided MDT (33.2 mo [95% CI, 19.6–41.5 mo] vs. 13.8 mo [95% CI, 11.8–76.1 mo]; hazard ratio [HR], 0.49 [95% CI, 0.36–0.67]; $P < 0.0001$; Fig. 2A). The median PFS2 was 41.5 mo (95% CI, 32.2–77.7 mo). The use of PSMA PET/CT as the guide for MDT was associated with a significantly increased median time to treatment change compared with choline PET/CT (median PFS2 not reached vs. 25.6 mo [95% CI, 19.3–37.7 mo]; HR, 0.42 [95% CI, 0.28–0.63]; $P < 0.0001$; Fig. 2B). The median OS was not reached for the overall cohort or the 2 subgroups. During the follow-up interval, 18 events were recorded, involving 4 and 14 patients in the PSMA and choline PET/CT subgroups, respectively (HR, 0.39 [95% CI, 0.15–0.99]; $P = 0.014$). Figure 2C displays the resulting Kaplan–Meier curves ($P < 0.05$). Notably, patients who underwent different imaging approaches before MDT experienced divergent OS even when OS was measured since PCa diagnosis (HR, 0.31; $P < 0.05$; Supplemental Fig. 1). The sensitivity analyses confirmed these findings (Supplemental Figs. 2–4). The temporal analysis (Supplemental Table 2) revealed that the year of MDT was not a significant predictor of PFS, PFS2, or OS, affirming the temporal robustness of our findings across imaging modalities.

Outcome in Patients Who Underwent PSMA PET/CT–Guided MDT

We subsequently compared 2 propensity score–matched cohorts of patients who underwent MDT guided by either [^{68}Ga]Ga-PSMA-11 or [^{18}F]F-PSMA-1007 PET/CT. The 2 cohorts, consisting of 44 patients, demonstrated well-balanced clinical, imaging, and treatment characteristics (Table 3). The nadir PSA serum level after MDT was significantly lower in patients who underwent [^{68}Ga]Ga-PSMA-11 than in those who underwent [^{18}F]F-PSMA-1007 (0.53 ± 0.91 vs. 1.69 ± 2.23 ng/mL; $P < 0.005$). Moreover, the use of [^{68}Ga]Ga-PSMA-11 as the guide for MDT was associated with significantly increased median PFS (41.5 mo [95% CI, 24.4–47.6 mo] vs. 22.4 mo [95% CI, 14.1–33.2 mo]; HR, 0.51 [95% CI, 0.26–1.00]; $P < 0.05$; Fig. 3A) and median PFS2 (not reached vs. 30.3 mo [95% CI, 21.0–35.2 mo]; HR, 0.24 [95% CI, 0.09–0.60]; $P < 0.005$; Fig. 3B) compared with [^{18}F]F-PSMA-1007. The sensitivity analyses confirmed these findings (Supplemental Figs. 5–6). Differences in OS were not assessed in this subgroup, as no events were recorded in patients undergoing [^{18}F]F-PSMA-1007 PET/CT–guided MDT. The temporal analysis confirmed the temporal robustness of our observations (Supplemental Table 3).

DISCUSSION

There is considerable uncertainty in interpreting and applying clinical trial findings for oligorecurrent PCa, mainly attributable to varied imaging approaches. Table 4 summarizes existing real-world retrospective studies (*13–17*) comparing the efficacy of different imaging-guided MDT approaches. Beyond providing a larger patient sample, our multiinstitutional observational study contributes additional valuable insights.

First, whereas previous studies focused on PFS, we observed differences in PFS2 and OS. Subject to confirmation by further studies, this may represent a relevant step forward in MDT validation, as PFS is a questionable surrogate of OS (*18*). A recent study suggested that the oligometastatic state defined by PSMA PET/CT may represent a less aggressive disease with slower progression, as it is associated with fewer high-risk DNA mutations (*19,20*). However, this finding should be interpreted cautiously, considering the evolving landscape of PCa treatment, where advancements in systemic therapies and radiation techniques during the study period may influence outcomes. We used temporal analyses to investigate these effects, yet the potential for residual confounding remains. Future prospective studies are essential to disentangle the specific impact of imaging modalities from these treatment advancements, ensuring a clearer understanding of their comparative effectiveness. Moreover, the higher sensitivity of PSMA PET/CT imaging likely leads to earlier detection of metastatic disease than is possible with choline PET/CT. Identifying metastases earlier introduces a potential lead-time bias known as the Will Rogers phenomenon (*21*). This occurs when a patient's disease is reclassified using more sensitive diagnostic tools. With earlier metastasis identification, the interval from imaging to treatment alteration or death may appear prolonged, even though the patient's life-span remains unchanged. Thus, the observed increase in survival could be attributed to early detection rather than an actual prolongation of life. However, in an exploratory analysis, we observed a difference in OS from the initial diagnosis of PCa rather than from the imaging time. On this basis, we can assume that our findings are not purely the result of the lead-time bias. Ongoing prospective randomized phase III trials (NCT03582774,

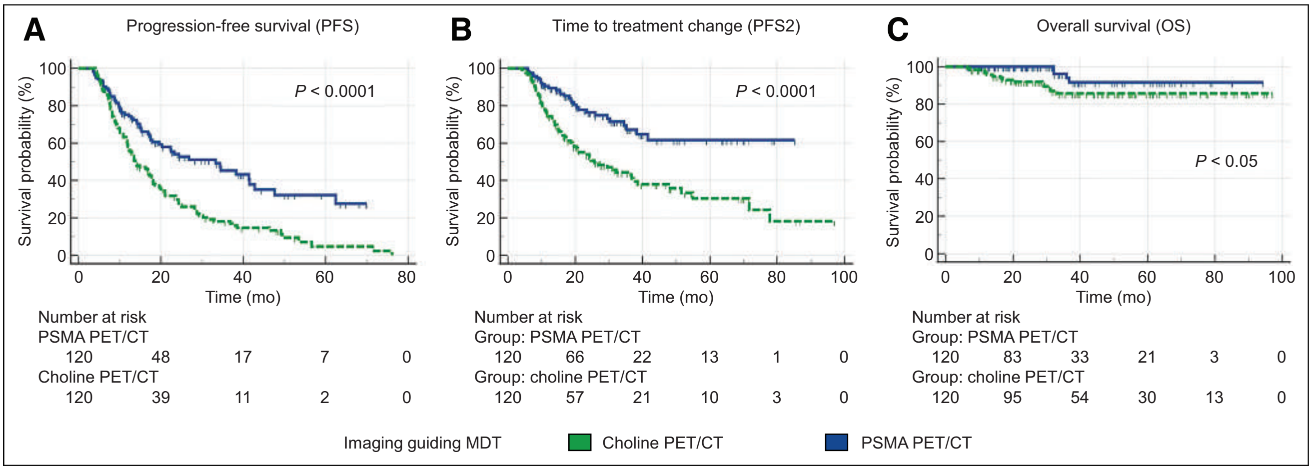

FIGURE 2. Survival curves according to imaging modality guiding MDT in PSMA and choline PET/CT matched cohorts ($n = 120$).

TABLE 3
Clinical, Imaging, and Treatment Characteristics of Patients Undergoing [^{18}F]F-PSMA-1007 or [^{68}Ga]Ga-PSMA-11 PET/CT–Guided MDT After Propensity Score Matching

Parameter	Overall (*n* = 88)	[^{18}F]F-PSMA-1007–guided MDT (*n* = 44)	[^{68}Ga]Ga-PSMA-11–guided MDT (*n* = 44)	*P*
Preimaging clinical characteristics				
Age (y)	73.07 ± 6.42	73.2 ± 7.23	72.94 ± 5.56	0.850
Initial AJCC stage				
I	4 (4.55%)	3 (6.82%)	1 (2.27%)	0.308
II	22 (25.00%)	9 (20.45%)	13 (29.55%)	0.327
III	54 (61.36%)	26 (59.09%)	28 (63.64%)	0.663
IV	8 (9.09%)	6 (13.64%)	2 (4.54%)	0.140
ISUP grade				
1	10 (11.36%)	4 (9.09%)	6 (13.64%)	0.504
2	19 (21.59%)	10 (22.73%)	9 (20.45%)	0.796
3	25 (28.41%)	12 (27.27%)	13 (29.55%)	0.814
4	19 (21.59%)	10 (22.73%)	9 (20.45%)	0.796
5	15 (17.05%)	8 (18.18%)	7 (15.91%)	0.778
Primary treatment				
Surgery	74 (84.09%)	34 (77.27%)	40 (90.91%)	0.082
Radiotherapy (±ADT)	14 (15.91%)	10 (22.73%)	4 (9.09%)	0.082
CRPC at time of MDT	15 (17.05%)	7 (15.91%)	8 (18.18%)	0.778
PSA at time of MDT (ng/mL)	2.42 ± 5.01	2.27 ± 3.80	2.58 ± 6.05	0.769
Imaging findings				
Number of metastatic lesions				
1	69 (78.41%)	34 (77.27%)	35 (79.55%)	0.796
2	13 (14.77%)	6 (13.54%)	7 (15.91%)	0.755
3–5	6 (6.82%)	4 (9.09%)	2 (4.54%)	0.400
Site of metastases				
Lymph node	59 (67.04%)	27 (61.36%)	32 (72.73%)	0.259
Bone	28 (31.82%)	16 (36.36%)	12 (27.27%)	0.367
Visceral	1 (1.14%)	1 (2.27%)	0 (0.00%)	0.318
MDT parameters and clinical follow-up				
MDT total dose (per lesion)	34.02 ± 4.86	33.84 ± 5.22	34.20 ± 4.51	0.731
MDT BED (per lesion)	117.89 ± 20.18	115.40 ± 11.77	120.11 ± 25.64	0.492
Concurrent systemic treatment in addition to MDT	29 (32.96%)	14 (31.82%)	15 (34.09%)	0.822
PSA nadir after MDT (ng/mL)	1.093 ± 1.77	1.70 ± 2.24	0.53 ± 0.91	0.003
Propensity score matching	0.52 ± 0.15	0.52 ± 0.15	0.52 ± 0.15	0.988

AJCC = American Joint Committee on Cancer; ISUP = International Society of Urological Pathology; BED = biologically effective dose.

Qualitative data are number and percentage; continuous data are mean ± SD.

NCT03762759, and NCT04557501, with estimated completion dates in 2023, 2025, and 2028, respectively) will further address these issues, providing more robust evidence on the topic.

Interestingly, we observed a hierarchy between PSMA-targeted radiopharmaceuticals in differentiating the PSA nadir after therapy and the oncologic outcome of patients who underwent MDT under the guidance of [^{68}Ga]Ga-PSMA-11 or [^{18}F]F-PSMA-1007. Only a few head-to-head studies comparing these 2 radiotracers are currently available in the literature, mainly from the diagnostic accuracy point of view (*22*). In a prospective cross-over study on 50 patients, [^{18}F]F-PSMA-1007 provided more equivocal results than [^{68}Ga]Ga-PSMA-11 (*23*). Seifert et al. used [^{68}Ga]Ga-PSMA-11 as part of a reference standard for [^{18}F] F-PSMA-1007 PET/CT bone-uncertain findings (*24*). An ongoing randomized comparative trial is assessing the noninferiority of [^{18}F]F-PSMA-1007 to [^{68}Ga]Ga-PSMA-11 (*25*). To the best of our knowledge, the present

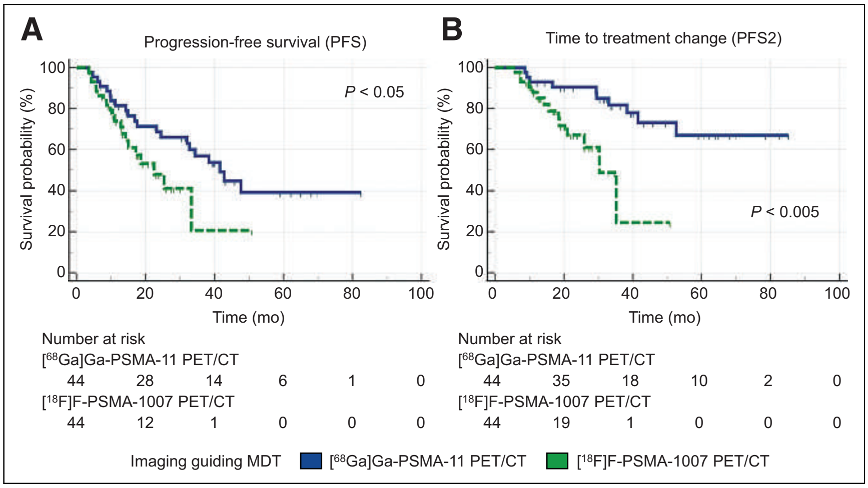

FIGURE 3. Survival curves according to imaging modality guiding MDT in $[^{68}\mathrm{Ga}]$Ga-PSMA-11 and $[^{18}\mathrm{F}]$F-PSMA-1007 PET/CT matched cohorts (*n* = 44).

study is the first to observe a difference in clinical outcomes in patients managed under the guidance of the 2 tracers. One possible explanation for our findings is the propensity of $[^{18}\mathrm{F}]$F-PSMA-1007 to exhibit unspecific bone uptake, potentially leading to false-positive results. Mistaking unspecific uptake for metastatic lesions could result in inappropriate targeting during stereotactic body radiotherapy, thereby affecting the tracer's effectiveness in guiding MDT. The literature emphasizes the need for sophisticated training in interpreting $[^{18}\mathrm{F}]$F-PSMA-1007 PET/CT images (*26*), pointing to a steeper learning curve and potential variability in physician interpretations. This is especially relevant in nuclear medicine facilities that perform a high volume of $[^{18}\mathrm{F}]$F-PSMA-1007 PET/CT scans, for which the understanding and interpretation of bone uptake are in constant evolution. This evolution suggests that future MDT outcomes may vary as methodologies and interpretive approaches adapt to these insights. On the one side, this dynamic underlines a limitation of our study, as the lack of a central imaging review may have introduced heterogeneity in interpretations and potentially affected MDT efficacy. On the other hand, it also underscores a practical challenge in achieving consistent readings across different observers when using this tracer in real-world settings. Further research using a more refined methodology is essential to investigate these concerns thoroughly.

It is important to acknowledge several further limitations of our study. The retrospective and observational design of the study might have resulted in limited statistical power. Additionally, although propensity score matching aimed to reduce heterogeneity in clinically relevant prognostic parameters between patient groups, it may not have completely addressed all disparities. In particular, although not significantly different, we observed a discernible trend toward more frequent use of concurrent ADT in addition to MDT between the PSMA and choline PET/CT matched cohorts. Moreover, we did not consider the type and duration of ADT before MDT in the matching process. Altogether, these limitations prevent drawing a secure causative relationship between the observed differences in oncologic outcome and imaging methods. Therefore, further studies with appropriate methodologies are needed in this

TABLE 4
Overview of Previous Studies Regarding SBRT-Delivered MDT Guided by Different Imaging Techniques in Oligorecurrent PCa

Author	Oligometastatic patients (*n*)	Disease phase*	Imaging-guided MDT	Treatment received	Median follow-up (mo)	Endpoint	Result
Schmidt Hegemann, 2020 (*13*)	272 (subgroup analysis)	HSPC (NA)	$[^{68}\mathrm{Ga}]$-PSMA-11 vs. $[^{18}\mathrm{F}]$fluorocholine or $[^{11}\mathrm{C}]$C-choline PET/CT	SBRT ± ADT	30	bPFS	Imaging-guided MDT did not predict bPFS
Mazzola, 2021 (*14*)	88	HSPC (≤3)	$[^{68}\mathrm{Ga}]$Ga-PSMA-11 vs. $[^{18}\mathrm{F}]$fluorocholine PET/CT	SBRT	25	dPFS, ADT-FS	Imaging-guided MDT predicted ADT-FS but not dPFS
Deijen, 2021 (*15*)	50	HSPC (≤4)	$[^{68}\mathrm{Ga}]$Ga-PSMA-11 vs. $[^{18}\mathrm{F}]$F-methylcholine PET/CT	SBRT ± ADT	24.3	bPFS, ADT-FS	Imaging-guided MDT predicted bPFS and ADT-FS
Lanfranchi, 2023 (*16*)	37	HSPC or CRPC (≤5)	$[^{68}\mathrm{Ga}]$Ga-PSMA-11 vs. $[^{18}\mathrm{F}]$fluorocholine PET/CT	SBRT ± ADT	40.9	PFS (composite)	Imaging-guided MDT predicted PFS
Metz, 2023 (*17*)	123	HSPC (≤5)	$[^{68}\mathrm{Ga}]$Ga-PSMA-11 vs. $[^{18}\mathrm{F}]$fluorocholine PET/CT	SBRT ± ADT	42.2	bPFS, ADT-FS	Imaging-guided MDT predicted bPFS and ADT-FS

*Data in parentheses are number of metastatic lesions.

HSPC = hormone-sensitive prostate cancer; NA = not applicable; SBRT = stereotactic body radiotherapy; bPFS = biochemical PFS; dPFS = distant PFS; ADT-FS = ADT-free survival.

field. Nevertheless, the retrospective design was essential for conducting a real-world study, mirroring actual clinical practices and patient care, and providing the advantages of a less selected patient population and more generalizable results. Lastly, in response to the growing interest in integrating systemic therapies with MDT in the CRPC setting (*7*), we included oligorecurrent CRPC patients in our study. A dedicated subanalysis for CRPC patients could have provided further insights. However, it was not feasible to apply propensity score matching to CRPC patients because of insufficient statistical power. Additional studies are needed to address this point.

CONCLUSION

Diverse imaging methods may influence outcomes in patients with oligometastatic PCa undergoing MDT. However, prospective head-to-head studies, ideally incorporating a randomized design, are necessary to provide definitive evidence and facilitate the practical application of these findings.

DISCLOSURE

This work was performed within the framework of the project "RAISE—Robotics and AI for Socioeconomic Empowerment" and has been supported by European Union–NextGenerationEU and by the Italian Ministry of Health (5 × 1000 funds 2020 and Ricerca Corrente Funds 2022 granted to Matteo Bauckneht). Matteo Bauckneht reports personal fees from AAA and GE Healthcare outside the submitted work. No other potential conflict of interest relevant to this article was reported.

KEY POINTS

QUESTION: Are PET tracers interchangeable for guiding MDT in oligorecurrent PCa patients?

PERTINENT FINDINGS: We observed increased PFS, PFS2, and OS in oligorecurrent PCa patients treated with MDT guided by PSMA PET/CT as opposed to choline PET/CT. A hierarchy among PSMA-targeted radiopharmaceuticals was also observed, favoring [^{68}Ga]Ga-PSMA-11 over [^{18}F]F-PSMA-1007.

IMPLICATIONS FOR PATIENT CARE: The choice of PET tracer may influence oncologic outcomes in PCa patients with limited metastases treated with MDT. Prospective, randomized, head-to-head studies are necessary to establish these findings conclusively.

REFERENCES

1. Prostate cancer. European Association of Urology website. https://uroweb.org/guidelines/prostate-cancer. Accessed May 15, 2024.
2. Ciccarese C, Iacovelli R, Sternberg CN, Gillessen S, Tortora G, Fizazi K. Triplet therapy with androgen deprivation, docetaxel, and androgen receptor signalling inhibitors in metastatic castration-sensitive prostate cancer: a meta-analysis. *Eur J Cancer.* 2022;173:276–284.
3. Tucci M, Leone G, Buttigliero C, et al. Hormonal treatment and quality of life of prostate cancer patients: new evidence. *Minerva Urol Nefrol.* 2018;70:144–151.
4. Ost P, Reynders D, Decaestecker K, et al. Surveillance or metastasis-directed therapy for oligometastatic prostate cancer recurrence: a prospective, randomized, multicenter phase II trial. *J Clin Oncol.* 2018;36:446–453.
5. Phillips R, Shi WY, Deek M, et al. Outcomes of observation vs stereotactic ablative radiation for oligometastatic prostate cancer: the ORIOLE phase 2 randomized clinical trial. *JAMA Oncol.* 2020;6:650–659.
6. Deek MP, Van der Eecken K, Sutera P, et al. Long-term outcomes and genetic predictors of response to metastasis-directed therapy versus observation in oligometastatic prostate cancer: analysis of STOMP and ORIOLE trials. *J Clin Oncol.* 2022;40:3377–3382.
7. Gillessen S, Bossi A, Davis ID, et al. Management of patients with advanced prostate cancer-metastatic and/or castration-resistant prostate cancer: report of the Advanced Prostate Cancer Consensus Conference (APCCC) 2022. *Eur J Cancer.* 2023;185:178–215.
8. Grünig H, Maurer A, Thali Y, et al. Focal unspecific bone uptake on [^{18}F]-PSMA-1007 PET: a multicenter retrospective evaluation of the distribution, frequency, and quantitative parameters of a potential pitfall in prostate cancer imaging. *Eur J Nucl Med Mol Imaging.* 2021;48:4483–4494.
9. Seifert R, Telli T, Opitz M, et al. Unspecific ^{18}F-PSMA-1007 bone uptake evaluated through PSMA-11 PET, bone scanning, and MRI triple validation in patients with biochemical recurrence of prostate cancer. *J Nucl Med.* 2023;64:738–743.
10. Fendler WP, Eiber M, Beheshti M, et al. PSMA PET/CT: joint EANM procedure guideline/SNMMI procedure standard for prostate cancer imaging 2.0. *Eur J Nucl Med Mol Imaging.* 2023;50:1466–1486.
11. Zilli T, Achard V, Dal Pra A, et al. Recommendations for radiation therapy in oligometastatic prostate cancer: an ESTRO-ACROP Delphi consensus. *Radiother Oncol.* 2022;176:199–207.
12. Robins JM, Hernán MA, Brumback B. Marginal structural models and causal inference in epidemiology. *Epidemiology.* 2000;11:550–560.
13. Schmidt Hegemann NS, Rogowski P, Eze C, et al. Outcome after ^{68}Ga-PSMA-11 versus choline PET-based salvage radiotherapy in patients with biochemical recurrence of prostate cancer: a matched-pair analysis. *Cancers (Basel).* 2020;12:3395.
14. Mazzola R, Francolini G, Triggiani L, et al. Metastasis-directed therapy (SBRT) guided by PET-CT ^{18}F-choline versus PET-CT ^{68}Ga-PSMA in castration-sensitive oligorecurrent prostate cancer: a comparative analysis of effectiveness. *Clin Genitourin Cancer.* 2021;19:230–236.
15. Deijen CL, Vrijenhoek GL, Schaake EE, et al. PSMA-11-PET/CT versus choline-PET/CT to guide stereotactic ablative radiotherapy for androgen deprivation therapy deferral in patients with oligometastatic prostate cancer. *Clin Transl Radiat Oncol.* 2021;30:1–6.
16. Lanfranchi F, Belgioia L, Marcenaro M, et al. Oligometastatic prostate cancer treated with metastasis-directed therapy guided by positron emission tomography: does the tracer matter? *Cancers (Basel).* 2023;15:323.
17. Metz R, Rauscher A, Vaugier L, et al. Comparison of hormone-sensitive oligorecurrent prostate cancer patients based on routine use of choline and/or PSMA PET/CT to guide metastasis-directed therapy. *Cancers (Basel).* 2023;15:1898.
18. Booth CM, Eisenhauer EA, Gyawali B, Tannock IF. Progression-free survival should not be used as a primary end point for registration of anticancer drugs. *J Clin Oncol.* 2023;41:4968–4972.
19. Sutera P, Song Y, Van der Eecken K, et al. Clinical and genomic differences between advanced molecular imaging-detected and conventional imaging-detected metachronous oligometastatic castration-sensitive prostate cancer. *Eur Urol.* 2023;84:531–535.
20. Deek MP, Van der Eecken K, Phillips R, et al. The mutational landscape of metastatic castration-sensitive prostate cancer: the spectrum theory revisited. *Eur Urol.* 2021;80:632–640.
21. Feinstein AR, Sosin DM, Wells CK. The Will Rogers phenomenon: stage migration and new diagnostic techniques as a source of misleading statistics for survival in cancer. *N Engl J Med.* 1985;312:1604–1608.
22. Evangelista L, Maurer T, van der Poel H, et al. [^{68}Ga]Ga-PSMA versus [^{18}F]PSMA positron emission tomography/computed tomography in the staging of primary and recurrent prostate cancer. A systematic review of the literature. *Eur Urol Oncol.* 2022;5:273–282.
23. Pattison DA, Debowski M, Gulhane B, et al. Prospective intra-individual blinded comparison of [^{18}F]PSMA-1007 and [^{68}Ga]Ga-PSMA-11 PET/CT imaging in patients with confirmed prostate cancer. *Eur J Nucl Med Mol Imaging.* 2022;49:763–776.
24. Seifert R, Telli T, Opitz M, et al. Unspecific ^{18}F-PSMA-1007 bone uptake evaluated through PSMA-11 PET, bone scanning, and MRI triple validation in patients with biochemical recurrence of prostate cancer. *J Nucl Med.* 2023;64:738–743.
25. Alberts I, Bütikofer L, Rominger A, Afshar-Oromieh A. A randomised, prospective and head-to-head comparison of [^{68}Ga]Ga-PSMA-11 and [^{18}F]PSMA-1007 for the detection of recurrent prostate cancer in PSMA-ligand PET/CT-protocol design and rationale. *PLoS One.* 2022;17:e0270269.
26. Rauscher I, Krönke M, König M, et al. Matched-pair comparison of ^{68}Ga-PSMA-11 PET/CT and ^{18}F-PSMA-1007 PET/CT: frequency of pitfalls and detection efficacy in biochemical recurrence after radical prostatectomy. *J Nucl Med.* 2020;61:51–57.

Prostate-Specific Membrane Antigen–Targeted Imaging and Its Correlation with HOXB13 Expression

Duminduni Hewa Angappulige*[1], Nimrod S. Barashi*[1], Nicholas Pickersgill*[1], Cody Weimholt[2], Jingqin Luo[3,4], Ghazal Shadmani[5], Ziad Tarcha[5], Sampanna Rayamajhi[5], Nupam P. Mahajan[1,4], Gerald L. Andriole[1], Barry A. Siegel[†4,5], Eric H. Kim[†1,4], and Kiran Mahajan[†1,4]

[1]Division of Urologic Surgery, Department of Surgery, Washington University in St. Louis, St. Louis, Missouri; [2]Department of Pathology and Immunology, Washington University in St. Louis, St. Louis, Missouri; [3]Division of Public Health, Department of Surgery, Washington University in St. Louis, St. Louis, Missouri; [4]Alvin J. Siteman Cancer Center, Washington University in St. Louis, St. Louis, Missouri; and [5]Division of Nuclear Medicine, Mallinckrodt Institute of Radiology, Washington University in St. Louis, St. Louis, Missouri

Homeobox 13 (HOXB13) is an oncogenic transcription factor that directly regulates expression of folate hydrolase 1, which encodes prostate-specific membrane antigen (PSMA). HOXB13 is expressed in primary and metastatic prostate cancers (PCs) and promotes androgen-independent PC growth. Since HOXB13 promotes resistance to androgen receptor (AR)–targeted therapies and regulates the expression of folate hydrolase 1, we investigated whether SUVs on PSMA PET would correlate with HOXB13 expression. **Methods:** We analyzed 2 independent PC patient cohorts who underwent PSMA PET/CT for initial staging or for biochemical recurrence. In the discovery cohort, we examined the relationship between HOXB13, PSMA, and AR messenger RNA (mRNA) expression in prostate biopsy specimens from 179 patients who underwent PSMA PET/CT with ^{18}F-piflufolastat. In the validation cohort, we confirmed the relationship between HOXB13, PSMA, and AR by comparing protein expression in prostatectomy and lymph node (LN) sections from 19 patients enrolled in ^{18}F-rhPSMA-7.3 PET clinical trials. Correlation and association analyses were also used to confirm the relationship between the markers, LN positivity, and PSMA PET SUVs. **Results:** We observed a significant correlation between PSMA and HOXB13 mRNA ($P < 0.01$). The association between HOXB13 and ^{18}F-piflufolastat SUVs was also significant (SUV$_{max}$, $P = 0.0005$; SUV$_{peak}$, $P = 0.0006$). Likewise, the PSMA SUV$_{max}$ was significantly associated with the expression of HOXB13 protein in the ^{18}F-rhPSMA-7.3 PET cohort ($P = 0.008$). Treatment-naïve patients with LN metastases demonstrated elevated HOXB13 and PSMA levels in their tumors as well as higher PSMA tracer uptake and low AR expression. **Conclusion:** Our findings demonstrate that HOXB13 correlates with PSMA expression and PSMA PET SUVs at the mRNA and protein levels. Our study suggests that the PSMA PET findings may reflect oncogenic HOXB13 transcriptional activity in PC, thus potentially serving as an imaging biomarker for more aggressive disease.

Key Words: prostate cancer; HOXB13; androgen receptor; PSMA; PSMA PET; metastasis

J Nucl Med 2024; 65:1210–1216
DOI: 10.2967/jnumed.123.267301

Biomarkers that can predict aggressive prostate cancers (PCs) early in development are critical to improve patient outcomes (*1–4*). One important biomarker of PC is prostate-specific membrane antigen (PSMA), which is overexpressed in most PCs (*5*,*6*); its higher expression is associated with castration-resistant disease (*7*,*8*) and inferior metastasis-free survival (*9–11*). Recently, the Society for Nuclear Medicine and Molecular Imaging and the National Comprehensive Cancer Network have recommended PSMA PET for the initial staging of patients with unfavorable intermediate-, high-, and very high–risk clinically localized PC, as well as for patients with biochemically recurrent PC (*12*,*13*). Thus, higher-risk patients may benefit from undergoing PSMA PET for treatment planning, with consideration of extended pelvic nodal dissection, pelvic nodal radiation, or the addition of chemohormonal agents (*12*).

PC demonstrates intra- and intertumor heterogeneity, which may increase in response to androgen deprivation (*1*,*14*). PSMA expression also demonstrates heterogeneity at the intra- and intertumoral levels (*15–17*). Although PSMA PET/CT has improved the detection of nonlocalized, recurrent, and metastatic PCs (*18*), understanding the molecular relationships associated with PSMA PET findings may enable improved selection of treatments to improve overall survival outcomes.

We and others have previously demonstrated that homeobox 13 (HOXB13) promotes androgen-independent growth of PC as a pioneer transcription factor and as a regulator of critical PC target genes including the androgen receptor (AR) and folate hydrolase 1 that encodes PSMA (*3*,*13*,*19–23*). Moreover, HOXB13 expression is increased in response to enzalutamide in PC cell lines, and its depletion increases enzalutamide sensitivity (*3*,*22*). As such, ours and other studies have reported the association of HOXB13 with more aggressive disease, specifically, in AR-negative castration-resistant PC (CRPC) and in some neuroendocrine PCs (*3*,*21–26*). To improve the understanding between clinical tools and molecular drivers of PC progression, we sought to evaluate the correlation between HOXB13, PSMA expression, and PSMA PET findings, as well as their association with lymph node (LN) metastasis.

Received Dec. 19, 2023; revision accepted May 24, 2024.

For correspondence or reprints, contact Kiran Mahajan (kiranm@wustl.edu).

*Contributed equally to this work.

†Contributed equally to this work.

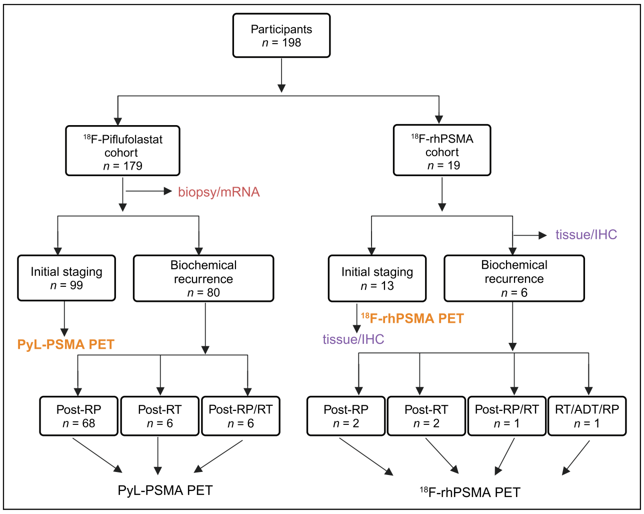

FIGURE 1. Study design of PSMA PET/CT and biomarker expression profiling in PC patients. Schematic diagram of patient stratification for retrospective analysis is shown. ADT = androgen-deprivation therapy; IHC = immunohistochemical; RP = radical prostatectomy; RT = radiation therapy.

MATERIALS AND METHODS

Study Design and Patient Demographics

The current study involving existing data was conducted under institutional review board approval with waiver of consent. We studied 2 independent subsets of patients imaged with 2 different PSMA radiopharmaceuticals. Group 1 was the discovery cohort, which included 179 patients who underwent PET/CT with ^{18}F-piflufolastat (PyL) (Lantheus), and group 2 was the validation cohort, which included 19 patients who underwent PET/CT with ^{18}F-rhPSMA-7.3 (Blue Earth Diagnostics) (Fig. 1). We performed a retrospective analysis of clinically obtained pathologic specimens (prostate biopsies before PSMA PET for group 1 and radical prostatectomy and LN sections after PSMA PET for group 2). Histopathologic examination was performed as a part of the standard clinical workflow for group 1 and group 2 specimens by board-certified genitourinary pathologists.

For the discovery cohort, messenger RNA (mRNA) expression profiling was performed using the Decipher GRID platform (Veracyte) (*27*). Normalized gene expression was obtained for all patients. For the validation cohort, deidentified formalin-fixed, paraffin-embedded (FFPE) radical prostatectomy and LN sections were used for immunohistochemical staining.

Immunohistochemical Staining and Quantification

Two FFPE radical prostatectomy sections from each patient were selected for immunohistochemical staining and were sufficient for quantification. FFPE tissue sections were stained with hematoxylin and eosin and with specific antibodies for HOXB13, folate hydrolase 1, and AR. The hematoxylin and eosin–stained and immunohistochemical-stained slides were digitally scanned at ×20 magnification using an Aperio whole-slide scanner, and digital quantitation was performed with Aperio ImageScope software (Leica Biosystems). An Aperio Positive Pixel Count algorithm (version 9; Leica Biosystems) was used to perform the analysis (*28*). Average positivity of immunohistochemical staining was obtained as the ratio of the number of positive pixels divided by the total number of positive plus negative pixels. The immunohistochemical slides were also manually analyzed by a board-certified genitourinary pathologist using the following formula: quick score = $P \times I$, where P represents the percentage of positive cells (0, 1+ [10%–25%], 2+ [25%–50%], 3+ [50%–75%], or 4+ [>75%]) and given as ordinal numbers and I represents intensity, scored as 1 (weak), 2 (moderate), or 3 (strong). More details are provided in the supplemental materials (supplemental materials are available at http://jnmt.snmjournals.org).

PSMA PET Imaging and Quantification

Group 1 patients underwent PSMA PET/CT after intravenous injection of 333 MBq ± 20% of PyL. Imaging was performed with a Biograph 40HD or an mCT PET/CT scanner (Siemens Healthineers). Group 2 patients underwent PSMA PET/CT with 296 MBq ± 20% of ^{18}F-rhPSMA-7.3 on a Siemens Biograph Vision 600 PET/CT scanner. The PSMA PET images were evaluated semiquantitatively by determination of SUV_{max} and SUV_{peak} of the most tracer-avid lesions identified on the scans (up to 3 foci in the prostate, if still present; up to 5 LN foci; and up to 2 osseous foci). In patients with multiple lesions in the prostate, the lesion with highest SUV_{max} was taken as the index lesion for correlation with mRNA or immunohistochemical analyses. For correlation of PSMA PET results with immunohistochemical results, the pathologist-defined lesion with the strongest (PSMA) or

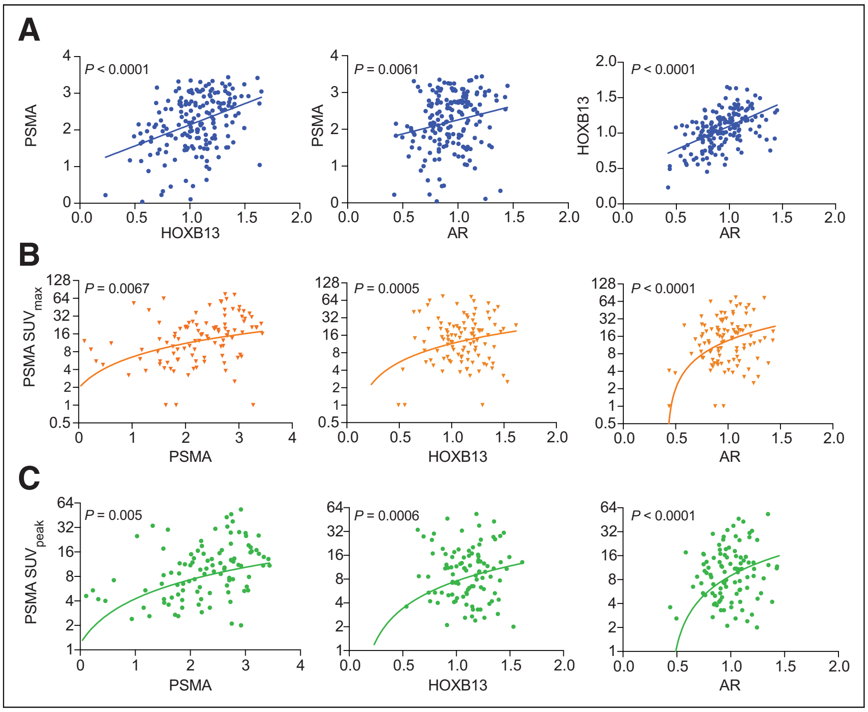

FIGURE 2. Association among HOXB13, PSMA, and AR with PSMA SUVs in PyL cohort. (A) Correlation among HOXB13, PSMA, and AR mRNA expression for each patient (n = 179). Lines represent linear regression. (B and C) Correlation among HOXB13, PSMA, and AR mRNA expression vs. prostate PSMA SUV_{max} (B) or prostate PSMA SUV_{peak} (C) for measurable lesions. Line represents linear regression (note logarithmic scale) (n = 105; initial staging PSMA PET–positive, n = 94; biochemical recurrence, n = 11).

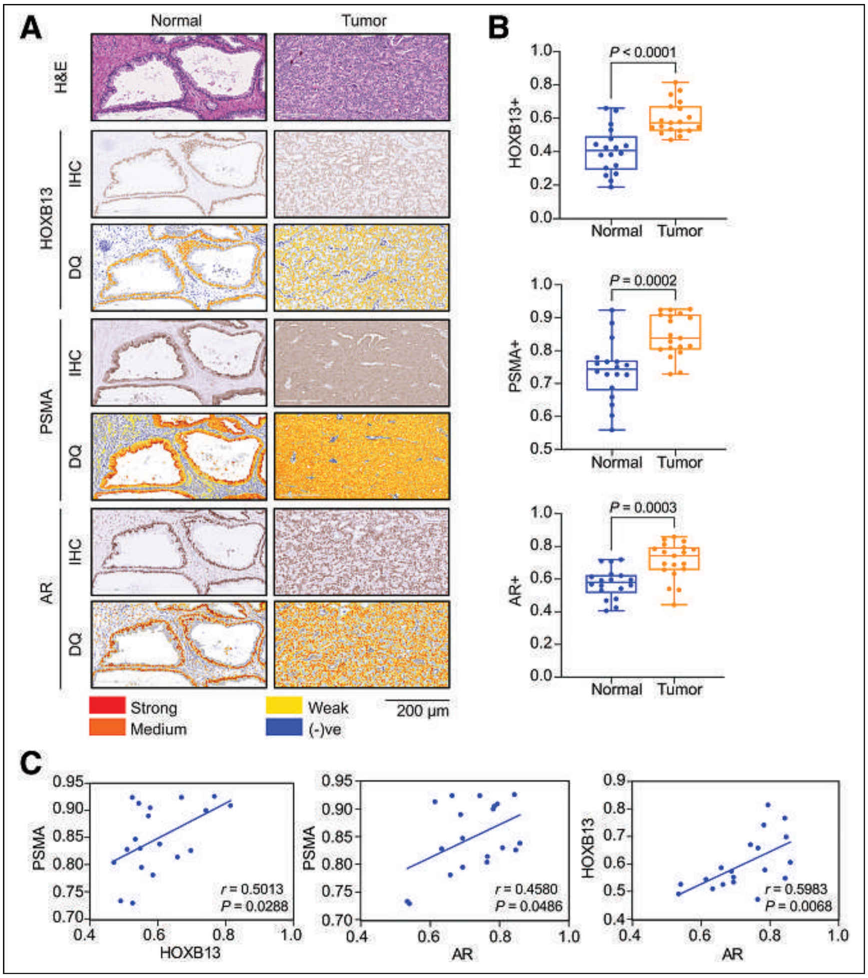

FIGURE 3. Correlation of HOXB13, PSMA, and AR protein expression in advanced PC. (A) Immunohistochemical (IHC) analysis shows representative normal and prostate tumor sections from individual FFPE patient specimens stained for AR, HOXB13, and PSMA. Digital quantification (DQ) analysis of marker expression is given below each panel. Scale bar = 200 μm. (B) Expression of HOXB13, AR, and PSMA in normal vs. tumor sections obtained by IHC and DQ determination was compared by Student *t* test (*****P* < 0.0001; *n* = 19). (C) Correlation analysis compares expression of each marker by IHC and DQ determination. Line represents linear regression, and *r* indicates Pearson correlation coefficient. H&E = hematoxylin and eosin; + = positive; (-)ve = negative.

median (AR and HOXB13) pixel positivity was plotted against PSMA SUV_{max} or SUV_{peak}. The PSMA PET and immunohistochemical parameters were correlated on a per-patient and per-lesion basis.

Statistical Analysis

Unpaired *t* tests were used to compare mRNA and protein expression of genes between normal tissue and tumors. To compare patient and tumor characteristics between PET negative and PET positive and lymph node or bone metastasis versus no metastasis, Wilcoxon rank sum test was used for continuous characteristics, whereas a Fisher exact test was used for categoric ones. A linear regression model was fit on HOXB13 mRNA gene expression on PSMA PET results (based on SUV_{max} or SUV_{peak}) and mRNA expression levels of AR, folate hydrolase 1, and prostate-specific antigen, adjusting for patient characteristics (age at scan, tumor stage, prostate-specific antigen level at scan, primary Gleason score, and time from radical prostatectomy). Pearson (parametric) and Spearman rank (nonparametric) correlation coefficients were calculated between 2 variables to quantify their correlation with *P* values reported testing the estimated correlation against 0. GraphPad Prism (version 9.0) and R (version 4.4.0, http://cran.r-project.org) were used for data analyses. *P* values of less than 0.05 were considered statistically significant.

RESULTS

Clinicopathologic Outcomes and Patient Stratification by Treatment

A summary of the clinicopathologic variables of the PyL (group 1) and ^{18}F-rhPSMA-7.3 (group 2) subjects is shown in Supplemental Tables 1 and 2. In group 1, of the 55.3% (99/179) treatment-naïve patients with newly diagnosed unfavorable intermediate-, high-, or very high–risk PC, according to the National Comprehensive Cancer Network, 93.9% (93/99) had positive PSMA PET results. Likewise, of the 44.6% (80/179) group 1 patients with biochemically recurrent PC, 47.5% (38/80) had positive PSMA PET results (Supplemental Table 1); group 2 consisted of 19 patients enrolled in the ^{18}F-rhPSMA-7.3 clinical trials, for whom FFPE was available. PSMA PET revealed metastasis in 46% (6/13) of the treatment-naïve patients (2 bone and 4 LN metastases). In patients with biochemical recurrence, 66.6% (4/6) had PSMA PET–positive LNs (Supplemental Table 2). Pathologically positive LNs were found at radical prostatectomy or pelvic LN dissection in 46% (6/13) of treatment-naïve patients.

Association of HOXB13 Expression with PSMA Tracer Uptake

Correlation analysis for PSMA, HOXB13, and AR mRNA expression in group 1 demonstrated strong correlation among each patient in this group (Fig. 2A). A significant correlation was also observed for the above 3 markers with the kallikrein genes *KLK2* and *KLK3,* encoding hexokinase 2 and prostate-specific antigen, respectively, according to the National Comprehensive Cancer Network guidelines on prostate-specific antigen serine proteases (Supplemental Figs. 1A–1C). In addition, PSMA and HOXB13 at mRNA levels (Spearman correlation [*r*] = 0.391; *P* < 0.0001) (Fig. 2A) and HOXB13 mRNA and PyL uptake showed significant correlations (*P* = 0.0005 and 0.0006 for SUV_{max} and SUV_{peak}, respectively) (Figs. 2B and 2C). This correlation observation was also noted for AR (*P* < 0.0001 for SUV_{max} and SUV_{peak}) and PSMA (*P* = 0.006 and 0.005 for SUV_{max} and SUV_{peak}, respectively) (Figs. 2B and 2C). Linear regression analysis of HOXB13 against the covariates indicated association with the Gleason subpattern 5 versus 3 (*P* = 0.048), AR (*P* = 0.018), and PSMA (*P* = 0.022) mRNA expression (Supplemental Table 3).

Coexpression of HOXB13 and PSMA in Primary PC and LN Metastases

PSMA, HOXB13, and AR protein expression was analyzed in group 2 FFPE specimens obtained from the prostate and LNs

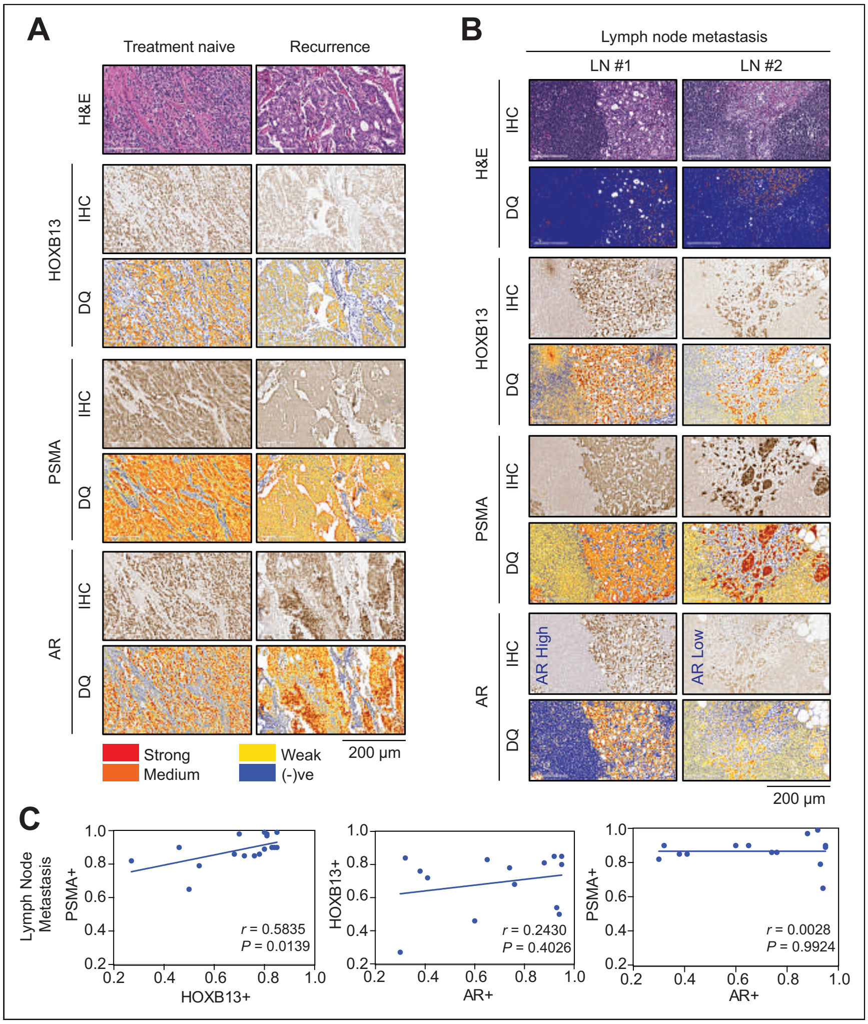

FIGURE 4. HOXB13 PSMA coexpression in recurrent and metastatic PC. (A) Representative normal and prostate tumor FFPE sections from treatment-naïve or recurrent PC immunohistochemically (IHC) stained for AR, HOXB13, and PSMA protein expression. Digital quantification (DQ) of staining is shown below each panel. Left panel: treatment-naïve. Right panel: recurrence with radiation plus androgen-deprivation therapy. (B) LN sections (GGG3 T3aN1 for LN 1 or GGG5 T3bN1 for LN 2). (C) Pearson correlation analysis comparing HOXB13 and PSMA protein expression in LNs. Line represents linear regression, and *r* indicates Pearson correlation coefficient. H&E = hematoxylin and eosin; + = positive; (-)ve = negative.

(Fig. 3A). Validation of the antibodies used for immunohistochemical analysis is provided in Supplemental Figures 2A and 2B. Digital quantification results of HOXB13, PSMA, and AR staining in these specimens are provided in Supplemental Table 4. All patient specimens had expression of the 3 targets with some degree of intra- and intertumoral heterogeneity (Supplemental Figs. 3A–3C). All 3 markers showed statistically significant differences between normal prostate and tumor, indicating increased protein expression overall in the tumor (Fig. 3B). Pearson correlation analysis comparing the expression of each marker in normal prostate and in tumor revealed a significant correlation between HOXB13 and PSMA for normal prostate ($r = 0.684$, $P = 0.001$) and tumor ($r = 0.501$, $P = 0.028$) (Fig. 3C; Supplemental Fig. 4A). This trend was maintained between AR and HOXB13, although slightly reduced in tumor (normal prostate: $r = 0.804$, $P = <0.0001$; tumor: $r = 0.598$, $P = 0.006$), and between PSMA and AR (normal prostate: $r = 0.878$, $P < 0.0001$; tumor: $r = 0.458$, $P = 0.048$) (Fig. 3C; Supplemental Figs. 4B and 4C).

Among the patients in group 2 who had biochemical recurrence, sustained AR, HOXB13, and PSMA expression levels were identified despite prior radiation and androgen-deprivation therapy (Fig. 4A). Kruskal–Wallis testing that compared the treatment-naïve patients with the biochemical-recurrence patients revealed a significant difference for both AR ($P < 0.00001$) and HOXB13 ($P < 0.00001$) (Supplemental Fig. 5). Analysis of LN FFPE sections from treatment-naïve PC patients with PSMA PET–positive LNs revealed coexpression of HOXB13 and PSMA. However, AR expression was variable among these PSMA PET–positive LNs, with some displaying low levels of AR expression (Fig. 4B). Pearson correlation analysis revealed a significant correlation between HOXB13 and PSMA ($r = 0.583$, $P = 0.014$) but not between AR and HOXB13 ($r = 0.243$, $P = 0.402$) or PSMA and AR ($r = 0.002$, $P = 0.992$) in LN metastasis (Fig. 4C).

HOXB13 and PSMA Expression and Correlation with PSMA SUVs

Analysis pipeline and corresponding immunohistochemical images of the PSMA PET scans for 2 representative cases are shown in Figures 5A and 5B. We observed statistically significant correlations for prostate tumor SUV_{peak} with immunohistochemical staining and digital quantitation for PSMA ($r = 0.737$, $P = 0.004$), HOXB13 ($r = 0.702$, $P = 0.007$), and AR ($r = 0.659$, $P = 0.014$) in the prostate lesions (Fig. 5C) or SUV_{max} with immunohistochemical staining and digital quantitation for PSMA ($r = 0.806$, $P = 0.001$), HOXB13 ($r = 0.697$, $P = 0.008$), and AR ($r = 0.743$, $P = 0.003$) in the prostate lesions (Fig. 5D; Supplemental Table 5).

DISCUSSION

In this study, we found a significant relationship between HOXB13 and PSMA in PC. PC uptake of the PSMA tracers PyL and ^{18}F-rhPSMA-7.3 was significantly associated with tissue-level HOXB13 expression, suggesting that PSMA PET findings may be an important prognostic biomarker for potentially lethal (i.e., castration-resistant) PC. An earlier study reported PSMA response heterogeneity in SUV_{max} in hormone-sensitive PC, whereas all men with metastatic CRPC showed an increase in SUV_{max} compared with that at baseline (*17*). In addition, for patients with advanced PC started on abiraterone and enzalutamide, a change in PyL uptake in PC lesions or development of new lesions was prognostic of time-to-therapy change and overall survival (*29*). This

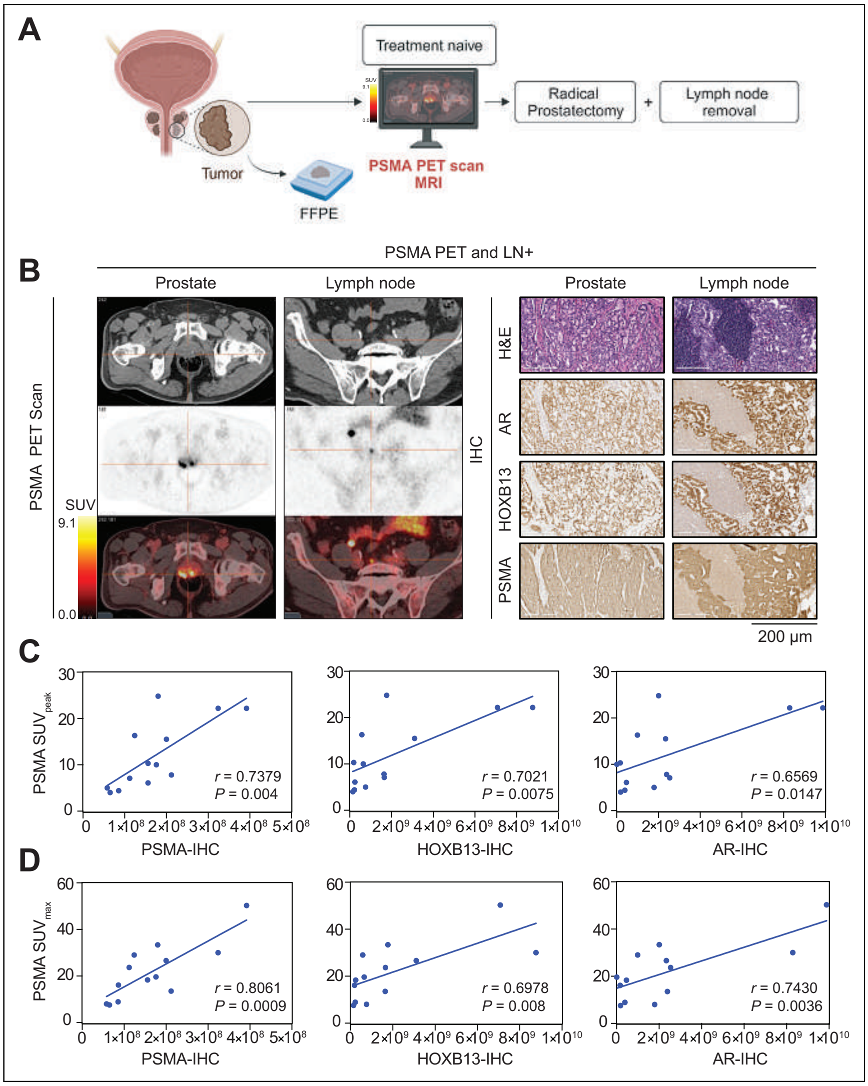

FIGURE 5. Detection of primary and metastatic prostate tumors by ^{18}F-rhPSMA-7.3 PSMA PET. (A) Schematic of screening of PC patients with PSMA PET. (B) ^{18}F-rhPSMA-7.3 PET/CT images of PSMA-positive prostate tumor and LN metastasis. Immunohistochemical (IHC) analysis shows representative FFPE-fixed prostate and LN patient sections stained for AR, HOXB13, and PSMA with corresponding hematoxylin and eosin (H&E) staining. Scale bar = 200 μm. (C and D) Pearson correlation analysis of the individual biomarker expression by IHC and digital quantification and prostate PSMA SUV_{peak} (C) ($n = 19$) and prostate PSMA SUV_{max} (D) ($n = 19$). Line represents linear regression, and *r* indicates Pearson correlation coefficient.

difference in PSMA response may be partially attributable to heterogeneous HOXB13 and AR expression as their levels significantly change in CRPCs compared with hormone-naïve PCs (*26*,*30*).

Our study findings are consistent with prior publications that have demonstrated PSMA expression positively correlating with higher Gleason scores ($P < 0.0001$ in biopsy specimens and $P = 0.007$ in prostatectomy samples) (*31*), with LN involvement ($P = 0.007$) (*32*) and reduced recurrence-free survival ($P < 0.001$) (*33*). In a treatment scenario, hormone-naïve men treated with androgen-deprivation therapy showed a reduction in PSMA tracer uptake initially on treatment, with a subsequent rise at some tumor sites (*17*,*34*). Furthermore, PSMA levels and ^{68}Ga-PSMA-11 uptake are increased in men with metastatic CRPC treated with enzalutamide (*7*,*17*,*35*,*36*). Thus, the clinical importance of PSMA PET imaging lies in its ability to redefine staging via its sensitivity to detect metastatic disease in patients with previously diagnosed nonmetastatic CRPC (*37*). Most importantly, the future of PC treatment will likely include ^{177}Lu-PSMA therapy, as it has demonstrated high response rates, low toxicity, and improved quality of life for men diagnosed with metastatic CRPC, despite prior treatment with docetaxel, cabazitaxel, or a second AR pathway antagonist, abiraterone, after enzalutamide (*38*,*39*).

This relatively novel description of the strong relationship between expression of HOXB13 and PSMA with the results of PSMA PET has several potential clinical implications. For example, HOXB13 expression in biopsy specimens might be useful to guide the appropriateness of PSMA PET for initial staging. Currently, the National Comprehensive Cancer Network's risk categories are used to determine who may benefit from PSMA PET, which is not personalized to an individual patient's PC biology. With HOXB13 expression and activity linked to castration-independent behavior (*21*,*22*,*24*,*25*,*40*), patients with high HOXB13 and PSMA expression may benefit from primary treatments that do not rely on androgen-deprivation therapy or castration to be therapeutically effective. Furthermore, HOXB13 and PSMA expression may be useful as a biomarker to better select patients for earlier use of PSMA-targeted radiopharmaceutical therapy, such as ^{177}Lu-PSMA-617 (*41*–*43*). In the currently ongoing trial PSMAddition (NCT04720157), which is comparing ^{177}Lu-PSMA-617 therapy plus the standard of care with the standard of care alone in newly diagnosed metastatic hormone-sensitive PC, secondary analysis of diagnostic prostate biopsy tissue for HOXB13 expression may reveal which patients are better suited for upfront PSMA-targeted radiopharmaceutical therapy.

The use of different PSMA tracers could be considered a limitation of our study. However, this is reflective of clinical practice, and in this study, the correlation with HOBX13 was maintained, irrespective of the specific tracer used. The LN studies are underpowered, and thus the significance of the finding remains to be determined. Technical limitations may have impacted colocalization between FFPE tissue samples and PET activity. However, the significant positive correlation we observed between markers in pathologist-confirmed lesions and PSMA PET findings in our large cohort suggests that we were able to overcome this limitation.

The correlations between HOXB13 and PSMA expression are statistically significant, but the magnitude of correlation is limited in the discovery cohort (group 1). This limited correlation may be due to gene expression methodology performed with Decipher GRID

(Decipher Bioscience). Previously, we reported a strong correlation between PSMA and HOXB13 expression in The Cancer Genome Atlas Prostate Adenocarcinoma ($n = 492$, $r = 0.51$, $P = 2.2 \times 10^{-37}$) and the Stand Up to Cancer–Prostate Cancer Foundation ($n = 444$, $r = 0.54$, $P = 3.66 \times 10^{-10}$) datasets, which are based on RNA sequencing (*3*). Compared with RNA sequencing, the Decipher GRID microarray hybridization technology may have limited gene-expression measurements because of the background signal at the low end and signal saturation at the high end ($>10^5$ for RNA sequence vs. 10^3 for arrays).

CONCLUSION

HOXB13 expression at both mRNA and protein levels correlates significantly with clinical PSMA PET findings, underscoring the likely mechanistic relationship between HOXB13 and PSMA expression in PC. Our findings of PSMA PET association with HOXB13 could pave the way for future studies incorporating HOXB13 and PSMA testing at earlier stages of PC diagnosis, which could then guide personalized PC care.

DISCLOSURE

Kiran Mahajan received financial support from the Department of Defense (W81XWH-21-1-0203) and the Department of Surgery at Washington University. Eric Kim is supported by funding from the Midwest Stone Institute, the American Cancer Society, the Siteman Investment Program, and NIH/NCI grant R01-CA258690. PET/CT analysis was supported in part by NCI Cancer Center support (P30 CA091842). Barry Siegel reports receiving grants from the American College of Radiology, Blue Earth Diagnostics, Curium Pharma, and Progenics Pharmaceuticals and receiving personal fees from the American College of Radiology, Capella Imaging, Curium Pharma, Evicore Health Care, GE Healthcare, Lantheus Medical Imaging, and Siemens Healthineers. Gerald Andriole has an advisory role with Invitae, Lantheus Medical Imaging, and Siemens Medical Solutions. Kiran Mahajan and Nupam Mahajan are cofounders of Technogenesys, a startup company that controls the intellectual property and patents on the ACK1 inhibitor (*R*)-**9b**. No other potential conflict of interest relevant to this article was reported.

ACKNOWLEDGMENTS

We thank the Siteman Cancer Center Imaging and Response Assessment Core for assistance with PET/CT analysis, our clinical coordinators Alex Klim and Karla Bergeron for regulatory support, and Blue Earth Diagnostics for use of the ^{18}F-rhPSMA-7.3 PET data.

KEY POINTS

QUESTION: Does the uptake of PSMA-targeted radiopharmaceuticals correlate with HOXB13 expression in PC lesions to enable improved molecular profiling of PC?

PERTINENT FINDINGS: Prostate tumor SUVs of PyL and ^{18}F-rhPSMA-7.3 were significantly associated with HOXB13 expression as assessed by mRNA analysis or by immunohistochemical staining.

IMPLICATIONS FOR PATIENT CARE: Combining PSMA PET with HOXB13 RNA or protein expression profiling of biopsy specimens or resected tumors may enable early improved profiling of high-risk PC in the clinical setting.

REFERENCES

1. Kim EH, Cao D, Mahajan NP, Andriole GL, Mahajan K. ACK1-AR and AR-HOXB13 signaling axes: epigenetic regulation of lethal prostate cancers. *NAR Cancer.* 2020;2:zcaa018.
2. Mahajan K, Malla P, Lawrence HR, et al. ACK1/TNK2 regulates histone H4 Tyr88-phosphorylation and AR gene expression in castration-resistant prostate cancer. *Cancer Cell.* 2017;31:790–803.e8.
3. Nguyen DT, Yang W, Renganathan A, et al. Acetylated HOXB13 regulated super enhancer genes define therapeutic vulnerabilities of castration-resistant prostate cancer. *Clin Cancer Res.* 2022;28:4131–4145.
4. Quintanal-Villalonga Á, Chan JM, Yu HA, et al. Lineage plasticity in cancer: a shared pathway of therapeutic resistance. *Nat Rev Clin Oncol.* 2020;17:360–371.
5. Hawkey NM, Sartor AO, Morris MJ, Armstrong AJ. Prostate-specific membrane antigen-targeted theranostics: past, present, and future approaches. *Clin Adv Hematol Oncol.* 2022;20:227–238.
6. Sokoloff RL, Norton KC, Gasior CL, Marker KM, Grauer LS. A dual-monoclonal sandwich assay for prostate-specific membrane antigen: levels in tissues, seminal fluid and urine. *Prostate.* 2000;43:150–157.
7. Wright GL Jr, Grob BM, Haley C, et al. Upregulation of prostate-specific membrane antigen after androgen-deprivation therapy. *Urology.* 1996;48:326–334.
8. Kessel K, Bernemann C, Bogemann M, Rahbar K. Evolving castration resistance and prostate specific membrane antigen expression: implications for patient management. *Cancers (Basel).* 2021;13:3556.
9. Chu CE, Alshalalfa M, Sjostrom M, et al. Prostate-specific membrane antigen and fluciclovine transporter genes are associated with variable clinical features and molecular subtypes of primary prostate cancer. *Eur Urol.* 2021;79:717–721.
10. Ross JS, Sheehan CE, Fisher HA, et al. Correlation of primary tumor prostate-specific membrane antigen expression with disease recurrence in prostate cancer. *Clin Cancer Res.* 2003;9:6357–6362.
11. Hofman MS, Iravani A. Gallium-68 prostate-specific membrane antigen PET imaging. *PET Clin.* 2017;12:219–234.
12. Jadvar H, Calais J, Fanti S, et al. Appropriate use criteria for prostate-specific membrane antigen PET imaging. *J Nucl Med.* 2022;63:59–68.
13. Barashi NS, Li T, Angappulige DH, et al. Symptomatic benign prostatic hyperplasia with suppressed epigenetic regulator HOXB13 shows a lower incidence of prostate cancer development. *Cancers (Basel).* 2024;16:213.
14. Vlachostergios PJ, Puca L, Beltran H. Emerging variants of castration-resistant prostate cancer. *Curr Oncol Rep.* 2017;19:32.
15. Corpetti M, Muller C, Beltran H, de Bono J, Theurillat JP. Prostate-specific membrane antigen-targeted therapies for prostate cancer: towards improving therapeutic outcomes. *Eur Urol.* 2024;85:193–204.
16. Mannweiler S, Amersdorfer P, Trajanoski S, Terrett JA, King D, Mehes G. Heterogeneity of prostate-specific membrane antigen (PSMA) expression in prostate carcinoma with distant metastasis. *Pathol Oncol Res.* 2009;15:167–172.
17. Emmett L, Yin C, Crumbaker M, et al. Rapid modulation of PSMA expression by androgen deprivation: serial ^{68}Ga-PSMA-11 PET in men with hormone-sensitive and castrate-resistant prostate cancer commencing androgen blockade. *J Nucl Med.* 2019;60:950–954.
18. Jochumsen MR, Bouchelouche K. PSMA PET/CT for primary staging of prostate cancer: an updated overview. *Semin Nucl Med.* 2024;54:39–45.
19. Pomerantz MM, Li F, Takeda DY, et al. The androgen receptor cistrome is extensively reprogrammed in human prostate tumorigenesis. *Nat Genet.* 2015; 47:1346–1351.
20. Pomerantz MM, Qiu X, Zhu Y, et al. Prostate cancer reactivates developmental epigenomic programs during metastatic progression. *Nat Genet.* 2020;52:790–799.
21. Bakht MK, Yamada Y, Ku SY, et al. Landscape of prostate-specific membrane antigen heterogeneity and regulation in AR-positive and AR-negative metastatic prostate cancer. *Nat Cancer.* 2023;4:699–715.
22. Nerlakanti N, Yao J, Nguyen DT, et al. Targeting the BRD4-HOXB13 coregulated transcriptional networks with bromodomain-kinase inhibitors to suppress metastatic castration-resistant prostate cancer. *Mol Cancer Ther.* 2018;17:2796–2810.
23. Angappulige DH, Mahajan NP, Mahajan K. Epigenetic underpinnings of tumor-immune dynamics in prostate cancer immune suppression. *Trends Cancer.* 2024; 10:369–381.
24. Patel RA, Sayar E, Coleman I, et al. Characterization of HOXB13 expression patterns in localized and metastatic castration-resistant prostate cancer. *J Pathol.* 2024;262:105–120.
25. Weiner AB, Faisal FA, Davicioni E, et al. Somatic HOXB13 expression correlates with metastatic progression in men with localized prostate cancer following radical prostatectomy. *Eur Urol Oncol.* 2021;4:955–962.
26. Ylitalo EB, Thysell E, Jernberg E, et al. Subgroups of castration-resistant prostate cancer bone metastases defined through an inverse relationship between androgen receptor activity and immune response. *Eur Urol.* 2017;71:776–787.

27. Dalela D, Loppenberg B, Sood A, Sammon J, Abdollah F. Contemporary role of the Decipher test in prostate cancer management: current practice and future perspectives. *Rev Urol.* 2016;18:1–9.
28. Jerome JA, Wenzel SE, Trejo Bittar HE. Digital imaging analysis reveals reduced alveolar α-smooth muscle actin expression in severe asthma. *Appl Immunohistochem Mol Morphol.* 2021;29:506–512.
29. Zukotynski KA, Emmenegger U, Hotte S, et al. Prospective, single-arm trial evaluating changes in uptake patterns on prostate-specific membrane antigen-targeted ^{18}F-DCFPyL PET/CT in patients with castration-resistant prostate cancer starting abiraterone or enzalutamide. *J Nucl Med.* 2021;62:1430–1437.
30. Chen Z, Wu D, Thomas-Ahner JM, et al. Diverse AR-V7 cistromes in castration-resistant prostate cancer are governed by HoxB13. *Proc Natl Acad Sci USA.* 2018; 115:6810–6815.
31. Bravaccini S, Puccetti M, Bocchini M, et al. PSMA expression: a potential ally for the pathologist in prostate cancer diagnosis. *Sci Rep.* 2018;8:4254.
32. Queisser A, Hagedorn SA, Braun M, Vogel W, Duensing S, Perner S. Comparison of different prostatic markers in lymph node and distant metastases of prostate cancer. *Mod Pathol.* 2015;28:138–145.
33. Hupe MC, Philippi C, Roth D, et al. Expression of prostate-specific membrane antigen (PSMA) on biopsies is an independent risk stratifier of prostate cancer patients at time of initial diagnosis. *Front Oncol.* 2018;8:623.
34. Malaspina S, Ettala O, Tolvanen T, et al. Flare on [^{18}F]PSMA-1007 PET/CT after short-term androgen deprivation therapy and its correlation to FDG uptake: possible marker of tumor aggressiveness in treatment-naive metastatic prostate cancer patients. *Eur J Nucl Med Mol Imaging.* 2023;50:613–621.
35. Hope TA, Truillet C, Ehman EC, et al. ^{68}Ga-PSMA-11 PET imaging of response to androgen receptor inhibition: first human experience. *J Nucl Med.* 2017;58:81–84.
36. Staniszewska M, Fragoso Costa P, Eiber M, et al. Enzalutamide enhances PSMA expression of PSMA-low prostate cancer. *Int J Mol Sci.* 2021;22:7431.
37. Fendler WP, Weber M, Iravani A, et al. Prostate-specific membrane antigen ligand positron emission tomography in men with nonmetastatic castration-resistant prostate cancer. *Clin Cancer Res.* 2019;25:7448–7454.
38. Violet J, Sandhu S, Iravani A, et al. Long-term follow-up and outcomes of retreatment in an expanded 50-patient single-center phase II prospective trial of ^{177}Lu-PSMA-617 theranostics in metastatic castration-resistant prostate cancer. *J Nucl Med.* 2020;61:857–865.
39. Calais J, Czernin J, Thin P, et al. Safety of PSMA-targeted molecular radioligand therapy with ^{177}Lu-PSMA-617: results from the prospective multicenter phase 2 trial RESIST-PC (NCT03042312). *J Nucl Med.* 2021;62:1447–1456.
40. Varinot J, Furudoi A, Drouin S, et al. HOXB13 protein expression in metastatic lesions is a promising marker for prostate origin. *Virchows Arch.* 2016;468:619–622.
41. Moradi Tuchayi AM, Yadav S, Jiang F, et al. Real-world experience with ^{177}Lu-PSMA-617 radioligand therapy after Food and Drug Administration approval. *J Nucl Med.* 2024;65:735–739.
42. Hofman MS, Emmett L, Sandhu S, et al. Overall survival with [^{177}Lu]Lu-PSMA-617 versus cabazitaxel in metastatic castration-resistant prostate cancer (TheraP): secondary outcomes of a randomised, open-label, phase 2 trial. *Lancet Oncol.* 2024; 25:99–107.
43. Sartor O, de Bono J, Chi KN, et al. Lutetium-177-PSMA-617 for metastatic castration-resistant prostate cancer. *N Engl J Med.* 2021;385:1091–1103.

The Role of Fibroblast Activation Protein in Glioblastoma and Gliosarcoma: A Comparison of Tissue, ^{68}Ga-FAPI-46 PET Data, and Survival Data

Christoph Oster[1,2], Lukas Kessler[3], Tobias Blau[4], Kathy Keyvani[4], Kim M. Pabst[3], Wolfgang P. Fendler[3], Pedro Fragoso Costa[3], Lazaros Lazaridis[1], Teresa Schmidt[1], Jonas Feldheim[1], Daniela Pierscianek[5,6], Hans Ulrich Schildhaus[7,8], Ulrich Sure[5], Yahya Ahmadipour[5], Christoph Kleinschnitz[1], Nika Guberina[9], Martin Stuschke[9], Cornelius Deuschl[10], Björn Scheffler[2,11], Ken Herrmann*[3,12], Sied Kebir*[1,2], and Martin Glas*[1,2]

[1]Department of Neurology and Center for Translational Neuro- and Behavioral Sciences (C-TNBS), Division of Clinical Neurooncology, University Medicine Essen, University Duisburg–Essen, Essen, Germany; [2]German Cancer Consortium (DKTK), Partner Site Essen–Düsseldorf, Partnership Between DKFZ and University Hospital Essen, Essen, Germany; and DKFZ–Division of Translational Neurooncology at West German Cancer Center (WTZ), University Medicine Essen, University Duisburg–Essen, Essen, Germany; [3]Department of Nuclear Medicine, University of Duisburg–Essen, and German Cancer Consortium (DKTK)–University Hospital Essen, Essen, Germany; and National Center for Tumor Diseases (NCT), NCT West, Essen, Germany; [4]Institute of Neuropathology, University Medicine Essen, University Duisburg-Essen, Essen, Germany; [5]Department of Neurosurgery and Spine Surgery, Center for Translational Neuro- and Behavioral Sciences (C-TNBS), University Medicine Essen, University Duisburg–Essen, Essen, Germany; [6]Department of Neurosurgery and Spine Surgery, St. Marienhospital Lünen, Lünen, Germany; [7]Institute of Pathology, University Medicine Essen, University Duisburg-Essen, Essen, Germany; [8]Discovery Life Sciences Biomarker Services GmbH, Kassel, Germany; [9]Department of Radiotherapy, University Medicine Essen, University Duisburg-Essen, Essen, Germany; [10]Institute for Diagnostic and Interventional Radiology and Neuroradiology, University Medicine Essen, University of Duisburg-Essen, Essen, Germany; [11]German Cancer Research Center (DKFZ), Heidelberg, Germany; and [12]National Center for Tumor Diseases (NCT), NCT West, Heidelberg, Germany

Despite their unique histologic features, gliosarcomas belong to the group of glioblastomas and are treated according to the same standards. Fibroblast activation protein (FAP) is a component of a tumor-specific subpopulation of fibroblasts that plays a critical role in tumor growth and invasion. Some case studies suggest an elevated expression of FAP in glioblastoma and a particularly strong expression in gliosarcoma attributed to traits of predominant mesenchymal differentiation. However, the prognostic impact of FAP and its diagnostic and therapeutic potential remain unclear. Here, we investigate the clinical relevance of FAP expression in gliosarcoma and glioblastoma and how it correlates with ^{68}Ga–FAP inhibitor (FAPI)–46 PET uptake. **Methods:** Patients diagnosed with gliosarcoma or glioblastoma without sarcomatous differentiation with an overall survival of less than 2.5 y were enrolled. Histologic examination included immunohistochemistry and semiquantitative scoring of FAP (0–3, with higher values indicating stronger expression). Additionally, ^{68}Ga-FAPI-46 PET scans were performed in a subset of glioblastomas without sarcomatous differentiation patients. The clinical SUVs were correlated with FAP expression levels in surgically derived tumor tissue and relevant prognostic factors. **Results:** Of the 61 patients who were enrolled, 13 of them had gliosarcoma. Immunohistochemistry revealed significantly more FAP in gliosarcomas than in glioblastomas without sarcomatous differentiation of tumor tissue ($P < 0.0001$). In the latter, FAP expression was confined to the perivascular space, whereas neoplastic cells additionally expressed FAP in gliosarcoma. A significant correlation of immunohistochemical FAP with SUV_{mean} and SUV_{peak} of ^{68}Ga-FAPI-46 PET indicates that clinical tracer uptake represents FAP expression of the tumor. Although gliosarcomas express higher levels of FAP than do glioblastomas without sarcomatous differentiation, overall survival does not significantly differ between the groups. **Conclusion:** The analysis reveals a significant correlation between SUV_{mean} and SUV_{peak} in ^{68}Ga-FAPI-46 PET and immunohistochemical FAP expression. This study indicates that FAP expression is much more abundant in the gliosarcoma subgroup of glioblastomas. This could open not only a diagnostic but also a therapeutic gap, since FAP could be explored as a theranostic target to enhance survival in a distinct subgroup of high-risk brain tumor patients with poor survival prognosis.

Key Words: FAP; ^{68}Ga-FAPI-46 PET; glioblastoma; gliosarcoma; theranostic

J Nucl Med 2024; 65:1217–1223
DOI: 10.2967/jnumed.123.267151

Glioblastoma multiforme, a highly malignant primary brain tumor, has a median survival of about 14 mo after optimal surgical resection and chemoradiotherapy (*1*). Its subtype, gliosarcoma, shows both glial and sarcomatous differentiation (*2*,*3*) and has a similar median survival of approximately 17 mo (*4*). Despite their different histologies, both are treated with the same standard therapies (*5*). For simplicity, the term *glioblastoma* will be used for *glioblastoma without sarcomatous differentiation* hereafter, even though gliosarcomas are naturally considered a subgroup of glioblastoma.

Recent focus on the tumor microenvironment has been to find new therapies, despite the lack of survival benefits from previous immunotherapy trials in glioblastoma. Current studies explore potential immunotherapies (e.g., NOA-16, NOA-21, or DCVax trials (*6*–*9*)). Targeting molecules such as human epidermal growth factor receptor 2 or endothelial growth factor receptor in immunotherapy has been

---

Received Dec. 2, 2023; revision accepted May 22, 2024.

For correspondence or reprints, contact Martin Glas (martin.glas@uk-essen.de).

*Contributed equally to this work.

suggested, though their presence in normal tissues raises concerns about side effects and their varied expression in glioma cells hinders efficacy (*10*,*11*).

Fibroblast activation protein (FAP), found in a specific subgroup of tumor-associated fibroblasts known as cancer-associated fibroblasts, promotes tumor growth and invasion (*12*). FAP, an unusual serine protease with dipeptidyl peptidase and endopeptidase activities, influences the extracellular matrix and cellular signaling, altering gene transcription related to cell cycle, proliferation, and invasion (*13*,*14*). FAP also contributes to an immunosuppressive tumor microenvironment and can confer resistance to temozolomide (*14*). FAP's regulation is influenced by factors such as transforming growth factor β-1 from astrocytes and glioma cells (*15*).

Although FAP is minimally expressed in normal tissues, its significant expression in glioblastoma, especially gliosarcoma, is likely linked to its mesenchymal differentiation (*16–18*). Ebert et al. observed that nearly 40% of glioblastomas were FAP-positive, whereas normal brain tissue was not (*10*). In vivo FAP-specific PET imaging shows higher FAP expression in more malignant tissues than in lower-grade gliomas, independent of cell counts (*19–21*). Inhibition of FAP leads to cell cycle arrest and decreased cell proliferation (*22*), yet the prognostic significance of FAP in glioblastoma and gliosarcoma remains uncertain.

MATERIALS AND METHODS

Study Design and Population

This retrospective analysis was conducted at the University Hospital Essen in Germany to investigate tumor tissue's FAP expression in patients diagnosed with isocitrate dehydrogenase wild-type glioblastoma or gliosarcoma and poor overall survival prognosis, with a life expectancy not exceeding 2.5 y after primary diagnosis. Only patients who died within 2.5 y of diagnosis were included in this study, as there is a great therapeutic need because of the still high rate of negative phase III studies in glioblastoma, especially for patients who are not long-term survivors (*23*). The aim of the study was therefore to evaluate a potential tumor-specific target protein for radiopharmaceutical therapy for most glioblastoma and gliosarcoma patients who are not among the rare long-term survivors of more than 2.5 y. In one of the largest phase III studies on glioblastoma published to date to our best knowledge, only 1 in 5 patients reached this mark (*24*). The study was approved by the local ethics committee (approval number 19-9092-BO). We analyzed the correlation between immunohistochemical FAP expression and tracer uptake in ^{68}Ga-FAP inhibitor (FAPI)–46 PET. Therefore, all glioblastoma patients who received a ^{68}Ga-FAPI-46 PET scan at the University Hospital Essen and whose tissue was available for further analyses were included. The studies involving ^{68}Ga-FAPI-46 PET imaging and the collection of patient-specific clinical data received approval from our institution's ethics committee (approval numbers 19-8991-BO for the observational study and 20-9485-BO for the supplemental study). Moreover, all participants provided their informed consent by signing consent forms, ensuring adherence to ethical standards and respect for patient autonomy. The study was conducted in accordance with the Declaration of Helsinki and national regulations.

FAP Immunohistochemistry Evaluation

We performed immunohistochemical staining on a BenchMark ULTRA Slide Staining System (Roche) using anti-FAP α-antibody (Abcam, ab227703, clone SP325, monoclonal, rabbit) diluted 1:100. According to the data sheet, the antibody is reactive with human tissues with no reported cross reactivity. We validated this antibody in our laboratory using positive and negative controls, confirming the lack of cross reactivity and supporting specificity for intended targets (detailed data not included). Antigen retrieval occurred for 60 min at 36°C with cell conditioning-1 buffer (Roche). FAP expression was scored from 0 to 3 according to a semiquantitative FAP immunopositivity scoring system with slight modifications as previously described (Table 1; Fig. 1) (*25*,*26*).

TABLE 1
Semiquantitative FAP Scoring System

FAP in cancer or perivascular cells	Score
Negative	0
1%–10% positive cells	1
11%–50% positive cells	2
51%–100% positive cells	3

^{68}Ga-FAPI-46 PET Imaging

We assessed imaging data in 15 patients as part of an observational trial (registered at clinicaltrials.gov under NCT04571086). We included patients from this study with suspected glioblastoma who underwent a ^{68}Ga-FAPI-46 PET scan before surgery and subsequent definitive histopathologic diagnosis.

PET scans were performed in the craniocaudal direction on a Biograph mMR or Biograph Vision 600 scanner (Siemens Healthineers). The mean injected activity was 115.2 ± 41.5 MBq. ^{68}Ga-FAPI-46 PET images were captured 20.2 ± 17.9 min after injection. PET images acquired with the Biograph mMR were reconstructed using an ordinary Poisson ordered-subset expectation maximization algorithm (3 iterations, 21 subsets) and a voxel size of 2.09 × 2.09 × 2.03 mm. A 4-mm gaussian filter was used for postsmoothing. Attenuation correction was performed using a Dixon-based segmentation approach. All PET/CT images were iteratively reconstructed using an ordinary Poisson ordered-subset expectation maximization algorithm (4 iterations, 5 subsets) using a time-of-flight option and a voxel size of 3.3 × 3.3 × 3.0

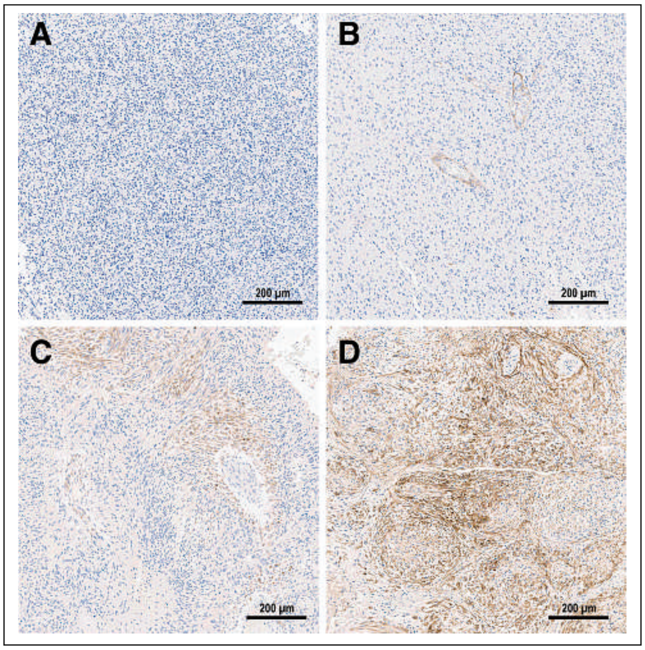

FIGURE 1. Semiquantitative FAP immunopositivity scoring examples. (A) Score 0: tumor negative (glioblastoma). (B) Score 1: <10% of cells with perivascular staining (glioblastoma). (C) Score 2: ~30% tumor cells positive (glioblastoma). (D) Score 3: >50% of tumor cells positive (gliosarcoma).

TABLE 2
Patient Characteristics

Parameter	Glioblastoma	Gliosarcoma
IDH status (wild type)	46/46 (100%)	13/13 (100%)
MGMT promotor methylation		
Methylated	19/46 (41%)	2/13 (15%)
Unmethylated	27/46 (59%)	11/13 (85%)
Karnofsky performance status	70% (40%–100%)*	80% (40%–90%)*
Extent of resection		
Complete resection	17/46 (37%)	3/13 (23%)
Partial resection	24/46 (52%)	9/13 (69%)
Biopsy	3/46 (7%)	0/13 (0%)
NA	2/46 (4%)	1/13 (8%)
Tissue investigated	46/46 (100%)	13/13 (100%)
Available FAP PET	15 (100%)	0 (0%)

*Data not available for 12 patients in glioblastoma category and 3 patients in gliosarcoma category.
IDH = isocitrate dehydrogenase; NA = not available.
Continuous data are median and range.

with a 4-mm postsmoothing gaussian filter. Images were reconstructed using dedicated manufacturer's software (syngo MI.PET/CT; Siemens Healthineers). Low-dose CT was acquired for attenuation correction (30 mAs, 120 keV, 512 × 512 matrix, 3-mm slice thickness) in the case of CT imaging. SUV_{max}, SUV_{mean}, and SUV_{peak} of intracranial lesions were measured with a region-growing algorithm with a threshold of 40% of the maximal uptake (Syngo.via software; Siemens Healthcare). PET/CT and PET/MR images were read by an experienced, masked nuclear medicine physician. For all patients, a preoperative MRI study was available. An automated postprocess coregistration was performed to match MRI with ^{68}Ga-FAPI-46 PET scans (Syngo.via software; Siemens Healthcare).

For the exclusively intracranially located lesions, SUV_{max}, SUV_{mean}, and SUV_{peak} were determined using a region-growing algorithm with a threshold set at 40% of maximum uptake. The study sought to determine the relationship between the semiquantitative FAP score in tissues, the PET data (SUV and tumor-to-brain ratio [TBR]), and the expression and uptake of FAP in tissues as revealed by the ^{68}Ga-FAPI-46 PET scan.

Statistical Analysis

Progression-free and overall survival were analyzed using the Kaplan–Meier method, with a Spearman rank correlation to assess the relationships between clinical data and FAP expression or uptake. Patients still alive or who had survived beyond 2.5 y as of March 12, 2023, were excluded. Data analysis was performed with SPSS (IBM) and Prism (GraphPad) software. Progression-free survival was defined as the period from the initial tumor resection to the time of first recurrence, as identified by MRI. Overall survival spanned the time from the date of the first tumor resection and histopathologic diagnosis to the date of death. Patients who did not show progression in MRI follow-ups were censored and remained part of the study cohort.

RESULTS

Patient Characteristics

The FAP score was analyzed using tissue specimens from 13 gliosarcoma patients and 46 glioblastoma patients. In the glioblastoma group, 19 tumors (41%) exhibited O^6-methylguanine-DNA methyltransferase (MGMT) promoter methylation, whereas in the gliosarcoma group, 2 tumors (15%) were MGMT promoter–methylated. For the glioblastoma cohort, the median initial Karnofsky performance status index stood at 70%, ranging from 40% to 100%. The gliosarcoma cohort had a median Karnofsky performance status index of 80%, ranging between 40% and 90%. Within the glioblastoma group, 17 patients (37%) experienced a complete surgical resection, characterized by the lack of any contrast-enhancing lesions in postoperative MRI scans taken within 72 h after the surgery. Conversely, 24 patients (52%) underwent a partial resection, and 3 patients (7%) had only a biopsy. For 2 patients, the extent of the resection could not be determined because of the unavailability of postoperative MRI scans. For the gliosarcoma group, complete resection was performed on 3 patients (23%) and partial resection on 9 patients (69%). One patient's resection extent remained undetermined because of the absence of postoperative MRI scans. Furthermore, 15 eligible glioblastoma patients underwent a

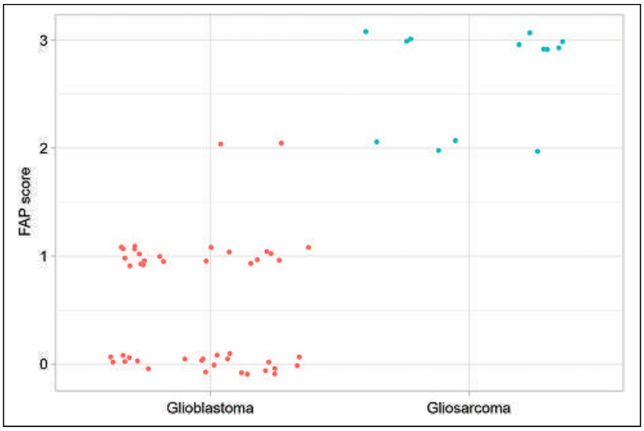

FIGURE 2. In gliosarcoma (green dots), FAP expression is more pronounced than in glioblastoma (red dots). Median FAP score in gliosarcoma was 3 (fractions: FAP score 2, $n = 4 \triangleq 31\%$; FAP score 3, $n = 9 \triangleq 69\%$) compared with 0.5 (fractions: FAP score 0, $n = 23 \triangleq 50\%$; FAP score 1, $n = 21 \triangleq 46\%$; FAP score 2, $n = 2 \triangleq 4\%$) in glioblastoma ($P < 0.0001$).

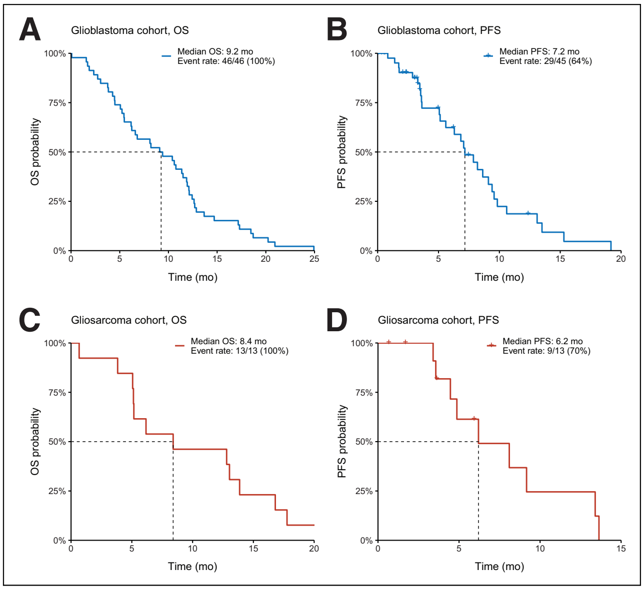

FIGURE 3. (A and B) Median overall survival (OS) and progression-free survival (PFS) were 9.2 and 7.2 mo in glioblastoma cohort, respectively. (C and D) In gliosarcoma cohort, median overall survival and progression-free survival were 8.4 and 6.2 mo, respectively.

^{68}Ga-FAPI-46 PET scan using ^{68}Ga-FAPI-46 before their surgical resection. Patient characteristics are provided in Table 2.

FAP Expression in Tumor Tissue

The expression of FAP was notably higher in gliosarcoma (median FAP score, 3) than in glioblastoma (median FAP score, 0.5) ($P < 0.0001$; Fig. 2). No glioblastoma samples achieved a maximum FAP score of 3, whereas gliosarcoma samples scored neither 0 nor 1. Glioblastoma with MGMT methylation had a median FAP score of 1 and without methylation had a median FAP score of 0. Gliosarcoma with MGMT methylation had a median FAP score of 2.5 and without methylation had a median FAP score of 3. In glioblastoma, FAP was expressed in perivascular regions, isolated tumor cells, and meninges. In gliosarcoma, abundant FAP was noted in mesenchymal tumor cells and perivascular regions. The study findings highlight differential FAP expression patterns between these brain tumors, with implications for diagnosis and treatment.

Survival Analyses

The glioblastoma cohort reported a median overall survival of 9.2 mo and a progression-free survival of 7.2 mo. The gliosarcoma cohort had slightly lower median overall and progression-free survival of 8.4 and 6.2 mo, respectively (Fig. 3). In a detailed breakdown, 46 glioblastoma patients were divided into 3 subgroups on the basis of FAP scores: 0 ($n = 23$), 1 ($n = 21$), and 2 ($n = 2$), with median overall survivals of 9.1, 8.2, and 15.9 mo, respectively ($P = 0.54$). Progression-free survival was 5.6, 9.6, and 10.2 mo for these groups ($P = 0.07$), indicating no significant correlation between the FAP score and survival. In the 13 gliosarcoma patients, those with a FAP score of 2 ($n = 4$) had a median overall survival of 4.4 mo, whereas those with a score of 3 ($n = 9$) lived longer, at 12.8 mo ($P = 0.16$). Progression-free survival was 8.5 mo for a FAP score of 2 and 6.2 mo for a FAP score of 3 ($P = 0.95$), also showing no significant correlation between FAP score and prognosis (Supplemental Fig. 1; supplemental materials are available at http://jnm.snmjournals.org). Additionally, glioblastoma patients with MGMT methylation had a median overall survival of 5.5 mo, surprisingly lower than the 11.4 mo for those without methylation, likely due to the study's limitation of including only patients who lived no longer than 2.5 y after diagnosis. In gliosarcomas, the median overall survival was 10.9 mo for MGMT-methylated patients compared with 8.4 mo for nonmethylated patients. The median progression-free survival for MGMT-methylated patients in the glioblastoma and gliosarcoma cohorts was 9.1 mo (event rate, 44%) and 13.6 mo (event rate, 50%), respectively, whereas for nonmethylated patients, it was 6.8 mo (event rate, 78%) and 6.2 mo (event rate, 72%) (Supplemental Fig. 2).

FAP Uptake and Its Correlation with FAP Score

We analyzed the correlation between FAP uptake in ^{68}Ga-FAPI-46 PET scans and FAP expression in tissue samples from 15 glioblastoma patients with preoperative MRI indications of malignant gliomas (Fig. 4). No patients from the gliosarcoma group underwent these scans. The results showed enhanced FAP uptake in the lesions, with a mean SUV_{max} (40% isocontour) of 4.24 ± 1.69, an SUV_{mean} (40% isocontour) of 2.18 ± 0.91, and an SUV_{peak} (40% isocontour) of 3.58 ± 4.14, compared with significantly lower values in the contralateral side (SUV_{max}, 0.55 ± 0.54; SUV_{mean}, 0.44 ± 0.62; SUV_{peak}, 0.35 ± 0.39). A significant positive correlation

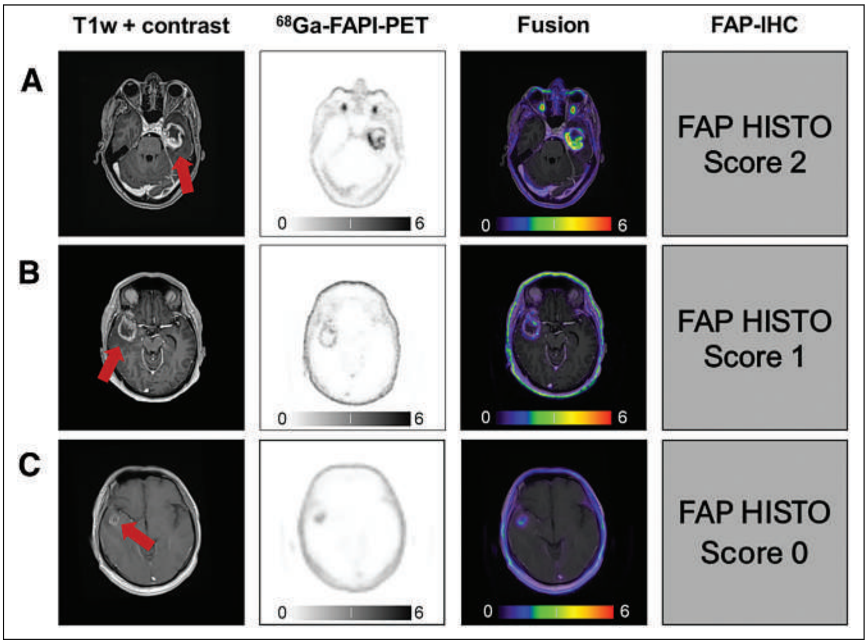

FIGURE 4. T1-weighted (T1w) contrast-enhanced MRI and ^{68}Ga-FAPI-46 PET (SUV, 0–6) of patients with glioblastoma (isocitrate dehydrogenase wild type) with FAP score of 2 and SUV_{max} of 7.6 (A), patient with glioblastoma (isocitrate dehydrogenase wild type) with FAP score of 1 and SUV_{max} of 3.5 (B), and patient with glioblastoma (isocitrate dehydrogenase wild type) with negative FAP score and SUV_{max} of 2.2 (C). Postprocess coregistration of MRI and ^{68}Ga-FAPI-46 was performed in all cases. HISTO = histopathology; IHC = immunohistochemical.

was found between tissue-based FAP expression and the lesions' $\mathrm{SUV_{mean}}$ ($r = 0.55$, $P = 0.035$) and $\mathrm{SUV_{peak}}$ ($r = 0.53$, $P = 0.044$), suggesting FAP's potential as a biomarker in PET imaging. However, no significant correlation was observed between the lesions' $\mathrm{SUV_{max}}$ ($r = 0.42$, $P = 0.12$) or the contralateral $\mathrm{SUV_{max}}$ ($r = -0.12$, $P = 0.68$) and tissue FAP expression. Additionally, maximum TBR ($r = 0.18$, $P = 0.52$), mean TBR ($r = 0.19$; $P = 0.5$), and peak TBR ($r = 0.15$; $P = 0.6$) did not show significant correlations, highlighting the limitations of the maximum TBR as a reliable indicator in ^{68}Ga-FAPI-46 PET scans due to low background uptake and variable interindividual contrast (Fig. 5).

DISCUSSION

Our study, to our knowledge, is the largest to have data on immunohistochemical FAP staining in gliosarcoma and glioblastoma patients with poor survival prognosis. The study shows FAP expression is more pronounced in gliosarcoma than in glioblastoma. In our glioblastoma cohort, $\mathrm{SUV_{mean}}$ and $\mathrm{SUV_{peak}}$ in ^{68}Ga-FAPI-46 PET correlated with immunohistochemical FAP expression. The FAP expression amount in ^{68}Ga-FAPI-46 PET depends on cancer type, with sarcoma, esophageal cancer, breast cancer, cholangiocarcinoma, and lung cancer showing a high $\mathrm{SUV_{max}}$, whereas pheochromocytoma, renal cell cancer, differentiated thyroid cancer, adenoid cystic cancer, and gastric cancer exhibit lower FAP uptake (*27*). There is a known positive correlation between ^{68}Ga-FAPI-46 $\mathrm{SUV_{max}}$ and the immunohistochemical FAP score in sarcoma (*28*). FAP PET quantifies the amount of FAP in tumors. Gross tumor volumes are shown to be larger with FAP PET plus MRI than with MRI alone in glioblastoma (*29*).

No correlation was found between progression-free or overall survival and FAP expression in our glioblastoma cohort, but FAP is a promising theranostic target in high-risk, poor-prognosis gliosarcoma. FAP has radiopharmaceutical therapy potential in xenografts (*30*). The correlation between SUV and tissue FAP expression suggests that ^{68}Ga-FAPI-46 PET could identify candidates who will respond to radiolabeled FAP therapy.

FAP's prognostic value remains unclear. Higher expression often correlates with aggressive tumors, but some studies show better prognosis. Higher FAP expression is associated with poorer glioblastoma survival (*10*), better breast cancer prognosis but poorer colon cancer prognosis (*31*,*32*), and decreased metastatic colon cancer survival (*26*). Positive correlations exist in osteosarcoma between higher FAP expression with advanced clinical stage, high histological grade, positive metastatic status, and shorter survival (*33*). In gastric cancer, higher FAP expression correlates with poorer differentiation, tumor stage, and invasion (*34*). FAP is highly expressed in pancreatic adenocarcinoma. Higher peritumoral expression increased the node positivity, recurrence, and death risk (*35*).

Interestingly, 3 additional grade 4 isocitrate dehydrogenase–mutated astrocytomas scored 0 for immunohistochemical FAP expression in our trial (data not shown). Isocitrate dehydrogenase mutation confers improved glioma survival (*36*). There is no elevated ^{68}Ga-FAPI-46 PET uptake in isocitrate dehydrogenase–mutant gliomas, allowing noninvasive differentiation from high-grade gliomas (*20*).

FAP-positive tumor cells correlate with glioblastoma neoangiogenesis, implicating FAP in disease progression (*25*), fitting our observation of perivascular FAP expression.

FAP antibody expression attenuated HT29 xenograft growth, indicating therapeutic potential (*37*). However, the clinical FAP inhibitor talabostat and FAP antibody sibrotuzumab trials showed minimal metastatic disease efficacy (*38*–*41*). Earlier administration might improve the results.

Our study has several limitations. As a retrospective analysis, we could not control potential confounding factors that may have influenced survival outcomes. The sample size, particularly for gliosarcoma patients, was relatively small. Our study was restricted to tissue samples from deceased patients who survived less than 2.5 y, as per our ethical approval. Consequently, we cannot extrapolate the prognostic value of FAP to all glioblastoma or gliosarcoma patients. A broader, representative sample or a prospective study would be needed to assess FAP's prognostic value across a more diverse patient cohort, a direction we find promising based on our current findings. We used immunohistochemistry to evaluate FAP expression, but including

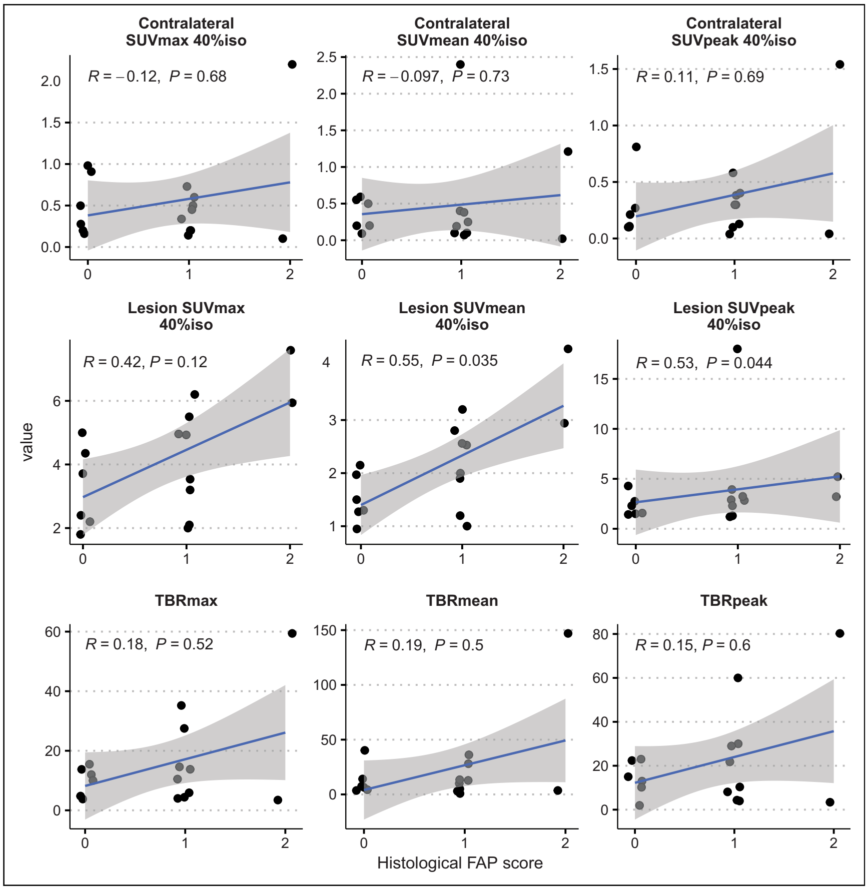

FIGURE 5. Lesion $\mathrm{SUV_{mean}}$ ($r = 0.55$, $P = 0.035$) and $\mathrm{SUV_{peak}}$ ($r = 0.53$; $P = 0.044$) show significant positive correlation between FAP uptake in PET and FAP expression in tissues. iso = isocontour; $\mathrm{TBR_{max}}$ = maximum tumor-to-brain ratio; $\mathrm{TBR_{mean}}$ = mean tumor-to-brain ratio; $\mathrm{TBR_{peak}}$ = peak tumor-to-brain ratio.

additional methods such polymerase chain reaction could provide more quantitative results. Regrettably, our cohort did not include patients with gliosarcoma who underwent ^{68}Ga-FAPI-46 PET imaging before their initial surgery. As a result, our analysis was limited to demonstrating the correlation between FAP expression in tissue samples and its uptake in PET scans, specifically in glioblastomas that lacked sarcomatous differentiation. We can draw associative conclusions only regarding FAP's role in prognosis and treatment response. The single-institution design may limit the generalizability of the findings. Further prospective research in more extensive, multicenter cohorts is warranted to validate the relationships suggested by our preliminary data and to determine the utility of FAP-directed therapies.

CONCLUSION

Our findings reveal greater FAP expression in gliosarcoma than in glioblastoma, suggesting potential therapeutic implications warranting further investigation. The correlation between FAP tissue expression and SUV in ^{68}Ga-FAPI-46 PET for glioblastoma without sarcomatous differentiation allows noninvasive identification of suitable patient populations for FAP radiopharmaceutical therapy by imaging. The PET–tissue staining correlation provides a noninvasive means to identify patients most likely to benefit from FAP-targeted treatment. However, additional studies are needed to clarify FAP's conflicting prognostic roles across cancer types.

DISCLOSURE

Christoph Oster has received travel support from Novocure and honoraria from Horizon and Novocure. He has received a Clinician Scientist Stipend of the University Medicine Essen Clinician Scientist Academy (UMEA) sponsored by the faculty of medicine and Deutsche Forschungsgemeinschaft (DFG). Kim Pabst has received a Clinician Scientist Stipend of the University Medicine Essen Clinician Scientist Academy (UMEA) sponsored by the faculty of medicine and Deutsche Forschungsgemeinschaft (DFG), travel fees from IPSEN, and research funding from Bayer and is a consultant for Novartis. Teresa Schmidt received honoraria and travel support from Novocure. Lazaros Lazaridis received honoraria and travel support from Novocure. Björn Scheffler is supported by the German Cancer Consortium (DKTK). Sied Kebir received honoraria and travel support from Novocure. Ken Herrmann reports receiving consultant fees from Advanced Accelerator Applications, a Novartis company, Amgen, AstraZeneca, Bain Capital, Bayer, Boston Scientific, Convergent, Curium, Debiopharm, EcoR1, Fusion, GE Healthcare, Immedica, Isotopen Technologien München, Janssen, Merck, Molecular Partners, NVision, POINT Biopharma, Pfizer, Radiopharm Theranostics, Rhine Pharma, Siemens Healthineers, SOFIE Biosciences, Telix, Theragnostics, and Ymabs; receiving research grants from Advanced Accelerator Applications, a Novartis company, Boston Scientific, and Janssen; and having stock or other ownership interests with AdvanCell, Aktis Oncology, Convergent, NVision, Pharma 15, and SOFIE Biosciences. Martin Glas has received research grants from Novocure. He has received honoraria from Roche, Seagan, Servier, Novartis, UCB, Abbvie, Daiichi Sankyo, Bayer, Janssen-Cilag, Kyowa Kirin, Medac, Merck, and Novocure. He has received travel support from Novocure and Medac. No other potential conflict of interest relevant to this article was reported.

KEY POINTS

QUESTION: How does FAP expression in gliosarcoma and glioblastoma correlate with ^{68}Ga-FAPI-46 PET uptake?

PERTINENT FINDINGS: Analysis showed a significant correlation between immunohistochemical FAP expression and SUV_{mean} and SUV_{peak} in ^{68}Ga-FAPI-46 PET, indicating FAP expression in the tissue.

IMPLICATIONS FOR PATIENT CARE: Correlation between PET imaging and tissue staining provides a noninvasive means to identify patients most likely to benefit from FAP-targeted therapy.

REFERENCES

1. Delgado-López PD, Corrales-Garcia EM. Survival in glioblastoma: a review on the impact of treatment modalities. *Clin Transl Oncol.* 2016;18:1062–1071.
2. Awadalla AS, Al Essa AM, Al Ahmadi HH, et al. Gliosarcoma case report and review of the literature. *Pan Afr Med J.* 2020;35:26.
3. Louis DN, Perry A, Wesseling P, et al. The 2021 WHO classification of tumors of the central nervous system: a summary. *Neuro Oncol.* 2021;23:1231–1251.
4. Amer A, Khose S, Alhasan H, et al. Clinical and survival characteristics of primary and secondary gliosarcoma patients. *Clin Neurol Neurosurg.* 2022;214:107146.
5. McAleer MF, Brown PD. Therapeutic management of gliosarcoma in the temozolomide era. *CNS Oncol.* 2015;4:171–178.
6. Liau LM, Ashkan K, Brem S, et al. Association of autologous tumor lysate-loaded dendritic cell vaccination with extension of survival among patients with newly diagnosed and recurrent glioblastoma: a phase 3 prospective externally controlled cohort trial. *JAMA Oncol.* 2023;9:112–121.
7. Bunse L, Rupp AK, Poschke I, et al. AMPLIFY-NEOVAC: a randomized, 3-arm multicenter phase I trial to assess safety, tolerability and immunogenicity of IDH1-vac combined with an immune checkpoint inhibitor targeting programmed death-ligand 1 in isocitrate dehydrogenase 1 mutant gliomas. *Neurol Res Pract.* 2022;4:20.
8. Platten M, Bunse L, Wick W. Emerging targets for anticancer vaccination: IDH. *ESMO Open.* 2021;6:100214.
9. Weller M, Roth P, Preusser M, et al. Vaccine-based immunotherapeutic approaches to gliomas and beyond. *Nat Rev Neurol.* 2017;13:363–374.
10. Ebert LM, Yu W, Gargett T, et al. Endothelial, pericyte and tumor cell expression in glioblastoma identifies fibroblast activation protein (FAP) as an excellent target for immunotherapy. *Clin Transl Immunol.* 2020;9:e1191.
11. Ravanpay AC, Gust J, Johnson AJ, et al. EGFR806-CAR T cells selectively target a tumor-restricted EGFR epitope in glioblastoma. *Oncotarget.* 2019;10:7080–7095.
12. Dendl K, Koerber SA, Kratochwil C, et al. FAP and FAPI-PET/CT in malignant and non-malignant diseases: a perfect symbiosis? *Cancers (Basel).* 2021;13:4946.
13. Hamson EJ, Keane FM, Tholen S, Schilling O, Gorrell MD. Understanding fibroblast activation protein (FAP): substrates, activities, expression and targeting for cancer therapy. *Proteomics Clin Appl.* 2014;8:454–463.
14. Shi Y, Kong Z, Liu P, et al. Oncogenesis, microenvironment modulation and clinical potentiality of FAP in glioblastoma: lessons learned from other solid tumors. *Cells.* 2021;10:1142.
15. Krepela E, Vanickova Z, Hrabal P, et al. Regulation of fibroblast activation protein by transforming growth factor beta-1 in glioblastoma microenvironment. *Int J Mol Sci.* 2021;22:1046.
16. Busek P, Hrabal P, Fric P, Sedo A. Co-expression of the homologous proteases fibroblast activation protein and dipeptidyl peptidase-IV in the adult human Langerhans islets. *Histochem Cell Biol.* 2015;143:497–504.
17. Park JE, Lenter MC, Zimmermann RN, Garin-Chesa P, Old LJ, Rettig WJ. Fibroblast activation protein, a dual specificity serine protease expressed in reactive human tumor stromal fibroblasts. *J Biol Chem.* 1999;274:36505–36512.
18. Mikheeva SA, Mikheev AM, Petit A, et al. TWIST1 promotes invasion through mesenchymal change in human glioblastoma. *Mol Cancer.* 2010;9:194.
19. Röhrich M, Floca R, Loi L, et al. FAP-specific PET signaling shows a moderately positive correlation with relative CBV and no correlation with ADC in 13 IDH wildtype glioblastomas. *Eur J Radiol.* 2020;127:109021.
20. Röhrich M, Loktev A, Wefers AK, et al. IDH-wildtype glioblastomas and grade III/IV IDH-mutant gliomas show elevated tracer uptake in fibroblast activation protein-specific PET/CT. *Eur J Nucl Med Mol Imaging.* 2019;46:2569–2580.
21. Windisch P, Zwahlen DR, Giesel FL, et al. Clinical results of fibroblast activation protein (FAP) specific PET for non-malignant indications: systematic review. *EJNMMI Res.* 2021;11:18.

22. Ma H, Li F, Shen G, et al. In vitro and in vivo evaluation of ^{211}At-labeled fibroblast activation protein inhibitor for glioma treatment. *Bioorg Med Chem.* 2022;55: 116600.
23. Oster C, Schmidt T, Agkatsev S, et al. Are we providing best available care to newly diagnosed glioblastoma patients? Systematic review of phase III trials in newly diagnosed glioblastoma 2005–2022. *Neurooncol Adv.* 2023;5:vdad105.
24. Stupp R, Taillibert S, Kanner A, et al. Effect of tumor-treating fields plus maintenance temozolomide vs maintenance temozolomide alone on survival in patients with glioblastoma: a randomized clinical trial. *JAMA.* 2017;318:2306–2316.
25. Balaziova E, Vymola P, Hrabal P, et al. Fibroblast activation protein expressing mesenchymal cells promote glioblastoma angiogenesis. *Cancers (Basel).* 2021;13:3043.
26. Henry LR, Lee HO, Lee JS, et al. Clinical implications of fibroblast activation protein in patients with colon cancer. *Clin Cancer Res.* 2007;13:1736–1741.
27. Kratochwil C, Flechsig P, Lindner T, et al. ^{68}Ga-FAPI PET/CT: tracer uptake in 28 different kinds of cancer. *J Nucl Med.* 2019;60:801–805.
28. Kessler L, Ferdinandus J, Hirmas N, et al. ^{68}Ga-FAPI as a diagnostic tool in sarcoma: data from the ^{68}Ga-FAPI PET prospective observational trial. *J Nucl Med.* 2022;63:89–95.
29. Windisch P, Röhrich M, Regnery S, et al. Fibroblast activation protein (FAP) specific PET for advanced target volume delineation in glioblastoma. *Radiother Oncol.* 2020;150:159–163.
30. Jeanjean P, Kwock S, Tse C, et al. Fibroblast activation protein (FAP) as a target for radioligand therapy in glioblastoma. *J Nucl Med.* 2022;63(suppl 2):4050.
31. Ariga N, Sato E, Ohuchi N, Nagura H, Ohtani H. Stromal expression of fibroblast activation protein/seprase, a cell membrane serine proteinase and gelatinase, is associated with longer survival in patients with invasive ductal carcinoma of breast. *Int J Cancer.* 2001;95:67–72.
32. Wikberg ML, Edin S, Lundberg IV, et al. High intratumoral expression of fibroblast activation protein (FAP) in colon cancer is associated with poorer patient prognosis. *Tumour Biol.* 2013;34:1013–1020.
33. Yuan D, Liu B, Liu K, Zhu G, Dai Z, Xie Y. Overexpression of fibroblast activation protein and its clinical implications in patients with osteosarcoma. *J Surg Oncol.* 2013;108:157–162.
34. Shan LH, Sun WG, Han W, et al. Roles of fibroblasts from the interface zone in invasion, migration, proliferation and apoptosis of gastric adenocarcinoma. *J Clin Pathol.* 2012;65:888–895.
35. Cohen SJ, Alpaugh RK, Palazzo I, et al. Fibroblast activation protein and its relationship to clinical outcome in pancreatic adenocarcinoma. *Pancreas.* 2008;37:154–158.
36. Zou P, Xu H, Chen P, et al. IDH1/IDH2 mutations define the prognosis and molecular profiles of patients with gliomas: a meta-analysis. *PLoS One.* 2013;8:e68782.
37. Cheng JD, Dunbrack RL Jr, Valianou M, Rogatko A, Alpaugh RK, Weiner LM. Promotion of tumor growth by murine fibroblast activation protein, a serine protease, in an animal model. *Cancer Res.* 2002;62:4767–4772.
38. Eager RM, Cunningham CC, Senzer N, et al. Phase II trial of talabostat and docetaxel in advanced non-small cell lung cancer. *Clin Oncol (R Coll Radiol).* 2009;21:464–472.
39. Narra K, Mullins SR, Lee HO, et al. Phase II trial of single agent Val-boroPro (talabostat) inhibiting fibroblast activation protein in patients with metastatic colorectal cancer. *Cancer Biol Ther.* 2007;6:1691–1699.
40. Scott AM, Wiseman G, Welt S, et al. A phase I dose-escalation study of sibrotuzumab in patients with advanced or metastatic fibroblast activation protein-positive cancer. *Clin Cancer Res.* 2003;9:1639–1647.
41. Hofheinz RD, al-Batran SE, Hartmann F, et al. Stromal antigen targeting by a humanised monoclonal antibody: an early phase II trial of sibrotuzumab in patients with metastatic colorectal cancer. *Onkologie.* 2003;26:44–48.

PET/CT-Based Absorbed Dose Maps in ^{90}Y Selective Internal Radiation Therapy Correlate with Spatial Changes in Liver Function Derived from Dynamic MRI

Zhonglin Lu[1–3], Daniel F. Polan[4], Lise Wei[4], Madhava P. Aryal[4], Kellen Fitzpatrick[3], Chang Wang[5], Kyle C. Cuneo[4], Joseph R. Evans[4], Molly E. Roseland[3], Joseph J. Gemmete[3], Jared A. Christensen[3], Baljendra S. Kapoor[3], Justin K. Mikell[6], Yue Cao[3,4,7], Greta S.P. Mok[1,2,8], and Yuni K. Dewaraja[3]

[1]Biomedical Imaging Laboratory, Department of Electrical and Computer Engineering, Faculty of Science and Technology, University of Macau, Taipa, China; [2]Center for Cognitive and Brain Sciences, Institute of Collaborative Innovation, University of Macau, Taipa, China; [3]Department of Radiology, University of Michigan Medical Center, Ann Arbor, Michigan; [4]Department of Radiation Oncology, University of Michigan, Ann Arbor, Michigan; [5]Department of Biostatistics, University of Michigan, Ann Arbor, Michigan; [6]Department of Radiation Oncology, Washington University in St. Louis, St. Louis, Missouri; [7]Department of Biomedical Engineering, University of Michigan, Ann Arbor, Michigan; and [8]Ministry of Education Frontiers Science Center for Precision Oncology, Faculty of Health Science, University of Macau, Taipa, China

Functional liver parenchyma can be damaged from treatment of liver malignancies with ^{90}Y selective internal radiation therapy (SIRT). Evaluating functional parenchymal changes and developing an absorbed dose (AD)–toxicity model can assist the clinical management of patients receiving SIRT. We aimed to determine whether there is a correlation between ^{90}Y PET AD voxel maps and spatial changes in the nontumoral liver (NTL) function derived from dynamic gadoxetic acid–enhanced MRI before and after SIRT. **Methods:** Dynamic gadoxetic acid–enhanced MRI scans were acquired before and after treatment for 11 patients undergoing ^{90}Y SIRT. Gadoxetic acid uptake rate (k_1) maps that directly quantify spatial liver parenchymal function were generated from MRI data. Voxel-based AD maps, derived from the ^{90}Y PET/CT scans, were binned according to AD. Pre- and post-SIRT k_1 maps were coregistered to the AD map. Absolute and percentage k_1 loss in each bin was calculated as a measure of loss of liver function, and Spearman correlation coefficients between k_1 loss and AD were evaluated for each patient. Average k_1 loss over the patients was fit to a 3-parameter logistic function based on AD. Patients were further stratified into subgroups based on lesion type, baseline albumin–bilirubin scores and alanine transaminase levels, dose–volume effect, and number of SIRT treatments. **Results:** Significant positive correlations ($\rho = 0.53$–0.99, $P < 0.001$) between both absolute and percentage k_1 loss and AD were observed in most patients (8/11). The average k_1 loss over 9 patients also exhibited a significant strong correlation with AD ($\rho \geq 0.92$, $P < 0.001$). The average percentage k_1 loss of patients across AD bins was 28%, with a logistic function model demonstrating about a 25% k_1 loss at about 100 Gy. Analysis between patient subgroups demonstrated that k_1 loss was greater among patients with hepatocellular carcinoma, higher alanine transaminase levels, larger fractional volumes of NTL receiving an AD of 70 Gy or more, and sequential SIRT treatments. **Conclusion:** Novel application of multimodality imaging demonstrated a correlation between ^{90}Y SIRT AD and spatial functional liver parenchymal degradation, indicating that a higher AD is associated with a larger loss of local hepatocyte function. With the developed response models, PET-derived AD maps can potentially be used prospectively to identify localized damage in liver and to enhance treatment strategies.

Key Words: SIRT; ^{90}Y PET/CT; DGAE MRI; dosimetry; absorbed dose–toxicity relationship

J Nucl Med 2024; 65:1224–1230
DOI: 10.2967/jnumed.124.267421

Selective internal radiation therapy (SIRT) with ^{90}Y is an effective treatment for patients with unresectable primary or metastatic liver cancer. During SIRT, intraarterial administration of ^{90}Y microspheres leads to preferential deposition of microspheres and absorbed dose (AD) in and around tumors (*1*). However, on the basis of the surrounding arterial blood supply, some of the microspheres can deliver dose to nontumoral liver (NTL), resulting in radiation-associated toxicity to the NTL (*2*). Despite the potential for local heterogeneity, historically only mean AD within the NTL has been analyzed in correlation with the whole-liver toxicity biomarkers for dose–toxicity evaluation (*3–7*). As a tool for establishing a dose–toxicity relationship for the NTL, post-SIRT dosimetry based on ^{90}Y PET/CT could be valuable, given its ability to capture the AD heterogeneity at the voxel level (*1,8*). Analysis of voxel level dosimetry and association with spatial liver parenchymal function can enable refinement of treatment strategies and mitigation of potential radiation-associated toxicity. This includes identifying high-functioning liver parenchymal regions receiving low doses (*9*), which can be spared in subsequent single- and multimodality treatments.

Imaging techniques for quantifying regional liver function include dynamic ^{99m}Tc-iminodiacetic acid SPECT/CT (*10*) and dynamic contrast-enhanced MRI (*11–13*). MRI-based techniques that assess liver function are based on contrast uptake by hepatocytes and demonstrate distinct advantages over SPECT/CT, including higher image resolution and higher soft-tissue contrast. Portal venous perfusion maps from dynamic contrast-enhanced MRI have been used as a surrogate of liver function (*11*). More recently, techniques for estimating direct hepatic parenchymal uptake have been developed

---

Received Jan. 9, 2024; revision accepted May 7, 2024.

For correspondence or reprints, contact Yuni K. Dewaraja (yuni@med.umich.edu) or Greta S.P. Mok (gretamok@um.edu.mo).

using dynamic gadoxetic acid–enhanced (DGAE) MRI, which applies a hepatobiliary contrast agent that is specifically absorbed and excreted by functioning hepatocytes. With DGAE MRI, gadoxetic acid uptake rate (k_1) maps can be derived, which uniquely allow for direct assessment of spatial liver parenchymal function (*12,13*).

Prior studies have established a correlation between degradation of regional liver parenchymal function, assessed via DGAE MRI, and radiation dose from stereotactic body radiation therapy (SBRT) (*14*). However, the impact of AD on regional liver function in the context of ^{90}Y SIRT remains unclear. Combining post-SIRT voxel level dosimetry with spatial k_1 maps could assist in improving the current clinical understanding of radioembolization-induced hepatotoxicity. In this pioneering study, we aimed to use multimodality imaging to establish a correlation between the voxel-level AD in the NTL from ^{90}Y PET/CT and the spatial liver function deterioration, that is, k_1 loss from DGAE MRI before and after ^{90}Y SIRT.

MATERIALS AND METHODS

Patient Population

Eleven patients with hepatocellular carcinoma (HCC) or metastatic liver cancer received ^{90}Y SIRT along with pre- and posttreatment DGAE MRI scans from 2020 to 2023 as part of a prospective clinical trial (ClinicalTrials.gov identifier NCT04518748) (Supplemental Tables 1 and 2; supplemental materials are available at http://jnm.snmjournals.org). All patients signed an Institutional Review Board–approved informed consent form and met prespecified inclusion criteria (*15*). Ten patients received either a single-hepatic-lobe or segmental treatment or 2 sequential bilobar treatments with about a 1-mo interval. One patient underwent 2 sequential unilobar treatments with about a 1-mo interval to administer microspheres through multiple arterial blood supplies to a single lesion. ^{90}Y glass microspheres (TheraSphere; Boston Scientific) were prescribed for each treatment session following standard dosimetry practices at the discretion of the treating clinician (*16*). The administered activity ranged from 0.92 to 5.97 GBq (median, 3.28 GBq) per treatment. Liver parenchymal function and injury were assessed by various biomarkers before the ^{90}Y SIRT (Supplemental Table 1) and at 1, 3, and 6 mo after therapy. These included common liver enzymes (alanine transaminase [ALT] and aspartate aminotransferase [AST]) and validated clinical scoring systems with prognostic relevance among patients with liver disease, including the albumin–bilirubin (ALBI) score ([log10 bilirubin (μmol/L) × 0.66] + [albumin (g/L) × −0.085]) (*17*) and the Child–Pugh score.

DGAE MRI Acquisition and Processing

DGAE MR images of the liver were acquired about 1 wk before and about 1 mo after completion of SIRT. After a median of 18 min following intravenous injection of a single standard dose of gadoxetic acid (Eovist; Bayer Healthcare Pharmaceuticals Inc.), patients underwent the DGAE MRI scans on a 3-T scanner (Skyra; Siemens Healthineers). The DGAE MRI sequence was adapted from Simeth et al. (*13*), for example, an echo time/repetition time of 1.16/2.68 ms, a flip angle of 13.5°, a median temporal sampling rate of 8.8 s, a matrix size of 384 × 384 × 64, and a voxel size of 1.09× 1.09 × 3.5–4.2 mm. Reference MRI volumes were selected for pre- and post-SIRT time-series DGAE MRI volumes. A rigid registration method, outlined by Johansson et al. (*18*), was used to register the DGAE MRI volumes to the reference volume for breathing motion correction, yielding acceptable results after review by the technologist for the current patient cohort. However, if the results were deemed unacceptable because of obvious misregistration for a patient, an in-house–developed deformable motion correction in k-space would be used as an alternative (*19*) in our general practice. Details of the k_1 map generation process have been reported previously (*12,13*). Briefly, the gadoxetic acid k_1, that is, k_1 maps (mL/100 g/min) quantifying liver function spatially, was derived by modeling DGAE MRI volumes through a single-input 2-compartment model. This process also facilitated the creation of blood distribution volume (v_{dis}) maps for reference in excluding main vessels in the NTL mask. Subsequently, k_1 and v_{dis} maps before and after SIRT were coregistered along with the rigid coregistration of corresponding reference MRI volumes (Fig. 1, step 1) using an in-house software (imFIAT) that has been rigorously evaluated in collaborative projects of the Quantitative Image Network of the National Cancer Institute (*14*).

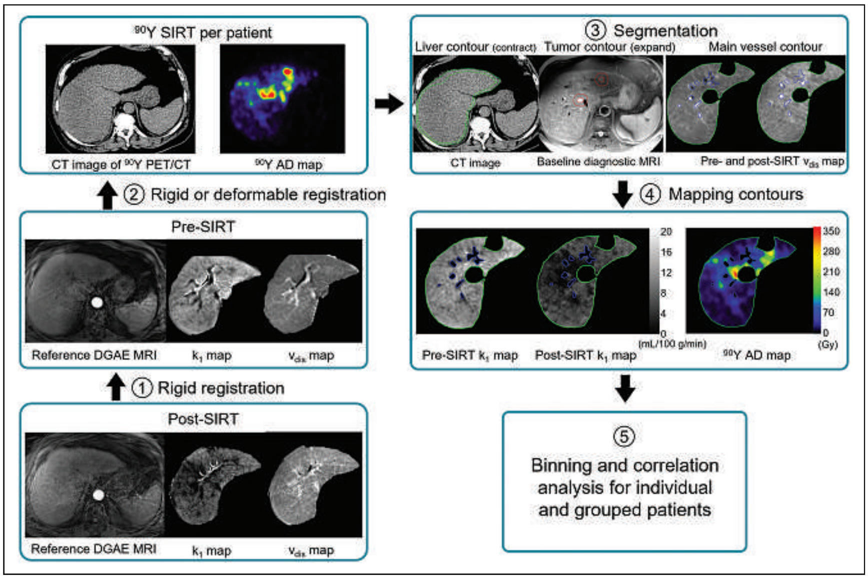

FIGURE 1. Flowchart illustrating correlation process between ^{90}Y AD and k_1 maps. Steps 1 and 2 involve aligning post-SIRT k_1, pre-SIRT k_1, and AD maps through coregistration of DGAE MRI and CT images. In step 3, liver is delineated on CT, excluding lesions and main vessels segmented on diagnostic MRI and v_{dis} maps. Step 4 entails mapping refined NTL regions onto both k_1 and AD maps for correlation analysis in step 5.

^{90}Y Microsphere PET/CT Imaging and Dosimetry

Details on post-SIRT ^{90}Y PET/CT imaging and dosimetry can be found in a previous publication (*6*). Briefly, within 4 h after SIRT, time-of-flight ^{90}Y PET/CT imaging was acquired on a Biograph mCT (Siemens Healthineers) for about 30 min and reconstructed using 3-dimensional ordered-subset expectation maximization (1 iteration, 21 subsets) and 5-mm gaussian postfiltering. The PET matrix size was 200 × 200 × 82–145 with a voxel size 4.07 × 4.07 × 3 mm. Voxel-based ^{90}Y AD maps were calculated directly from the quantitative ^{90}Y PET/CT (in Bq/cm^3) using the dose-planning method Monte Carlo code (*20*). For patients receiving sequential administrations, the CT image from the latter treatment was registered to the CT image from the first treatment, and the 2 corresponding aligned AD maps were summed to generate 1 AD map.

k_1 Maps and ^{90}Y AD Map Alignment and Processing

The liver contours were segmented on the pre-SIRT reference MRI and CT images using deep learning–based segmentation tools (MIM Software Inc.) for registration guidance. Then, the reference MRI volumes were coregistered to the CT images using the surface-based rigid or regularized deformable registration in MIM software (Fig. 1, step 2). Subsequently, k_1 maps and v_{dis} maps were aligned to AD maps and linearly interpolated to match their size.

Lesions were contoured by an experienced radiologist on baseline MR images or contrast-enhanced CT images and transferred to the CT of the PET/CT. To mitigate edge artifacts in k_1 maps, spill-out effects, and blurring of lesions on NTL in AD maps, the NTL masks were created by contracting the liver contour by a 0.5-cm margin and excluding the lesion contours expanded by 1 cm (*14*). Additionally, as a k_1 map is valid for assessing the function of only nontumoral hepatocytes, main vessels were excluded from the NTL mask by excluding voxels with v_{dis} values of less than 0.02 or more than 0.25 for refinement (Fig. 1, step 3) (*13*). For patients with unilobar involvement in SIRT, the NTL mask was further split into treated and untreated lobes. The NTL area was then mapped out for AD and pre- and post-SIRT k_1 maps (Fig. 1, step 4).

Data Analysis

Dosimetry Metrics. Dose–volume histogram metrics, including mean AD and minimum AD to percentage NTL volume (from 30% to 90% with increments of 20%), were computed to provide additional insights into the AD distribution among patients. The percentage of the whole NTL volume receiving at least 70 Gy (denoted as $V_{70\ Gy}$ in %) were also evaluated, as 70 Gy has been suggested as the AD limit of NTL for SIRT (*4*).

Regional Liver Function–to–Dose Correlation Analysis. To analyze the regional function degradation after ^{90}Y SIRT for individual patients, the AD maps were binned in 5-Gy increments from 0 to 100 Gy, in 10-Gy increments from 100 to 150 Gy, and in 25-Gy increments for more than 150 Gy for noise reduction in higher-AD regions with a smaller number of voxels. Additionally, bins encompassing fewer than 100 voxels (equivalent to 0.19 cm^3), potentially more subjective to noise, were excluded from the study. k_1 maps of both pre-SIRT and post-SIRT were spatially binned on the basis of the AD binning, and the k_1 values were averaged over each bin. Both the absolute loss (Eq. 1) and percentage loss (Eq. 2) of mean k_1 values before and after SIRT were calculated. This strategy of binning first and then subtracting was confirmed to be more robust against noise and misregistration (*14*):

$$\Delta k_{1,i}(\text{mL}/100\ \text{g/min}) = k_{1,i}^{\text{pre}} - k_{1,i}^{\text{post}}, \qquad \text{Eq. 1}$$

$$\Delta k_{1,i}(\%) = (k_{1,i}^{\text{pre}} - k_{1,i}^{\text{post}})/k_{1,i}^{\text{pre}} \times 100, \qquad \text{Eq. 2}$$

where $k_{1,i}^{\text{pre}}$ and $k_{1,i}^{\text{post}}$ stand for the mean k_1 in the *i*-th dose bin before and after SIRT, respectively. In patients with unilobar treatment only, the k_1 loss of the untreated lobe (~0 Gy) was calculated and compared with the first bin in the treated lobe, that is, low-AD (≤ 5 Gy) region. The linear regression model and Wilcoxon signed-rank testing were applied to assess numeric and statistical differences, respectively. If there was no obvious discrepancy in the values or a statistically significant difference ($P > 0.05$), the untreated lobe was combined with the treated lobe to incorporate more volume for greater correlation assessment.

The Spearman correlation analysis was used to evaluate the relationship between k_1 loss and AD for each patient.

For evaluation of the entire patient cohort, the absolute/percentage k_1 loss and AD were averaged over all patients for each bin, denoted as $\overline{\Delta k}_{1,i}$ and $\overline{AD}_i$, respectively. To develop a dose-function response model, a 3-parameter logistic function (Eq. 3) was fit, based on normal-tissue complication probability modeling:

$$\overline{\Delta k}_{1,i} = \frac{\alpha}{1 + e^{(D_c - \overline{AD}_i)/\gamma}}, \qquad \text{Eq. 3}$$

where α represents an asymptote indicating the maximum achievable k_1 loss, D_c denotes a characteristic dose at 50%-asymptotic height of the maximum loss, and γ is proportional to the inverse of the dose–response slope at D_c. This function was fit by applying a nonlinear least-squares function implemented in R (*21*). The goodness of fit was assessed using the coefficient of determination R^2 by the aomisc package in R (*22*) and the SE of fit variables. The k_1 loss averaged over all patients and all bins was computed for comparison. The patient cohort was further stratified into subgroups based on specific characteristics, including HCC or liver metastases, baseline ALBI scores, baseline ALT and AST levels, dose–volume effects ($V_{70\ Gy}$), and single versus sequential treatments. ALBI scores, ALT and AST levels, and $V_{70\ Gy}$ subgroups were defined using their respective median values as thresholds to ensure balanced subgroup sizes.

Global Liver Function Assessment Comparison. Global liver function measured through imaging (k_1 maps) and biomarkers (ALBI scores) was compared. Mean k_1 multiplied by NTL volume (k_1V_L) as functional volume (*13*) were calculated before and after SIRT, and the difference represented global k_1 loss. Meanwhile, the change in ALBI scores after SIRT, corresponding to the time of the second DGAE MRI acquisition, was computed relative to the baseline. Pearson correlation analysis was performed between k_1V_L loss and the ALBI score increase.

RESULTS

Dosimetry Metrics

The dose–volume histogram plots and metrics in the entire NTL, including mean AD, D_{xx} (xx = 30%, 50%, 70%, and 90%), and $V_{70\ Gy}$ for 11 patients, are shown in Supplemental Figure 1 and Supplemental Table 2, respectively. The median value of the mean AD of the whole NTL was 35.1 Gy (range, 2.4–61.6 Gy), The median value of $V_{70\ Gy}$ was 7.8% (range, 0%–35.0%).

Regional Liver Function–to–AD Correlation Analysis

Individual Patient Assessment. The linear regression analysis between k_1 loss in the low-AD (≤ 5 Gy) region of the treated lobe versus the untreated lobe (Fig. 2) for 7 patients who received only unilobar treatment demonstrated an approximate line of equality (slope, 1.01; intercept, −3.83%). This trend suggested nearly identical k_1 loss between the low-AD region of the treated lobe and the untreated lobe. Additionally, no statistically significant difference was observed between the two (P = 0.237 for Wilcoxon

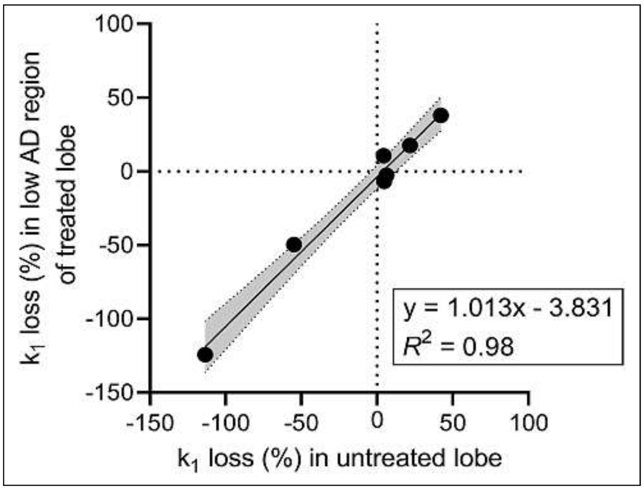

FIGURE 2. Scatterplot of k_1 loss in low-AD ($\leq$5 Gy) region of treated lobe vs. untreated lobe. Best-fit line (solid line) combines with its 95% CI (gray area) as linear regression model.

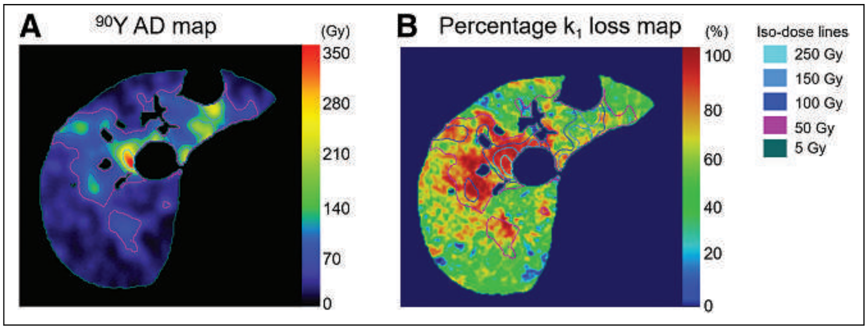

FIGURE 3. Sample visual correlation of ^{90}Y AD maps (A) and percentage k_1 loss (B) in refined NTL area, overlaid with isodose lines. Central hepatic region (segment 8) with higher AD presents larger k_1 loss. Percentage k_1 loss map is shown to visually illustrate its association with AD but was not directly used in correlation calculation analysis.

signed-rank test). Consequently, the untreated lobe was included in the correlation assessment between k_1 loss and AD.

Visual correlation between the percentage k_1 loss and AD maps in the refined NTL area, overlaid with isodose lines, is shown for a sample patient (patient 2) in Figure 3.

Scatterplots and Spearman correlation coefficients illustrate the relationship between k_1 loss and AD for 11 patients in Supplemental Figure 2 and Table 1, respectively. A significant and strong positive correlation ($\rho > 0.5$, $P < 0.001$) between both absolute and percentage k_1 loss and AD was observed in most patients (8/11), whereas 3 patients exhibited a poor or negative correlation. Most patients showed regional liver function degradation, particularly in higher-AD regions, except for 2 patients (patients 7 and 11) who demonstrated globally increased k_1 values after SIRT and were subsequently excluded from the grouped assessment because of this unexpected behavior.

Grouped Patient Assessment. Both absolute and percentage k_1 loss averaged over 9 patients exhibited a significantly strong positive correlation with the AD in the NTL (Fig. 4), with ρ values of at least 0.92 ($P < 0.001$) (Table 2). Logistic function modeling for k_1 loss and AD demonstrated an R^2 value of at least 0.91 for the percentage and absolute k_1 loss. The fit variables are given in Table 2. The average absolute and percentage k_1 loss over 9 patients across all AD bins was 2.2 mL/100 g/min and 28.1%, respectively.

Stratifying by patient characteristics, we found that most subgroups demonstrated a significantly strong correlation between AD and both absolute and percentage k_1 loss ($\rho > 0.9$, $P < 0.001$) (Supplemental Table 3), as well as a high R^2 for logistic model fitting ($\geq$0.79), except subgroups with an ALBI of at least -2.93 and a lower $V_{70\ Gy}$. Because patients stratified by baseline ALT had results similar to those stratified by baseline AST, only the results of ALT are presented here. The 3-parameter logistic model fit variables for subgroups are provided in Supplemental Table 3. Absolute (Supplemental Fig. 3) and percentage (Fig. 5) k_1 loss results displayed similar trends. When patients with HCC and liver metastases were compared, the HCC group exhibited a notably larger k_1 loss. Patients with a baseline ALT level of at least 45 IU/L had a more pronounced k_1 loss than did those with an ALT of less than 45 IU/L. In contrast, the subgroup with a baseline ALBI score of at least -2.93 presented a smaller k_1 loss than did the subgroup with an ALBI lower than -2.93. A lower $V_{70\ Gy}$ was associated with a generally smaller k_1 loss than was a higher $V_{70\ Gy}$. Additionally, patients with 2 sequential treatments demonstrated a larger k_1 loss than did patients with a single treatment.

Global Liver Function Assessment Comparison

Liver function changes after SIRT derived by imaging (k_1 maps) and biomarkers (change in ALBI score) showed a positive correlation ($r = 0.60$) for all 11 patients (Fig. 6), that is, a larger k_1V_L loss with increasing, less negative, ALBI scores (indicating rising bilirubin and lower albumin levels).

DISCUSSION

This study incorporated information from multimodality imaging (PET/CT and MRI) to establish a dose–toxicity relationship within normal liver after ^{90}Y SIRT; to our knowledge, this was the first attempt to assess this relationship at a spatial level. We demonstrated a strong and significant correlation between higher AD and an increasing k_1 loss for both individual ($\rho = 0.53$–0.99, $P < 0.001$ for 8/11) and grouped ($\rho \geq 0.92$, $P < 0.001$) patient studies. Additionally, in the grouped patient study, the average percentage k_1 loss across AD bins was 28.1%, with a logistic function model indicating that 25.8% of k_1 loss occurred at an AD of 102.1 Gy (Table 2).

The consistency for k_1 loss in the low-AD region of the treated lobe and untreated lobe suggests that at these low AD levels, k_1 loss is primarily the result of natural progression of liver malignancy. As AD levels increased, a corresponding increase in regional k_1 loss was observed, mirroring results from a prior study of patients undergoing SBRT (*14*). For patients exhibiting a poor or negative correlation, potential factors include the relatively dispersed and small perfused NTL volumes for patients 4 and 8 (~350 cm^3) and the narrow NTL AD ranges (0 to ~25 Gy) for

TABLE 1
Spearman Correlation Coefficients Between Absolute and Percentage k_1 Loss and AD

	Patient no.										
Loss	1	2	3	4	5	6	7	8	9	10	11
Absolute k_1	0.97*	0.53*	0.79*	−0.03	0.93*	0.72*	0.93*	0.09	−1.00*	0.67*	0.91*
Percentage k_1	0.98*	0.99*	0.89*	0.17	0.91*	0.76*	0.69*	0.18	−0.70	0.82*	0.89*

*$P < 0.001$.

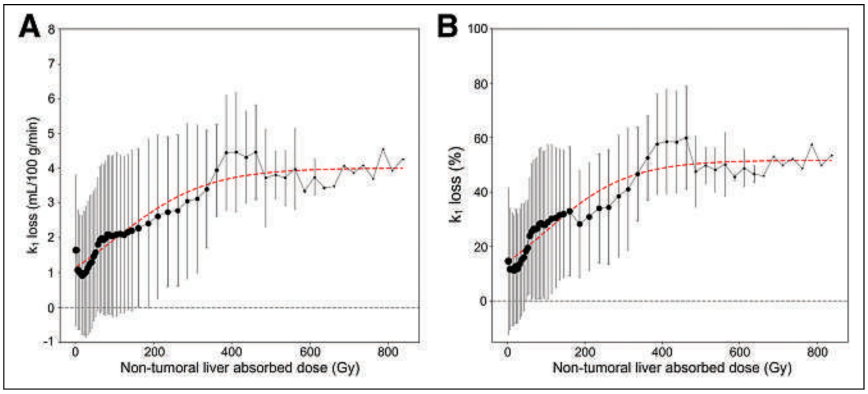

FIGURE 4. Absolute loss (A) and percentage k_1 loss (B) vs. AD in NTL for 9 patients, with average and SD computed over all k_1 measurements. Red lines indicate fit 3-parameter logistic curves. Data point radius is proportional to patient count included in each bin.

patient 9, which may not provide enough sampling to establish a robust correlation. Generally, liver function degraded after therapy (i.e., lower k_1 values after SIRT for all except patients 7 and 11). This is an expected occurrence, inherent in SIRT, in the setting of radiation-induced liver injury. Interestingly, both patients who saw an unanticipated rise in k_1 values had received prior antivascular endothelial growth factor therapy with bevacizumab. It is possible this drug altered the vascular response or recovery after SIRT (which may alter enhancement and therefore k_1 values on DGAE MRI), although the small number of patients limits confident assessment. Nonetheless, the potential of such immunotherapy to generate spurious results warranted exclusion of these patients from our overall dose–response analysis.

For the grouped study, both curves in Figure 4 resemble a logistic function. Initially, there is a sharp rise in k_1 loss for an AD of less than 100 Gy, signifying pronounced functional decline. As AD increases, the rate of change in k_1 loss slows at about 200 Gy, indicating milder functional decline. However, fluctuations occur thereafter and are particularly notable after 400 Gy, which could be attributed to the reduced patient count within those bins. Specifically, large changes in slope at about 180 and 480 Gy may be attributed to patient dropout at higher-dose bins, marked by higher k_1 loss than in other patients. This possibility also may explain the slope change in Figures 5B and 5D at about 180 Gy.

Patient characteristics influenced the extent of k_1 loss in response to AD (Fig. 5). The HCC group exhibited a more pronounced k_1 loss, a more severe maximum liver function decline (α), and a lower AD to reach half this decline (D_c), than did the liver metastasis group, suggesting higher sensitivity to radiation in HCC (*23–25*). One explanation for this finding is not the HCC itself but the higher incidence of cirrhosis among the HCC cohort (2/4 vs. 0/5 for HCC vs. liver metastases), which would limit the ability of background liver parenchyma to undergo repair and regeneration after radiation injury. Thus, we stratified patients into cirrhosis and noncirrhosis subgroups, with the cirrhosis subgroup showing a notably larger k_1 loss, albeit only 2 patients in our cohort had cirrhosis (Supplemental Fig. 4).

Child–Pugh scores and ascites were not used as stratification criteria because of limited variation (8/9 with A5 and no ascites). ALBI scores served as a surrogate for liver function over time and have been predictive of radiation-induced liver injury in HCC patients (*17*). Surprisingly, patients with initially normal ALBI scores showed higher k_1 loss, possibly because of having more functioning hepatocytes at baseline and, thus, a higher relative liver parenchymal loss resulting from any radiation-induced injury. However, the low median baseline ALBI score used as our cutoff (-2.93) and the limited number of cirrhosis and HCC patients in our study may make this score less reliable for predicting liver dysfunction in this subset. Conversely, higher baseline ALT and AST values were both associated with greater k_1 loss; because these markers indicate acute hepatocellular injury or cell death, it is unsurprising that subsequent radiation treatment would accentuate loss of liver function.

Regarding dose–volume effects, patients with a larger relative volume of the NTL receiving 70 Gy demonstrated generally larger k_1 loss and derived α. This implies a volume-based correlation between total irradiated volume and hepatic function damage, which is supported by prior studies (*23,26*). For assessment intervals, patients with sequential treatments had a longer (~3-mo) gap between pre- and post-SIRT MRI scans, whereas those with a single treatment had scans about 1 mo apart. Greater k_1 loss among the group with the sequential treatments also suggests that liver function could decline over time, compounding the effects of AD. However, the liver is known for its dynamic vascular reorganization and regeneration, which likely affects the comparison of these scans. Thus, a more detailed time interval stratification could be designed and assessed for a larger patient population in the future.

A comparison of the change in global liver function before and after SIRT estimated by k_1 maps and ALBI scores yielded a correlation of 0.60 (Fig. 6), consistent with the results of a previous

TABLE 2

Spearman Correlation Coefficients and 3-Parameter Logistic Model Fit Variables for Grouped 9 Patients

		Fit variable			
Loss	ρ	α	D_c (Gy)	γ (Gy)	R^2
Absolute k_1	0.93*	4.0 mL/100 g/min (0.1)	106.5 (10.1)	115.5 (13.2)	0.92
Percentage k_1	0.92*	51.6% (1.3)	102.1 (10.1)	105.6 (13.2)	0.91

---

*$P < 0.001$.

Data in parentheses are SE.

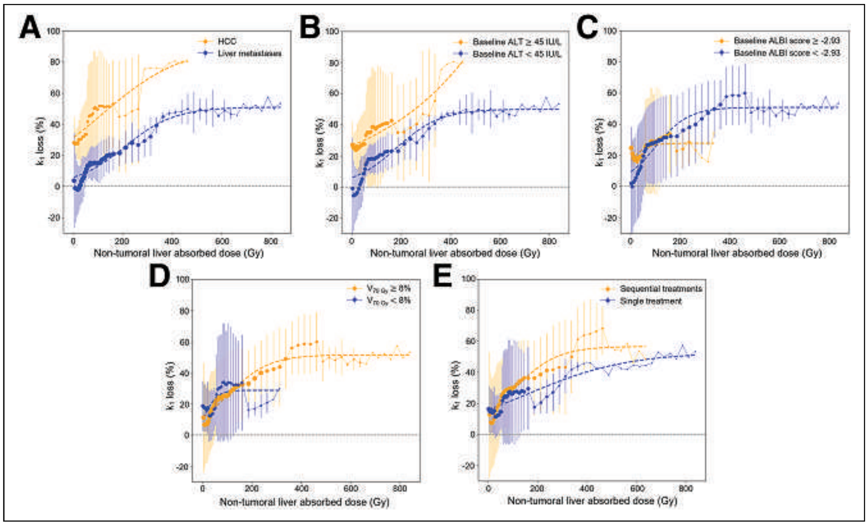

FIGURE 5. Percentage k_1 loss vs. AD in NTL for 9 patients subgrouped by HCC and liver metastases (A), baseline ALT $\geq$ and $<$ 45 IU/L (B), baseline ALBI score $\geq$ and < -2.93 (C), $V_{70\ Gy}$ above and below median $V_{70\ Gy}$ (D), and single and sequential treatments (E). Dashed lines indicate fit 3-parameter logistic curves. Data point radius is proportional to patient count included in each bin.

study (*13*). Notably, the largest increase in ALBI score after SIRT was only 0.34, which may be reasonable considering most patients had good baseline liver function and all patients received a mean AD of less than 70 Gy. However, because of the heterogeneous distribution of AD and functional tissue in the NTL, radiation-induced liver damage may not be sufficiently captured by the ALBI biomarker. Furthermore, the regional dose–toxicity relationship for the NTL after SIRT in this study was more pronounced than in a prior study of whole-liver dose–toxicity relationships among patients with colorectal liver metastases by Alsultan et al. (*3*). They correlated the mean AD in the NTL from ^{90}Y PET/CT images with toxicity grades and changes in general liver biomarkers, such as total bilirubin, but a reliable association was not well established. In another study, by Chiesa et al. (*4*), the mean ADs in the NTL based on ^{99m}Tc-macroaggregated albumin SPECT/CT images and basal bilirubin ($\geq$1.1 mg/dL) were reported as prognostic indicators for liver decompensation in patients with HCC. To explore this further, we stratified our patients into similar subgroups based on baseline bilirubin and found that patients with bilirubin of at least 1.1 mg/dL exhibited a larger percentage k_1 loss (Supplemental Fig. 5). However, with only 2 patients within this subgroup, only a limited assessment could be performed.

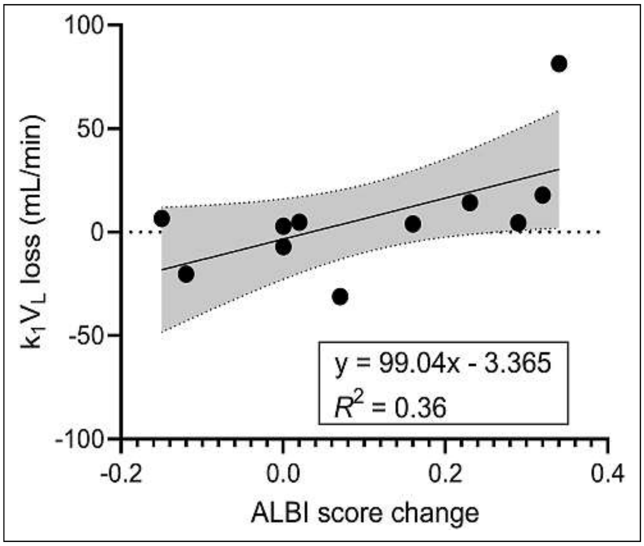

FIGURE 6. Scatterplot of global liver function changes after SIRT derived by k_1 maps vs. change in ALBI score. Best-fit line (solid line) combines with its 95% CI (gray area) as linear regression model.

In an ongoing clinical trial (NCT04518748) of combinational therapy, the SBRT planning after SIRT is optimized to spare high-functioning regions of the liver based on pre-SBRT k_1 maps. The spatial level dose–toxicity correlations demonstrated in the current study could further facilitate refinement of SIRT dose selection and post-SIRT treatments, including SBRT. However, studies with larger patient cohorts are needed to establish the current findings. The small patient cohort limits statistical analysis and may compound errors in the analysis. Besides, there is a high variation in k_1 loss among individuals, as inferred from the large SD of k_1 loss when averaging over patients. Although a mixed model considering the dose as the fixed effect and patient as the random effect has been preliminarily explored, the limited number of patients rendered the modeling unrobust. An additional limitation associated with the small sample is that we chose to stratify subgroups on the basis of median values to ensure balanced groups, although a different approach (e.g., grade for ALBI) may be more relevant.

Another limitation is potential misregistration between single- and multimodality images due to involuntary and voluntary patient motion (*27*) and to hepatic volume changes (*28*), even with careful registration efforts. Our study used rigid registration between pre- and post-SIRT MRI scans, with results deemed acceptable after review by the technologist. However, further improvement may be achieved through nonrigid methods, which can better accommodate the deformable liver shape during patient motion, despite requiring careful deformation constraints and smoothness to avoid artifacts. To further alleviate the impact of misregistration, a binning strategy (*14*) was implemented by aggregating voxels with similar AD and spatial proximity into regions within a bin, which reduces susceptibility to misregistration compared with individual voxels. Motion correction strategies such as data-driven gating (*29*) were not used in this study because of lack of validation for ^{90}Y with low-count statistics. However, the impact of motion in ^{90}Y SIRT imaging may be less significant given the 5-mm image filter and the large untreated liver volumes in some patients. Moreover, a single snapshot of DGAE MRI was obtained after the completion of treatment, limiting this study to a short-term hepatic function assessment, whereas long-term dysfunction could be further explored.

Considering the technical aspect of this study, implementing DGAE MRI in clinical settings involves straightforward procedures for image acquisition and pharmacokinetic modeling. However, motion correction may present challenges and currently requires custom software, particularly if addressing respiratory motion in k-space. Additionally, advancements in newer generations of technology (*8*) offer superior sensitivity and event statistics, particularly beneficial for ^{90}Y imaging. This facilitates achieving smaller voxel sizes while maintaining or enhancing signal-to-noise ratio. Consequently, we may be able to include the smaller dose-voxel bins (<100 voxels) that we currently exclude from our model. Furthermore, a smaller postprocessing filter kernel size may suffice, helping to maintain a higher spatial resolution in PET images and subsequent AD maps in the future.

CONCLUSION

In this pioneering study, information derived from multimodal imaging facilitated the correlation of regional liver function degradation, as quantified through DGAE MRI, with voxel-level AD in the NTL as determined by ^{90}Y PET/CT images after ^{90}Y SIRT. Higher AD levels are associated with a larger loss of liver function. Modeling demonstrates that patients with certain characteristics, such as HCC and a larger NTL fractional volume receiving an AD of 70 Gy or more and sequential SIRT treatments, could experience greater loss of liver function after treatment, warranting greater attention for their treatment. Future research with the inclusion of a larger and more diverse patient population is warranted to verify these findings.

DISCLOSURE

This research was supported by the National Institute of Biomedical Imaging and Bioengineering under award R01EB022075 and by the Science and Technology Development Fund (FDCT) of Macau (0099/2021/A). Yuni Dewaraja is a consultant for MIM Software Inc. No other potential conflict of interest relevant to this article was reported.

KEY POINTS

QUESTION: Is there a correlation between the ^{90}Y PET/CT-derived AD to the NTL and spatial liver function deterioration as assessed by dynamic MRI after ^{90}Y SIRT?

PERTINENT FINDINGS: A direct correlation between regions of higher ADs and increased liver function deterioration after SIRT has been demonstrated, with notably severer hepatic function loss in patients with HCC than in those with liver metastases.

IMPLICATIONS FOR PATIENT CARE: The nonuniform hepatic function loss is induced because of heterogeneous AD deposition. The spatial dose–toxicity information can potentially be used to enhance ^{90}Y SIRT strategies, including combination therapy.

REFERENCES

1. Chiesa C, Sjogreen-Gleisner K, Walrand S, et al. EANM dosimetry committee series on standard operational procedures: a unified methodology for ^{99m}Tc-MAA pre- and ^{90}Y peri-therapy dosimetry in liver radioembolization with ^{90}Y microspheres. *EJNMMI Phys.* 2021;8:77.
2. Sangro B, Gil-Alzugaray B, Rodriguez J, et al. Liver disease induced by radioembolization of liver tumors: description and possible risk factors. *Cancer.* 2008;112:1538–1546.
3. Alsultan AA, van Roekel C, Barentsz MW, et al. Dose–response and dose–toxicity relationships for glass ^{90}Y radioembolization in patients with liver metastases from colorectal cancer. *J Nucl Med.* 2021;62:1616–1623.
4. Chiesa C, Mira M, Bhoori S, et al. Radioembolization of hepatocarcinoma with ^{90}Y glass microspheres: treatment optimization using the dose-toxicity relationship. *Eur J Nucl Med Mol Imaging.* 2020;47:3018–3032.
5. Garin E, Lenoir L, Edeline J, et al. Boosted selective internal radiation therapy with ^{90}Y-loaded glass microspheres (B-SIRT) for hepatocellular carcinoma patients: a new personalized promising concept. *Eur J Nucl Med Mol Imaging.* 2013;40:1057–1068.
6. Dewaraja YK, Devasia T, Kaza RK, et al. Prediction of tumor control in ^{90}Y radioembolization by logit models with PET/CT-based dose metrics. *J Nucl Med.* 2020;61:104–111.
7. Strigari L, Sciuto R, Rea S, et al. Efficacy and toxicity related to treatment of hepatocellular carcinoma with ^{90}Y-SIR spheres: radiobiologic considerations. *J Nucl Med.* 2010;51:1377–1385.
8. Costa G, Spencer B, Omidvari N, et al. Radioembolization dosimetry with total-body ^{90}Y PET. *J Nucl Med.* 2022;63:1101–1107.
9. Matuszak MM, Kashani R, Green M, et al. Functional adaptation in radiation therapy. *Semin Radiat Oncol.* 2019;29:236–244.
10. Wang H, Cao Y. Spatially resolved assessment of hepatic function using ^{99m}Tc-IDA SPECT. *Med Phys.* 2013;40:092501.
11. Cao Y, Wang H, Johnson TD, et al. Prediction of liver function by using magnetic resonance-based portal venous perfusion imaging. *Int J Radiat Oncol Biol Phys.* 2013;85:258–263.
12. Simeth J, Johansson A, Owen D, et al. Quantification of liver function by linearization of a two-compartment model of gadoxetic acid uptake using dynamic contrast-enhanced magnetic resonance imaging. *NMR Biomed.* 2018;31:e3913.
13. Simeth J, Aryal M, Owen D, Cuneo K, Lawrence TS, Cao Y. Gadoxetic acid uptake rate as a measure of global and regional liver function as compared with indocyanine green retention, albumin-bilirubin score, and portal venous perfusion. *Adv Radiat Oncol.* 2022;7:100942.
14. Wei L, Simeth J, Aryal MP, et al. The effect of stereotactic body radiation therapy for hepatocellular cancer on regional hepatic liver function. *Int J Radiat Oncol Biol Phys.* 2023;115:794–802.
15. Combined Y-90 selective internal radiation therapy (Y-90 SIRT) and stereotactic body radiation therapy (SBRT) in hepatic malignancy. ClinicalTrials.gov website. https://clinicaltrials.gov/ct2/show/NCT04518748. Updated October 16, 2023. Accessed May 15, 2024.
16. Instructions for use: TheraSphere^{TM} ytrium-90 glass microspheres. Boston Scientific website. https://www.bostonscientific.com/content/dam/elabeling/pi/OTT-00221_Rev1_TheraSphere_en_s.pdf. Revised March 2021. Accessed May 15, 2024.
17. Lescure C, Estrade F, Pedrono M, et al. ALBI score is a strong predictor of toxicity following SIRT for hepatocellular carcinoma. *Cancers (Basel).* 2021;13:3794.
18. Johansson A, Balter J, Feng M, Cao Y. An overdetermined system of transform equations in support of robust DCE-MRI registration with outlier rejection. *Tomography.* 2016;2:188–196.
19. Johansson A, Balter JM, Cao Y. Abdominal DCE-MRI reconstruction with deformable motion correction for liver perfusion quantification. *Med Phys.* 2018;45:4529–4540.
20. Wilderman SJ, Dewaraja Y. Method for fast CT/SPECT-based 3D Monte Carlo absorbed dose computations in internal emitter therapy. *IEEE Trans Nucl Sci.* 2007;54:146–151.
21. bbmle: tools for general maximum likelihood estimation. The Comprehensive R Archive Network website. https://cran.r-project.org/web/packages/bbmle/index.html. Published December 9, 2023. Accessed May 15, 2024.
22. Schabenberger O, Pierce FJ. *Contemporary Statistical Models for the Plant and Soil Sciences*: CRC Press; 2001:251–261.
23. Dawson LA, Normolle D, Balter JM, McGinn CJ, Lawrence TS, Ten Haken RK. Analysis of radiation-induced liver disease using the Lyman NTCP model. *Int J Radiat Oncol Biol Phys.* 2002;53:810–821.
24. Xu Z-Y, Liang S-X, Zhu J, et al. Prediction of radiation-induced liver disease by Lyman normal-tissue complication probability model in three-dimensional conformal radiation therapy for primary liver carcinoma. *Int J Radiat Oncol Biol Phys.* 2006;65:189–195.
25. Miften M, Vinogradskiy Y, Moiseenko V, et al. Radiation dose-volume effects for liver SBRT. *Int J Radiat Oncol Biol Phys.* 2021;110:196–205.
26. Pan CC, Kavanagh BD, Dawson LA, et al. Radiation-associated liver injury. *Int J Radiat Oncol Biol Phys.* 2010;76(suppl):S94–S100.
27. Lu Z, Chen G, Jiang H, Sun J, Lin K-H, Mok GS. SPECT and CT misregistration reduction in [^{99m}Tc]Tc-MAA SPECT/CT for precision liver radioembolization treatment planning. *Eur J Nucl Med Mol Imaging.* 2023;50:2319–2330.
28. Polan DF, Feng M, Lawrence TS, Ten Haken RK, Brock KK. Implementing radiation dose-volume liver response in biomechanical deformable image registration. *Int J Radiat Oncol Biol Phys.* 2017;99:1004–1012.
29. Dias AH, Schleyer P, Vendelbo MH, Hjorthaug K, Gormsen LC, Munk OL. Clinical feasibility and impact of data-driven respiratory motion compensation studied in 200 whole-body ^{18}F-FDG PET/CT scans. *EJNMMI Res.* 2022;12:16.

Clinical Trial Protocol for VIOLET: A Single-Center, Phase I/II Trial Evaluation of Radioligand Treatment in Patients with Metastatic Castration-Resistant Prostate Cancer with [^{161}Tb]Tb-PSMA-I&T

James P. Buteau[1,2], Louise Kostos[2,3], Ramin Alipour[1,2], Price Jackson[1,2], Lachlan McInstosh[1,2], Brittany Emmerson[1,2], Mohammad B. Haskali[2,4], Jing Xie[5], Elizabeth Medhurst[1,2], Rajeev Ravi[6], Brian D. Gonzalez[7], Heidi Fettke[2,8], Benjamin Blyth[2,8], Luc Furic[2,8], Katie Owen[2,8], Shahneen Sandhu[2,3], Declan G. Murphy[2,9], Arun A. Azad*[2,3], and Michael S. Hofman*[1,2]

[1]Prostate Cancer Theranostics and Imaging Centre of Excellence, Molecular Imaging and Therapeutic Nuclear Medicine, Cancer Imaging, Peter MacCallum Cancer Centre, Melbourne, Victoria, Australia; [2]Sir Peter MacCallum Department of Oncology, University of Melbourne, Melbourne, Victoria, Australia; [3]Department of Medical Oncology, Peter MacCallum Cancer Centre, Melbourne, Victoria, Australia; [4]Radiopharmaceutical Production and Research Laboratory, Peter MacCallum Cancer Centre, Melbourne, Victoria, Australia; [5]Centre for Biostatistics and Clinical Trials, Peter MacCallum Cancer Centre, Melbourne, Victoria, Australia; [6]Department of Cancer Imaging, Peter MacCallum Cancer Centre, Melbourne, Victoria, Australia; [7]Department of Health Outcomes and Behavior, Moffitt Cancer Center, Tampa, Florida; [8]Cancer Research Division, Peter MacCallum Cancer Centre, Melbourne, Victoria, Australia; and [9]Division of Cancer Surgery, Peter MacCallum Cancer Centre, Melbourne, Victoria, Australia

[^{177}Lu]Lu-PSMA is an effective class of therapy for patients with metastatic castration-resistant prostate cancer (mCRPC); however, progression is inevitable. The limited durability of response may be partially explained by the presence of micrometastatic deposits, which are energy-sheltered and receive low absorbed radiation with ^{177}Lu due to the approximately 0.7-mm mean pathlength. ^{161}Tb has abundant emission of Auger and conversion electrons that deposit a higher concentration of radiation over a shorter path, particularly to single tumor cells and micrometastases. ^{161}Tb has shown in vitro and in vivo efficacy superior to that of ^{177}Lu. We aim to demonstrate that [^{161}Tb]Tb-PSMA-I&T will deliver effective radiation to sites of metastatic prostate cancer with an acceptable safety profile. **Methods:** This single-center, single-arm, phase I/II trial will recruit 30 patients with mCRPC. Key eligibility criteria include a diagnosis of mCRPC with progression after at least one line of taxane chemotherapy (unless medically unsuitable) and androgen receptor pathway inhibitor; prostate-specific membrane antigen–positive disease on [^{68}Ga]Ga-PSMA-11 or [^{18}F]DCFPyL PET/CT (SUV$_{max}$ ≥ 20); no sites of discordance on [^{18}F]FDG PET/CT; adequate bone marrow, hepatic, and renal function; an Eastern Cooperative Oncology Group performance status of no more than 2, and no prior treatment with another radioisotope. The dose escalation is a 3 + 3 design to establish the safety of 3 prespecified activities of [^{161}Tb]Tb-PSMA-I&T (4.4, 5.5, and 7.4 GBq). The maximum tolerated dose will be defined as the highest activity level at which a dose-limiting toxicity occurs in fewer than 2 of 6 participants. The dose expansion will include 24 participants at the maximum tolerated dose. Up to 6 cycles of [^{161}Tb]Tb-PSMA-I&T will be administered intravenously every 6 wk, with each subsequent activity reduced by 0.4 GBq. The coprimary objectives are to establish the maximum tolerated dose and safety profile (Common Terminology Criteria for Adverse Events version 5.0) of [^{161}Tb]Tb-PSMA-I&T. Secondary objectives include measuring absorbed radiation dose (Gy), evaluating antitumor activity (prostate-specific antigen 50% response rate, radiographic and prostate-specific antigen progression-free survival, overall survival, objective response rate), and evaluating pain (Brief Pain Inventory–Short Form) and health-related quality of life (Functional Assessment of Cancer Therapy–Prostate and Functional Assessment of Cancer Therapy–Radionuclide Therapy). **Conclusion:** Enrollment was completed in February 2024. Patients are still receiving [^{161}Tb]Tb-PSMA-I&T.

Key Words: prostate cancer; PSMA; ^{161}Tb; Auger electrons; theranostics

J Nucl Med 2024; 65:1231–1238
DOI: 10.2967/jnumed.124.267650

Although [^{177}Lu]Lu-PSMA has been established as a safe and effective radiopharmaceutical therapy, enhancing overall survival and quality of life in patients with metastatic castration-resistant prostate cancer (mCRPC), disease progression remains inevitable (*1*). A likely contributing factor for the limited durability of response is the presence of micrometastatic deposits. Single tumor cells and micrometastases are considered energy-sheltered deposits. They receive vanishingly low absorbed radiation from ^{177}Lu because of the approximately 0.7-mm mean pathlength (range, 0.04–1.8 mm). In comparison, the diameters of circulating tumor cells from prostate cancer patients and cultured prostate cancer cells measure on average 7.97 and 13.38 μm, respectively (*2*). Although a complete response of macroscopic disease is observed with [^{177}Lu]Lu-PSMA, these small energy-sheltered deposits do not receive lethal radiation and eventually progress.

^{161}Tb has physical properties that indicate it could be superior for medical use to the currently used ^{177}Lu because of its abundant emission of Auger and conversion electrons. These ejected inner

---

Received Feb. 21, 2024; revision accepted May 28, 2024.

For correspondence or reprints, contact James P. Buteau (james.buteau@petermac.org) or Michael S. Hofman (michael.hofman@petermac.org).

*Contributed equally to this work.

TABLE 1
Decay Characteristics of ^{177}Lu and ^{161}Tb (*5*)

Characteristic	^{177}Lu	^{161}Tb
Half-life (d)	6.647	6.906
Type of decay (%)	β^- (100%)	β^- (100%)
β particles mean energy (keV)	133.3	154.3
Daughter	^{177}Hf (stable)	^{161}Dy (stable)
Conversion electrons (keV per decay)	13.52	39.28
Conversion electron energy range (keV)	6.2–206.3 (weighted average, 87)	3.3–98.3 (weighted average, 28)
Auger electrons (keV per decay)	1.13	8.94
Auger electron energy range (keV)	0.01–61.7 (weighted average, 1)	0.018–50.9 (weighted average, 0.8)
Total electron energy per decay (keV)	147.9	202.5
γ for imaging: energy in keV (% abundance)	208 (11%); 113 (6.4%)	75 (10.2%)
Photon X and γ (total energy per decay in keV)	35.1	36.35

orbital electrons deposit their energy over a much shorter distance (nanometers to micrometers), with an order-of-magnitude higher linear energy transfer than β-electrons, resulting in greater cell death (*3*,*4*). ^{161}Tb delivers higher radiation doses to single tumor cells and micrometastases than does ^{177}Lu when calculating different scenarios of the radionuclide distribution (*5*). Several other studies have also supported theoretic dose calculations in favor of ^{161}Tb (*6–9*). The physical characteristics of ^{161}Tb and ^{177}Lu are otherwise similar (Table 1).

^{161}Tb has been shown superior to ^{177}Lu in tumor cell killing and growth suppression in vitro and in vivo (*10–12*), supporting an additional contribution of Auger and conversion electrons. [^{161}Tb]Tb-PSMA-617 was evaluated in tumor-bearing murine models, and the in vitro properties, pharmacokinetics, and biodistribution profile were similar to [^{177}Lu]Lu-PSMA-617 (*10*). Theoretic dose calculations also confirmed an additive therapeutic effect of ^{161}Tb when comparing both radiopharmaceutical therapies. Whether the promising theoretic and preclinical data will translate into clinical benefit has yet to be determined. We hypothesize that [^{161}Tb]Tb-PSMA-I&T will deliver effective radiation to sites of metastatic prostate cancer with an acceptable safety profile.

MATERIALS AND METHODS

Design, Study Population, and Objectives

VIOLET is an investigator-initiated and -led, open-label, single-arm, single-center, phase I/II dose-escalation and -expansion study designed to evaluate the safety and efficacy of [^{161}Tb]Tb-PSMA-I&T in patients with mCRPC. The dose-escalation phase is a traditional 3 + 3 design, with 3 prespecified activity levels. Recruitment will be halted after each cohort of 3 patients is enrolled until the dose-limiting toxicities (DLTs) have been assessed (Table 2) and the activity for the next cohort of 3 patients has been determined. The DLT assessment period is 6 wk from cycle 1 day 1. Once the maximum tolerated dose or maximum administered dose has been determined, the trial will proceed to the dose-expansion stage. The trial schema is illustrated in Figure 1.

Patients with mCRPC who have progressed on at least one line of taxane chemotherapy (unless medically unsuitable) and an androgen receptor pathway inhibitor will be eligible for this study. Other key eligibility criteria include prostate-specific membrane antigen (PSMA)–positive disease on [^{68}Ga]Ga-PSMA-11 or [^{18}F]DCFPyL PET/CT ($SUV_{max} \geq 20$); no sites of discordance on [^{18}F]FDG PET/CT; adequate bone marrow, hepatic, and renal function; an Eastern Cooperative Oncology Group performance status of no more than 2; and no prior treatment with another radioisotope (Table 3).

TABLE 2
Definitions of DLTs

Toxicity	Exception	Duration
Grade ≥ 3 nonhematologic adverse event	Grade 3 nausea, vomiting, or diarrhea that is optimally treated and resolves to grade of ≤2 in ≤5 d	
	Grade 3 fatigue	
	Grade 3 tumor flare (local pain) that resolves to grade of ≤2 in ≤7 d	
Grade 4 neutropenia		>7 d
Febrile neutropenia		>7 d
Grade 4 anemia		>7 d
Grade 3 thrombocytopenia		>7 d

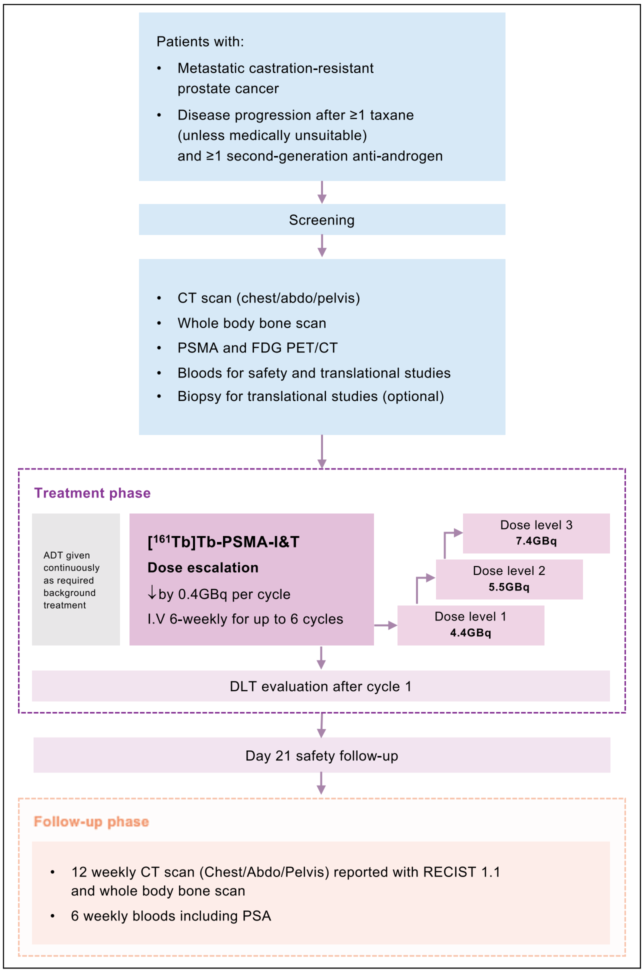

FIGURE 1. Trial schema.

The phase I primary objectives are to determine maximum tolerated dose, DLTs, and the recommended phase II dose of [^{161}Tb]Tb-PSMA-I&T in patients with mCRPC. The phase II primary objective is to evaluate its safety. Secondary and exploratory objectives include estimating the absorbed radiation dose in normal organs and metastases, evaluating antitumor activity (prostate-specific antigen [PSA] response rate, radiographic and PSA progression-free survival, overall survival, objective response rate), evaluating dynamic changes in circulating tumor DNA, and evaluating pain (Brief Pain Inventory–Short Form) and health-related quality of life (Functional Assessment of Cancer Therapy–Prostate and Functional Assessment of Cancer Therapy–Radionuclide Therapy) (Table 4).

The study protocol was approved by the Human Research Ethics Committee at Peter MacCallum Cancer Centre, and all participants will provide signed informed consent. The VIOLET trial is registered with ClinicalTrials.gov (NCT05521412) and sponsored by the Peter MacCallum Cancer Centre. The funders of the study had no role in study design or writing of this article.

[^{161}Tb]Tb-PSMA-I&T Production, Administration, and Posttherapy Dosimetry

PSMA-I&T will be radiolabeled with no-carrier-added ^{161}Tb using the same chelator (DOTAGA) as [^{177}Lu]Lu-PSMA-I&T in the onsite hospital radiopharmacy. The production of [^{161}Tb]Tb-PSMA-I&T will be automated on the iPHASE MultiSyn radiochemistry module using a kit formulation (Isotopia Molecular Imaging) encompassing labeling buffer and a precursor/stabilizer combination. [^{161}Tb]Tb-PSMA-I&T production and quality control will undergo rigorous process validation leading to a product that meets all prerelease criteria matching or exceeding the Australasian Radiopharmaceutical Network production guidelines. This includes tests for radionuclidic purity, radiochemical purity, and radiochemical identity using high-pressure liquid chromatography and radio–thin-layer chromatography, as well as endotoxin and sterility testing.

[^{161}Tb]Tb-PSMA-I&T will be administered by slow intravenous injection in an ambulatory treatment setting every 6 wk ± 1 wk, for a maximum of 6 cycles. A minimum of 500 mL of normal saline hydration over 1–2 h is recommended with radiopharmaceutical therapy, unless fluids are contraindicated. In the dose-escalation phase, there are 3 planned activity levels starting at 4.4, 5.5, and 7.4 GBq. The dose-escalation results will determine the activity of [^{161}Tb]Tb-PSMA-I&T in the expansion phase. In both phases, the activity of [^{161}Tb]Tb-PSMA-I&T will decrease by 0.4 GBq every cycle. All patients will receive androgen deprivation therapy continuously throughout the trial.

The subsequent activities of [^{161}Tb]Tb-PSMA-I&T will be reduced by 20% for patients who have the following toxicities from the preceding cycle: dry mouth (grade 2), dry eyes (grade 2), nadir platelet count of less than 100×10^9/L, nadir neutrophil count of less than 1.0×10^9/L, or other significant dose-related toxicities (grade 3 or worse) that are considered both attributable to [^{161}Tb]Tb-PSMA-I&T and activity-related. A maximum of 3 activity reductions per patient is permitted, and there are no reescalations.

Posttherapy SPECT/CT imaging will be performed after each cycle. In the dose-escalation phase, 3-time-point SPECT/CT from vertex to mid thigh will be acquired at 4 h (±2 h), 24 h (±4 h), and 96 h (±24 h) after cycle 1 and optionally thereafter. Acquisitions will be obtained on low-energy high-resolution collimators, using a double energy window peaked at 74 keV with lower scatter limits (*13–15*). Retention of [^{161}Tb]Tb-PSMA-I&T will be estimated from voxel-based time–activity curves based on a multiphase exponential clearance model and convolved using a Geant4 Application for Emission Tomography–derived voxel dose kernel based on decay of ^{161}Tb in International Commission on Radiological Protection soft tissue to yield 3-dimensional absorbed dose maps (*16–18*).

Assessment of Safety, Efficacy, and Patient-Reported Outcome Measures

During the treatment phase, patients will have weekly safety reviews and a full blood count performed during cycle 1. Adverse events will be graded and causality assigned according to Common Terminology Criteria for Adverse Events version 5.0 at each clinical review. For subsequent cycles, safety reviews and blood tests (full blood count, urea, creatinine, electrolytes, liver function tests, and PSA) will be repeated on day 22 and within 3 d before the next cycle. If the platelet count is less than 50×10^9/L, it will be rechecked 1 wk later and every week thereafter until it is rising. Administration of the next cycle can proceed if pretreatment bloods show a platelet level of at least 75×10^9/L and rising ($\geq 100 \times 10^9$/L for cycle 1), a hemoglobin level of at least 80 g/L, and an absolute neutrophil count of at least 1.5×10^9/L. [^{161}Tb]Tb-PSMA-I&T can be delayed for a maximum of 6 wk. Treatment will be withheld during grade 3 or 4 adverse events with the exception of fatigue or lymphocytopenia and not restarted until improvement to grade 0–2 or baseline.

Contrast-enhanced CT of the chest, abdomen, and pelvis, as well as whole-body bone scans, will be performed every 12 wk ± 1 wk from cycle 1 day 1, until radiologic progression. [^{68}Ga]Ga-PSMA-11 or [^{18}F]DCFPyL, and [^{18}F]FDG PET/CT, will be repeated 12 wk ± 1 wk from cycle 1 day 1, and before cycle 3 day 1. Peripheral blood for

TABLE 3
Eligibility Criteria

Category	Criterion
Inclusion criteria	Patient has provided written informed consent
	Patient is 18 y or older at time of written informed consent
	Patient has histologically or cytologically confirmed adenocarcinoma of prostate or unequivocal diagnosis of metastatic prostate cancer (i.e., involving bone or pelvic lymph nodes or paraaortic lymph nodes) with elevated serum PSA
	Eastern Cooperative Oncology Group performance status is ≤2
	Patient had prior treatment with at least one line of taxane chemotherapy, unless medically unsuitable
	Patient had prior treatment with at least one androgen receptor pathway inhibitor (e.g., enzalutamide, abiraterone, apalutamide, or darolutamide)
	Patient has progressive disease defined according to Prostate Cancer Clinical Trials Working Group 3 as any one of the following:
	PSA progression: minimum of 2 rising PSA values from baseline measurement with interval of ≥1 wk between each measurement
	Soft-tissue progression: per RECIST 1.1
	Bone progression: ≥2 new lesions on bone scan
	Patient had prior surgical orchiectomy or chemical castration maintained on luteinizing hormone–releasing hormone analog (agonist or antagonist)
	Patient has serum testosterone level of ≤1.75 nmol/L (≤50 ng/dL)
	Patient has significant PSMA avidity on [^{68}Ga]Ga-PSMA-11 or [^{18}F]DCFPyL PET/CT, defined as minimum SUV$_{max}$ of 20 at site of disease and SUV$_{max}$ of >10 at sites of measurable soft-tissue disease 15 mm or smaller (unless subject to factors explaining lower uptake, e.g., respiratory motion or reconstruction artifact)
	Patient has life expectancy of ≥6 mo
	Patient has adequate bone marrow, hepatic, and renal function, defined as …
	Hemoglobin ≥ 100 g/L independently of transfusions (no red blood cell transfusion in last 4 wk)
	Absolute neutrophil count ≥ 1.5 × 10^{9}/L
	Platelets ≥ 150 × 10^{9}/L
	Total bilirubin ≤ 1.5 times ULN except for patients with known Gilbert syndrome, where this applies for unconjugated bilirubin component
	Aspartate transaminase and alanine transaminase ≤ 3 times ULN if there is no evidence of liver metastasis or ≤ 5 times ULN in presence of liver metastases
	Creatinine clearance estimate of ≥40 mL/min using Cockcroft–Gault equation
	Sexually active patient is willing to use medically acceptable forms of barrier contraception
	Patient is willing and able to comply with all study requirements, including treatments and timing, as well as nature of required assessments
	At least 3 wk has passed since completion of surgery or radiotherapy before registration
Exclusion criteria	Patient has undergone prior treatment with another radioisotope (e.g., PSMA radioligands, ^{223}Ra, ^{89}Sr, or ^{153}Sm)
	Patient has sites of discordant disease on PET imaging ([^{18}F]FDG-positive and minimal PSMA uptake)
	Patient had other malignancies in addition to prostate cancer within previous 2 y before registration, other than basal cell or squamous cell carcinoma of skin or other cancers unlikely to recur within 24 mo
	Patient has symptomatic brain metastases or leptomeningeal metastases
	Patient has symptomatic or impending cord compression unless appropriately treated beforehand and clinically stable for >4 wk
	Patient has concurrent illness, including severe infection that may jeopardize ability to undergo procedures outlined in this protocol with reasonable safety

ULN = upper limit of normal.

translational research will be collected immediately before day 1 for cycles 1, 2, and 4 and within 10 d after unequivocal progression.

Three patient-reported outcome measure instruments will be used in this study. The Brief Pain Inventory–Short Form (*19*) will assess the location and severity of pain; the impact of pain on, or its interference with, daily functions; and the extent of pain relief. The Functional Assessment of Cancer Therapy–Prostate (*20*) will assess health-related quality of life in patients with prostate cancer, including physical,

TABLE 4
Study Objectives

Objective	Description
Primary	
Phase I	To establish maximum tolerated dose, DLTs, and recommended phase II dose of [^{161}Tb]Tb-PSMA-I&T in patients with mCRPC
Phase II	To evaluate safety of [^{161}Tb]Tb-PSMA-I&T in patients with mCRPC
Secondary	To establish absorbed radiation dose (Gy) in normal tissue and sites of metastatic disease after 1 cycle of [^{161}Tb]Tb-PSMA-I&T
	To evaluate antitumor activity of [^{161}Tb]Tb-PSMA-I&T in patients with mCRPC by…
	PSA response rate
	Radiographic progression-free survival
	PSA progression-free survival
	Progression-free survival
	Overall survival
	Objective response rate
	To evaluate health-related quality of life within 12 mo of treatment commencement
	To evaluate pain within 12 mo of treatment commencement
Exploratory	To evaluate associations among [^{68}Ga]Ga-PSMA-11 or [^{18}F]DCFPyL PET/CT, [^{18}F]FDG PET/CT, posttherapy SPECT/CT, baseline characteristics, and outcomes
	To evaluate dynamic changes in circulating tumor DNA fraction and utility of circulating tumor DNA genomic aberrations as predictive biomarker of response
	To evaluate molecular alterations in tissue and their correlation with clinical outcome
	To evaluate treatment-related quality of life using Functional Assessment of Cancer Therapy–Radionuclide Therapy questionnaire within 12 mo of treatment commencement

functional, emotional, and social well-being, as well as additional concerns specific to prostate cancer. The Functional Assessment of Cancer Therapy–Radionuclide Therapy is a 15-item questionnaire that has been developed for use with patients receiving radiopharmaceutical therapy and provides information about treatment-specific symptoms. Validation of the Functional Assessment of Cancer Therapy–Radionuclide Therapy and determination of the optimal subscales remain ongoing (*21*).

Statistical Considerations

This study will assess the toxicities associated with [^{161}Tb]Tb-PSMA-I&T, recruiting 30–36 patients. Between 12 and 18 patients will be enrolled in the dose-escalation phase, with the number of enrolled patients dependent on the number of activity levels evaluated and the number of patients at each activity level. An additional 18 patients will be recruited in the dose-expansion phase, with a total of 24 patients treated at the maximum tolerated dose.

For the dose-escalation phase, analysis will focus primarily on adverse events, particularly DLTs. These will be tabulated descriptively for each activity level separately. The probability of observing toxicity in at least one patient is 90% for toxicities with true DLT incidence rates of 4.2% (95% CI, 0.3%–13.4%). The safety analysis will include all patients who received at least one cycle of [^{161}Tb]Tb-PSMA-I&T. Safety will be assessed using Common Terminology Criteria for Adverse Events version 5.0, and the maximum toxicity grade per patient of each adverse event will be derived and presented in tabular form. All adverse events will be described overall and separately by activity level. The safety analysis will be reported once for all adverse events regardless of relatedness to treatment and once considering only adverse events related to treatment. The efficacy analysis will be reported for all patients who received at least one cycle of [^{161}Tb]Tb-PSMA-I&T. PSA response rate and objective response rate will be described as percentages with 95% CIs using exact methods.

DISCUSSION

Targeting PSMA-expressing prostate cancer cells with ^{161}Tb is a potent alternative to ^{177}Lu. The additional clustered damage from Auger and conversion electrons within micrometastases may improve the durability of the response (Fig. 2). Preclinical data form the strong rationale for in-human investigation of [^{161}Tb]Tb-PSMA-I&T. The VIOLET trial will establish the recommended activity and safety profile and provide the preliminary efficacy of [^{161}Tb]Tb-PSMA-I&T in patients with mCRPC. The first patient was recruited on October 9, 2022 (Fig. 3). The VIOLET trial is named in honor of Dr. John Violet (*22*), who passed away unexpectedly in 2020 and had an enduring interest in Auger electron therapy.

Limited use of terbium isotopes in humans has not reported any adverse events. Two studies using ^{152}Tb, a positron emitter, provided important data because ^{161}Tb has identical chemical characteristics and resultant pharmacokinetics. In these first-in-human studies, [^{152}Tb]Tb-DOTATOC was administered to a patient with a metastatic neuroendocrine neoplasm (*23*), and [^{152}Tb]Tb-PSMA-617 was administered to a patient with mCRPC (*24*). When terbium-labeled tracers were compared with their respective ^{68}Ga-labeled tracers, all known metastases were visualized. The imaging procedures had no adverse events noted during or after the infusion. The first-in-human administration using ^{161}Tb reported single-cycle administrations (596 and 1,300 MBq) of [^{161}Tb]Tb-DOTATOC radiopharmaceutical

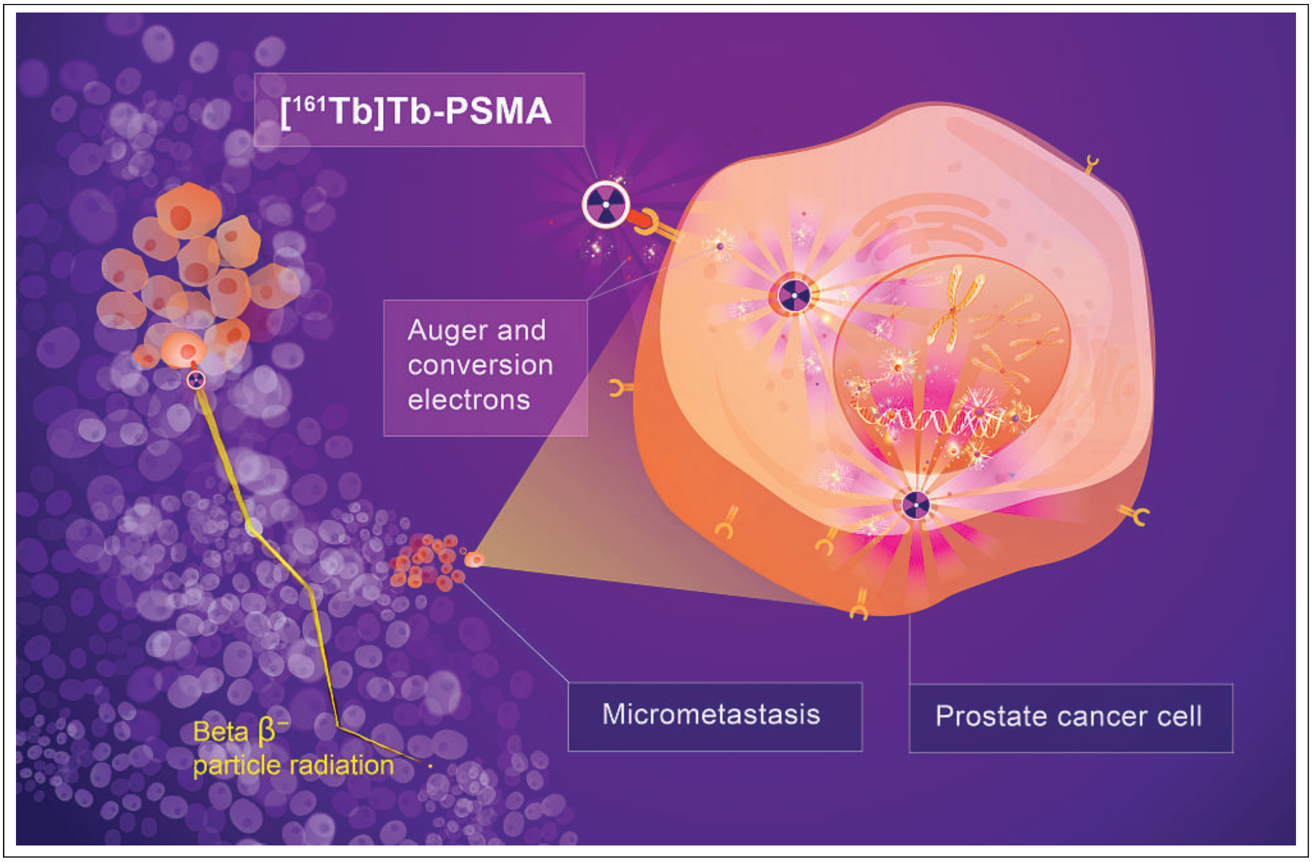

FIGURE 2. High radiation delivery to micrometastases with [^{161}Tb]Tb-PSMA-I&T Auger and conversion electrons from [^{161}Tb]Tb-PSMA-I&T have high linear energy transfer, delivering more radiation to micrometastases as illustrated in enlarged prostate cancer cell (right). In contrast, β-particles deposit their energy over greater distance (left) and have lower probability of causing lethal damage to micrometastases.

therapy in 2 patients, without adverse events or significant laboratory abnormalities reported (*25*). After commencement of the VIOLET trial, 2 case reports of patients with mCRPC have described administration of single cycles (6.5 GBq and 5,550 MBq) of [^{161}Tb]Tb-PSMA-617 (*26*,*27*). In both case reports, no immediate adverse events were reported. Posttherapy planar imaging and SPECT/CT were performed, without dosimetry calculations. To our knowledge, VIOLET is the first prospective clinical trial assessing [^{161}Tb]Tb-PSMA in patients with mCRPC. A German prospective registry (REALITY; NCT04833517) is assessing various radionuclide therapies, including [^{161}Tb]Tb-PSMA, in patients with advanced prostate cancer. The only other registered clinical trial investigating ^{161}Tb is a Swiss randomized, crossover, prospective, single-center, open-label phase 0 study comparing the dosimetry of [^{177}Lu]Lu-DOTATOC and [^{161}Tb]Tb-DOTA-LM3 (Beta plus; NCT05359146) in 16 patients with neuroendocrine tumors.

We expect [^{161}Tb]Tb-PSMA-I&T to be well tolerated, analogous to [^{177}Lu]Lu-PSMA (*28*). The delivery of radiation is expected to mirror [^{177}Lu]Lu-PSMA to off-target PSMA-expressing tissues including salivary glands, lacrimal glands, duodenum, and kidneys. The additional Auger emission from ^{161}Tb is not expected to cause adverse events because of its subcellular (2–500 nm) path-length range. Furthermore, ^{161}Tb decays to the stable isotope ^{161}Dy, which would not lead to subsequent radiation. Unbound ^{161}Tb is not expected but would be tightly bound to diethylenetriaminepentaacetic acid with renal excretion. [^{161}Tb]Tb-folate and [^{177}Lu]Lu-folate have been compared to assess long-term renal damage in nude mice (*29*). The additional Auger and conversion electrons at similar activities did not worsen renal damage in this model. In the VIOLET trial population, delayed renal toxicity is not anticipated to be clinically relevant, as patients with mCRPC have a life expectancy in the 15- to 18-mo range after effective radiopharmaceutical therapy (*30*). The 6-wk DLT period chosen for VIOLET mirrors our definition in other clinical trials evaluating [^{177}Lu]Lu-PSMA. The rationale is that hemotoxicity is expected in this window, as the nadir after ^{177}Lu is less than 30 d. On the basis of the preclinical and clinical data available, we expect a similar nadir for ^{161}Tb and all potential hematologic toxicities to be resolved or improving by the end of the 6-wk period.

The absorbed electron energy fraction per decay dose differs between ^{161}Tb and ^{177}Lu. On the basis of the biodistribution results and Monte Carlo simulations, the absorbed radiation dose from β-emission of [^{161}Tb]Tb-PSMA-617 is approximately 35%–40% higher per decay than that of [^{177}Lu]Lu-PSMA-617 (*10*,*31*). In the VIOLET trial, the starting activities of [^{161}Tb]Tb-PSMA-I&T for each level are 4.4, 5.5, and 7.4 GBq, which are approximately equivalent to 5.9, 7.4, and 10.0 GBq of [^{177}Lu]Lu-PSMA, respectively, and do not account for additional radiation from Auger and conversion electrons. Before the TheraP and VISION trials, few dose-escalation studies of [^{177}Lu]Lu-PSMA were performed (*32*). The activities and cycle schedules were largely empiric based on experience using [^{177}Lu]Lu-DOTATATE in

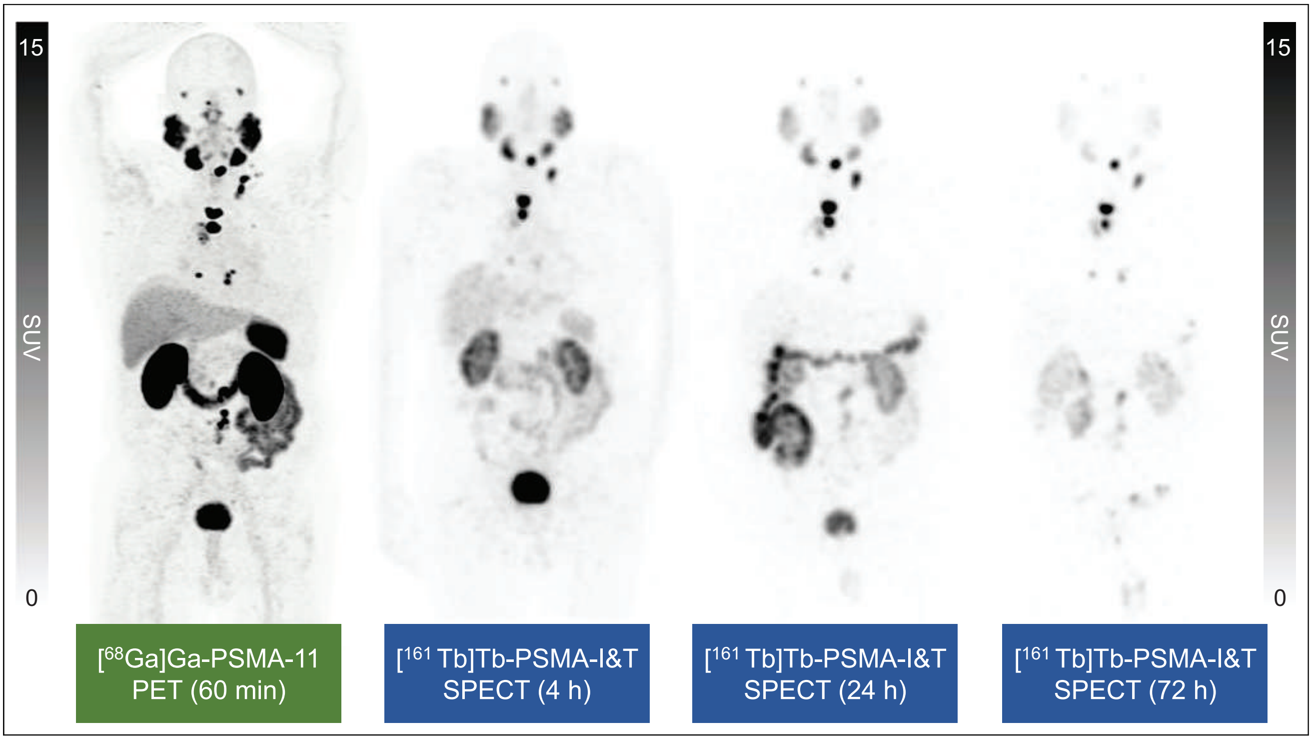

FIGURE 3. Screening [^{68}Ga]Ga-PSMA-11 PET and 3-time-point SPECT after cycle 1 of first patient recruited.

neuroendocrine tumors and dosimetry safety data from [^{177}Lu]Lu-PSMA. Nevertheless, we took a conservative approach by adopting a dose-escalation design to enable clinical evaluation for adverse effects and performing multiple-time-point posttherapy quantitative SPECT/CT enabling robust calculation of the actual radiation dose delivered to normal organs and tumors. This provides a significant layer of safety oversight that is not possible with conventional drugs. We chose PSMA-I&T as the small-molecule inhibitor to target PSMA, as [^{177}Lu]Lu-PSMA-I&T is considered radioequivalent to [^{177}Lu]Lu-PSMA-617. The European Association of Nuclear Medicine procedure guidelines for ^{177}Lu-labeled PSMA ligands consider the current available data and do not indicate differences in efficacy between [^{177}Lu]Lu-PSMA-617 and [^{177}Lu]Lu-PSMA-I&T (*33*) because of equivalent clinical responses and toxicities (*34*).

The VIOLET trial will generate robust data for appropriate activities of [^{161}Tb]Tb-PSMA in patients with mCRPC. High yields of no-carrier-added ^{161}Tb can be produced for clinical application by neutron irradiation of ^{160}Gd targets, analogous to the production of ^{177}Lu (*35,36*). Upscaling the production is expected to be feasible, similar to ^{177}Lu production (*37*). Since the physical properties of ^{161}Tb and ^{177}Lu are similar, no additional radioprotection measures would be required. The question of greatest interest is whether ^{161}Tb will be superior to ^{177}Lu in humans, particularly for killing micrometastases. In similar cohorts of patients with mCRPC treated with [^{177}Lu]Lu-PSMA, median progression-free survival was 5.1 mo (95% CI, 3.4–5.7 mo) and overall survival was 16.4 mo (95% CI, 13.7–19.4 mo) in TheraP (*38*), and median radiographic PFS was 8.7 mo and median overall survival was 15.3 mo in VISION (*30*). This study will provide initial data on PFS and OS with [^{161}Tb]Tb-PSMA but is not designed to enable direct comparison with [^{177}Lu]Lu-PSMA.

CONCLUSION

VIOLET is a phase I/II clinical trial with enrollment completed in February 2024. Patients are still receiving [^{161}Tb]Tb-PSMA-I&T.

DISCLOSURE

This study is funded by the Challenge Award from the Prostate Cancer Foundation through funds from CANICA AS and the Peter MacCallum Foundation. Isotopia is supplying [^{161}Tb]Tb and PSMA-I&T kits as part of a commercialization agreement with the Peter MacCallum Cancer Centre. James Buteau receives support from a Prostate Cancer Foundation Young Investigator Award and PhD support through an Australian Government Research Training Program Scholarship. Louise Kostos received PhD support through an Australian Government Research Training Program Scholarship. Michael Hofman is supported through an NHMRC investigator grant. Shahneen Sandhu is supported through an NHMRC investigator grant. Brian Gonzalez received fees unrelated to this work from Sure Med Compliance and Elly Health. No other potential conflict of interest relevant to this article was reported.

ACKNOWLEDGMENTS

The protocol of this study was presented as a poster at the ASCO Genitourinary Cancers Symposium, San Francisco, February 16–18, 2023. We thank the participating patients and their families; Annette Van Der Heyden (ProsTIC program manager); Claire Martin and Richelle Linklater (trial coordination with the Parkville Cancer Clinical Trials Unit); Petra Opar (clinical trial project management with the Centre of Biostatistics and Clinical Trials); the cancer imaging nuclear medicine and radiology consultants, technologists, and nurses; and Nicole Ng, Maria Docanto, and Patricia Bukczynska (Cancer Research Division).

KEY POINTS

QUESTION: Is [^{161}Tb]Tb-PSMA-I&T a safe and effective radiopharmaceutical therapy for patients with mCRPC?

PERTINENT FINDINGS: We describe the protocol for the VIOLET trial, an investigator-initiated and -led, open-label, single-arm, single-center, phase I/II dose-escalation and expansion study designed to evaluate the safety and efficacy of [^{161}Tb]Tb-PSMA-I&T. Recruitment was completed in February 2024.

IMPLICATIONS FOR PATIENT CARE: The VIOLET trial will generate robust data on the appropriate activity of [^{161}Tb]Tb-PSMA in patients with mCRPC.

REFERENCES

1. Violet J, Sandhu S, Iravani A, et al. Long-term follow-up and outcomes of retreatment in an expanded 50-patient single-center phase II prospective trial of ^{177}Lu-PSMA-617 theranostics in metastatic castration-resistant prostate cancer. *J Nucl Med.* 2020;61:857–865.
2. Park S, Ang RR, Duffy SP, et al. Morphological differences between circulating tumor cells from prostate cancer patients and cultured prostate cancer cells. *PLoS One.* 2014;9:e85264.
3. Ku A, Facca VJ, Cai Z, Reilly RM. Auger electrons for cancer therapy: a review. *EJNMMI Radiopharm Chem.* 2019;4:27.
4. Bolcaen J, Gizawy MA, Terry SYA, et al. Marshalling the potential of Auger electron radiopharmaceutical therapy. *J Nucl Med.* 2023;64:1344–1351.
5. Alcocer-Ávila ME, Ferreira A, Quinto MA, Morgat C, Hindié E, Champion C. Radiation doses from ^{161}Tb and ^{177}Lu in single tumour cells and micrometastases. *EJNMMI Phys.* 2020;7:33.
6. Hindié E, Zanotti-Fregonara P, Quinto MA, Morgat C, Champion C. Dose deposits from ^{90}Y, ^{177}Lu, ^{111}In, and ^{161}Tb in micrometastases of various sizes: implications for radiopharmaceutical therapy. *J Nucl Med.* 2016;57:759–764.
7. Uusijärvi H, Bernhardt P, Rösch F, Maecke HR, Forssell-Aronsson E. Electron- and positron-emitting radiolanthanides for therapy: aspects of dosimetry and production. *J Nucl Med.* 2006;47:807–814.
8. Champion C, Quinto MA, Morgat C, Zanotti-Fregonara P, Hindié E. Comparison between three promising β-emitting radionuclides, ^{67}Cu, ^{47}Sc and ^{161}Tb, with emphasis on doses delivered to minimal residual disease. *Theranostics.* 2016;6:1611–1618.
9. Bernhardt P, Svensson J, Hemmingsson J, et al. Dosimetric analysis of the short-ranged particle emitter ^{161}Tb for radionuclide therapy of metastatic prostate cancer. *Cancers (Basel).* 2021;13:2011.
10. Müller C, Umbricht CA, Gracheva N, et al. Terbium-161 for PSMA-targeted radionuclide therapy of prostate cancer. *Eur J Nucl Med Mol Imaging.* 2019;46:1919–1930.
11. Müller C, Reber J, Haller S, et al. Direct in vitro and in vivo comparison of ^{161}Tb and ^{177}Lu using a tumour-targeting folate conjugate. *Eur J Nucl Med Mol Imaging.* 2014;41:476–485.
12. Grünberg J, Lindenblatt D, Dorrer H, et al. Anti-L1CAM radioimmunotherapy is more effective with the radiolanthanide terbium-161 compared to lutetium-177 in an ovarian cancer model. *Eur J Nucl Med Mol Imaging.* 2014;41:1907–1915.
13. Juget F, Talip Z, Buchillier T, et al. Determination of the gamma and X-ray emission intensities of terbium-161. *Appl Radiat Isot.* 2021;174:109770.
14. Marin I, Rydèn T, Van Essen M, et al. Establishment of a clinical SPECT/CT protocol for imaging of ^{161}Tb. *EJNMMI Phys.* 2020;7:45.
15. McIntosh L, Jackson P, Emmerson B, et al. Quantitative calibration of Tb-161 SPECT/CT in view of personalised dosimetry assessment studies. *EJNMMI Phys.* 2024;11:18.
16. Jackson P, McIntosh L, Hofman MS, Kong G, Hicks RJ. Technical note: rapid multiexponential curve fitting algorithm for voxel-based targeted radionuclide dosimetry. *Med Phys.* 2020;47:4332–4339.
17. Jackson PA, Beauregard J-M, Hofman MS, Kron T, Hogg A, Hicks RJ. An automated voxelized dosimetry tool for radionuclide therapy based on serial quantitative SPECT/CT imaging. *Med Phys.* 2013;40:112503.
18. Jackson PA, Hofman MS, Hicks RJ, Scalzo M, Violet J. Radiation dosimetry in ^{177}Lu-PSMA-617 therapy using a single posttreatment SPECT/CT scan: a novel methodology to generate time- and tissue-specific dose factors. *J Nucl Med.* 2020;61:1030–1036.
19. Cleeland CS. *The Brief Pain Inventory User Guide.* M.D. Anderson Cancer Center; 2009.
20. Esper P, Mo F, Chodak G, Sinner M, Cella D, Pienta KJ. Measuring quality of life in men with prostate cancer using the functional assessment of cancer therapy-prostate instrument. *Urology.* 1997;50:920–928.
21. Gudenkauf LM, Chavez MN, Maconi ML, et al. Developing a patient-reported outcome measure for radionuclide therapy for prostate cancer. *J Nucl Med.* 2023;64:869–872.
22. Yamey G. John Violet: radiation oncologist and physician scientist who pioneered targeted radionuclide therapy for prostate cancer. *BMJ.* 2020;371:m4803.
23. Baum RP, Singh A, Benešová M, et al. Clinical evaluation of the radiolanthanide terbium-152: first-in-human PET/CT with ^{152}Tb-DOTATOC. *Dalton Trans.* 2017;46:14638–14646.
24. Müller C, Singh A, Umbricht CA, et al. Preclinical investigations and first-in-human application of ^{152}Tb-PSMA-617 for PET/CT imaging of prostate cancer. *EJNMMI Res.* 2019;9:68.
25. Baum RP, Singh A, Kulkarni HR, et al. First-in-humans application of ^{161}Tb: a feasibility study using ^{161}Tb-DOTATOC. *J Nucl Med.* 2021;62:1391–1397.
26. Rosar F, Maus S, Schaefer-Schuler A, Burgard C, Khreish F, Ezziddin S. New horizons in radioligand therapy: ^{161}Tb-PSMA-617 in advanced mCRPC. *Clin Nucl Med.* 2023;48:433–434.
27. Al-Ibraheem A, Doudeen RM, Juaidi D, Abufara A, Maus S. ^{161}Tb-PSMA radioligand therapy: first-in-humans SPECT/CT imaging. *J Nucl Med.* 2023;64:1322–1323.
28. Hofman MS, Emmett L, Sandhu S, et al. [^{177}Lu] Lu-PSMA-617 versus cabazitaxel in patients with metastatic castration-resistant prostate cancer (TheraP): a randomised, open-label, phase 2 trial. *Lancet.* 2021;397:797–804.
29. Haller S, Pellegrini G, Vermeulen C, et al. Contribution of Auger/conversion electrons to renal side effects after radionuclide therapy: preclinical comparison of ^{161}Tb-folate and ^{177}Lu-folate. *EJNMMI Res.* 2016;6:13.
30. Sartor O, de Bono J, Chi KN, et al. Lutetium-177-PSMA-617 for metastatic castration-resistant prostate cancer. *N Engl J Med.* 2021;385:1091–1103.
31. Verburg FA, de Blois E, Koolen S, Konijnenberg MW. Replacing Lu-177 with Tb-161 in DOTA-TATE and PSMA-617 therapy: potential dosimetric implications for activity selection. *EJNMMI Phys.* 2023;10:69.
32. Tagawa ST, Osborne JR, Hackett A, et al. Preliminary results of a phase I/II dose-escalation study of fractionated dose ^{177}Lu-PSMA-617 for progressive metastatic castration resistant prostate cancer (mCRPC) [abstract]. *Ann Oncol.* 2019;30(suppl 5):v329–v330.
33. Kratochwil C, Fendler WP, Eiber M, et al. EANM procedure guidelines for radionuclide therapy with ^{177}Lu-labelled PSMA-ligands (^{177}Lu-PSMA-RLT). *Eur J Nucl Med Mol Imaging.* 2019;46:2536–2544.
34. Schuchardt C, Zhang J, Kulkarni HR, Chen X, Müller D, Baum RP. Prostate-specific membrane antigen radioligand therapy using ^{177}Lu-PSMA I&T and ^{177}Lu-PSMA-617 in patients with metastatic castration-resistant prostate cancer: comparison of safety, biodistribution, and dosimetry. *J Nucl Med.* 2022;63:1199–1207.
35. Gracheva N, Müller C, Talip Z, et al. Production and characterization of no-carrier-added ^{161}Tb as an alternative to the clinically-applied ^{177}Lu for radionuclide therapy. *EJNMMI Radiopharm Chem.* 2019;4:12.
36. Lehenberger S, Barkhausen C, Cohrs S, et al. The low-energy β^- and electron emitter ^{161}Tb as an alternative to ^{177}Lu for targeted radionuclide therapy. *Nucl Med Biol.* 2011;38:917–924.
37. Müller C, van der Meulen NP, Schibli R. Opportunities and potential challenges of using terbium-161 for targeted radionuclide therapy in clinics. *Eur J Nucl Med Mol Imaging.* 2023;50:3181–3184.
38. Hofman MS, Emmett L, Sandhu S, et al. Overall survival with [^{177}Lu]Lu-PSMA-617 versus cabazitaxel in metastatic castration-resistant prostate cancer (TheraP): secondary outcomes of a randomised, open-label, phase 2 trial. *Lancet Oncol.* 2024;25:99–107.

Interreader and Intrareader Reproducibility of ^{18}F-Flotufolastat Image Interpretation in Patients with Newly Diagnosed or Recurrent Prostate Cancer: Data from Two Phase 3 Prospective Multicenter Studies

Phillip H. Kuo[1], Giuseppe Esposito[2], Gary A. Ulaner[3,4], Don Yoo[5], Katherine Zukotynski[6], Gregory C. Ravizzini[7], Ross Penny[8], Matthew P. Miller[8], Albert Chau[8], Phillip Davis[9], Brian F. Chapin[10], and David M. Schuster[11]
on behalf of the SPOTLIGHT and LIGHTHOUSE study groups

[1]Departments of Medical Imaging, Medicine, and Biomedical Engineering, University of Arizona, Tucson, Arizona; [2]Department of Nuclear Medicine, Medstar Georgetown University Hospital, Washington, District of Columbia; [3]Department of Molecular Imaging and Therapy, Hoag Family Cancer Institute, Irvine, California; [4]Radiology and Translational Genomics, University of Southern California, Los Angeles, California; [5]Warren Alpert Medical School of Brown University, Providence, Rhode Island; [6]Department of Radiology, McMaster University, Hamilton, Ontario, Canada; [7]Division of Diagnostic Imaging, Department of Nuclear Medicine, University of Texas MD Anderson Cancer Center, Houston, Texas; [8]Blue Earth Diagnostics Ltd., Oxford, United Kingdom; [9]Blue Earth Diagnostics Inc., Monroe Township, New Jersey; [10]Department of Urology, University of Texas MD Anderson Cancer Center, Houston, Texas; and [11]Division of Nuclear Medicine and Molecular Imaging, Department of Radiology and Imaging Sciences, Emory University, Atlanta, Georgia

Interreader and intrareader reproducibility of ^{18}F-flotufolastat PET/CT scans in newly diagnosed and recurrent prostate cancer patients was assessed from masked image evaluations from two phase 3 studies. **Methods:** ^{18}F-flotufolastat PET/CT images of newly diagnosed (n = 352) or recurrent (n = 389) patients were evaluated by 3 masked readers. Cohen κ was used to assess pairwise patient- and region-level interreader agreement. Agreement among all readers was assessed using Fleiss κ. Intrareader agreement between the first and repeat read (20% of images, ≥4 wk later) was assessed using Cohen κ. **Results:** Pairwise interreader agreement was 95% or better (newly diagnosed) and 75% or better (recurrent). The κ coefficients were impacted by the high-agreement–low-κ paradox: Cohen κ ranged from not estimable to 0.55, whereas Fleiss κ was 0.50 (newly diagnosed) and 0.41 (recurrent). Agreement was highest in the prostate of newly diagnosed patients (≥95%) and in the pelvic lymph nodes in recurrent patients (≥87%). Intrareader agreement was 86% or better across both populations. **Conclusion:** ^{18}F-flotufolastat PET/CT images can be reliably interpreted, with a high degree of inter- and intrareader agreement.

Key Words: molecular imaging; oncology; PET/CT; PSMA; interreader variability

J Nucl Med 2024; 65:1239–1243
DOI: 10.2967/jnumed.123.267306

Prostate-specific membrane antigen (PSMA) PET has become a standard of care for prostate cancer (PCa) imaging, as demonstrated by its inclusion in the most recent guidelines from the National Comprehensive Cancer Network (*1*).

^{18}F-flotufolastat is a high-affinity PSMA-targeting PET diagnostic radiopharmaceutical developed from a radiohybrid technology platform that enables engineering of PSMA ligands that can be labeled with ^{18}F for diagnostic imaging or with α- or β-emitting radiometals for radiopharmaceutical therapy (*2*). The data from two phase 3 clinical studies, LIGHTHOUSE (NCT04186819) and SPOTLIGHT (NCT04186845), show ^{18}F-flotufolastat to be well tolerated and to provide clinically useful information regarding the presence of N1 and M1 disease before surgery in newly diagnosed PCa patients (*3*) and for localization of recurrent PCa (*4*). Data from the SPOTLIGHT study showed the patient-level verified detection rate of ^{18}F-flotufolastat in patients with recurrent prostate cancer to be 51%–54% (*4*), whereas data from the LIGHTHOUSE study showed that in newly diagnosed prostate cancer, ^{18}F-flotufolastat had a sensitivity of 23%–30% and a specificity of 93%–97% for the detection of pelvic lymph node (PLN) metastases (*3*). ^{18}F-flotufolastat was recently approved by the U.S. Food and Drug Administration for diagnostic PET imaging of PSMA-positive lesions in men with PCa (*5*) and was included in the most recent guideline updates from National Comprehensive Cancer Network and the American Society of Clinical Oncology (*1,6*).

Here, we evaluate the results of masked image evaluations from the LIGHTHOUSE and SPOTLIGHT studies to investigate whether masked readers could, after training, reliably interpret ^{18}F-flotufolastat PET/CT images in the newly diagnosed or recurrent setting. We report the interreader and intrareader reproducibility of ^{18}F-flotufolastat for each population.

MATERIALS AND METHODS

The full methods of the LIGHTHOUSE and SPOTLIGHT studies have been reported previously (*3,4*). In brief, treatment-naïve men

---

Received Dec. 19, 2023; revision accepted May 13, 2024.

For correspondence or reprints, contact Phillip H. Kuo (kuoradiology@gmail.com).

aged older than 18 y with biopsy-proven PCa and unfavorable intermediate-risk to high-risk disease classification who were scheduled for radical prostatectomy with regional PLN dissection were enrolled in the LIGHTHOUSE study. The SPOTLIGHT study recruited men aged older than 18 y with elevated prostate-specific antigen (PSA) suspected to be biochemical recurrence after curative-intent treatment of localized PCa if they were eligible for curative-intent salvage therapy. Patients in both studies received 296 MBq (8 mCi ± 20%) of ^{18}F-flotufolastat, and PET/CT imaging was conducted 50–70 min after injection. Each site used either a current- or previous-generation dedicated PET/CT system, with time-of-flight capabilities. All systems were approved by the imaging core lab before patients were scanned.

In both studies, all scans were evaluated by 3 masked central readers. Two individuals were readers on both studies. The readers were all board-certified nuclear medicine physicians with more than 15 y of experience who underwent protocol-specific, ^{18}F-flotufolastat–specific training that included marked assessment cases to ensure alignment with an expert reader. The readers were masked to all clinical information. The readers were instructed that lesions should be considered suggestive if ^{18}F-flotufolastat uptake was greater than physiologic uptake in that tissue or greater than the adjacent background if no physiologic uptake was expected (*3,4*).

Pairwise Inter- and Intrareader Agreement

Pairwise inter- and intrareader agreements were assessed as secondary endpoints in both studies and were reported at a patient level and for the prostate and prostate bed, PLN, and other (extrapelvic) regions (i.e., extra-PLN, soft tissue or parenchyma, and bone). The Cohen κ statistic (*7*) was used to test pairwise agreement between any 2 readers, giving 3 κ statistics. To assess intrareader agreement, each reader conducted a reread of a random selection of 20% of the images, with the repeat read taking place at least 4 wk after the first read. Cohen κ was used to assess agreement between the 2 reads.

Overall Interreader Agreement Among All 3 Readers

The patient-level agreement among all 3 readers was performed as a post hoc assessment during regulatory review using the Fleiss κ statistic (*8*). For this metric, agreement on lesions in 5 distinct regions (prostate or prostate bed, PLN, extra-PLN, soft tissue or parenchyma, and bone) was considered part of the assessment.

Statistical Analyses

All κ coefficients were calculated using SAS (version 9.4; SAS Institute) and are presented with approximate 95% CIs.

RESULTS

Patients

In total, 352 scans from patients in the LIGHTHOUSE study and 389 scans from patients in the SPOTLIGHT study were assessed by the readers to determine the inter- and intrareader agreement. The 352 patients in the LIGHTHOUSE study with newly diagnosed PCa had a median age of 65 y and a median PSA of 8.8 ng/mL, and 32% of those patients were considered to have unfavorable intermediate-risk disease. The 389 patients in the SPOTLIGHT study with recurrent PCa had a median age of 69 y and a median PSA of 1.1 ng/mL, and 79% of those patients had previously undergone radical prostatectomy.

^{18}F-Flotufolastat–Positive Lesions

In the LIGHTHOUSE study, across the 3 readers, 335–352 (95%–100%) of the 352 patients with newly diagnosed PCa had ^{18}F-flotufolastat–positive lesions. On a regional basis, 333–352 (95%–100%) patients were positive in the prostate, 44–61 (13%–17%) patients were positive in PLN, and 56–98 (16%–28%) patients were positive in extrapelvic sites.

In the SPOTLIGHT study, across the 3 readers, 264–358 (68%–92%) of the 389 patients with recurrent PCa had ^{18}F-flotufolastat–positive lesions. In total, 101–256 (26%–66%) patients were positive in the prostate region, 111–138 (29%–36%) patients were positive in PLN, and 146–173 (38%–44%) patients were positive in extrapelvic sites.

Interreader Agreement

Patient-level, pairwise interreader agreement comparisons were 95% or better in the newly diagnosed population and 75% or better in the recurrent population (Fig. 1). On a regional basis, the pairwise agreement was greater than 80% for all regions except the prostate or prostate bed in the recurrent population. The pairwise agreement was highest in the prostate among the newly diagnosed population and highest in PLN in the recurrent population (Fig. 1).

Cohen κ for the pairwise interreader agreement is presented in Figure 2. Across both populations, Cohen κ for pairwise interreader agreement ranged from nonestimable to 0.55 at the patient level, from nonestimable to 0.65 in the prostate or prostate bed, from 0.68 to 0.79 in PLN, and from 0.45 to 0.69 in extrapelvic sites. Supplemental Table 1 provides the interreader agreement and Cohen κ for the various subcategories of extrapelvic regions (supplemental materials are available at http://jnm.snmjournals.org).

Figure 3 presents a case study of a discordant read in an external iliac lymph node in a patient with newly diagnosed PCa.

As shown in Supplemental Tables 2 and 3, which present the patient-level interreader agreement stratified by PSA level, although the small numbers of patients in some PSA categories limit the conclusions that can be drawn, high levels of agreement were seen irrespective of PSA levels among newly diagnosed patients, and the recurrent data suggest a trend toward higher agreement in patients with a PSA level greater than 1 ng/mL than in patients with a PSA level less than 1 ng/mL.

Fleiss κ, which was used to assess reader agreement for all 3 readers across 5 regions in each patient, was 0.50 (95% CI, 0.46–0.53) in the newly diagnosed population and 0.41 (95% CI, 0.39–0.43) in the recurrent population.

Intrareader Agreement

In total, 70 scans from the LIGHTHOUSE study and 78 scans from the SPOTLIGHT study were reread at least 4 wk after the initial read to determine the intrareader agreement. Figure 4 presents the intrareader agreement between the 2 reads.

Across both studies, the patient-level intrareader agreement was 86% or better for each reader. On a regional basis, intrareader agreement was broadly high for each reader, with agreement highest in the prostate region for newly diagnosed patients and in extraprostatic regions in patients with recurrent PCa.

Cohen κ for the intrareader agreement is shown in Figure 5. Cohen κ was higher for PLN and other (extrapelvic) regions than for the prostate or prostate bed. In scans from newly diagnosed patients, Cohen κ was estimable for the prostate for only 1 reader.

DISCUSSION

The phase 3 LIGHTHOUSE and SPOTLIGHT studies show ^{18}F-flotufolastat to have a clinically meaningful diagnostic performance in newly diagnosed and recurrent PCa (*3,4*). However, determining that results can be consistently and reliably interpreted is imperative for its clinical use. Here, we report data from these

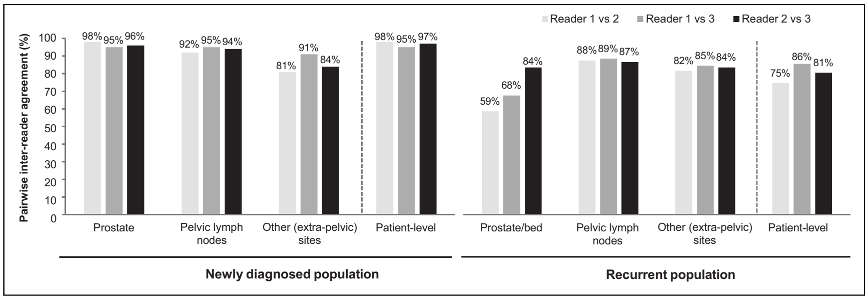

FIGURE 1. Pairwise patient- and region-level interreader agreement for 352 newly diagnosed and 389 recurrent PCa patients with evaluable ^{18}F-flotufolastat PET/CT scan.

2 trials to evaluate the inter- and intrareader agreement of ^{18}F-flotufolastat PET/CT image interpretation.

Although some differences among the readers were noted, particularly in the prostate or prostate bed of patients with recurrent PCa, overall, the data demonstrate that naïve readers who had received specific ^{18}F-flotufolastat reader-interpretation training were able to achieve good reproducibility when staging newly diagnosed or recurrent PCa.

In newly diagnosed patients, patient-level interreader agreement was 95% or better. As might be expected in this newly diagnosed treatment-naïve population, the region-level agreement was highest in the prostate. Reassuringly, however, there was also good agreement in extraprostatic regions among readers. Interreader agreement in PLN ranged from 92% to 95%. The corresponding Cohen κ was 0.68–0.79, marginally higher than that reported for ^{68}Ga-PSMA-11 PET imaging (*9*). Reliably determining the presence of nodal and metastatic disease is particularly important in these patients given that such findings would be more likely to influence treatment decisions (*1*). We observed low or nonestimable κ coefficients for corresponding high agreement data in some analyses. This high-agreement–low-κ paradox is a consequence of the κ coefficient's propensity to be affected by the prevalence of rare findings. For example, as the readers rarely reported the prostate region in newly diagnosed patients to be negative, inter- and intrareader κ coefficients for the prostate and patient level were affected despite high levels of agreement.

Although slightly lower levels of interreader agreement were observed in the recurrent population than in the newly diagnosed population, the patient-level interreader agreement for ^{18}F-flotufolastat was still high at 75%–86% and was comparable with other PSMA PET agents. The CONDOR trial data show an interreader agreement of 75% among 3 readers of ^{18}F-DCFPyL scans from 208 patients with recurrent PCa (*10*), whereas pairwise patient-level interreader agreement data for ^{68}Ga-PSMA-11 PET imaging in 125 patients with metastatic castration-resistant PCa are reported as 82%–88% (*11*). Our interreader agreement data in the recurrent population were impacted by findings from reader 1, who read considerably more scans as positive in the prostate region than did the other masked readers (*4*) and the onsite readers (Supplemental Table 4). Reproducibility in extraprostatic regions was high and of a similar level to that seen in newly diagnosed patients.

Interpretation standards for strength of agreement based on κ coefficients have been proposed (*12,13*), and although these standards, particularly those by Landis and Koch (*12*), are widely applied to the interpretation of the κ coefficient, they are somewhat arbitrary and should be used with caution given the effects of

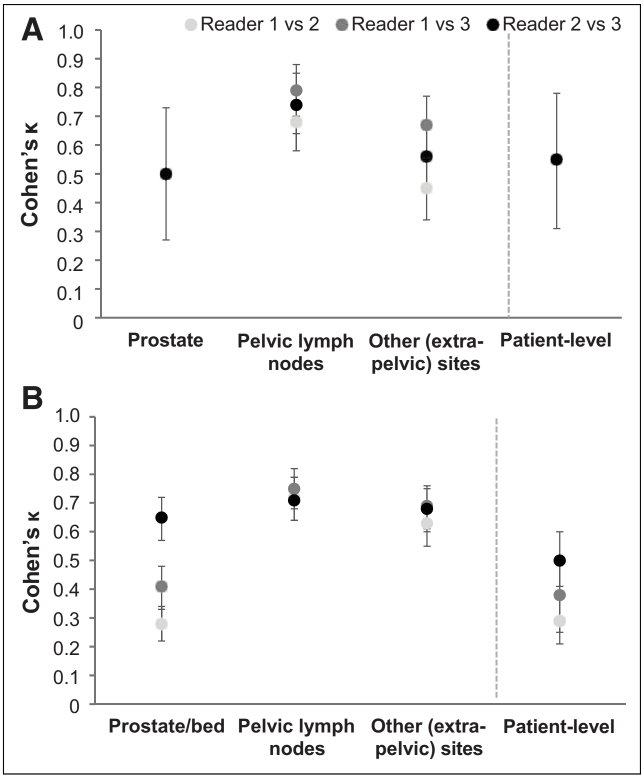

FIGURE 2. (A and B) Cohen κ for pairwise patient- and region-level interreader agreement of reads or images from 352 newly diagnosed (A) and 389 recurrent (B) PCa patients with evaluable ^{18}F-flotufolastat PET/CT scan. Cohen κ was not estimable in prostate or at patient level for reader 1 vs. reader 2 or for reader 1 vs. reader 3 because of lack of negative prostate reads in newly diagnosed population.

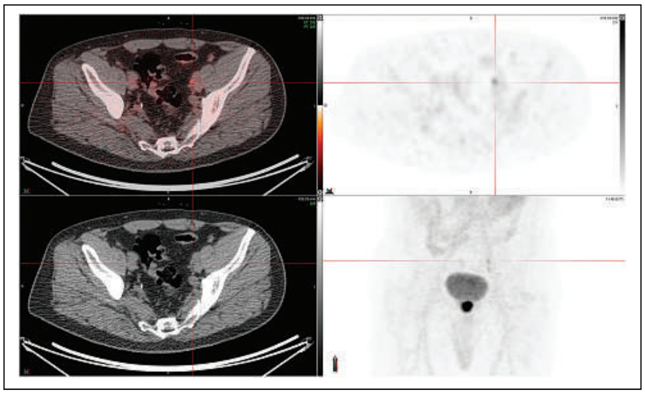

FIGURE 3. Discordant case in left external iliac lymph node. Fused PET/CT and ^{18}F-flotufolastat PET (right) images (SUV, 0–10) from newly diagnosed high-risk PCa patient (PSA, 17.8 ng/mL) are shown. One of 3 masked readers identified metastasis in left external iliac lymph node, which other 2 readers did not read as positive. Lesion was later confirmed as true positive by histopathology, resulting in majority-read false-negative result.

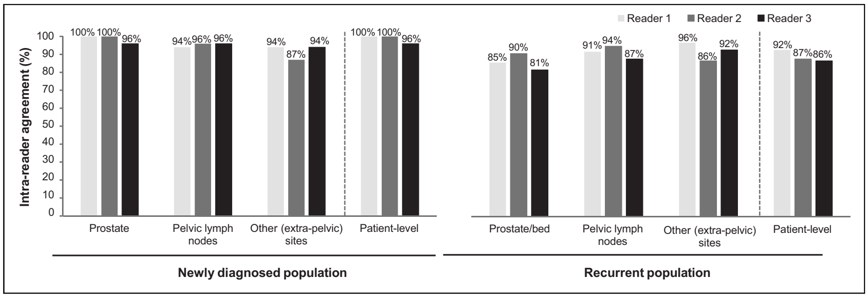

FIGURE 4. Patient- and region-level intrareader agreement for reread of ^{18}F-flotufolastat PET/CT images from newly diagnosed (n = 70) or recurrent (n = 78) PCa patients.

prevalence and bias on the κ coefficient and the high-agreement–low-κ paradox discussed above (*14*). Landis's and Koch's scale ranks agreement as poor ($\kappa < 0$), slight ($0.0 > \kappa < 0.20$), fair ($0.21 > \kappa < 0.40$), moderate ($0.41 > \kappa < 0.60$), substantial ($0.61 > \kappa < 0.80$), or almost perfect ($0.81 > \kappa < 1.0$). Application of these interpretation scales here suggests that the Fleiss κ for agreement among all 3 readers, which were likely impacted by the prostate region reporting discussed above, shows moderate κ coefficients (*12*). Patient-level intrareader agreement was high throughout, again similar to that of other PSMA PET agents (*11*) but with κ coefficients that would broadly be considered moderate to substantial in the recurrent population and, where estimable, fair in the newly diagnosed population.

There are some limitations to the present analysis. First, as noted above, we observed a low κ coefficient for corresponding high-agreement data in some inter- and intrareader analyses across both populations, perhaps suggesting the unsuitability of the κ coefficient for these data. The κ coefficient can be unreliable for rare observations (such as negative ^{18}F-flotufolastat PET/CT in the prostate), because of its propensity to be affected by the prevalence of the finding under consideration (*15,16*). This is perhaps demonstrated by the numerically lower κ coefficients (range, 0.29–0.5) for the patient-level pairwise interreader agreement in our recurrent population compared with the ^{68}Ga-PSMA-11 PET data discussed above, which correspond with a κ coefficient of 0.54–0.67 despite similar levels of pairwise interreader agreement. Second, as is typical for trials of this type, scans were read by only a small number of readers, which means the impact of any outlier data such as the increased positive reads in a particular region by one of the readers is amplified. In a real-world environment, with access to patients' clinical information, and with learning from follow-up of subjects, further increases in diagnostic accuracy and interreader agreement might be expected. Comparison of the reads between the onsite readers and the masked readers (Supplemental Table 4) perhaps exemplifies this and further highlights the outlier data in the prostate region in recurrent patients from reader 1. Among all cases in which the prostate was read negative by the unmasked onsite readers, positive reads by readers 2 and 3 were relatively uncommon at 3%–12%, whereas reader 1 read the prostate positive in 34% of these cases.

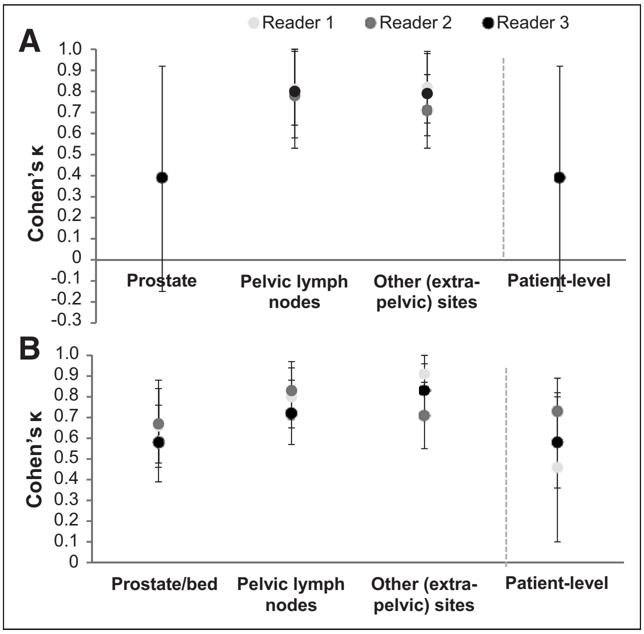

FIGURE 5. Cohen κ for patient- and region-level intrareader agreement for reread of ^{18}F-flotufolastat PET/CT images from newly diagnosed (A) (n = 70) and recurrent (B) (n = 78) PCa patients. Cohen κ was not estimable in prostate or at patient level for readers 1 and 2 because of lack of negative prostate reads in newly diagnosed population.

CONCLUSION

The data here show ^{18}F-flotufolastat PET/CT scans of patients with newly diagnosed and recurrent PCa can be reliably interpreted with a high degree of inter- and intrareader agreement. The high reproducibility of results observed here offers further support of the clinical utility of ^{18}F-flotufolastat PET/CT imaging for patients with PCa.

DISCLOSURE

Phillip Kuo is a consultant or speaker for Blue Earth Diagnostics, Chimerix, Eli Lilly, Fusion Pharma, GE Healthcare, Invicro, Novartis, Radionetics, and Telix Pharmaceuticals. He is a recipient of research grants from Blue Earth Diagnostics and GE Healthcare. Gary Ulaner has served as a speaker, received grant support, or served on a scientific advisory board for GE Healthcare, Lantheus, Nuclidium, and RayzeBio. Katherine Zukotynski has served on an advisory board for AAA/Novartis and as a consultant for Fusion Pharmaceuticals. Gregory Ravizzini is a recipient of research grants from GE Healthcare, Curium, ABX, Bayer, Novartis, Clarity, and Fusion. David Schuster has acted as a consultant for Global Medical Solutions Taiwan; Progenics Pharmaceuticals, Inc.; Heidelberg University; and DuChemBio Co. Ltd. He participates through the Emory Office of Sponsored Projects in full compliance with Emory University sponsored research and conflict-of-interest regulations in sponsored grants including those funded or partially funded by Blue Earth Diagnostics; Nihon Medi-Physics Co., Ltd.; Telix Pharmaceuticals (U.S.) Inc.; Advanced Accelerator Applications; FUJIFILM Pharmaceuticals U.S.A., Inc; and Amgen Inc. He participates in educational initiatives with School of Breast Oncology and PrecisCa and provides medicolegal consulting vetted through Emory School of Medicine. No other potential conflict of interest relevant to this article was reported.

ACKNOWLEDGMENTS

We thank all LIGHTHOUSE and SPOTLIGHT investigators and their patients. Editorial support was provided by Dr. Catriona Turnbull (Blue Earth Diagnostics).

KEY POINTS

QUESTION: How reliably can ^{18}F-flotufolastat scans of patients with newly diagnosed and recurrent PCa be interpreted?

PERTINENT FINDINGS: ^{18}F-flotufolastat scan interpretation by 3 masked readers in two phase 3 clinical trials show the pairwise interreader agreement to be 95% or higher in newly diagnosed patients and 75% or higher in patients with recurrent PCa. Intrareader agreement was 86% or higher in both populations.

IMPLICATIONS FOR PATIENT CARE: As this newly approved PET/CT imaging agent moves into clinical use, the present study shows that it can be reliably interpreted to give consistent results across individual readers.

REFERENCES

1. Clinical practice guidelines in oncology: prostate cancer, version 4.2024. National Comprehensive Cancer Network website. https://www.nccn.org/professionals/physician_gls/pdf/prostate.pdf. Updated May 17, 2024. Accessed May 23, 2024.
2. Wurzer A, Di Carlo D, Schmidt A, et al. Radiohybrid ligands: a novel tracer concept exemplified by ^{18}F- or ^{68}Ga-labeled rhPSMA inhibitors. *J Nucl Med.* 2020;61:735–742.
3. Surasi DS, Eiber M, Maurer T, et al. Diagnostic performance and safety of positron emission tomography with ^{18}F-rhPSMA-7.3 in patients with newly diagnosed unfavourable intermediate to very high-risk prostate cancer: results from a phase 3, prospective, multicentre study (LIGHTHOUSE). *Eur Urol.* 2023;84:361–370.
4. Jani AB, Ravizzini G, Gartrell BA, et al. Diagnostic performance and safety of ^{18}F-rhPSMA-7.3 PET in men with suspected prostate cancer recurrence: results from a phase 3, prospective, multicenter study (SPOTLIGHT). *J Urol.* 2023;210:299–311.
5. Highlights of prescribing information: POSLUMA (flotufolastat F 18) injection. FDA website. https://www.accessdata.fda.gov/drugsatfda_docs/label/2023/216023s000lbl.pdf. Revised May 2023. Accessed May 23, 2024.
6. Garje R, Rumble RB, Parikh RA. Systemic therapy update on ^{177}lutetium-PSMA-617 for metastatic castration-resistant prostate cancer: ASCO guideline rapid recommendation update. *J Clin Oncol.* November 6, 2023 [Epub ahead of print].
7. Cohen J. A coefficient of agreement for nominal scales. *Educ Psychol Meas.* 1960;20:37–46.
8. Fleiss JL. Measuring nominal scale agreement among many raters. *Psychol Bull.* 1971;76:378–382.
9. Hope TA, Eiber M, Armstrong WR, et al. Diagnostic accuracy of ^{68}Ga-PSMA-11 PET for pelvic nodal metastasis detection prior to radical prostatectomy and pelvic lymph node dissection: a multicenter prospective phase 3 imaging trial. *JAMA Oncol.* 2021;7:1635–1642.
10. Morris MJ, Rowe SP, Gorin MA, et al. Diagnostic performance of ^{18}F-DCFPyL-PET/CT in men with biochemically recurrent prostate cancer: results from the CONDOR phase III, multicenter study. *Clin Cancer Res.* 2021;27:3674–3682.
11. Kuo PH, Yoo DC, Avery R, et al. A VISION substudy of reader agreement on ^{68}Ga-PSMA-11 PET/CT scan interpretation to determine patient eligibility for ^{177}Lu-PSMA-617 radioligand therapy. *J Nucl Med.* 2023;64:1259–1265.
12. Landis JR, Koch GG. The measurement of observer agreement for categorical data. *Biometrics.* 1977;33:159–174.
13. Fleiss JL. *Statistical Methods for Rates and Proportions.* 2nd ed. John Wiley; 1981:18.
14. Sim J, Wright CC. The kappa statistic in reliability studies: use, interpretation, and sample size requirements. *Phys Ther.* 2005;85:257–268.
15. Viera AJ, Garrett JM. Understanding interobserver agreement: the kappa statistic. *Fam Med.* 2005;37:360–363.
16. Feinstein AR, Cicchetti DV. High agreement but low kappa: I—the problems of two paradoxes. *J Clin Epidemiol.* 1990;43:543–549.

Spleen Volume Reduction Is a Reliable and Independent Biomarker for Long-Term Risk of Leukopenia Development in Peptide Receptor Radionuclide Therapy

Lisa Steinhelfer*[1], Friederike Jungmann*[1], Lukas Endrös[1], Patrick Wenzel[2], Bernhard Haller[3], Manuel Nickel[3], Eva Haneder[1], Fabian Geisler[2], Katharina Götze[4], Alexander von Werder[2], Matthias Eiber[5,6], Markus R. Makowski[1], Rickmer Braren†[1,6], and Fabian Lohöfer†[1]

[1]Department of Radiology, School of Medicine, Klinikum Rechts der Isar, Technical University of Munich, Munich, Germany; [2]Medical Clinic and Polyclinic II, School of Medicine, Klinikum Rechts der Isar, Technical University of Munich, Munich, Germany; [3]Institute of AI and Informatics in Medicine, School of Medicine, Klinikum Rechts der Isar, Technical University of Munich, Munich, Germany; [4]Medical Clinic and Polyclinic III, School of Medicine, Klinikum Rechts der Isar, Technical University of Munich, Munich, Germany; [5]Department of Nuclear Medicine, School of Medicine, Klinikum Rechts der Isar, Technical University of Munich, Munich, Germany; and [6]German Cancer Consortium, a Partnership Between DKFZ and School of Medicine, Technical University of Munich, Munich, Germany

^{177}Lu-DOTATATE therapy is an effective treatment for advanced neuroendocrine tumors, despite its dose-limiting hematotoxicity. Herein, the significance of off-target splenic irradiation is unknown. Our study aims to identify predictive markers of peptide receptor radionuclide therapy–induced leukopenia. **Methods:** We retrospectively analyzed blood counts and imaging data of 88 patients with histologically confirmed, unresectable metastatic neuroendocrine tumors who received ^{177}Lu-DOTATATE treatment at our institution from February 2009 to July 2021. Inclusion criterium was a tumor uptake equivalent to or greater than that in the liver on baseline receptor imaging. We excluded patients with less than 24 mo of follow-up and those patients who received fewer than 4 treatment cycles, additional therapies, or blood transfusions during follow-up. **Results:** Our study revealed absolute and relative white blood cell counts and relative spleen volume reduction as independent predictors of radiation-induced leukopenia at 24 mo. However, a 30% decline in spleen volume 12 mo after treatment most accurately predicted patients proceeding to leukopenia at 24 mo (receiver operating characteristic area under the curve of 0.91, sensitivity of 0.93, and specificity of 0.90), outperforming all other parameters by far. **Conclusion:** Automated splenic volume assessments demonstrated superior predictive capabilities for the development of leukopenia in patients undergoing ^{177}Lu-DOTATATE treatment compared with conventional laboratory parameters. The reduction in spleen size proves to be a valuable, routinely available, and quantitative imaging-based biomarker for predicting radiation-induced leukopenia. This suggests potential clinical applications for risk assessment and management.

Key Words: PRRT; spleen volumetry; imaging-based biomarker; ^{177}Lu-DOTATATE; leukopenia

J Nucl Med 2024; 65:1244–1249
DOI: 10.2967/jnumed.123.267098

Peptide receptor radionuclide therapy (PRRT) using ^{177}Lu-labeled somatostatin analogs has emerged as an effective treatment approach for patients with somatostatin receptor–positive advanced neuroendocrine tumors. This therapy has demonstrated clinically significant effects, including symptom relief, improved quality of life, and radiologic response (*1–3*). Notably, the NETTER-1 study showed that ^{177}Lu-DOTATATE treatment led to longer progression-free survival and higher response rates than did high-dose octreotide long-acting release in patients with midgut neuroendocrine tumors (*4*).

Although PRRT is generally well tolerated, it is known that the kidneys and bone marrow receive off-target radiation doses, potentially leading to hematologic toxicity (*2,5–9*). Another factor that may contribute to hematologic toxicity is radiation exposure of the spleen. The spleen, as a major immune system organ, also plays a role in blood cell production and storage (*10*). Histophysiologic examinations have confirmed significant expression of somatostatin receptor subtype 2A in the spleen with a strong affinity for somatostatin analogs, including octreotide and octreotate, which are frequently used in the treatment of neuroendocrine tumors, including ^{177}Lu-DOTATATE treatment (*11–14*). Consequently, this distinctive receptor affinity contributes to high splenic uptake, resulting in elevated absorbed doses during PRRT (*9*).

Previous studies on external radiotherapy targeting the spleen have shown a decline in hemoglobin, white blood cell (WBC), and platelet counts (*15–17*). Herein, a correlation of spleen radiation dose and leukopenia has been revealed, as well as a decrease in spleen volume associated with an increased incidence of infectious events and poorer survival outcomes (*18,19*).

In this retrospective study, we aimed to evaluate the correlation between splenic volume and the emergence of leukopenia in a large cohort of patients with metastatic neuroendocrine tumors treated with ^{177}Lu-DOTATATE. Our investigation focused on assessing the prognostic significance of alterations in spleen volume in relation to the potential development of leukopenia. Notably, the integration of automated splenic volume assessments through deep learning has streamlined the process, rendering it more practical for daily clinical applications, particularly when considering the time-consuming and potentially variable manual assessments on CT or MR images.

Received Nov. 20, 2023; revision accepted May 22, 2024.

For correspondence or reprints, contact Lisa Steinhelfer (lisa.steinhelfer@tum.de) or Rickmer Braren (rbraren@tum.de).

*Contributed equally to this work.

†Contributed equally to this work.

MATERIALS AND METHODS

Patients

In a retrospective analysis, all patients who underwent ^{177}Lu-DOTATATE treatment at our institution between February 2009 and July 2021 were extracted from the institution's database. Inclusion criteria were histologically confirmed, unresectable, metastatic neuroendocrine tumors; sufficient tumor uptake, equivalent to or greater than liver uptake on baseline receptor imaging; a baseline glomerular filtration rate above 50 mL/min/1.73 m^2; adequate bone marrow function with a WBC count of 4,000/μL or higher; a hemoglobin level of 8 g/dL or higher; a platelet level of 70,000/μL or higher; and adequate liver function with a total bilirubin level no more than 2 times the upper limit of normal, a transaminase level no more than 5 times the upper limit of normal, and a serum albumin level of more than 3 g/dL with normal prothrombin time ($>$70%). Each fraction was administered as a 30-min intravenous infusion, coinfused with kidney-protecting amino acids (2.5% lysine and 2.5% arginine in 1 L of 0.9% NaCl; infusion rate, 250 mL/h), and was preceded by an antiemetic regime consisting of a 5-HT3 antagonist (e.g., granisetron or ondansetron). Long-acting somatostatin analogs were discontinued approximately 4 wk before the treatment start date. We excluded patients with a follow-up duration of less than 24 mo and those who had fewer than 4 cycles of ^{177}Lu-DOTATATE treatment, who received additional treatments, or who required blood product transfusions during the follow-up period. Ethical approval for this retrospective analysis was obtained from the local institutional review boards (reference 87/18S). Patients who underwent PRRT in our study received the treatment under compassionate use (§13.2b Arzneimittelgesetz). Therefore, the number of cycles was not limited to the approval status of Lutathera (Novartis). Supplemental Figure 1 illustrates the recruitment flowchart (supplemental materials are available at http://jnm.snmjournals.org).

CT and MRI Scans

Diagnostic CT or MRI scans were used to assess spleen volumes before treatment and at the 12-mo follow-up (12 ± 1 mo) after the start of treatment. To estimate the spleen volume from CT scans, a pretrained and publicly available deep-learning segmentation model (TotalSegmentator; University Hospital Basel) was used (*20*). The algorithm was applied to contrast-enhanced and native CT scans with a slice thickness of 3 or 5 mm (Fig. 1). Each segmentation was manually reviewed, and adjustments were made to the automatically measured contour if necessary ($n = 2$). In cases where only MRI scans were available ($n = 3$), spleen volume measurements were manually performed by segmenting the spleen parenchyma on all slices using the Philips IntelliSpace Radiology image platform.

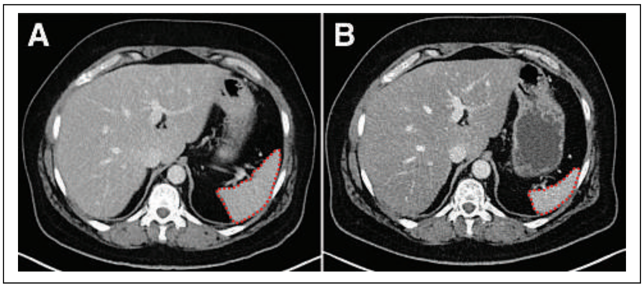

FIGURE 1. CT images from patient with ileal neuroendocrine tumor presenting with hepatic and bone metastases. Patient underwent total of 8 cycles of ^{177}Lu-DOTATATE treatment. (A) Baseline splenic volume was measured at 161 cm^3. (B) At 1-y follow-up after initiation of treatment, splenic volume was reduced to 79 cm^3, representing volume reduction of 51%.

Assessment of Hematologic Response

Hemoglobin, WBC, and platelet counts were systematically monitored throughout the treatment duration, with blood samples collected at 3- to 4-wk intervals according to standard hospital protocols. The decline in hemoglobin, WBC, and platelet counts was evaluated at 12 and 24 mo after the start of treatment. The relative decline ($\Delta_{\%}$) was defined as the percent change from baseline and then correlated with the splenic volume. Additionally, the severity of leukopenia, lymphopenia, and neutropenia was subsequently defined according to the Common Terminology Criteria for Adverse Events at the 12- and 24-mo follow-up.

Statistical Methods

Statistical analyses were performed using Python 3.10.5 (Python) and R (R Project for Statistical Computing) (*21*) with a 2-sided level of significance of less than 0.05. Descriptive statistics were used to illustrate patient characteristics. Mean values with SD or median and interquartile ranges were reported, unless indicated otherwise. Overall correlation between the decline of spleen volume and blood count data was assessed using the Spearman correlation coefficient. To determine potential confounders, further clinical data of all patients, including age, weight, comorbidities, tumor characteristics, and therapy details, were analyzed. Continuous variables were tested for normality using the Shapiro–Wilk test. Differences among patients developing leukopenia after 24 mo were analyzed using the 2-sided *t* test for normally distributed features and the Mann–Whitney *U* test for nonnormally distributed or ordinal features. Binary data between the groups were analyzed using the Fisher exact test. The level of significance was adjusted using Bonferroni adjustment. Furthermore, uni- and multivariate logistic regression tests of features significantly associated with the development of leukopenia were performed to assess both the predictive value of spleen decline compared with the other significant features and the relative risk of developing leukopenia with respect to those features. To assess the overlap of significant features between patients developing leukopenia and those who did not, the Bhattacharyya coefficient was used. Furthermore, analysis of receiver operating characteristics (ROC) was applied to determine specific cutoff values to distinguish between the 2 groups. Thresholds were selected using the Youden index.

RESULTS

Patients

In total, 88 patients with metastatic neuroendocrine tumors and a follow-up time of at least 24 mo were selected for the analysis. All patients exhibited tumor progression before receiving ^{177}Lu-DOTATATE treatment and underwent a total number of 547 cycles.

The median administered activity per cycle and median total administered activity of ^{177}Lu-DOTATATE were 7.4 GBq (interquartile range, 6.5–7.9 GBq) and 44 GBq (interquartile range, 29.6–57.7 GBq), respectively. The median number of cycles was 6 (interquartile range, 4–8), and the median time interval between 2 cycles was approximately 8 wk. Before initiation of PRRT, 62 patients were receiving long-acting octreotide every 4 wk. The median time interval between their last octreotide dose and PRRT initiation was 28 d (range, 27–31.5 d). Patient characteristics are presented in Table 1.

Correlation of Changes in Spleen Volume and Blood Count

A strong and statistically significant correlation emerged between the early-onset decrease in spleen volume after 12 mo and the late-onset decrease in WBC counts after 24 mo (correlation coefficient, 0.603; $P < 0.001$). Based on these insights, further investigation was

TABLE 1
Patient Characteristics

Parameter	Data
Age (y)	62 (13)
Sex	
Male	n = 51 (65%)
Female	n = 37 (35%)
Baseline leukocytes (μL)	6.57 (1.69)
Baseline spleen volume (mL)	239 (133)
Prior treatment	
Primary surgery	n = 42 (48%)
Somatostatin analog	n = 62 (77%)
Primary tumor	
Pancreas	34 (38)
Small intestine	31 (35)
Colon	6 (7)
Lung	6 (7)
Rectum	3 (3)
Stomach	3 (3)
Other	8 (9)

Continuous data are mean with SD in parentheses.

conducted to identify additional parameters predictive of the development of leukopenia during the follow-up period.

Development of Leukopenia After 24 Months

Of 88 patients, 29 developed leukopenia after 24 mo, which was defined as a WBC count below 4,000/μL, with at least grade 1 severity. Mild leukopenia (grades 1 and 2) occurred in 24% of patients, with grade 3 leukopenia noted in 8% of patients and grade 4 in 1% of patients. Lymphocytopenia, grades 1 and 2, was observed in 22% of patients, with the most severe toxicity at grade 3 in 3% of patients. Notably, neutrophil toxicity, primarily at grades 3 and 4, affected 7% of patients (Table 2). Importantly, none developed myelodysplastic syndrome. Clinical parameters were also examined for potential confounding factors. The t test was significant on 3 parameters: baseline WBC count, $\Delta_{\%}$ of WBC count, and $\Delta_{\%}$ of spleen volume after 12 mo; therefore, they were significantly associated with leukopenia development (Table 3). The results for all tested variables are presented in Supplemental Tables 1–3.

Patients developing leukopenia after 24 mo had an average spleen volume reduction of 36% ± 14%, whereas those with normal WBC levels after 24-mo follow-up had a spleen volume reduction of 19% ± 10%. When categorizing patients on the basis of their leukocyte decline after 24 mo, we found that those with a greater $\Delta_{\%}$ in leukocytes also exhibited a larger $\Delta_{\%}$ in spleen volume after 12 mo (Supplemental Fig. 2). Patients with higher baseline WBC levels were less likely to develop leukopenia (leukopenia group: 5,750 ± 1,150/μL; normal WBC level group: 6,980 ± 1,790/μL). Patients with leukopenia at 24 mo exhibited a smaller $\Delta_{\%}$ in WBC counts after 12 mo than did those without leukopenia, indicating that the early dynamics of hematologic parameters may not consistently result in long-term leukopenia.

However, in the multivariate logistic regression, only the $\Delta_{\%}$ in spleen volume remained significantly associated with the development of leukopenia (OR, 1.16; 95% CI, 1.09–1.26; $P < 0.001$), the results of which are shown in Supplemental Table 4. No other confounding features were identified (Supplemental Table 3).

Based on these results, ROC analyses provided specific threshold values to distinguish among patients developing leukopenia after 24 mo and those who would not. The best cutoff values regarding the univariate significant features are shown in Table 4.

A 30% decline in spleen volume most effectively differentiated between the 2 groups, achieving an excellent ROC area under the curve of 0.91 with a sensitivity of 0.93 and a specificity of 0.90. The $\Delta_{\%}$ in spleen volume in relation to the presence of leukopenia after 24 mo is presented in Figure 2.

TABLE 2
Distribution of Patients in Subgroups Based on Severity of Leukopenia, Lymphopenia, and Neutropenia at 12 and 24 Months After Initiation of PRRT (n = 88)

	Toxicity grade				
Parameter	0	I	II	III	IV
Total WBC count (per μL)	≥4,000	3,000–3,999	2,000–2,999	1,000–1,999	<1,000
12 mo	87 (99)	1 (1)	0 (0)	0 (0)	0 (0)
24 mo	59 (67)	8 (9)	13 (15)	7 (8)	1 (1)
ALC (per μL)	≥1,000	800–999	500–799	200–499	<200
12 mo	83 (94)	4 (5)	1 (1)	0 (0)	0 (0)
24 mo	65 (73)	16 (18)	4 (4)	3 (3)	0 (0)
ANC (per μL)	≥2,000	1,500–1,999	1000–1499	500–999	<500
12 mo	85 (97)	2 (2)	1 (1)	0 (0)	0 (0)
24 mo	63 (72)	9 (10)	10 (11)	5 (6)	1 (1)

ALC = absolute lymphocyte count; ANC = absolute neutrophil count.
Values for 12 and 24 mo are number with percentage in parentheses.

TABLE 3

Significant Clinical and Imaging Characteristics Differentiating Patients Developing Leukopenia After 24 Months from Those with Normal WBC Counts

Feature	Patients with leukopenia at 24 mo	Patients with normal WBC counts at 24 mo	*P*
$\Delta_{\%}$ of spleen volume after 12 mo	0.36 ± 0.14	0.19 ± 0.10	<0.001
$\Delta_{\%}$ of WBC after 12 mo	0.07 ± 0.10	0.19 ± 0.17	0.002
Baseline WBC count (×1,000/μL)	5.75 ± 1.15	6.98 ± 1.79	<0.001

Data are presented as mean ± SD, with feature decline relative to baseline values. Full analysis results are available in supplemental materials.

TABLE 4

Decline in Spleen Volume from Baseline After 12 Months Enables Discrimination Between Patients with Low and Normal WBC Levels After 24 Months*

Feature	Cutoff value	Sensitivity	Specificity	ROC-AUC	95% CI	*P*
Baseline WBC count (×1,000/μL)	6.0	0.68	0.69	0.68	0.60–0.83	<0.001
$\Delta_{\%}$ of spleen volume after 12 mo	0.3	0.93	0.90	0.91	0.80–0.98	<0.001
$\Delta_{\%}$ of WBC count after 12 mo	0.2	0.54	0.90	0.72	0.62–0.83	<0.001

*High sensitivity and specificity outperforming differences in baseline WBC levels and $\Delta_{\%}$ of WBC levels after 12 mo.

AUC = area under curve.

A baseline WBC level cutoff of 6,000/μL showed an ROC area under the curve of 0.68 for distinguishing among patients with reduced and normal WBC levels after 24 mo. Sensitivity was 0.68, and specificity was 0.69. The discrimination capability of this parameter was lower than that for the spleen volume.

Decline in Spleen Volume as an Independent, Imaging-Based Predictor of Leukopenia

The $\Delta_{\%}$ in spleen volume after 12 mo emerged as a robust indicator for the future development of leukopenia in patients undergoing PRRT, surpassing all other identified predictive parameters. This is shown by the decreased degree of overlap in the distribution of spleen volume decline between the 2 patient groups compared with other parameters. By setting a threshold of 30% decline, a highly accurate discrimination was achieved between patients developing leukopenia after 24 mo and those with normal WBC levels, as evident from the high ROC area under the curve of 0.91. Figure 3 emphasizes this aspect by illustrating the correlation between the decrease in spleen volume after 12 mo and the reduction in WBC levels after 24 mo. Furthermore, the mean and 2 SDs are displayed. As can be seen, the 2 patient groups can be distinctly separated on the basis of the $\Delta_{\%}$ in spleen volume after 12 mo.

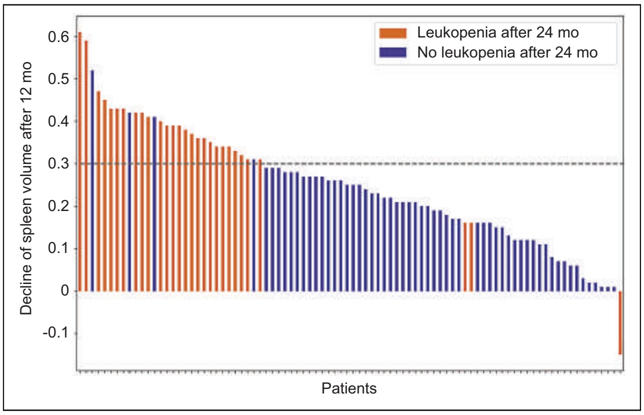

FIGURE 2. Waterfall plot showing distinct decline in spleen volume for all patients, including identified cutoff value for optimal differentiation between 2 patient groups. Decline of 30% in spleen volume after 12 mo demonstrates accuracy in distinguishing between patients who will develop leukopenia and those with normal WBC counts after 24 mo.

DISCUSSION

This retrospective analysis investigates the prognostic significance of changes in splenic volume and their relationship to leukopenia development in patients undergoing ^{177}Lu-DOTATATE treatment. For the fully automated extraction of spleen volume from routine CT imaging data, we used an open-source tool. In our retrospective analysis, a 30% reduction in spleen volume at 12 mo proved to be a highly accurate predictor for identifying patients at risk of developing leukopenia at 24 mo, with an excellent ROC area under the curve of 0.91, demonstrating excellent sensitivity of 0.93 and specificity of 0.90, outperforming all other tested parameters.

Regarding the irradiation effect on the spleen and subsequent hematologic changes, our findings demonstrate results comparable to those observed with radiation exposure in palliative splenic irradiation or off-target splenic irradiation during external radiotherapy. Lavrenkov et al. reported that palliative splenic irradiation reduced spleen size in over 75% of cases (*17,22*). Trip et al. in

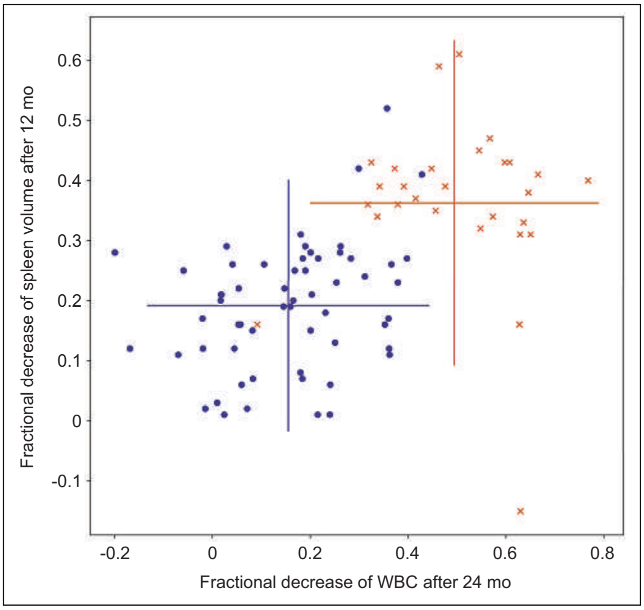

FIGURE 3. Correlation between $\Delta_{\%}$ in spleen volume after 12 mo and late reduction in WBC levels at 24-mo follow-up. Representation of mean (intersection) and 2 SDs (lines) for change in feature values for both groups is provided. Good discrimination between patients developing leukopenia (orange) and those with normal WBC counts (blue) is achieved on basis of early changes in spleen volume.

2015 first classified the spleen as an organ at risk, studying radiation-induced dose-dependent changes in spleen volume and hematologic toxicity after chemoradiation therapy (*23*). This finding has been confirmed in several studies related to external radiotherapy of neighboring organs. For example, Chadha et al. established a relationship between splenic radiation exposure in palliatively treated pancreatic cancer patients and lymphocyte count, showing a significant correlation between severe lymphopenia and the medium spleen dose and fraction exposed to low radiation doses (*24*).

Similarly, Liu et al. found a significant correlation between spleen irradiation dose and peripheral blood lymphocytes in their study of 59 patients with hepatocellular carcinoma (*18*). Saito et al.'s retrospective study with 61 esophageal cancer patients demonstrated that each 1-Gy increase in mean splenic dose resulted in a 2.9% decline in absolute lymphocyte count, with the mean splenic dose predicting grade 4 lymphopenia (*25*). In addition, histopathologic changes in the parenchyma of irradiated spleens from lymphoma patients revealed parenchymal collapse, diffuse fibrosis, and lymphocyte depletion, suggesting structural alterations responsible for the observed changes in spleen volume and resultant leukopenia (*25*). However, the pathophysiology of irradiation-induced damage to the spleen and its effects on the hematopoietic system are complex and suggest a dose dependency, since acute high radiation exposure resulted in complete ablation of the spleen and limited hematotoxicity (*26,27*). Furthermore, a study conducted on blood cell migration in mice indicated a notable change in the distribution of WBC counts from spleen tissue cavities to the bloodstream after surgical spleen removal (*28*). Therefore, surgical and radiotherapeutic splenectomy might impact the peripheral WBC count through a comparable mechanism.

The correlation observed between a higher $\Delta_{\%}$ in leukocytes after 24 mo and a larger decline in spleen volume after 12 mo suggests that spleen volume could serve as a predictive marker for hematologic toxicity in patients undergoing PRRT. In alignment with our findings, Svensson et al. identified a substantial association between hematologic toxicity and the cumulative radiation dose absorbed by the spleen during PRRT (*29*). Notably, baseline risk factors such as diabetes, hypertension, and the number of therapy cycles were not significantly associated with a more pronounced reduction in splenic volume at the 24-mo follow-up. Furthermore, there was no correlation observed with prior therapies or patient age. In summary, our findings indicate a significant physiologic impact of PRRT on hematopoietic functions, suggesting that radiation-induced alterations in the spleen involve intricate interactions with leukopenia, extending beyond the established effects on bone marrow and WBC dynamics. Although our study did not directly investigate the correlation between infections and leukocyte reduction, existing literature underscores the association between hematotoxicity and susceptibility to infections, particularly in cancer patients (*30–32*). Using spleen volume as a biomarker holds promise in identifying patients at risk and in facilitating proactive management of hematologic issues.

The retrospective design of this study introduces the potential for bias from unidentified confounding factors, emphasizing the need for further investigations using different datasets to validate these findings. To avoid investigator bias, blood count and splenic volumetry were done independently. Further research is needed to validate the results of our study, given the lack of standard reference values for splenic size reduction and the increased risk of leukopenia in patients undergoing ^{177}Lu-DOTATATE treatment.

CONCLUSION

Despite these limitations, our findings highlight the feasibility of applying automated splenic volumetry from routine imaging data in patients receiving ^{177}Lu-DOTATATE treatment. The automated approach offers several advantages, including a reduction in the time required for image analysis and the potential to effectively mitigate investigator bias.

A 30% reduction in spleen volume at 12 mo emerged as a highly accurate predictor for identifying patients at risk of developing leukopenia at 24 mo. Stratifying patients on the basis of this biomarker could prompt the implementation of a more rigorous follow-up protocol, enabling the early detection and proactive management of hematologic issues in patients receiving ^{177}Lu-DOTATATE treatment. This might involve adjusting treatment cycles, considering reinduction of PRRT, or using more sensitive patient monitoring for further treatments that can cause leukopenia. Additionally, administering granulocyte colony-stimulating factor preventively could be an option.

Further research including prospective multicenter testing of spleen volume reduction as an independent biomarker is warranted to identify and validate a universal cutoff value, validate its utility, and further explore its broader applicability in risk stratification and treatment optimization for this patient population.

DISCLOSURE

Matthias Eiber reports fees from Blue Earth Diagnostics Ltd. (consultant, research funding), Novartis/AAA (consultant, speaker), Telix (consultant), Bayer (consultant, research funding), RayzeBio (consultant), Point Biopharma (consultant), Eckert & Ziegler (speaker), Janssen Pharmaceuticals (consultant, speakers bureau), Parexel (image review), and Bioclinica (image review) outside the submitted work and a patent application for rhPSMA.

KEY POINTS

QUESTION: Can predictive biomarkers be used to identify PRRT-induced leukopenia?

PERTINENT FINDINGS: In this retrospective study, early spleen volume reduction was identified as a predictive imaging-based biomarker for radiation-induced WBC count changes in 88 patients undergoing ^{177}Lu-DOTATATE treatment. A 30% decline in spleen volume 12 mo after treatment accurately identifies patients at risk of developing leukopenia at 24 mo, with excellent sensitivity and specificity.

IMPLICATIONS FOR PATIENT CARE: Changes in spleen volume serve as a highly accurate and independent quantitative biomarker, automatically extracted from routine clinical imaging data, to predict radiation-induced leukopenia.

REFERENCES

1. Bodei L, Kidd M, Prasad V, Modlin IM. Peptide receptor radionuclide therapy of neuroendocrine tumors. *Front Horm Res.* 2015;44:198–215.
2. Kwekkeboom DJ, Bakker WH, Kam BL, et al. Treatment of patients with gastro-entero-pancreatic (GEP) tumours with the novel radiolabelled somatostatin analogue [^{177}Lu-DOTA^{0},Tyr^{3}]octreotate. *Eur J Nucl Med Mol Imaging.* 2003;30:417–422.
3. Pavel M, Valle JW, Eriksson B, et al. ENETS consensus guidelines for the standards of care in neuroendocrine neoplasms: systemic therapy—biotherapy and novel targeted agents. *Neuroendocrinology.* 2017;105:266–280.
4. Strosberg J, El-Haddad G, Wolin E, et al. Phase 3 trial of ^{177}Lu-Dotatate for midgut neuroendocrine tumors. *N Engl J Med.* 2017;376:125–135.
5. Bodei L, Kidd M, Paganelli G, et al. Long-term tolerability of PRRT in 807 patients with neuroendocrine tumours: the value and limitations of clinical factors. *Eur J Nucl Med Mol Imaging.* 2015;42:5–19.
6. Delpassand ES, Samarghandi A, Zamanian S, et al. Peptide receptor radionuclide therapy with ^{177}Lu-DOTATATE for patients with somatostatin receptor-expressing neuroendocrine tumors: the first US phase 2 experience. *Pancreas.* 2014;43:518–525.
7. Gupta SK, Singla S, Bal C. Renal and hematological toxicity in patients of neuroendocrine tumors after peptide receptor radionuclide therapy with ^{177}Lu-DOTATATE. *Cancer Biother Radiopharm.* 2012;27:593–599.
8. Pfeifer AK, Gregersen T, Gronbaek H, et al. Peptide receptor radionuclide therapy with ^{90}Y-DOTATOC and ^{177}Lu-DOTATOC in advanced neuroendocrine tumors: results from a Danish cohort treated in Switzerland. *Neuroendocrinology.* 2011;93:189–196.
9. Sabet A, Ezziddin K, Pape UF, et al. Long-term hematotoxicity after peptide receptor radionuclide therapy with ^{177}Lu-octreotate. *J Nucl Med.* 2013;54:1857–1861.
10. Cesta MF. Normal structure, function, and histology of the spleen. *Toxicol Pathol.* 2006;34:455–465.
11. Baković D, Eterovic D, Saratlija-Novakovic Z, et al. Effect of human splenic contraction on variation in circulating blood cell counts. *Clin Exp Pharmacol Physiol.* 2005;32:944–951.
12. Ferone D, Pivonello R, Kwekkeboom DJ, et al. Immunohistochemical localization and quantitative expression of somatostatin receptors in normal human spleen and thymus: implications for the in vivo visualization during somatostatin receptor scintigraphy. *J Endocrinol Invest.* 2012;35:528–534.
13. Spencer RP, Gupta SM. The spleen: diagnosis of splenic diseases using radiolabeled tracers. *Crit Rev Clin Lab Sci.* 1989;27:299–318.
14. Wyffels JT, Luer CA, Walsh CJ, Bodine AB. In vivo exposure of clearnose skates, *Raja eglanteria,* to ionising X-radiation: acute effects on the peripheral blood, spleen, and epigonal and Leydig organs. *Fish Shellfish Immunol.* 2007;23:401–418.
15. Ishibashi N, Maebayashi T, Aizawa T, et al. Myelosuppression toxicity of palliative splenic irradiation in myelofibrosis and malignant lymphoma. *Hematology.* 2015;20:203–207.
16. Kriz J, Micke O, Bruns F, et al. Radiotherapy of splenomegaly: a palliative treatment option for a benign phenomenon in malignant diseases. *Strahlenther Onkol.* 2011;187:221–224.
17. Pistevou-Gombaki K, Zygogianni A, Kantzou I, et al. Splenic irradiation as palliative treatment for symptomatic splenomegaly due to secondary myelofibrosis: a multi-institutional experience. *J BUON.* 2015;20:1132–1136.
18. Liu J, Zhao Q, Deng W, et al. Radiation-related lymphopenia is associated with spleen irradiation dose during radiotherapy in patients with hepatocellular carcinoma. *Radiat Oncol.* 2017;12:90.
19. Celik E, Baues C, Trommer M, et al. Dose-dependent effects of unintended splenic irradiation after neoadjuvant radiochemotherapy for esophageal cancer. *Anticancer Res.* 2023;43:2733–2739.
20. Wasserthal J, Breit H-C, Meyer MT, et al. TotalSegmentator: robust segmentation of 104 anatomical structures in CT images. arXiv website. https://arxiv.org/abs/2208.05868. Published August 11, 2022. Accessed June 26, 2024.
21. Wang X, Jiang B, Liu JS. Generalized R-squared for detecting dependence. *Biometrika.* 2017;104:129–139.
22. Lavrenkov K, Krepel-Volsky S, Levi I, Ariad S. Low dose palliative radiotherapy for splenomegaly in hematologic disorders. *Leuk Lymphoma.* 2012;53:430–434.
23. Trip AK, Sikorska K, van Sandick JW, et al. Radiation-induced dose-dependent changes of the spleen following postoperative chemoradiotherapy for gastric cancer. *Radiother Oncol.* 2015;116:239–244.
24. Chadha AS, Liu G, Chen HC, et al. Does unintentional splenic radiation predict outcomes after pancreatic cancer radiation therapy? *Int J Radiat Oncol Biol Phys.* 2017;97:323–332.
25. Saito T, Toya R, Yoshida N, et al. Spleen dose-volume parameters as a predictor of treatment-related lymphopenia during definitive chemoradiotherapy for esophageal cancer. *In Vivo.* 2018;32:1519–1525.
26. Chin AL, Aggarwal S, Pradhan P, et al. The role of bone marrow and spleen irradiation in the development of acute hematologic toxicity during chemoradiation for esophageal cancer. *Adv Radiat Oncol.* 2018;3:297–304.
27. Weinmann M, Becker G, Einsele H, Bamberg M. Clinical indications and biological mechanisms of splenic irradiation in autoimmune diseases. *Strahlenther Onkol.* 2001;177:105–111.
28. Djaldetti M, Bergman M, Salman H, Cohen AM, Fibach E, Bessler H. On the mechanism of post-splenectomy leukocytosis in mice. *Eur J Clin Invest.* 2003;33:811–817.
29. Svensson J, Hagmarker L, Magnander T, Wangberg B, Bernhardt P. Radiation exposure of the spleen during ^{177}Lu-DOTATATE treatment and its correlation with haematological toxicity and spleen volume. *EJNMMI Phys.* 2016;3:15.
30. Schwarzberg AB, Stover EH, Sengupta T, et al. Selective lymphopenia and opportunistic infections in neuroendocrine tumor patients receiving temozolomide. *Cancer Invest.* 2007;25:249–255.
31. Terrones-Campos C, Ledergerber B, Specht L, Vogelius IR, Helleberg M, Lundgren J. Risk of bacterial, viral, and fungal infections in patients with solid malignant tumors treated with curative intent radiation therapy. *Adv Radiat Oncol.* 2022;7:100950.
32. Warny M, Helby J, Nordestgaard BG, Birgens H, Bojesen SE. Lymphopenia and risk of infection and infection-related death in 98,344 individuals from a prospective Danish population-based study. *PLoS Med.* 2018;15:e1002685.

Synthesis of ^{64}Cu-, ^{55}Co-, and ^{68}Ga-Labeled Radiopharmaceuticals Targeting Neurotensin Receptor-1 for Theranostics: Adjusting In Vivo Distribution Using Multiamine Macrocycles

German O. Fonseca Cabrera*[1], Xinrui Ma*[1,2], Wilson Lin*[3], Tao Zhang[1], Weiling Zhao[1], Liqin Pan[1], Xiaomei Li[4], Todd E. Barnhart[3], Eduardo Aluicio-Sarduy[3], Huaifu Deng[1], Xuedan Wu[1], Kadalipura P. Rakesh[1], Zibo Li[1], Jonathan W. Engle[2], and Zhanhong Wu[1]

[1]Biomedical Research Imaging Center, Department of Radiology, UNC Lineberger Comprehensive Cancer Center, University of North Carolina at Chapel Hill, Chapel Hill, North Carolina; [2]Joint Department of Biomedical Engineering, University of North Carolina at Chapel Hill and North Carolina State University, Chapel Hill, North Carolina; [3]Department of Medical Physics, University of Wisconsin, Madison, Wisconsin; and [4]Accunovo Biotechnologies, Inc., Chapel Hill, North Carolina

The development of theranostic radiotracers relies on their binding to specific molecular markers of a particular disease and the use of corresponding radiopharmaceutical pairs thereafter. This study reports the use of multiamine macrocyclic moieties (MAs), as linkers or chelators, in tracers targeting the neurotensin receptor-1 (NTSR-1). The goal is to achieve elevated tumor uptake, minimal background interference, and prolonged tumor retention in NTSR-1–positive tumors. **Methods:** We synthesized a series of neurotensin antagonists bearing MA linkers and metal chelators. The MA unit is hypothesized to establish a strong interaction with the cell membrane, and the addition of a second chelator may enhance water solubility, consequently reducing liver uptake. Small-animal PET/CT imaging of [^{64}Cu]Cu-DOTA-SR-3MA, [^{64}Cu]Cu-NT-CB-NOTA, [^{68}Ga]Ga-NT-CB-NOTA, [^{64}Cu]Cu-NT-CB-DOTA, and [^{64}Cu]Cu-NT-Sarcage was acquired at 1, 4, 24, and 48 h after injection using H1299 tumor models. [^{55}Co]Co-NT-CB-NOTA was also tested in HT29 (high NTSR-1 expression) and Caco2 (low NTSR-1 expression) colorectal adenocarcinoma tumor models. Saturation binding assay and internalization of [^{55}Co]Co-NT-CB-NOTA were used to test tracer specificity and internalization in HT29 cells. **Results:** In vivo PET imaging with [^{64}Cu]Cu-NT-CB-NOTA, [^{68}Ga]Ga-NT-CB-NOTA, and [^{55}Co]Co-NT-CB-NOTA revealed high tumor uptake, high tumor-to-background contrast, and sustained tumor retention (≤48 h after injection) in NTSR-1–positive tumors. Tumor uptake of [^{64}Cu]Cu-NT-CB-NOTA remained at 76.9% at 48 h after injection compared with uptake 1 h after injection in H1299 tumor models, and [^{55}Co]Co-NT-CB-NOTA was retained at 60.2% at 24 h compared with uptake 1 h after injection in HT29 tumor models. [^{64}Cu]Cu-NT-Sarcage also showed high tumor uptake with low background and high tumor retention 48 h after injection **Conclusion:** Tumor uptake and pharmacokinetic properties of NTSR-1–targeting radiopharmaceuticals were greatly improved when attached with different nitrogen-containing macrocyclic moieties. The study results suggest that NT-CB-NOTA labeled with either ^{64}Cu/^{67}Cu, ^{55}Co/^{58m}Co, or ^{68}Ga (effect of ^{177}Lu in tumor to be determined in future studies) and NT-Sarcage labeled with ^{64}Cu/^{67}Cu or ^{55}Co/^{58m}Co may be excellent diagnostic and therapeutic radiopharmaceuticals targeting NTSR-1–positive cancers. Also, the introduction of MA units to other ligands is warranted in future studies to test the generality of this approach.

Key Words: radiotheranostic agent; prostate cancer; PET; neurotensin receptor; ^{64}Cu; ^{55}Co; ^{68}Ga

J Nucl Med 2024; 65:1250–1256
DOI: 10.2967/jnumed.124.267469

Prostate cancer is the most frequently diagnosed noncutaneous malignancy and the second leading cause of cancer-related death among men in the United States (*1*). Although several treatments exist, there is a need for significantly improved prostate cancer management (*2,3*). Indeed, a new targeted radionuclide therapy has been developed for advanced prostate cancer patients by targeting prostate-specific membrane antigen (PSMA) (*4*). In 2022, [^{177}Lu]Lu-PSMA-617 (Pluvicto; Novartis) received U.S. Food and Drug Administration approval for prostate cancer treatment (*5,6*). Despite this progress, a proportion of prostate cancer patients exhibit inherent resistance to this therapy (*7,8*). It has been estimated that up to 30% of patients may not respond effectively to PSMA-based radionuclide therapy (*9–12*). Furthermore, acquired resistance to PSMA-based radionuclide therapy can also occur over time. Cancer cells may adapt and develop mechanisms to evade therapy effects. Resistance might arise because of various mechanisms, such as alterations in PSMA expression or changes in DNA repair mechanisms. There is a necessity to develop new therapeutic and prognostic methods for the management of advanced-stage prostate cancer. Although multiple factors may contribute to prostate cancer development, progression, and resistance to therapy, increasing evidence suggests that intraprostate neuroendocrinelike cells play an important role in androgen-independent recurrent prostate cancer (*13–17*). Prostate cancer may even become enriched in (or entirely composed of) neuroendocrine cell clusters after long-term antiandrogen therapy. Secreted by neuroendocrinelike prostate cells, neurotensin has numerous physiologic effects predominantly mediated through its high-affinity receptor, neurotensin receptor-1 (NTSR-1), which is expressed and activated in aggressive prostate cancer cells

---

Received Jan. 22, 2024; revision accepted May 7, 2024.

For correspondence or reprints, contact Zibo Li (ziboli@med.unc.edu), Jonathan W. Engle (jwengle@wisc.edu), or Zhanhong Wu (zhanhong_wu@med.unc.edu).

*Contributed equally to this work.

but not in normal prostate epithelial cells (*17–19*). In advanced prostate cancer, NTSR-1 is recruited as an alternative growth pathway in the absence of androgens (*20–22*). Thus, NTSR-1–targeted radiopharmaceuticals hold great potential as novel treatments for the management of NTSR-1–positive prostate cancer. Moreover, NTSR-1 has been found to be overexpressed in a large portion of lung, breast, pancreatic, and colorectal cancers, all of which can also benefit from NTSR-1–targeted agents.

With the ability to see what we treat and treat what we see, radiotheranostic agents can be screened quickly using an imaging radionuclide and subsequently used for treatment once the isotope is changed to a matched therapeutic radionuclide. For example, tracers labeled with positron-emitting radionuclides (β^+) are used for diagnosis and patient screening by PET, whereas the same agent labeled with ionizing particle–emitting radionuclides (emitters of β-particles [β^-], α-particles, or Auger electrons) can be used for therapy purposes (*23*). Although ^{68}Ga/^{177}Lu is a widely used theranostic pair, their half-lives do not match, and the use of 2 different elements may increase the chance of pharmacokinetic discrepancy. A true theranostic pair involves the use of same-element radioisotopes for both imaging and therapy. Two of such matched pairs are ^{64}Cu (PET isotope for imaging, half-life = 12.7 h, $I_{\beta^+} = 18\%$, $<E_{\beta^+}> = 280$ keV)/^{67}Cu (β-emitter for therapy, half-life = 62 h, $I_{\beta^-} = 100\%$, $<E_{\beta^-}> = 141$ keV) and ^{55}Co (PET isotope, half-life = 17.5 h, $I_{\beta^+} = 77\%$, $<E_{\beta^+}> = 570$ keV)/^{58m}Co (Auger electron emitter for therapy, half-life = 9.1 h, 100% internal conversion). Metal-binding chelators such as bicyclic Sarcage (1-*N*-(4-aminobenzyl)-3,6,10,13,16,19-hexaazabicyclo[6.6.6]-eicosane-1,8-diamine), NOTA, and DOTA readily form stable complexes in vivo with both copper and cobalt cations (*24–26*).

To develop NTSR-1–targeted radiotheranostic agents, an appropriate ligand must be used. NTSR-1 is activated by the endogenous 13-amino-acid peptide agonist neurotensin and the hexapeptide neuromedin N (section 12 of the supplemental materials; supplemental materials are available at http://jnm.snmjournals.org). The C-terminal hexapeptide portion of neurotensin, NT8-13, represents the binding epitope and contains all determinants for NTSR-1 activation (*27*). Initial NTSR-1–targeted radiopharmaceuticals were focused on stabilized peptide agonists, which were labeled with ^{18}F, ^{11}C, ^{68}Ga, and ^{64}Cu and showed high-contrast imaging of NTSR-1–positive tumor models (*28,29*). However, fast clearance profiles and moderate tumor uptake values made these peptides unsuitable for targeted radionuclide therapy. Nonpeptidic antagonists (Fig. 1A) represent another category of NTSR-1 ligands, which were labeled with ^{18}F and ^{68}Ga for PET imaging and ^{177}Lu for therapy applications (*28,29*). For example, Schulz et al. evaluated 3BP-227 for ^{177}Lu radiotherapy of colon carcinoma in a preclinical study in 2017 (*30*), and Baum et al. initiated a radiotherapy trial on patients with metastatic or locally advanced NTSR-1–expressing cancers with promising results (*31*). Tracer ^{225}Ac-FPI-2059 is currently in preclinical development for the treatment of solid tumors expressing NTSR-1 (*32,33*). Previously, we developed SR142948A-related derivatives and found that those attached to chelators based on 1,4,8,11-tetraazabicyclo[6.6.2]hexadecane (CB)-cyclam (Fig. 1B) can greatly reduce the background uptake and enhance tumor retention of ^{64}Cu-labeled agents compared with [^{64}Cu]Cu-3BP-227. Liver was the only major organ that showed uptake of the NTSR-1–targeted agents (*34*).

In this report, we developed NTSR-1–targeted constructs with the potential for ^{64}Cu/^{67}Cu, ^{55}Co/^{58m}Co, and ^{68}Ga/^{177}Lu labeling. PET imaging with ^{64}Cu, ^{55}Co, and ^{68}Ga was used to study in vivo radiotracer distribution. To synthesize agents with improved tumor uptake, improved tumor-to-background ratios, and extended tumor residence time, we hypothesized that the net charge around the tracer is a key factor in determining how a tracer interacts with its receptor and other cell substructures such as the cell membrane. Thus, we used a synthetic antagonistic NTSR-1–targeting ligand, and charge modification was performed by introducing structural changes at the linker and chelator moieties of the tracer (Fig. 1A). Multiamine macrocyclic moieties (MAs) affect the distribution of SR142948A derivatives (*28,29,35*), possibly by enhancing the linkage with the negatively charged external surface of the cell membrane, through ionic interactions, with the MAs' positively charged basic nitrogens (section 5 of the supplemental materials) (*36*). This would increase the tracer concentration and the time the tracer spends near its receptor. MAs may also improve the target-to-background ratio of tracers by modifying their pharmacokinetic properties. Furthermore, MAs such as CB-cyclam and Sarcage are rigid macrocycles with several nitrogen atoms capable of establishing additional hydrogen bonding to water molecules, which makes the tracer more hydrophilic and helps minimize undesired liver uptake.

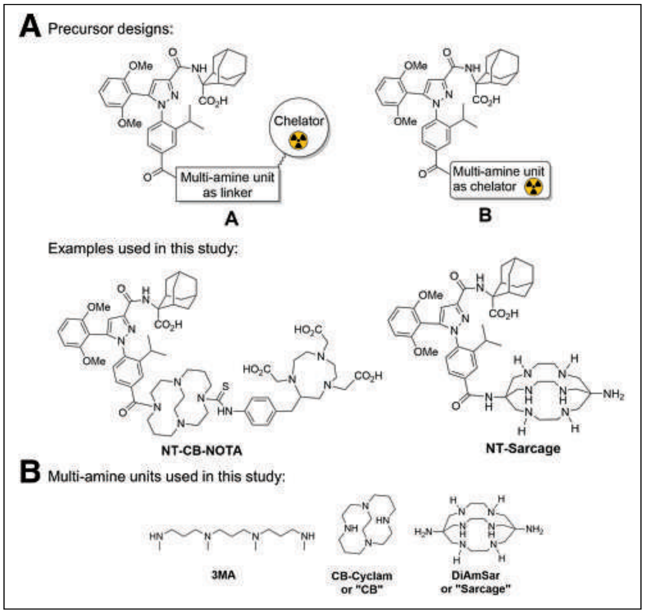

FIGURE 1. (A) Precursor designs and examples that illustrate rational design. (B) Multiamine units used in this study.

MATERIALS AND METHODS

Small-Animal PET/CT Imaging and Biodistribution of [^{64}Cu]Cu-DOTA-SR-3MA, [^{64}Cu]Cu-NT-CB-NOTA, [^{68}Ga]Ga-NT-CB-NOTA, [^{64}Cu]Cu-NT-CB-DOTA, and [^{64}Cu]Cu-NT-Sarcage

All animal studies were conducted under a protocol approved by the Institutional Animal Care and Use Committee of the University of North Carolina at Chapel Hill. Female nude mice (nu/nu immunodeficient, 5–6 wk old) were obtained from the Animal Facility at University of North Carolina at Chapel Hill. Approximately 5 million H1299 cells in a 1:1 mixture of Matrigel (BD Biosciences) and phosphate-buffered saline were injected subcutaneously into the left or right shoulder and leg to establish the tumor xenograft. Animals were ready for imaging studies after the tumor reached a volume of 200 mm^3.

For PET/CT imaging, each mouse ($n = 3$) was injected with 3–6 MBq of [^{64}Cu]Cu-DOTA-SR-3MA. The same settings were applied to the

PET images acquired with [^{64}Cu]Cu-NT-CB-NOTA, [^{64}Cu]Cu-NT-CB-DOTA, and [^{64}Cu]Cu-NT-Sarcage. PET imaging acquired pharmacokinetic profiles at 1, 4, 24, and 48 h after injection. CT scans were acquired before PET imaging for anatomic reference. Mice were awakened between tracer injection and imaging times. Images were acquired with the PET/CT imaging system SuperArgus 4R (Sedecal Inc.). List-mode data were collected and reconstructed using the algorithm described before (*37*). Regions of interest were drawn using AMIDE software (Amide's a Medical Image Data Examiner). Organ uptake was expressed as mean ± SD of percentage injected dose per gram and corrected for radioactivity decay.

Small-Animal PET/CT Imaging and Biodistribution of [^{55}Co]Co-NT-CB-NOTA

All animal studies were conducted under a protocol approved by the University of Wisconsin Institutional Animal Care and Use Committee. Female athymic nude mice (5–6 wk old) were purchased from Jackson Laboratory. HT29 and Caco2 tumor inoculation, in vivo PET imaging, and ex vivo biodistribution were performed following methods reported by Lin et al. (*38*). Each mouse (*n* = 4) received 2.1 MBq of [^{55}Co]Co-NT-CB-NOTA. PET imaging acquired pharmacokinetic profiles at 1, 4, 9, and 24 h after injection. Ex vivo biodistribution studies were performed immediately after the 24-h PET scan to validate the in vivo PET imaging results.

The supplemental materials provide the synthetic schemes and protocols for new compounds and radiotracers (sections 2 and 3); radiolabeling details (section 4); saturation binding assay and internalization of [^{55}Co]Co-NT-CB-NOTA results (section 6); quantification of organ uptake and tumor-to-muscle ratios and comparison of tumor uptake, residence half-life, and tumor-to-muscle ratios between tracers (sections 7–9); and statistical analysis (section 10) (*39,40*).

RESULTS

Synthesis and In Vivo Biodistribution of Precursor DOTA-SR-3MA

First, we synthesized intermediate SR-3MA-NH (**2**) from the phenyl-Br (**1**) (*41*), and then it was conjugated to a DOTA chelator to obtain precursor DOTA-SR-3MA (**3**). Compound **3** has an additional nitrogen center compared with 3BP-227 (section 2.1 of the supplemental materials). After **3** was labeled with ^{64}Cu, in vivo PET imaging results showed high tumor uptake for [^{64}Cu]Cu-DOTA-SR-3MA (in H1299-tumor–bearing nu/nu mice) with relatively low background except for moderate uptake in the liver (Fig. 2). The linker homologation with the presence of an extra nitrogen atom seemed to have a positive impact on the in vivo PET imaging biodistribution, but the tumor uptake was moderately reduced. A more dramatic change in the MA structure was needed to reduce undesired liver uptake.

Synthesis and In Vivo Biodistribution of NT-CB–Based Precursors

Next, we explored whether the more rigid structure of macrocycle CB-cyclam could be used as an MA to improve the tumor-to-liver ratio obtained with **3.** NT-CB (**5**) was obtained in high yield from the corresponding precursor **1,** via its phenyl-carboxylic acid (**4**) derivative (section 2.2 of the supplemental materials). Next, precursors NT-CB-CA (**7**), NT-CB-Sarcage (**8**), NT-CB-NOTA (**9**), and NT-CB-DOTA (**10**) were easily synthesized in good yield (section 2.3 of the supplemental materials). Two additional precursors, NT-CB-succinimide-NOTA (**11**) and NT-CB-succinimide-DOTA (**12**), were successfully synthesized from **5,** but they were not tested for their in vivo PET imaging biodistribution during this study (section 2.4 of the supplemental materials). Next, we performed the ^{64}Cu labeling and in vivo PET imaging of **7** and **8.** [^{64}Cu]Cu-NT-CB-CA and [^{64}Cu]Cu-NT-CB-Sarcage both showed relatively low tumor uptake in our pilot PET imaging studies. We then focused our efforts on testing the biodistribution of **9** and **10.** Gratifyingly, in vivo PET imaging results with [^{64}Cu]Cu-NT-CB-NOTA, [^{68}Ga]Ga-NT-CB-NOTA (both in H1299-tumor–bearing mice), and [^{55}Co]Co-NT-CB-NOTA (in HT29-tumor–bearing mice) revealed high tumor uptake with low background and sustained tumor retention for up to 48 h after injection (Figs. 3–5, respectively). The presence of the CB-NOTA moiety in the tracer structure clearly improved the ratio of the tumor-to-background signal compared with [^{64}Cu]Cu-DOTA-SR-3MA. Unexpectedly, chemical replacement of the NOTA chelator with its DOTA analog and subsequent ^{64}Cu labeling to generate [^{64}Cu]Cu-NT-CB-DOTA did not provide the same level of improvement in H1299-tumor–bearing mice. Tumor uptake levels were similar to those of the NOTA analog; however, higher liver and kidney radiosignals were detected (Fig. 6). This might be caused by the in vivo stability limitation of the Cu-DOTA complex. This agent is worth further investigation given its α-particle therapy applications.

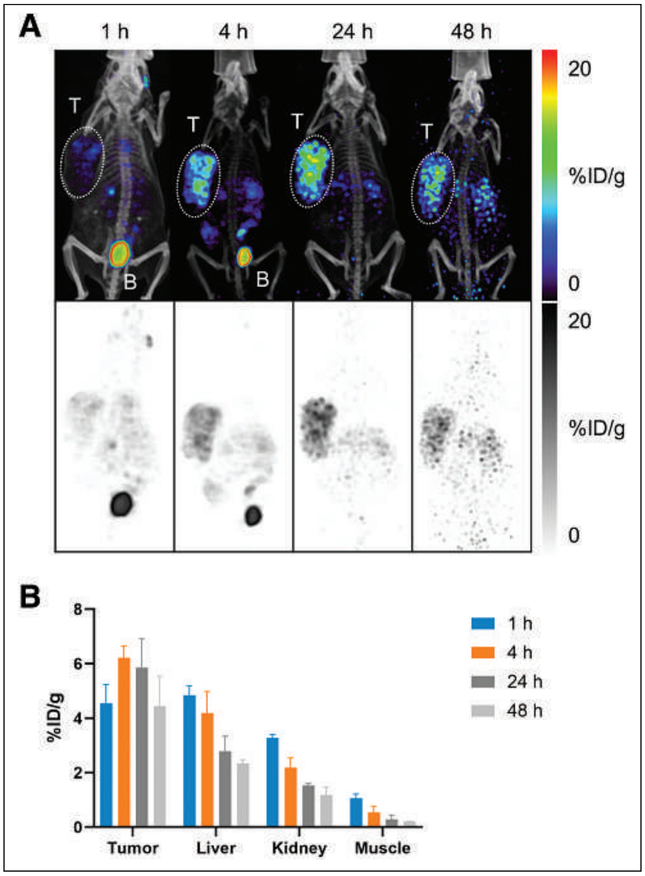

FIGURE 2. (A) Three-dimensional PET/CT images of [^{64}Cu]Cu-DOTA-SR-3MA in H1299-tumor–bearing nu/nu mice at 1, 4, 24, and 48 h after injection. (B) In vivo biodistribution analysis of approximately 4.5 MBq of [^{64}Cu]Cu-DOTA-SR-3MA at 1, 4, 24, and 48 h after injection (via tail vein). B = bladder; %ID/g = percentage injected dose per gram; T = tumor.

Synthesis and In Vivo Biodistribution of NT-Sarcage

Given the unexpected imaging result obtained with **8** and to remove any negative chemical interaction between Sarcage and other linkers present in the tracer, we decided to modify this precursor and synthesize an agent in which the neurotensin ligand

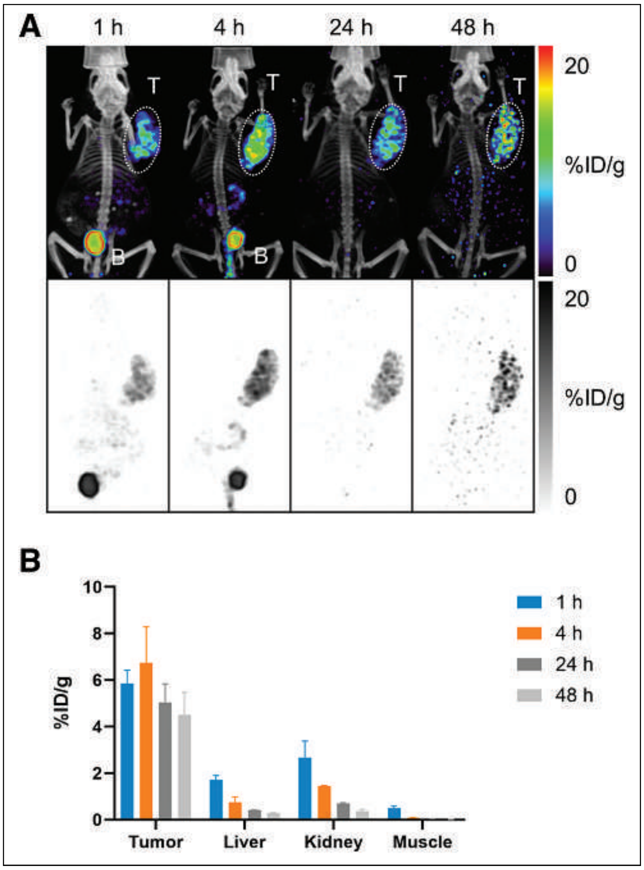

FIGURE 3. (A) In vivo biodistribution experiments showing 3-dimensional PET/CT images of [^{64}Cu]Cu-NT-CB-NOTA in H1299-tumor–bearing nu/nu mice at 1, 4, 24, and 48 h after injection. (B) Quantitative analysis of [^{64}Cu]Cu-NT-CB-NOTA in H1299-tumor–bearing mice at 1, 4, 24, and 48 h after injection. B = bladder; %ID/g = percentage injected dose per gram; T = tumor.

and the Sarcage chelator were directly connected, without any linker present between. NT-Sarcage (**6**) was then synthesized in one pot with a large yield from **4** (section 2.2 of the supplemental materials). The Sarcage moiety is directly attached through an amide functional group to the neurotensin ligand. With **6** in hand, we performed in vivo PET imaging studies of [^{64}Cu]Cu-NT-Sarcage in H1299-tumor–bearing mice (Fig. 7). [^{64}Cu]Cu-NT-Sarcage showed high tumor uptake with low background and high tumor retention at 48 h after injection. Initial labeling with Co also revealed interesting results (*42*). Remarkably, **6** can be modified further to add a second ligand to the cage. In this regard, a PSMA ligand (Lys-Glu-urea or *N*-[[[(1*S*)-5-amino-1-carboxypentyl]amino]carbonyl]-L-glutamic acid (**13**)) was linked to **6,** which may serve as a dual-targeting agent to address tumor heterogeneity limitations (**16a** and **16b**; section 2.5 of the supplemental materials). Detailed biologic evaluations of NT-Sarcage-PSMA compounds **16a** and **16b** as well as NT-CB–based precursors **11** and **12** will be performed in follow-up studies.

Tracer-Specific Binding to NTSR-1

We validated that the high tumor uptake was due to the specific binding of [^{64}Cu]Cu-NT-CB-NOTA to NTSR-1 by performing in vivo blocking experiments. The experiments were conducted by injecting a 100-fold molar excess of unlabeled neurotensin peptide (blocking agent) before the radioactive tracer in H1299-tumor–bearing nu/nu mice (section 11 of the supplemental materials). Also, the different tumor uptake of [^{55}Co]Co-NT-CB-NOTA between HT29 (high NTSR-1 expression) and Caco2 (low NTSR-1 expression) tumor models suggested specificity of the tracer for NTSR-1 (Fig. 5). Furthermore, the [^{55}Co]Co-NT-CB-NOTA cell surface binding and internalization potentials were tested in NTSR-1–positive HT29 cells. The binding saturation assays determined a dissociation constant of 3 ± 2 nM and an NTSR-1 density of $(0.7 \pm 0.2) \times 10^5$ per HT29 cell using a one-site binding model (section 6 of the supplemental materials; Supplemental Fig. 7A). [^{55}Co]Co-NT-CB-NOTA internalization reached a calculated plateau of 34% ± 2% cell-associated activity and a monoexponential internalization rate of $(1.7 \pm 0.3) \times 10^{-2}$ min^{-1} (section 6 of the supplemental materials; Supplemental Fig. 7B).

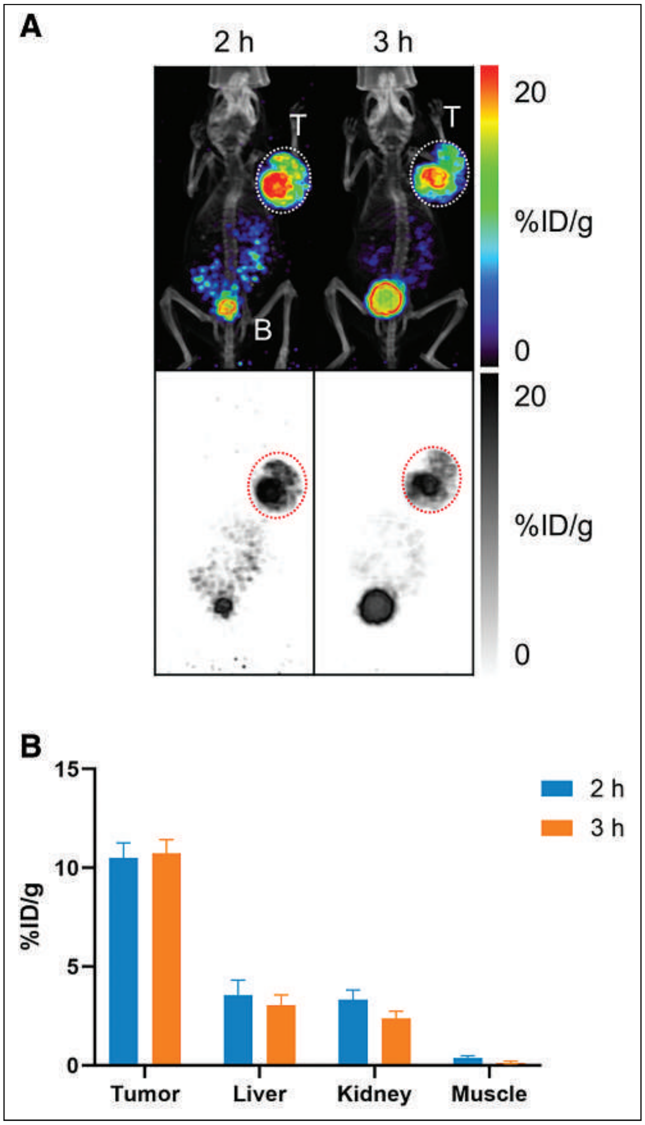

FIGURE 4. (A) Three-dimensional PET/CT images of [^{68}Ga]Ga-NT-CB-NOTA in H1299-tumor–bearing nu/nu mice at 2 and 3 h after injection. (B) Quantitative analysis of [^{68}Ga]Ga-NT-CB-NOTA in H1299-tumor–bearing mice at 2 and 3 h after injection. B = bladder; %ID/g = percentage injected dose per gram; T = tumor.

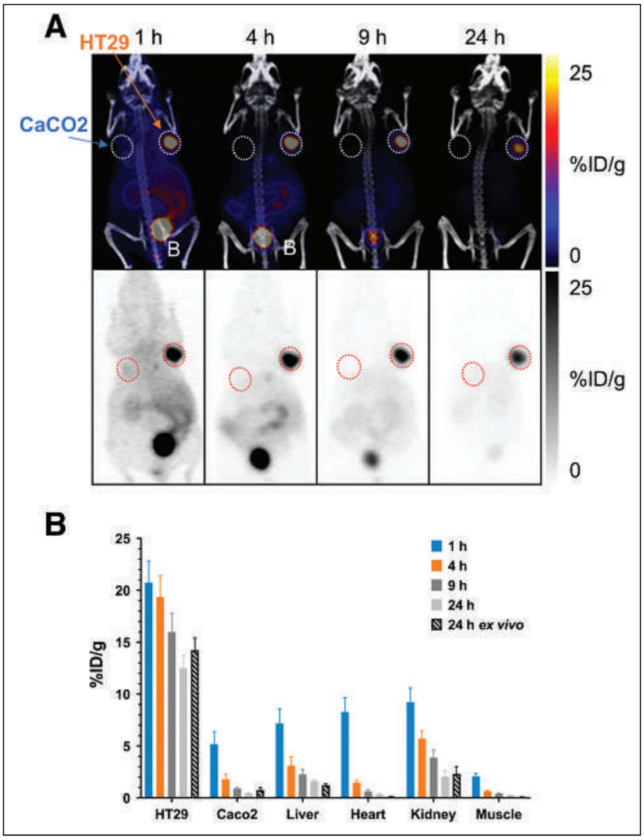

FIGURE 5. (A) Three-dimensional PET/CT images of [^{55}Co]Co-NT-CB-NOTA in HT29-tumor–bearing mice at 1, 4, 9, and 24 h after injection. Caco2 tumor is shown on left shoulder; HT29 tumor is shown on right shoulder. (B) Quantitative analysis of [^{55}Co]Co-NT-CB-NOTA in HT29-tumor–bearing mice at 1, 4, 9, 24, and 24 h ex vivo after injection. B = bladder; %ID/g = percentage injected dose per gram; T = tumor.

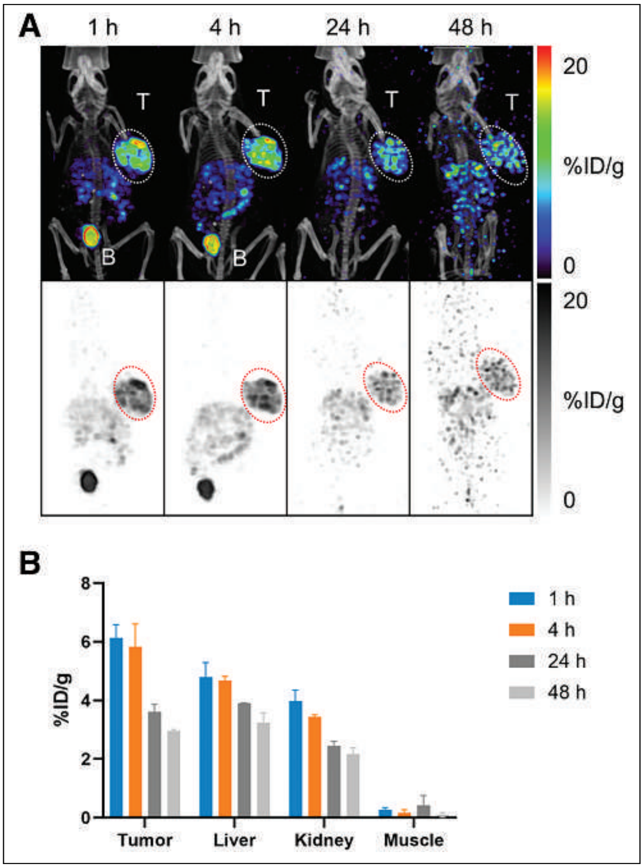

FIGURE 6. (A) Three-dimensional PET/CT representative images of [^{64}Cu]Cu-NT-CB-DOTA in H1299-tumor–bearing mice at 1, 4, 24, and 48 h after injection. (B) Quantitative analysis of [^{64}Cu]Cu-NT-CB-DOTA in H1299-tumor–bearing mice at 1, 4, 24, and 48 h after injection. B = bladder; %ID/g = percentage injected dose per gram; T = tumor.

DISCUSSION

To develop novel NTSR-1–targeting radiopharmaceuticals with improved tumor uptake, improved tumor-to-background ratio, and extended tumor residence, we elaborated a strategy to attach MAs to a synthetic antagonistic NTSR-1 ligand. The hypothesis was based on the fact that the net charge around the tracer may be modified by introducing chelators or linker–chelator combinations with several basic nitrogen atoms. Our results showed that the combination of CB-NOTA (linker–chelator) and the bicyclic Sarcage (chelator) directly attached to the neurotensin ligand significantly improved the in vivo PET imaging tumor uptake and tumor-to-background ratio (especially tumor-to-liver ratios) even up to 48 h after injection.

It is worth addressing some future directions of this study. First, our platform showed promising results in the NTSR-1 system. Other target/ligand systems should be used together with CB-NOTA and Sarcage to evaluate the generality of this approach. Second, macrocycles CB-cyclam and Sarcage were the 2 MAs we put to the test. It remains to be seen how other macrocycles may affect these results in terms of size, number of nitrogen atoms, and attachment to the ligand. Third, we were focused on the characterization of **9** because of its ability to chelate multiple radiometals. However, [^{64}Cu]Cu-NT-Sarcage showed increased tumor uptake compared with [^{64}Cu]Cu-NT-CB-NOTA. Fourth, [^{64}Cu]Cu-NT-CB-NOTA and [^{55}Co]Co-NT-CB-NOTA also showed different uptake values in 2 tumor models. Whether the different uptake was caused by the radioisotope or the tumor model needs to be confirmed further. Fifth, in the case of [^{64}Cu]Cu-NT-CB-NOTA and [^{64}Cu]Cu-NT-CB-DOTA, there may be concerns that the ^{64}Cu chelation may have occurred at both the CB-cyclam unit and the chelator. However, CB-cyclam generally requires 90°C heating to form a stable complex with ^{64}Cu during labeling, and it is reasonable to assume that the chelation happened at the NOTA or DOTA locations when heated at 37°C (conditions used in this study). Nonetheless, direct evidence is still needed to confirm this assumption. Sixth, direct comparison with 3BP-227 would have resulted in a better reference to compare with the data obtained from our tracers. Nevertheless, the focus of this research was to improve tumor uptake and retention and to reduce liver uptake. We, therefore, did not compare our agent with 3BP-227 in this research. Finally, the effect of ^{177}Lu with precursors **9** and **10** also remains to be determined, which was not done in this study.

Recently, Garrison et al. used the same synthetic antagonistic NTSR-1–targeting ligand with a different approach to extend the tumor residence time (*43–45*). They proposed a strategy in which low-molecular-weight targeted ligands were attached to irreversible cysteine cathepsin inhibitors. Once the ligand was internalized and transported to the endolysosomal compartments of the cell, the cysteine cathepsin inhibitors (or endolysosomal trapping agents)

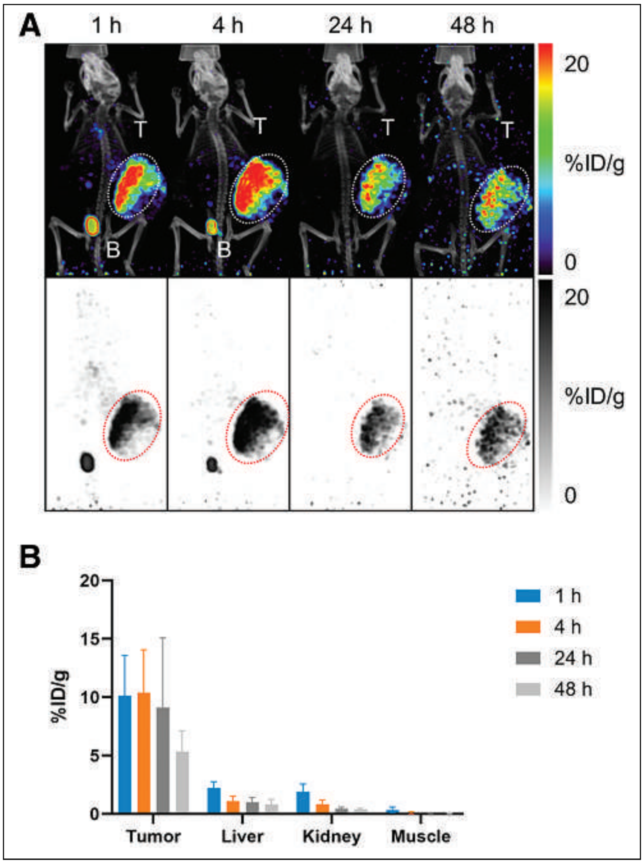

FIGURE 7. (A) Three-dimensional PET/CT images of [^{64}Cu]Cu-NT-Sarcage in H1299-tumor–bearing nu/nu mice at 1, 4, 24, and 48 h after injection. Note that animal-to-animal and tumor size differences were mainly responsible for data spread observed within this group. (B) Quantitative analysis of [^{64}Cu]Cu-NT-Sarcage in H1299-tumor–bearing mice at 1, 4, 24, and 48 h after injection. B = bladder; %ID/g = percentage injected dose per gram; T = tumor.

formed high-molecular-weight irreversible adducts with cysteine proteases. In this way, the receptor-targeted constructs were able to increase tumor retention. In the same study, the impact of charge modification around the cysteine cathepsin inhibitors was also tested in vitro and in vivo using HT29 colon cancer models (*45*). This approach introduced another structural motif to the tracer (cysteine inhibitor), and the construct needed to interact with cysteine proteases. In the future, it would be interesting to perform a side-by-side comparison with our approach that requires the selection of only a chelator or linker–chelator construct and interaction with only 1 target. We also point out that our initial in vivo studies are being conducted using lung and colorectal cancer models to avoid direct competition with Pluvicto. In a follow-up study, it would be interesting to investigate the potential complementary role of NTSR-1–targeted agents alongside Pluvicto in prostate cancer.

CONCLUSION

In this study, we synthesized several new NTSR-1–targeting radiopharmaceuticals based on a nonpeptidic antagonist ligand. Our synthetic rationale was based on the hypothesis that MAs can modulate the net charge around the tracer, which in turn favors its tumor retention through the interaction with the negatively charged external surface of a cell. In this regard, CB-NOTA and Sarcage moieties were found to improve tumor uptake, tumor-to-background ratio, and tumor retention even at 48 h after injection compared with the acyclic 3MA unit. The results of this study suggest that **9** labeled with ^{64}Cu/^{67}Cu, ^{55}Co/^{58m}Co, or ^{68}Ga and **6** labeled with ^{64}Cu/^{67}Cu or ^{55}Co/^{58m}Co may be excellent diagnostic and therapeutic radiopharmaceuticals for NTSR-1–positive cancers that could progress into the clinic. Given the common presence of MAs in drug molecules, it is possible that these MAs could be replaced with CB-NOTA or Sarcage for easy conversion to radiotheranostic agents.

DISCLOSURE

This work was supported in part by the National Science Foundation under grant CHE-1726291 and by National Institutes of Health grants 5R01CA247769, 1R43CA261503, NIH/NCI P01-CA250972, and NCI P30 CA014520. PET/CT imaging was carried out in the UNC Small Animal Imaging Core Facility. The imaging core is supported in part by NIH grant P30-CA016086, and the PET/CT system was funded by NIH grant S10-OD023611. A patent has been filed on intellectual property relating to this work that has been licensed from UNC Chapel Hill to Accunovo Biotech. Zibo Li is one of the cofounders of Accunovo Biotech. No other potential conflict of interest relevant to this article was reported.

ACKNOWLEDGMENTS

We thank the University of North Carolina's Department of Chemistry Mass Spectrometry Core Laboratory, especially Antonio Lazaro Toledo Machin and Brandie Michelle Ehrmann, for their assistance with mass spectrometry analysis. We gratefully acknowledge Justin Jeffery, Ashley Weichmann, and Dr. Zachary Rosenkrans at the University of Wisconsin Carbone Cancer Center for their assistance with animal experiments.

KEY POINTS

QUESTION: Is it possible to develop NTSR-1–targeted radiopharmaceuticals with high tumor uptake, sustained tumor retention, and low background uptake that hold potential for theranostic applications in the clinic?

PERTINENT FINDINGS: With MAs introduced to the NTSR-1 ligand, the resulting agents [^{64}Cu]Cu-NT-CB-NOTA, ^{68}Ga]Ga-NT-CB-NOTA, [^{55}Co]Co-NT-CB-NOTA, and [^{64}Cu]Cu-NT-Sarcage showed high tumor uptake and retention with low background on PET imaging.

IMPLICATIONS FOR PATIENT CARE: This study suggests that leading precursors NT-CB-NOTA and NT-Sarcage are excellent diagnostic and therapeutic candidates as NTSR-1–targeted theranostic agents, which may benefit prostate cancer patients with low PSMA expression.

REFERENCES

1. Annual report to the nation 2022: overall cancer statistics. NIH website. https://seer.cancer.gov/report_to_nation/statistics.html. Updated December 20, 2023. Accessed May 15, 2024.
2. Rebello RJ, Oing C, Knudsen KE, et al. Prostate cancer. *Nat Rev Dis Primers.* 2021;7:9.
3. Posdzich P, Darr C, Hilser T, et al. Metastatic prostate cancer: a review of current treatment options and promising new approaches. *Cancers (Basel).* 2023;15:461.

4. Malcolm J, Falzone N, Lee BQ, Vallis KA. Targeted radionuclide therapy: new advances for improvement of patient management and response. *Cancers (Basel).* 2019;11:268.
5. FDA approves Pluvicto/Locametz for metastatic castration-resistant prostate cancer. *J Nucl Med.* 2022;63(5):13N.
6. Jadvar H. The VISION forward: recognition and implication of PSMA−/^{18}F-FDG+ mCRPC. *J Nucl Med.* 2022;63:812–815.
7. Cai M, Son XL, Li XA, et al. Current therapy and drug resistance in metastatic castration-resistant prostate cancer. *Drug Resist Updat.* 2023;68:100962.
8. AlSadi R, Bouhali O, Dewji S, Djekidel M. ^{177}Lu-PSMA therapy for metastatic castration-resistant prostate cancer: a mini-review of state-of-the-art. *Oncologist.* 2022;27:e957–e966.
9. Juzeniene A, Stenberg VY, Bruland ØS, Larsen RH. Preclinical and clinical status of PSMA-targeted alpha therapy for metastatic castration-resistant prostate cancer. *Cancers (Basel).* 2021;13:779.
10. Inderjeeth AJ, Iravani A, Subramaniam S, Conduit C, Sandhu S. Novel radionuclide therapy combinations in prostate cancer. *Ther Adv Med Oncol.* 2023;15: 17588359231187202.
11. Sandhu S, Guo C, Hofman MS. Radionuclide therapy in prostate cancer: from standalone to combination PSMA theranostics. *J Nucl Med.* 2021;62:1660–1668.
12. El Fakiri M, Geis NM, Ayada N, Eder M, Eder AC. PSMA-targeting radiopharmaceuticals for prostate cancer therapy: recent developments and future perspectives. *Cancers (Basel).* 2021;13:3967.
13. Falkmer S, Askensten U, Grimelius L, Abrahamsson PA. Cytochemical markers and DNA content of neuroendocrine cells in carcinoma of the prostate gland during tumour progression. *Acta Histochem Suppl.* 1990;38:127–132.
14. Huang J, Wu C, di Sant'Agnese PA, Yao JL, Cheng L, Na Y. Function and molecular mechanisms of neuroendocrine cells in prostate cancer. *Anal Quant Cytol Histol.* 2007;29:128–138.
15. Oesterling JE, Hauzeur CG, Farrow GM. Small cell anaplastic carcinoma of the prostate: a clinical, pathological and immunohistological study of 27 patients. *J Urol.* 1992;147:804–807.
16. Lee LF, Guan J, Qiu Y, Kung HJ. Neuropeptide-induced androgen independence in prostate cancer cells: roles of nonreceptor tyrosine kinases Etk/Bmx, Src, and focal adhesion kinase. *Mol Cell Biol.* 2001;21:8385–8397.
17. Swift SL, Burns JE, Maitland NJ. Altered expression of neurotensin receptors is associated with the differentiation state of prostate cancer. *Cancer Res.* 2010;70:347–356.
18. Amorino GP, Deeble PD, Parsons SJ. Neurotensin stimulates mitogenesis of prostate cancer cells through a novel c-Src/Stat5b pathway. *Oncogene.* 2007;26:745–756.
19. Elek J, Pinzon W, Park KH, Narayanan R. Relevant genomics of neurotensin receptor in cancer. *Anticancer Res.* 2000;20:53–58.
20. Abrahamsson PA, Wadström LB, Alumets J, Falkmer S, Grimelius L. Peptide-hormone- and serotonin-immunoreactive tumour cells in carcinoma of the prostate. *Pathol Res Pract.* 1987;182:298–307.
21. Sehgal I, Powers S, Huntley B, Powis G, Pittelkow M, Maihle NJ. Neurotensin is an autocrine trophic factor stimulated by androgen withdrawal in human prostate cancer. *Proc Natl Acad Sci USA.* 1994;91:4673–4677.
22. Seethalakshmi L, Mitra SP, Dobner PR, Menon M, Carraway RE. Neurotensin receptor expression in prostate cancer cell line and growth effect of NT at physiological concentrations. *Prostate.* 1997;31:183–192.
23. Burkett BJ, Bartlett DJ, McGarrah PW, et al. A review of theranostics: perspectives on emerging approaches and clinical advancements. *Radiol Imaging Cancer.* 2023; 5:e220157.
24. Li M, Wang S, Kong Q, et al. Advances in macrocyclic chelators for positron emission tomography imaging. *VIEW.* 2023;4:20230042.
25. Barrett KE, Houson HA, Lin W, Lapi SE, Engle JW. Production, purification, and applications of a potential theranostic pair: cobalt-55 and cobalt-58m. *Diagnostics (Basel).* 2021;11:1235.
26. Liu S, Li Z, Conti PS. Development of multi-functional chelators based on sarcophagine cages. *Molecules.* 2014;19:4246–4255.
27. Deng H, Wang H, Zhang H, et al. Imaging neurotensin receptor in prostate cancer with ^{64}Cu-labeled neurotensin analogs. *Mol Imaging.* 2017;16:1536012117711369.
28. Iyer MR, Kunos G. Therapeutic approaches targeting the neurotensin receptors. *Expert Opin Ther Pat.* 2021;31:361–386.
29. Maschauer S, Prante O. Radiopharmaceuticals for imaging and endoradiotherapy of neurotensin receptor-positive tumors. *J Labelled Comp Radiopharm.* 2018;61: 309–325.
30. Schulz J, Rohracker M, Stiebler M, et al. Proof of therapeutic efficacy of a ^{177}Lu-labeled neurotensin receptor 1 antagonist in a colon carcinoma xenograft model. *J Nucl Med.* 2017;58:936–941.
31. Baum RP, Singh A, Schuchardt C, et al. ^{177}Lu-3BP-227 for neurotensin receptor 1–targeted therapy of metastatic pancreatic adenocarcinoma: first clinical results. *J Nucl Med.* 2018;59:809–814.
32 . Fusion Pharmaceuticals announces first patient dosed in phase 1 study of FPI-2059, a targeted alpha therapy (TAT) for the treatment of solid tumors expressing NTSR1. Fusion Pharmaceuticals website. https://ir.fusionpharma.com/2023-03-20-Fusion-Pharmaceuticals-Announces-First-Patient-Dosed-in-Phase-1-Study-of-FPI-2059,-a-Targeted-Alpha-Therapy-TAT-for-the-Treatment-of-Solid-Tumors-Expressing-NTSR1. Updated March 20, 2023. Accessed May 15, 2024.
33. Engle JW. The production of Ac-225. *Curr Radiopharm.* 2018;11:173–179.
34. Zhang T, Ma X, Xu M, et al. Chelator boosted tumor-retention and pharmacokinetic properties: development of ^{64}Cu labeled radiopharmaceuticals targeting neurotensin receptor. *Eur J Nucl Med Mol Imaging*. May 21, 2024 (Epub ahead of print].
35. Holik HA, Ibrahim FM, Elaine AA, Putra BD, Achmad A, Kartamihardja AHS. The chemical scaffold of theranostic radiopharmaceuticals: radionuclide, bifunctional chelator, and pharmacokinetics modifying linker. *Molecules.* 2022;27:3062.
36. Metwally S, Stachewicz U. Surface potential and charges impact on cell responses on biomaterials interfaces for medical applications. *Mater Sci Eng C Mater Biol Appl.* 2019;104:109883.
37. Li M, Ma X, Molnar CJ, et al. Modular PET agent construction strategy through strain-promoted double-click reagent with efficient photoclick step. *Bioconjugate Chem.* 2022;33:2088–2096.
38. Lin W, Aluicio-Sarduy E, Houson HA, et al. Theranostic cobalt-55/58m for neurotensin receptor-mediated radiotherapy in vivo: a pilot study with dosimetry. *Nucl Med Biol.* 2023;118:108329.
39. Avila-Rodriguez MA, Nye JA, Nickles RJ. Simultaneous production of high specific activity ^{64}Cu and ^{61}Co with 11.4 MeV protons on enriched ^{64}Ni nuclei. *Appl Radiat Isot.* 2007;65:1115–11120.
40. Lin W, Aluicio-Sarduy E, Barrett KE, et al. Separation of cyclotron-produced cobalt-55/58m from iron targets using cation exchange chromatography with non-aqueous solvents and extraction chromatography. *Appl Radiat Isot.* 2023;200: 110980.
41. Lang C, Gmeiner P. Efficient synthesis of heterocyclic neurotensin receptor ligands by microwave-assisted aminocarbonylation. *Synthesis.* 2013;45:2474–2480.
42. Lin W, Fonseca Cabrera GO, Aluicio-Sarduy E, et al. Radiolabeling diaminosarcophagine with cyclotron-produced cobalt-55 and [^{55}Co]Co-NT-Sarcage as a proof of concept in a murine xenograft model. *Bioconjugate Chem*. 2024;35:412–418.
43. Fan W, Zhang W, Allen S, et al. Examination of charge modifications of an endolysosomal trapping inhibitor in an antagonistic NTSR1-targeted construct for colon cancer. *Bioconjug Chem.* 2022;33:1363–1376.
44. Fan W, Zhang W, Alshehri S, Garrison JC. Examination of the impact molecular charge has on NTSR1-targeted agents incorporated with cysteine protease inhibitors. *Eur J Med Chem.* 2022;234:114241.
45. Fan W, Zhang W, Alshehri S, Neeley TR, Garrison JC. Enhanced tumor retention of NTSR1-targeted agents by employing a hydrophilic cysteine cathepsin inhibitor. *Eur J Med Chem.* 2019;177:386–400.

Design of a Fibroblast Activation Protein–Targeted Radiopharmaceutical Therapy with High Tumor–to–Healthy-Tissue Ratios

Ramesh Mukkamala[1], Daniel J. Carlson[1], Nicholas Kaine Miller[1], Spencer D. Lindeman[1], Emily Renee Bowen[1], Pooja Tudi[1], Taylor Schleinkofer[1], Owen C. Booth[1], Abigail Cox[2], Madduri Srinivasarao[1], and Philip S. Low[1]

[1]Department of Chemistry and Institute for Drug Discovery, Purdue University, West Lafayette, Indiana; and [2]Department of Comparative Pathobiology, Purdue College of Veterinary Medicine, West Lafayette, Indiana

Because of upregulated expression on cancer-associated fibroblasts, fibroblast activation protein (FAP) has emerged as an attractive biomarker for the imaging and therapy of solid tumors. Although many FAP ligands have already been developed for radiopharmaceutical therapies (RPTs), most suffer from inadequate tumor uptake, insufficient tumor residence times, or off-target accumulation in healthy tissues, suggesting a need for further improvements. **Methods:** A new FAP-targeted RPT with a novel ligand (FAP8-PEG$_3$-IP-DOTA) was designed by combining the desirable features of several previous ligand-targeted RPTs. Uptake and retention of [^{111}In]In or [^{177}Lu]Lu-FAP8-PEG$_3$-IP-DOTA were assessed in KB, HT29, MDA-MB-231, and 4T1 murine tumor models by radioimaging or ex vivo biodistribution analyses. Radiotherapeutic potencies and gross toxicities were also investigated by monitoring tumor growth, body weight, and tissue damage in tumor-bearing mice. **Results:** FAP8-PEG$_3$-IP-DOTA exhibited high affinity (half-maximal inhibitory concentration, 1.6 nM) and good selectivity for FAP relative to its closest homologs, prolyl oligopeptidase (half-maximal inhibitory concentration, ~14.0 nM) and dipeptidyl peptidase-IV (half-maximal inhibitory concentration, ~860 nM). SPECT/CT scans exhibited high retention in 2 different solid tumor models and minimal uptake in healthy tissues. Quantitative biodistribution analyses revealed tumor–to–healthy-tissue ratios of more than 5 times for all major organs, and live animal studies demonstrated 65%–93% suppression of tumor growth in all 4 models tested, with minimal or no evidence of systemic toxicity. **Conclusion:** We conclude that [^{177}Lu]Lu-FAP8-PEG$_3$-IP-DOTA constitutes a promising and safe RPT candidate for FAPα-targeted radionuclide therapy of solid tumors.

Key Words: radionuclide therapy; fibroblast activation protein; albumin binder; cancer-associated fibroblast; tumor microenvironment

J Nucl Med 2024; 65:1257–1263
DOI: 10.2967/jnumed.124.267756

Fibroblast activation protein α (FAP) is a serine protease that is overexpressed on cancer-associated fibroblasts in about 90% of human epithelial tumors (*1*). Because FAP is minimally expressed in healthy tissues (*1*), the cell surface receptor has become an attractive biomarker for the diagnosis and treatment of human cancers. Indeed, a FAP-targeted ^{68}Ga-radioimaging agent has been recently shown to image 28 different human cancer types (*2*), and multiple FAP-targeted radioligands have entered clinical trials for imaging or therapy of solid tumors (*3–7*). However, whereas preclinical development of FAP-targeted radioligands has been steadily expanding, their radiotherapeutic potencies have frequently suffered from insufficient tumor uptake, inadequate tumor residence times, or unacceptable accumulation in the healthy tissues, especially when physiologically relevant tumor models have been used (*8–10*). Although we and others have attempted to address these inadequacies with improved versions of FAP-targeted radiopharmaceutical therapies (RPTs) (*11–13*), none have achieved the tumor–to–healthy-tissue dosimetry ratios needed to eradicate tumors without causing significant off-target damage (*14,15*).

We report here the design, synthesis, and evaluation in vitro and in vivo of a new FAP-targeted radioligand (FAP8-PEG$_3$-IP-DOTA) that exhibits superior properties to previous candidates. To achieve these improvements, we have incorporated the optimal features of 3 ligand-targeted RPTs described by others, namely the basic ligand scaffold of Šimková et al. (*16*), which reports picomolar affinity for FAP; the gem-difluoro modification of Jansen et al. (*17*), which endows their compound **60** with excellent ligand specificity for FAP over prolyl oligopeptidase (PREP); and the albumin-binding moiety of the radiofolate cm09 of Müller et al., which increases its pharmacokinetics and accumulation in solid tumors (*18*). We then demonstrate that this novel trifunctional conjugate, FAP8-PEG$_3$-IP-DOTA, exhibits the improved affinity, enhanced organ specificity, elevated tumor accumulation, and reduced healthy-tissue toxicity expected of the composite RPT and propose that it should qualify for possible preclinical development.

MATERIALS AND METHODS

Synthetic schemes for FAP8 (**2**), FAP8-PEG$_3$-IP-DOTA (**3**), FAP8-PEG$_3$-DOTA (**4**), and FAP8-PEG$_3$-FITC (**5**) are given in Figure 1, with complete experimental procedures presented in Supplemental Schemes 1–4 (supplemental materials are available at http://jnm.snmjournals.org). Protocol details for all studies are also presented in the supplemental material (*19–20*).

Cell Culture

Cancer cell lines 4T1, KB, HT29, and MDA-MB-231 were purchased from ATCC and cultured as formerly reported (*21*). HEK-293T cells transduced to express high levels of human FAP (HEK-hFAP) were previously generated (*22*).

Received Mar. 9, 2024; revision accepted May 13, 2024.
For correspondence or reprints, contact Philip S. Low (plow@purdue.edu).

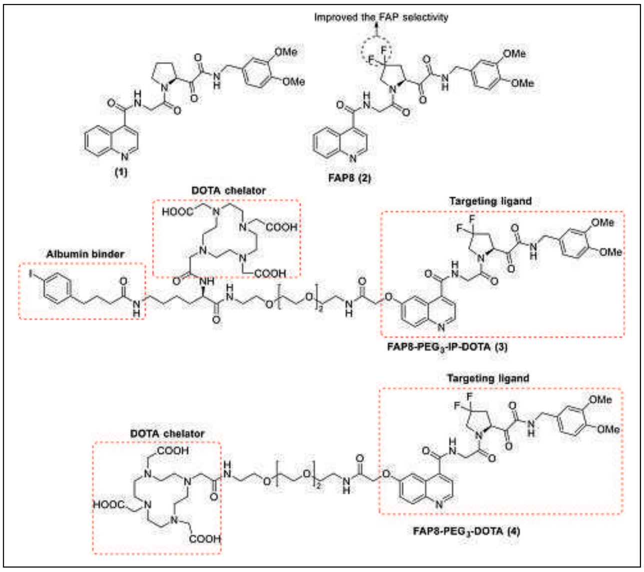

FIGURE 1. Chemical structures of inhibitor (**1**) (*16*), FAP-targeting ligand (FAP8) (**2**), FAP8-PEG$_3$-IP-DOTA (**3**), and FAP8-PEG$_3$-DOTA (**4**).

Radiolabeling

FAP8-PEG$_3$-DOTA or FAP8-PEG$_3$-IP-DOTA was dissolved in NH$_4$OAc buffer (1.0 M, pH 7.0) and labeled with [^{111}In]In^{3+} (BWMX Canada) or [^{177}Lu]Lu^{3+} (National Isotope Development Center).

Animal Husbandry

Mice were provided normal rodent chow and water ad libitum and maintained on a standard 12-h light–dark cycle. All animal procedures were approved by the Purdue Animal Care and Use Committee.

Tumor Models

BALB/c mice were inoculated on their shoulders with 1 × 10^5 4T1 cells, whereas nu/nu mice were inoculated on their shoulders with 5 × 10^6 HT29, KB, MDA-MB-231, or HEK-hFAP cells.

SPECT/CT Scans

HT29 and KB tumor–bearing mice were injected intravenously with [^{111}In]In-FAP8-PEG$_3$-IP-DOTA (∼15 MBq/mouse), and SPECT/CT scans were taken at multiple time points over the course of 1 wk.

Ex Vivo Radioligand Biodistribution

Mice implanted with 4T1 or HEK-hFAP tumors were intravenously injected with [^{177}Lu]Lu-FAP8-PEG$_3$-IP-DOTA, and ex vivo biodistribution measurements of select organs were taken at several time points.

Dosimetry Analysis

From the biodistribution data, the total absorbed radiation doses (mGy/MBq) were calculated using OLINDA 2.2.3 software as previously described (*11,23*).

Radiopharmaceutical Therapy

4T1, HT29, KB, and MDA-MB231 tumor–bearing mice were randomized into control and treatment groups to ensure similar average starting tumor volumes. Each cohort received a single intravenous injection of saline or [^{177}Lu]Lu-FAP8-PEG$_3$-IP-DOTA on day 0, as indicated.

Toxicology

Mice were weighed every other day during RPT to evaluate gross toxicity. Tissue sections from organs of interest (1–8/organ per mouse) were preserved and examined for lesions in a masked manner by a board-certified veterinary pathologist.

Statistical Analysis

Data were analyzed using GraphPad Prism 9 unless otherwise stated. All results are presented as mean ± SE.

RESULTS

Evaluation of Binding Affinity and Specificity of FAP8 Conjugates

To determine the binding affinity and specificity of the new FAP8 ligand (compound **2**) and FAP8-PEG$_3$-IP-DOTA conjugate (compound **3**) (Fig. 1), we measured the inhibition potency of each compound against FAP and its closest homologs, PREP and DPP-IV. As detailed in Figure 2A and Supplemental Table 1, FAP8 preferentially inhibited FAP over PREP and DPP-IV, with half-maximal inhibitory concentrations of 0.76, 13, and more than 3,000 nM, respectively, whereas FAP8-PEG$_3$-IP-DOTA exhibited half-maximal inhibitory concentrations for the same 3 peptidases of 1.6, 14, and 860 nM, respectively (Fig. 2B). Introduction of the gem-difluoro moiety onto the proline of FAP8 ligand improved its selectivity for FAP over PREP by 7.5-fold relative to inhibitor **1** (*16*) as anticipated. The same modification also stabilized the linear form of inhibitor **1** over its cyclized tautomer, thereby increasing its affinity for FAP. Moreover, analysis of the direct binding of fluorescent (FAP8-PEG$_3$-FITC) (**5**) (Supplemental Scheme 2) and radiolabeled ([^{177}Lu]Lu-FAP8-PEG$_3$-IP-DOTA) FAP8 conjugates to HEK-hFAP cells revealed dissociation constants of about 1.2 and 3.0 nM, respectively (Figs. 2C and 2D). Because this binding could be significantly inhibited on coincubation with excess unlabeled FAP8

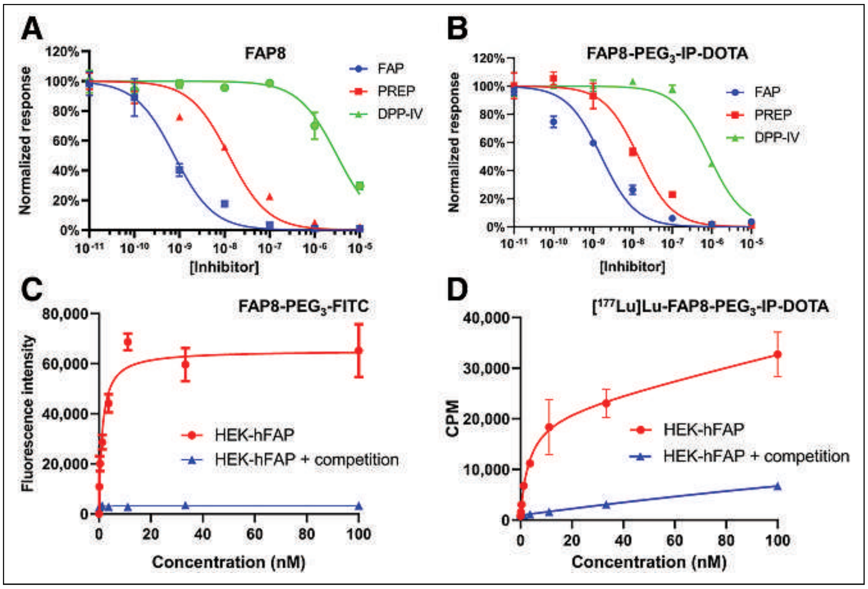

FIGURE 2. Measurements of enzyme inhibition of FAP, PREP, and DPP-IV by FAP8 ligand (**2**) (A) and FAP8-PEG$_3$-IP-DOTA (**3**) (B). Binding of FAP8-PEG$_3$-FITC (C) and [^{177}Lu] Lu-FAP8-PEG$_3$-IP-DOTA (D) to HEK-hFAP cells.

conjugate (Figs 2C and 2D), we conclude that both of these binding interactions were FAP-mediated.

Ex Vivo Biodistribution Analysis

Motivated by the encouraging binding affinity and specificity of FAP8 conjugates for FAP, we next evaluated the impact of an albumin binder on both the uptake and the specificity of the FAP8-PEG$_3$-DOTA conjugate for the tumor. For this purpose, the biodistributions of [^{177}Lu]Lu-FAP8-PEG$_3$-IP-DOTA and [^{177}Lu]Lu-FAP8-PEG$_3$-DOTA were compared, where the only difference between the 2 compounds was the 4-iodophenylbutyryllysine (IP) inserted between the PEG and the DOTA (Fig. 1, structure **4**). As shown in Supplemental Figure 2, insertion of the IP increased the net tumor uptake of conjugate by about 10 times while improving both the tumor-to-kidney and the tumor-to-liver ratios by more than 2 times. These results argued in favor of including the IP insertion in all further forms of FAP8 RPTs.

Next, to determine the preferred mass dose for achieving an ideal tumor–to–healthy-tissue ratio, we chelated a fixed amount of [^{177}Lu]LuCl$_3$ (7.4 MBq/mouse) with 3 different concentrations of FAP8-PEG$_3$-IP-DOTA (0.3, 1.0, and 5.0 nmol/mouse) and injected the radioligands into mice bearing syngeneic 4T1 breast cancer cells in which the only FAP+ cells were derived from naturally infiltrating cancer-associated fibroblasts. Analysis of the resulting ex vivo biodistribution data revealed that mice injected with lower doses of [^{177}Lu]Lu-FAP8-PEG$_3$-IP-DOTA (0.3 and 1.0 nmol/mouse) exhibited slightly lower tumor uptake at early time points (5–6 percentage injected dose [%ID]/g at 1 h after injection and 5%–9 %ID/g at 4 h after injection) than did mice injected with 5 nmol/mouse (~9 %ID/g at 1 h after injection and 11 %ID/g at 4 h after injection) (Figs. 3A–3C; Supplemental Tables 2–4). These initial tumor uptake values gradually decreased to 3.4 ± 1 %ID/g, 5 ± 1.6 %ID/g, and 2.2 ± 0.3 %ID/g for the 0.3, 1.0, and 5 nmol/mouse doses, respectively, by 168 h after injection. In mice injected with 5 nmol of FAP8-PEG$_3$-IP-DOTA, there was rapid clearance from both the liver (decreasing from 5.3 ± 0.90 %ID/g to ~1 %ID/g) and the kidneys (decreasing from 4.8 ± 2.4 to 0.30 ± 0.39 %ID/g by 168 h after injection), leading to a steady increase in tumor–to–healthy-tissue ratio in these organs (Fig. 3G). In contrast, mice injected with 0.3 or 1 nmol exhibited consistently higher uptake in the liver (7.1 ± 2.0 %ID/g to 4.9 ± 0.5 %ID/g), spleen (4.1 ± 1.8 to 1.9 ± 0.45 %ID/g), and kidneys (4.9 ± 3.3 to 1.6 ± 0.7 %ID/g) at all time points tested, resulting in decreased tumor–to–healthy-tissue ratios (Figs. 3E and 3F). Although tumor uptake was slightly higher for doses of 0.3 and 1.0 nmol/mouse (3.4 ± 1 %ID/g and 5 ± 1.6 %ID/g, respectively) than for 5 nmol/mouse (2.2 ± 0.3 %ID/g) at 168 h after injection, the tumor–to–healthy-tissue ratios were lower for the 0.3- and 1.0-nmol doses than for the 5-nmol dose. From this experiment, we conclude that the best tumor–to–healthy-tissue ratios were achieved when 5 nmol of FAP8-PEG$_3$-IP-DOTA per mouse were administered.

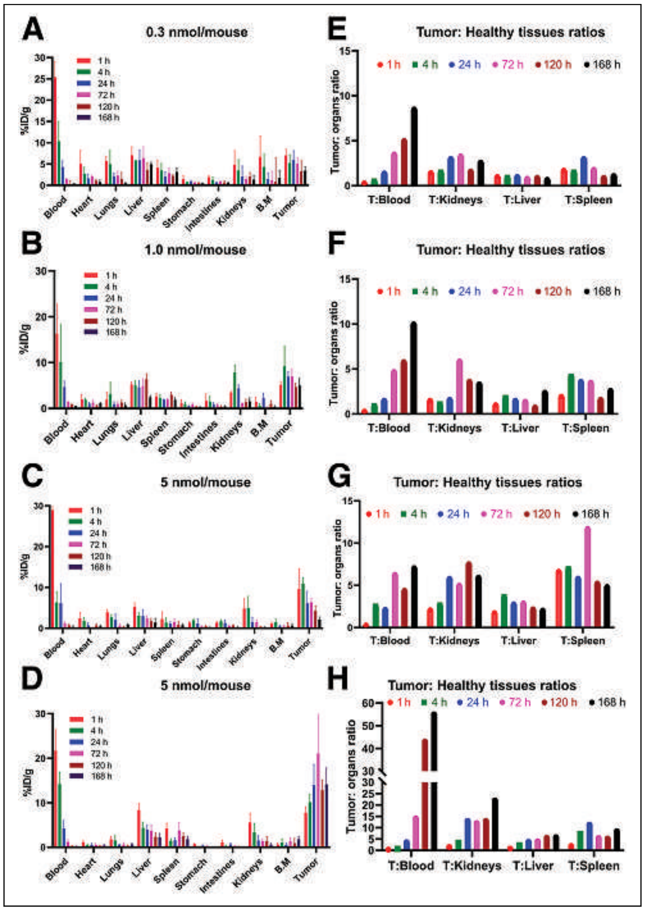

FIGURE 3. (A–D) Biodistribution analyses of [^{177}Lu]Lu-FAP8-PEG$_3$-IP-DOTA in 4T1 (A–C) and HEK-hFAP (D) tumor–bearing mice (4/time point). (E, F, G, and H) Calculated tumor-to-healthy tissues ratios from data in panels A, B, C, and D, respectively. B.M = bone marrow.

Because most previously published data on FAP-targeted radioligands have used tumor models in which the cancer cells were artificially transduced to express FAP (e.g., HEK-hFAP or HT1080-FAP) (*8,24–26*), for purposes of comparison, we elected to similarly evaluate the biodistribution of [^{177}Lu]Lu-FAP8-PEG$_3$-IP-DOTA in a tumor model in which the cancer cells were transduced with FAP. For this purpose, HEK-hFAP tumor–bearing mice were injected intravenously with 5 nmol of FAP8-PEG$_3$-IP-DOTA radiolabeled with 7.4 MBq of [^{177}Lu]Lu^{3+}. Measurement of the biodistribution at 1, 4, and 24 h after injection revealed tumor uptake of 7.8 ± 1.3 %ID/g, 10 ± 1.7 %ID/g, and 14 ± 4.6 %ID/g, respectively. This uptake further increased to 22 ± 13 %ID/g by 72 h after injection and then gradually decreased to about 14 ± 5 %ID/g by 168 h after injection (Fig. 3D). Because the total tumor uptake at 168 h was about 7 times higher than that seen in mice implanted with FAP-negative cancer cells, we conclude that nonphysiologic induction of FAP expression in cancer cells can artificially elevate the radiation doses received in a tumor mass relative to healthy tissues (Fig. 3H; Supplemental Table 5). We therefore elected to continue characterizing our FAP8 RPT only in nontransduced tumor cell lines in which FAP naturally occurs.

Comparative Dosimetry Analyses

To determine whether 5 nmol of FAP8-PEG$_3$-IP-DOTA per mouse might saturate available FAP receptors in an average 4T1 tumor, we computed the total absorbed dose of [^{177}Lu]Lu-FAP8-PEG$_3$-IP-DOTA in both solid tumors and healthy tissues (area under the curve over 168 h). As shown in Figures 4A–4C and Supplemental Tables 6–7, increasing the amount of injected FAP8-PEG$_3$-IP-DOTA by a factor of 16.7 (i.e., from 0.3 to 1.0 to 5 nmol/mouse) raised the total absorbed dose in the tumor masses only from 904 to 994 and 1,140 mGy/MBq, respectively. Because the tumor dose increased only 25% after about a 17-times increase in FAP8-PEG$_3$-IP-DOTA concentration, we conclude that the

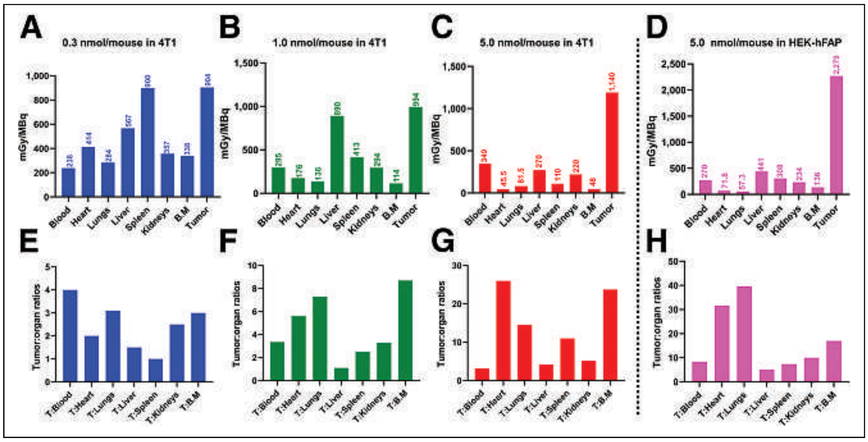

FIGURE 4. (A–D) Comparison of absorbed radiation doses by select organs in 4T1 (A–C) and HEK-hFAP (D) tumor–bearing mice. (E, F, G, and H) Calculated tumor-to-healthy tissues ratios from data in panels A, B, C, and D, respectively. B.M = bone marrow.

5 nmol/mouse dose nearly saturates the FAP receptors in 4T1 tumors. As anticipated, the total absorbed doses were approximately 2-fold higher in HEK-hFAP tumors than in 4T1 tumors (2,270 vs. 1140 mGy/MBq), whereas dosimetry for healthy tissues was more similar irrespective of the tumor model. Thus, in healthy tissues such as the kidneys and bone marrow, which are at risk for radiation toxicity (*27*), absorbed doses were 220 and 48 mGy/MBq in 4T1 tumor–bearing mice, respectively, but 234 and 134 mGy/MBq, respectively in HEK-hFAP tumor–bearing mice. Because these values are both substantially lower than the absorbed doses of 1,140 mGy/MBq in 4T1 tumors and 2,270 mGy/MBq in HEK-hFAP tumors, we conclude that FAP8-PEG$_3$-IP-DOTA delivers significantly more radiation to tumors than to healthy tissues (>5 times), regardless of the tumor model used.

Radiopharmaceutical Therapy and Toxicology

Encouraged by the favorable biodistribution and dosimetry data, we proceeded to examine the therapeutic efficacy of a single dose of [^{177}Lu]Lu-FAP8-PEG$_3$-IP-DOTA in mice bearing human breast (MDA-MB-231), cervical (KB), and colorectal (HT29) tumor xenografts. As mentioned for the 4T1 tumors described above, MDA-MB-231, KB, and HT29 cancer cells were selected for this study because the only FAP expression in the derived tumors is found on the infiltrating fibroblasts, that is, similar to the FAP expression pattern found in human tumors (*1*). As shown in Figures 5A–5C, mice treated with 37 MBq of [^{177}Lu]Lu-FAP8-PEG$_3$-IP-DOTA exhibited reductions in tumor growth rates of 93%, 65%, and 75% in the MDA-MB-231, KB, and HT29 tumor xenograft models, respectively. Although treated mice experienced a 5%–10% body weight loss during the first week of therapy, all mice subsequently recovered and survived without any obvious health complications. Moreover, whereas our Institutional Animal Care and Use Committee regulations required euthanasia of the mice before their overall survivals could be determined, the stalled tumor growth and prolonged survival rates in all 3 models suggested that a significant improvement in overall survival might be achievable with the single RPT dose.

To determine whether any overt toxicities were caused by [^{177}Lu]Lu-FAP8-PEG$_3$-IP-DOTA RPT, tissue sections from the heart, lung, liver, and kidneys of all treated and untreated control groups were examined by a board-certified veterinary pathologist after hematoxylin and eosin staining. Although no diagnostic lesions or other morphologic abnormalities were detected in the HT29 tumor–bearing mice (Figs. 5D and 5E), 2 of 5 MDA-MD-231 tumor–bearing mice and one of the KB tumor–bearing mice had liver lesions marked by a periportal mononuclear cells, mainly lymphocytes and plasma cells and localized hepatocellular necrosis (Supplemental Figs. 3–4). It was concluded that the therapy was generally safe, though the lesions were mild to moderate in severity.

Because the number of RPT doses that a cancer patient can receive is limited by the cumulative radioactive exposure of healthy tissues in a patient, we decided to determine whether tumor growth might still be suppressed by lower doses of [^{177}Lu]Lu-FAP8-PEG$_3$-IP-DOTA. For this purpose, 4 different specific activities of ^{177}Lu (0, 9.25, 18.5, and 37 MBq) were administered to 4T1 tumor–bearing mice. The syngeneic 4T1 breast cancer model was selected because its more aggressive growth rate would allow

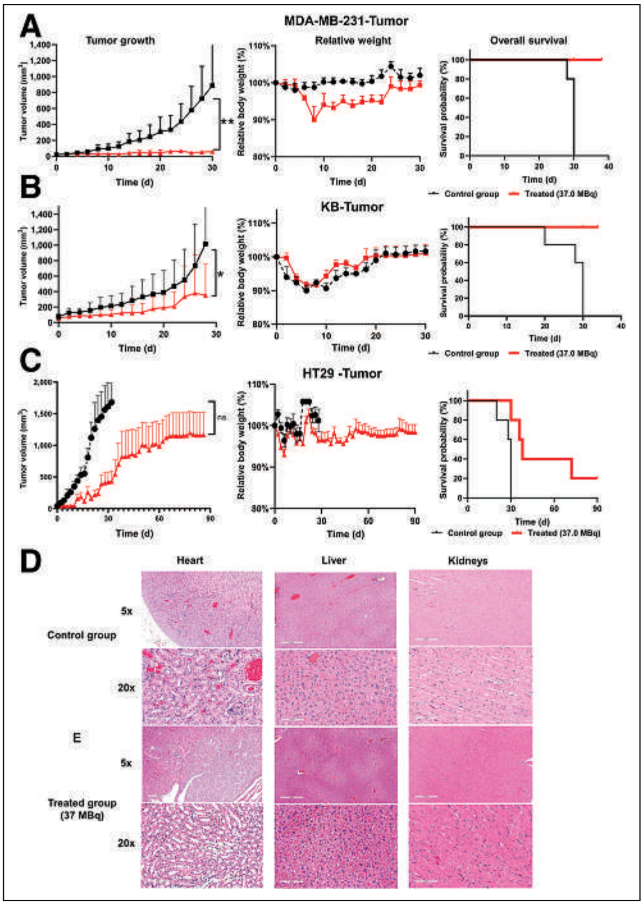

FIGURE 5. (A–C) Antitumor efficacy of [^{177}Lu]Lu-FAP8-PEG$_3$-IP-DOTA (37 MBq on day 0) in MDA-MB-231 (5/group) (A), KB (3/group) (B), and HT29 (5/group) (C) tumor–bearing mice. (D and E) Representative micrographs of 4-μm hematoxylin- and eosin-stained sections of fixed heart, liver, and kidney tissues after administration of vehicle (D) or [^{177}Lu]Lu-FAP8-PEG$_3$-IP-DOTA (E) in HT29 tumor–bearing mice. ns = nonsignificant. $^*P < 0.05$. $^{**}P < 0.01$.

for greater differentiation in responses among treatment groups. As shown in Figure 6A, tumors in untreated mice reached their maximum allowed volumes (1,500 mm^3) by day 12, whereas tumors in all 3 treatment groups stopped growing before reaching this maximum allowed volume, suggesting that their tumor progression may have been measurably inhibited. Although mice in the 9.25-MBq and 18.5-MBq cohorts did not experience any body weight loss, mice treated with 37 MBq exhibited about 5%–10% body weight loss (Fig. 6B), suggesting that 9.25- and 18.5-MBq doses may be well tolerated but that higher doses may be toxic.

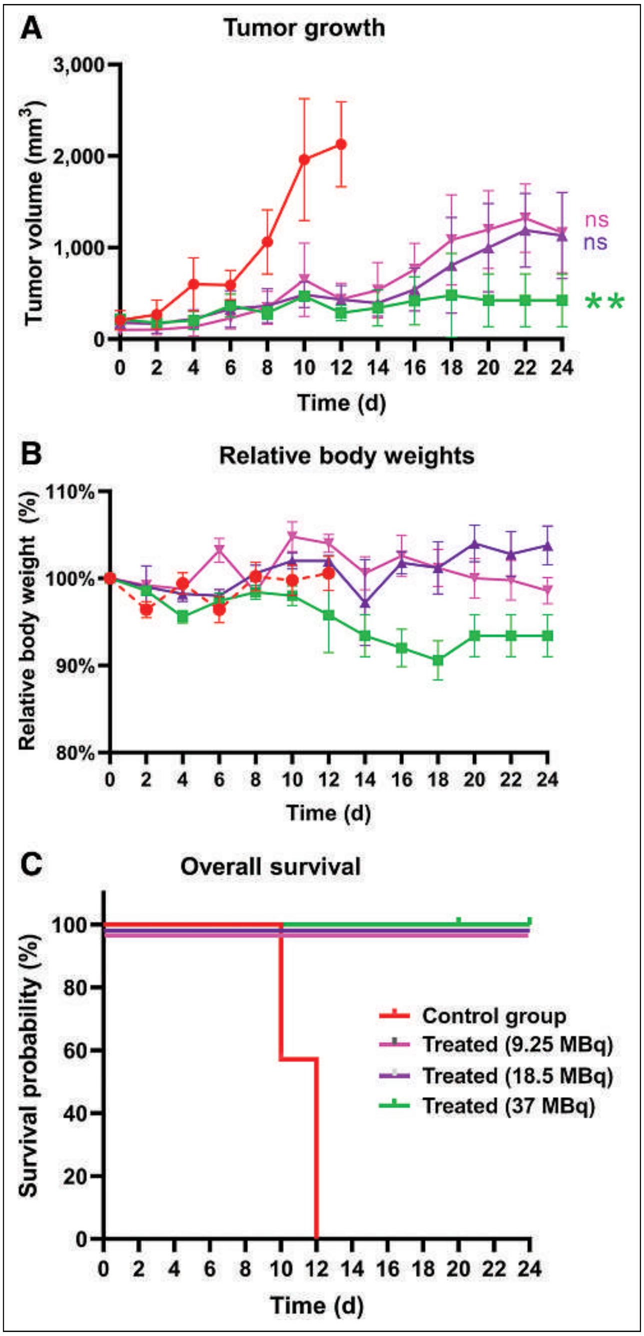

FIGURE 6. Dose response of $[^{177}Lu]Lu$-FAP8-PEG_3-IP-DOTA in BALB/c mice bearing 4T1 tumors (5/group). Cohorts were treated with single dose of $[^{177}Lu]Lu$-FAP8-PEG_3-IP-DOTA on day 0 and then measured for tumor growth (A), body weight (B), and overall survival (C). ns = nonsignificant. $^{**}P < 0.01$.

Analysis of SPECT/CT Imaging in Multiple Tumor Models

Finally, because response rates to RPTs have been shown to correlate with expression levels of the targeted receptors (*28*), it became important to determine whether our FAP8-PEG_3-IP-DOTA might also be used as an imaging agent to stratify cancer patients by FAP expression. Therefore, HT29 and KB tumor–bearing mice were intravenously injected with a 5 nmol/mouse dose of FAP8-PEG_3-IP-DOTA in which the FAP8 conjugate was labeled with the SPECT imaging agent $[^{111}In]In^{3+}$ rather than the radiotherapeutic agent $[^{177}Lu]Lu^{3+}$. Whole-body SPECT/CT scans collected at various time points (Figs. 7A and 7B) revealed that $[^{111}In]In$-FAP8-PEG_3-IP-DOTA accumulated rapidly in both HT29 and KB tumors, where it persisted for at least 168 h. In contrast, most of the radioactivity in the healthy tissues was cleared within 24 hours after injection. Because this uptake could be blocked by coadministration of a 100-fold excess of unlabeled FAP8-PEG_3-IP-DOTA, we conclude that retention of $[^{111}In]In$-FAP8-PEG_3-IP-DOTA in the tumors was FAP-mediated (Supplemental Figs. 5 and 6). This prolonged retention in tumors combined with only transient residence in healthy tissues portends well for the potential safety of $[^{177}Lu]Lu$-FAP8-PEG_3-IP-DOTA as an RPT in humans.

DISCUSSION

The overarching goal of this study was to improve FAP-targeted RPT tumor–to–healthy-tissue dosimetry ratios sufficiently to comply with Food and Drug Administration guidelines for radiotherapies. On the basis of external-beam radiation (not RPT) studies, the Food and Drug Administration has recommended that total cumulative radiation doses to healthy tissues be limited to less than 20 Gy for heart, less than 7 Gy for lungs, less than 30 Gy for liver, less than 23 Gy for kidneys, and less than 2–5 Gy for bone marrow (*29*). Because radiosensitive tumors respond at about 40 Gy whereas radioresistant tumors may require up to 100 Gy to shrink (*29–31*), the tumor–to–healthy-organ dosimetry ratios necessary for a safe therapeutic index can be determined. Assuming

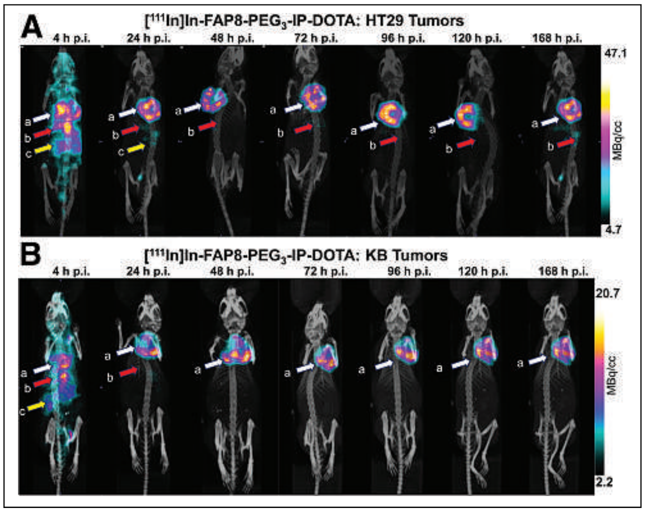

FIGURE 7. In vivo SPECT/CT imaging of $[^{111}In]In$-FAP8-PEG_3-IP-DOTA conjugate in mice bearing HT29 ($n = 2$) (A) and KB (B) ($n = 2$) tumors. White arrow (a) indicates tumor, red arrow (b) indicates liver, and yellow arrow (c) indicates kidneys. p.i. = after injection.

that tumor radiation doses should exceed about 100 Gy, with maximum kidney, liver, and bone marrow cumulative exposures remaining below 23, 30, and 5 Gy, respectively, a conservative estimate suggests that tumor-to-kidney, tumor-to-liver, and tumor–to–bone marrow ratios need to exceed 4.34, 3.3, and 20 times, respectively. Compliance with these minimum ratios would ensure effective tumor shrinkage without significant normal-tissue toxicity. On the basis of the above dose escalation data, a 5 nmol/mouse dose of [^{177}Lu]Lu-FAP8-PEG$_3$-IP-DOTA achieved a total tumor-absorbed dose of 1,140 mGy/MBq in the 4T1 mice, which was 25.3, 14.0, 4.2, 10.3, 5.2, and about 24.0 times higher than the total absorbed doses in the heart, lungs, liver, spleen, kidney, and bone marrow, respectively (Fig. 4G). We therefore conclude that [^{177}Lu]Lu-FAP8-PEG$_3$-IP-DOTA should meet the safety requirements for an effective RPT in humans. Although it is difficult to compare data from different labs using different FAP-transduced tumor models (*25,26,32*), our previous FAP6-targeted RPT did not meet these Food and Drug Administration requirements. Thus, [^{177}Lu]Lu-FAP8-PEG$_3$-IP-DOTA exhibited an 8-times higher total tumor dose than did FAP6-IP-DOTA conjugate in the same 4T1 tumor–bearing mouse model at the same 5 nmol/mouse concentration, and its tumor-to-kidney ratio ($>5\times$ vs. $2\times$) was also superior. Not surprisingly, [^{177}Lu]Lu-FAP8-PEG$_3$-IP-DOTA also induced greater tumor growth inhibition than did [^{177}Lu]Lu-FAP6-IP-DOTA (80% vs. 40%), even though about 6-times less radioactivity (9.25 vs. 55 MBq) was used than for the former therapy (*11*).

We have also repeatedly noted that better tumor–to–healthy-tissue ratios are achieved at higher mass doses, regardless of the amount of radionuclide chelated by the RPT. We propose that this can be explained by the relative rates of perfusion of the tumor versus healthy tissues such as the lungs, kidneys, gastrointestinal tract, and liver. Although 100%, 22%, 21%, and 6% of the blood perfuses the lungs, kidneys, gastrointestinal tract, and liver, respectively (*33*), during each circulatory cycle through the body, only a very minor fraction ($<2\%$) will perfuse a small solid tumor (*34–36*). Thus, when the administered amount of FAP8-PEG$_3$-IP-DOTA is low (e.g., at 0.3 and 1.0 nmol/mouse), most of the individual radioligands will be captured either by scavenger receptors or by the very low numbers of FAP+ fibroblasts that may exist in healthy tissues, leaving very little [^{177}Lu]Lu-FAP8-PEG$_3$-IP-DOTA to perfuse the solid tumor. At higher mass doses, however, both healthy and malignant tissues can conceivably be saturated, enabling the radioligand biodistribution to reflect the relative expression levels of the targeted receptor rather than their relative rates of blood perfusion. Because FAP+ cancer-associated fibroblasts are much more abundant in solid tumors than in healthy tissues, it will be important to treat a patient with sufficient compound to nearly saturate all FAP receptors in the tumor mass and then adjust the amount of radionuclide delivered to ensure that the allowed radiation exposure of healthy tissues is not exceeded. Estimation of this amount of RPT precursor will require a dose escalation study in an appropriate tumor-bearing patient population.

We observed a significant improvement in both total tumor dose and tumor–to–healthy-tissue ratios on insertion of the albumin binder, IP, into our FAP8-PEG$_3$-DOTA conjugate, presumably because it extended the drug's circulatory half-life in the vasculature (*37*). Other groups have similarly inserted albumin binders into their FAP-targeted RPTs with the same goal of prolonging pharmacokinetics (*12,13*). Although the anticipated enhanced tumor uptake was achieved in all cases, these labs also reported significantly compromised tumor–to–healthy-tissue ratios, perhaps because their Evans blue albumin binder exhibited nonspecific affinity for many proteins (*38*). Nevertheless, one of these RPTs (^{177}Lu-LNC1004) has shown encouraging results in a phase 1 human clinical trial (*39*), suggesting that perhaps the toxicities associated with low radiation exposures to healthy tissues in preclinical models may be overestimated. A limitation to our present study is the absence of a head-to-head comparison between our RPT with the other FAP-targeted RPTs currently in the clinic (e.g., FAP-2286 and FAPI-46).

CONCLUSION

We have designed a superior FAP-targeted RPT that provides tumor–to–healthy-tissue ratios that exceed the requirements established by the Food and Drug Administration, suggesting that it should be considered a viable candidate for human clinical evaluation.

DISCLOSURE

Ramesh Mukkamala, Spencer D. Lindeman, Madduri Srinivasarao, and Philip S. Low hold a patent on FAP-targeted RPT. Financial support was provided through a Purdue professorship. No other potential conflict of interest relevant to this article was reported.

ACKNOWLEDGMENTS

We acknowledge the Purdue Imaging Facility for its general support of the SPECT/CT studies and the assistance of MacKenzie McIntosh and the Purdue University Histology Research Laboratory. Ramesh Mukkamala thanks Charity Campbell, Mar, Brandon Chuck-Wang Mar, Jackson N. Moss, Autumn Horner, and Losha Dasol Jung for their help in select studies.

KEY POINTS

QUESTION: Can a FAP-targeted radioligand demonstrate sufficient tumor–to–healthy-tissue ratios and efficacy for preclinical development in murine tumor models in which FAP expression is limited to cancer-associated fibroblasts?

PERTINENT FINDINGS: [^{177}Lu]Lu-FAP8-PEG$_3$-IP-DOTA exhibited superior tumor–to–healthy-tissue ratios and successfully treated multiple murine tumor models generated from FAP-negative cancer cells.

IMPLICATIONS FOR PATIENT CARE: These data suggest that [^{177}Lu]Lu-FAP8-PEG$_3$-IP-DOTA constitutes a promising candidate for development of FAP-targeted RPT for solid tumors.

REFERENCES

1. Garin-Chesa P, Old LJ, Rettig WJ. Cell surface glycoprotein of reactive stromal fibroblasts as a potential antibody target in human epithelial cancers. *Proc Natl Acad Sci USA*. 1990;87:7235–7239.
2. Kratochwil C, Flechsig P, Lindner T, et al. ^{68}Ga-FAPI PET/CT: tracer uptake in 28 different kinds of cancer. *J Nucl Med*. 2019;60:801–805.
3. Ferdinandus J, Costa PF, Kessler L, et al. Initial clinical experience with ^{90}Y-FAPI-46 radioligand therapy for advanced-stage solid tumors: a case series of 9 patients. *J Nucl Med*. 2022;63:727–734.
4. Fendler WP, Pabst KM, Kessler L, et al. Safety and efficacy of ^{90}Y-FAPI-46 radioligand therapy in patients with advanced sarcoma and other cancer entities. *Clin Cancer Res*. 2022;28:4346–4353.
5. Baum RP, Schuchardt C, Singh A, et al. Feasibility, biodistribution, and preliminary dosimetry in peptide-targeted radionuclide therapy of diverse adenocarcinomas using ^{177}Lu-FAP-2286: first-in-humans results. *J Nucl Med*. 2022;63:415–423.

6. Ballal S, Yadav MP, Moon ES, et al. First-in-human results on the biodistribution, pharmacokinetics, and dosimetry of [^{177}Lu] Lu-DOTA.SA.FAPi and [^{177}Lu] Lu-DOTAGA.(SA.FAPi) 2. *Pharmaceuticals (Basel).* 2021;14:1212.
7. Ballal S, Yadav MP, Kramer V, et al. A theranostic approach of [^{68}Ga]Ga-DOTA.-SA.FAPi PET/CT-guided [^{177}Lu]Lu-DOTA.SA.FAPi radionuclide therapy in an end-stage breast cancer patient: new frontier in targeted radionuclide therapy. *Eur J Nucl Med Mol Imaging.* 2021;48:942–944.
8. Loktev A, Lindner T, Burger EM, et al. Development of fibroblast activation protein-targeted radiotracers with improved tumor retention. *J Nucl Med.* 2019;60: 1421–1429.
9. Watabe T, Liu Y, Kaneda-Nakashima K, et al. Theranostics targeting fibroblast activation protein in the tumor stroma: ^{64}Cu-and ^{225}Ac-labeled FAPI-04 in pancreatic cancer xenograft mouse models. *J Nucl Med.* 2020;61:563–569.
10. Liu Y, Watabe T, Kaneda-Nakashima K, et al. Fibroblast activation protein targeted therapy using [^{177}Lu]FAPI-46 compared with [^{225}Ac]FAPI-46 in a pancreatic cancer model. *Eur J Nucl Med Mol Imaging.* 2022;49:871–880.
11. Lindeman SD, Mukkamala R, Horner A, et al. Fibroblast activation protein-targeted radioligand therapy for treatment of solid tumors. *J Nucl Med.* 2023;64: 759–766.
12. Wen X, Xu P, Shi M, et al. Evans blue-modified radiolabeled fibroblast activation protein inhibitor as long-acting cancer therapeutics. *Theranostics.* 2022;12: 422–433.
13. Xu M, Zhang P, Ding J, Chen J, Huo L, Liu Z. Albumin binder–conjugated fibroblast activation protein inhibitor radiopharmaceuticals for cancer therapy. *J Nucl Med.* 2022;63:952–958.
14. Kratochwil C, Fendler WP, Eiber M, et al. EANM procedure guidelines for radionuclide therapy with ^{177} Lu-labelled PSMA-ligands (^{177}Lu-PSMA-RLT). *Eur J Nucl Med Mol Imaging.* 2019;46:2536–2544.
15. Rubin P. Law and order of radiation sensitivity. Absolute versus relative. *Front Radiat Ther Oncol.* 1989;23:7–40.
16. Šimková A, Ormsby T, Sidej N, et al. Structure-activity relationship and biochemical evaluation of novel fibroblast activation protein and prolyl endopeptidase inhibitors with α-ketoamide warheads. *Eur J Med Chem.* 2021;224:113717.
17. Jansen K, Heirbaut L, Verkerk R, et al. Extended structure–activity relationship and pharmacokinetic investigation of (4-quinolinoyl) glycyl-2-cyanopyrrolidine inhibitors of fibroblast activation protein (FAP). *J Med Chem.* 2014;57:3053–3074.
18. Müller C, Struthers H, Winiger C, Zhernosekov K, Schibli R. DOTA conjugate with an albumin-binding entity enables the first folic acid-targeted ^{177}Lu-radionuclide tumor therapy in mice. *J Nucl Med.* 2013;54:124–131.
19. Spencer DL, Ramesh M, Autumn H, et al. Fibroblast activation protein–targeted radioligand therapy for treatment of solid tumors. *J Nucl Med.* 2023;64:759–766.
20. Patil P, Ahmadian-Moghaddam M, Dömling A. Isocyanide 2.0. *Green Chem.* 2020;22:6902–6911.
21. Roy J, Hettiarachchi SU, Kaake M, Mukkamala R, Low PS. Design and validation of fibroblast activation protein alpha targeted imaging and therapeutic agents. *Theranostics.* 2020;10:5778–5789.
22. Mukkamala R, Lindeman SD, Kragness KA, Shahriar I, Srinivasarao M, Low PS. Design and characterization of fibroblast activation protein targeted pan-cancer imaging agent for fluorescence-guided surgery of solid tumors. *J Mater Chem B.* 2022;10:2038–2046.
23. Nicolas GP, Mansi R, McDougall L, et al. Biodistribution, pharmacokinetics, and dosimetry of ^{177}Lu-, ^{90}Y-, and ^{111}In-labeled somatostatin receptor antagonist OPS201 in comparison to the agonist ^{177}Lu-DOTATATE: the mass effect. *J Nucl Med.* 2017; 58:1435–1441.
24. Galbiati A, Zana A, Bocci M, et al. A dimeric FAP-targeting small-molecule radioconjugate with high and prolonged tumor uptake. *J Nucl Med.* 2022;63:1852.
25. Poplawski SE, Hallett RM, Dornan MH, et al. Preclinical development of PNT6555, a boronic acid–based, fibroblast activation protein-α (FAP)–targeted radiotheranostic for imaging and treatment of FAP-positive tumors. *J Nucl Med.* 2024;65:100–108.
26. Zboralski D, Hoehne A, Bredenbeck A, et al. Preclinical evaluation of FAP-2286 for fibroblast activation protein targeted radionuclide imaging and therapy. *Eur J Nucl Med Mol Imaging.* 2022;49:3651–3667.
27. Camus B, Cottereau AS, Palmieri LJ, et al. Indications of peptide receptor radionuclide therapy (PRRT) in gastroenteropancreatic and pulmonary neuroendocrine tumors: an updated review. *J Clin Med.* 2021;10:1267.
28. Bodei L, Herrmann K, Schöder H, Scott AM, Lewis JS. Radiotheranostics in oncology: current challenges and emerging opportunities. *Nat Rev Clin Oncol.* 2022;19:534–550.
29. Wahl RL, Sgouros G, Iravani A, et al. Normal-tissue tolerance to radiopharmaceutical therapies, the knowns and the unknowns. *J Nucl Med.* 2021;62:23S–35S.
30. Yang G, Yuan Z, Ahmed K, et al. Genomic identification of sarcoma radiosensitivity and the clinical implications for radiation dose personalization. *Transl Oncol.* 2021;14:101165.
31. Rubin P, Siemann DW. Principles of radiation oncology and cancer radiotherapy. In: Rubin P ed. *Clinical Oncology: A Multidisciplinary Approach for Physicians and Students.* Saunders; 1993:71–90.
32. Galbiati A, Zana A, Bocci M, et al. A dimeric FAP-targeting small-molecule radioconjugate with high and prolonged tumor uptake. *J Nucl Med.* 2022;63:1852–1858.
33. Germann WJ, Stanfield CL, Cannon JG, et al. The Immune System. In: Brassert C, ed. *Principles of Human Physiology*: Benjamin Cummings; 2002:708–740.
34. Gullino PM. Tumor pathophysiology: the perfusion model. In: Mihich E, Eckhardt S, eds. *Design of Cancer Chemotherapy: Experimental and Clinical Approaches.* Vol 28. S. Karger AG; 1980:35–42.
35. Vaupel P, Fortmeyer HP, Runkel S, Kallinowski F. Blood flow, oxygen consumption, and tissue oxygenation of human breast cancer xenografts in nude rats. *Cancer Res.* 1987;47:3496–3503.
36. Gillies RJ, Schornack PA, Secomb TW, Raghunand N. Causes and effects of heterogeneous perfusion in tumors. *Neoplasia.* 1999;1:197–207.
37. Hoogenboezem EN, Duvall CL. Harnessing albumin as a carrier for cancer therapies. *Adv Drug Deliv Rev.* 2018;130:73–89.
38. Tsopelas C, Sutton R. Why certain dyes are useful for localizing the sentinel lymph node. *J Nucl Med.* 2002;43:1377–1382.
39. Fu H, Huang J, Zhao T, et al. Fibroblast activation protein-targeted radioligand therapy with ^{177}Lu-EB-FAPI for metastatic radioiodine-refractory thyroid cancer: first-in-human, dose-escalation study. *Clin Cancer Res.* 2023;29:4740–4750.

Dosimetry of [^{177}Lu]Lu-PSMA–Targeted Radiopharmaceutical Therapies in Patients with Prostate Cancer: A Comparative Systematic Review and Metaanalysis

Zachary Ells[1], Tristan R. Grogan[2], Johannes Czernin[1], Magnus Dahlbom*[1], and Jeremie Calais*[1]

[1]*Ahmanson Translational Theranostics Division, Department of Molecular and Medical Pharmacology, UCLA, Los Angeles, California; and* [2]*Department of Medicine Statistics Core, David Geffen School of Medicine, UCLA, Los Angeles, California*

Novel theranostic approaches using radiopharmaceuticals targeting prostate-specific membrane antigen (PSMA) have emerged for treating metastatic castration-resistant prostate cancer. The physical properties and commercial availability of ^{177}Lu make it one of the most used radionuclides for radiopharmaceutical therapy (RPT). In this literature review, we aimed at comparing the dosimetry of the most used [^{177}Lu]Lu-PSMA RPT compounds. **Methods:** This was a systematic review and metaanalysis of [^{177}Lu]Lu-PSMA RPT (617, I&T, and J591) dosimetry in patients with prostate cancer. Absorbed doses in Gy/GBq for each organ at risk (kidney, parotid and submandibular glands, bone marrow, liver, and lacrimal glands) and for tumor lesions (bone and nonbone lesions) were extracted from included articles. These were used to estimate the pooled average absorbed dose of each agent in Gy/GBq and in Gy/cycle, normalized to the injected activity (per cycle) used in the VISION (7.4 GBq), SPLASH (6.8 GBq), and PROSTACT trials (5.8 GBq). **Results:** Twenty-nine published articles comprising 535 patients were included in the metaanalysis. The pooled doses (weighted average across studies) of [^{177}Lu]Lu-PSMA-617 and [^{177}Lu]Lu-PSMA-I&T were 4.04 Gy/GBq (17 studies, 297 patients) and 4.70 Gy/GBq (10 studies, 153 patients) for the kidney ($P = 0.10$), 5.85 Gy/GBq (14 studies, 216 patients) and 2.62 Gy/GBq (5 studies, 86 patients) for the parotids ($P < 0.01$), 5.15 Gy/GBq (5 studies, 81 patients) and 4.35 Gy/GBq (1 study, 18 patients) for the submandibular glands ($P = 0.56$), 11.03 Gy/GBq (6 studies, 121 patients) and 19.23 Gy/GBq (3 studies, 53 patients) for the lacrimal glands ($P = 0.20$), 0.24 Gy/GBq (12 studies, 183 patients) and 0.19 Gy/GBq (4 studies, 68 patients) for the bone marrow ($P = 0.31$), and 1.11 Gy/GBq (9 studies, 154 patients) and 0.56 Gy/GBq (4 studies, 56 patients) for the liver ($P = 0.05$), respectively. Average tumor doses tended to be higher for [^{177}Lu]Lu-PSMA-617 than for [^{177}Lu]Lu-PSMA-I&T in soft tissue tumor lesions (4.19 vs. 2.94 Gy/GBq; $P = 0.26$). Dosimetry data of [^{177}Lu]Lu-J591 were limited to one published study of 35 patients with reported absorbed doses of 1.41, 0.32, and 2.10 Gy/GBq to the kidney, bone marrow, and liver, respectively. **Conclusion:** In this metaanalysis, there was no significant difference in absorbed dose between [^{177}Lu]Lu-PSMA-I&T and [^{177}Lu]Lu-PSMA-617. There was a possible trend toward a higher kidney dose with [^{177}Lu]Lu-PSMA-I&T and a higher tumor lesion dose with [^{177}Lu]Lu-PSMA-617. It remains unknown whether this finding has any clinical impact. The dosimetry methodologies were strikingly heterogeneous among studies, emphasizing the need for standardization.

Key Words: ^{177}Lu; PSMA; dosimetry; theranostics; metaanalysis; prostate cancer

J Nucl Med 2024; 65:1264–1271
DOI: 10.2967/jnumed.124.267452

Novel theranostic approaches using radiopharmaceuticals have emerged for treating metastatic castration-resistant prostate cancer. Because of its overexpression by most prostate cancers, prostate-specific membrane antigen (PSMA) represents a valid molecular target for radionuclide imaging and therapy. The physical properties and commercial availability of ^{177}Lu make it one of the most used radionuclides for radioligand therapy. After the positive results of the VISION trial (*1*), [^{177}Lu]Lu-PSMA-617 therapy (Pluvicto; Novartis) was approved by the Food and Drug Administration, and this treatment is now included in the National Comprehensive Cancer Network guidelines and reimbursed by the Centers for Medicare and Medicaid Services for patients with metastatic castration-resistant prostate cancer progressing after chemotherapy. Randomized phase 3 trials testing [^{177}Lu]Lu-PSMA-617 at earlier disease stages have completed their enrollment (PSMAfore NCT04689828 for prechemotherapy metastatic castration-resistant prostate cancer patients, PSMAddition NCT04720157 for patients with metastatic hormone-sensitive prostate cancer). Another small-molecule radioligand, [^{177}Lu]Lu-PSMA-I&T, is being investigated in 2 randomized phase 3 trials (SPLASH NCT04647526 and ECLIPSE NCT05204927), which also completed enrollment. The radiolabeled monoclonal antibody [^{177}Lu]Lu-J591 is being investigated in an ongoing randomized phase 3 trial (PROSTACT NCT04876651).

^{177}Lu decays by β^- emission with a half-life of 6.7 d. The average energy of the β-particles is 134 keV (maximum of 498 keV), with an average travel path of 0.670 mm in soft tissue. The energies of the primary γ-emissions are 113 keV (6.6%) and 208 keV (11%) (*2*). The γ-ray emissions allow for imaging of the drug biodistribution over multiple days using planar scintigraphy or SPECT/CT. Estimations of the radiation dose deposition in normal organs at risk and tumor lesions are required for regulatory purposes and essential for risk determinations. Dosimetry also carries the potential to assist in individualized patient management, including optimization of drug administration (injected activity per cycle, number of cycles, time interval between cycles).

With the expected approval of various [^{177}Lu]Lu-PSMA–targeted compounds, the question of how their efficacy and safety

---

Received Jan. 16, 2024; revision accepted Apr. 29, 2024.

For correspondence or reprints, contact Jeremie Calais (jcalais@mednet.ucla.edu).

*Contributed equally to this work.

Guest Editor: Rodney Hicks, University of Melbourne

profiles compare arises. However, to our knowledge, no head-to-head dosimetry comparison of the different [^{177}Lu]Lu-PSMA–targeted compounds has been conducted. Moreover, the reported radiation dose estimates for [^{177}Lu]Lu-PSMA can vary considerably because multiple technical parameters and methods impact organ and tumor dose estimates, such as image reconstruction parameters, acquisition practices, segmentation methods, dose calculation models, lesion sizes, or use of partial-volume correction (*3–5*).

Because direct comparisons among different therapeutic radiopharmaceutical are not feasible, we conducted a systematic review and metaanalysis to summarize the dosimetry of [^{177}Lu]Lu-PSMA-617, [^{177}Lu]Lu-PSMA-I&T, and [^{177}Lu]Lu-J591 in articles published as of November 2023.

MATERIALS AND METHODS

The Preferred Reporting Items for Systematic Reviews and Meta-Analyses (PRISMA) 2020 guidelines were followed to conduct this study (*6*) (checklist provided in supplemental materials, available at http://jnm.snmjournals.org).

Article Search

We created a comprehensive list of all dosimetry studies involving [^{177}Lu]Lu-PSMA therapy for prostate cancer and performed a systematic review and metaanalysis. We conducted an article search using advanced settings in PubMed and Google Scholar as of November 2023 (Fig. 1). Within articles, referenced publications regarding the dosimetry of [^{177}Lu]Lu-PSMA were also added to the database if not initially found on either platform.

Data Inclusion

The dosimetry data were extracted from each article in Gy/GBq for the normal organs (kidney, parotid and submandibular glands, lacrimal glands, liver, and bone marrow) at risk and for tumor lesions, which were separated into bone and nonbone lesions (soft tissue; i.e., visceral, lung, liver, and lymph nodes). Biological effective dose was not included.

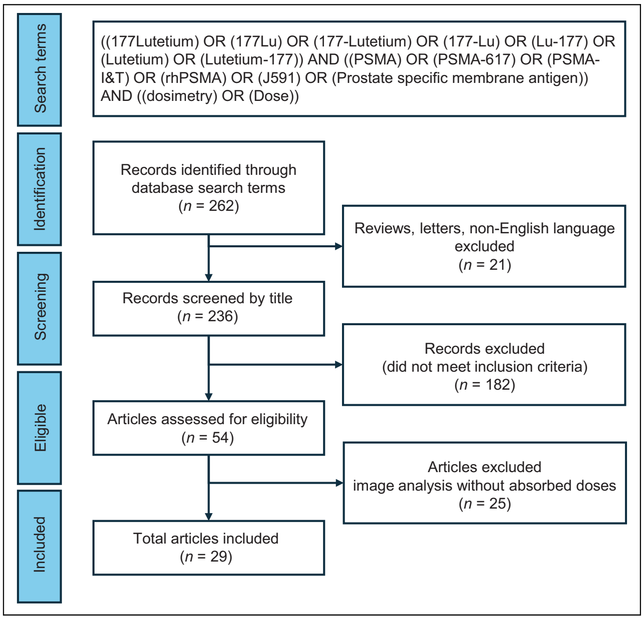

FIGURE 1. Study selection for metaanalysis. Using PRISMA criteria, we selected 29 studies for this metaanalysis. Only conference abstracts or fully published articles that were in English and reported absorbed dose to organs at risk or tumors were included.

Because of the different injected activities per cycle in each study, we also calculated the pooled dose normalized to a fixed amount of injected activity per cycle (Gy/cycle): 7.4 GBq for [^{177}Lu]Lu-PSMA-617 based on the VISION trial, 6.8 GBq for [^{177}Lu]Lu-PSMA-I&T based on the SPLASH trial, and 5.6 GBq (76 mCi ×2) for [^{177}Lu]Lu-J591 based on the PROSTACT trial.

Factors Affecting Dosimetry Calculations

We collected the multiple factors that could affect the dosimetry calculations. Three different image protocols were recorded: planar whole-body scans, 3-dimensional SPECT/CT scans, and a hybrid approach combining both. To convert activity to dose, multiple dosimetry tools were used, primarily including voxelwise and RADAR (Radiation Dose Assessment Resource; https://www.doseinfo-radar.com/) schema (OLINDA/EXM) or MIRD. In addition, different reconstruction parameters were used in the various studies. The 2 methods used to determine the average absorbed dose to bone marrow were based on blood sampling and on imaging.

Statistics

A metaanalysis was conducted for each organ (kidney, parotid and submandibular glands, lacrimal glands, bone marrow, and liver) and for tumor lesions. We reported the pooled estimated average dose of each radiopharmaceutical (617, I&T, and J591) with standard errors or CIs estimated using inverse variance weighting. Most studies reported their sample size, means, and SDs, which were used as inputs to the metaanalysis; however, some studies reported medians and quartiles instead. For those studies, we estimated the mean and SD by assuming the median was the mean and estimating the SD by taking the difference in quartiles divided by 1.35, as suggested by the *Cochrane Handbook for Systematic Reviews of Interventions* (*7*). The Cochran Q statistic and I^2 index (the percentage of variation across studies that is due to heterogeneity rather than chance) were used to assess heterogeneity. Because significant heterogeneity was observed, the random-effects metaanalytic model was used as opposed to the fixed-effects pooled estimate. Within each organ, we used the subgroup option of the package to test for differences in radionuclides. If the overall test was significant, we conducted pairwise comparisons between groups. However, if it was not significant, no further testing for that organ was done. Tumor dosimetry was analyzed for all lesions, as well as stratified by bone only or nonbone lesions. Statistical analyses were performed using R version 4.1.0 (www.r-project.org) with the meta package, which is the general package for metaanalysis. *P* values of less than 0.05 were considered statistically significant. The *P* values shown throughout the article denote comparisons between [^{177}Lu]Lu-PSMA-617 and [^{177}Lu]Lu-PSMA-I&T, as [^{177}Lu]Lu-J591 data were limited, unless otherwise indicated as overall *P* value.

RESULTS

Twenty-nine published articles comprising 535 patients were included in the metaanalysis. The number of studies and included patients for individual organs and tumor lesions are summarized in Supplemental Tables 1 and 2. The patient population is summarized in Supplemental Table 3. Overall, 90% of the studies in this metaanalysis included metastatic castration-resistant prostate cancer, whereas 10% included metastatic hormone-sensitive prostate cancer. Of note, one study included only low-volume metastatic hormone-sensitive prostate cancer ($n = 10$ patients) (*8,9*). The dosimetry protocol parameters and reconstruction protocols used in each study are included in Supplemental Tables 4 and 5.

The dosimetry data extracted from each article are summarized in Table 1 for the normal organs at risk and in Table 2 for the tumor lesions. Table 3 lists the average absorbed dose in Gy/GBq and the dose normalized to the injected activity (Gy). The pooled

TABLE 1
Reported Dosimetry for Organs at Risk

Author	Isotope	Injected activity (GBq)	Kidney (Gy/GBq)	Parotid (Gy/GBq)	Submandibular (Gy/GBq)	Marrow (Gy/GBq)	Liver (Gy/GBq)	Lacrimal (Gy/GBq)
Kabasakal (*39*)	617	0.2	0.88 ± 0.4	1.17 ± 0.31	–	0.03 ± 0.01	0.28 ± 0.09	–
Delker (*15*)	617	3.6	0.6 ± 0.18	1.4 ± 0.53	–	0.01 ± 0.01	0.11 ± 0.06	–
Fendler (*10*)	617	3.7	0.55 ± 0.25	1 ± 0.6	–	0.1	< 0.1	–
Hohberg (*40*)	617	5.5	0.53 ± 0.17	0.72 ± 0.14	–	–	–	2.82 ± 0.76
Kratochwil (*33*)	617	3.0	0.75 ± 0.19	1.28 ± 0.4	1.48 ± 0.37	0.03 ± 0.01	–	–
Yadav (*12*)	617	2.5	0.99 ± 0.31	1.24 ± 0.27	–	0.05 ± 0.06	0.36 ± 0.11	–
Scarpa (*19*)	617	6.1	0.6 ± 0.36	0.56 ± 0.25	0.5 ± 0.15	0.04 ± 0.03	–	1.01 ± 0.69
Gosewisch (*41*)	617	3.7	–	–	–	0.01 (0.01–0.02)	–	–
Gosewisch (*42*)	617	5.2	–	–	–	0.012	–	–
Sarnelli (*43*)	617	5.0	0.67 ± 0.27	0.81 ± 0.74	–	0.04 ± 0.02	0.16 ± 0.15	–
Violet (*20*)	617	7.8	0.39 ± 0.15	0.58 ± 0.43	0.44 ± 0.36	0.11 ± 0.1	0.1 ± 0.05	0.36 ± 0.18
Paganelli (*44*)	617	4.4	0.41 ± 0.19	1.04 ± 0.82	0.67 ± 0.36	0.04 ± 0.02	0.18 ± 0.14	2.06 ± 1.24
Mix (*34*)	617	6.0	0.67 ± 0.24	–	–	–	–	–
Privé/Peters (*8,9*)	617	3.0	0.49 ± 0.11	0.39 ± 0.17	–	0.02 ± 0.01	0.09 ± 0.01	–
Rosar (*11*)	617	6.4	0.54 ± 0.28	0.81 ± 0.34	0.72 ± 0.39	–	0.1 ± 0.05	–
Völter (*45*)	617	6.0	–	–	–	–	–	–
Kamaldeep (*16*)	617	4.4	0.49 ± 0.17	0.53 ± 0.2	–	0.03 ± 0.02	0.07 ± 0.04	1.23 ± 0.7
Schuchardt (*46*)	617	6.5	0.8	0.5	–	–	–	5.1
Herrmann/Krause (*47,48*)	617	7.4	0.43 ± 0.16	0.63 ± 0.36	–	0.04 ± 0.02	–	2.1 ± 0.47
Uijen (*22*)	617	3.0	0.49 (0.34–0.66)	–	–	–	–	–
Okamoto (*35*)	I&T	7.4	0.72 ± 0.21	0.55 ± 0.14	0.64 ± 0.4	–	0.12 ± 0.06	3.8 ± 1.4
Baum (*17*)	I&T	5.8	0.8 (0.2–1.9)	1.3 (0.3–9.5)	–	0.03 (0.01–0.04)	–	–
Barna (*13*)	I&T	7.4	0.71 ± 0.24	0.77	–	–	0.27	–
Chatachot (*14*)	I&T	6.7	0.81 ± 0.24	0.21 ± 0.14	–	0.02 ± 0.01	0.13 ± 0.10	3.62 ± 1.78
Schuchardt (*46*)	I&T	6.1	0.9	0.5	–	–	–	3.7
Kelk (*49*)	I&T	7.4	0.305	0.11	0.24	–	0.03	0.8
Feuerecker (*18*)	I&T	7.3	0.73 ± 0.18	0.8 ± 0.41	–	0.28 ± 0.2	0.07 ± 0.03	–
Beauregard (*50*)	I&T	6.8	0.73 ± 0.33	0.34 ± 0.27	–	0.03 ± 0.02	0.05 ± 0.04	1.2 ± 1.2
Uijen (*22*)	I&T	7.4	0.73 (0.42–1.31)	–	–	–	–	–
Resch (*51*)	I&T	7.4	2 (1.2–2.4)	–	–	–	–	–
Hohberg (*21*)	I&T	7.2	0.53 ± 0.21	–	–	–	–	–
Bander/Vallabhajosula (*27,52*)	J591	2.8	1.41 ± 0.35	–	–	0.32 ± 0.01	2.1 ± 0.6	–

Data are reported as mean ± SD or as median followed by range in parentheses.

TABLE 2
Reported Tumor Lesion Dosimetry

Author	Isotope	Injected activity (GBq)	Unspecified/single-study exploration (Gy/GBq)	Skeletal lesion (Gy/GBq)	Nodal lesion (Gy/GBq)	Liver lesion (Gy/GBq)
Delker (*15*)	617	3.6	2.1 ± 0.8*	5.3 ± 3.7	4.2 ± 5.3	–
Fendler (*10*)	617	3.7	2.16 ± 0.85*	4.92 ± 3.54	11.64 ± 5.44	–
Scarpa (*19*)	617	6.1	–	3.4 ± 1.9	2.6 ± 0.4	2.4 ± 0.8
Violet (*20*)	617	7.8	–	5.28 ± 2.46	3.91 ± 3.93	–
Paganelli (*44*)	617	4.4	–	4.7 (0.74–55.86)	3.64 (0.25–15.10)	–
Privé/Peters (*8,9*)	617	3.0	3.25 ± 3.19	1.1 (0.3–3.1)	3.1 (0.6–13)	–
Rosar (*11*)	617	6.4	–	1.68 ± 1.32	–	–
Volter (*45*)	617	6.0	–	4.7 ± 3.9	7.7 ± 9.7	–
Schuchardt (*46*)	617	6.5	–	6	7.1	–
Herrmann/Krause (*47,48*)	617	7.4	–	14.6 ± 29.8	12.5 ± 15.9	–
Okamoto (*35*)	I&T	7.4	1.75 ± 0.92†	3.4 ± 2.7	3.2 ± 2.2	1.2 ± 0.67
Baum (*17*)	I&T	5.8	–	3 (0.2–40)	4 (0.14–78)	–
Barna (*13*)	I&T	7.4	–	4.38	5.47	4.95
Schuchardt (*46*)	I&T	6.1	–	5.9	6.9	–
Feuerecker (*18*)	I&T	7.3	–	1.7 ± 1.13	4.51 ± 2.69	–
Hohberg (*21*)	I&T	7.2	–	3.47 ± 2	3.73 ± 1.65	–
Resch (*51*)	I&T	7.5	–	5.8 ± 3.1	7.7 ± 4.5	–

*Tumor was deemed soft tissue in nature.
†Tumor was deemed lung lesion.
Data are reported as mean ± SD or as median followed by range in parentheses.

averages and CIs are shown in Figures 2 and 3 for the kidney and tumors and in the supplemental materials for the other organs.

Kidneys

Twenty-eight studies including 485 patients reported kidney dosimetry. The absorbed kidney dose was not significantly different but tended to be higher for [^{177}Lu]Lu-PSMA-I&T than for [^{177}Lu]Lu-PSMA-617 (4.70 Gy [CI, 4.16–5.24 Gy] vs. 4.04 Gy [CI, 3.94–4.60 Gy]; $P = 0.10$). For [^{177}Lu]Lu-J591, the reported kidney dose was 3.95 Gy (CI, 3.62–4.27 Gy; overall $P = 0.06$) (Table 3). Figure 2 depicts the pooled average absorbed kidney dose along with the CI from the included studies.

Of note, Fendler et al. ([^{177}Lu]Lu-PSMA-617) reported the dose to the left and right kidneys individually, and we averaged the data

TABLE 3
Weighted Average of Absorbed Doses for Organs at Risk and Tumors

	617		I&T		J591			
Organ or group	Gy/GBq	Gy/7.4-GBq cycle	Gy/GBq	Gy/6.8-GBq cycle	Gy/GBq	Gy/5.6-GBq cycle	617 vs. I&T *P*	Overall *P*
Kidney	0.58	4.04	0.71	4.70	1.41	3.95	0.10	0.06
Parotid	0.84	5.85	0.43	2.62	–	–	<0.01	–
Submandibular	0.74	5.15	0.64	4.35	–	–	0.56	–
Bone marrow	0.03	0.24	0.03	0.19	0.32	0.90	0.31	<0.01
Liver	0.16	1.11	0.09	0.56	2.10	5.88	0.05	<0.01
Lacrimal glands	1.58	11.03	2.83	19.23	–	–	0.20	–
Tumor lesion, bone only	3.57	26.43	4.10	27.87	–	–	0.38	–
Tumor lesion, soft-tissue only	4.19	31.00	2.94	19.98	–	–	0.23	–

Data are summary of pooled doses for organs at risk and tumor lesions from different ^{177}Lu-based molecules shown as average (CI can be seen for kidney and tumors in Figs. 2 and 3 and for rest of organs in Supplemental Figs. 1–5).

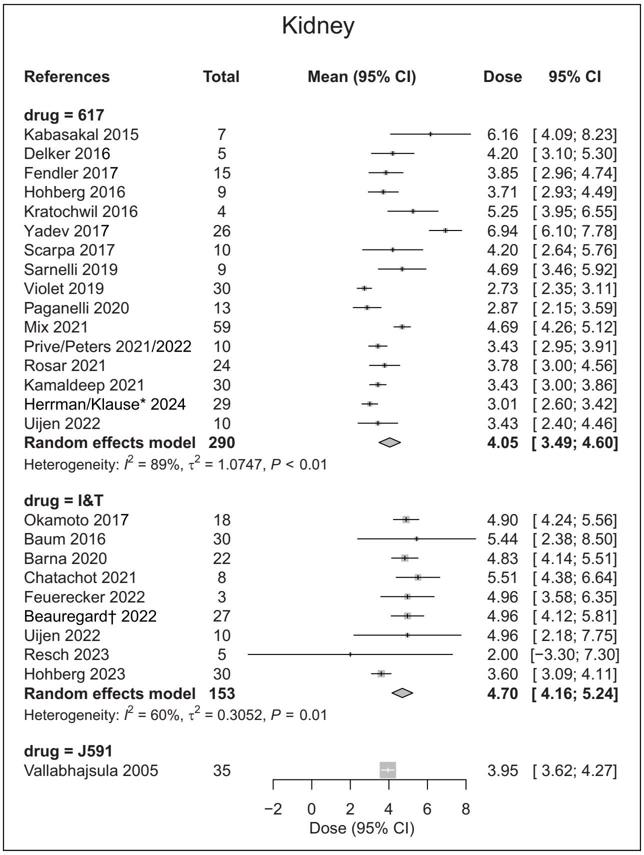

FIGURE 2. Reported absorbed doses (Gy/cycle) to kidney from selected studies, allowing for computation of pooled average absorbed dose. *As reported in VISION trial. †As reported in SPLASH trial.

to match other reports (*10*). Rosar et al. ([^{177}Lu]Lu-PSMA-617) reported dosimetry from multiple methods (*11*). We elected to include the values derived from the 3-dimensional SPECT images (highest reliability). Yadav et al. used a 2-L cocktail of lysine and arginine in saline to protect the kidneys 30–60 min before infusion, which may have affected dosimetry (*12*).

Liver

Fourteen studies reported liver dosimetry in 245 patients. The pooled liver doses are summarized in Table 3 and Supplemental Figure 1. The average absorbed dose to the liver was higher for [^{177}Lu]Lu-PSMA-617 than for [^{177}Lu]Lu-PSMA-I&T (1.11 Gy [CI, 0.65–1.58 Gy] vs. 0.56 Gy [0.28–0.84 Gy]; $P = 0.05$). The absorbed dose to the liver was highest for [^{177}Lu]Lu-PSMA-J591 (5.88 Gy [CI, 5.32–6.44 Gy]; overall $P < 0.01$). Two articles were excluded as the data were presented without SE or CIs (*10,13*).

Salivary Glands

Parotid and submandibular gland dosimetry was available from 20 and 7 studies that included 309 and 100 patients in total, respectively. The absorbed parotid gland dose was significantly higher for [^{177}Lu]Lu-PSMA-617, at 5.85 Gy (CI, 4.67–7.02 Gy), than for [^{177}Lu]Lu-PSMA-I&T, at 2.62 Gy (CI, 1.33–3.80 Gy) ($P < 0.01$). No significant difference was noted for the dose to the submandibular glands ($P = 0.56$) (Table 3; Supplemental Figs. 2 and 3). Absorbed dose values for the salivary glands have yet to be reported for [^{177}Lu]Lu-J591.

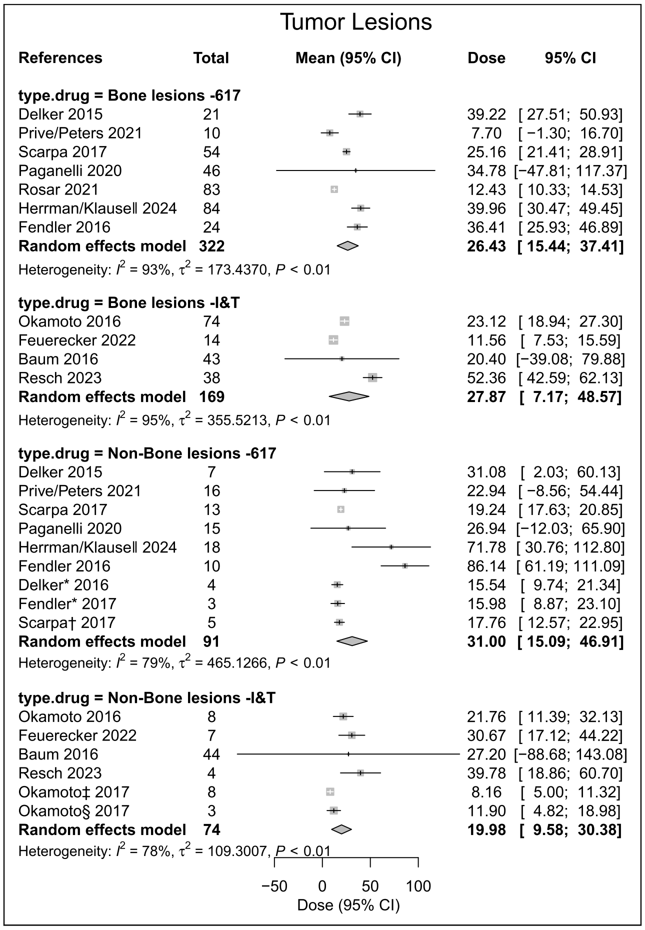

FIGURE 3. Reported absorbed doses (Gy/cycle) to tumor lesions from selected studies that were used to compute pooled average absorbed dose. Individual study estimates: gray box with black bar, each study's effect estimate (mean) is represented by gray box, with size of box proportional to study's weight in metaanalysis; black bar through box indicates CI for estimate; white cross in gray box, studies with very precise estimates; white cross indicates point estimate (mean), with gray box showing narrow CI; pooled estimate (diamond): Diamond Shape: The pooled estimate, or overall effect estimate, of the meta-analysis is shown as a diamond at the bottom of the plot. Width of the Diamond: The width of the diamond represents the confidence interval for the pooled estimate. The left and right tips of the diamond correspond to the lower and upper bounds of the CI, respectively. Center of the Diamond: The center of the diamond represents the overall effect estimate (mean) calculated from combining the individual study estimates. *Lesion location reported as soft tissue. †Lesion location reported as visceral tissue. ‡Lesion location reported within liver. §Lesion location reported within lung. ‖Tumor dosimetry reported from VISION trial.

Applying ice packs locally to the neck to reduce blood flow did not affect the absorbed dose to the parotid glands (Table 1) (*10,14,15*).

Lacrimal Glands

Nine studies including 174 patients reported lacrimal gland dosimetry. The average absorbed dose to the lacrimal glands tended to be lower for [^{177}Lu]Lu-PSMA-617 than for [^{177}Lu]Lu-PSMA-I&T (11.03 Gy [CI, 6.00–16.06 Gy] vs. 19.23 Gy [CI, 7.69–30.78 Gy]; $P = 0.20$) (Table 3; Supplemental Fig. 4). Lacrimal gland dose has not been reported for [^{177}Lu]Lu-J591.

Bone Marrow

Eighteen studies including 293 patients reported bone marrow dosimetry. The absorbed doses reported were derived from blood sampling or SPECT/CT images ($n = 2$) for [^{177}Lu]Lu-PSMA-617 (*15,16*) and [^{177}Lu]Lu-PSMA-I&T (*14,17,18*). For [^{177}Lu]Lu-J591, the imaging method was used.

Absorbed dose values were similar for [^{177}Lu]Lu-PSMA-617 and [^{177}Lu]Lu-PSMA-I&T (0.24 Gy [CI, 0.17–0.31 Gy] vs. 0.19 Gy [CI, 0.13–0.25 Gy]; $P = 0.31$) but were significantly higher for [^{177}Lu]Lu-PSMA-J591 (0.90 Gy [CI, 0.89–0.91 Gy]; overall $P < 0.1$) (Table 3; Supplemental Fig. 5).

Tumor Lesion Dosimetry

In total, 339 patients and 656 lesions were reported from the studies seen in Table 2; 491 lesions from 161 patients were bone lesions, whereas 165 lesions from 178 patients were soft-tissue lesions. Although included in the absorbed dose analysis, the number or location of lesions present in the patient cohorts were not reported for several studies (*8,9,19–21*). The pooled average absorbed dose along with the CI from the included studies for the tumors can be seen in Table 3 and Figure 3.

Average tumor doses tended to be higher for [^{177}Lu]Lu-PSMA-617 than for [^{177}Lu]Lu-PSMA-I&T in soft tissue (31.00 Gy [CI, 15.09–46.91 Gy] vs. 19.98 Gy [CI, 9.58–30.38 Gy]; $P = 0.26$). [^{177}Lu]Lu-PSMA-617 and [^{177}Lu]Lu-PSMA-I&T achieved comparable bone lesion doses (26.43 Gy [CI, 15.44–37.41 Gy] vs. 27.78 Gy [CI, 7.17–48.57 Gy]; $P = 0.90$).

Impact of Image Acquisition Protocol on Reported Doses

Supplemental Table 4 denotes the imaging protocol, scanner, and activity-to-dose conversion method used in the study. We completed a simple comparison of the published absorbed doses between SPECT/CT, hybrid, and planar acquisition methods (Supplemental Figs. 6 and 7). Briefly, the difference between the average dose reported based on the imaging acquisition protocols was influenced primarily by the size of the organ (Supplemental Fig. 6). As the organ volume decreased, the reported absorbed dose decreased when serial SPECT imaging was used as opposed to the other methods. This trend continued when the tumor lesions were evaluated (Supplemental Fig. 7).

Although differences between scanners do not play a large role in the absorbed dose calculation, the reconstruction parameters have been shown to affect measurements (*5*). Although seldom reported, in Supplemental Table 5 we show the reconstruction parameters used. It is unknown to what extent these influenced the absorbed dose calculation.

DISCUSSION

In this systematic review and metaanalysis, we compared the organ and tumor dose estimates of 3 [^{177}Lu]Lu-PSMA–targeted radiopharmaceuticals provided by 29 studies that included 535 patients. All 3 [^{177}Lu]Lu-PSMA compounds had absorbed doses to organs at risk well below the regulatory threshold. Historically, the kidney is the dose-limiting organ for regulatory purposes, restricting the therapeutic injection of higher injected activities. For [^{177}Lu]Lu-PSMA-617 and [^{177}Lu]Lu-PSMA-I&T, however, the dose-limiting organs by regulatory threshold are the salivary and lacrimal glands (*22,23*). For [^{177}Lu]Lu-J591, in contrast, the liver and bone marrow are dose-limiting and the dosimetry of other organs has not been reported (*24,25*).

[^{177}Lu]Lu-PSMA-I&T and [^{177}Lu]Lu-PSMA-617 differed only in absorbed dose to the parotid glands ($P < 0.01$). There was no significant difference in absorbed dose between [^{177}Lu]Lu-PSMA-I&T and [^{177}Lu]Lu-PSMA-617 in the other organs or tumor lesions even if there was a possible trend toward a higher kidney dose with [^{177}Lu]Lu-PSMA-I&T (weighted average, 4.04 vs. 4.70 Gy; $P = 0.10$). The trend toward lower kidney doses from [^{177}Lu]Lu-PSMA-617 than from [^{177}Lu]Lu-PSMA-I&T may be explained by the neutrally charged chelator DOTA of [^{177}Lu]Lu-PSMA-617 compared with the negatively charged chelator DOTAGA of [^{177}Lu]Lu-PSMA-I&T (-1). This negatively charged chelator can increase reabsorption of the ligand by the proximal tubule of the kidney and thus may result in a higher absorbed kidney dose (*26*). [^{177}Lu]Lu-PSMA-617 and [^{177}Lu]Lu-PSMA-I&T showed similar binding characteristics in tumors.

Clinical studies investigating [^{177}Lu]Lu-J591 tumor doses have not been published. However, tumor uptake may be higher because of longer radiopharmaceutical retention as shown in preclinical models (*27*).

Dosimetry protocols and technical parameters varied substantially among studies (image acquisition parameters, image reconstruction parameters, quantification methods, dose calculation methodologies, bone marrow dosimetry, first cycle vs. multiple cycles, etc.). Three-dimensional SPECT/CT, planar imaging, or a combination of the two (hybrid) can be performed on patients injected with [^{177}Lu]Lu-PSMA compounds. Multiple-time-point 3-dimensional SPECT/CT is viewed as the most accurate imaging technique to perform these calculations. We performed a simple comparison of the imaging techniques from the various published articles to the effect on the dosimetry and support the findings of Rosar et al. (*9*). Using planar-only imaging in dosimetry calculations results in higher uncertainty than using hybrid or SPECT/CT protocols (*5,11*). A detailed analysis of the impact of acquisition and reconstruction parameters on the derived doses was not feasible because of the limited information in the respective publications (Supplemental Tables 4 and 5). Most of the authors used the OLINDA/EXM software (based on MIRDDOSE 3.0/3.1 (*28*)) in their calculations of absorbed dose (https://www.doseinfo-radar.com/RADAROver.html). The difference between OLINDA/EXM and voxel-based techniques is the use of dose point kernels with patient-specific geometries of both organs and tumors in the latter, whereas OLINDA/EXM relies on phantom data.

Organ dosimetry of all 3 compounds was well within regulatory limits. It is worth mentioning that dose thresholds applied by regulatory agencies are likely inappropriate for RPT as there has been no formal dose–toxicity analysis. The current thresholds are derived from one work done in 1991 using conventional fractionated external-beam radiation therapy (*29*). Some authors correct the data presented from external-beam radiation therapy for RPT, suggesting that the absorbed kidney dose limit is closer to 39 Gy (expanded further in the supplemental materials) (*30–32*). Only a few studies have reported whether the number of RPT cycles (*14–16,33–35*) has an impact on kidney doses (*36,37*) or whether the injected activity has an impact on outcomes (*38*). There is a need to provide new thresholds specific to RPT along with developing proven radioprotection methods (prior methods are given in the supplemental materials). Monitoring of the short-term and long-term toxicity of RPT, and the correlation of observed clinical toxicity with dosimetry, is further warranted. Efforts to obtain a new expert consensus on these topics, such as the RPT-TEC group, should be encouraged and promoted.

This study had some limitations. The included studies were heterogeneous in terms of patient population and treatment protocols. Although seldom noted, the reconstruction parameters used were vastly different, which has been shown to have a profound effect on absorbed dose calculations. Partial-volume effect corrections were not mentioned in any of the published articles. The lack of standardization in imaging and dosimetry is the major obstacle in comparing results from many studies and pooling data.

CONCLUSION

In this metaanalysis, we provided doses estimates of [^{177}Lu]Lu-PSMA radiopharmaceuticals from 29 studies and 535 patients. There was no significant difference in absorbed dose between [^{177}Lu]Lu-PSMA-I&T and [^{177}Lu]Lu-PSMA-617 even if there was a possible trend toward a higher kidney dose with [^{177}Lu]Lu-PSMA-I&T and toward a higher tumor lesion dose with [^{177}Lu]Lu-PSMA-617. It remains unknown whether the higher tumor-to-kidney dose for PSMA-617 has any relevant impact on clinical outcomes such as progression-free or overall survival. The dosimetry methodologies were strikingly heterogeneous among studies, emphasizing the need for standardization.

DISCLOSURE

Jeremie Calais reports grants from support to his institution from Lantheus, Novartis, and POINT Biopharma. He also reports consulting activities (advisory board member, speaker, blinded reader) for Advanced Accelerator Applications, Amgen, Astellas, Bayer, Blue Earth Diagnostics Inc., Curium Pharma, DS Pharma, Fibrogen, GE Healthcare, Isoray, IBA RadioPharma, Janssen Pharmaceuticals, Monrol, Lightpoint Medical, Lantheus, Novartis, Pfizer, POINT Biopharma, Progenics, Radiomedix, Sanofi, Siemens-Varian, SOFIE, and Telix Pharmaceuticals, outside the submitted work. Statistical analyses for this research were supported by the National Center for Advancing Translational Science (NCATS) of the National Institutes of Health under UCLA Clinical and Translational Science Institute grant UL1TR001881. No other potential conflict of interest relevant to this article was reported.

KEY POINTS

QUESTION: Are there any differences among the dosimetry of [^{177}Lu]Lu-PSMA-617, [^{177}Lu]Lu-PSMA-I&T, and [^{177}Lu]Lu-J591?

PERTINENT FINDINGS: In this metaanalysis, we provided doses estimates of [^{177}Lu]Lu-PSMA radiopharmaceuticals from 29 studies and 535 patients. There was no significant difference in absorbed dose between [^{177}Lu]Lu-PSMA-I&T and [^{177}Lu]Lu-PSMA-617, although there was a possible trend toward a higher kidney dose with [^{177}Lu]Lu-PSMA-I&T and toward a higher tumor lesion dose with [^{177}Lu]Lu-PSMA-617. The lack of standardization in imaging and dosimetry is a major obstacle in comparing results from many studies and pooling data.

IMPLICATIONS FOR PATIENT CARE: [^{177}Lu]Lu-PSMA-617, [^{177}Lu]Lu-PSMA-I&T, and [^{177}Lu]Lu-J591 absorbed doses were all below regulatory thresholds for all organs. Although [^{177}Lu]Lu-PSMA-I&T seems to have a lower tumor dose and higher kidney dose than those of [^{177}Lu]Lu-PSMA-617, the clinical relevance of this finding remains unknown. Standardized dosimetry practices are warranted for further clinical implementation.

REFERENCES

1. Sartor O, de Bono J, Chi KN, et al. Lutetium-177-PSMA-617 for metastatic castration-resistant prostate cancer. *N Engl J Med.* 2021;385:1091–1103.
2. Dash A, Pillai MR, Knapp FF Jr. Production of ^{177}Lu for targeted radionuclide therapy: available options. *Nucl Med Mol Imaging.* 2015;49:85–107.
3. Jackson PA, Hofman MS, Hicks RJ, Scalzo M, Violet J. Radiation dosimetry in ^{177}Lu-PSMA-617 therapy using a single posttreatment SPECT/CT scan: a novel methodology to generate time- and tissue-specific dose factors. *J Nucl Med.* 2020; 61:1030–1036.
4. Mora-Ramirez E, Santoro L, Cassol E, et al. Comparison of commercial dosimetric software platforms in patients treated with ^{177}Lu-DOTATATE for peptide receptor radionuclide therapy. *Med Phys.* 2020;47:4602–4615.
5. Tran-Gia J, Denis-Bacelar AM, Ferreira KM, et al. A multicentre and multi-national evaluation of the accuracy of quantitative Lu-177 SPECT/CT imaging performed within the MRTDosimetry project. *EJNMMI Phys.* 2021;8:55.
6. Page MJ, McKenzie JE, Bossuyt PM, et al. The PRISMA 2020 statement: an updated guideline for reporting systematic reviews. *Rev Esp Cardiol (Engl Ed).* 2021;74:790–799.
7. Higgens JPT, Green S, eds. *Cochrane Handbook for Systematic Reviews of Interventions.* Wiley Blackwell; 2008:section 7.7.3.5.
8. Peters SMB, Privé BM, de Bakker M, et al. Intra-therapeutic dosimetry of [^{177}Lu]Lu-PSMA-617 in low-volume hormone-sensitive metastatic prostate cancer patients and correlation with treatment outcome. *Eur J Nucl Med Mol Imaging.* 2022;49:460–469.
9. Privé BM, Peters SMB, Muselaers CHJ, et al. Lutetium-177-PSMA-617 in low-volume hormone-sensitive metastatic prostate cancer: a prospective pilot study. *Clin Cancer Res.* 2021;27:3595–3601.
10. Fendler WP, Reinhardt S, Ilhan H, et al. Preliminary experience with dosimetry, response and patient reported outcome after ^{177}Lu-PSMA-617 therapy for metastatic castration-resistant prostate cancer. *Oncotarget.* 2017;8:3581–3590.
11. Rosar F, Schon N, Bohnenberger H, et al. Comparison of different methods for post-therapeutic dosimetry in [^{177}Lu]Lu-PSMA-617 radioligand therapy. *EJNMMI Phys.* 2021;8:40.
12. Yadav MP, Ballal S, Tripathi M, et al. Post-therapeutic dosimetry of ^{177}Lu-DKFZ-PSMA-617 in the treatment of patients with metastatic castration-resistant prostate cancer. *Nucl Med Commun.* 2017;38:91–98.
13. Barna S, Haug AR, Hartenbach M, et al. Dose calculations and dose-effect relationships in ^{177}Lu-PSMA I&T radionuclide therapy for metastatic castration-resistant prostate cancer. *Clin Nucl Med.* 2020;45:661–667.
14. Chatachot K, Shiratori S, Chaiwatanarat T, Khamwan K. Patient dosimetry of ^{177}Lu-PSMA I&T in metastatic prostate cancer treatment: the experience in Thailand. *Ann Nucl Med.* 2021;35:1193–1202.
15. Delker A, Fendler WP, Kratochwil C, et al. Dosimetry for ^{177}Lu-DKFZ-PSMA-617: a new radiopharmaceutical for the treatment of metastatic prostate cancer. *Eur J Nucl Med Mol Imaging.* 2016;43:42–51.
16. Kamaldeep, Wanage G, Sahu SK, et al. Examining absorbed doses of indigenously developed ^{177}Lu-PSMA-617 in metastatic castration-resistant prostate cancer patients at baseline and during course of peptide receptor radioligand therapy. *Cancer Biother Radiopharm.* 2021;36:292–304.
17. Baum RP, Kulkarni HR, Schuchardt C, et al. ^{177}Lu-labeled prostate-specific membrane antigen radioligand therapy of metastatic castration-resistant prostate cancer: safety and efficacy. *J Nucl Med.* 2016;57:1006–1013.
18. Feuerecker B, Chantadisai M, Allmann A, et al. Pretherapeutic comparative dosimetry of ^{177}Lu-rhPSMA-7.3 and ^{177}Lu-PSMA I&T in patients with metastatic castration-resistant prostate cancer. *J Nucl Med.* 2022;63:833–839.
19. Scarpa L, Buxbaum S, Kendler D, et al. The ^{68}Ga/^{177}Lu theragnostic concept in PSMA targeting of castration-resistant prostate cancer: correlation of SUV_{max} values and absorbed dose estimates. *Eur J Nucl Med Mol Imaging.* 2017;44: 788–800.
20. Violet J, Jackson P, Ferdinandus J, et al. Dosimetry of ^{177}Lu-PSMA-617 in metastatic castration-resistant prostate cancer: correlations between pretherapeutic imaging and whole-body tumor dosimetry with treatment outcomes. *J Nucl Med.* 2019;60:517–523.
21. Hohberg M, Reifegerst M, Drzezga A, Wild M, Schmidt M. Prediction of response to $_{177}$Lu-PSMA therapy based on tumor-to-kidney ratio on pretherapeutic PSMA PET/CT and posttherapeutic tumor-dose evaluation in mCRPC. *J Nucl Med.* 2023;64:1758–1764.
22. Uijen MJM, Prive BM, van Herpen CML, et al. Kidney absorbed radiation doses for [^{177}Lu]Lu-PSMA-617 and [^{177}Lu]Lu-PSMA-I&T determined by 3D clinical dosimetry. *Nucl Med Commun.* 2023;44:270–275.
23. Mahajan S, Grewal RK, Friedman KP, Schoder H, Pandit-Taskar N. Assessment of salivary gland function after ^{177}Lu-PSMA radioligand therapy: current concepts in imaging and management. *Transl Oncol.* 2022;21:101445.

24. Tagawa ST, Milowsky MI, Morris M, et al. Phase II study of lutetium-177-labeled anti-prostate-specific membrane antigen monoclonal antibody J591 for metastatic castration-resistant prostate cancer. *Clin Cancer Res.* 2013;19:5182–5191.
25. Hartrampf PE, Weinzierl FX, Buck AK, et al. Matched-pair analysis of [^{177}Lu]Lu-PSMA I&T and [^{177}Lu]Lu-PSMA-617 in patients with metastatic castration-resistant prostate cancer. *Eur J Nucl Med Mol Imaging.* 2022;49:3269–3276.
26. Vegt E, de Jong M, Wetzels JF, et al. Renal toxicity of radiolabeled peptides and antibody fragments: mechanisms, impact on radionuclide therapy, and strategies for prevention. *J Nucl Med.* 2010;51:1049–1058.
27. Bander NH, Milowsky MI, Nanus DM, Kostakoglu L, Vallabhajosula S, Goldsmith SJ. Phase I trial of ^{177}lutetium-labeled J591, a monoclonal antibody to prostate-specific membrane antigen, in patients with androgen-independent prostate cancer. *J Clin Oncol.* 2005;23:4591–4601.
28. Stabin MG, Sparks RB, Crowe E. OLINDA/EXM: the second-generation personal computer software for internal dose assessment in nuclear medicine. *J Nucl Med.* 2005;46:1023–1027.
29. Emami B, Lyman J, Brown A, et al. Tolerance of normal tissue to therapeutic irradiation. *Int J Radiat Oncol Biol Phys.* 1991;21:109–122.
30. Zechmann CM, Afshar-Oromieh A, Armor T, et al. Radiation dosimetry and first therapy results with a ^{124}I/^{131}I-labeled small molecule (MIP-1095) targeting PSMA for prostate cancer therapy. *Eur J Nucl Med Mol Imaging.* 2014;41:1280–1292.
31. Bodei L, Cremonesi M, Grana CM, et al. Peptide receptor radionuclide therapy with ^{177}Lu-DOTATATE: the IEO phase I-II study. *Eur J Nucl Med Mol Imaging.* 2011;38:2125–2135.
32. Sandström M, Freedman N, Fross-Baron K, Kahn T, Sundin A. Kidney dosimetry in 777 patients during ^{177}Lu-DOTATATE therapy: aspects on extrapolations and measurement time points. *EJNMMI Phys.* 2020;7:73.
33. Kratochwil C, Giesel FL, Stefanova M, et al. PSMA-targeted radionuclide therapy of metastatic castration-resistant prostate cancer with ^{177}Lu-labeled PSMA-617. *J Nucl Med.* 2016;57:1170–1176.
34. Mix M, Renaud T, Kind F, et al. Kidney doses in ^{177}Lu-based radioligand therapy in prostate cancer: is dose estimation based on reduced dosimetry measurements feasible? *J Nucl Med.* 2022;63:253–258.
35. Okamoto S, Thieme A, Allmann J, et al. Radiation dosimetry for ^{177}Lu-PSMA I&T in metastatic castration-resistant prostate cancer: absorbed dose in normal organs and tumor lesions. *J Nucl Med.* 2017;58:445–450.
36. Garin E, Tselikas L, Guiu B, et al. Personalised versus standard dosimetry approach of selective internal radiation therapy in patients with locally advanced hepatocellular carcinoma (DOSISPHERE-01): a randomised, multicentre, open-label phase 2 trial. *Lancet Gastroenterol Hepatol.* 2021;6:17–29.
37. Minczeles NS, de Herder WW, Feelders RA, Verburg FA, Hofland J, Brabander T. Long-term outcomes of submaximal activities of peptide receptor radionuclide therapy with ^{177}Lu-DOTATATE in neuroendocrine tumor patients. *J Nucl Med.* 2023;64:40–46.
38. Sundlöv A, Gleisner KS, Tennvall J, et al. Phase II trial demonstrates the efficacy and safety of individualized, dosimetry-based ^{177}Lu-DOTATATE treatment of NET patients. *Eur J Nucl Med Mol Imaging.* 2022;49:3830–3840.
39. Kabasakal L, AbuQbeitah M, Aygun A, et al. Pre-therapeutic dosimetry of normal organs and tissues of ^{177}Lu-PSMA-617 prostate-specific membrane antigen (PSMA) inhibitor in patients with castration-resistant prostate cancer. *Eur J Nucl Med Mol Imaging.* 2015;42:1976–1983.
40. Hohberg M, Eschner W, Schmidt M, et al. Lacrimal glands may represent organs at risk for radionuclide therapy of prostate cancer with [^{177}Lu]DKFZ-PSMA-617. *Mol Imaging Biol.* 2016;18:437–445.
41. Gosewisch A, Delker A, Tattenberg S, et al. Patient-specific image-based bone marrow dosimetry in Lu-177-[DOTA^0,Tyr^3]-octreotate and Lu-177-DKFZ-PSMA-617 therapy: investigation of a new hybrid image approach. *EJNMMI Res.* 2018;8:76.
42. Gosewisch A, Ilhan H, Tattenberg S, et al. 3D Monte Carlo bone marrow dosimetry for Lu-177-PSMA therapy with guidance of non-invasive 3D localization of active bone marrow via Tc-99m-anti-granulocyte antibody SPECT/CT. *EJNMMI Res.* 2019;9:76.
43. Sarnelli A, Belli ML, Di Iorio V, et al. Dosimetry of ^{177}Lu-PSMA-617 after mannitol infusion and glutamate tablet administration: preliminary results of EUDRACT/RSO 2016-002732-32 IRST protocol. *Molecules.* 2019;24:621.
44. Paganelli G, Sarnelli A, Severi S, et al. Dosimetry and safety of ^{177}Lu PSMA-617 along with polyglutamate parotid gland protector: preliminary results in metastatic castration-resistant prostate cancer patients. *Eur J Nucl Med Mol Imaging.* 2020; 47:3008–3017.
45. Völter F, Mittlmeier L, Gosewisch A, et al. Correlation of an index-lesion-based SPECT dosimetry method with mean tumor dose and clinical outcome after ^{177}Lu-PSMA-617 radioligand therapy. *Diagnostics (Basel).* 2021;11:428.
46. Schuchardt C, Zhang J, Kulkarni HR, Chen X, Muller D, Baum RP. Prostate-specific membrane antigen radioligand therapy using ^{177}Lu-PSMA I&T and ^{177}Lu-PSMA-617 in patients with metastatic castration-resistant prostate cancer: comparison of safety, biodistribution, and dosimetry. *J Nucl Med.* 2022;63:1199–1207.
47. Herrmann K, Rahbar K, Eiber M, et al. Renal and multiorgan safety of ^{177}Lu-PSMA-617 in patients with metastatic castration-resistant prostate cancer in the VISION dosimetry substudy. *J Nucl Med.* 2024;65:71–78.
48. Krause BJ, Chi KN, Sartor AO, et al. Tumor dosimetry of [^{177}Lu]Lu-PSMA-617 for the treatment of metastatic castration-resistant prostate cancer: results from the VISION trial sub-study [abstract]. *J Clin Oncol.* 2023;41:5046.
49. Kelk E, Ruuge P, Rohtla K, Poksi A, Kairemo K. Radiomics analysis for ^{177}Lu-DOTAGA-(l-y)fk(Sub-KuE) targeted radioligand therapy dosimetry in metastatic prostate cancer: a model based on clinical example. *Life (Basel).* 2021;11:170.
50. Beauregard J-M. Dosimetry results from the SPLASH trial. Paper presented at: 2022 Virtual SNMMI Mid-Winter and ACNM Annual Meeting; February 25–27, 2022.
51. Resch S, Takayama Fouladgar S, Zacherl M, et al. Investigation of image-based lesion and kidney dosimetry protocols for ^{177}Lu-PSMA-I&T therapy with and without a late SPECT/CT acquisition. *EJNMMI Phys.* 2023;10:11.
52. Vallabhajosula S, Goldsmith SJ, Hamacher KA, et al. Prediction of myelotoxicity based on bone marrow radiation-absorbed dose: radioimmunotherapy studies using ^{90}Y- and ^{177}Lu-labeled J591 antibodies specific for prostate-specific membrane antigen. *J Nucl Med.* 2005;46:850–858.

Impact of the Reference Multiple-Time-Point Dosimetry Protocol on the Validity of Single-Time-Point Dosimetry for [^{177}Lu]Lu-PSMA-I&T Therapy

Sandra Resch[1], Sibylle I. Ziegler[1], Gabriel Sheikh[1], Lena M. Unterrainer[1,2], Mathias J. Zacherl[1], Peter Bartenstein[1], Guido Böning[1], Julia Brosch-Lenz[3], and Astrid Delker[1]

[1]Department of Nuclear Medicine, LMU University Hospital, LMU, Munich, Germany; [2]Ahmanson Translational Theranostics Division, Department of Molecular and Medical Pharmacology, UCLA, Los Angeles, California; and [3]Department of Nuclear Medicine, Technical University of Munich, Munich, Germany

Internal dosimetry supports safe and effective patient management during radionuclide therapy. Yet, it is associated with high clinical workload, costs, and patient burden, as patient scans at multiple time points (MTPs) must be acquired. Dosimetry based on imaging at a single time point (STP) has continuously gained popularity. However, MTP protocols, used as a reference to judge the validity of STP dosimetry, differ depending on local requirements and deviate from the unknown patient-specific ground truth pharmacokinetics. The aim of this study was to compare the error and optimum time point for different STP approaches using different reference MTP protocols. **Methods:** Whole-body SPECT/CT scans of 7 patients (7.4–8.9 GBq of [^{177}Lu]Lu-PSMA-I&T) were scheduled at 24, 48, 72, and 168 h after injection. Sixty lesions, 14 kidneys, and 10 submandibular glands were delineated in the SPECT/CT data. Two curve models, that is, a mono- and a biexponential model, were fitted to the MTP data, in accordance with goodness-of-fit analysis (coefficients of variation, sum of squared errors). Three population-based STP approaches were compared: one method published by Hänscheid et al., one by Jackson et al., and one using population-based effective half-lives in the mono- or biexponential curve models. Percentage differences between STP and MTP dosimetry were evaluated. **Results:** Goodness-of-fit parameters show that a monoexponential function and a biexponential function with shared population-based parameters and physical tail are reasonable reference models. When comparing both reference models, we observed maximum differences of −44%, −19%, and −28% in the estimated absorbed doses for lesions, kidneys, and salivary glands, respectively. STP dosimetry with an average deviation of less than 10% from MTP dosimetry may be feasible; however, this deviation and the optimum imaging time point showed a dependence on the chosen reference protocol. **Conclusion:** STP dosimetry for [^{177}Lu]Lu-PSMA therapy is promising to boost the integration of dosimetry into clinical routine. According to our patient cohort, 48 h after injection may be regarded as a compromise for STP dosimetry for lesions and at-risk organs. The results from this analysis show that a common gold standard for dosimetry is desirable to allow for reliable and comparable STP dosimetry.

Key Words: PSMA; ^{177}Lu; dosimetry; single time point

J Nucl Med 2024; 65:1272–1278
DOI: 10.2967/jnumed.123.266871

Targeting of the prostate-specific membrane antigen (PSMA) with [^{177}Lu]Lu-PSMA therapy evolved as a promising strategy for the treatment of metastasized castration-resistant prostate cancer, which is one of the main worldwide causes of death in men (*1*). The VISION trial led to the approval of [^{177}Lu]Lu-vipivotide tetraxetan (Pluvicto; Novartis) by the U.S. Food and Drug Administration in March 2022 and by the European Medicines Agency in December 2022 (*2*). Patient-specific internal dosimetry supports safe and efficient patient management during radionuclide therapy by monitoring the absorbed radiation dose to both healthy and malignant tissues (*3,4*). However, internal dosimetry requires quantitative images, preferably SPECT or PET, at multiple time points (MTPs) at least over the initial days after injection (*5–7*). The associated high number of examinations poses a high workload and additional costs to the clinics in cases of unclear reimbursement. These factors have so far limited the routine implementation of clinical dosimetry, although it is more and more legally requested (*8,9*). The rising number of therapies as expected after the U.S. Food and Drug Administration and European Medicines Agency approval of [^{177}Lu]Lu-vipivotide tetraxetan will probably further complicate the integration of routine dosimetry into the clinical workflow. On the other hand, only routine dosimetry with reasonable accuracy can provide the empiric knowledge that is necessary to tailor PSMA therapy more to the individual patient characteristics, as for example, with respect to treatment activity per cycle or number of cycles.

To handle the workload associated with increasing routine use of dosimetry, dosimetry based on fewer image acquisitions and even single-time-point (STP) dosimetry methods are being intensively investigated for ^{177}Lu-based treatments (*10–25*). Depending on the selected imaging time point, these protocols lay within an acceptable agreement of around 10% compared with a selected ground truth protocol that is based on serial quantitative imaging. To derive the time-integrated activity (TIA) for each tissue of interest, most of the proposed STP methods measure the uptake per tissue based on a single quantitative image and combine this single uptake measurement with some prior knowledge about the tissue-specific effective half-life. The latter could be a population-based effective half-life or the patient-specific effective half-life of a former therapy cycle. Besides the exact STP method used for the calculation of the TIA itself, so far published methods differ regarding the considered reference model (Table 1). The reference model for MTP dosimetry is defined by the number and timing of

---

Received Oct. 17, 2023; revision accepted Apr. 22, 2024.

For correspondence or reprints, contact Sandra Resch (sandra.resch@med.uni-muenchen.de).

TABLE 1
Overview of STP Dosimetry for [^{177}Lu]Lu-PSMA Therapy

Study	Compound	Reference time points	Reference fit	Optimum STP (h): Kidneys	Optimum STP (h): Lesions	Optimum STP (h): Salivary glands	Criterion for optimal STP
Brosch-Lenz et al. (*10*)	[^{177}Lu]Lu-PSMA-617	24, 48, 72 h	Monoexponential	48	72	NA	Percentage difference
Jackson et al. (*11*)	[^{177}Lu]Lu-PSMA-617	4, 24, 96 h	Triexponential	<48	≥72	<48	Mean absolute deviation
Rinscheid et al. (*18*)	[^{177}Lu]Lu-PSMA-I&T	30–120 min, 24 h, 168 h	PBPK/monoexponential	52	72 h	NA	Root-mean-squared error
Peters et al. (*17*)	[^{177}Lu]Lu-PSMA-617	1, 24, 48, 72, 168 h	Compartment-specific combination of linear interpolation and monoexponential	24/48	168	24/48	Various (e.g., Lin concordance correlation coefficient)
Kurth et al. (*13*)	[^{177}Lu]Lu-PSMA-617	2, 24, 48, 72 h	Rapid uptake + biexponential	48	—	48	Bland–Altman analysis, rmANOVA

NA = not applicable; PBPK = physiologically based pharmacokinetics; rmANOVA = repeated-measures ANOVA.

the image acquisition itself and the mathematic fit model that is applied to the data points. These reference protocols are highly variable between institutions, as internal dosimetry still lacks standardization, and as site-specific protocols must be tailored to the local situation. Because the reference model is usually already limited by clinical feasibility, it cannot be considered a real ground truth but already represents an approximation with some protocol-dependent error. Thus, findings on STP dosimetry such as optimum time point and percentage deviation compared with MTP dosimetry cannot necessarily be transferred from one considered MTP reference protocol to another. The aim of this study was to investigate how the choice of reference model affects selection of the optimum method for STP dosimetry in the scope of [^{177}Lu]Lu-PSMA-I&T therapy.

MATERIALS AND METHODS

Patients

This study included 7 patients diagnosed with metastasized castration-resistant prostate cancer in their first cycle of [^{177}Lu]Lu-PSMA-I&T therapy (Table 2). All patients gave written consent to undergo radiopharmaceutical therapy. The institutional review board approved this retrospective study, and the requirement to obtain informed consent was waived (reference 22-0552).

Imaging

SPECT/CT measurements were scheduled 24, 48, 72, and 168 h after injection on a dual-head Symbia Intevo T16 SPECT/CT (Siemens Healthineers) using a standard ^{177}Lu protocol (*26*) (Supplemental Fig. 1; supplemental materials are available at http://jnm.snmjournals.org).

Dosimetry

Sixty lesions, 14 kidneys, and 10 submandibular glands were delineated daywise in the SPECT/CT data. Kidney volumes of interest (VOIs) were drawn manually on the CT data. Lesions and submandibular glands were delineated using a 30% isocontour of the average within a spheric VOI of 12-mm diameter centered at the tissue maximum (*26,27*). To allow for a more robust quantification, only lesions with volumes larger than 5 cm^3 were included. Only 10 submandibular glands could be investigated since segmentation was not possible for 2 patients because the field of view was too small. The parotid glands could not be evaluated, as they were not completely covered in the SPECT acquisitions. Mean activity concentrations and volumes were extracted. Absorbed doses were estimated using an in-house routine and mass-scaled organ and tumor S values as extracted from OLINDA/EXM version 2.0 (lesions: 2.33e−05 Gy/[MBq × s], 1 g; kidneys: 7.74e−08 Gy/[MBq × s], 310 g; salivary glands: 2.76e−07 Gy/[MBq × s], 85 g) (*28*).

TABLE 2
Patient Information

Patient no.	Age (y)	Weight (kg)	Height (cm)	PSA (ng/mL)	Activity (GBq)	Number of lesions in field of view	Location of segmented lesions
1	68	83	173	84	7.40	7	Bone
2	83	58	166	197	7.45	8	Bone
3	68	95	180	286	7.39	4	Lymph node
4	83	84	187	551	7.43	9	Bone
5	76	75	170	1,500	8.93	15	Bone
6	55	68	170	4.6	7.94	4	Bone
7	68	85	183	52	7.84	13	Bone

Reference MTP Dosimetry

The TIA was first estimated for each compartment by fitting and integrating all available imaging time points using a monoexponential model and a biexponential model. For the latter, all possible realizations with up to 3 free parameters as proposed by Hardiansyah et al. were considered (*29*). All fit functions were evaluated by common goodness-of-fit criteria, that is, the coefficients of variation (CV) and the sum of squared errors (*30,31*). Finally, the following 2 functions were used to fit the reference MTP model:

$$f_{\mathrm{mono}}(t) = A_0 e^{-(\lambda_{\mathrm{bio}}+\lambda_{\mathrm{phys}})t},$$

$$f_{\mathrm{bi1,s}\gamma}(t) = A_0 \gamma e^{-(\lambda_{\mathrm{bio}}+\lambda_{\mathrm{phys}})t} + A_0(1-\gamma)e^{-(\lambda_{\mathrm{phys}})t} \text{ with shared } \gamma.$$

A_0 refers to $A(t = 0)$, and λ_{bio} and λ_{phys} are the biologic and physical clearance rates, respectively. The population-based γ-parameter modulates the transition from the phase with biologic clearance to the phase without biologic clearance and was determined by the jackknife method. For the latter, the respective function is fitted to the data of all patients except the one currently being investigated. The CV refer to the 2 free parameters A_0 (CV_A) and λ_{bio} (CV_λ).

STP Dosimetry

Three different STP approaches were evaluated with a single SPECT/CT acquisition at 24, 48, 72, or 168 h after injection: a monoexponential (STP_{mono}) or a biexponential (STP_{bi}) function with population-based biologic clearance rates; the method by Hänscheid et al., originally established for ^{177}Lu-DOTATE/DOTATOC therapy (STP_H) (*12*); and the method proposed by Jackson et al. (STP_J) (*11*).

The TIA for STP_{mono} is given by

$$TIA_{\mathrm{mono}} = \frac{1}{(\lambda_{\mathrm{bio}}+\lambda_{\mathrm{phys}})} \frac{A(t_{\mathrm{SPECT}})}{\exp(-(\lambda_{\mathrm{bio}}+\lambda_{\mathrm{phys}}) \cdot t_{\mathrm{SPECT}})}.$$

t_{SPECT} and $A(t_{\mathrm{SPECT}})$ refer to imaging time point and the VOI activity measured for that time point, respectively. Two population-based parameters, λ_{bio} and γ, were used for STP_{bi}, with the TIA being given by

$$TIA_{\mathrm{bi}} = \frac{A(t_{\mathrm{SPECT}})}{\gamma \exp(-(\lambda_{\mathrm{bio}}+\lambda_{\mathrm{phys}}) \cdot t_{\mathrm{SPECT}}) + (1-\gamma) \cdot \exp(-\lambda_{\mathrm{phys}}\, t_{\mathrm{SPECT}})} \cdot \left(\frac{\gamma}{\lambda_{\mathrm{bio}}+\lambda_{\mathrm{phys}}} + \frac{1-\gamma}{\lambda_{\mathrm{phys}}}\right).$$

For STP_H, the TIA is estimated by

$$TIA_H = A(t_{\mathrm{SPECT}}) \cdot \frac{2}{\ln(2)} \cdot t_{\mathrm{SPECT}}.$$

Hänscheid et al. stated that if imaging is performed between $0.75\, t_{1/2,\mathrm{eff}}$ and $2.5\, t_{1/2,\mathrm{eff}}$ ($t_{1/2,\mathrm{eff}}$ is effective half-life), the error in the TIA is less than 10% (*12*). In this study, we investigated all available time points, assuming that time points that do not fulfil this criterion will automatically show a larger deviation from the reference. More information about the VOIs and time points t_{SPECT} for which the criterion $0.75\, t_{1/2,\mathrm{eff}} < t_{\mathrm{SPECT}} < 2.5\, t_{1/2,\mathrm{eff}}$ was applied is given in Supplemental Table 2.

For STP_J, it is assumed that

$$TIA_J = A(t_{\mathrm{SPECT}}) \cdot f_{\mathrm{tissue}}(t_{\mathrm{SPECT}}),$$

with f_{tissue} being a scaling factor depending on time point and compartment. The factors were recalculated for our patient cohort according to the method described by Jackson et al. because of the different PSMA compound used in this study (Supplemental Table 2) (*11*).

Data Evaluation

The Wilcoxon signed-rank test was used to compare the dosimetry estimates and the goodness-of-fit parameters for the reference models monoexponential MTP (MTP_{mono}) and biexponential MTP (MTP_{bi}). Mean absolute deviations of STP methods from MTP_{mono} and MTP_{bi} were determined per compartment, whereupon STP_{mono} was compared only with MTP_{mono} and STP_{bi} only with MTP_{bi}. The best imaging time point or STP method was defined as the one with the lowest mean absolute deviation. The percentage of VOIs with a deviation of less than |10|% was used as a secondary criterion.

RESULTS

Table 3 shows the goodness-of-fit parameters for both the mono- and biexponential reference model, as well as the statistical evaluation. For the salivary glands, MTP_{bi} seemed to be superior to MTP_{mono}, as both the CV and the sum of squared errors were significantly lower ($P < 0.05$). Such was not the case for the kidneys. The average goodness-of-fit parameters would favor MTP_{bi} but without statistical significance ($P > 0.05$). For the lesions, CV λ_{bio} significantly favored MTP_{mono} ($P < 0.05$), whereas the sum of squared errors significantly favored MTP_{bi} ($P < 0.05$). However, the monoexponential reference model yielded significantly lower absorbed doses than did the biexponential fit (Table 3). Although for both the kidneys and the lesions, no reference model was deemed to be superior, maximum absorbed dose deviations of −19% and −44% were found for kidneys and lesions, respectively (Table 3). As expected, CV λ_{bio} was found to be larger for lesions than for kidneys and salivary glands, indicating a larger pharmacokinetic variability for lesions. Average (±SD) effective half-lives were found to be 56.5 ± 18.8, 32.9 ± 5.9, and 22.5 ± 2.8 h for lesions, kidneys, and salivary glands, respectively. More information on the distribution of effective half-lives and some exemplary time–activity curves are shown in Supplemental Figures 3–5.

The deviations of all STP methods and imaging time points from the reference models are listed in Supplemental Tables 3 and 4.

Kidneys

For both reference models, 48 h after injection was found to be the optimum imaging time point (Figs. 1A and 1B). STP_{mono} and STP_H showed the smallest mean absolute deviations from the monoexponential reference model MTP_{mono}, at 3% ± 4% and 4% ± 4%, respectively. Compared with the biexponential reference model MTP_{bi}, STP_{bi} and STP_J indicated the smallest mean absolute deviations of 4% ± 4% and 4% ± 5%, respectively, with a slight preference for STP_{bi} since for 86% (vs. 71%) of VOIs the renal absorbed doses deviated less than 10% from the reference (Fig. 1D).

Salivary Glands

SPECT/CT imaging at 24 h after injection in combination with STP_{bi} resulted in the lowest mean absolute dose deviation of 4% ± 4% (all VOIs within |10|%), when compared with the best-suited reference model, that is, MTP_{bi} (Figs. 2B and 2D). At 48 h after injection, STP_{bi} showed the best performance as well (mean absolute deviation of 10% ± 14%, with 70% of all VOIs within |10|%) (Figs. 2B and 2D).

Lesions

Larger deviations from the reference models were observed for lesions than for at-risk organs, with 48–72 h being the best-suited time point (Figs. 3A and 3B). Compared with MTP_{mono}, STP_{mono} and STP_H—both with imaging at 72 h after injection—showed a similar performance (average deviation, 8% ± 9% and 7% ± 9%, respectively, with 73% and 70% of lesions deviating less than 10% from MTP_{mono}) (Figs. 3A and 3C). Compared with MTP_{bi},

TABLE 3
Fit and Dosimetry Results for Reference Models

Parameter	Kidneys (*n* = 14)	Salivary glands (*n* = 10)	Lesions (*n* = 60)
Volume ± SD (cm^3)	216 ± 58	10 ± 2	25 ± 25
MTP$_{mono}$ goodness of fit			
CV$_A$/CV$_\lambda$ (%)	3.3 ± 2.3/6.3 ± 5.3	11.1 ± 7.6/14.9 ± 9.1	8.3 ± 4.5/25.8 ± 18.6
SSE	6.2 ± 5.6	0.05 ± 0.02	8.3 ± 17.0
Dose ± SD* (Gy/GBq)	0.32 ± 0.07	0.21 ± 0.08	0.95 ± 0.50
Half-life ± SD (h) (CV)	32.9 ± 5.9 (17.8%)	22.5 ± 2.8 (12.3%)	56.5 ± 18.8 (33.2%)
MTP$_{bi}$ goodness of fit			
CV$_A$/CV$_\lambda$ (%)	3.1 ± 2.2/6.0 ± 5.1	8.2 ± 8.1/9.9 ± 7.0	8.9 ± 6.0/28.3 ± 22.2
SSE	3.8 ± 3.2	0.01 ± 0.01	6.4 ± 12.0
Dose ± SD† (Gy/GBq)	0.36 ± 0.09	0.28 ± 0.1	1.10 ± 0.70
Comparison of calculated absorbed dose: MTP$_{mono}$ vs. MTP$_{bi}$			
AD ± SD† (%)	−10.6 ± 3.8	−24.2 ± 3.1	−13.9 ± 9.7
Maximum deviation† (%)	−19	−28	−44
P value‡	<0.001	0.002	<0.001
Comparison of goodness-of-fit parameters: MTP$_{mono}$ vs. MTP$_{bi}$			
P values‡ CV$_A$/CV$_\lambda$	0.583/0.761	0.027/0.020	0.233/0.026
P values‡ SSE	0.135	0.002	<0.001

---

*Values without recovery correction.

†Calculated via $\frac{(\mathrm{MTP}_{mono}-\mathrm{MTP}_{bi})}{\mathrm{MTP}_{bi}}\cdot 100\%$.

‡Wilcoxon signed-rank test.

CV$_A$/CV$_\lambda$ = CV A_0/CV λ_{bio}; AD ± SD = average deviation ± SD of absorbed dose; SSE = sum of squared errors.

similar average deviations for all 3 STP methods could be obtained (STP$_{bi}$, 10% ± 13%; STP$_H$, 16% ± 10%; and STP$_J$, 10% ± 10%) but with use of different optimum imaging time points (72 h for STP$_H$ and STP$_J$, 48 h for STP$_{bi}$) (Figs. 3B and 3D).

DISCUSSION

The aim of this study was to compare different STP approaches for 2 reference models and—apart from the bone marrow—the main compartments of interest during [^{177}Lu]Lu-PSMA treatment, that is, lesions, kidneys, and salivary glands. Although MTP$_{bi}$ could be identified as the best-suited reference model for the salivary glands, no superiority of MTP$_{bi}$ or MTP$_{mono}$ could be established for kidney and lesion dosimetry using SPECT acquisitions at 24, 48, 72, and 168 h after injection. However, absorbed dose estimates were found to be significantly different for both reference models. A higher number of image acquisitions may help to reduce the ambiguity of the optimum reference model for lesion and kidney dosimetry. Yet, the number of image acquisitions available in a clinical setting is inherently limited. For example, although the late pharmacokinetics has a significant impact on dosimetry estimates (*32*), image acquisitions are usually terminated, at the latest, at around 7–9 d after injection for logistic reasons and because SPECT imaging at late time points is limited by a decreasing activity concentration. Although STP dosimetry is feasible, Figures 1, 2, 3A, and 3B highlight that the error of each STP method depends on the reference MTP protocol. Thus, an uncertainty in the reference MTP protocol automatically translates into the selection of the optimum STP method. Comparability of STP dosimetry from different studies requires careful consideration of the reference protocols that were used to define the STP methodology. In this sense, the popularity of STP dosimetry also strengthens the request for standardization of clinically feasible but reliable MTP protocols.

The optimum imaging time point for renal STP dosimetry is clearly 48 h for all STP methods and both reference models. As no superiority for MTP$_{bi}$ or MTP$_{mono}$ could be proven and, thus, the underlying pharmacokinetics is not well known, STP$_{mono}$ and STP$_{bi}$ should be avoided. Thus for kidney STP dosimetry, STP$_H$ is recommended over STP$_J$ because the number of VOIs with a deviation of less than 10% is high for both MTP$_{mono}$ and MTP$_{bi}$. Similarly, STP$_J$ with imaging at 72 h can be recommended for lesion STP dosimetry. For the salivary glands, MTB$_{bi}$ could be identified as the optimum reference model, with imaging at 24 h after injection and STP$_{bi}$ being the best choice for STP dosimetry.

The definition of a specific STP methodology is further complicated by the fact that the optimal STP dosimetry for different compartments is usually associated with different optimum imaging time points. From a clinical perspective, STP approaches should be available with similar performance for lesions and organs at risk. However, considering the results in both Figure 1 and Figure 2, compared with Figure 3, a trade-off between the accuracy of dosimetry for lesions and at-risk organs is necessary. The optimum time point is also likely to depend on the question of whether the

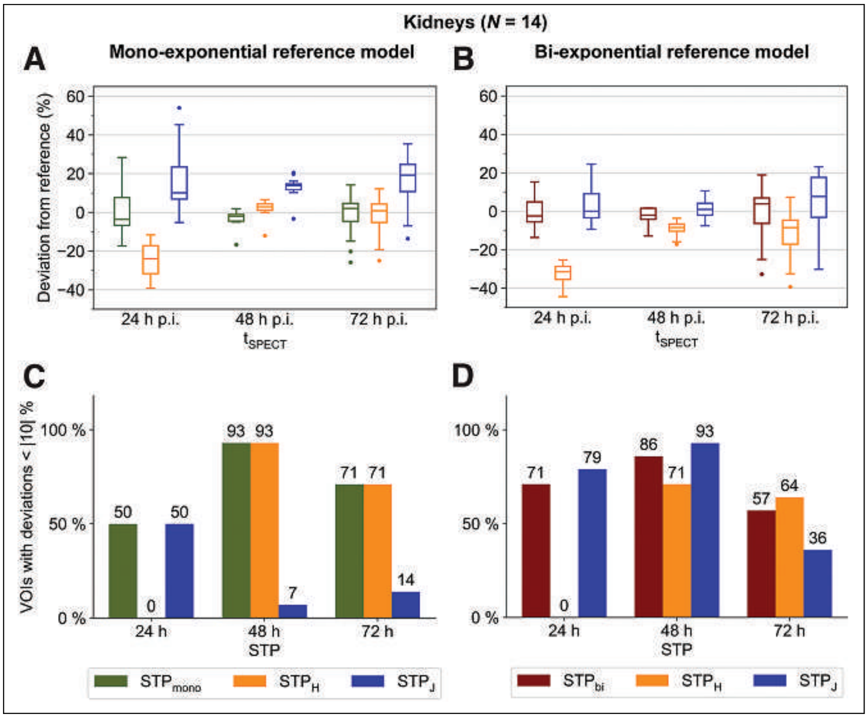

FIGURE 1. (A and B) Deviation of kidney STP dosimetry from MTP dosimetry using monoexponential (A) or biexponential (B) MTP reference models and for different imaging time points. (C and D) Percentage of VOIs with deviation less than |10|% using monoexponential (C) or biexponential (D) MTP reference models and for different imaging time points. Numbers above each bar indicate exact percentages. For better visualization, data for 168 h after injection are shown in Supplemental Figure 6 and Supplemental Tables 5 and 6. p.i. = after injection.

primary objective of dosimetry is safety or efficacy. It may be possible to merge STP dosimetry for lesions, kidneys, and salivary glands based on imaging at 48 h after therapy, although this will result in a lower level of accuracy for lesions (optimum, 72 h after injection) and salivary glands (optimum, 24 h after injection). For the salivary glands with MTP_{bi} as the optimum reference protocol, STP_{bi} is suggested for imaging at 48 h after injection. For lesion dosimetry, STP_J is recommended for imaging at 48 h after injection, as it shows a more balanced performance for MTP_{bi} and MTP_{mono} than does STP_H.

The overall number of patients in this study was low. Especially, the used biexponential reference model applies a population-based shared parameter γ that should be reevaluated for a larger patient cohort. Further, this population-based parameter may vary over the course of subsequent therapy cycles, whereas only the first therapy cycle was investigated in this study. However, Hardiansyah et al. found a value of 0.963 ± 0.004 for the renal biokinetics of 13 [^{177}Lu]Lu-PSMA-I&T patients (*29*), compared with a very similar value of 0.956 ± 0.007 (CV, 0.7%) for 14 kidneys and 7 patients in this study (0.8% deviation). In addition, the method proposed by Hänscheid et al. (*12*) was originally developed for monoexponential pharmacokinetics but was compared with a biexponential reference model in this study as well. However, the intention was to show the effect of an unknown ground truth model on STP methodology. For example, for the salivary glands, with clearly biexponential pharmacokinetics, STP_H showed poor performance. Despite the smaller patient cohort, the optimum time points proposed in this study agreed well with previously published data (*10,11,13,17,18*). As data with a late SPECT scan at around 7 d after injection were available for only a selected number of patients undergoing their first treatment cycle in this study, no prior information on the compartment-specific effective half-life was available, limiting this study to population-based approaches only. Brosch-Lenz et al. investigated a prior-information approach based on the patient-specific effective half-life of the previous treatment cycle in comparison to the method proposed by Hänscheid et al. for kidney and lesion STP dosimetry and for [^{177}Lu]Lu-PSMA-I&T therapy (*10,12*). The reference model was a monoexponential fit with SPECT/CT imaging at 24, 48, and 72 h after treatment. The method by Hänscheid et al. was slightly superior for the kidneys, whereas for lesion STP dosimetry the prior-information approach showed better performance, possibly because the lesion pharmacokinetics usually shows a larger interpatient and intrapatient variability.

Population-based approaches assume an average patient with average pharmacokinetics. It should be further investigated whether patient-specific factors, such as changes in tumor volume, kidney function, or any other patient-specific factors that deviate from the average patient, may guide the decision between MTP and STP dosimetry. Scheduling MTP dosimetry intermittently (e.g., alternating between MTP and STP dosimetry) may be a trade-off between clinical efficiency and accuracy. Further, in view of the observed outliers for different STP approaches, quality control is an important aspect of STP dosimetry. The use of mixed-linear-effects models, which consider each parameter as a combination of a mixed population-based effect and a random patient-specific effect, has already been shown to be promising for reducing outliers within STP dosimetry (*19,24*).

Current research also focuses on speeding the SPECT acquisition, a development that is lately being driven by the integration of artificial intelligence into molecular imaging (*33–35*). This should be considered as an opportunity to maintain MTP-based protocols, at least in centers that hospitalize patients or where multiple examinations are feasible on an outpatient basis.

CONCLUSION

STP dosimetry is becoming more popular because it allows for efficient integration of internal dosimetry into clinical routine. Usually, however, the considered reference MTP protocol already approximates the real but unknown clinical ground truth, and its error is in addition to the error of STP dosimetry itself. The intercomparison of different STP methods shows a different optimum time point and error depending on the compartment and the reference MTP protocol. According to our patient cohort, 48 h after injection may be regarded as a compromise for STP dosimetry for lesions and at-risk organs.

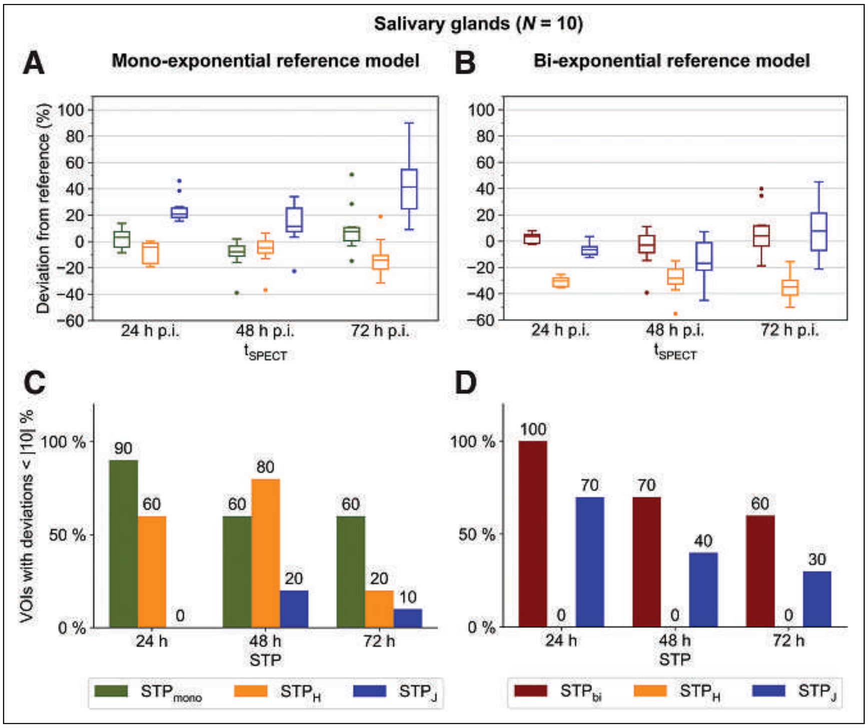

FIGURE 2. (A and B) Deviations of salivary gland STP dosimetry from MTP dosimetry using monoexponential (A) and biexponential (B) reference models and different imaging time points. (C and D) Percentage of VOIs with deviation less than |10|% using monoexponential (C) and biexponential (D) reference models and different imaging time points. Numbers above each bar indicate exact percentages. For better visualization, data for 168 h after injection are shown in Supplemental Figure 6 and Supplemental Tables 5 and 6. p.i. = after injection.

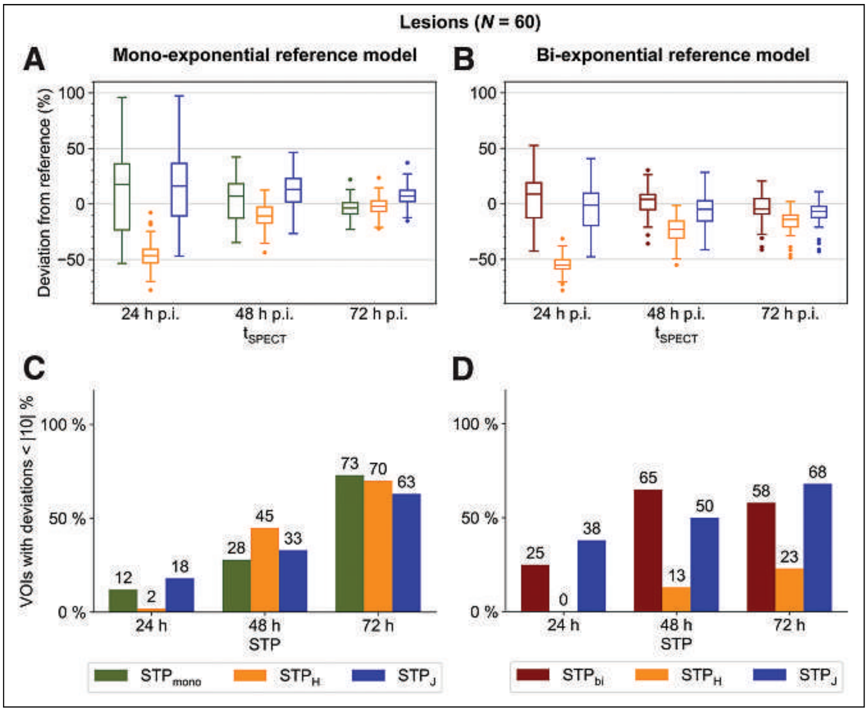

FIGURE 3. (A and B) Deviation of lesion STP dosimetry from MTP dosimetry using monoexponential (A) or biexponential (B) MTP reference models and for different imaging time points. (C and D) Percentage of VOIs with deviation less than |10|% using monoexponential (C) or biexponential (D) MTP reference models and for different imaging time points. Numbers above each bar indicate exact percentages. For better visualization, data for 168 h after injection are shown in Supplemental Figure 6 and Supplemental Tables 5 and 6. p.i. = after injection.

DISCLOSURE

Astrid Delker is partially funded by the Federal Ministry of Education and Research (funding number 02NUK065C). No other potential conflict of interest relevant to this article was reported.

KEY POINTS

QUESTION: Does the reference model impact findings on STP dosimetry for [^{177}Lu]Lu-PSMA-I&T therapy?

PERTINENT FINDINGS: The error of each STP dosimetry method depends on compartment, time point, and reference MTP protocol. In our patient cohort, 48 h may be regarded as a compromise for dosimetry for lesions and healthy tissues.

IMPLICATIONS FOR PATIENT CARE: STP dosimetry for [^{177}Lu]Lu-PSMA-I&T can be performed, but at the cost of some level of accuracy. Further efforts to standardize internal dosimetry are important to harmonize MTP and STP dosimetry among centers.

REFERENCES

1. Ljungberg M, Celler A, Konijnenberg MW, et al. MIRD pamphlet no. 26: joint EANM/MIRD guidelines for quantitative ^{177}Lu SPECT applied for dosimetry of radiopharmaceutical therapy. *J Nucl Med.* 2016;57:151–162.
2. Sartor O, De Bono J, Chi KN, et al. Lutetium-177–PSMA-617 for metastatic castration-resistant prostate cancer. *N Engl J Med.* 2021;385:1091–1103.
3. Strigari L, Konijnenberg M, Chiesa C, et al. The evidence base for the use of internal dosimetry in the clinical practice of molecular radiotherapy. *Eur J Nucl Med Mol Imaging.* 2014;41:1976–1988.
4. Ilan E, Sandström M, Wassberg C, et al. Dose response of pancreatic neuroendocrine tumors treated with peptide receptor radionuclide therapy using ^{177}Lu-DOTATATE. *J Nucl Med.* 2015;56:177–182.
5. Siegel JA, Thomas SR, Stubbs JB, et al. MIRD pamphlet no. 16: techniques for quantitative radiopharmaceutical biodistribution data acquisition and analysis for use in human radiation dose estimates. *J Nucl Med.* 1999;40:37S–61S.
6. Cremonesi M, Ferrari ME, Bodei L, et al. Correlation of dose with toxicity and tumour response to ^{90}Y- and ^{177}Lu-PRRT provides the basis for optimization through individualized treatment planning. *Eur J Nucl Med Mol Imaging.* 2018;45:2426–2441.
7. Rosar F, Schön N, Bohnenberger H, et al. Comparison of different methods for post-therapeutic dosimetry in [^{177}Lu]Lu-PSMA-617 radioligand therapy. *EJNMMI Phys.* 2021;8:40.
8. Konijnenberg M, Herrmann K, Kobe C, et al. EANM position paper on article 56 of the Council Directive 2013/59/Euratom (basic safety standards) for nuclear medicine therapy. *Eur J Nucl Med Mol Imaging.* 2021;48:67–72.

9. Graves SA, Bageac A, Crowley JR, Merlino DAM. Reimbursement approaches for radiopharmaceutical dosimetry: current status and future opportunities. *J Nucl Med.* 2021;62(suppl 3):48S–59S.
10. Brosch-Lenz J, Delker A, Völter F, et al. Toward single-time-point image-based dosimetry of ^{177}Lu-PSMA-617 therapy. *J Nucl Med.* 2023;64:767–774.
11. Jackson PA, Hofman MS, Hicks RJ, Scalzo M, Violet J. Radiation dosimetry in ^{177}Lu-PSMA-617 therapy using a single posttreatment SPECT/CT scan: a novel methodology to generate time- and tissue-specific dose factors. *J Nucl Med.* 2020; 61:1030–1036.
12. Hänscheid H, Lapa C, Buck AK, Lassmann M, Werner RA. Dose mapping after endoradiotherapy with ^{177}Lu-DOTATATE/DOTATOC by a single measurement after 4 days. *J Nucl Med.* 2018;59:75–81.
13. Kurth J, Heuschkel M, Tonn A, et al. Streamlined schemes for dosimetry of ^{177}Lu-labeled PSMA targeting radioligands in therapy of prostate cancer. *Cancers (Basel).* 2021;13:3884.
14. Willowson KP, Eslick E, Ryu H, Poon A, Bernard EJ, Bailey DL. Feasibility and accuracy of single time point imaging for renal dosimetry following ^{177}Lu-DOTATATE ('Lutate') therapy. *EJNMMI Phys.* 2018;5:33.
15. Madsen MT, Menda Y, O'Dorisio TM, O'Dorisio MS. Technical note: single time point dose estimate for exponential clearance. *Med Phys.* 2018;45: 2318–2324.
16. Mix M, Renaud T, Kind F, et al. Kidney doses in ^{177}Lu-based radioligand therapy in prostate cancer: is dose estimation based on reduced dosimetry measurements feasible? *J Nucl Med.* 2022;63:253–258.
17. Peters SMB, Mink MCT, Privé BM, et al. Optimization of the radiation dosimetry protocol in lutetium-177-PSMA therapy: toward clinical implementation. *EJNMMI Res.* 2023;13:6.
18. Rinscheid A, Kletting P, Eiber M, Beer AJ, Glatting G. Influence of sampling schedules on [^{1177}Lu]Lu-PSMA dosimetry. *EJNMMI Phys.* 2020;7:41.
19. Hardiansyah D, Riana A, Beer AJ, Glatting G. Single-time-point dosimetry using model selection and nonlinear mixed-effects modelling: a proof of concept. *EJNMMI Phys.* 2023;10:12.
20. Hou X, Brosch J, Uribe C, et al. Feasibility of single-time-point dosimetry for radiopharmaceutical therapies. *J Nucl Med.* 2021;62:1006–1011.
21. Peterson AB, Mirando DM, Dewaraja YK. Accuracy and uncertainty analysis of reduced time point imaging effect on time-integrated activity for ^{177}Lu-DOTATATE PRRT in patients and clinically realistic simulations. *EJNMMI Res.* 2023; 13:57.
22. Chicheportiche A, Sason M, Zidan M, et al. Impact of single-time-point estimates of ^{177}Lu-PRRT absorbed doses on patient management: validation of a trained multiple-linear-regression model in 159 patients and 477 therapy cycles. *J Nucl Med.* 2023;64:1610–1616.
23. Pirozzi Palmese V, D'Ambrosio L, Di Gennaro F, et al. A comparison of simplified protocols of personalized dosimetry in NEN patients treated by radioligand therapy (RLT) with [^{177}Lu]Lu-DOTATATE to favor its use in clinical practice. *Eur J Nucl Med Mol Imaging.* 2023;50:1753–1764.
24. Devasia TP, Dewaraja YK, Frey KA, Wong KK, Schipper MJ. A novel time-activity information-sharing approach using nonlinear mixed models for patient-specific dosimetry with reduced imaging time points: application in SPECT/CT after ^{177}Lu-DOTATATE. *J Nucl Med.* 2021;62:1118–1125.
25. Chicheportiche A, Sason M, Godefroy J, et al. Simple model for estimation of absorbed dose by organs and tumors after PRRT from a single SPECT/CT study. *EJNMMI Phys.* 2021;8:63.
26. Resch S, Takayama Fouladgar S, Zacherl M, et al. Investigation of image-based lesion and kidney dosimetry protocols for ^{177}Lu-PSMA-I&T therapy with and without a late SPECT/CT acquisition. *EJNMMI Phys.* 2023;10:11.
27. Frings V, van Velden FH, Velasquez LM, et al. Repeatability of metabolically active tumor volume measurements with FDG PET/CT in advanced gastrointestinal malignancies: a multicenter study. *Radiology.* 2014;273:539–548.
28. Stabin MG, Sparks RB, Crowe E. OLINDA/EXM: the second-generation personal computer software for internal dose assessment in nuclear medicine. *J Nucl Med.* 2005;46:1023–1027.
29. Hardiansyah D, Riana A, Kletting P, et al. A population-based method to determine the time-integrated activity in molecular radiotherapy. *EJNMMI Phys.* 2021;8:82.
30. Kletting P, Schimmel S, Kestler HA, et al. Molecular radiotherapy: the NUKFIT software for calculating the time-integrated activity coefficient. *Med Phys.* 2013; 40:102504.
31. Bonate LP. *Pharmacokinetic-Pharmacodynamic Modeling and Simulation.* 2nd ed. Springer; 2011:14–29.
32. Delker A, Ilhan H, Zach C, et al. The influence of early measurements onto the estimated kidney dose in [^{177}Lu][DOTA^0,Tyr^3]octreotate peptide receptor radiotherapy of neuroendocrine tumors. *Mol Imaging Biol.* 2015;17:726–734.
33. Rydén T, Van Essen M, Marin I, Svensson J, Bernhardt P. Deep-learning generation of synthetic intermediate projections improves ^{177}Lu SPECT images reconstructed with sparsely acquired projections. *J Nucl Med.* 2021; 62:528–535.
34. Sohlberg A, Kangasmaa T, Constable C, Tikkakoski A. Comparison of deep learning-based denoising methods in cardiac SPECT. *EJNMMI Phys.* 2023;10:9.
35. Liu J, Yang Y, Wernick MN, Pretorius PH, King MA. Deep learning with noise-to-noise training for denoising in SPECT myocardial perfusion imaging. *Med Phys.* 2021;48:156–168.

Factors Associated with Myocardial Uptake on Oncologic Somatostatin PET Investigations and Differentiation from Myocardial Uptake of Acute Myocarditis

Thomas Larive[1,2], Caroline Boursier[1–3], Marine Claudin[1,2], Jeanne Varlot[4], Laura Filippetti[4], Olivier Huttin[4,5], Véronique Roch[2], Laetitia Imbert[1–3], Matthieu Doyen[3,6], Aurélien Lambert[7], Damien Mandry[3,8], Zohra Lamiral[9], Elodie Chevalier[1,2], and Pierre-Yves Marie[1–3]

[1]Department of Nuclear Medicine, CHRU Nancy, Université de Lorraine, Nancy, France; [2]Nancyclotep Imaging Platform, CHRU Nancy, Université de Lorraine, Nancy, France; [3]UMR 1254, INSERM, Université de Lorraine, Nancy, France; [4]Department of Cardiology, CHRU Nancy, Nancy, France; [5]UMR 1116, INSERM, Université de Lorraine, Nancy, France; [6]Université de Lorraine, Nancy, France; [7]Department of Medical Oncology, Institut de Cancérologie de Lorraine, Vandœuvre-lès-Nancy, France; [8]Department of Radiology, CHRU Nancy, Université de Lorraine, Nancy, France; [9]CIC 1433, INSERM, CHRU Nancy, Nancy, France

Myocardial somatostatin PET uptake is observed not only in most patients with acute myocarditis (AM) but also in some oncology patients referred for routine somatostatin PET. This raises concerns about the specificity of somatostatin PET for detecting myocarditis. The current study aims to identify factors associated with the detection of myocardial uptake on somatostatin PET scans recorded for oncology indications and differential PET criteria that characterize myocardial uptake in AM patients. **Methods:** We analyzed factors associated with the detection of myocardial [^{68}Ga]Ga-DOTATOC uptake in 508 [^{68}Ga]Ga-DOTATOC PET scans from 178 patients, performed for confirmed or suspected oncologic disease (Onc-PET) and PET criteria that could differentiate myocardial [^{68}Ga]Ga-DOTATOC uptake in 31 patients with MRI-ascertained AM (AM-PET) from that in the Onc-PET group. **Results:** Significant myocardial uptake was detected in 137 (26.9%) Onc-PET scans and was independently associated with somatostatin analog treatment (exp(β), 0.805; 95% CI, 0.728–0.890; $P < 0.001$) and age (exp(β), 1.005; 95% CI, 1.001–1.009; $P = 0.012$). A comparable model was selected for predicting the myocardial-to-blood SUV$_{max}$ ratio using somatostatin analog treatment ($P < 0.001$) and history of coronary artery disease ($P = 0.022$). Myocardial uptake was detected in 12.9% (25/193) of Onc-PET scans from patients treated with somatostatin analogs but in 43.4% (59/136) of untreated patients over the median age of 64 y. Myocardial uptake was apparent in all 31 AM-PET scans, with volume and intensity of uptake dramatically higher than in the 137 Onc-PET scans showing myocardial uptake. A myocardial-to-blood SUV$_{max}$ ratio threshold of 2.20 provided a sensitivity of 87% (27/31) and a specificity of 88% (44/50) for differentiating myocardial uptake between the AM-PET group and an Onc-PET group restricted to patients with clinical characteristics comparable to those of patients in the AM-PET group (≤64 y of age, no coronary artery disease history, and no somatostatin agonists). A myocardial uptake volume threshold of 18 cm^3 provided comparable diagnostic accuracy (sensitivity, 84% [26/31]; specificity, 94% [47/50]). **Conclusion:** Myocardial uptake was detected in 26.9% of somatostatin PET scans recorded for oncology indications. This rate was decreased by somatostatin analog treatments and increased in older individuals. However, somatostatin PET scans, analyzed with the quantitative criterion of uptake intensity or volume, are able to identify AM and to differentiate it from myocardial uptake of other origins.

Key Words: [^{68}Ga]Ga-DOTATOC; PET; myocardial inflammation; somatostatin receptor; acute myocarditis

J Nucl Med 2024; 65:1279–1285
DOI: 10.2967/jnumed.123.267219

Myocarditis is far from being infrequent. It sometimes mimics an acute coronary syndrome, with some cases presenting or evolving toward left ventricular (LV) dysfunction, heart failure, and arrhythmia (*1*).

An endomyocardial biopsy, analyzed using the Dallas criteria, remains the gold standard for myocarditis diagnosis, even though it has low sensitivity for detecting focal forms (*2*). MRI is an efficient noninvasive diagnostic tool when analyzed using the 2018 revised Lake Louise criteria (*3*). However, MRI suffers from low sensitivity for detecting subacute or chronic myocarditis, characterized by cardiomyopathylike or arrhythmia presentations (*4*).

[^{68}Ga]DOTA peptides were developed for PET imaging of somatostatin receptor (SSTR) subtypes to diagnose or monitor neuroendocrine tumors. However, SSTRs are overexpressed in lymphocytes and activated macrophages, the primary cell subsets involved in myocarditis (*1,2*).

Previous pilot somatostatin PET studies have reported myocardial radiopeptide uptake in most patients with acute myocarditis (AM) (*5–10*). For reasons that are still poorly understood, myocardial uptake is also observed in numerous patients undergoing somatostatin PET for routine oncology indications (*11–13*), raising concerns about the specificity of somatostatin PET to identify AM.

This study aims to identify the factors associated with myocardial uptake observed on somatostatin PET scans recorded for routine oncology indications and define differential PET criteria that characterize myocardial uptake in AM patients.

MATERIALS AND METHODS

Study Populations

This study analyzed a retrospectively constituted group of patients with consecutive [^{68}Ga]Ga-DOTATOC PET/CT scans recorded in our

---

Received Dec. 7, 2023; revision accepted May 22, 2024.

For correspondence or reprints, contact Pierre-Yves Marie (py.marie@chru-nancy.fr).

nuclear medicine department between January 2019 and December 2023 (Onc-PET group). Patients were referred from the Regional University Hospital Center of Nancy or the neighboring Regional Oncology Center (Institut de Cancerologie de Lorraine) to investigate conventional oncology indications. PET/CT scans from patients with carcinoid syndrome or a cardiac tumor location were excluded. We extracted the variables listed in Table 1 from electronic medical databases, including sex, age, tumor data, history of oncologic and cardiac interventions, ongoing oncologic treatments, and cardiovascular risk factors.

We analyzed a second group of [^{68}Ga]Ga-DOTATOC PET/CT patients recorded between July 2020 and April 2023 as part of a prospective study of AM ascertained by MRI according to the 2018 Lake Louise criteria (AM-PET group), with our CMR methodology being described in the supplemental materials (supplemental materials are available at http://jnm.snmjournals.org) (*3,14*). Both the AM-PET and the Onc-PET study protocols were approved by dedicated ethics committees (Comité de Protection des Personnes–Ouest IV and Comité d'Éthique du Centre Hospitalier Régional Universitaire de Nancy, respectively) and released on the ClinicalTrials.gov website under the identifiers NCT03347760 and NCT05478733, respectively. All participants from the AM prospective study signed an informed-consent form to participate. The requirement to obtain informed consent was waived for the Onc-PET patients, but they had been informed that their medical data could be used retrospectively for research purposes.

PET/CT Recording and Analysis

All PET scans were recorded 60 min after the intravenous injection of 2 MBq/kg of [^{68}Ga]Ga-DOTATOC on a digital PET/CT system

TABLE 1
Main Data Recorded at Time of PET/CT in Overall Onc-PET Group, Onc-PET Subgroup with Myocardial Uptake, and AM-PET Group

Characteristic	Overall Onc-PET	Onc-PET with myocardial uptake	AM-PET	*P*
All patients (*n*)	508	137	31	
Female patients (*n*)	246 (48.3)	64 (46.7)	1 (3.2)	<0.0001
Age (y)	64.0 (54.8–72.0)	65.7 (55.0–73.4)	26.5 (21.9–33.8)	<0.0001
Body mass index (kg/m^2)	25.5 (22.5–29.1)	26.1 (23.1–29.5)	24.9 (23.2–27.7)	0.27
CV history and risk factors (*n*)				
CAD history	40 (7.9)	14 (10.2)	0 (0)	0.075
Myocardial infarction history	24 (4.7)	9 (6.6)	0 (0)	0.21
No. CV risk factors	1 (0–2)	1 (0–2)	0 (0–1)	0.005
Active smoking	7 (1.4)	2 (1.5)	7 (22.6)	0.0001
Obesity	102 (20.1)	29 (21.3)	5 (16.7)	0.80
Treated hypertension	207 (40.7)	58 (42.3)	1 (3.2)	<0.0001
Treated dyslipidemia	78 (15.3)	20 (14.6)	1 (3.2)	0.13
Treated diabetes	102 (20.0)	26 (19.0)	0 (0)	0.005
Oncologic data (*n*)				
Diagnosed cancer	466 (91.5)	124 (90.5)		
Diagnosed NET	423 (83.1)	111 (81.0)		
≥2 tumor grade	275 (54.3)	68 (49.6)		
External radiotherapy history	100 (19.6)	28 (20.4)		
Internal radiotherapy history	87 (17.1)	17 (12.4)		
Oncologic surgery history	266 (52.3)	62 (45.3)		
Current chemotherapy	61 (12.0)	26 (19.0)		
Current immunotherapy	67 (13.2)	14 (10.2)		
Somatostatin analog treatment*	193 (37.9)	25 (18.2)		
CV PET/CT data				
Presence of myocardial uptake (*n*)	137 (26.9)	137 (100)	31 (100)	1
Segments with myocardial uptake (*n*)	0.0 (0.0–3.0)	6.0 (3.0–9.0)	15.0 (10.0–17.0)	<0.0001
Myocardial uptake volume (cm^3)	0.0 (0.0–0.09)	2.2 (0.6–9.5)	47.3 (24.0–135.0)	<0.0001
Myocardial-to-blood SUV_{max} ratio	1.44 (1.25–1.79)	2.00 (1.76–2.18)	2.80 (2.29–3.00)	<0.0001

---

*Somatostatin analogs were not administered in 4 wk preceding PET.

CV = cardiovascular; NET = neuroendocrine tumor.

P values relate to comparison between AM-PET group and Onc-PET group with myocardial uptake. Qualitative data are number and percentage; continuous data are median and range.

(Vereos; Philips). In patients treated with somatostatin analogs, the PET/CT procedures were scheduled before the monthly treatment dose (*15*).

Both Onc-PET and AM-PET scans were reconstructed with 2-mm^3 voxels, a similar iterative algorithm, and additional corrections detailed elsewhere (*5*). A 3-min PET recording was scheduled per bed position for Onc-PET scans, and a single 15-min cardiac-centered bed position was scheduled for AM-PET scans.

Areas of LV myocardial uptake of [^{68}Ga]Ga-DOTATOC were detected visually with an SUV scaling range of 0–3 (*5*) and localized according to 17-segment LV division (Supplemental Fig. 1) (*16*). These uptake areas were considered significant only when they involved at least 2 contiguous LV segments; were associated with both a myocardial-to-blood SUV$_{max}$ ratio of more than 1.5, with this ratio determined using 2-cm-diameter spheric volumes of interest, and a right atrium center location for blood activity; and were located more than 1 cm from liver activity (*5*).

In addition, a myocardial PET uptake volume was quantified using isocontours and the same criteria as used for the visual analysis (i.e., myocardial-to-blood SUV$_{max}$ ratio > 1.5 and $>$1-cm distance from liver activity). This volume was considered zero when no myocardial uptake was detected visually.

Statistical Analysis

Continuous variables are represented as medians, with interquartile ranges, and categoric variables are represented as frequencies and percentages. Two-group comparisons were performed with χ^2 tests (or Fisher exact tests when more appropriate) for categoric variables and with Mann–Whitney tests. Receiver operating characteristic curves were additionally performed for continuous variables, and associations between continuous variables were tested with the nonparametric Spearman rank correlation method. The significance threshold was set at a *P* value of less than 0.05, and the closest-to-(0,1) corner approach was used to define the optimal threshold value from receiver operating characteristic curves.

In the Onc-PET group, generalized linear mixed-effects models using SAS software (SAS Institute) for repeat measurements were used to identify factors associated with significant myocardial [^{68}Ga]Ga-DOTATOC uptake (dichotomous variable), among those listed in Table 1, and linear mixed-effects models for repeat measurements (mixed SAS procedure) were used to determine factors associated with the log-transformed myocardial-to-blood SUV$_{max}$ ratio. This log transformation was required to meet the normality assumptions of the linear models. Odds ratios (generalized linear mixed-effects models) and exp(β) (mixed models) with 95% CIs were reported, and *P* values of 0.15 and 0.05 were used as thresholds for, respectively, entering and removing variables from the models. Log linearity and linearity assumptions for continuous variables in generalized linear mixed-effects and mixed models were checked using the restricted cubic splines method, with knot locations based on Harrell's recommended percentiles (*17*).

All analyses were conducted using SAS version 9.4.

RESULTS

Analysis of the Onc-PET Group

In total, 511 consecutive [^{68}Ga]Ga-DOTATOC PET/CT scans were considered. Three were excluded because of confirmed or suspected cardiac metastasis or a technical PET problem, leaving 508 [^{68}Ga]Ga-DOTATOC PET recordings from 178 patients in the current analysis. Seventy-six patients had a single PET scan, 56 patients had 2–3 PET scans, and 46 patients had more than 3 PET scans.

As detailed in Table 1, 423 (83.1%) of the Onc-PET scans were recorded from patients with a confirmed neuroendocrine tumor, but only 40 (7.9%) scans were recorded from patients with a history of coronary artery disease (CAD; myocardial infarction or coronary revascularization). Oncology surgery was documented in 266 (52.3%) cases, and the Onc-PET scans were recorded during periods of analog somatostatin treatment in 193 (37.9%) cases.

Significant myocardial uptake was detected in 137 (26.9%) Onc-PET scans and, as detailed in Table 2, the multivariate predictors of this uptake were somatostatin analog treatment (exp(β), 0.805; 95% CI, 0.728–0.890; $P < 0.001$) and age (exp(β), 1.005; 95% CI, 1.001–1.009; $P = 0.012$). A comparable model was selected for predicting the logarithm of the myocardial-to-blood SUV$_{max}$ ratio—that is, somatostatin analog treatment ($P < 0.001$) and CAD history ($P = 0.022$).

The detection rate of myocardial uptake was only 12.9% (25/193) in somatostatin analog–treated patients. This rate was higher, 29.4% (53/180), when the absence of somatostatin analog treatment was associated with an age of no more than 64 y, which was the median of the Onc-PET population, and was even higher, 43.4% (59/136), when associated with the older age group. These data are illustrated in the graphical abstract.

Analysis of the AM-PET Group

Thirty-one patients were recruited at the time of AM diagnosis, with elevated plasma troponin I levels (median peak, 12.0 ng/mL; interquartile range, 6.9–17.4 ng/mL) and chest pain in 27 cases. Symptoms evocative of a gastrointestinal or respiratory tract infection were documented for 15 of these patients, and a recent (≤3 d) history of messenger RNA–based coronavirus disease 2019 vaccination was documented for 3 other patients. Ten AM patients had an abnormal LV ejection fraction (<50%) on MRI. The PET scan was performed a median of 4 d (range, 3–5 d) after peak troponin.

As detailed in Figure 1, the PET parameters considered (myocardial-to-blood SUV$_{max}$ ratio and myocardial uptake volume) were unrelated to the MRI parameters used for tissue characterization (T1, T2, and the number of segments with late gadolinium enhancement). However, the LV ejection fraction, determined by MRI, was inversely correlated to the myocardial-to-blood SUV$_{max}$ ratio ($P = 0.008$) and myocardial PET uptake volume ($P = 0.013$).

Comparison Between the Onc-PET and the AM-PET Groups

As shown in Table 1, men were overrepresented in the AM-PET group compared with the Onc-PET group with myocardial uptake. Patients in the AM-PET group were also younger and had lower rates of most cardiovascular risk factors. None of the AM-PET group patients had a history of cancer or cardiac disease.

Significant myocardial uptake was detected in all 31 AM-PET scans, with the volume and intensity of uptake dramatically higher than in the 137 Onc-PET scans with myocardial uptake. The respective medians in these 2 groups were 2.80 (range, 2.29–3.00) and 2.00 (range, 1.76–2.18; $P < 0.001$) for the myocardial-to-blood SUV$_{max}$ ratio and 47.3 cm^3 (range, 24.0–135.0 cm^3) and 2.2 cm^3 (range, 0.6–9.5 cm^3; $P < 0.001$) for the myocardial uptake volume (Fig. 2). Higher rates of myocardial uptake were also observed in the AM-PET group than in the Onc-PET group in a per-segment analysis, with the difference particularly marked for inferior and inferior-lateral segments (Fig. 2).

On the receiver operating characteristic curve analysis shown in Figure 3, both the myocardial uptake volume and the myocardial-to-blood SUV$_{max}$ ratio were able to differentiate myocardial

TABLE 2

Univariate and Multivariate Predictors of Myocardial Uptake and Log-Transformed Myocardial-to-Blood SUV_{max} Ratio in Onc-PET Group

	Myocardial uptake				Ln of SUV_{max} ratio			
	Univariate		Multivariate		Univariate		Multivariate	
Characteristic	exp(β)	*P*	exp(β)	*P*	exp(β)	*P*	exp(β)	*P*
Women	1.070 (0.620–1.848)	0.81			0.973 (0.877–1.079)	0.60		
Age (y)	1.018 (0.993–1.044)	0.16	1.005 (1.001–1.009)	0.012	1.003 (0.999–1.006)	0.16		
Body mass index (kg/m^2)	1.049 (0.995–1.106)	0.075			1.006 (0.996–1.015)	0.23		
CV history and risk factors								
CAD history	1.646 (0.758–3.572)	0.21			1.184 (1.024–1.369)	0.023	1.177 (1.024–1.353)	0.022
Myocardial infarction history	1.887 (0.717–4.964)	0.20			1.214 (1.015–1.451)	0.034		
≥1 CV risk factor	0.970 (0.587–1.602)	0.91			1.015 (0.922–1.118)	0.76		
Active smoking	0.962 (0.127–7.285)	0.97			1.007 (0.676–1.500)	0.97		
Obesity	1.329 (0.723–2.442)	0.36			1.043 (0.944–1.152)	0.41		
Treated hypertension	1.076 (0.619–1.871)	0.80			0.957 (0.862–1.063)	0.42		
Treated dyslipidemia	1.045 (0.482–2.264)	0.91			1.064 (0.924–1.225)	0.39		
Treated diabetes	0.872 (0.433–1.756)	0.70			1.036 (0.910–1.178)	0.59		
Oncologic data								
Diagnosed cancer	0.829 (0.380–1.805)	0.64			0.881 (0.769–1.009)	0.069		
Diagnosed NET	0.730 (0.383–1.391)	0.34			0.978 (0.870–1.099)	0.70		
≥2 tumor grade	0.839 (0.481–1.463)	0.54			0.869 (0.783–0.963)	0.008		
External radiotherapy history	1.090 (0.500–2.378)	0.83			1.044 (0.911–1.195)	0.54		
Internal radiotherapy history	0.532 (0.264–1.071)	0.078			0.950 (0.848–1.065)	0.38		
Oncologic surgery history	0.771 (0.459–1.297)	0.33			0.900 (0.820–0.989)	0.028		
Current chemotherapy	1.639 (0.712–3.772)	0.25			1.008 (0.888–1.145)	0.90		
Current immunotherapy	0.820 (0.399–1.686)	0.59			1.053 (0.939–1.180)	0.38		
Current somatostatin analog treatment*	0.325 (0.171–0.619)	0.0007	0.805 (0.728–0.890)	<0.0001	0.759 (0.695–0.830)	<0.0001	0.761 (0.698–0.831)	<0.001

---

*Somatostatin analogs were not administered in 4 wk preceding PET.

CV = cardiovascular; NET = neuroendocrine tumor.

P values relate to comparison between AM-PET group and Onc-PET group with myocardial uptake. Data in parentheses are 95% CI.

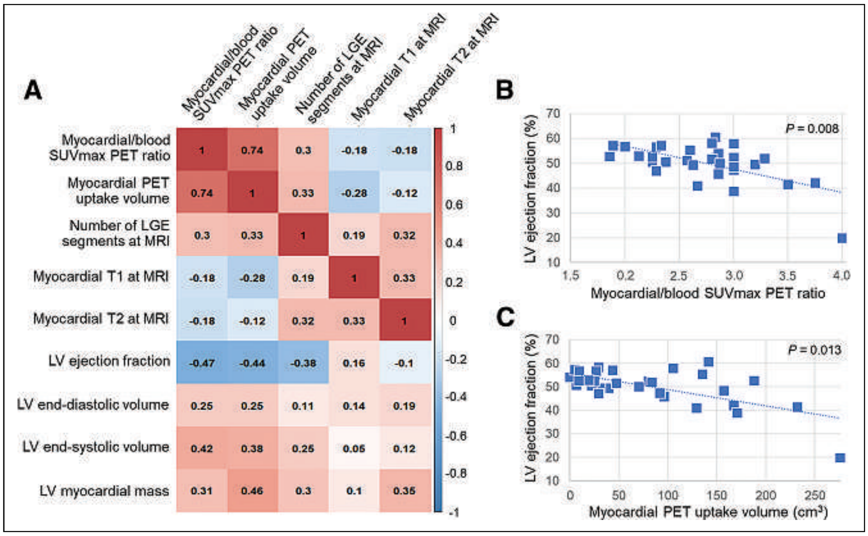

	Myocardial/blood SUVmax PET ratio	Myocardial PET uptake volume	Number of LGE segments at MRI	Myocardial T1 at MRI	Myocardial T2 at MRI
Myocardial/blood SUVmax PET ratio	1	0.74	0.3	-0.18	-0.18
Myocardial PET uptake volume	0.74	1	0.33	-0.28	-0.12
Number of LGE segments at MRI	0.3	0.33	1	0.19	0.32
Myocardial T1 at MRI	-0.18	-0.28	0.19	1	0.33
Myocardial T2 at MRI	-0.18	-0.12	0.32	0.33	1
LV ejection fraction	-0.47	-0.44	-0.38	0.16	-0.1
LV end-diastolic volume	0.25	0.25	0.11	0.14	0.19
LV end-systolic volume	0.42	0.38	0.25	0.05	0.12
LV myocardial mass	0.31	0.46	0.3	0.1	0.35

FIGURE 1. (A) Spearman correlation coefficients for associations between tissue characterization parameters provided by PET (myocardial-to-blood SUV_{max} ratio and myocardial uptake volume) or MRI (T1, T2, and number of late gadolinium enhancement [LGE] LV segments) and all considered PET and MRI variables. (B) Relationship between LV ejection fraction and myocardial-to-blood SUV_{max} ratio. (C) Relationship between LV ejection fraction and myocardial uptake volume.

uptake in the AM-PET group from that in the Onc-PET group, with areas under the curve of 0.888 (95% CI, 0.817–0.960) and 0.879 (95% CI, 0.814–944), respectively. The criteria of a myocardial-to-blood SUV_{max} of more than 2.2 allowed differentiation of myocardial uptake between the AM-PET and the Onc-PET groups with a sensitivity of 87% (27/31) and a specificity of 77.4% (106/137). The criteria of a myocardial uptake volume of more than 18 cm^3 provided comparable results (sensitivity, 84% [26/31]; specificity, 83% [114/137]).

Specificities of 88% (44/50) for the criteria of a myocardial-to-blood SUV_{max} ratio of more than 2.2 and of 94% (47/50) for that of a myocardial uptake volume of more than 18 cm^3 were obtained when the Onc-PET group with myocardial uptake was restricted to a subgroup with characteristics more comparable to those of the AM group (i.e., age ≤ 64 y, no CAD history, and no somatostatin agonists).

Representative AM-PET and Onc-PET group scans are shown in Figure 4.

DISCUSSION

Our study found that up to 26.9% somatostatin PET scans recorded for routine oncology indications show significant myocardial uptake. This is consistent with the prevalence reported in the literature (*11–13*). The uptake detection rate was decreased by somatostatin analogs and increased with patient age. Moreover, uptake in oncology cases was generally less intense and less extensive than uptake measured in AM cases, which supports the notion that somatostatin PET may be able to specifically detect AM.

Results obtained in our AM-PET group, where [^{68}Ga]Ga-DOTATOC PET scans were recorded in MRI-ascertained AM cases, confirm our previously published preliminary results (*5*)—that is, consistently observed increased myocardial uptake relative to the blood activity on at least 2 contiguous LV segments, associated with a marked decrease in blood activity, and with myocardial uptake predominantly localizing to inferior and inferior-lateral LV segments (Fig. 2). The main technical limitations remain the relatively low activity of the myocardial uptake areas (mean SUV_{max}, 1.8 in the present AM-PET group) and the inability to analyze certain inferior LV segments proximal to liver activity.

In [^{68}Ga]Ga-DOTATOC PET scans recorded for oncology indications, differences in SUV_{max} between organs from the same patient were previously shown to correlate with differences in SSTR expression (*18*). However, tissue-to-blood SUV ratios of [^{68}Ga]Ga-DOTATOC are known to be a more accurate measure of SSTR density than SUV (*19*), and in the present study, the myocardial-to-blood SUV_{max} ratio was a better predictor of AM than was SUV_{max}. The lower blood SUV_{max} observed in the AM-PET group than in the Onc-PET group is also likely to enhance the difference in the myocardial-to-blood SUV_{max} ratio between the 2 groups.

The specificity of detecting AM could be undermined by the frequent observation of myocardial uptake in somatostatin PET recordings of common oncology indications. Such incidental observations were previously found to correlate with older patient age, a CAD history, and cardiovascular risk factors (*11*). In our large sample of [^{68}Ga]Ga-DOTATOC PET scans recorded for an oncology indication, we also found a significant correlation between age and detection of myocardial uptake, as well as between a CAD history and the myocardial-to-blood SUV_{max} ratio. However, these 2 cardiac PET parameters were primarily associated with ongoing somatostatin antagonist treatment. Somatostatin analogs were prescribed in up to 37.9% of Onc-PET group cases, which is in line with their antiproliferative and antisecretory action in neuroendocrine tumors.

The myocardial uptake rate was only 12.9% in Onc-PET scans recorded in patients treated with somatostatin analogs. According to current recommendations (*15*), an Onc-PET scan was scheduled a few days before the monthly administration of somatostatin agonists and thus as long as 4 wk after the last administration. Nevertheless, such long-acting treatments are known to decrease tracer uptake in somatostatin PET for up to 25 d after their administration (*20*), and a primary consequence of this reduced uptake is an apparent increase in blood activity (as shown in the graphical abstract).

The detection rate of significant myocardial uptake was thus even higher when considering only the population not treated with somatostatin analogs and specifically the older subgroup of this cohort (43.4% uptake in the >64-y-old subgroup). This observation is not fully understood, although it is supported by the general concept that cardiovascular aging involves an overall increased level of heart inflammation (*21*).

Consistent with previous reports (*6,22*), we also observed myocardial uptake in patients with a history of myocardial infarction (Fig. 3). The previous observations of SSTR expression in fibroblasts could explain the detection of somatostatin PET uptake within myocardial scars (*23,24*). However, of the 24 Onc-PET scans from patients that presented a history of myocardial infarction, myocardial uptake was documented only in 10 cases. Certain areas of somatostatin PET uptake could also occur within the atherosclerotic plaques of coronary arteries, as previously reported (*25*).

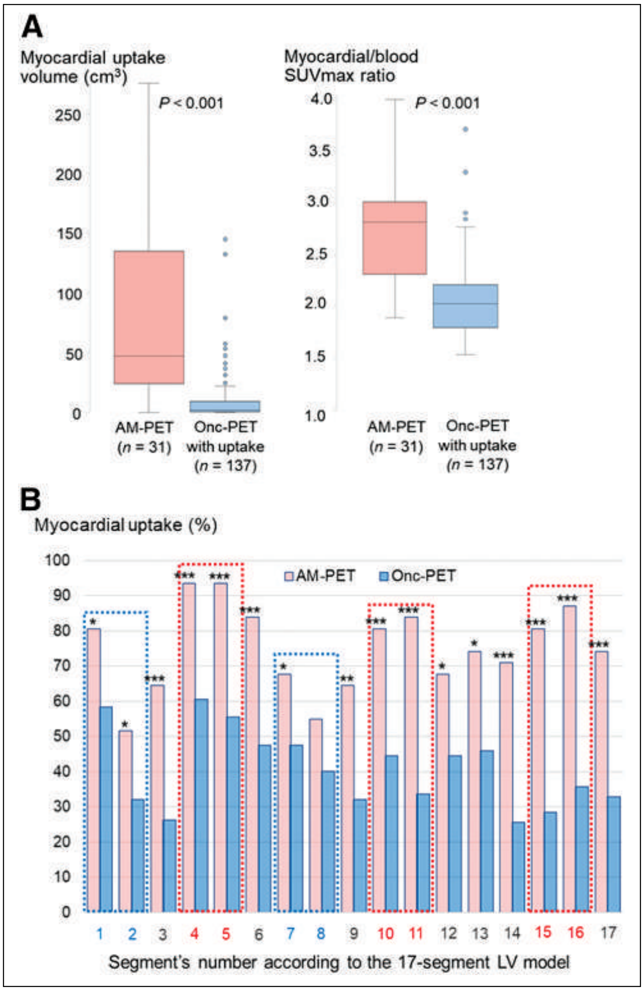

FIGURE 2. (A–C) Comparison of myocardial uptake in AM-PET and Onc-PET groups in terms of myocardial uptake volume (A), myocardial-to-blood SUV_{max} ratio (B), and myocardial uptake detection rate on each of 17 LV segments (C). Difference in uptake detection rates between AM-PET and Onc-PET groups is particularly marked ($P < 0.001$) in inferior and inferior-lateral segments (columns delimited with dashed red lines) and weaker ($P = \sim 0.05$) in anterior and anterior-septal segments located in basal and median parts of LV (columns delimited with dashed blue lines).

The anterior and anterior-septal segments, located in the basal and median parts of the LV, exhibited the slightest difference in uptake rate between the AM-PET and the Onc-PET groups (Fig. 2). However, this uptake location was previously considered to correspond to the atheromatous left anterior descending arteries (the PTCA history patient in Fig. 4). (*26*).

The main finding of the present study is that AM-PET is best differentiated from Onc-PET on the basis of the objective quantitative criteria of uptake intensity and volume—that is, myocardial-to-blood SUV_{max} ratio and myocardial uptake volume. These parameters were strongly interrelated in the present study population (Fig. 1), and using optimized thresholds, respective sensitivities of 87% and 84% were achieved. The respective specificities were 88% and 94% when the Onc-PET group with myocardial uptake was restricted to a subgroup with clinical characteristics more comparable to those of the AM group. Patients from this subgroup did not exhibit factors previously shown to affect myocardial uptake in our Onc-PET population, factors that are unlikely to be present in AM patients (>64 y old, somatostatin analog treatment, and history of CAD).

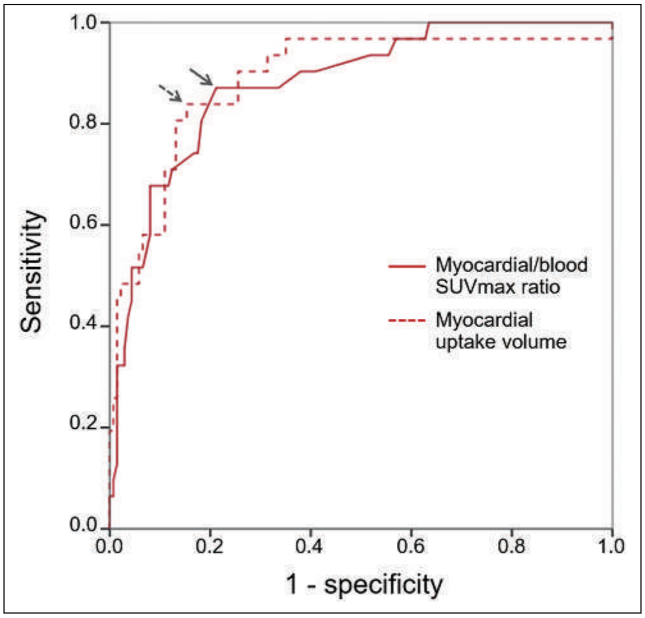

FIGURE 3. Receiver operating characteristic curves optimized to differentiate AM-PET group from Onc-PET group on basis of myocardial-to-blood SUV_{max} ratio and myocardial uptake volume. According to closest-to-(0,1) corner approach, we selected thresholds of 2.2 for myocardial-to-blood SUV_{max} ratio and 18 cm^3 for myocardial uptake volume (arrows).

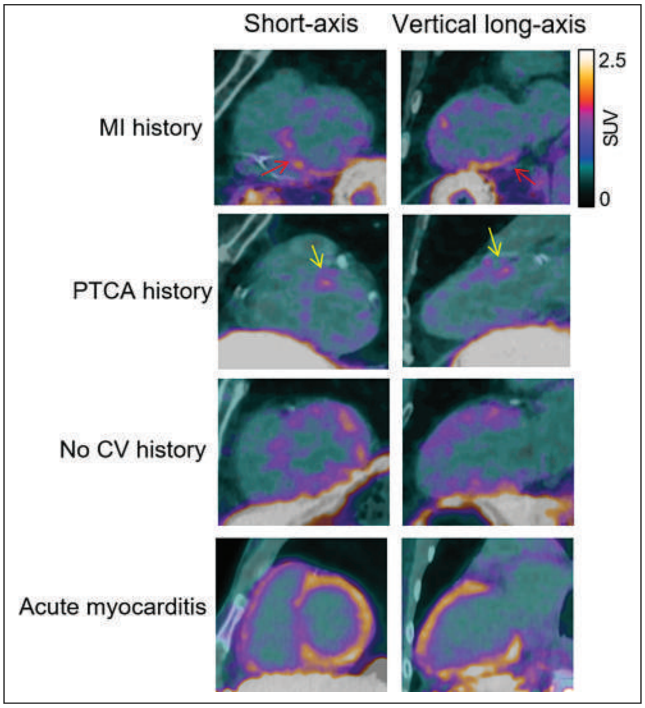

FIGURE 4. Representative fused PET/CT slices, on 0-to-2.5 SUV scale, of 41-y-old man in AM-PET group (diffuse and intense LV uptake) and of 3 Onc-PET patients with myocardial uptake: 71-y-old man with history of inferior myocardial infarction (MI; arrows mark uptake on inferior and inferoseptal segments),76-y-old woman with history of percutaneous transluminal angioplasty (PTCA; arrows mark uptake on proximal parts of anterior and septal walls), and 81-y-old man with no cardiovascular (CV) history (diffuse LV uptake). Myocardial-to-blood SUV_{max} ratio was 4.0 in AM-PET patient and ranged from 2.13 to 2.18 in Onc-PET patients.

Our results appear to be more satisfactory than those previously published with [^{18}F]FDG PET for detecting myocarditis (*27*). This most likely results from the difficulties of suppressing physiologic myocardial [^{18}F]FDG uptake, despite diet or fasting. No preparation is recommended before a cardiac somatostatin PET scan except the withdrawal of corticosteroid or somatostatin analog treatment. Finally, the pathologic significance of the myocardial-to-blood SUV_{max} ratio and the myocardial uptake volume are strengthened by our additional observations of inverse associations with the LV ejection fraction in myocarditis patients (Fig. 1).

Our results need to be confirmed in other populations and require a dedicated cardiac somatostatin PET recording protocol for control groups. It would be interesting to determine whether this PET methodology could also detect cardiac sarcoidosis or chronic forms of myocarditis and to what extent our findings may be extrapolated to other somatostatin PET tracers, such as [^{68}Ga]Ga-DOTANOC (*28*).

CONCLUSION

Significant myocardial uptake is observed in up to 26.9% of somatostatin PET scans recorded for routine oncology indications. This rate is even higher in the absence of somatostatin agonist treatments, particularly in older individuals. However, somatostatin PET scans, analyzed with the objective quantitative criterion of uptake intensity or volume, are able to identify AM and differentiate it from myocardial uptake of other origins.

DISCLOSURE

The sponsor was the Regional University Hospital Center (Centre Hospitalier Régional Universitaire) of Nancy, and this study was supported by a grant from the French Ministry of Health (APJ 2015) and by Advanced Accelerator Applications, a Novartis company, which provided the SomaKit TOC free of charge. No other potential conflict of interest relevant to this article was reported.

ACKNOWLEDGMENTS

We thank Dr. Petra Neufing for critically reviewing the article and the staff of Nancyclotep for technical support.

KEY POINTS

QUESTION: What are the parameters associated with the detection of myocardial uptake on somatostatin PET scans recorded for routine oncology indications, and what are the PET criteria for differentiating from AM?

PERTINENT FINDINGS: Myocardial uptake is frequently detected on oncologic somatostatin PET scans, especially in older patients not treated with somatostatin analogs, but this uptake is mostly less extensive and less intense than that observed in AM.

IMPLICATIONS FOR PATIENT CARE: Somatostatin PET scans, analyzed with the objective quantitative criterion of uptake intensity or volume, have the potential to diagnose AM and differentiate it from myocardial uptake of other origins.

REFERENCES

1. Tschöpe C, Ammirati E, Bozkurt B, et al. Myocarditis and inflammatory cardiomyopathy: current evidence and future directions. *Nat Rev Cardiol.* 2021;18:169–193.
2. Vidusa L, Kalejs O, Maca-Kaleja A, Strumfa I. Role of endomyocardial biopsy in diagnostics of myocarditis. *Diagnostics (Basel).* 2022;12:2104.
3. Ferreira VM, Schulz-Menger J, Holmvang G, et al. Cardiovascular magnetic resonance in nonischemic myocardial inflammation: expert recommendations. *J Am Coll Cardiol.* 2018;72:3158–3176.
4. Francone M, Chimenti C, Galea N, et al. CMR sensitivity varies with clinical presentation and extent of cell necrosis in biopsy-proven acute myocarditis. *JACC Cardiovasc Imaging.* 2014;7:254–263.
5. Boursier C, Chevalier E, Varlot J, et al. Detection of acute myocarditis by ECG-triggered PET imaging of somatostatin receptors compared to cardiac magnetic resonance: preliminary results. *J Nucl Cardiol.* 2023;30:1043–1049.
6. Lapa C, Reiter T, Li X, et al. Imaging of myocardial inflammation with somatostatin receptor based PET/C: a comparison to cardiac MRI. *Int J Cardiol.* 2015;194:44–49.
7. Boughdad S, Latifyan S, Fenwick C, et al. ^{68}Ga-DOTATOC PET/CT to detect immune checkpoint inhibitor-related myocarditis. *J Immunother Cancer.* 2021;9:e003594.
8. Boursier C, Weizman O, Chevalier E, et al. Acute left atrial myocarditis due to close contact with inflammatory nodes and identified by combined cardiac magnetic resonance and ^{68}Ga-DOTATOC positron emission tomography image analysis. *Circ Cardiovasc Imaging.* 2023;16:e014770.
9. Polte CL, Bollano E, Oldfors A, et al. Somatostatin receptor positron emission tomography/computed tomography in giant cell myocarditis: a promising approach to molecular myocardial inflammation imaging. *Circ Cardiovasc Imaging.* 2022;15:e013551.
10. Boursier C, Chevalier E, Filippetti L, et al. ^{68}Ga-DOTATOC digital-PET imaging of inflammatory cell infiltrates in myocarditis following COVID-19 vaccination. *Eur J Nucl Med Mol Imaging.* 2022;49:1433–1434.
11. Itani M, Haq A, Amin M, et al. Myocardial uptake of ^{68}Ga-DOTATATE: correlation with cardiac disease and risk factors. *Acta Radiol.* 2022;63:1166–1172.
12. Bobbio E, Dudás A, Bergström A, et al. Incidental cardiac findings on somatostatin receptor PET/CT: what do they indicate and are they of clinical relevance? *J Nucl Cardiol.* 2022;29:1159–1165.
13. Moyade P, Vinjamuri S. The heart matters: a review of incidental cardiac uptake on Ga-68 DOTA peptide PET-CT scans. *Nucl Med Commun.* 2019;40:1081–1085.
14. Filippetti L, Pace N, Louis JS, et al. Long-lasting myocardial and skeletal muscle damage evidenced by serial CMR during the first year in COVID-19 patients from the first wave. *Front Cardiovasc Med.* 2022;9:831580.
15. Bozkurt MF, Virgolini I, Balogova S, et al. Guideline for PET/CT imaging of neuroendocrine neoplasms with ^{68}Ga-DOTA-conjugated somatostatin receptor targeting peptides and ^{18}F-DOPA. *Eur J Nucl Med Mol Imaging.* 2017;44:1588–1601.
16. Cerqueira MD, Weissman NJ, Dilsizian V, et al. Standardized myocardial segmentation and nomenclature for tomographic imaging of the heart: a statement for healthcare professionals from the Cardiac Imaging Committee of the Council on Clinical Cardiology of the American Heart Association. *Circulation.* 2002;105:539–542.
17. Harrell FE. *Regression Modeling Strategies: With Applications to Linear Models, Logistic Regression, and Survival Analysis.* Springer; 2001:24–28.
18. Boy C, Heusner TA, Poeppel TD, et al. ^{68}Ga-DOTATOC PET/CT and somatostatin receptor (sst1–sst5) expression in normal human tissue: correlation of sst2 mRNA and SUV_{max}. *Eur J Nucl Med Mol Imaging.* 2011;38:1224–1236.
19. Ilan E, Velikyan I, Sandström M, Sundin A, Lubberink M. Tumor-to-blood ratio for assessment of somatostatin receptor density in neuroendocrine tumors using ^{68}Ga-DOTATOC and ^{68}Ga-DOTATATE. *J Nucl Med.* 2020;61:217–221.
20. Ayati N, Lee ST, Zakavi R, et al. Long-acting somatostatin analog therapy differentially alters ^{68}Ga-DOTATATE uptake in normal tissues compared with primary tumors and metastatic lesions. *J Nucl Med.* 2018;59:223–227.
21. Liberale L, Badimon L, Montecucco F, Lüscher TF, Libby P, Camici GG. Inflammation, aging, and cardiovascular disease: JACC review topic of the week. *J Am Coll Cardiol.* 2022;79:837–847.
22. Tarkin JM, Calcagno C, Dweck MR, et al. ^{68}Ga-DOTATATE PET identifies residual myocardial inflammation and bone marrow activation after myocardial infarction. *J Am Coll Cardiol.* 2019;73:2489–2491.
23. Borie R, Fabre A, Prost F, et al. Activation of somatostatin receptors attenuates pulmonary fibrosis. *Thorax.* 2008;63:251–258.
24. Ambrosini V, Zompatori M, De Luca F, et al. ^{68}Ga-DOTANOC PET/CT allows somatostatin receptor imaging in idiopathic pulmonary fibrosis: preliminary results. *J Nucl Med.* 2010;51:1950–1955.
25. Tarkin JM, Joshi FR, Evans NR, et al. Detection of atherosclerotic inflammation by ^{68}Ga-DOTATATE PET compared to [^{18}F]FDG PET imaging. *J Am Coll Cardiol.* 2017;69:1774–1791.
26. Rominger A, Saam T, Vogl E, et al. In vivo imaging of macrophage activity in the coronary arteries using ^{68}Ga-DOTATATE PET/CT: correlation with coronary calcium burden and risk factors. *J Nucl Med.* 2010;51:193–197.
27. Ko WS, Kim SJ. Diagnostic performance of ^{18}F-FDG PET or PET/CT for detection of myocarditis. *Hell J Nucl Med.* 2023;26:132–139.
28. Kaushik P, Patel C, Chandra KB, et al. Semiquantitative evaluation of ^{68}Ga-DOTANOC uptake in the normal myocardium: establishment of reference values. *J Nucl Cardiol.* 2023;30:1121–1128.

Performing [^{18}F]MFBG Long–Axial-Field-of-View PET/CT Without Sedation or General Anesthesia for Imaging of Children with Neuroblastoma

Lise Borgwardt[1], Jesper Brok[2], Kim Francis Andersen[1], Jacob Madsen[1], Nicholas Gillings[1], Marie Øbro Fosbøl[1], Charlotte Lund Denholt[1], Ida Nymann Petersen[1], Louise Sørup Sørensen[1], Lotte Hahn Enevoldsen[1], Peter Sandor Oturai[1], Helle Hjort Johannesen[1], Liselotte Højgaard[1], Christina Schulze[1], Eunice Saxtoft[1], Flemming Andersen[1], and Barbara Malene Fischer[1]

[1]Department of Clinical Physiology and Nuclear Medicine, Copenhagen University Hospital–Rigshospitalet, Copenhagen, Denmark; and [2]Department of Paediatrics, Copenhagen University Hospital–Rigshospitalet, Copenhagen, Denmark

Meta-[^{123}I]iodobenzylguanidine ([^{123}I]MIBG) scintigraphy with SPECT/CT is the standard of care for diagnosing and monitoring neuroblastoma. Replacing [^{123}I]MIBG with the new PET tracer meta-[^{18}F]fluorobenzylguanidine ([^{18}F]MFBG) and further improving sensitivity and reducing noise in a new long-axial-field-of-view (LAFOV) PET/CT scanner enable increased image quality and a faster acquisition time, allowing examinations to be performed without sedation or general anesthesia (GA). Focusing on feasibility, we present our first experience with [^{18}F]MFBG LAFOV PET/CT and compare it with [^{123}I]MIBG scintigraphy plus SPECT/CT for imaging in neuroblastoma in children. **Methods:** A pilot of our prospective, single-center study recruited children with neuroblastoma who were referred for [^{123}I]MIBG scintigraphy with SPECT/CT. Within 1 wk of [^{123}I]MIBG scintigraphy and SPECT/low-dose CT, [^{18}F]MFBG LAFOV PET/ultra–low-dose CT was performed 1 h after injection (1.5–3 MBq/kg) without sedation or GA, in contrast to the 24-h postinjection interval needed for scanning with [^{123}I]MIBG, the 2- to 2.5-h acquisition time, and the GA often needed in children less than 6 y old. Based on the spirocyclic iodonium-ylide precursor, [^{18}F]MFBG was produced in a fully automated good manufacturing practice–compliant procedure. We present the feasibility of the study. **Results:** In the first paired scans of the first 10 children included (5 at diagnosis, 2 during treatment, 2 during surveillance, and 1 at relapse), [^{18}F]MFBG PET/CT scan showed a higher number of radiotracer-avid lesions in 80% of the cases and an equal number of lesions in 20% of the cases. The SIOPEN score was higher in 50% of the cases, and the Curie score was higher in 70% of the cases. In particular, intraspinal, retroperitoneal lymph node, and bone marrow involvement was diagnosed with much higher precision. None of the children (median age, 1.6 y; range, 0.1–7.9 y) had sedation or GA during the PET procedure, whereas 80% had GA during [^{123}I]MIBG scintigraphy with SPECT/CT. A PET acquisition time of only 2 min without motion artifacts was the data requirement of the 10-min acquisition time for reconstruction to provide a clinically useful image. **Conclusion:** This pilot study demonstrates the feasibility of performing [^{18}F]MFBG LAFOV PET/CT for imaging of neuroblastoma. Further, an increased number of radiotracer-avid lesions, an increased SIOPEN score, and an increased Curie score were seen on [^{18}F]MFBG LAFOV PET/CT compared with [^{123}I]MIBG scintigraphy with SPECT/CT, and GA and sedation was avoided in all patients. Thus, with a 1-d protocol, a significantly shorter scan time, a higher sensitivity, and the avoidance of GA and sedation, [^{18}F]MFBG LAFOV PET/CT shows promise for future staging and response assessment and may also have a clinical impact on therapeutic decision-making for children with neuroblastoma.

Key Words: pediatrics; [^{18}F]MFBG; [^{18}F]MFBG LAFOV PET/CT; total-body PET/CT; neuroblastoma

J Nucl Med 2024; 65:1286–1292
DOI: 10.2967/jnumed.123.267256

Neuroblastoma is the most common extracranial solid tumor in children, with an overall survival of 70% (*1*,*2*). More than 50% of patients present with distant skeletal or bone marrow involvement or soft-tissue metastases at diagnosis, with an overall survival of about 50% (*1*,*2*). For decades, scanning with the norepinephrine analog meta-[^{123}I]iodobenzylguanidine ([^{123}I]MIBG) has been part of the initial staging, response assessment, and follow-up of neuroblastoma. The scanning procedure is a 2-d protocol due to a 24-h tracer uptake period. Sedation or general anesthesia (GA) is often used because of the lengthy scan time (often >2 h), and thyroid-protecting medication is necessary (*3*). PET is a more sensitive technique than scintigraphy with SPECT/CT; therefore, a shorter scan time and a higher resolution are possible. Some PET radiotracers with different molecular targets have been introduced for neuroblastoma imaging in the past few years, such as [^{124}I]MIBG, [^{18}F]FDG, [^{18}F]F-DOPA, and [^{68}Ga]Ga-DOTA peptides, generally identifying a higher number of lesions on PET scans than on [^{123}I]MIBG scans (*3*,*4*). Meta-[^{18}F]fluorobenzylguanidine ([^{18}F]MFBG) has a molecular target similar to that of [^{123}I]MIBG but is radiolabeled with ^{18}F instead of ^{123}I and is therefore different from most of the other PET tracers. It is furthermore a 1-d protocol without the need for thyroid-protecting medication (*5*). Few reports have described the use of [^{18}F]MFBG PET/CT in neuroblastomas (*5*–*8*). Three clinical studies have yet been published. In the first study of 5 patients with metastasized neuroblastoma, [^{18}F]MFBG showed overall physiologic and pathologic distributions similar to those of [^{123}I]MIBG, but with detection of additional lesions on [^{18}F]MFBG PET/CT (*5*). The results were confirmed in 20 patients in the second study (*6*) and in

---

Received Dec. 15, 2023; revision accepted May 7, 2024.

For correspondence or reprints, contact Lise Borgwardt (lise.borgwardt@regionh.dk).

40 patients in the third study (*7*), with paired scans in patients with neuroblastoma. In these studies, [^{18}F]MFBG PET/CT was performed with an older-generation Discovery 710 PET/CT scanner (GE Healthcare) (*5*) and on a digital Vision 600 (Siemens Healthineers) (*6*) and Polestar m660 (Medical Supply Professionals) (*7*) PET/CT scanner. In our study, we performed [^{18}F]MFBG PET/CT on the new long-axial-field-of-view (LAFOV) PET/CT scanner without sedation or GA. The sensitivity of the LAFOV PET/CT scanner is about 10 times higher than that of a digital PET/CT scanner.

We initiated a prospective study to evaluate the diagnostic value and feasibility of neuroblastoma imaging using [^{18}F]MFBG LAFOV PET/CT in children compared with [^{123}I]MIBG scintigraphy with SPECT/CT. This paper presents the preliminary data and feasibility of the proposed imaging protocol.

MATERIALS AND METHODS

Study Design and Participants

This pilot of our prospective, single-center study was performed at Rigshospitalet, Copenhagen University Hospital, and was approved by the local ethics committee (H-21009982; registered at ClinicalTrials.gov, identifier NCT05826158). We recruited the first 10 pediatric patients with suggested or confirmed neuroblastoma who were referred for [^{123}I]MIBG scintigraphy with SPECT/CT as part of their regular clinical care (suspicion of disease, staging at diagnosis, or any treatment-response assessment) and their first paired scans. If parents or caretakers gave written informed consent, [^{18}F]MFBG LAFOV PET/CT was performed within 1 wk of [^{123}I]MIBG scintigraphy with SPECT/CT. Exclusion criteria included being age 18 y or older and pregnancy. The differences in acquisition protocols for [^{123}I]MIBG scintigraphy with SPECT/CT in clinical routines compared with [^{18}F]MFBG LAFOV PET/CT are listed in Table 1.

[^{18}F]MFBG Preparation

[^{18}F]MFBG was synthesized in our department. The radiosynthesis of [^{18}F]MFBG was fully automated using a Synthera+ high-performance liquid chromatography synthesis module (IBA Radio Pharma Solutions) by ^{18}F-fluorination and deprotection of the spirocyclic ylide precursor (SPIAd-MBG), in compliance with good manufacturing practices (supplemental materials; available at http://jnm.snmjournals.org).

[^{18}F]MFBG LAFOV PET/Ultra–Low-Dose (ULD) CT

Patients received an intravenous injection of [^{18}F]MFBG (1.5–3 MBq/kg) depending on age, with no minimum activity, and without any restrictions in food or medication intake before administration of the radiotracer. Whole-body LAFOV PET/CT was performed on a Biograph Vision Quadra PET/CT scanner (Siemens Healthineers) 1 h after injection (*5*). To limit radiation use, an ULD CT image was acquired with a fixed tube voltage of 100 kVp and a current modulation of 7 mAs using Siemens CareDose. ULD CT was used for attenuation correction of PET data and large-scale localization. Anatomic localization and correlation with CT were performed with low-dose (LD) CT from the SPECT/CT scan. Whole-body PET was then performed in list mode in 1–2 fields of view (at 106 cm) for 5–10 min per field of view. From previous experience (*8*), we estimated that a minimum 2-min acquisition time without a motion artifact is required to provide images of clinically acceptable quality with an activity of 3 MBq/kg. The PET procedure was performed without GA or sedation (Table 2). PET images were reconstructed using point-spread-function modeling and time of flight with 4 iterations and 5 subsets, a maximum ring difference of 85, and a gaussian postprocessing filter of 2 mm. The image matrix was 440 × 440, resulting in a 1.65-mm in-plane voxel size. The PET slice thickness was 2 mm, which matched the CT spacing.

Dosimetry estimation was not performed because it is well described by Pandit-Taskar et al. (*5*) and Samin et al. (*6*).

[^{123}I]MIBG Scintigraphy with SPECT/LD CT

Patients were prescribed oral thyroid-protecting medication (potassium iodide for 2 d, starting 1 d before [^{123}I]MIBG injection). Scintigraphy images with SPECT/LD CT scans were obtained 24 h after injection of [^{123}I]MIBG (European Association of Nuclear Medicine dose calculator: maximum, 200; minimum, 80 MBq) (*9*) on a Symbia Intevo 16 Bold SPECT/LD CT scanner (Siemens Healthineers). Planar (anterior and posterior) whole-body scintigraphy images were acquired with a 512 × 1,024 matrix size, low- and medium-energy collimators, and a 5 cm/min scan speed. SPECT of the thorax and abdomen and other areas of interest was acquired with a 128 × 128 matrix size, low- and medium-energy collimators, a 15% wide photopeak window centered at 159 keV and similarly sized upper and lower scatter windows, a 20-s acquisition time per view, 64 views per head (90-s views in 2-bed-position tomography), 180 projections in total with step-and-shoot technique for a single bed position and continuous acquisition for 2 bed positions, and a noncircular orbit. An LD CT scan was acquired using 110 kV and 25 mAs, depending on the height and weight of the patient, and 5.0-mm slices. Images were reconstructed using attenuation correction, triple-energy-window scatter correction, and a 4.0-mm gaussian filter, with Flash 3D (Siemens Healthineers), 8 iterations, 4 subsets, and S31 median filter smoothing.

Image Analysis

Any [^{123}I]MIBG or [^{18}F]MFBG uptake in bone marrow was regarded as radiotracer-avid lesions of neuroblastoma, and uptake in the soft tissue, not representing physiological uptake, was regarded as radiotracer-avid lesions of neuroblastoma. Planar whole-body scintigraphy, SPECT/LD CT, PET/ULD CT, and maximum-intensity projection images were assessed visually, while taking morphologic data from both LD CT and

TABLE 1

Acquisition Protocols for [^{123}I]MIBG Scintigraphy with SPECT/CT in Clinical Routine and [^{18}F]MFBG LAFOV PET/CT

Parameter	[^{123}I]MIBG scintigraphy with SPECT/CT	[^{18}F]MFBG LAFOV PET/CT
Acquisition time	∼150 min*	5–10 min
Effective dose of tracer	3.7 mSv	1.7–3.4 mSv
Time from injection to scan	24 h after injection	60 min after injection
Protocol length	2 d	1 d
GA or sedation	Yes†	No

*Dependent on length of child (planar + 2 SPECT/CT scans).
†GA or sedation needed for children < 6 y old.

TABLE 2
Procedures for Avoiding GA and Sedation with [^{18}F]MFBG LAFOV PET/CT

Age range	Procedure
0–9 mo	PET/CT planned during nap time
	Parents contacted and procedure and preparation explained at least 1–2 d before scheduled scan
	Sleep and food deprivation, advised starting 1–2 h before scan
	Wrapped, fed, and rested in scanner room
	Scanned without GA or sedation with activity of 1.5 MBq/kg
9 mo to 3 y	PET/CT planned during nap time
	Parents contacted and procedure and preparation explained at least 1–2 d before scheduled scan
	Sleep and food deprivation, advised starting 1–2 h before scan
	Wrapped if possible, light dimmed, fed and rested in scanner room
	Scanned without GA or sedation at activity of 3 MBq/kg*
≥4 y	Parents contacted and preparation explained at least 1–2 d before scan
	Food and drink with lower glycemic index to keep child calm offered in tracer uptake period
	In scanner room, light is dimmed and story is read by parents or caretakers
	Scan performed without GA or sedation at activity of 1.5 MBq/kg

*To be able to reconstruct in only 2 min.

ULD CT scans into account. Two masked readers independently scored the [^{18}F]MFBG scans, and 2 other masked readers scored the [^{123}I]MIBG scans for the presence of any pathologic lesions, as the number of lesions in total were counted and the SIOPEN score and the Curie score were calculated. Discrepancies between the pairs of readers were resolved by consensus. All readers were nuclear medicine physicians with more than 10 y of experience in pediatric oncology. The lesions on the paired [^{123}I]MIBG and [^{18}F]MFBG scans were compared.

Anti-GD2 Staining

Anti-GD2 staining is not the gold standard, but it is a new and more sensitive method than bone marrow staining, and of all the neuroectodermally derived tumor cell lines and tissues studied by researchers, neuroblastoma is the one known to have the highest expression of GD2 (~98% expression in all neuroblastoma cell lines, so not just a certain biologic subtype of neuroblastoma cells), estimated at 5–10 million molecules per cell, making it an obvious biomarker for neuroblastoma (*10*). In our study, GD2 staining was used to confirm bone marrow involvement when the bone marrow staining and [^{123}I]MIBG results were negative but the [^{18}F]MFBG results were positive.

Statistical Analysis

Continuous data are presented as median with ranges, whereas categoric data are presented as a percentage. A paired-samples *t* test was applied to assess the differences between the 2 scan methods. Statistical analyses were performed using SPSS, version 24.0 (IBM), with *P* values of less than 0.05 indicating a significant difference.

RESULTS

[^{18}F]MFBG was synthesized (1,600–3,800 MBq) in an overall time of 120 min, with radiochemical yields of 22% ± 8% ($n = 8$). The radiochemical purity was greater than 98%. The product remained stable for at least 6 h at activities of up to 9,500 MBq of [^{18}F]MFBG.

Ten children with a median age of 1.6 y (range, 0.1–7.9 y) underwent paired [^{123}I]MIBG scintigraphy with SPECT/LD CT and [^{18}F]MFBG LAFOV PET/ULD CT. Five children were scanned at the time of diagnosis, 2 during treatment, 2 during off-therapy surveillance, and 1 at verified relapse. The neuroblastoma staging of the children was at diagnosis: $n = 4$ stage L2 (low risk), $n = 1$ stage L2 (intermediate risk), $n = 1$ stage L2 (high risk/relapse), $n = 2$ stage M (high risk), $n = 1$ stage M (high risk/relapse), $n = 1$ stage MS, according to the International Neuroblastoma Risk Group Staging System (Table 3).

None of the children underwent sedation or GA during the [^{18}F]MFBG LAFOV PET/ULD CT scan, whereas GA was performed in 80% of patients during [^{123}I]MIBG scintigraphy with SPECT/LD CT. Only 1 of the 10 children did not fall asleep before or during the [^{18}F]MFBG PET/ULD CT scan and was talked to through the procedure by the parents. Two of the 10 children moved during sleep. All PET acquisitions were performed in list mode for 5–10 min. Depending on the age and the expected cooperability of the child, 2-min periods with no movements were identified in these 3 cases and subsequently reconstructed into images of clinically acceptable quality, as illustrated in Figure 1. To be able to identify a 2-min period without motion artifacts, we performed the scans for a longer period than required, as described previously (*8*), and the utility of this method was confirmed when the lesion counts were compared and found to be equal in all

TABLE 3
International Neuroblastoma Risk Group Staging System

Stage	Definition
L1	Localized tumor without image-defined risk factors for surgery
L2	Locoregional tumor with image-defined risk factors
M	Metastatic
MS	Metastatic in infant < 18 mo old with metastases limited to liver, skin, and bone marrow

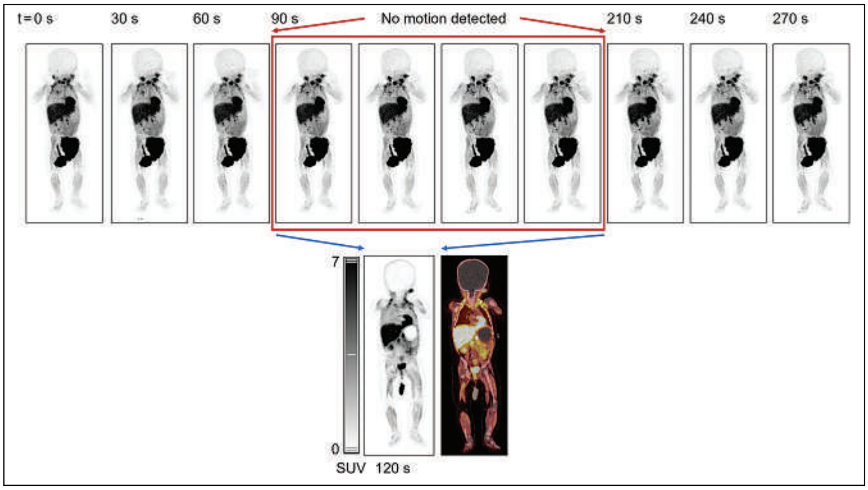

FIGURE 1. PET images obtained in list mode in 30-s increments, excluding periods of motion artifacts in reconstruction of images.

10 scans with simulated acquisition times of 2, 5, and 10 min. The mean scan time for [^{18}F]MFBG LAFOV PET/ULD CT (7.7 ± 2.6 min) was significantly shorter than that for [^{123}I]MIBG scintigraphy with SPECT/LD CT (76.3 ± 17.8 min) ($P < 0.01$). The effective dose from CT was, on average, 0.39 mSv (range, 0.36–0.43 mSv) for ULD CT (whole body including the legs) as part of the [^{18}F]MFBG PET/CT scan and 1.27 mSv (range, 1.16–2.08 mSv) for LD CT (whole body including the mid thigh) as part of the [^{123}I]MIBG SPECT/CT scan. Individual data are available in Supplemental Table 1.

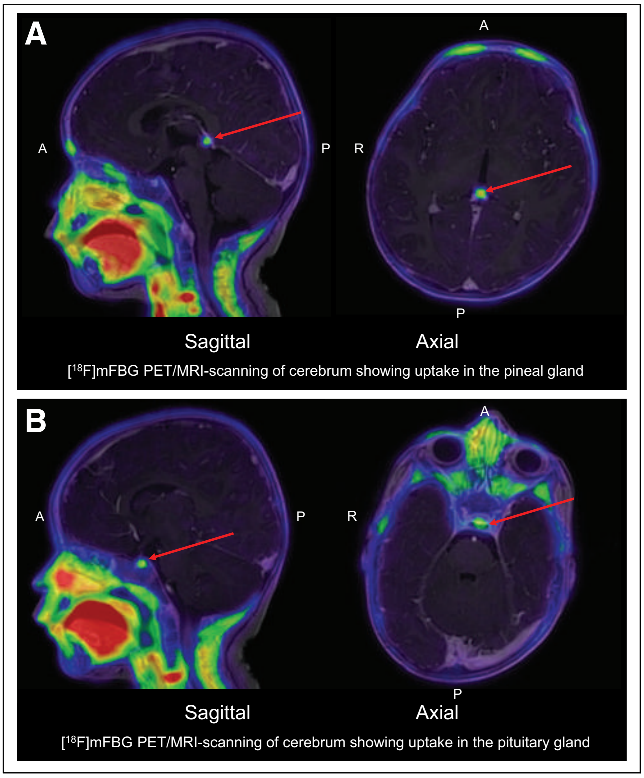

FIGURE 2. Sagittal and axial view of tracer uptake in pineal gland (arrows, A) and pituitary gland (arrows, B) seen on [^{18}F]MFBG LAFOV PET/MRI. A = anterior; P = posterior.

The physiologic uptake observed for [^{18}F]MFBG LAFOV PET/ULD CT was similar to the well-known uptake pattern for [^{123}I]MIBG scintigraphy (*3*), such as in the urinary tract, salivary glands, liver, heart wall, adrenal glands, intestines, pancreas, and brown fat; however, uptake in the brown fat, the lacrimal glands, and the pancreas can be more prominent in [^{18}F]MFBG LAFOV PET/ULD CT than in [^{123}I]MIBG scintigraphy. We also observed physiologic uptake, also seen on follow-up, in the pineal gland (Fig. 2A) in 2 of 10 children when the images were coregistered with MR images (MRI performed for other clinical purposes), as well as discrete physiologic uptake in the pituitary gland (Fig. 2B) in all children. The SUV in structures ($\text{SUV}_{\text{structure}}$) with physiologic uptake and the SUV ratio ($\text{SUV}_{\text{structure}}$/$\text{SUV}_{\text{liver}}$) as the average for [^{18}F]MFBG in all 10 patients are shown in Table 4.

Compared with [^{123}I]MIBG scintigraphy with SPECT/LD CT, [^{18}F]MFBG LAFOV PET/ULD CT showed a higher number of radiotracer-avid lesions in 80% of the cases and an equal number in 20% when lesions were counted in the scans. In particular, intraspinal, retroperitoneal lymph node, and bone marrow involvement was diagnosed with much higher precision in [^{18}F]MFBG LAFOV PET/ULD CT than in [^{123}I]MIBG scintigraphy with SPECT/LD CT (Figs. 3A and 3B). Further, in cases of equivocal [^{123}I]MIBG findings, for example, if [^{123}I]MIBG scintigraphy with SPECT/LD CT showed suspicion of involvement at these sites, it was diagnosed on [^{18}F]MFBG LAFOV PET/ULD CT with a greater diagnostic confidence because of the increased spatial resolution and improved target-to-nontarget contrast of LAFOV PET/CT. When SIOPEN and Curie scores were analyzed and compared, the SIOPEN score was higher in 50% of the cases and the Curie score was higher in 70% of the cases (Table 5).

TABLE 4
SUV of Structures with Physiologic Uptake in [^{18}F]MFBG PET Scanning

Structure	SUV	Ratio with liver SUV
Pituitary gland	1.1 (0.4–2.6)	0.3 (0.2–0.9)
Pineal gland	0.7 (0.2–2.1)	0.2 (0.0–0.4)
Lacrimal glands	3.3 (0.8–6.5)	0.9 (0.6–1.3)
Parotid glands	6.4 (3.0–10.6)	2.6 (1.0–4.4)
Submandibular glands	8.4 (4.1–13.1)	2.8 (1.3–5.6)
Thyroid gland	5.0 (1.3–9.9)	1.4 (0.9–2.0)
Heart	6.4 (3.2–9.0)	1.8 (1.1–2.0)
Intestines	2.1 (1.0–2.5)	0.6 (0.5–0.7)
Brown fat	1.6 (1.5–1.7)	0.4 (0.4–0.5)
Pancreas	4.2 (1.0–6.6)	1.2 (0.7–1.8)
Liver	4.0 (3.7–4.9)	

Data are average and range.

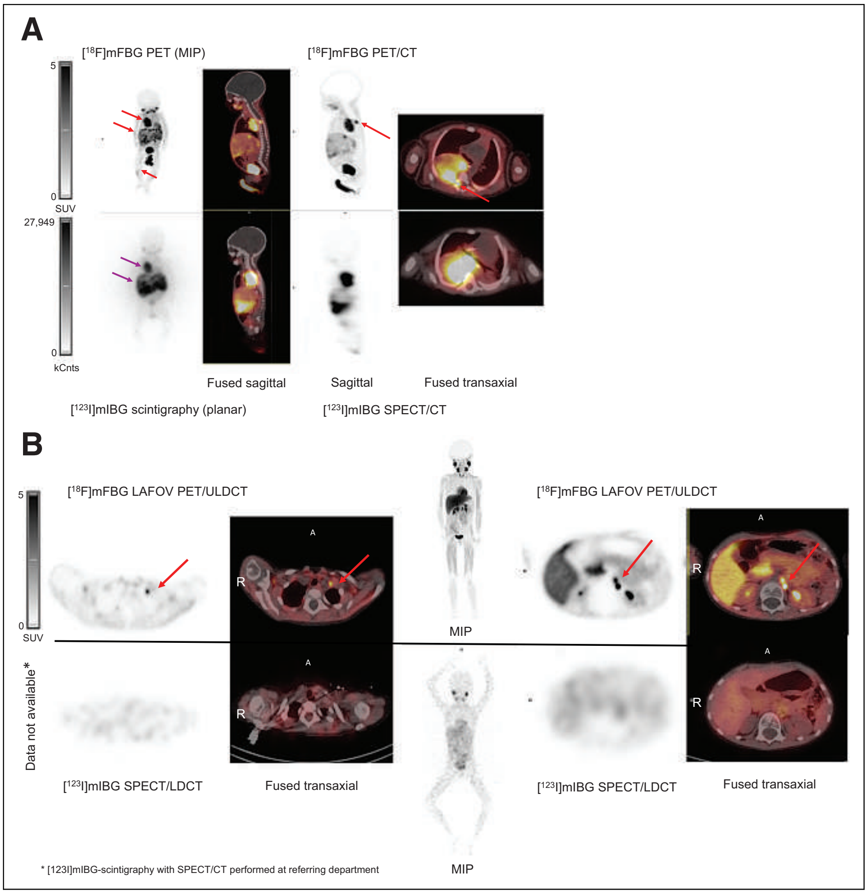

FIGURE 3. (A) [^{18}F]MFBG LAFOV PET/ULD CT (top) and [^{123}I]MIBG scintigraphy with SPECT/LD CT images (bottom) of 7-wk-old girl with neuroblastoma. [^{18}F]MFBG image shows intraspinal and bone marrow involvement not seen on [^{123}I]MIBG image. [^{18}F]MFBG PET/ULD CT image shows uptake in tumor in right hemithorax with intraspinal involvement with direct extension into neural foramina and spinal canal between thoracic vertebrae 4/5 and 5/6 (top red arrow), several liver lesions (middle red arrow), and in bone marrow of right tibia (bottom red arrow). [^{123}I]MIBG scintigraphy with SPECT/LD CT image shows only large thoracic tumor (top purple arrow) and liver metastases (bottom purple arrow). Spinal involvement and bone marrow involvement could not be identified on [^{123}I]MIBG scintigraphy with SPECT/LD CT. (B) [^{18}F]MFBG LAFOV PET/ULD CT and [^{123}I]MIBG scintigraphy with SPECT/LD CT images of 6-y-old girl with paravertebral relapse of neuroblastoma stage IV in left adrenal gland without N-Myc gene amplification. [^{18}F]MFBG image shows lymph node involvement not seen on [^{123}I]MIBG image. [^{18}F]MFBG PET/ULD CT postoperative image, after resection of paravertebral relapse, shows uptake in left-side cervical lymph node (top left red arrows) and 2 retroperitoneal lymph nodes (top right red arrows), not identified on [^{123}I]MIBG scintigraphy with SPECT/LD CT. A = anterior; MIP = maximum-intensity projection.

DISCUSSION

To the best of our knowledge, this is the first demonstration of the feasibility of using [^{18}F]MFBG LAFOV PET/ULD CT for imaging of neuroblastoma in children. We have presented the results of paired [^{123}I]MIBG and [^{18}F]MFBG scans of the first 10 children who were included in our prospective study. [^{18}F]MFBG PET/ULD CT scans can be performed without sedation or GA in the most critical age group of 0–4 y because of the possibility of obtaining high-quality PET images, despite short acquisition time, because of the high sensitivity of the LAFOV PET/CT scanner.

We also showed the feasibility of producing tracers in our chemistry laboratory (*11–16*). These details are provided in the supplemental materials.

None of the children had GA or sedation during the PET/ULD CT scanning procedure. This study demonstrates that close collaboration with the parents before arrival at the clinic and during the procedure, along with prioritizing space with extended time slots on the scanner, can create a calm atmosphere so that GA and sedation can be avoided. Samim et al. (*6*) reduced use of GA and sedation to 10% (*n* = 20; median age, 4.9 y) because of the shorter scan time, but they were not able to avoid the use of GA or sedation in all patients (the median age in our study was 1.6 y). It might be more difficult to perform PET with diagnostic CT with intravenous contrast, because injection of the intravenous contrast could potentially wake up the sleeping child.

Regarding physiologic uptake, we experienced the same pitfalls for [^{18}F]MFBG as for [^{123}I]MIBG. This is in accordance with the 3 studies on [^{18}F]MFBG PET/CT performed on the older-generation PET/CT (*5*) and digital PET/CT scanners (*6*,*7*). In addition, we found discrete uptake in the pituitary gland and, in some children, also in the pineal gland on [^{18}F]MFBG PET/CT, which was not reported earlier. This is most likely due to the increased sensitivity and resolution of LAFOV PET/CT. As both the posterior pituitary gland and the pineal gland are outside the blood–brain barrier (*17*), this suggests that, as with [^{123}I]MIBG (*17*), [^{18}F]MFBG does not seem to cross the blood–brain barrier; however, this needs to be further explored in future studies. We also found that the radiotracer uptake in the pancreas, lacrimal glands, and brown fat may be markedly increased on [^{18}F]MFBG PET/CT compared with [^{123}I]MIBG scintigraphy with SPECT/CT.

Compared with [^{123}I]MIBG scintigraphy with SPECT/LD CT, [^{18}F]MFBG LAFOV PET/ULD CT detected more lesions in 80% of the cases and detected an equal number of lesions in the remaining 20% of the patients. This finding suggests that replacing [^{123}I]MIBG SPECT/LD CT with [^{18}F]MFBG PET/ULD CT will result in higher scores in a significant number of neuroblastoma patients if using either the North American Curie score or the European SIOPEN score (*3*). In our study, the SIOPEN score was higher in 50% of patients and the Curie score was higher in 70% of patients. Thus, it is important to explore this observation further, as well as to explore the clinical impact in larger studies and consider the potential impact on initial diagnosis, treatment decision-making, treatment-response assessment, and off-therapy surveillance.

It is difficult to define a gold standard, but since [^{123}I]MIBG and [^{18}F]MFBG are the same molecule, differing only in radiolabel (^{123}I and ^{18}F, respectively), it is assumed that the increased number of lesions detected when applying the latter radiotracer are true positives found as a result of the increased sensitivity and resolution on PET imaging. We performed the more sensitive GD2

TABLE 5

Comparison of SIOPEN Scores, Curie Scores, and Lesion Counts for [^{123}I]MIBG Scintigraphy with SPECT/CT and [^{18}F]MFBG LAFOV PET/CT

Patient	Tracer	SIOPEN score	Curie score	Lesion count	[^{18}F]MFBG addition
1	[^{18}F]MFBG	2	3	3	Bone marrow involvement
	[^{123}I]MIBG	0	1	1	
2	[^{18}F]MFBG	1	4	4	Intraspinal involvement and bone marrow involvement
	[^{123}I]MIBG	0	3	2	
3	[^{18}F]MFBG	17	12	21	Bone marrow involvement
	[^{123}I]MIBG	0	0	0	
4	[^{18}F]MFBG	0	3	2	Confidence in intraspinal involvement
	[^{123}I]MIBG	0	3	1	
5	[^{18}F]MFBG	0	0	0	No addition
	[^{123}I]MIBG	0	0	0	
6	[^{18}F]MFBG	4	6	9	Confidence in intraspinal involvement and bone marrow involvement
	[^{123}I]MIBG	0	3	2	
7	[^{18}F]MFBG	0	2	3	LN cerv. and retro.
	[^{123}I]MIBG	0	0	0	
8	[^{18}F]MFBG	4	7	8	LN cerv., retro., iliac, and bone marrow involvement
	[^{123}I]MIBG	3	6	3	
9	[^{18}F]MFBG	0	1	1	No addition
	[^{123}I]MIBG	0	1	1	
10	[^{18}F]MFBG	0	2	3	LN retro.
	[^{123}I]MIBG	0	1	1	

LN = lymph node; cerv. = cervical; retro. = retroperitoneal.

antigen tests in some of the patients with bone marrow lesions seen only on [^{18}F]MFBG PET/ULD CT and with negative results on bone marrow aspiration. In all cases, GD2 antigen testing confirmed the uptake in the bone marrow seen on the [^{18}F]MFBG scan.

CONCLUSION

The clinical benefit of [^{18}F]MFBG LAFOV PET/ULD CT compared with [^{123}I]MIBG scintigraphy with SPECT/LD CT is that it is a 1-d protocol, has a much shorter scan time, and avoids the need for GA and sedation in most patients with neuroblastoma. Preliminary results demonstrate that in most patients, more neuroblastoma lesions were detected on [^{18}F]MFBG LAFOV PET/ULD CT than on [^{123}I]MIBG scintigraphy with SPECT/LD CT, with increased SIOPEN and Curie scores in 50% and 70% of cases, respectively. [^{18}F]MFBG LAFOV PET/ULD CT shows promise for future staging and response assessment in children with neuroblastoma. The impact on staging, treatment decision-making, treatment-response assessment, and off-therapy surveillance remains to be explored.

DISCLOSURE

No potential conflict of interest relevant to this article was reported.

KEY POINTS

QUESTION: Is [^{18}F]MFBG LAFOV PET/CT feasible in a clinical setting, and do we see more lesions on [^{18}F]MFBG LAFOV PET/CT than on [^{123}I]MIBG scintigraphy with SPECT/LD CT?

PERTINENT FINDINGS: This study included 10 patients in our prospective study to compare [^{18}F]MFBG LAFOV PET/CT with [^{123}I]MIBG scintigraphy with SPECT/LD CT in children with neuroblastoma. In total, 80% of [^{18}F]MFBG LAFOV PET/CT studies showed more lesions than did studies acquired using [^{123}I]MIBG scintigraphy with SPECT/LD CT, and 20% showed the same number of lesions and with increased SIOPEN and Curie scores in 50% and 70%, respectively. [^{18}F]MFBG LAFOV PET/CT could be performed without sedation or GA in all patients.

IMPLICATIONS FOR PATIENT CARE: The clinical benefit of [^{18}F]MFBG LAFOV PET/ULD CT compared with [^{123}I]MIBG scintigraphy with SPECT/LD CT is that it is a 1-d protocol, has a much shorter scan time, and avoids the need for GA and sedation in most patients with neuroblastoma. The influence of this result for clinical decision-making seems promising.

REFERENCES

1. Monclair T, Brodeur GM, Ambros PF, et al. The International Neuroblastoma Risk Group (INRG) staging system: an INRG Task Force report. *J Clin Oncol.* 2009;10:298–303.

2. Simon T, Berthold F, Borkhardt A, Kremens B, De Carolis B, Hero B. Treatment and outcomes of patients with relapsed, high-risk neuroblastoma: results of German trials. *Pediatr Blood Cancer.* 2011;56:578–583.
3. Bar-Sever Z, Biassoni L, Shulkin B, et al. Guidelines on nuclear medicine imaging in neuroblastoma. *Eur J Nucl Med Mol Imaging.* 2018;45:2009–2024.
4. Piccardo A, Treglia G, Fiz F, et al. The evidence-based role of catecholaminergic PET tracers in neuroblastoma: a systematic review and a head-to-head comparison with mIBG scintigraphy. *Eur J Nucl Med Mol Imaging.* 2024;51:756–767.
5. Pandit-Taskar N, Zanzonico P, Staton KD, et al. Biodistribution and dosimetry of ^{18}F-meta-fluorobenzylguanidine: a first-in-human PET/CT imaging study of patients with neuroendocrine malignancies. *J Nucl Med.* 2018;59:147–153.
6. Samim A, Blom T, Poot AJ, et al. [^{18}F]mFBG PET-CT for detection and localisation of neuroblastoma: a prospective pilot study. *Eur J Nucl Med Mol Imaging.* 2023;50:1146–1157.
7. Wang P, Li T, Liu Z, et al. [^{18}F]MFBG PET/CT outperforming [^{123}I]MIBG SPECT/CT in the evaluation of neuroblastoma. *Eur J Nucl Med Mol Imaging.* 2023;50:3097–3106.
8. Borgwardt L, Brok JS, Andersen KF, et al. [^{18}F]mFBG long axial field of view PET-CT without general anaesthesia reveals concise extension of neuroblastoma in a 9-month-old boy. *Eur J Nucl Med Mol Imaging.* 2023;50:2563–2564.
9. Metrard G, Besse H, Darsin-Bettinger D, Mouzoune S, Gauvain S. New EANM paediatric dosage card: optimization of F-18 FDG-administered activities. *Eur J Nucl Med Mol Imaging.* 2014;41:1635.
10. Sabbih GO, Danquah MK. Neuroblastoma GD2 expression and computational analysis of aptamer-based bioaffinity targeting. *Int J Mol Sci.* 2021; 22:9101.
11. Garg PK, Garg S, Zalutsky MR. Synthesis and preliminary evaluation of para- and meta-[^{18}F]fluorobenzylguanidine. *Nucl Med Biol.* 1994;21:97–103.
12. Zhang H, Huang R, Pillarsetty N, et al. Synthesis and evaluation of ^{18}F-labeled benzylguanidine analogs for targeting the human norepinephrine transporter. *Eur J Nucl Med Mol Imaging.* 2014;41:322–332.
13. Hu B, Vavere AL, Neumann KD, Shulkin BM, DiMagno SG, Synder SE. A practical, automated synthesis of meta-[^{18}F]fluorobenzylguanidine for clinical use. *ACS Chem Neurosci.* 2015;6:1870–1879.
14. Preshlock S, Calderwood S, Verhoog S, et al. Enhanced copper-mediated ^{18}F-fluorination of aryl boronic esters provides eight radiotracers for PET applications. *Chem Commun (Camb).* 2016;52:8361–8364.
15. Rotstein BH, Wang L, Liu RY, et al. Mechanistic studies and radiofluorination of structurally diverse pharmaceuticals with spirocyclic iodonium(III) ylides. *Chem Sci.* 2016;7:4407–4417.
16. Pauwels E, Celen S, Baete K, et al. [^{18}F] MFBG PET imaging: biodistribution, pharmacokinetics, and comparison with [^{123}I] MIBG in neural crest tumour patients. *Eur J Nucl Med Mol Imaging.* 2023;50:1134–1145.
17. Gourand F, Patin D, Henry A, et al. Chemical delivery system of MIBG to the central nervous system: synthesis,^{11}C-radiosynthesis, and in vivo evaluation. *ACS Med Chem Lett.* 2019;10:352–357.

Noninvasive Diagnostic Method to Objectively Measure Olfaction and Diagnose Smell Disorders by a Molecularly Targeted Fluorescence Imaging Agent

Dauren Adilbay*[1,2], Junior Gonzales*[1], Marianna Zazhytska[3], Paula Demetrio de Souza Franca[1,4], Sheryl Roberts[1], Tara D. Viray[1], Raik Artschwager[1], Snehal Patel[2], Albana Kodra[3,5], Jonathan B. Overdevest[6], Chun Yuen Chow[7,8], Glenn F. King[7,8], Sanjay K. Jain[9–11], Alvaro A. Ordonez[9,10], Laurence S. Carroll[9,11], Stavros Lomvardas[3], Thomas Reiner[†1,12], and Nagavarakishore Pillarsetty[†1,12]

[1]Department of Radiology, Memorial Sloan Kettering Cancer Center, New York, New York; [2]Department of Surgery, Memorial Sloan Kettering Cancer Center, New York, New York; [3]Mortimer B. Zuckerman Mind, Brain and Behavior Institute, Columbia University, New York, New York; [4]Department of Otorhinolaryngology and Head and Neck Surgery, Federal University of São Paulo, São Paulo, Brazil; [5]Department of Genetics and Development, Columbia University Irving Medical Center, Vagelos College of Physicians and Surgeons, Columbia University, New York, New York; [6]Department of Otolaryngology—Head and Neck Surgery, Columbia University Irving Medical Center, Vagelos College of Physicians and Surgeons, Columbia University, New York, New York; [7]Institute for Molecular Bioscience, University of Queensland, St. Lucia, Queensland, Australia; [8]Australian Research Council Centre of Excellence for Innovations in Peptide and Protein Science, University of Queensland, St. Lucia, Queensland, Australia; [9]Center for Infection and Inflammation Imaging Research, Johns Hopkins University School of Medicine, Baltimore, Maryland; [10]Department of Pediatrics, Johns Hopkins University School of Medicine, Baltimore, Maryland; [11]Russell H. Morgan Department of Radiology and Radiological Sciences, Johns Hopkins University School of Medicine, Baltimore, Maryland; and [12]Department of Radiology, Weill Cornell Medical College, New York, New York

Despite the recent advances in understanding the mechanisms of olfaction, no tools are currently available to noninvasively identify loss of smell. Because of the substantial increase in patients presenting with coronavirus disease 2019–related loss of smell, the pandemic has highlighted the urgent need to develop quantitative methods. **Methods:** Our group investigated the use of a novel fluorescent probe named Tsp1a-IR800$_P$ as a tool to diagnose loss of smell. Tsp1a-IR800$_P$ targets sodium channel 1.7, which plays a critical role in olfaction by aiding the signal propagation to the olfactory bulb. **Results:** Intuitively, we have identified that conditions leading to loss of smell, including chronic inflammation and coronavirus disease 2019, correlate with the downregulation of sodium channel 1.7 expression in the olfactory epithelium, both at the transcript and at the protein levels. We demonstrated that lower Tsp1a-IR800$_P$ fluorescence emissions significantly correlate with loss of smell in live animals—thus representing a potential tool for its semiquantitative assessment. Currently available methods rely on delayed subjective behavioral studies. **Conclusion:** This method could aid in significantly improving preclinical and clinical studies by providing a way to objectively diagnose loss of smell and therefore aid the development of therapeutic interventions.

Key Words: optical; anosmia; COVID-19; fluorescence imaging; olfaction; smell

J Nucl Med 2024; 65:1293–1300
DOI: 10.2967/jnumed.123.266123

Olfaction (sense of smell) is crucial for the survival of most animals, including humans, attributed to its vital transfer of information about the food and environment, which instinctively serves as a tool for inter- and intraspecies communication (*1*). Over the past 3 y, mostly as a result of the coronavirus disease 2019 (COVID-19) pandemic, loss of smell (anosmia) has captured the attention not only of the scientific community but also of the general public and has highlighted the need for a deeper mechanistic understanding of this sense. Most importantly, the lack of rapid assessments has exposed the need for objective tools to assess anosmia (*2,3*). It is estimated that about 13.3 million adults in the United States have a vast range of smell disorders and that 3.4 million endure severe hyposmia or complete anosmia (*4*). These studies were performed before the COVID-19 virus pandemic and therefore severely underestimate people currently with smell disorders (*5–7*).

Despite the fundamental importance of the sense of smell in the quality of life and the high prevalence of anosmia, no quantitative method to assess the perception of smell is currently available either clinically or for use in human or research animal settings. In humans, the perception of smell is subjectively reported and registered as a nonindependent measure. In animals, we rely on behavioral studies, such as the buried-food test, which measures time to find food as negatively correlated with the sense of smell (*8*). These tests not only are challenging to perform but also are indirect and highly subjective. Developing new diagnostic methods is, therefore, a clinical and scientific need.

Received Jul. 21, 2023; revision accepted May 22, 2024.

For correspondence or reprints, contact Thomas Reiner (c2c90cavma7122@gmail.com) or Nagavarakishore Pillarsetty (pillarsn@mskcc.org).

*Contributed equally to this work.

†Contributed equally to this work.

Voltage-gated sodium channels (ranging from $Na_V1.1$ to $Na_V1.9$) are crucial in neurotransmission and aid in the propagation of an action potential, and therefore neurologic impulses, along the nerve bundles. $Na_V1.7$ is encoded by the SCN9A gene and is expressed predominantly in the peripheral sensory neurons. Its dysfunction has been correlated with impaired olfaction (*9,10*). It is highly expressed in the axons of human olfactory sensory neurons (OSNs), where it plays a critical role in transmitting olfactory cues provided by olfactory receptor activation to higher-order neurons in the brain (*10*). Dysfunction of $Na_V1.7$, originating from mutations in the SCN9A gene or loss of $Na_V1.7$ channels at the level of the olfactory bulb and olfactory epithelium, results in smell disorders (*10*). The presence of $Na_V1.7$ in the superficial layer of the olfactory epithelium presents an unprecedented opportunity to develop optic probes that can noninvasively image the expression of $Na_V1.7$. By objectively measuring changes in $Na_V1.7$ expression in the olfactory epithelium, we can potentially identify smell disorders immediately.

Taking advantage of a potent and exquisite Hsp1a peptide (Supplemental Fig. 1; supplemental materials are available at http://jnm.snmjournals.org), which was isolated from a Peruvian tarantula and targets solely $Na_V1.7$ (*11–13*), our group has previously developed fluorescent and PET imaging agents that can aid visualization of peripheral nerves in vivo without any side effects (*12–15*). For this work, amenable Tsp1a-Pra0 was derived from Hsp1a and was the starting compound for Tsp1a-$IR800_P$ (Supplemental Fig. 1). A fluorescent peptide is used to demarcate olfactory epithelium and $Na_V1.7$ changes triggered by inflammation. As a model for smell disorders (allergy, viral infection, etc.), we have used methimazole injections to induce inflammation in the nasal cavity (*16*). After intraperitoneal methimazole administration, various cell types in the olfactory epithelium, including OSNs and sustentacular cells, exhibit swollen organelles within 4 h, which is subsequently followed by detachment of cells from the basal lamina. In the current article, we establish a robust correlation between anosmia resulting from methimazole treatment or COVID-19 and a decrease in $Na_V1.7$ expression in the superficial layer of the olfactory epithelium of mice, hamsters, primates, and humans, and we demonstrate the utility of $Na_V1.7$-targeted fluorescent Tsp1a peptides in detecting the changes in $Na_V1.7$ expression in OSNs. Our findings suggest that our fluorescent Tsp1a peptide has the potential to serve as a noninvasive imaging tool for detecting loss of smell.

MATERIALS AND METHODS

General

Acetonitrile of high-performance liquid chromatography (HPLC) grade and liquid chromatography–mass spectrometry grade was purchased from Fisher Scientific. Water ($>18.2\ M\Omega cm^{-1}$) was obtained from an AlphaQ Ultrapure water system. Reverse-phase HPLC purifications were performed on a Shimadzu HPLC system equipped with a DGU-20A degasser, an SPD-M20A ultraviolet detector, an LC-20AB pump system, and a CBM-20A communication bus module using a reverse-phase HPLC column (Atlantis T3 C18, 5 μm, 4.6 × 250 mm, Waters product number 186003748). Regarding the HPLC solvents, buffer A was H_2O plus 0.1% trifluoroacetic acid, and buffer B was acetonitrile plus 0.1% trifluoroacetic acid. HPLC purification and analysis were performed at a flow rate of 1 mL/min with a gradient of 5%–95% B for 60 min. Electrospray ionization mass spectroscopy spectra were recorded on a Waters Aquity ultra-performance liquid chromatograph with an electrospray ionization single-quadrupole detector. Compounds were lyophilized on a Labconco FreeZone 2.5 plus. The concentration of Tsp1a-$IR800_P$ was determined by measuring the absorbance. Details are provided in Supplemental Figure 1. Regarding the solvents for the mobile phase for the liquid chromatography–mass spectrometry, buffer A was H_2O plus 0.05% formic acid, and buffer B was acetonitrile plus 0.05% formic acid. The liquid chromatography–mass spectrometry analysis was performed at a flow rate of 1 mL/min with a gradient of 5%–95% B for 15 min.

Synthesis of Tsp1a-Pra0 and Fluorescent Tsp1a-$IR800_P$

On the basis of our previous success with the Hsp1a peptide, we prepared a synthetic version named Tsp1a that incorporates a propargylglycine at the N terminus (Tsp1a-Pra0) to facilitate the click chemistry, following protocols similar to what has been reported before (*12–14*). Our Tsp1a—which features a propargylglycine—was used to conjugate the peptide to IR800 azide via copper-catalyzed click chemistry to afford Tsp1a-$IR800_P$. IR800cw azide dye (50 μg, 44 nmol, LI-COR BioSciences product number 929-60000, in 50 μL of acetonitrile) was conjugated to Tsp1a-Pra0 (propargylglycine modified at the N terminus) peptide (0.72 mM, 250 μg in 100 μL of H_2O) in a buffer. The Tsp1a-Pra0 peptide was diluted with an aqueous Tris-buffered solution (25 mM, pH 7.4); further, L-ascorbic acid in H_2O (50 mM), $CuSO_4$ solution in H_2O (50 mM), and IR800cw azide (50 μg, 44 nmol) were added to the reaction mixture. The reaction mixture was stirred at room temperature in the dark for 4 h. The crude mixture was purified via reverse-phase HPLC, fractions containing the product were pooled and lyophilized, and pure Tsp1a-$IR800_P$ was obtained as a blue solid (44 μg, 10 nmol; 26% yield). The final HPLC analysis for the Tsp1a-$IR800_P$ showed 96% purity after the isolation. On liquid chromatography–mass spectrometry (electrospray ionization–positive), the mass-to-charge ratio for Tsp1a-$IR800_P$ was successful and showed ions corresponding to the calculated mass of Tsp1a-$IR800_P$. The calculated mass of Tsp1a-$IR800_P$ was 4,682.87 for $(3H)C_{207}H_{293}N_{48}O_{57}S_{10}$ and 1,563.03 for $(3H)C_{207}H_{293}N_{48}O_{57}S_{10}$ $[M+3H]^{3+}$, the found mass was 1,564.11 for $C_{207}H_{293}N_{48}O_{57}S_{10}$ $[M+3H]^{3+}$, the calculated mass was 1,172.20 for $(3H)C_{207}H_{293}N_{48}O_{57}S_{10}$ $[M+4H]^{4+}$, and the found mass was 1,173.02 for $C_{207}H_{293}N_{48}O_{57}S_{10}$ $[M+4H]^{4+}$. The HPLC retention time for the Tsp1a-$IR800_P$ was 21.7 min ($R_t = 21.7$ min).

Animal Work

All animal care and procedures were approved by the Animal Care and Use Committees of Memorial Sloan Kettering Cancer Center.

Mouse Experiments

Hsd:athymic female mice (Nude-$Foxn1^{nu}$, 6–8 wk old) were acquired from Jackson Laboratory. We first assessed the possibility of visualizing the olfactory nerve in normosmic mice using Tsp1a-$IR800_P$. Nine mice were divided into 3 groups: experimental, control, and blocking. The experimental group was intravenously injected with Tsp1a-$IR800_P$ (1 nmol in 100 μL of phosphate-buffered saline [PBS]), the control group was injected with 100 μL of PBS, and the blocking group was injected with a combination of Tsp1a-$IR800_P$ and unmodified Tsp1a-Pra0 (1 nmol of Tsp1a-$IR800_P$ plus 5 nmol of Tsp1a-Pra0 to form the blocking agent in 100 μL of PBS). Epifluorescence images were acquired 3 min after injection.

Fluorescence Imaging of Mice

Fluorescence imaging was performed to identify fluorescence emitted by olfactory epithelium after injection of the compound. All mice were anesthetized using an intraperitoneal injection of a cocktail of 90 mg of ketamine and 10 mg of xylazine per kilogram, and in vivo epifluorescence images were obtained using an IVIS Spectrum imaging system (PerkinElmer) with filters set for 745-nm excitation and 800-, 820-, 840-nm emission. The animals were euthanized using CO_2 asphyxiation, and olfactory nerve/bulb, muscle, heart, spleen, kidney, and liver were removed and imaged ex vivo using the IVIS Spectrum system. Autofluorescence was removed through spectral unmixing.

Semiquantitative analysis of the Tsp1a-IR800$_P$ signal was conducted by measuring the average radiant efficiency (in units of [p/s/cm^2/sr]/[μW/cm^2]) in regions of interest that were placed on the region of the olfactory bulb and nerve. Radiant efficiency was calculated using the following formula: radiant efficiency (p/s/cm^2/sr)/(μW/cm^2) = flux (photons/s)/excitation power (μW). Flux is the total photon flux emitted by the sample, which can be determined from the emission images. Excitation power is the power of the excitation light used for imaging.

Regarding mice infected with severe acute respiratory syndrome coronavirus 2 (SARS-CoV-2), the protocol has been described by Ordonez et al. (*17*). The supplemental materials provide details.

Olfactory Ablation (Animal Model for Smell Disorders)

Methimazole treatment was performed to ablate the olfactory nerve as described by Bergman et al. (*18*). Mice were injected with methimazole dissolved in 0.9% saline (50 mg/kg of body weight) via intraperitoneal administration on days 0 and 3 from the start of treatment. In vivo, fluorescence imaging was performed on day 8. For this part of the experiment, we used 3 groups of mice, a group treated with methimazole ($n = 3$, 1 nmol in 100 μL of PBS), a normosmic group ($n = 3$, 1 nmol in 100 μL of PBS), and a blocking group ($n = 3$, normosmic mice injected with blocking agent in 100 μL of PBS). After imaging, all mice were euthanized, and organs of interest were dissected. Epifluorescence images were acquired 3 min after injection.

Behavioral Experiment

The buried-food test was performed to prove the sense of smell impairment in olfactory-ablated mice. The buried-food test was performed as previously described (*8*). The supplemental materials provide more details.

Dissection of Olfactory Bulb and Epithelium in Mice

Mouse olfactory bulb and epithelium were dissected to confirm our findings of the in vivo fluorescent experiments. Mice were anesthetized with ketamine and xylazine (100 and 20 μg/g of body weight, respectively) and perfused transcardially with 0.1 M phosphate buffer followed by a phosphate buffer fixative containing 4% paraformaldehyde as described by Lin et al. (*19*). The dissection was divided into 2 components: removal of the brain from the body and removal of the skin and lower jaw. Under ×2 loupe magnification, we removed the hard palate and the bones covering the brain, keeping nasal bones in place. The head was fixed in 4% paraformaldehyde overnight. Tissues were further processed, decalcified, and paraffin-embedded using a standard protocol (*20*).

Nonmouse Animal Experiments

Hamsters. The protocol for hamsters has been described by Zazhytska et al. (*3*). The supplemental materials provide details.

Nonhuman Primates (NHPs). Three NHPs (*Chlorocebus aethiops* [2 male and 1 female]) aged 5–8 y old were acquired from Worldwide Primates Inc. and allowed to acclimate in the vivarium for 3 mo. The animals were intravenously injected (brachial vein) with Tsp1a-IR800$_P$ (200 μg/kg in 5 mL of 0.9% saline) and euthanized after 120 min using an intravenous barbiturate overdose (pentobarbital $\geq$ 150 mg/kg). Tissues of the olfactory epithelium, olfactory bulb, muscle, and frontal lobes of the brain were isolated and resected during necropsy. The tissues were further fixed in 4% paraformaldehyde for 12 h and imaged using the Quest imaging system.

Fluorescence Imaging of NHP Tissues Using Clinically Available Fluorescent Camera

After intravenous injection of Tsp1a-IR800$_P$, the animals were euthanized (using an intravenous barbiturate overdose) and tissues including olfactory epithelium, olfactory bulb, muscles, and brain were harvested. To image those tissues, we used a fluorescent camera that is clinically available (Quest Medical Imaging). The tissues were placed on top of nonreflective black paper to minimize reflection. The camera of the Quest near-infrared (NIR) imaging system was fixated 15 cm above the tissues. We used the same settings that are normally used for a typical imaging procedure (30-ms exposure time, 100% excitation power, and 25.5-dB gain, at 24 frames per second). Analysis and quantifications were performed on the QIFS research tool (Quest Medical Imaging). Regions of interest were drawn on the dissected tissues to determine differences.

Methods Used to Work on Dissected Tissues

Immunohistochemistry and Quantification of Na$_V$1.7 Expression. Na$_V$1.7 staining was performed by the Molecular Cytology Core Facility of the Memorial Sloan Kettering Cancer Center using a Discovery XT processor (Ventana Medical Systems), according to our previously described protocol using anti-Na$_V$1.7 antibody (N68/6; NeuroMab) that binds to both human and mouse Na$_V$1.7 (0.5 μg/mL) (*12*). Na$_V$1.7 quantification was performed on digitalized slides. The supplemental materials provide details.

Hematoxylin and Eosin Staining. We used a standard staining procedure. In short, tissue sections were deparaffinized in xylene and rehydrated through ethanol solutions. Hematoxylin was applied to stain nuclei, and after differentiation, eosin was used to stain cytoplasm. The slides were dehydrated with ascending ethanol concentrations, cleared with xylene, and mounted with a medium. After drying, the slides were examined under a microscope to visualize tissue structure and morphology.

Obtaining Human Cadaveric Specimens

This study, conducted at Columbia University Irving Medical Center, involved 25 patients who had been previously diagnosed with COVID-19 by SARS-CoV-2 reverse transcription polymerase chain reaction analysis and underwent full-body autopsy. The study was approved by the Ethics and Institutional Review Board of Columbia University Medical Center (approvals AAAT0689 and AAAS7370). The supplemental materials provide details.

Statistical Analysis

Statistical analysis of Na$_V$1.7 expression was performed using R version 3.6.3 (R Core Team) and Prism 9 (GraphPad Software). The Student *t* test was used to compare Na$_V$1.7 expression (ratio of Nav1.7 expression to total tissue area) and the fluorescent intensity difference between different groups of mice. A normal distribution of the variables was confirmed using the Shapiro–Wilk test. The Pearson correlation coefficient was used to examine the correlation between the time on the buried-food test and radiant efficiency. Results with a *P* value equal to or lower than 0.05 were considered statistically significant. Data points represent mean values, and error bars represent SD.

RESULTS

Na$_V$1.7 Is Abundantly Expressed in Region of Olfactory Epithelium and Bulb (ROEB) of Normosmic Mice

We isolated and dissected olfactory bulb and epithelium regions from normosmic nude mice and used immunohistochemistry (hematoxylin and eosin and anti-Na$_V$1.7 antibody staining) to identify areas of high Na$_V$1.7 expression. Consistent with previous reports (*9,10*), we found that Na$_V$1.7 is moderately expressed in layers of primary OSNs and highly expressed in olfactory nerve bundles located in the lamina propria, including all the paths toward the olfactory bulb (Figs. 1A and 1B). The olfactory bulbs abundantly express Na$_V$1.7 in peripheral areas, which correspond to the olfactory nerve layer. The glomerular layer, a layer deeper to the olfactory nerve layer, corresponds to terminal synapses of

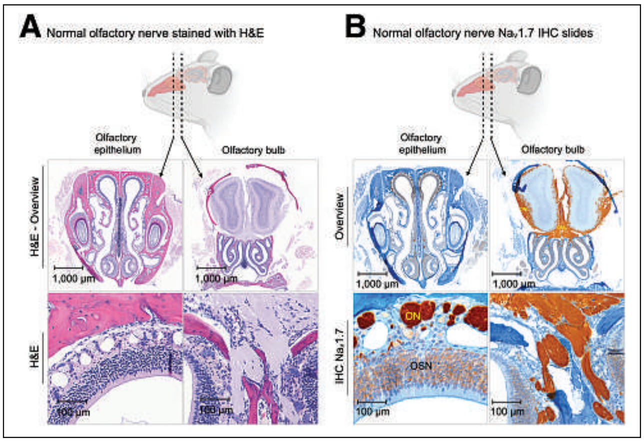

FIGURE 1. Histologic slides of olfactory bulb and olfactory epithelium of normosmic mice. (A) Hematoxylin and eosin staining. (B) Na$_V$1.7 immunohistochemistry. H&E = hematoxylin and eosin; IHC = immunohistochemistry; ON = olfactory nerve bundles; ONL = olfactory nerve layer.

OSN axons, with the dendrites of mitral and tufted cells lightly stained for Na$_V$1.7 (Fig. 1B).

Na$_V$1.7 Expression Is Downregulated in Chemically Induced Anosmia and COVID-19–Infected Mice

Our immunohistochemistry data suggest that the expression of Na$_V$1.7 was significantly diminished after olfactory ablation using methimazole and in SARS-CoV-2–infected mice (Figs. 2A–2E). Of the total tissue area in the olfactory epithelium of normosmic mice, 15.7% (±0.83%) was positive for Na$_V$1.7 expression, compared with 8.5% (±0.94%) in mice that had their olfactory sense ablated by methimazole and 9.7% (±1.2%) in mice infected with SARS-CoV-2 (Fig. 2D, $P \leq 0.01$). The olfactory nerve layer of the olfactory bulb also showed a decrease in Na$_V$1.7 expression in both olfactory-ablated and SARS-CoV-2 infected mice (Fig. 2E). Normosmic mice have a 25.4% (±2.4%) positive Na$_V$1.7 area compared with 11.8% (±1.7%) in ablated and 15.4% (±0.9%) in SARS-CoV-2–infected mice (Fig. 2E).

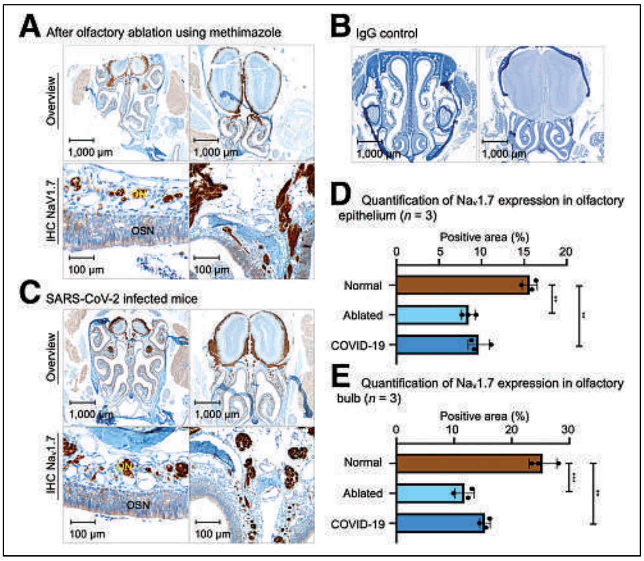

FIGURE 2. Histologic slides of olfactory bulb and olfactory epithelium of mice with olfactory ablation using methimazole and mouse infected with COVID-19. (A) Immunohistochemistry slide of mouse after olfactory ablation. (B) Immunohistochemistry slide of olfactory tissue with IgG isotype primary antibody, as control for possible unspecific binding. (C) Immunohistochemistry slides of mouse with SARS-CoV-2 infection. (D) Quantification of Na$_V$1.7 expression in olfactory epithelium of 3 mouse groups. (E) Quantification of Na$_V$1.7 expression in olfactory bulb of 3 mouse groups. ** $P \leq 0.01$. *** $P \leq 0.001$. IHC = immunohistochemistry; ON = olfactory nerve bundles; ONL = olfactory nerve layer.

RNA Sequencing Reveals Temporal Downregulation of SCN9A Gene Expression in OSN Cells from Hamsters Infected with SARS-CoV-2 and Correlates with Loss and Gain of Olfactory Function

We performed bulk and single-cell RNA sequencing of SARS-CoV-2–infected and mock hamsters' olfactory epithelium tissues at 1, 3, and 10 d after infection. For single-cell RNA sequencing, we analyzed 68,951 cells and identified 13 cell subtypes using previously described markers (*21*). SCN9A was expressed predominantly in OSNs and olfactory glia, with minimal to zero expression in other cell subtypes in the olfactory epithelium. In SARS-CoV-2–infected hamsters, we observed a 3-fold drop in expression of the SCN9A gene transcripts in OSNs at 3 d after infection and full recovery of expression at 10 d after infection with bulk RNA sequencing analysis ($P < 0.001$). These changes in SCN9A transcripts can be followed on Uniform Manifold Approximation and Projection for Dimension Reduction clustering maps that show temporal downregulation of SCN9A. At 3 d after infection, the transcript levels were significantly diminished compared with the control and first day after infection, and at 10 d after infection, they were restored to preinfection levels, as is clearly visible in the figures (Figs. 3A and 3B; Supplemental Fig. 2A).

SARS-CoV-2 Infection Induces Downregulation of SCN9A Gene in Human OSN

To verify whether changes in SCN9A expression in ROEB observed in COVID-19–infected mice and hamsters were also observed in humans, we tested the Na$_V$1.7 expression in the OSNs of cadavers. The region of the cribriform plate, located at the roof of the nasal cavity, in 23 human cadavers—18 COVID-19–infected and 5 controls—was dissected. This region has a high density of mature OSNs and therefore is suitable for the experimental plan. We then performed bulk RNA sequencing of olfactory epithelium tissues from the resected specimens. Cadavers were donated from patients of different sexes (9 male and 14 female), with the median age of patients being 73 y (interquartile range, 65–78 y), representing a variety of infection durations, hospital stays, treatments, and postmortem intervals. We have previously demonstrated that despite different postmortem times for collecting the samples, only a minimal influence on the cellular constitution of tissues and immune cells in the olfactory epithelium of humans could be observed (*3*). Therefore, we extrapolated this for the Na$_V$1.7 expression. SARS-CoV-2 was detected in all positive olfactory epithelium tissues with variations in the viral load (*3*). SCN9A gene expression is 4-fold lower in SARS-CoV-2–infected olfactory epithelium tissue samples than in healthy controls ($P < 0.001$) (Fig. 3C; Supplemental Fig. 2B).

Na$_V$1.7 Expression in ROEB of Healthy Mice Can Be Imaged Using Tsp1a-IR800$_P$

Using a widely available IVIS Spectrum imaging system, we could clearly visualize Na$_V$1.7 expression in mouse ROEB using fluorescence imaging without the need for any surgical intervention.

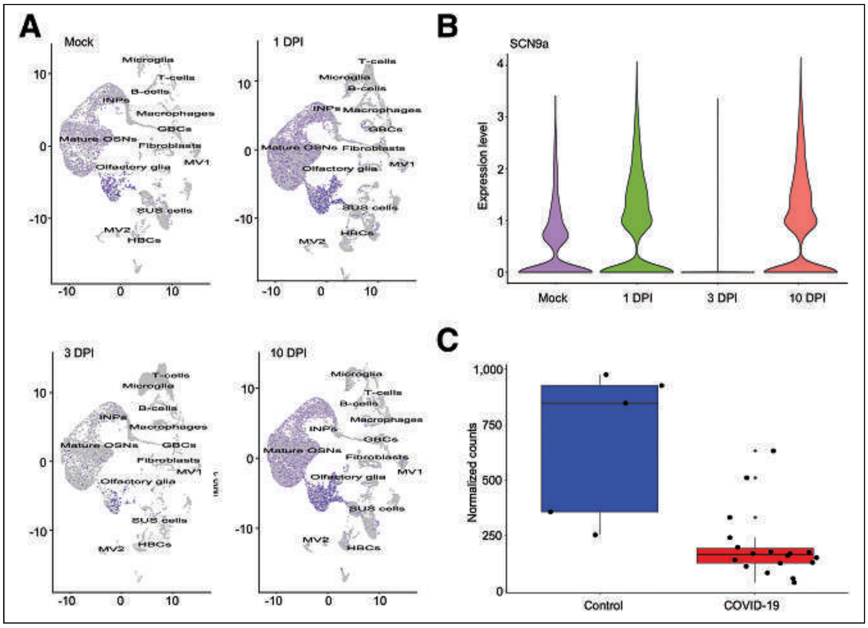

FIGURE 3. SCN9A gene expression in olfactory epithelium of hamsters and humans infected with SARS-CoV-2. (A) Uniform manifold approximation and projection for dimension reduction plots of SCN9A gene expression in different cell types of olfactory epithelium in mock and SARS-CoV-2–infected hamsters at 1, 3, and 10 d after infection. (B) Violin plots of SCN9A gene expression in olfactory epithelium bulk tissues in mock and SARS-CoV-2–infected hamsters at 1, 3, 10 d after infection. (C) SCN9A gene expression in human olfactory epithelium tissues in control and SARS-CoV-2–infected cadavers. DPI = days after infection; GBC = glucose basal cells; HBC = horizontal basal cells; INP = immediate neuronal precursors; MV2 = microvillus cells 2; OSN = olfactory sensory neurons; SUS = sustentacular cells.

Excitation was set to 745 nm, and emission was set to 800, 820, and 840 nm. We designed our probe to have these features because there is minimal background at these wavelengths, thus providing a highly specific signal. Because of the superficial expression of $Na_V1.7$ in the mouse ROEB, we were able to obtain images of the mice without the need to expose the olfactory epithelium. Epifluorescence in vivo images in mice receiving intravenous injection with the imaging agent Tsp1a-$IR800_P$ generated high contrast between the ROEB and its surrounding regions. The radiant efficiency was significantly less in both mice injected with PBS and mice injected with the unmodified peptide (blocking agent) in combination with the imaging agent (Figs. 4A and 4B). We observed a 150-fold ($[5.9 \pm 3.4] \times 10^8$ vs. $[3.9 \pm 1.9] \times 10^6$ $[\text{p/s/cm}^2\text{/sr}]/[\mu\text{W/cm}^2]$, $P < 0.0001$) increase in radiant efficiency compared with mice injected with PBS. To demonstrate specificity, we coadministered our imaging probe with a non–fluorophore-labeled Tsp1a and observed a 61-fold decrease in signal emanating from the mouse olfactory epithelium.

Tsp1a-$IR800_P$ Can Differentiate Healthy from Anosmic Mice Through Its Fluorescence Emission

The group of mice that were treated with methimazole, widely known to cause damage to the olfactory nerves of those animals, had an 8-fold decrease in radiant efficiency signal compared with normosmic control mice when imaged with Tsp1a-$IR800_P$ (Figs. 4C and 4D). The average radiant efficiency of the olfactory region of normosmic mice imaged from both sides was $(4.08 \pm 2.11) \times 10^9$, compared with $(5.33 \pm 2.08) \times 10^8$ for mice with an olfactory ablation (unpaired t test, $P = 0.045$). Ex vivo images showed a similar statistically significant difference between mouse groups in the ROEB. The heart and kidneys were the only internal organs with higher fluorescence signals than in normosmic mice and mice treated with a blocking agent.

Tsp1a-$IR800_P$ Shows Fluorescence Signals in OSN

For further confirmation, we resected the olfactory epithelium region of these mice and obtained regular tabletop fluorescent microscopy images of sectioned tissue (Fig. 5). The fluorescent microscopy images confirmed the results of in vivo epifluorescence imaging and immunohistochemistry. OSN and olfactory nerve bundles located in the lamina propria showed the most intense fluorescence. Normosmic mice and mice treated with a blocking agent were negative for any signal (red staining), whereas only nucleus-associated blue staining was visible corresponding to nuclear staining by Hoechst dye.

Time to Completion of Buried-Food Test Correlates with ROEB Fluorescence Emissions

Normosmic mice were able to find buried food in less than 30 s (mean, 17 ± 5.2 s), compared with a mean time of 117 s (±44 s) for olfactory-ablated mice, showing that mice with olfactory ablation needed a significantly longer time ($P < 0.001$) than normosmic mice to find the buried food (Figs. 6A and 6B). Furthermore, there was an inverse correlation between the Tsp1a-$IR800_P$ radiant efficiency and the time required to find buried food ($r = –0.79$, $n = 10$, $P = 0.006$; Fig. 6C).

$Na_V1.7$ Expression in Olfactory Epithelium of NHPs Can Be Detected Using Tsp1a-$IR800_P$ and Clinically Approved NIR Camera

To validate the clinical potential of our approach of using $Na_V1.7$ expression as a surrogate marker for the sense of smell, we imaged NHP specimens using a clinically applied Food and Drug Administration–approved commercial Quest NIR system. The bright fluorescence was clearly visible over the olfactory epithelium, and weak or no fluorescence was detected over the muscle, olfactory bulb, and brain. The fluorescence intensity of olfactory epithelium was significantly higher ($P < 0.001$) than that of any other measured tissue (Figs. 7A and 7B).

Confocal Microscopy of NHP Tissues Corroborates Results from Clinically Approved NIR Device

To confirm our macroscopic results, we also performed fluorescence microscopy on the dissected NHP tissues (Fig. 7C). The fluorescence signal from the NHP olfactory epithelium was clearly brighter than that from other tissues. It is important to stress that the olfactory bulb expresses $Na_V1.7$ but that the blood–brain barrier prevents entry of our imaging agent in the current setting. For the current application, this significant advantage reduces the potential background signal from the olfactory bulb, which could be immediately applicable to the clinical setting (Fig. 7D).

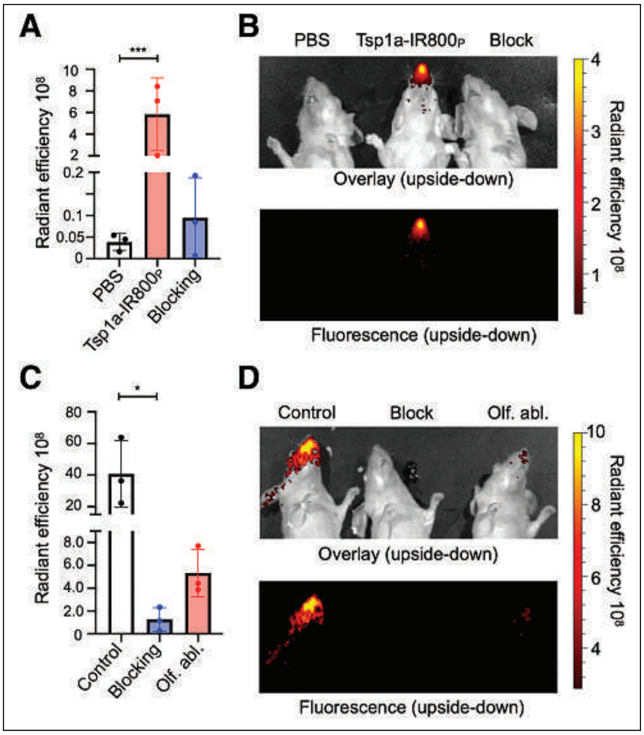

FIGURE 4. Tsp1a-IR800$_P$ accumulation in ROEB in normosmic mice and mice with olfactory ablation. (A and B) Fluorescence quantification and epifluorescence images of animals injected with PBS, Tsp1a-IR800$_P$, and Tsp1a-IR800$_P$/Tsp1a blocking formulation. (C and D) Epifluorescence images and fluorescence intensity quantification of normosmic animals injected with Tsp1a-IR800$_P$ (control) and Tsp1a-IR800$_P$/Tsp1a (blocking) and mice with prior olfactory ablation using methimazole injected with Tsp1a-IR800$_P$. All images were taken 30 min after tail vein injection. $^{*}P \leq 0.05$. $^{***}P \leq 0.001$. Olf. abl. = olfactory ablation.

DISCUSSION

We describe the development of a novel semiquantitative diagnostic method based on selective targeting of Na$_V$1.7 expression in olfactory epithelium for the detection of smell disorders induced by different insults and inflammatory conditions such as COVID-19. The fluorescence signal emanating from mouse olfactory epithelium shows decreased intensity when mice have anosmia. We observed an inverse linear relationship between signal intensity and the degree of damage. Therefore, we believe that the described method has the potential to serve as an objective guide for assessing disease progression and treatment response both in animal and in human subjects and to aid drug development. We hypothesize that the absence of fluorescence may indicate a low probability of recovery of the smell and that fluorescence intensity restoration may be an early indicator of treatment response, preceding perceptible or clinical smell restoration. This is a significant development because the current tests are subjective by design and methods are culturally specific and individually subjective (*22*). In addition, current methods rely on invasive biopsy, which may deter patients and limit the number of times testing can be performed. Our method is noninvasive, can be performed repeatedly on animal subjects, and therefore has the potential to detect the posttreatment restoration process before improvement in the sense of smell can be noticed (*23*).

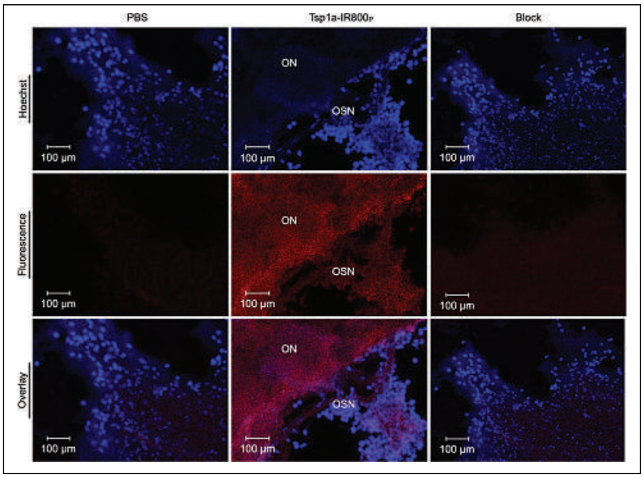

FIGURE 5. Fluorescent confocal microscopy images of olfactory epithelium of animals injected with PBS, Tsp1a-IR800$_P$, and Tsp1a-IR800$_P$/Tsp1a-Pra0 blocking formulation. Blue fluorescence indicates nucleus of cells, and red fluorescence indicates infrared fluorescence coming from Na$_V$1.7 of olfactory nerve bundles. ON = olfactory nerve (bundles).

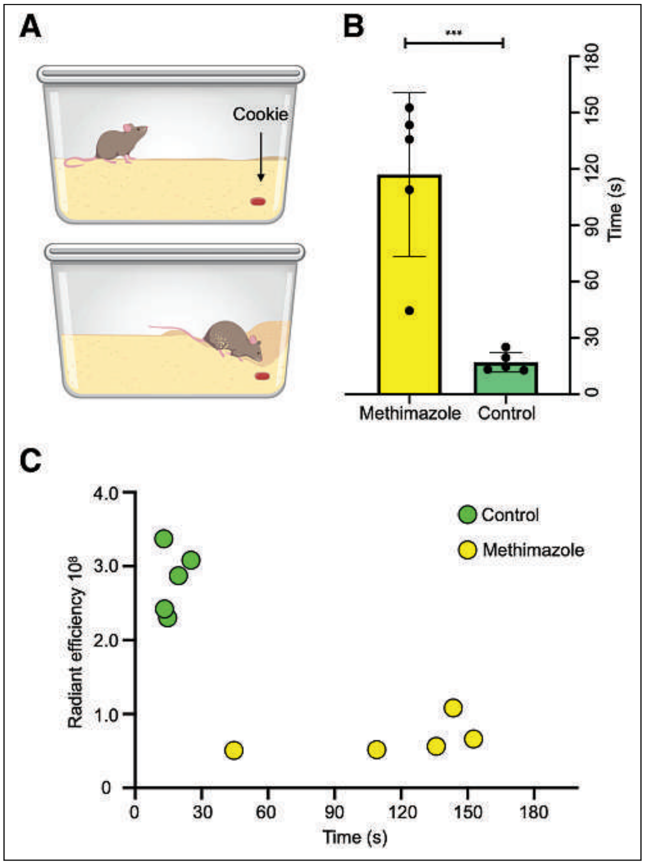

FIGURE 6. Buried-food test. (A) Schematic of experimental design illustrating mouse cage with cookie buried in upper right corner. (B) Average time (seconds) spent per mouse treated with PBS ($n = 5$) or methimazole ($n = 5$) to find buried food. Graph indicates that healthy mice found buried food much more quickly than ones treated with methimazole ($P < 0.001$), suggesting presence of olfactory dysfunction in the latter. (C) Correlation of Tsp1a-IR800$_P$ radiant efficiency at ROEB and time on buried-food test demonstrating that the more quickly mice find buried food, the brighter is fluorescence detected from olfactory nerve region.

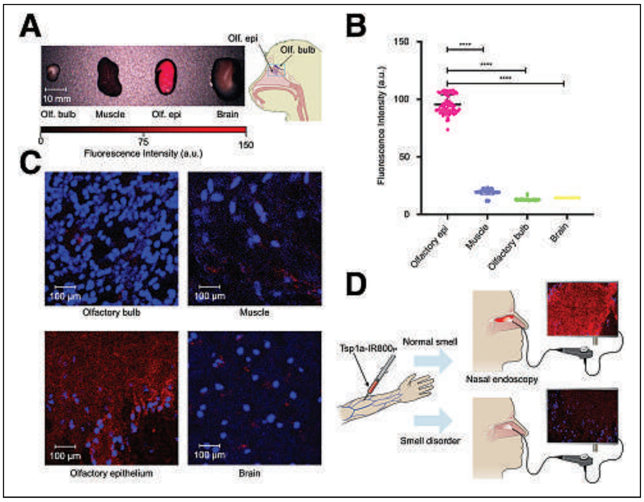

FIGURE 7. Imaging olfactory epithelium of NHPs. (A) Images were taken using Quest system (approved for clinical use) of olfactory bulb, muscle, olfactory epithelium, and brain of 4 NHPs, after intravenous injection of $\text{Tsp1a-IR800}_\text{P}$. (B) Quantification of near-fluorescence intensity demonstrates that signal from olfactory epithelium is significantly higher than that from surrounding tissues. (C) Fluorescent confocal microscopy images of olfactory bulb, muscle, olfactory epithelium, and brain tissues of same NHPs. (D) Schematic depiction of potential use of $\text{Tsp1a-IR800}_\text{P}$ in physician's office setting using Quest or other vendor NIR fluorescence imaging systems. $^{****}P \leq 0.0001$. a.u. = arbitrary units; olf. bulb = olfactory bulb; olf. epi = olfactory epithelium.

We have found that smell loss due to chronic inflammation in the nasal cavity or viral infection is accompanied by diminished expression of $\text{Na}_\text{V}1.7$ in OSNs. We observed loss of $\text{Na}_\text{V}1.7$ expression after olfactory ablation using methimazole (Fig. 2). Expression of $\text{Na}_\text{V}1.7$ was substantially reduced in OSNs and in nerve bundles located in the lamina propria, whereas expression was less affected at the level of the olfactory bulbs. This probably happens because of the location of the olfactory bulbs—much deeper in the tissues and protected by the blood–brain barrier and cribriform plate.

Further, we assessed whether COVID-19–related olfaction loss is also accompanied by loss of $\text{Na}_\text{V}1.7$. COVID-19–related smell disorders are possibly caused by multiple mechanisms. There is a direct tropism of the virus to sustentacular and microvillar cells covering OSNs; inflammatory damage to OSNs, as they are exposed to environmental factors; and inflammation involving focal mucosal swelling and obstruction to airways (*24*). Recently, our collaborators (Lomvardas Lab at Columbia University) reported that the downregulation in odor detection pathways could be a potential cause of COVID-19–induced anosmia (*3*). We found that these mechanisms cause diminished $\text{Na}_\text{V}1.7$ expression in OSNs and olfactory nerve bundles located in the nasal cavity as shown by immunohistochemistry and RNA sequencing on tissues from mice, hamsters, and humans.

Our compound $\text{Tsp1a-IR800}_\text{P}$ selectively binds to $\text{Na}_\text{V}1.7$, making it an ideal candidate for measuring smell perception using fluorescent measurement techniques. We tested our imaging agent using a mouse model in which olfactory ablation via methimazole injections (*25*) led to reduced fluorescence in mouse nasal epithelium. This damage follows a sensorineural smell loss pattern similar to that seen in upper-respiratory viral infection or chronic inflammation due to seasonal allergies (*16,26*). Furthermore, we demonstrated that the radiant efficiency of the $\text{Na}_\text{V}1.7$ imaging agent correlated inversely with the time that mice spent finding food in a buried-food test. These studies indicate that $\text{Tsp1a-IR800}_\text{P}$ uptake inversely correlates with loss of $\text{Na}_\text{V}1.7$ expression and therefore with loss of the sense of smell.

The difference between rodents and humans can be substantial, and to validate the possibility that olfaction can be imaged in humans, we tested our compound on healthy NHPs and measured fluorescence using a clinically approved NIR imaging system. We observed bright fluorescence from the olfactory epithelium, and the fluorescence measurements were significantly higher than in surrounding tissues.

It is crucial to develop a noninvasive, fast, and objective method to diagnose smell disorders. Intravenously injected $\text{Tsp1a-IR800}_\text{P}$ selectively accumulates in OSNs and olfactory nerve bundles located in the nasal cavity. For the experiment, we used a clinically applied camera that can detect infrared wavelength fluorescence using a rigid endoscope. Existing flexible endoscopes from several medical technology companies (Quest, Stryker, Olympus, etc.) can detect the infrared wavelength emitted by $\text{Tsp1a-IR800}_\text{P}$ (Fig. 7D). Because of the minimally invasive nature of the nasal cavity endoscope, and the correlation of fluorescence with the magnitude of smell loss, the method can be used as a treatment-monitoring tool and in drug development. In addition, the method can be widely used in an experimental setting to objectively measure smell in animals, replacing the need to perform behavioral experiments and streamlining the development of new therapeutics. An obvious limitation of the technique is that if loss of olfaction is a result of olfactory receptor or olfactory bulb dysfunction, the applicability of our imaging technique might be limited, though further studies are needed on the influence of such dysfunction on $\text{Na}_\text{V}1.7$ expression in OSNs.

CONCLUSION

The described method of applying the novel fluorescent probe $\text{Tsp1a-IR800}_\text{P}$ could help significantly improve preclinical and clinical studies by providing an objective way to diagnose smell disorders and aid in the development of therapeutic interventions.

DISCLOSURE

This work was supported by National Institutes of Health grants R01 EB029769 (Nagavarakishore Pillarsetty and Glenn King), R01 CA204441 (Thomas Reiner), K99 GM145587 (Junior Gonzales), and R01 CA204441-03S1 (Junior Gonzales); the Australian National Health and Medical Research Council (principal research fellowship APP1136889 to Glenn King); and the Australia Research Council (Centre of Excellence grant CE200100012 to Glenn King). Support is acknowledged from Mr. William H. Goodwin and Mrs. Alice Goodwin and the Commonwealth Foundation for Cancer Research and the Center for Experimental Therapeutics of Memorial Sloan Kettering Cancer Center. The funding sources were not involved in study design, data collection and analysis, writing of the report, or the decision to submit this article for publication. Funding from Memorial Sloan Kettering Cancer Center grant P30 CA008748 for core facility support is also acknowledged. Snehal Patel and Thomas Reiner are shareholders of Summit Biomedical Imaging. Thomas Reiner is now an employee of Evergreen Theragnostics. Junior Gonzales, Paula Demetrio de Souza Franca, Glenn King, and Thomas Reiner are coinventors on a Tsp1a-related patent

application. No other potential conflict of interest relevant to this article was reported.

ACKNOWLEDGMENTS

We thank the Memorial Sloan Kettering Cancer Center Animal Imaging Core Facility and Molecular Cytology Core Facility for its support. We especially thank Eric Chan for help with the Image J plugins for Na$_V$1.7 quantifications. We also thank Terry Helms for creating illustrations, and we thank the members of the Pillarsetty Lab for helpful discussions.

KEY POINTS

QUESTION: Is it possible to image the olfactory nerve and diagnose smell disorders by a molecularly targeted (Na$_V$1.7) fluorescent agent?

PERTINENT FINDINGS: In this animal study, we have shown that several causal factors of smell disorders, such as chronic inflammation, allergy, and viral infection including COVID-19, result in substantially diminished expression of Na$_V$1.7 at the transcript and protein levels. We have shown that a new fluorescently labeled agent, Tsp1a-IR800$_P$, molecularly targets Na$_V$1.7 and can be used to semiquantitatively measure olfaction and diagnose smell disorders in animals and humans.

IMPLICATIONS FOR PATIENT CARE: To study smell and smell disorders, there will be no need for behavioral experiments on animals. Furthermore, smell disorders such as anosmia in humans potentially can be diagnosed in a physician's office setting using our agent and endoscope.

REFERENCES

1. Asahina K, Pavlenkovich V, Vosshall LB. The survival advantage of olfaction in a competitive environment. *Curr Biol.* 2008;18:1153–1155.
2. Nalbandian A, Sehgal K, Gupta A, et al. Post-acute COVID-19 syndrome. *Nat Med.* 2021;27:601–615.
3. Zazhytska M, Kodra A, Hoagland DA, et al. Non-cell-autonomous disruption of nuclear architecture as a potential cause of COVID-19-induced anosmia. *Cell.* 2022;185:1052–1064.e12.
4. Hoffman HJ, Rawal S, Li CM, Duffy VB. New chemosensory component in the US National Health and Nutrition Examination Survey (NHANES): first-year results for measured olfactory dysfunction. *Rev Endocr Metab Disord.* 2016;17:221–240.
5. Burges Watson DL, Campbell M, Hopkins C, Smith B, Kelly C, Deary V. Altered smell and taste: anosmia, parosmia and the impact of long Covid-19. *PLoS One.* 2021;16:e0256998.
6. Mendes Paranhos AC, Nazareth Dias AR, Machado da Silva LC, et al. Sociodemographic characteristics and comorbidities of patients with long COVID and persistent olfactory dysfunction. *JAMA Netw Open.* 2022;5:e2230637.
7. Boscolo-Rizzo P, Tirelli G, Meloni P, et al. Coronavirus disease 2019 (COVID-19)-related smell and taste impairment with widespread diffusion of severe acute respiratory syndrome-coronavirus-2 (SARS-CoV-2) omicron variant. *Int Forum Allergy Rhinol.* 2022;12:1273–1281.
8. Yang M, Crawley JN. Simple behavioral assessment of mouse olfaction. *Curr Protoc Neurosci.* 2009;48:8.24.1–8.24.12.
9. Rupasinghe DB, Knapp O, Blomster LV, et al. Localization of Nav1.7 in the normal and injured rodent olfactory system indicates a critical role in olfaction, pheromone sensing and immune function. *Channels.* 2012;6:103–110.
10. Weiss J, Pyrski M, Jacobi E, et al. Loss-of-function mutations in sodium channel Na$_v$1.7 cause anosmia. *Nature.* 2011;472:186–190.
11. Jiang Y, Castro J, Blomster LV, et al. Pharmacological inhibition of the voltage-gated sodium channel Na$_V$1.7 alleviates chronic visceral pain in a rodent model of irritable bowel syndrome. *ACS Pharmacol Transl Sci.* 2021;4:1362–1378.
12. Gonzales J, Franca PDD, Jiang Y, et al. Fluorescence imaging of peripheral nerves by a Na$_v$1.7-targeted inhibitor cystine knot peptide. *Bioconjug Chem.* 2019;30:2879–2888.
13. Gonzales J, Adilbay D. Franca PDdS, et al. NaV1.7 targeted fluorescence imaging agents for nerve identification during intraoperative procedures. bioRxiv website. https://www.biorxiv.org/content/10.1101/2024.04.06.588368v1. Published April 6, 2024. Accessed June 4, 2024.
14. Gonzales J, Hernández-Gil J, Wilson TC, et al. Bimodal imaging of mouse peripheral nerves with chlorin tracers. *Mol Pharm.* 2021;18:940–951.
15. Hernández-Gil J, Chow CY, Chatras H, et al. Development and validation of nerve-targeted bacteriochlorin sensors. *J Am Chem Soc.* 2023;145:14276–14287.
16. Håglin S, Bohm S, Berghard A. Single or repeated ablation of mouse olfactory epithelium by methimazole. *Bio Protoc.* 2021;11:e3983.
17. Ordonez AA, Bullen CK, Villabona-Rueda AF, et al. Sulforaphane exhibits antiviral activity against pandemic SARS-CoV-2 and seasonal HCoV-OC43 coronaviruses in vitro and in mice. *Commun Biol.* 2022;5:242.
18. Bergman U, Ostergren A, Gustafson AL, Brittebo EB. Differential effects of olfactory toxicants on olfactory regeneration. *Arch Toxicol.* 2002;76:104–112.
19. Lin W, Ogura T, Margolskee RF, Finger TE, Restrepo D. TRPM5-expressing solitary chemosensory cells respond to odorous irritants. *J Neurophysiol.* 2008;99:1451–1460.
20. Alaeddini M, Bashizadehfakhar H, Amirinia F, et al. The effect of different combinations of fixatives and decalcifying agents on rat and rabbit hard tissues, a guide for histologic processing. *Acta Histochem.* 2022;124:151962.
21. Durante MA, Kurtenbach S, Sargi ZB, et al. Single-cell analysis of olfactory neurogenesis and differentiation in adult humans. *Nat Neurosci.* 2020;23:323–326.
22. Hummel T, Whitcroft KL, Andrews P, et al. Position paper on olfactory dysfunction. *Rhinology.* 2016;56:1–30.
23. Mainland JD, Barlow LA, Munger SD, et al. Identifying treatments for taste and smell disorders: gaps and opportunities. *Chem Senses.* 2020;45:493–502.
24. Mastrangelo A, Bonato M, Cinque P. Smell and taste disorders in COVID-19: from pathogenesis to clinical features and outcomes. *Neurosci Lett.* 2021;748:135694.
25. Bergström U, Giovanetti A, Piras E, Brittebo EB. Methimazole-induced damage in the olfactory mucosa: effects on ultrastructure and glutathione levels. *Toxicol Pathol.* 2003;31:379–387.
26. Jung AY, Kim YH. Reversal of olfactory disturbance in allergic rhinitis related to OMP suppression by intranasal budesonide treatment. *Allergy Asthma Immunol Res.* 2020;12:110–124.

*h*HEPATO-Cy5, a Bimodal Tracer for Image-Guided Hepatobiliary Surgery

Daphne D.D. Rietbergen*[1,2], Tessa Buckle*[1], Leon J. Slof[1], Maarten P. van Meerbeek[1], Clarize M. de Korne[1,3], Mick M. Welling[1], Matthias N. van Oosterom[1], Kevin Bauwens[4], Meta Roestenberg[3], Julia Kloetzl[5], and Fijs W.B. van Leeuwen[1]

[1]Interventional Molecular Imaging Laboratory, Leiden University Medical Center, Leiden, The Netherlands; [2]Section of Nuclear Medicine, Department of Radiology, Leiden University Medical Center, Leiden, The Netherlands; [3]Department of Parasitology, Leiden University Medical Center, Leiden, The Netherlands; [4]Orsi Academy, Melle, Belgium; and [5]Karl Storz SE & Co. KG, Tuttlingen, Germany

Liver cancer is a leading cause of cancer deaths worldwide. Surgical resection of superficial hepatic lesions is increasingly guided by the disrupted bile excretion of the fluorescent dye indocyanine green (ICG). To extend this approach to deeper lesions, a dedicated bimodal tracer that facilitates both fluorescence guidance and radioguidance was developed. **Methods:** A tracer comprising a methylated cyanine-5 (Cy5) fluorescent dye and a mercaptoacetyltriserine chelate (*h*HEPATO-Cy5) was synthesized and characterized. Cellular uptake and excretion were evaluated in hepatocyte cultures (2-dimensional culture and in vitro lesion model), using a fluorescent bile salt, MitoTracker dye, and methylated Cy5 as a control. After radiolabeling, the pharmacokinetics of ^{99m}Tc-*h*HEPATO-Cy5 were assessed in mice over 24 h (percentage injected dose and percentage injected dose per gram of tissue, SPECT/CT imaging and fluorescence imaging). The ability to provide real-time fluorescence guidance during robot-assisted hepatobiliary surgery was evaluated in a porcine model using ICG as a reference. **Results:** The unique molecular signature of *h*HEPATO-Cy5 promotes hepatobiliary excretion. In vitro studies on hepatocytes showed that where methylated Cy5 remained internalized, *h*HEPATO-Cy5 showed fast clearance (10 min) similar to that of fluorescent bile salt. In vivo use of ^{99m}Tc-*h*HEPATO-Cy5 in mice revealed liver accumulation and rapid biliary clearance. The effectiveness of bile clearance was best exemplified by the 2-orders-of-magnitude reduction in count rate for the gallbladder ($P = 0.008$) over time. During hepatobiliary surgery in a porcine model, *h*HEPATO-Cy5 enabled fluorescence-based lesion identification comparable to that of ICG. **Conclusion:** The bimodal ^{99m}Tc-*h*HEPATO-Cy5 provides an effective means to identify liver lesions. Uniquely, it helps overcome the shortcomings of fluorescence-only approaches by allowing for an extension to in-depth radioguidance.

Key Words: image-guided surgery; fluorescence imaging; hepatobiliary surgery; bimodal tracer; minimally invasive surgery

J Nucl Med 2024; 65:1301–1306
DOI: 10.2967/jnumed.123.266715

Annually, liver cancer accounts for an estimated 748,300 new cases and 695,900 cancer deaths worldwide. Next to primary liver cancer (e.g., hepatocellular carcinoma), tumorous lesions in the liver are often metastases of cancer with a different origin, such as colorectal cancer, neuroendocrine tumors, ocular melanoma, and breast cancer (*1–5*).

For both primary and metastatic liver cancer, surgical resection is considered essential to ensure long-term survival and to achieve a potential cure. The improvement in diagnostic imaging, the effectiveness of neoadjuvant systemic therapies, and the development of local treatment strategies has led to a 20%–30% increase in patients who are considered eligible for de novo surgery or surgery after neoadjuvant treatment (*6*). The success of these surgeries depends on the ability to achieve radical resection with preservation of normal liver tissue function (*7*). The high chance of hepatic recurrence (≤29% (*8*)) and complications (60% of cases (*9*)) indicates that substantial improvements can still be made in this line of therapy.

Accurate preoperative lesion identification, procedural planning, and intraoperative image guidance are of vital importance for precision surgery. Whereas preoperative lesion identification generally occurs via MRI, CT, or ^{18}F-FDG PET (*8*), intraoperative identification often relies on the limited sensitivity and resolution of palpation, optical inspection, and intraoperative ultrasound (*7,9*). With the shift from open surgery to minimally invasive laparoscopic and robotic surgery (*10*), the reliance on image guidance technologies has increased. Especially, the use of fluorescence guidance is gaining ground. In 2009, Ishizawa et al. started to exploit the pharmacologic clearance profile of the fluorescent dye indocyanine green (ICG) to identify hepatic lesions with a high spatial resolution (*11*). Since then, this image guidance approach has been widely adopted, resulting in lower complications (odds ratio, 0.523) and shorter hospital stays (weighted mean difference, −1.8 (*12*)). A downside of the ICG-guided approach is that lesions located more than 5 mm below the surface cannot be reliably identified (*9*). Conversely, the use of separate techniques for pre- and intraoperative imaging can cause misalignment between the two (*13*). This problem not only limits planning and logistics but may also result in excision of additional (i.e., false-positive) tissue. Ideally, nuclear medicine diagnostics and intraoperative fluorescence guidance are integrated. In nuclear medicine, there are several radiotracers available that can be used to assess liver function (e.g., iminodiacetic acid (*14*) and ^{99m}Tc-mebrofenin (*15*)). However, to support approaches that combine noninvasive nuclear and intraoperative fluorescence imaging, there is a need

---

Received Sep. 25, 2023; revision accepted May 28, 2024.

For correspondence or reprints, contact Fijs W.B. van Leeuwen (f.w.b.van_leeuwen@lumc.nl).

*Contributed equally to this work.

for new bimodal or hybrid biliary tracers that contain both a radiolabel and a fluorescent label. Such a combined approach has already demonstrated clinical value in another surgical indication, that is, sentinel node resection (*13*).

Although the exact mechanism of ICG accumulation in liver lesions remains unclear, the fluorescence signal has been shown to accumulate at the transition between healthy and diseased tissue (*9*). In particular, disruptions in biliary clearance of the tracer are thought to play an important role in the localization of fluorescence in diseased tissues (*16*). With this feature in mind, we designed a small-molecule hybrid tracer to support bimodal imaging of liver lesions. After tracer synthesis, uptake and excretion were evaluated in vitro in hepatocytes, and in vivo tracer pharmacokinetics were assessed in mice. The surgical utility of the tracer was assessed during robot-assisted fluorescence-based hepatobiliary surgery in a porcine model.

MATERIALS AND METHODS

Synthesis and Chemical Evaluation of Hybrid Tracer h*HEPATO-Cy5*

Mercaptoacetyltriserine (mas$_3$), *N*-Boc-aminophenol-Merrifield resin, and methyl-cyanine-5 (Cy5)-NH$_2$ (also used as a Cy5 control) were synthesized according to previously described procedures (*17,18*). Methyl-Cy5-mas$_3$ (*h*HEPATO-Cy5) (Fig. 1; Supplemental Figs. 1–4; supplemental materials are available at http://jnm.snmjournals.org) was synthesized as follows: mas$_3$ (27 mg, 68 μmol), hexafluorophosphate azabenzotriazole tetramethyl uronium (26 mg, 68 μmol), and *N*-methylmorpholine (34 mg, 340 μmol) were dissolved in dimethyl sulfoxide (2 mL). Methyl-Cy5-amineC4 (30 mg, 68 μmol) was added, and the reaction mixture was stirred at room temperature for 25 min. A mixture of H$_2$O/MeCN (85%/15%, 8 mL) with 0.1% trifluoroacetic acid was then added, and the crude product was purified through preparative high-performance liquid chromatography. Lyophilization yielded the product as a vibrant blue solid (30 mg, 54% yield). Compound characterization, including nuclear magnetic resonance (Supplemental Figs. 1–2), proton MR spectroscopy (Supplemental Fig. 3), high-performance liquid chromatography (Supplemental Fig. 4), absorption and emission (Supplemental Fig. 5), and brightness and serum protein binding, was performed as previously described (*17*).

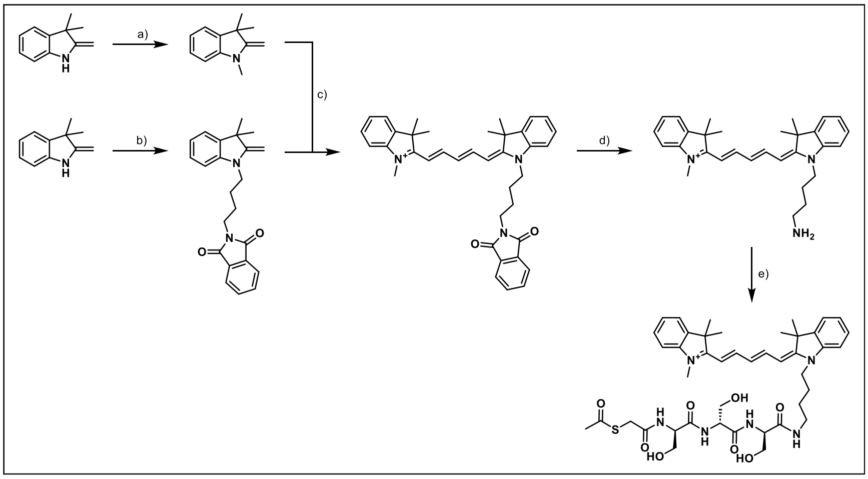

FIGURE 1. Reaction scheme for synthesis of *h*HEPATO-Cy5: (a) methyl iodide, K$_2$CO$_3$, dimethylformamide; (b) *N*-(4-bromobutyl)phthalimide, sulfolane; (c) first, malonaldehyde dianilide HCl, 1:1 Ac$_2$O:AcOH, followed by indole-amineC4Phth, 3:1 pyridine:Ac$_2$O; (d) 33 wt % MeNH$_2$ in EtOH; (e) L-mas$_3$, hexafluorophosphate azabenzotriazole tetramethyl uronium, *N,N*-diisopropylethylamine.

In Vitro Tracer Metabolism in Hepatocytes

HC04 hepatocyte (*19*) and GEB3 epithelial control (*20*) cells were cultured in Gibco minimum essential medium enriched with 10% fetal bovine serum and penicillin/streptomycin (all Life Technologies Inc.). Three days before fluorescence confocal imaging, cells were seeded onto glass-bottom culture dishes (MatTek Corp.). An in vitro model for hepatic lesions was created by placing a heated metal rod in the center of the culture dish for 1–2 s, 1 h before imaging.

Samples were stained with 1 μM *h*HEPATO-Cy5 or 100 nM Cy5 control for 10 or 30 min at 37°C (6 samples per tracer and condition). Staining with 1 μM of the bile salt cholyl-Lys-fluorescein (*21*) or MitoTracker green (2 μL/mL M7514; Thermo Fisher) was used to confirm the staining pattern of *h*HEPATO-Cy5. Hoechst stain (33342, 1 mg/mL; Thermo Fisher) was added to all samples as a nuclear reference. Before imaging, samples were washed 3 times with phosphate-buffered saline.

Fluorescence confocal microscopy was performed as previously described using a Leica SP8 WL at sequential settings (*22*). Images were analyzed using the accompanying confocal software (LAS X; Leica Microsystems). Color selection was matched to the emission profile of the dye (Hoechst stain, 420–270 nm in blue; cholyl-Lys-fluorescein and MitoTracker, 500–550 nm in green; Cy5, 650–700 nm in red), using the color options in the LAS X software. For visualization of in vitro lesions, a tile scan consisting of a 5 × 5 grid at ×20 magnification was made. Semiquantitative image analysis and 3-dimensional surface plotting were performed using Fiji software as previously described (*23*).

Frozen excised tissue samples that contained a liver lesion were cut into 5-μm sections and imaged without further pretreatment. Additional sections were cut for standard hematoxylin and eosin staining, which was performed as previously described (*24*) and served as a reference for tissue morphology.

Animal Experiments

All rodent experiments were granted a license by the competent authority after receiving approval from the Animal Experiments Committee Leiden (AVD1160020173304). Experiments on pigs were approved by the ethical board of the University of Ghent (EC2019/79). Experiments were performed in an establishment licensed for the use of experimental animals (Leiden University Medical Center or Orsi Academy). Experiments were performed in accordance with the Experiments on Animals Act (2014), which is the applicable legislation in The Netherlands and Belgium, in accordance with the European guidelines (European Union directive 2010/63/EU) regarding the protection of animals used for scientific purposes.

Pigs were housed at the animal facility at Orsi Academy until used for imaging experiments during surgical training (weight per animal, ∼40 kg). Pigs were reused after surgical training and remained under anesthesia until being euthanized when the examination was completed.

In Vivo Tracer Biodistribution in Mice

Radiolabeling of *h*HEPATO-Cy5 resulted in ^{99m}Tc-*h*HEPATO-Cy5 (high-performance liquid chromatograms are shown in Supplemental Fig. 4), and in vivo SPECT imaging (at 1, 2, 4, and 24 h) was performed according to previously described procedures (*17*). Reconstructions were visualized and analyzed with a custom MATLAB script (The MathWorks Inc.) that included correction for radioactive decay at the respective time point. Maximum-intensity projections with batlow color maps (*25*) were chosen, using identical color scaling at all time points for ease of comparison. Using the 2-dimensional scintigrams, we drew regions of interest over the gallbladder and liver for semiquantitative comparison of tracer uptake at every time point (decay-corrected). To reference the amount of radioactivity in these regions of interest, 1 MBq ^{99m}Tc point sources were imaged and analyzed under identical settings.

For quantitative assessment of the biodistribution of (hot) ^{99m}Tc-*h*HEPATO-Cy5, 10 MBq (0.5 nmol in 0.1 mL) of the labeled tracer were intravenously administered into female Swiss OF1 mice (6–7 wk old; Charles River). The percentage injected dose (%ID) and %ID per gram of tissue (%ID/g) were assessed at 2 and 24 h after intravenous tracer administration, as previously described (n = 9 (*20,26*)).

Semiquantitative assessment of fluorescence in the liver or gallbladder and intestines was assessed before γ-counting, to exemplify the effective hepatobiliary clearance and to complement the quantitative biodistribution, using an IVIS Spectrum preclinical imaging system (Perkin Elmer) and Living Image software (version 3.2 (*26*)). Images were acquired after excitation at 640 nm, and light was collected at more than 680 nm (acquisition time, 5 s). The fluorescent content was measured in photons/s/cm^2. Because of the limited choice in color mapping in the commercial IVIS software, a hot color map was selected.

In Vivo Pharmacokinetic Assessments in Porcine Model: Surgical Fluorescence Imaging

Since porcine models do not naturally yield liver metastases, superficial heat-induced necrotic lesions were created using bipolar robotic instruments (da Vinci Maryland or fenestrated forceps [Intuitive Surgical]). These lesions served as a model for lesions that disrupt the hepatic anatomy.

A 3.75-mg quantity of *h*HEPATO-Cy5 was dissolved in 150 μL of ethanol, after which 1,350 μL of polysorbate 80 and saline were added to achieve a 2.5 mg/mL solution, which was subsequently intravenously injected into individual animals (n = 6). At 4–6 h after tracer administration, intraoperative imaging using both white light and Cy5 filtered light was performed using a modified clinical-grade IMAGE1 S camera system including a D-Light P light source (integrated customized Cy5 filter) and a customized 10 mm 0° laparoscope (Karl Storz SE & Co. KG (*27*)). The use of radiotracers and a more extended time window could not be pursued under the available ethical approval for the surgical training setting.

As a reference, identical experiments were conducted after administration of a similar dye concentration of ICG (3.75 mg, n = 2). In those experiments, imaging was performed using the fluorescence setting of a Firefly camera mounted on a Da Vinci surgical robot. The Da Vinci vision cart depicts ICG fluorescence as green on a black-and-white background without any form of scale bar. After imaging, the animals were euthanized, and lesions were excised for ex vivo fluorescence imaging and pathologic examination. To facilitate appreciation of the tracer uptake in these models, in-house–developed image processing was applied, using custom algorithms written in MATLAB. The fluorescence signal was segmented on the basis of color and visualized as an overlay on a black-and-white representation of the anatomy. Regions of interest were drawn on healthy liver tissue for background fluorescence assessments. The median fluorescence background signal was used to calculate the signal-to-background ratio for each fluorescent pixel. The signal-to-background ratios were depicted using a batlow color map with scale bar (*25*).

Statistical Analysis

Statistical evaluation to compare uptake values (%ID and %ID/g for radioactive assessment and photons/s/cm^2 for the fluorescence signal) at different time points in the biodistribution was performed using an unpaired 2-sided Student t test. Values of P that were less than 0.05 were considered significant.

RESULTS

Synthesis and Characterization

*h*HEPATO-Cy5 was successfully synthesized (Fig. 1; Supplemental Figs. 1–4) and presented favorable chemical properties (serum protein binding, 94%; logP, 0.80 ± 0.03) and fluorescent properties (absorption/emission, 640/665 nm [Supplemental Fig. 5]; brightness, 3,445 M^{-1}). After radiolabeling, ^{99m}Tc-*h*HEPATO-Cy5 was obtained with a radiochemical yield of 83% ± 5%.

In Vitro Excretion Hepatocytes

Using an in vitro lesion model and assessment in hepatocyte cultures, the difference in uptake of *h*HEPATO-Cy5 in damaged and healthy hepatocytes was compared (Supplemental Fig. 6; Fig. 2). In the in vitro lesion model, a high-intensity Cy5 fluorescence signal was detected in a ring of damaged hepatocytes (Supplemental Fig. 6). In these cells, uptake was distributed evenly over the whole cell. A change in distribution of the fluorescence signal was seen with increasing distance from the lesion. At an approximately 500-μm distance, the overall uptake pattern was like that in healthy hepatocytes. Here, no intracellular uptake was seen, but focalized uptake of *h*HEPATO-Cy5 was positioned in bile cannulas between cells (Fig. 2; Supplemental Fig. 6 (*28*)). As this pattern was shown to be similar to that of fluorescent bile salts (Fig. 2), this suggests that *h*HEPATO-Cy5 is functionally excreted.

Incubation of epithelial cells with *h*HEPATO-Cy5 resulted in mitochondrial uptake (Supplemental Fig. 7), which was similar to the uptake of the fluorescent component alone (methylated

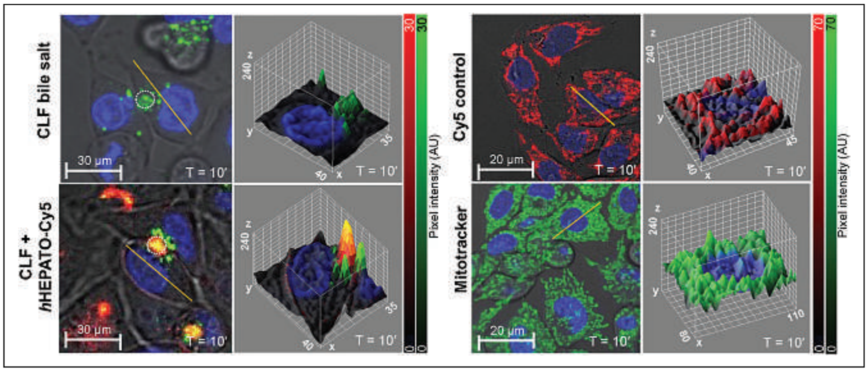

FIGURE 2. Fluorescence confocal imaging of HC04 hepatocytes after 10 min of incubation with fluorescent bile salt cholyl-Lys-fluorescein or coincubation of hHEPATO-Cy5 and cholyl-Lys-fluorescein), Cy5 control, or MitoTracker. Left images in each panel are 2-dimensional fluorescence confocal images (LAS X software). Right images in each panel are 3-dimensional representations of tracer distribution throughout cell (Fiji software). Nuclear staining is in blue, Cy5 is in red, and MitoTracker is in green. Dashed circle is example of bile canula, and yellow lines are orientation 3-dimensional analysis. Color bars show pixel intensity (arbitrary units) obtained with same software. AU = arbitrary units; CLF = cholyl-Lys-fluorescein; T = time after incubation.

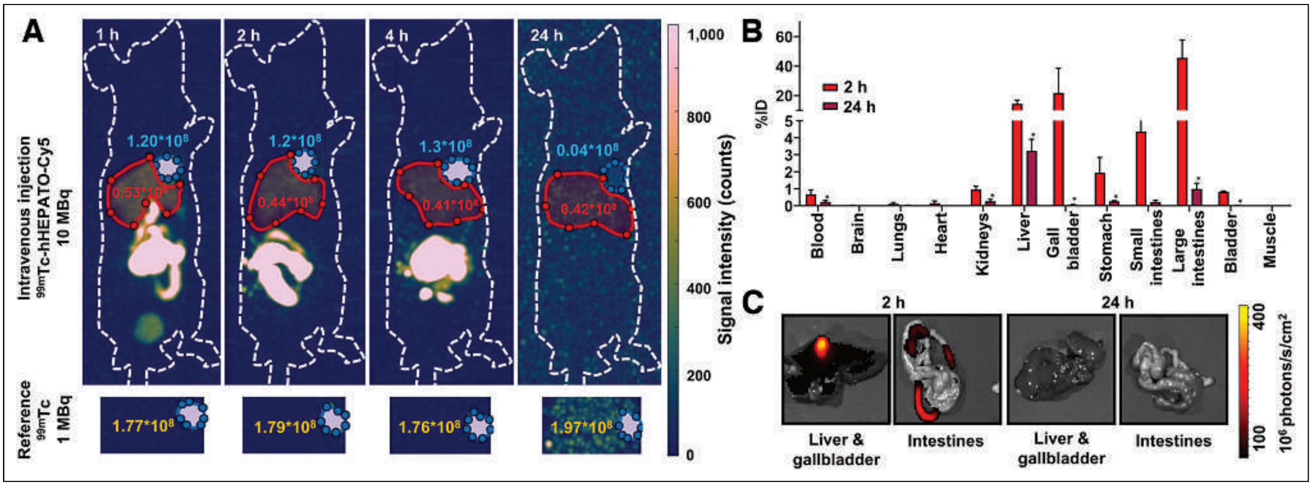

FIGURE 3. Biodistribution of ^{99m}Tc-*h*HEPATO-Cy5 in mice. (A) In vivo SPECT imaging (batlow color map) at 1, 2, 4, and 24 h after tracer administration. Shown are decay-corrected signal intensity (counts) for liver and gallbladder (in red and blue regions of interest, respectively; top images) and for ^{99m}Tc reference source (bottom images). (B) Quantitative biodistribution presented as %ID at 2 and 24 h after intravenous administration in mice. (C) IVIS fluorescence imaging of liver and gallbladder and intestines using hot map (Living Image Software [Perkin Elmer]; photons/s/cm^2) at 2 and 24 h. $^*P > 0.01$ for 2- vs. 24-h uptake values.

Cy5 [control]) in both hepatocytes and epithelial cells (Fig. 2; Supplemental Fig. 7). Excretion of *h*HEPATO-Cy5 was underlined by semiquantitative assessment of the fluorescence signal over time (Supplemental Fig. 8). In healthy hepatocytes, a decrease in *h*HEPATO-Cy5–related fluorescence signal was seen after 30 min. In contrast, a substantially higher ($P > 0.0001$) intracellular signal that did not decrease over time was seen for the Cy5 control. Hence, the focal uptake of *h*HEPATO-Cy5 is exclusive to hepatocytes, and the addition of the mas$_3$ moiety in *h*HEPATO-Cy5 is crucial for the hepatobiliary excretion.

In Vivo Biodistribution in Mice

As early as 1 h after intravenous administration, hot ^{99m}Tc-*h*HEPATO-Cy5 (0.5 nmol) yielded dominant hepatobiliary excretion, exemplified by the prominent signal seen in the liver, gallbladder, and intestines on SPECT (Fig. 3A). Biliary excretion was further substantiated by a significant 2-orders-of-magnitude reduction in count rate for the gallbladder (Fig. 3B; Supplemental Table 1; $P = 0.008$) over time. Instrumental for imaging of liver lesions, a 5-fold decrease in count rate was observed in the liver (Supplemental Table 1; $P = 0.002$) and was further substantiated via ex vivo tissue examination at 2 and 24 h (Fig. 3C). At 2 h after tracer injection, high fluorescence intensities were seen in the gallbladder ($2.6 \times 10^8 \pm 5.9 \times 10^7$ photons/s/cm^2), whereas intensities in the liver were significantly lower ($3.3 \times 10^7 \pm 7.9 \times 10^6$ photons/s/cm^2; $P > 0.0001$). After 24 h, fluorescence signal intensities in the liver had further reduced to $1.6 \times 10^7 \pm 2.8 \times 10^6$ photons/s/cm^2, which correlated to a negligible background staining in this tissue (Fig. 3C).

In Vivo Pharmacokinetic Assessments in Porcine Models: Surgical Fluorescence Imaging

In vivo imaging in a porcine model for robot-assisted hepatobiliary lesion resection was performed to show the similarities in staining pattern with the current clinical fluorescence-only approach (using ICG) and compatibility of *h*HEPATO-Cy5 with clinical-grade robotic surgery and imaging devices. Fluorescence imaging in this model underscored the hepatobiliary clearance profile for *h*HEPATO-Cy5. A clear fluorescence signal was seen in the gallbladder and intestines. And importantly, at 4 h after injection, the background uptake in the nonaffected liver was already negligible (Fig. 4).

In vivo created liver lesions (Fig. 5) demonstrated a characteristic fluorescent rim around the border of the lesion ($n >$ 25 lesions tested). Clear discrimination could be made between the liver and surrounding tissue of the abdominal wall, and this discrimination was especially evident for lesions on the outer edge of a liver segment. The rimlike staining pattern was comparable to the accumulation seen in the in vitro model (Supplemental Fig. 6) and in line with that of ICG in the same model (Supplemental Fig. 9) but also of ICG in patients with liver cancer (*16*).

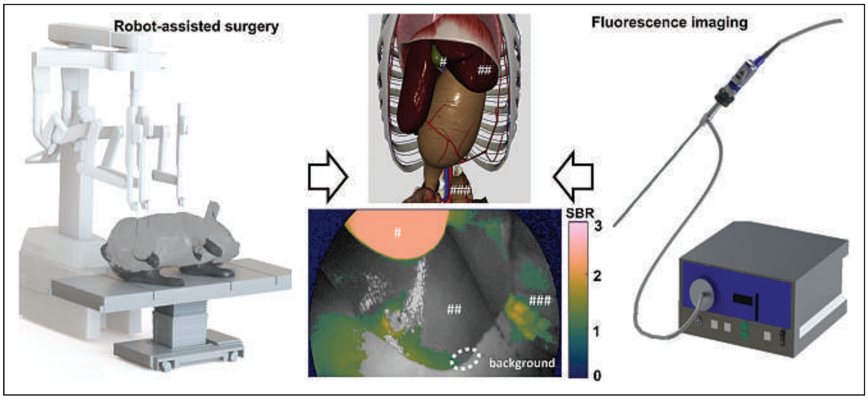

FIGURE 4. Surgical imaging setup in porcine model. Use of clinical-grade equipment allowed combination of robot-assisted surgery and laparoscopic fluorescence imaging (*22*) for assessment of tracer distribution over hepatobiliary system and excretion toward intestines. At center top is schematic localization of organs of interest, and at center bottom is batlow laparoscopic fluorescence image showing signal-to-background ratios of *h*HEPATO-Cy5-related fluorescence. Dashed circle represents area used to define background signal. # = gallbladder; ## = liver; ### = intestines; SBR = signal-to-background ratio.

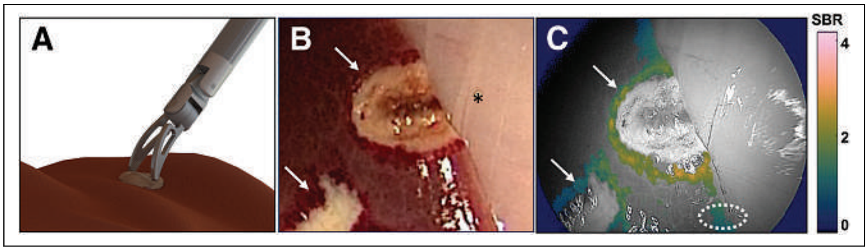

FIGURE 5. Robot-assisted in vivo imaging of liver lesions in porcine model. (A) Schematic representation of creation of heat-induced lesions using coagulation setting of bipolar robotic forceps. (B and C) In vivo laparoscopic imaging of liver lesions (arrows) and surrounding tissue of abdominal wall (*) using white-light imaging (B) and custom image-processing algorithms (C) support batlow intensity-based assessment of fluorescence uptake. Dashed circle is area used to define background signal. SBR = signal-to-background ratio (*27*).

Microscopic pathologic examination of the excised lesions underscored the difference in morphology between the healthy liver tissue and the lesion (Figs. 6A and 6B). Accumulation of *h*HEPATO-Cy5 occurred within a transitional rim bridging the lesion and healthy liver tissue (Fig. 6C). This suggests that damaged hepatocytes in the transitional rim are unable to facilitate bile transport, resulting in local retention of *h*HEPATO-Cy5.

DISCUSSION

By directly conjugating a lipophilic Cy5 dye to a mas$_3$ chelate, we generated a hybrid hepatic tracer (*h*HEPATO-Cy5). This tracer portrays a unique biliary excretion profile (Fig. 2; Supplemental Figs. 7 and 9) in hepatobiliary cultures. In vivo, the tracer allowed reliable delineation of liver lesions in real time using fluorescence-guided robot-assisted surgery in a porcine model (Fig. 5).

The hybrid nature of ^{99m}Tc-*h*HEPATO-Cy5 extends fluorescence imaging by giving it the ability to identify preoperative lesions (SPECT). In other oncologic surgical applications, this combination has been shown to provide value that is greater than the sum of the benefit of the individual techniques (*29*). Preoperative knowledge of the exact location of the lesion before tissue exploration, along with visual assessment and validation of the excision of the targeted tissue, is a feature likely to provide steps toward overcoming existing challenges in hepatobiliary surgery.

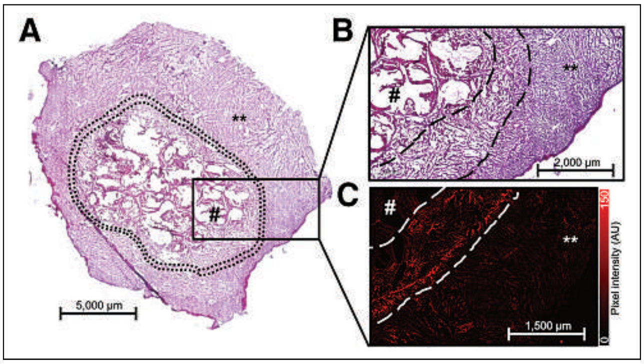

FIGURE 6. Localization fluorescence signal in liver lesions. (A) Immunohistochemistry (hematoxylin and eosin staining) of excised liver sample containing healthy liver tissue (**) and heat-induced liver lesion (encircled). (B and C) Zoomed area showing transitional rim (between dashed lines) between necrotic liver tissue (#) and healthy liver tissue (B) and fluorescence confocal imaging in sequential tissue section with fluorescence uptake (in red [Leica LAS X software]) in transitional rim (C). Color bar shows pixel intensity (arbitrary units) obtained with same software. AU = arbitrary units.

Although the correlation between nuclear and fluorescence imaging based on *h*HEPATO-Cy5 was shown in mice, constraints within the ethical license prohibited use of radioactivity in the porcine model. As such, in the latter model, use of only the fluorescent readout and subsequent assessment of superficial lesions was allowed. Nevertheless, the literature indicates that intraoperative extension of fluorescence imaging with in-depth drop-in radioguidance (*30*) is likely to help facilitate the resection of deeper lesions. This assumption is supported by studies in other clinical indications that provide clear evidence of the superior in-depth image guidance that can be achieved when a hybrid tracer is used rather than a fluorescence-only tracer (*31*).

The mechanism behind ICG uptake in hepatobiliary lesions remains a subject of study. Our work clearly indicates that uptake of *h*HEPATO-Cy5 around a lesion can be attributed to disrupted hepatocytes and is related to the excretion of bile (Fig. 2; Supplemental Fig. 6). Further mechanistic studies are needed to help understand if this relates to specific transporter proteins (*16*).

Fluorescent emissions used for image-guided surgery are classified into 3 categories according to the International Union of Pure and Applied Chemistry regulations: near-infrared, far-red, and visible fluorescence (*31*). Despite the popular demand for near-infrared analogs (e.g., ICG; maximum emission wavelength, 750–1,000 nm), there are clear arguments to be made for the surgical use of far-red dyes (e.g., Cy5; maximum emission wavelength, 650–750 nm). For example, previous investigations have shown that Cy5 has better photophysical properties than ICG (*32*) and that clinical systems have higher sensitivity to Cy5 than to ICG, both aiding deeper detection. Surprisingly, Cy5 is quite often falsely referred to as being a near-infrared dye (*24,33*). Using a range of clinical-grade Cy5 camera prototypes has resulted in the successful in-patient use of far-red dyes (*24,27,34*). The depiction of Cy5 fluorescence in vivo (Fig. 5) has even been shown to be compatible with imaging of near-infrared dyes (in the same patient), allowing unique multispectral imaging strategies (*32,35*).

Creation of relevant in vivo large-animal models for resection of hepatic lesions is not trivial. To the best of our knowledge, this is the first report of such a model that can be used to evaluate image guidance technologies for hepatobiliary lesions. The lesions displayed ICG uptake that is in line with literature reports (*16,36*). Clinical follow-up studies will be required to confirm the translational value of *h*HEPATO-Cy5.

CONCLUSION

By creating a small molecule comprising a fluorescent Cy5 dye and a mas$_3$ chelate, we have designed a unique bile-excreted hybrid tracer—one that is capable of providing both fluorescence guidance and radioguidance during excision of liver lesions. The hybrid nature of this tracer also paves the way for the future implementation of nuclear medicine road maps to plan and guide fluorescence-based hepatobiliary surgery.

DISCLOSURE

This research was funded by an NWO-TTW-VICI (TTW BGT16141) grant supported by the Dutch Research Council. Julia Kloetzl is an employee of Karl Storz SE & Co. KG. No other potential conflict of interest relevant to this article was reported.

ACKNOWLEDGMENTS

We thank Danny van Willigen and Thom van den Eng for their contributions to tracer synthesis, evaluation, and in vitro analysis.

KEY POINTS

QUESTION: Is it possible to design a hybrid radiolabeled and fluorescently labeled tracer that allows visualization of liver lesions in a manner similar to the clinical application of the fluorescent dye ICG?

PERTINENT FINDINGS: The unique molecular composition of the tracer ^{99m}Tc-*h*HEPATO-Cy5 promotes hepatobiliary excretion via a mechanism like that of bile salts. The hybrid nature of the tracer means it allows both in vivo SPECT of hepatic clearance in mice and fluorescence-guided liver lesion resection in a porcine model.

IMPLICATIONS FOR PATIENT CARE: The hybrid nature of ^{99m}Tc-*h*HEPATO-Cy5 helps extend the current clinically applied fluorescence-only approach to one that supports in-depth target identification and one that can be supported by road maps generated through preoperative tracer imaging.

REFERENCES

1. Balasubramanya R, Selvarajan SK, Cox M, et al. Imaging of ocular melanoma metastasis. *Br J Radiol.* 2016;89:20160092.
2. Carvajal RD, Schwartz GK, Tezel T, Marr B, Francis JH, Nathan PD. Metastatic disease from uveal melanoma: treatment options and future prospects. *Br J Ophthalmol.* 2017;101:38–44.
3. Engstrand J, Nilsson H, Strömberg C, Jonas E, Freedman J. Colorectal cancer liver metastases: a population-based study on incidence, management and survival. *BMC Cancer.* 2018;18:78.
4. Riihimäki M, Hemminki A, Sundquist K, Sundquist J, Hemminki K. The epidemiology of metastases in neuroendocrine tumors. *Int J Cancer.* 2016;139:2679–2686.
5. Wang R, Zhu Y, Liu X, Liao X, He J, Niu L. The clinicopathological features and survival outcomes of patients with different metastatic sites in stage IV breast cancer. *BMC Cancer.* 2019;19:1091.
6. Nordlinger B, Sorbye H, Glimelius B, et al. Perioperative chemotherapy with FOLFOX4 and surgery versus surgery alone for resectable liver metastases from colorectal cancer (EORTC intergroup trial 40983): a randomised controlled trial. *Lancet.* 2008;371:1007–1016.
7. Jones AD, Wilton JC. Can intra-operative fluorescence play a significant role in hepatobiliary surgery? *Eur J Surg Oncol.* 2017;43:1622–1627.
8. Freitas PS, Janicas C, Veiga J, Matos AP, Herédia V, Ramalho M. Imaging evaluation of the liver in oncology patients: a comparison of techniques. *World J Hepatol.* 2021;13:1936–1955.
9. Piccolo G, Barabino M, Pesce A, et al. Role of indocyanine green fluorescence imaging in minimally invasive resection of colorectal liver metastases. *Surg Laparosc Endosc Percutan Tech.* 2022;32:259–265.
10. Kow AWC. Hepatic metastasis from colorectal cancer. *J Gastrointest Oncol.* 2019;10:1274–1298.
11. Ishizawa T, Fukushima N, Shibahara J, et al. Real-time identification of liver cancers by using indocyanine green fluorescent imaging. *Cancer.* 2009;115:2491–2504.
12. Hu Y, Fu T, Zhang Z, Hua L, Zhao Q, Zhang W. Does application of indocyanine green fluorescence imaging enhance clinical outcomes in liver resection? A meta-analysis. *Photodiagnosis Photodyn Ther.* 2021;36:102554.
13. van Leeuwen FWB, Schottelius M, Brouwer OR, et al. Trending: radioactive and fluorescent bimodal/hybrid tracers as multiplexing solutions for surgical guidance. *J Nucl Med.* 2020;61:13–19.
14. Snyder EKS, Lopez PP. Hepatobiliary iminodiacetic acid scan. NIH website. https://www.ncbi.nlm.nih.gov/books/NBK539781/. Updated July 24, 2023. Accessed June 20, 2024.
15. Marie S, Hernández-Lozano I, Langer O, Tournier N. Repurposing ^{99m}Tc-mebrofenin as a probe for molecular imaging of hepatocyte transporters. *J Nucl Med.* 2021;62:1043–1047.
16. Franz M, Arend J, Wolff S, et al. Tumor visualization and fluorescence angiography with indocyanine green (ICG) in laparoscopic and robotic hepatobiliary surgery: valuation of early adopters from Germany. *Innov Surg Sci.* 2021;6:59–66.
17. Hensbergen AW, Buckle T, van Willigen DM, et al. Hybrid tracers based on cyanine backbones targeting prostate-specific membrane antigen: tuning pharmacokinetic properties and exploring dye-protein interaction. *J Nucl Med.* 2020;61:234–241.
18. Winkel BMF, de Korne CM, van Oosterom MN, et al. A tracer-based method enables tracking of *Plasmodium falciparum* malaria parasites during human skin infection. *Theranostics.* 2019;9:2768–2778.
19. Wonganan P, Jonsson-Schmunk K, Callahan SM, Choi JH, Croyle MA. Evaluation of the HC-04 cell line as an in vitro model for mechanistic assessment of changes in hepatic cytochrome P450 3A during adenovirus infection. *Drug Metab Dispos.* 2014;42:1191–1201.
20. Bunschoten A, van Willigen DM, Buckle T, et al. Tailoring fluorescent dyes to optimize a hybrid RGD-tracer. *Bioconjug Chem.* 2016;27:1253–1258.
21. Tanimizu N, Ichinohe N, Sasaki Y, et al. Generation of functional liver organoids on combining hepatocytes and cholangiocytes with hepatobiliary connections ex vivo. *Nat Commun.* 2021;12:3390.
22. Buckle T, Hensbergen AW, van Willigen DM, et al. Intraoperative visualization of nerves using a myelin protein-zero specific fluorescent tracer. *EJNMMI Res.* 2021;11:50.
23. Berehova N, van Meerbeek MP, Azargoshasb S, et al. A truncated 14-amino-acid myelin protein-zero-targeting peptide for fluorescence-guided nerve-preserving surgery. *Biomolecules.* 2023;13:942.
24. Burggraaf J, Kamerling IM, Gordon PB, et al. Detection of colorectal polyps in humans using an intravenously administered fluorescent peptide targeted against c-Met. *Nat Med.* 2015;21:955–961.
25. Crameri F, Shephard GE, Heron PJ. The misuse of colour in science communication. *Nat Commun.* 2020;11:5444.
26. Buckle T, Kuil J, van den Berg NS, et al. Use of a single hybrid imaging agent for integration of target validation with in vivo and ex vivo imaging of mouse tumor lesions resembling human DCIS. *PLoS One.* 2013;8:e48324.
27. Buckle T, van Alphen M, van Oosterom MN, et al. Translation of c-Met targeted image-guided surgery solutions in oral cavity cancer: initial proof of concept data. *Cancers (Basel).* 2021;13:2674.
28. Gary Hong Chun C, Jemima JB, Maëlle L, Paul G, Christopher JS. ER-PM contacts regulate apical domain formation in hepatocytes. bioRxiv website. https://www.biorxiv.org/content/10.1101/2020.04.23.057521v1.full. Published April 24, 2020. Accessed June 20, 2024.
29. Wit EMK, KleinJan GH, Berrens AC, et al. A hybrid radioactive and fluorescence approach is more than the sum of its parts; outcome of a phase II randomized sentinel node trial in prostate cancer patients. *Eur J Nucl Med Mol Imaging.* 2023;50:2861–2871.
30. Meershoek P, van Oosterom MN, Simon H, et al. Robot-assisted laparoscopic surgery using DROP-IN radioguidance: first-in-human translation. *Eur J Nucl Med Mol Imaging.* 2019;46:49–53.
31. van Leeuwen FW, Hardwick JC, van Erkel AR. Luminescence-based imaging approaches in the field of interventional molecular imaging. *Radiology.* 2015;276:12–29.
32. van Willigen DM, van den Berg NS, Buckle T, et al. Multispectral fluorescence guided surgery; a feasibility study in a phantom using a clinical-grade laparoscopic camera system. *Am J Nucl Med Mol Imaging.* 2017;7:138–147.
33. Mieog JSD, Achterberg FB, Zlitni A, et al. Fundamentals and developments in fluorescence-guided cancer surgery. *Nat Rev Clin Oncol.* 2022;19:9–22.
34. Zanoni DK, Stambuk HE, Madajewski B, et al. Use of ultrasmall core-shell fluorescent silica nanoparticles for image-guided sentinel lymph node biopsy in head and neck melanoma: a nonrandomized clinical trial. *JAMA Netw Open.* 2021;4:e211936.
35. van Beurden F, van Willigen DM, Vojnovic B, et al. Multi-wavelength fluorescence in image-guided surgery, clinical feasibility and future perspectives. *Mol Imaging.* 2020;19:1536012120962333.
36. van der Vorst JR, Schaafsma BE, Hutteman M, et al. Near-infrared fluorescence-guided resection of colorectal liver metastases. *Cancer.* 2013;119:3411–3418.

RadShap: An Explanation Tool for Highlighting the Contributions of Multiple Regions of Interest to the Prediction of Radiomic Models

Nicolas Captier[1], Fanny Orlhac[1], Narinée Hovhannisyan-Baghdasarian[1], Marie Luporsi[1,2], Nicolas Girard[3], and Irène Buvat[1]

[1]Laboratoire d'Imagerie Translationnelle en Oncologie, Institut Curie, INSERM U1288, PSL Research University, Orsay, France; [2]Department of Nuclear Medicine, Institut Curie, Paris, France; and [3]Institut du Thorax Curie-Montsouris, Institut Curie, Paris, France

Explaining the decisions made by a radiomic model is of significant interest, as it can provide valuable insights into the information learned by complex models and foster trust in well-performing ones, thereby facilitating their clinical adoption. Promising radiomic approaches that aggregate information from multiple regions within an image currently lack suitable explanation tools that could identify the regions that most significantly influence their decisions. Here we present a model- and modality-agnostic tool (RadShap, https://github.com/ncaptier/radshap), based on Shapley values, that explains the predictions of multiregion radiomic models by highlighting the contribution of each individual region. **Methods:** The explanation tool leverages Shapley values to distribute the aggregative radiomic model's output among all the regions of interest of an image, highlighting their individual contribution. RadShap was validated using a retrospective cohort of 130 patients with advanced non–small cell lung cancer undergoing first-line immunotherapy. Their baseline PET scans were used to build 1,000 synthetic tasks to evaluate the degree of alignment between the tool's explanations and our data generation process. RadShap's potential was then illustrated through 2 real case studies by aggregating information from all segmented tumors: the prediction of the progression-free survival of the non–small cell lung cancer patients and the classification of the histologic tumor subtype. **Results:** RadShap demonstrated strong alignment with the ground truth, with a median frequency of 94% for consistently explained predictions in the synthetic tasks. In both real-case studies, the aggregative models yielded superior performance to the single-lesion models (average [±SD] time-dependent area under the receiver operating characteristic curve was 0.66 ± 0.02 for the aggregative survival model vs. 0.55 ± 0.04 for the primary tumor survival model). The tool's explanations provided relevant insights into the behavior of the aggregative models, highlighting that for the classification of the histologic subtype, the aggregative model used information beyond the biopsy site to correctly classify patients who were initially misclassified by a model focusing only on the biopsied tumor. **Conclusion:** RadShap aligned with ground truth explanations and provided valuable insights into radiomic models' behaviors. It is implemented as a user-friendly Python package with documentation and tutorials, facilitating its smooth integration into radiomic pipelines.

Key Words: artificial intelligence; explainability; radiomics; Shapley values; python package

J Nucl Med 2024; 65:1307–1312
DOI: 10.2967/jnumed.124.267434

Radiomics has gained significant popularity in precision medicine, using both deep features and engineered ones that characterize shape, intensity, or texture (*1*). Although radiomics initially focused on a single region of interest (ROI), such as the primary tumor, more and more models now aggregate information from multiple ROIs in the same image. For instance, many radiomic approaches extract information from multiple tumors and regions within healthy organs to effectively predict cancer patients' outcomes (*2–4*). The motivation is to better leverage the image content and, hopefully, improve predictive performance.

These aggregative approaches raise an interesting question: can we identify the ROIs within each image that most influence the model's prediction? Indeed, understanding which ROIs drive the model's decision may not only enhance the model explainability but also provide valuable medical insights. However, the tools commonly used to explain predictive models (*5*) may not be well suited to address this question. They usually assign a global importance to aggregated features used by the model, without straightforward identification of the role of individual ROIs.

The Shapley value, a concept originally designed to fairly distribute the overall gain of a cooperative game among its players, has recently proven successful to explain the outputs of machine learning models (*6,7*). It offers a promising approach to answer our question. Considering that the different ROIs of an image (i.e., the players) collaborate to obtain the model's prediction (i.e., the overall gain), the Shapley value assigns a score to each ROI related to its contribution to the prediction.

Here we introduce an original explanation tool, named RadShap (https://github.com/ncaptier/radshap), that leverages Shapley values to highlight the influence of every ROI included into a radiomic model. We first evaluate the tool on a synthetic task for which the ground truth is known. We then illustrate its relevance through its application to radiomic models trained to address histologic classification and survival prediction tasks.

MATERIALS AND METHODS

Dataset

A retrospective cohort consisting of 130 individuals diagnosed with advanced non–small cell lung cancer (NSCLC) was used (Supplemental

---

Received Jan. 16, 2024; revision accepted May 22, 2024.

For correspondence or reprints, contact Nicolas Captier (nicolas.captier@polytechnique.org) or Irène Buvat (irene.buvat@curie.fr).

Table 1; supplemental materials are available at http://jnm.snmjournals.org) (*8–10*). Each patient received anti–programmed-death 1 and anti–programmed-death ligand 1 immunotherapy, specifically pembrolizumab, combined with chemotherapy, as their first-line treatment. Response to immunotherapy was assessed through progression-free survival (PFS). Clinical data and a baseline [^{18}F]FDG PET scan were collected for each patient in compliance with the General Data Protection Regulation. The study was approved by the institutional review board of Institut Curie (DATA200053), and written informed consent from all patients was obtained through institutional processes.

For each PET scan, intensities were converted to SUVs and all tumor foci were delineated by an experienced nuclear medicine physician (12 y of experience) using LIFEx software version 7.3 (www.lifexsoft.org) (*11*). Subsequently, all images were resampled to a fixed $2 \times 2 \times 2$ mm^3 voxel size, and a fixed threshold of 2.5 SUV units was applied to refine the segmented tumor regions.

For all the segmented lesions, we used Image Biomarker Standardization Initiative–compliant PyRadiomics version 3.0.1 (*12,13*) to compute 4 shape radiomic features (sphericity, elongation, flatness, and voxel volume) and 6 first-order radiomic features (SUV$_{\text{max}}$, SUV$_{\text{mean}}$, skewness, kurtosis, entropy, and quantile dispersion).

Computation of Shapley Values for Local Explanations

The RadShap explanation tool provides a local explanation for each prediction made by a radiomic model. This is achieved by calculating the Shapley values (*6*) of the aggregated ROIs used as input, assigning an importance score to each ROI based on its contribution to the final prediction. In short, the Shapley value of an ROI quantifies the impact of including this ROI in the model on the model's prediction. It corresponds to the average change in prediction observed when the ROI is added to any combination of other ROIs in the predictive model's input. The Shapley values distribute the model's output among the various ROIs, as their sum corresponds to the model's overall prediction.

For an input image I characterized by K ROIs $(r_1, r_2 \ldots, r_K)$, a trained predictive model f, and an aggregation function g (Figs. 1A and 1B), the Shapley value of region r_i is calculated by averaging its marginal contribution across all possible subsets of ROIs that exclude r_i. The marginal contribution of r_i to the subset of ROIs S is the difference observed in the model's prediction when r_i is included in subset S (Fig. 1C).

$$\Delta_{f \circ g}(r_i, S) = f\Big(g(S \cup \{r_i\})\Big) - f\Big(g(S)\Big) \qquad \text{(Eq. 1)}$$

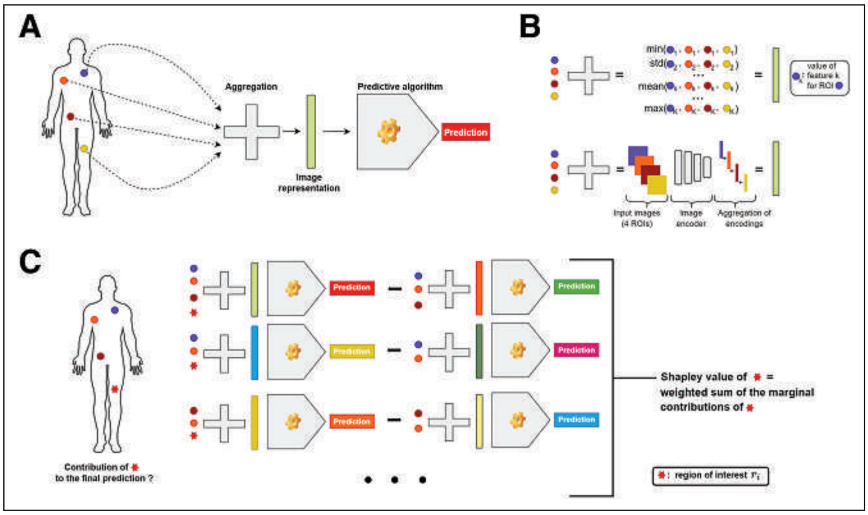

FIGURE 1. (A) Schematic representation of generic aggregative radiomic model. (B) Examples of aggregation function with engineered radiomic features (top) or deep radiomic features (bottom). (C) Schematic representation of explanation tool.

A detailed mathematic formulation is presented in Supplemental Section A, along with the description of a computational approximation scheme used to speed the estimation.

RadShap is both model- and modality-agnostic and, thus, applicable to any trained radiomic model that uses aggregated information from multiple ROIs as input. In the standard setting, the ROIs are assumed to be optional, meaning that aggregating any subset of ROIs will still produce a valid input for the predictive model. For instance, if the predictive model takes as input the average volume computed across all lesions of a metastatic patient, each lesion is optional. Indeed, removing a lesion will result only in the average volume's being computed across the remaining lesions, still yielding a valid input for the model. However, if the model also considers the SUV$_{\text{max}}$ in an ROI delineated in a healthy spleen region (i.e., SUV$_{\text{max(spleen)}}$), this ROI is not optional since removing it will result in a missing value for the SUV$_{\text{max(spleen)}}$ feature and therefore an invalid input for the predictive model. Our explanation tool includes a solution to address the scenario in which certain ROIs are not optional. Following a strategy used in the Shapley additive explanation (SHAP) method (*7*), the missing values resulting from the removal of nonoptional ROIs are replaced by all possible values observed in a background dataset (i.e., set of data samples representative of the general data distribution that the model is expected to encounter, typically the training set). The final prediction is then obtained by averaging the predictions made with every possible background value (Supplemental Sections B and C).

Building a Synthetic Task

To validate the explanation tool, we first built a synthetic radiomic signature as a linear combination of a random subset of the 10 radiomic features listed above and computed the signature value for every lesion of each NSCLC patient (Supplemental Section D). A binary label was then assigned to each patient: 1 if the patient had at least 1 lesion with the radiomic signature value above a predetermined threshold and 0 otherwise. The threshold was selected to ensure that the 2 classes were reasonably balanced, with the minority class frequency exceeding 30%. To achieve this, the maximum signature value was calculated for each patient, and the q$^{\text{th}}$ percentile (with q ranging from 30% to 70%) was randomly selected. This ensured that over q% of the patients had at least 1 lesion with a signature value exceeding this threshold, resulting in their label being set to 1. To enhance the robustness of our results, we repeated this experiment 1,000 times, with a different radiomic signature and a different threshold for each iteration (Fig. 2).

We then addressed this binary classification task using a logistic regression model with ridge regularization (i.e., scikit-learn implementation with default parameters and balanced class weights). The model's input consisted of the 10 radiomic features measured for all the patient's lesions. Specifically, these features were aggregated into a 20-feature vector using min and max functions, which involved computing the minimum and maximum of each of the 10 features across all lesions and concatenating these 20 values in a single vector. Importantly, no information related to the radiomic signature or label generation was provided to the model. Training and test were performed with a stratified 5-fold cross-validation scheme. To collect the Shapley values associated with each patient's lesions, our tool was applied to

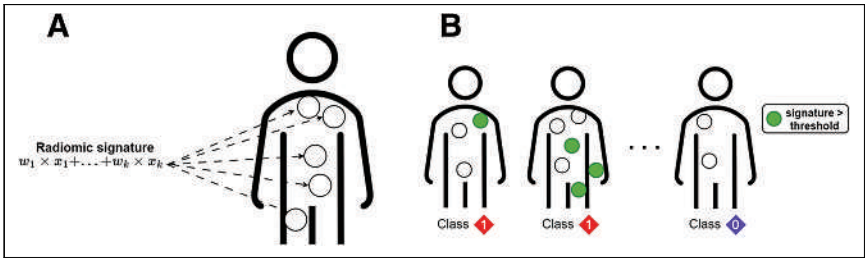

FIGURE 2. (A) Computation of synthetic radiomic signature for every lesion of each patient. (B) Each patient was assigned binary label based on presence of high-scored lesions, meaning lesions with radiomic signature above specified threshold.

every patient within the test set of each fold using the model trained on the corresponding training set.

Validation of the Tool Using a Synthetic Task

When the model accurately predicted the binary labels, we assumed that the model used information related to the presence of lesions with a high radiomic signature to make its decision. Thus, we evaluated the consistency of the tool's explanations by measuring the frequency with which the model correctly predicted a "1" label and the Shapley values identified a lesion with a high radiomic signature as the most influential factor affecting the model's decision. We also calculated the number of true-positive cases for which all lesions with a high radiomic signature value were assigned a higher Shapley value than any other lesion with a low signature value.

Survival Task: Explaining the Prediction of PFS Under Immunotherapy

The first case study addressed the prediction of PFS, comparing a standard approach involving radiomic features extracted from the segmented primary tumor (called primary model hereafter) with an approach using all segmented lesions (called aggregative model hereafter). Specifically, within the aggregative model, we used as input 2 multilesion features: the total metabolic tumor volume and the standardized D_{max}—defined as the maximum distance between 2 lesions normalized by the body surface area—a metric previously associated with outcomes in lymphoma patients (*14*). In total, we identified 115 NSCLC patients for whom both the primary tumor was visible on the PET scan and PFS data were available.

In the primary model, we included the 10 radiomic features extracted by PyRadiomics and listed in the Dataset section above. We then applied 2 successive feature selection preprocessing steps each time the primary model was trained. Initially, a backward elimination process based on the variance inflation factor was used to remove collinear features. Subsequently, another backward elimination step based on the Akaike information criterion was applied to discard unnecessary features for prediction. Both the primary and the aggregative models were trained using a Cox proportional-hazards algorithm (default settings of Lifelines Python package).

Classification Task: Explaining the Prediction of Lung Cancer Histologic Subtype

The second case study addressed the prediction of the NSCLC histologic subtype (adenocarcinoma vs. other subtypes). We compared a standard approach that used features extracted only from the biopsied lesion (called biopsy model hereafter) with an approach that aggregated features extracted from all segmented lesions (called aggregative model hereafter). We excluded patients for whom the biopsied tumor was not present in the PET scan or the localization of the biopsy site was not available, resulting in a final dataset of 117 patients (87 adenocarcinomas and 30 other subtypes). For 88 patients, the biopsy was performed on their primary lung tumor, whereas for the remaining 29 patients, the biopsy was performed on another lesion.

A logistic regression model with elastic net regularization (i.e., scikit-learn implementation with balanced class weights, C = 0.1, and l1_ratio = 0.5) was used for both biopsy and aggregative models. For the aggregative model, several combinations of simple functions were tested to aggregate the feature values extracted from all the lesions of a patient (min, max, mean, and SD).

Statistical Analysis

For the 1,000 synthetic tasks, the significance of the tool was assessed using a right-tailed test associated with the null hypothesis: the explanations were generated with a random ranking of lesions, and therefore, the number of consistent explanations followed a Poisson binomial distribution. We report the number of tasks for which this hypothesis was rejected after controlling the false discovery rate with the Benjamini–Yekutieli procedure.

For the PFS prediction and histologic classification studies, the models were trained and tested using a 5-fold cross-validation scheme repeated 100 times. The folds were stratified on the basis of censorship rate for the survival task (i.e., PFS prediction) and class proportion for the classification task (i.e., histologic classification). The performance of the binary classifiers was evaluated using 4 metrics: the area under the receiver operating characteristic curve (AUC), balanced accuracy, sensitivity, and specificity (0.5 threshold). For Cox models, evaluation was based on 2 metrics: Uno's concordance index (C-index) and the average time-dependent AUC (tAUC) over the observed time range. These metrics were averaged over 100 repetitions, and their SD was calculated to measure the variability resulting from the random partition of the data into 5 folds. The AUCs and C-indices were compared with 1-sided paired permutation tests (*15*), adjusted for multiple testing. Finally, an additional cross-validation scheme was used to collect the Shapley values associated with the lesions of each patient for the aggregative models.

RESULTS

Synthetic Tasks

The logistic regression model trained using aggregated radiomic features demonstrated high classification performance: for half the 1,000 synthetic tasks, it yielded a cross-validation AUC greater than or equal to 0.95 (Fig. 3A). Furthermore, both the cross-validation sensitivity and specificity median values were 87% (Supplemental Fig. 1). This demonstrates the model's ability to learn discriminative information for accurate patient classification in this synthetic setting.

In half the experiments, for more than 94% of the true-positive cases the explanation tool assigned the highest importance to a lesion with a high radiomic signature value (Fig. 3B; Supplemental Fig. 2A). For 997 experiments of 1,000, the number of these consistently explained cases was significant against a random ranking of lesions (false discovery rate controlled at level 0.001; Supplemental Fig. 3). In 50% of the experiments, for more than 73% of the true-positive cases the explanation tool ranked all the lesions with a high signature value above any lesion with a low signature value (Fig. 3C; Supplemental Fig. 2B).

Survival Task

The aggregative model outperformed the primary model for both C-index and tAUC metrics (mean tAUC primary [±SD], 0.55 ± 0.04; mean tAUC aggregative, 0.66 ± 0.02) (Fig. 4A). The

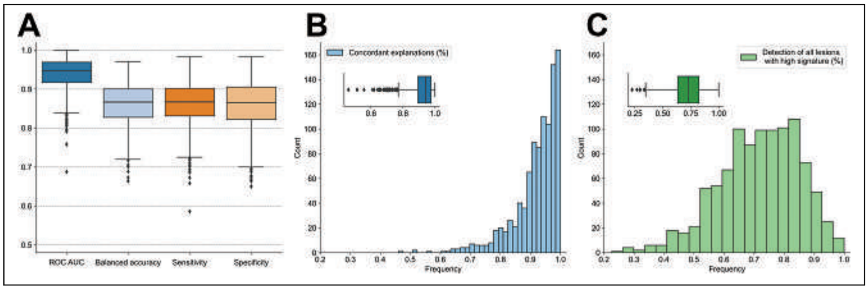

FIGURE 3. (A) Box plots of performance of logistic regression model trained and tested with stratified 5-fold cross-validation scheme across 1,000 synthetic tasks. (B) Distribution across 1,000 tasks of frequency of true-positive cases for which RadShap provided explanation aligned with synthetic data generation process, ranking lesion with high radiomic signature value as most impactful lesion. (C) Distribution across 1,000 tasks of frequency of true-positive cases for which RadShap ranked all lesions with high signature value above any lesion with low signature value.

difference in C-index between the primary and aggregative models was statistically significant in 60 of 100 repetitions of the cross-validation scheme, after correction of *P* values for multiple testing using the Benjamini–Hochberg method (false discovery rate controlled at level 0.05) (Supplemental Fig. 4). Additionally, Kaplan–Meier analysis demonstrated that predictions of the aggregative model, obtained from the test sets of a cross-validation scheme, resulted in better risk stratification than did predictions of the primary model, obtained from the same cross-validation scheme, as measured by the log-rank test *P* values (Fig. 4B).

The RadShap tool offered explanations consistent with our understanding of the aggregative model, which combines total metabolic tumor volume and standardized D_{max}. Specifically, for each patient in a test set of the cross-validation scheme, RadShap ranked lesions on the basis of their influence on the aggregative model's prediction, correctly identifying large and distant lesions as the most impactful for high-risk predictions (Fig. 4C).

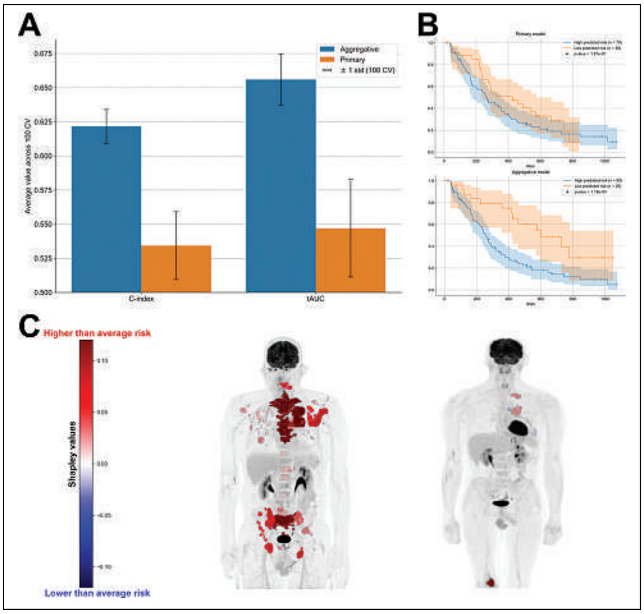

FIGURE 4. (A) Comparison of performance between primary and aggregative survival models for predicting PFS. (B) Kaplan–Meier survival curves for group of patients with high-risk predictions and group of patients with low-risk predictions for both primary (top) and aggregative (bottom) models. Predictions were collected from test sets of cross-validation scheme, and thresholds to define high- and low-risk groups were selected to maximize log-rank statistic. (C) Shapley values for explaining high-risk predictions made by aggregative model for 2 patients with high predicted risk, displayed on maximum-intensity projection of each [^{18}F]FDG PET scan.

Classification Task

The maximum values of the 10 radiomic features across all segmented lesions consistently yielded the highest average classification performance for the 100 cross-validation schemes. This approach outperformed the model trained on features extracted from only the biopsied tumor for all figures of merit (Fig. 5; Supplemental Fig. 5). Although the increase in AUC was not significant with paired permutation tests (Supplemental Fig. 6), the observed improvements still motivate the use of our explanation tool to gain insights into the complementary information leveraged by the aggregative model.

In the test sets, predictions differed between the biopsy and the aggregative model for 28 patients of 117. Among those, the aggregative model correctly classified 18 of 28 patients (64%). For patients diagnosed with adenocarcinoma (15/18), the explanation tool consistently highlighted that the biopsied tumor influenced the model's prediction toward a nonadenocarcinoma subtype (or had no influence in 1 case), whereas at least 1 metastasis directed it toward an adenocarcinoma. This observation confirmed that the sensitivity of the aggregative model was increased by the integration of information beyond the biopsied tumor. Our tool unveiled such information, prompting further exploration to determine whether the highlighted metastatic patterns are indeed related to adenocarcinoma (Fig. 6). Lastly, for the 3 patients for whom the aggregative model, unlike the biopsy model, correctly identified a nonadenocarcinoma subtype, the biopsied lesion influenced the model's prediction toward the correct subtype in 2 cases. This observation suggests that the aggregative model did not retain the same information as the primary model, leading to distinct considerations for certain biopsied tumors.

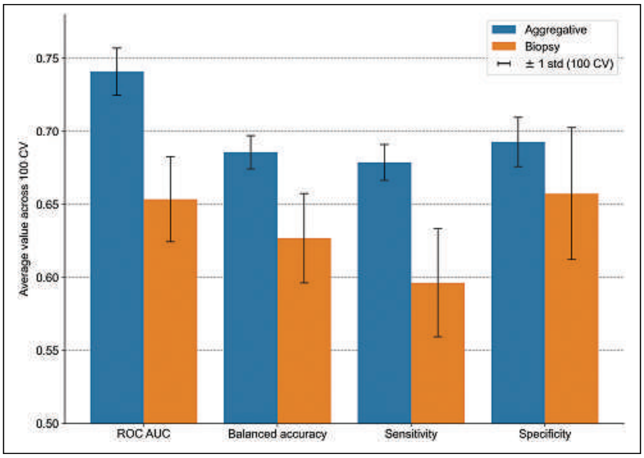

FIGURE 5. Comparison of classification performance between biopsy and aggregative classification models for prediction of lung cancer subtype. CV = cross-validation; ROC AUC = area under receiver operating characteristic curve.

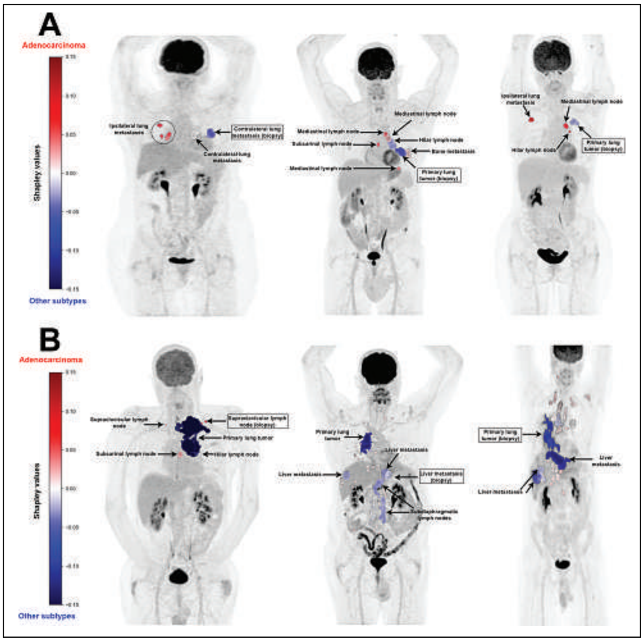

FIGURE 6. Shapley values for explaining correct prediction made by aggregative model, displayed on maximum-intensity projection of each [^{18}F]FDG PET scan. (A) Shapley values for 3 patients diagnosed with adenocarcinoma who were correctly classified by aggregative model and misclassified by biopsy model. (B) Shapley values for 3 patients diagnosed with nonadenocarcinoma subtype who were correctly classified by aggregative model and misclassified by biopsy model.

DISCUSSION

Many radiomic studies now use explanation tools to gain insight into the behavior of their predictive models (*16*). However, new approaches that involve combining multiple regions within an image to comprehensively characterize patient phenotypes and thereby build powerful predictors still lack well-suited explanation tools. Tools capable of highlighting the most impactful regions within an image hold great interest, as they could help in deciphering the information learned by predictive models, detecting potential biases (e.g., a region with no clear medical relevance is consistently highlighted across patients), or providing valuable medical insights (e.g., within all the metastases of a patient, a subset is identified as strongly associated with the prediction of the patient's outcome). Some studies proposed strategies, such as using attention weights (*17*), to assess the contribution of individual regions to a prediction, but these methods were closely tied to the developed predictive model. In this study, we introduced a novel model- and modality-agnostic tool to explain the outputs of multiregion radiomic models by highlighting the impact of each individual region on the model prediction.

The RadShap explanation tool was first validated with 1,000 synthetic classification tasks. In each task, a binary label was assigned to each patient within a cohort of 130 metastatic NSCLC cases, based on the presence of lesions with a high value of a randomly defined radiomic signature. Subsequently, a model, blinded to the data generation process, was trained to predict the binary label from radiomic features aggregated at the patient level. As expected, across the 1,000 tasks, most of the models were able to accurately classify patients and learn the underlying label generation process. RadShap successfully provided explanations well aligned with the ground truth, highlighting the pivotal role of lesions with a high signature value and, consequently, retrieving the label generation process learned by the models.

We then applied RadShap to the prediction of PFS for metastatic patients undergoing first-line immunotherapy and the classification of their histologic subtype, using their baseline [^{18}F]FDG PET scan. Cross-validation experiments demonstrated an increase in performance for both survival and classification tasks when aggregating information from all lesions of each patient, compared with radiomic models relying solely on a single lesion—either the primary tumor for the survival task or the biopsied lesion for the classification task. For the survival task, a model combining total metabolic tumor volume and standardized D_{max} significantly outperformed a model based on the primary tumor only, thus confirming the promising predictive and prognostic value of these 2 aggregated features for metastatic NSCLC (*18,19*). The RadShap explanations offered valuable insights into understanding the behavior of the aggregative models and their differences with the single-lesion models. Specifically, for the classification task, it highlighted that for most patients correctly classified by the aggregative model and misclassified by the biopsy model, information from the biopsied tumor influenced the aggregative model toward an incorrect prediction, whereas information from other lesions guided it toward the correct prediction.

We implemented RadShap in a user-friendly Python package and made it available for the radiomic community. It is applicable to any radiomic models that aggregate information from multiple regions as input, with the most appropriate setting being when all the regions are optional with the aggregation function (as described in the Materials and Methods section). Furthermore, RadShap is a fast-running tool, as it applies to an already trained radiomic model and uses only its prediction function; there is no need to retrain the model. RadShap explanations are grounded in the robust theoretic background of the Shapley values. In contrast to several explanation methods, such as SHAP (*7*), in the standard setting (i.e., when the ROIs are optional), there is no need to approximate the effect of removing an ROI from the predictive model to compute its marginal contribution.

The use of RadShap requires some Python coding skills, especially for defining custom aggregation functions. However, Python is a widely used programming language within the radiomic community for developing machine learning models. Additionally, like other explanation tools, RadShap offers no guarantee regarding the validity of the information that the model learned. Its application should be coupled with rigorous validation experiments to evaluate the robustness and generalization ability of the model. Finally, making sense of the impactful regions highlighted by RadShap is not always straightforward. Leveraging medical expertise and conducting additional experiments can aid in formulating relevant hypotheses based on the RadShap explanations.

Our study had limitations. First, we worked with a limited number of samples in the real case applications. Therefore, the performance scores should be interpreted cautiously, although they were not the primary focus of this study. Additionally, the aggregative model used for the survival task could have been explained with human intuition alone. Nevertheless, this task demonstrated that RadShap's explanations aligned with human understanding in a real-world context and highlighted the potential benefits of multiregion radiomic models, thereby supporting the relevance of RadShap. Finally, whereas we provided supportive evidence for the utility of the tool in elucidating complex aggregated strategies, we did not explore its full potential across a wide range of real-world scenarios and models. We believe that such a comprehensive evaluation will naturally emerge as the community starts experimenting with it. This is why we have made substantial efforts to ensure that our tool is easily and freely accessible through a user-friendly Python package.

CONCLUSION

We developed and validated a tool, implemented as the Python package RadShap, to offer local explanations for decisions of radiomic models involving several regions of interest. It complements the existing explanation strategies, focusing on multiregion approaches, to improve the understanding of radiomic models. These efforts toward explainable radiomics might both facilitate the adoption of well-performing models and provide relevant medical insights.

DISCLOSURE

This work was supported by Fondation ARC (TIPIT project SIGNIT202001322) and the French national agency ANR as part of the "Investissements d'avenir" program, reference ANR-19-P3IA-0001 (PRAIRIE 3IA Institute). No other potential conflict of interest relevant to this article was reported.

KEY POINTS

QUESTION: Can we identify the ROIs within an image that most influence a radiomic model's prediction?

PERTINENT FINDINGS: Our explanation tool demonstrated a strong alignment with the ground truth for 1,000 synthetic tasks. It also provided relevant insights to understand multilesion radiomic models' behavior, highlighting the most impactful lesions for the classification of the NSCLC subtype or the prediction of PFS.

IMPLICATIONS FOR PATIENT CARE: RadShap may improve the understanding of well-performing radiomic models, thus fostering their adoption in clinical practice.

REFERENCES

1. Lambin P, Rios-Velazquez E, Leijenaar R, et al. Radiomics: extracting more information from medical images using advanced feature analysis. *Eur J Cancer.* 2012; 48:441–446.
2. Yu K, Zhang Y, Yu Y, et al. Radiomic analysis in prediction of human papilloma virus status. *Clin Transl Radiat Oncol.* 2017;7:49–54.
3. Eertink JJ, Zwezerijnen GJC, Cysouw MCF, et al. Comparing lesion and feature selections to predict progression in newly diagnosed DLBCL patients with FDG PET/CT radiomics features. *Eur J Nucl Med Mol Imaging.* 2022;49:4642–4651.
4. Qiu HZ, Zhang X, Liu SL, et al. M1 stage subdivisions based on ^{18}F-FDG PET-CT parameters to identify locoregional radiotherapy for metastatic nasopharyngeal carcinoma. *Ther Adv Med Oncol.* 2022;14:17588359221118785.
5. Linardatos P, Papastefanopoulos V, Kotsiantis S, Explainable AI. A review of machine learning interpretability methods. *Entropy (Basel).* 2020;23:18.
6. Rozemberczki B, Watson L, Bayer P, et al. The Shapley value in machine learning. arXiv website. https://arxiv.org/abs/2202.05594. Published February 11, 2022. Revised May 26, 2022. Accessed May 30, 2024.
7. Lundberg SM, Lee SI. A unified approach to interpreting model predictions. arXiv website. https://arxiv.org/abs/1705.07874. Published May 22, 2017. Revised November 25, 2017. Accessed May 30, 2024.
8. Shapley LS. *A Value for N-Person Games.* RAND Corp.; 1953.
9. Kennedy T. *Monte Carlo Methods: A Special Topics Course.* University of Arizona; 2016.
10. Castro J, Gómez D, Tejada J. Polynomial calculation of the Shapley value based on sampling. *Comput Oper Res.* 2009; 36:1726–1730.
11. Nioche C, Orlhac F, Boughdad S, et al. LIFEx: a freeware for radiomic feature calculation in multimodality imaging to accelerate advances in the characterization of tumor heterogeneity. *Cancer Res.* 2018;78:4786–4789.
12. Zwanenburg A, Vallières M, Abdalah MA, et al. The Image Biomarker Standardization Initiative: standardized quantitative radiomics for high-throughput image-based phenotyping. *Radiology.* 2020;295:328–338.
13. van Griethuysen JJM, Fedorov A, Parmar C, et al. Computational radiomics system to decode the radiographic phenotype. *Cancer Res.* 2017;77:e104–e107.
14. Cottereau AS, Meignan M, Nioche C, et al. Risk stratification in diffuse large B-cell lymphoma using lesion dissemination and metabolic tumor burden calculated from baseline PET/CT. *Ann Oncol.* 2021;32:404–411.
15. Bandos AI, Rockette HE, Gur D. A permutation test sensitive to differences in areas for comparing ROC curves from a paired design. *Stat Med.* 2005;24:2873–2893.
16. de Vries BM, Zwezerijnen GJC, Burchell GL, van Velden FHP, Menke-van der Houven van Oordt CW, Boellaard R. Explainable artificial intelligence (XAI) in radiology and nuclear medicine: a literature review. *Front Med (Lausanne).* 2023;10:1180773.
17. Chen J, Zeng H, Zhang C, et al. Lung cancer diagnosis using deep attention-based multiple instance learning and radiomics. *Med Phys.* 2022;49:3134–3143.
18. Tan W, Zhang Y, Wang J, et al. FDG PET/CT tumor dissemination characteristic predicts the outcome of first-line systemic therapy in non-small cell lung cancer. *Acad Radiol.* 2023;30:2904–2912.
19. Seban RD, Assié JB, Giroux-Leprieur E, et al. Association of the metabolic score using baseline FDG-PET/CT and dNLR with immunotherapy outcomes in advanced NSCLC patients treated with first-line pembrolizumab. *Cancers (Basel).* 2020;12:2234.

Validation and Evaluation of a Vendor-Provided Head Motion Correction Algorithm on the uMI Panorama PET/CT System

Fei Kang*[1], Zhaojuan Xie*[1], Wenhui Ma*[1], Zhiyong Quan[1], Guiyu Li[1], Kun Guo[1], Xiang Li[1], Taoqi Ma[1], Weidong Yang[1], Yizhang Zhao[2], Hongyuan Yi[2], Yumo Zhao[2], Yihuan Lu[2], and Jing Wang[1]

[1]Department of Nuclear Medicine, Xijing Hospital, Fourth Military Medical University, Xi'an, China; and [2]United Imaging Healthcare, Shanghai, China

Brain PET imaging often faces challenges from head motion (HM), which can introduce artifacts and reduce image resolution, crucial in clinical settings for accurate treatment planning, diagnosis, and monitoring. United Imaging Healthcare has developed NeuroFocus, an HM correction (HMC) algorithm for the uMI Panorama PET/CT system, using a data-driven, statistics-based approach. The HMC algorithm automatically detects HM using a centroid-of-distribution technique, requiring no parameter adjustments. This study aimed to validate NeuroFocus and assess the prevalence of HM in clinical short-duration ^{18}F-FDG scans. **Methods:** The study involved 317 patients undergoing brain PET scans, divided into 2 groups: 15 for HMC validation and 302 for evaluation. Validation involved patients undergoing 2 consecutive 3-min single-bed-position brain ^{18}F-FDG scans—one with instructions to remain still and another with instructions to move substantially. The evaluation examined 302 clinical single-bed-position brain scans for patients with various neurologic diagnoses. Motion was categorized as small or large on the basis of a 5% SUV change in the frontal lobe after HMC. Percentage differences in $\mathrm{SUV}_{\mathrm{mean}}$ were reported across 11 brain regions. **Results:** The validation group displayed a large negative difference (−10.1%), with variation of 5.2% between no-HM and HM scans. After HMC, this difference decreased dramatically (−0.8%), with less variation (3.2%), indicating effective HMC application. In the evaluation group, 38 of 302 patients experienced large HM, showing a 10.9% ± 8.9% SUV increase after HMC, whereas most exhibited minimal uptake changes (0.1% ± 1.3%). The HMC algorithm not only enhanced the image resolution and contrast but also aided in disease identification and reduced the need for repeat scans, potentially optimizing clinical workflows. **Conclusion:** The study confirmed the effectiveness of NeuroFocus in managing HM in short clinical ^{18}F-FDG studies on the uMI Panorama PET/CT system. It found that approximately 12% of scans required HMC, establishing HMC as a reliable tool for clinical brain ^{18}F-FDG studies.

Key Words: PET; data-driven; head motion detection; head motion correction; COD; uMI Panorama

J Nucl Med 2024; 65:1313–1319
DOI: 10.2967/jnumed.124.267446

In brain PET imaging, head motion (HM) can lead to errors in uptake estimation and introduce artifacts, compromising diagnostic accuracy. For advanced scanners such as the uMI Panorama PET/CT (United Imaging Healthcare) (*1*), patient HM significantly hinders achieving the intended spatial resolutions, such as a full width at half maximum of under 3 mm. In clinical settings in which precise quantification is crucial for diagnosis, treatment planning, and response evaluation (*2*), HM undermines diagnostic confidence. Additionally, HM can cause misalignment between PET and CT images, resulting in attenuation mismatch artifacts and localization issues. In severe cases, substantial HM blurring may necessitate discarding the images and rescanning the patient.

Standard practices to minimize HM during scans include proper patient positioning, clear communication about the procedure, instructions to remain still, sedation, and HM monitoring. However, these measures may not suffice for patients who cannot voluntarily control HM, such as patients with parkinsonian disorders, cognitive impairment, dementia, brain tumors, or neuroinfectious diseases; young pediatric patients; and patients being scanned after trauma or neurosurgery. Therefore, a robust HM correction (HMC) algorithm is highly demanded in clinical practice.

Previous HMC approaches, such as frame-based image registration and hardware-based HM tracking, have their limitations (*3–9*). Frame-based image registration cannot correct for intraframe HM and attenuation mismatch artifacts. Although hardware-based HM tracking is more accurate and effective (*10*), its clinical application is hampered by the need to attach a tracking device to the patient, complicating the setup and impacting clinical workflow.

To address these issues, data-driven methods for HMC have emerged as promising alternatives. These techniques, including principal-component analysis (*11,12*) and centroid of distribution (COD) (*13,14*), estimate rigid HM using PET raw data, offering software-based solutions that integrate seamlessly into routine clinical workflows. A notable advancement is the NeuroFocus algorithm (United Imaging Healthcare), developed for the uMI Panorama PET/CT system, which is equipped with 189-ps time-of-flight resolution and a 35-cm axial field of view. This algorithm, based on a statistics-based method by Revilla et al. (*15*), detects HM without parameter tuning and differentiates HM-induced COD changes.

Received Feb. 17, 2024; revision accepted May 13, 2024.

For correspondence or reprints, contact Jing Wang (13909245902@163.com) or Fei Kang (fmmukf@qq.com).

*Contributed equally to this work.

This paper presents a 3-fold contribution, first validating the quantitative accuracy of NeuroFocus for the uMI Panorama PET/CT system, then demonstrating the algorithm's clinical efficacy in diagnosing brain disorders, and finally reporting the frequency and magnitude of HM for the clinical ^{18}F-FDG brain studies in this paper. The validation involved a prospective study with 15 volunteers performing instructed HM during PET scans, followed by the application of NeuroFocus on a large clinical cohort of 302 retrospective brain ^{18}F-FDG studies. This study is the first to apply an HMC algorithm to a large clinical cohort with short-duration PET acquisitions.

MATERIALS AND METHODS

Validation Study Data Acquisition

Fifteen volunteers were enlisted for the prospective validation study, each undergoing a 3-min single-bed-position ^{18}F-FDG brain scan (52.2 ± 9.2 min after injection) while instructed to remain still (no HM [NoMo]), followed by another 3-min scan with instructions for substantial translational and rotational HM (instructed HM [InstrMo]). A CT scan for attenuation correction preceded each PET scan. Additionally, T1-weighted, contrast-enhanced T1-weighted, and T2-weighted MR images were acquired for each subject on the same day. The study was approved by the Ethics Committee of the Medical University of Xijing Hospital, Xi'an, China (approval KY-20212145-F-1), which conformed with the revised Declaration of Helsinki (1964). Written informed consent was obtained from all participants.

Evaluation Study Data Acquisition

The algorithm's clinical efficacy was evaluated through a retrospective analysis of 302 clinical single-bed-position brain ^{18}F-FDG studies, each with a 3.0-min acquisition at 75.0 ± 19.9 min after injection. The studies were categorized as being acquired with no HMC (NMC) or with HMC. Each study included a CT scan for attenuation correction, but no MRI was performed. Detailed patient information is available in Table 1. The institutional review board approved the retrospective study with a waiver of informed consent.

HMC Algorithm

The HMC algorithm consists of 3 steps, that is, HM detection, estimation, and correction. To detect HM, a COD algorithm (*14*) was used. A COD trace was generated at 1 Hz. By estimating and separating the variation due to count statistics and HM on the COD trace, we could divide the entire study into consecutive HM-free frames (MFFs) separated by the detected HM time points (*15*). MFFs shorter than 5 s were discarded and excluded from subsequent processing. To estimate and correct the detected HM for MFFs, each MFF was first reconstructed using ordered-subset expectation maximization (OSEM) without attenuation correction. HM estimation was performed by rigidly registering other frames to the reference frame, that is, the first MFF in time. The mutual-information difference was used as the similarity metric. The first MFF was assumed to be aligned with the CT image in space, thus assuming that no HM occurred between the CT and PET acquisitions. The transformation matrix T(i) was used to denote the estimate for the ith MFF. To generate a matched attenuation map for the ith MFF, the CT attenuation map was transformed using the inverse of T(i). Subsequently, OSEM (3 iterations × 10 subsets) with attenuation correction was then performed for each MFF using the aligned attenuation map. After reconstruction, the images using OSEM with attenuation correction for all MFFs were transformed back to the reference MFF space using T and were summed to generate the final HMC image. A voxel size of 1.20 × 1.20 × 1.45 mm was used for all reconstructions.

TABLE 1
Patient Information for Validation and Evaluation Datasets

Parameter	Validation (with MRI)	Evaluation (without MRI)
Total participants (*n*)	15	302
Mean age ± SD (y)	34.1 ± 13.1	58.2 ± 14.4
Male (*n*)	6	171
Female (*n*)	9	131

Evaluation

For the validation dataset, FreeSurfer (*16,17*) segmented paired T1-weighted MR images into 109 brain regions of interest (ROIs), which were then resliced to individual PET spaces and were merged into 11 gray matter (GM) regions: amygdala, caudate, cerebellum cortex, frontal lobe, hippocampus, insula, occipital lobe, parietal lobe, putamen, temporal lobe, and thalamus. SUV_{mean} percentage differences between InstrMo and NoMo scans, and between InstrMo with HMC and NoMo, were reported for each GM region.

For the evaluation dataset, brain ROIs were generated via an in-house CT-based segmentation algorithm. After rigid and nonrigid registration with the Montreal Neurological Institute brain MRI template, 116 automated anatomic labeling brain ROIs were warped to individual CT spaces. Cerebellum uptake and SUV_{mean} ratio images were calculated, with a threshold applied to generate a binary GM mask. The cerebellum ROI was used to calculate the cerebellum uptake on the reference frame (first MFF in time) using OSEM with attenuation correction. Additionally, the SUV_{mean} ratio image of the reference frame was calculated using cerebellum uptake as the reference value.

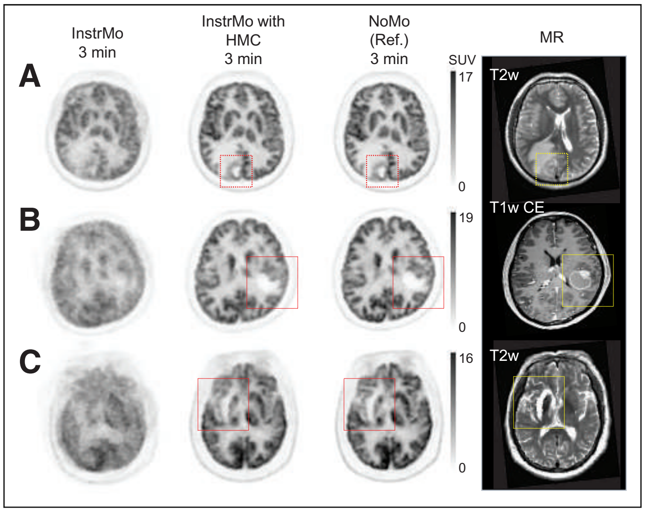

FIGURE 1. PET and MR images from 3 distinct cases in validation study, comparing InstrMo, HMC, and NoMo. (A) Annular hypermetabolic cerebral syphilitic gumma with surrounding edema in right parietooccipital lobe. (B) Hypermetabolic nodules on PET aligning with nodular wall thickening in cystic-appearing lesion observed on MRI associated with brain metastases from small cell lung cancer. (C) Encephalomalacia and gliosis of right basal ganglia and right temporal lobe and mild *ex vacuo* dilatation of right lateral ventricle in geriatric patient with history of right middle cerebral artery territory infarction. Averaged and maximal HM distance of frontal lobe are 8.5 and 26.3 mm (A), 9.5 and 17.3 mm (B), and 19.0 and 54.2 mm (C), respectively. Injected dose, postinjection time, duration, and body weight are 273.8 MBq, 56.1 min, 3 min, and 69 kg (A); 214.6 MBq, 65.6 min, 3 min, and 56 kg (B); and 270.1 MBq, 67.8 min, 3 min, and 70 kg (C), respectively. T1w CE = T1-weighted contrast-enhanced; T2w = T2-weighted.

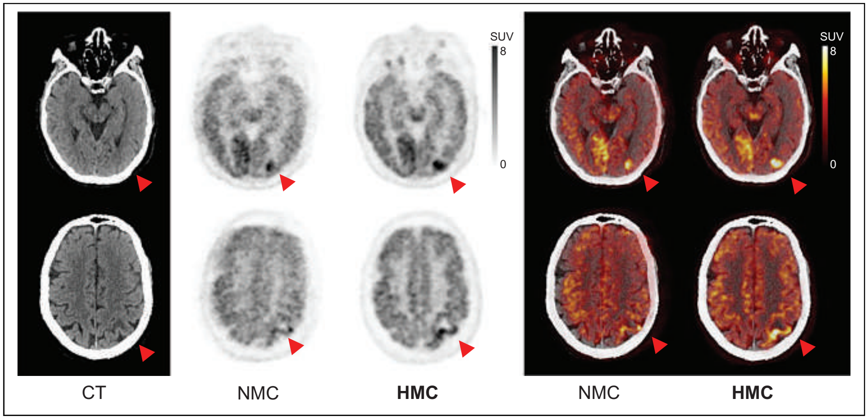

FIGURE 2. CT, PET, and PET/CT with HM before and after HMC in case of angioimmunoblastic T-cell lymphoma with suspected cerebral infiltration due to acute onset of neurologic symptoms. HM blur and misregistration were corrected after HMC. Areas of annular hypermetabolism with central hypometabolism in left parietal lobe (arrowheads) were revealed after HMC. Injected dose was 251.6 MBq, postinjection time was 90 min, frame duration was 3 min at single bed position, and body weight was 65 kg. Averaged and maximal HM distance of frontal lobe was 10.9 and 18.8 mm, respectively.

A threshold of 1.0 was applied to the SUV_{mean} ratio image to generate a binary GM mask. The intersecting areas between this mask and the 116 ROIs resulted in refined GM ROIs, which were further merged into 11 GM regions according to the automated anatomic labeling definition (*18*). Supplemental Figure 1 illustrates this ROI generation process (supplemental materials are available at http://jnm.snmjournals.org).

To quantify HM amplitude, the HM distance of each ROI was estimated using image registration. The HM distances of all 116 ROIs for different MFFs were computed first and then averaged per minute. The final HM amplitude for the composite 11 GM ROIs was determined as the average HM distances of the merged sub-ROIs. The maximal HM distance for each case study was also reported.

RESULTS

Prospective Validation Study

In Figure 1, 3 cases from the validation study are shown. Overall, InstrMo images displayed substantial HM-introduced image blur. However, after HMC, these images exhibited marked improvements in both contrast and resolution, closely resembling the NoMo studies. Additionally, the accompanying MR images provided a clear visualization of anatomic structures corresponding to the NoMo studies. Detailed clinical diagnoses for these 3 cases are provided in the caption of Figure 1.

Figure 2 presents a patient from the evaluation study diagnosed with angioimmunoblastic T-cell lymphoma. This figure includes 2 axial slices each from the CT, NMC, and HMC images. Notably, the HMC images revealed areas of annular hypermetabolism with central hypometabolism in the left parietal lobe. These areas were largely obscured and indistinct in the NMC images because of the blurring effects of HM.

In Figure 3, a case is shown in which focal hypometabolism in the left thalamic and basal ganglia regions was evident in the HMC image. Conversely, in the NMC image, extensive HM obscured these regions of hypometabolic activity, rendering them invisible.

Numeric analysis of the 15 validation studies is provided in Table 2, showcasing the SUV_{mean} percentage error results for each ROI. The InstrMo scans generally yielded substantial negative differences (−10%), with large variation across different brain regions when compared with the NoMo scans. For instance, the frontal region exhibited a larger discrepancy (−16%) than did the amygdala. The results after HMC showed much smaller differences (∼−1%), with a notably reduced variation (3%), indicating effective compensation for HM in all validation studies.

Retrospective Evaluation Study

Figure 4 illustrates 2 clinical evaluation studies involving patients with suspected nervous system lymphoma and thalamic lacunar infarction. During the initial PET scans, large HM was detected, prompting the technician to recall the patients for rescanning. Both patients remained still during these subsequent scans. Remarkably, the HMC applied to the initial scans produced images comparable to the rescans, effectively demonstrating the clinical utility of HMC in reducing the need for additional scans due to HM.

Figure 5 features a non–small cell lung cancer patient who exhibited large involuntary HM during both the initial scan and the rescan. The images from these scans without HMC were unsuitable for clinical diagnosis. However, after the application of HMC, both sets of scans showed substantial improvements in resolution and contrast. The images revealed hypometabolic edema surrounding a potential brain metastasis, visible only after HMC application.

For the evaluation studies, Table 3 presents the numeric results of SUV_{mean} changes across different brain regions after HMC. Participants were divided into 2

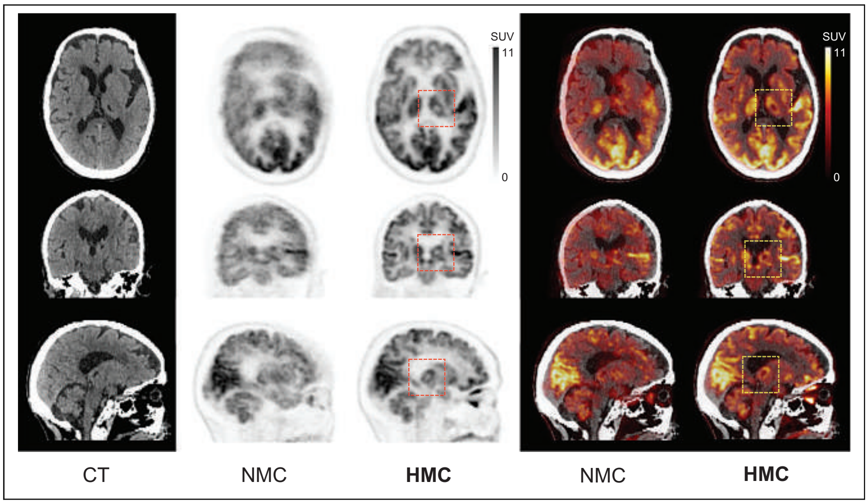

FIGURE 3. CT, PET, and PET/CT with HM before and after HMC in case of focal hypometabolism observed in left thalamic and basal ganglia region after HMC. Injected dose was 229.4 MBq, postinjection time was 69 min, frame duration was 3 min, and body weight was 48 kg. Averaged and maximal HM distance of frontal lobe was 13.7 and 25.4 mm, respectively.

TABLE 2
Percentage Error in SUV_{mean} in Validation Study as Compared with NoMo Study

ROI	NoMo SUV_{mean}	Percentage error: InstrMo	Percentage error: InstrMo with HMC
Amygdala	4.4 ± 0.5	−4.3 ± 4.7	−0.1 ± 1.8
Caudate	6.6 ± 1.2	−14.9 ± 8.4	−2.8 ± 5.4
Cerebellum	5.6 ± 0.8	−5.6 ± 3.2	−2.2 ± 1.5
Frontal lobe	6.8 ± 0.9	−16.3 ± 5.3	−1.0 ± 3.8
Hippocampus	4.9 ± 0.7	−2.4 ± 5.3	0.7 ± 4.4
Insula	5.6 ± 0.7	−5.0 ± 3.6	−0.2 ± 2.8
Occipital lobe	7.9 ± 1.1	−13.9 ± 3.7	−3.1 ± 4.2
Parietal lobe	6.6 ± 0.9	−14.1 ± 4.7	0.5 ± 3.6
Putamen	7.3 ± 1.3	−12.1 ± 7.7	−0.3 ± 2.2
Temporal lobe	6.0 ± 0.7	−11.3 ± 5.8	−0.1 ± 3.7
Thalamus	6.4 ± 0.9	−11.1 ± 4.8	−0.2 ± 1.4
Mean average	6.2	−10.1	−0.8
SD average	0.9	5.2	3.2

groups based on the extent of HM: small HM and large HM. This categorization used a 5% threshold in SUV_{mean} change in the frontal lobe after HMC application. In the small-HM category, the mean HM distance was relatively consistent across all brain regions (2.4 mm), with low variability (1.9 mm). Conversely, in the large-HM group, the mean HM distances increased for all ROIs, ranging from 7.3 mm in the cerebellum to 15.0 mm in the frontal region, with a notable increase in both the mean average and variation (10.9 ± 5.9 mm).

Of the 302 participants, 38 experienced large HM, resulting in an average SUV increase of 11% after HMC, whereas the rest showed a minimal uptake increase (0.1%). As depicted in Figure 6, the SUV_{mean} change in the large-HM group was significantly higher than in the small-HM group. The caudate region displayed the most substantial SUV increase, whereas the cerebellum showed the least. Consistent with expectations, Figure 7 reveals that HM

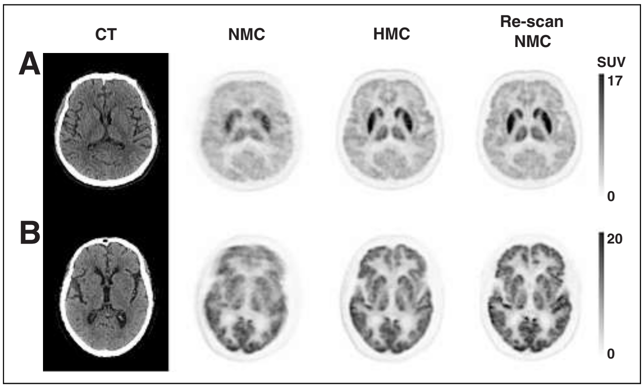

FIGURE 4. Comparison between PET with NMC, PET with HMC, and PET rescan with minimal HM. (A) Bilateral hypermetabolism in thalami and striatum in patient with suspected nervous system lymphoma. Injected dose was 266.4 MBq, postinjection time was 71 min, frame duration was 3 min, and body weight was 65 kg. (B) Hypometabolic foci in left thalamus indicating lacunar infarcts. Both HMC images are comparable to rescan images. Injected dose was 366.3 MBq, postinjection time was 66 min, frame duration was 3 min, and body weight was 80 kg. Averaged and maximal HM distance of frontal lobe was 9.6 and 47.2 mm (A) and 10.0 and 16.0 mm (B), respectively.

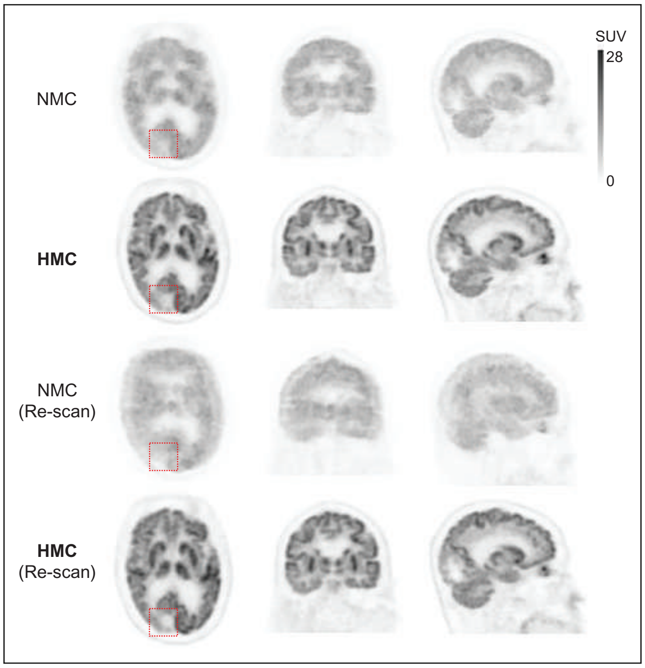

FIGURE 5. Images corrupted by involuntary HM in both initial PET scan and rescan with NMC. Spatial resolution and contrast were significantly improved after HMC. Dotted box indicates region of hypometabolic edema surrounding suspected metastatic lesion in occipital lobe in patient whose non–small cell lung cancer was revealed after HMC. Injected dose was 314.5 MBq; postinjection first scan and rescan were at 61 and 69 min, respectively; frame duration was 3 min; and body weight was 77 kg. Averaged and maximal HM distance of frontal lobe was 5.0 and 12.6 mm (first scan) and 12.1 and 27.7 mm (rescan), respectively.

TABLE 3

SUV$_{mean}$ Change from NMC after HMC for Evaluation Study and Mean HM Distance for Each Brain Region

ROI	Small HM (n = 264)		Large HM (n = 38)	
	Mean HM distance (mm)	SUV$_{mean}$ change (%)	Mean HM distance (mm)	SUV$_{mean}$ change (%)
Amygdala	2.5 ± 1.9	0.4 ± 2.6	11.8 ± 6.3	19.9 ± 20.8
Caudate	2.6 ± 2.0	0.6 ± 2.6	12.7 ± 7.0	22.9 ± 13.7
Cerebellum	2.1 ± 1.7	−0.2 ± 0.7	7.3 ± 3.9	2.9 ± 3.7
Frontal	2.9 ± 2.0	0.3 ± 1.3	15.0 ± 8.1	12.9 ± 8.3
Hippocampus	2.3 ± 1.8	−0.3 ± 1.4	10.1 ± 5.3	10.6 ± 9.0
Insula	2.6 ± 1.9	0.1 ± 1.1	13.0 ± 7.0	10.0 ± 6.2
Occipital lobe	2.2 ± 1.7	−0.2 ± 0.7	6.7 ± 4.4	2.9 ± 3.9
Parietal lobe	2.4 ± 1.8	−0.0 ± 0.8	9.5 ± 5.2	6.8 ± 6.0
Putamen	2.5 ± 1.9	0.3 ± 1.3	12.4 ± 6.7	12.2 ± 10.4
Temporal lobe	2.5 ± 1.8	0.1 ± 1.0	11.8 ± 6.2	10.0 ± 8.1
Thalamus	2.2 ± 1.8	−0.1 ± 0.8	9.9 ± 5.3	8.2 ± 7.8
Mean average	2.4	0.1	10.9	10.9
SD average	1.9	1.3	5.9	8.9

Data are mean ± SD.

amplitude escalated over the course of the scan. For instance, in the large-HM category, the frontal lobe showed increasing HM amplitudes of 2, 5.2, and 7.6 mm at 0–1, 1–2, and 2–3 min into the scan, respectively.

DISCUSSION

In this study, we conducted both a prospective validation and a retrospective evaluation of an HMC algorithm provided by the uMI Panorama PET/CT scanner. The prospective validation included 15 studies in which participants were instructed to perform HM, and for the retrospective evaluation, 302 clinical brain studies using ^{18}F-FDG with a duration of 3 min each were analyzed. Results from the validation study indicated that the HMC algorithm was highly effective, with an average quantitative discrepancy of less than 1% compared with scans without HM. In the retrospective evaluation, it was found that approximately 12% (38/302) of the clinical brain studies exhibited large HM, necessitating the use of HMC. The clinical utility of the HMC algorithm was demonstrated across a variety of brain diseases and clinical scenarios, underscoring its effectiveness in real-world applications. Regarding the efficiency of the HMC, that is, reconstruction time, for the InstrMo studies, it took 11.0 ± 1.1 min to perform the reconstruction using the reconstruction console. All the reconstructions were submitted after the acquisition was finished. For all the evaluation studies, 2.0 ± 9.7 s of data were rejected for each case.

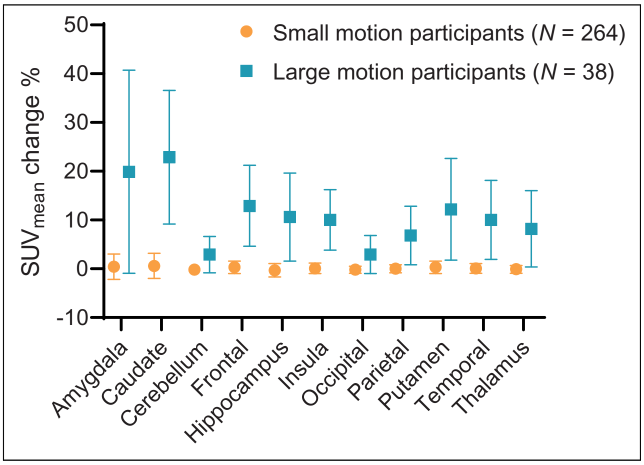

FIGURE 6. In evaluation studies, SUV$_{mean}$ change at all regions for large-HM group was substantially larger than for small-HM group.

The European Association of Nuclear Medicine guidelines (*19*) emphasize the importance of neurologic PET imaging for diagnosing cognitive and movement disorders, localizing epileptic foci, detecting neuroinfections such as encephalitis and meningitis, and assessing brain tumors. The guidelines recommend using small-voxel reconstructions to enhance the visualization of brain structures, a method that typically requires longer acquisition times to maintain adequate signal-to-noise ratios. For routine ^{18}F-FDG brain scans using a scanner with a short axial field of view, the guidelines suggest acquisition times of 10–15 min per bed position. Non–^{18}F-FDG imaging may necessitate even longer times, up to 20–30 min per bed position (*19*). However, in our study using the uMI Panorama scanner (*1*), known for its high sensitivity, we completed each clinical scan in just 3 min while preserving sufficient image quality for diagnostic purposes. Notably, within these brief scans, 12% of patients exhibited substantial HM, indicating a potential increase in the need for HMC in longer scans.

The introduction of HMC to PET imaging has significantly improved image quality and brought practical benefits. HMC reduces the need for rescans, decreasing patient waiting times and enhancing comfort by minimizing additional radiation exposure from repeated CT scans. This reduction in rescans also streamlines patient scheduling and workflows, ensuring that appointments run

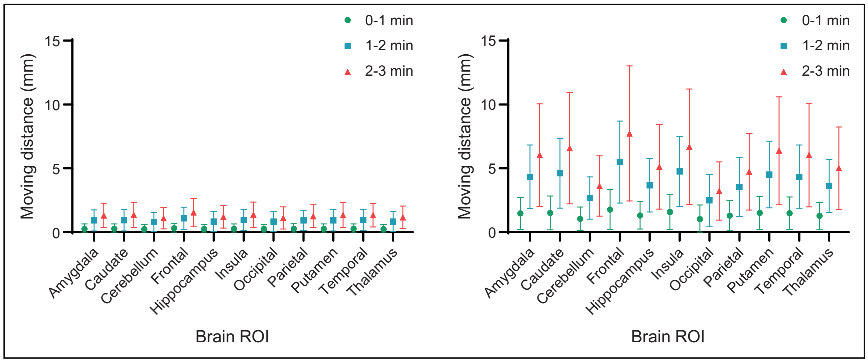

FIGURE 7. Brain-averaged HM distance across evaluation studies. (Left) Participants ($n = 268$) with small HM amplitude. (Right) Participants ($n = 38$) with large HM amplitude. Averaged HM distances are shown along with time course, that is, 0–1, 1–2, and 2–3 min into PET scan.

on time, reducing health care providers' workloads, and allowing for more efficient resource and time management. Additionally, HMC is particularly advantageous for patients who have difficulty remaining still during scans, reducing the need for tight head restraints or sedation and improving patient comfort. The benefits are not only to patients but also to the scanning process, simplifying it and reducing complications from patient HM, ultimately increasing clinical work efficiency.

This paper reviews several significant research efforts in HMC for PET imaging, comparing them with the proposed data-driven method. An alternative approach involves markerless HM tracking using an optical camera, as used by Spangler-Bickell et al. (*20*), who applied an optical camera attached to the head coil of a PET/MRI system, tracking HM with a large, curved marker on the patient's forehead. Zeng et al. (*21*) evaluated a markerless, hardware-based device using stereovision cameras with infrared structured light to capture the patient's facial surface and create an HM-tracking point cloud. Similar techniques were explored by Olesen et al. and Kyme et al. (*22,23*). However, these methods may be compromised by nonrigid facial movements and lack full validation. Another strategy used the Kinect system (*24*) by Microsoft for monitoring and tracking HM. More recently, Zeng et al. (*25*) investigated neural networks to predict HM between short frames to expedite HM estimation, though this requires further development for adequate correction accuracy. Additionally, 2 other groups (*26,27*) focused on deep learning methods to enhance PET image quality by synthesizing high-count PET images from low-count images, improving registration accuracy. Rezaei et al. (*28*) proposed computing inertia tensors from time-of-flight back projections for direct estimation of rigid HM parameters. Each method provides a unique perspective and potential solution for addressing HMC challenges in PET brain imaging, underscoring the ongoing and varied research in this critical field.

In concluding our analysis, we acknowledge certain limitations of the current HMC algorithm: its limited applicability to dynamic PET studies, as it is not designed for scenarios requiring tracking of physiologic changes over time; the inability to correct for HM between PET and CT acquisitions, which can result in attenuation mismatch artifacts; and the inability to correct continuous HM, such as tremors in patients with Parkinson disease, because of its frame-based nature. These limitations underscore the need for ongoing improvements and innovation in HMC technology to enhance the accuracy and utility of PET imaging.

CONCLUSION

We conducted a clinical study with 15 participants using ^{18}F-FDG to evaluate the accuracy of the NeuroFocus HMC algorithm for the uMI Panorama PET/CT system. In our validation tests, which included InstrMo, the SUV error after HMC was minimal, averaging −1% ± 3% across all brain ROIs and participants. This was a significant improvement from the −10% ± 5% error observed before applying HMC. In a broader evaluation involving 302 participants, approximately 12% of the short-duration (3-min) clinical brain scans showed substantial HM that required correction. The HMC algorithm effectively corrected HM across various brain diseases, confirming its suitability for clinical brain ^{18}F-FDG studies.

DISCLOSURE

Funding was provided by the National Natural Science Foundation of China (92259304 and 82122033), the Key Program of the Ministry of Industry and Information Technology of the People's Republic of China (CEIEC-2022-ZM02-0219), and the Shaanxi Province Key Industry Innovation Chain (2022ZDLSF04-12). No other potential conflict of interest relevant to this article was reported.

ACKNOWLEDGMENTS

We extend our gratitude to Chen Xi, Yue Li, Hao Liu, and Lei Shi for supporting NeuroFocus software and data acquisition. Special thanks are due to Enette Mae Revilla and Duo Zhang for manuscript editing. We also thank Bingbing Zhao, Wenjun Yu, and Fenggang Jia for their support with the image processing software.

KEY POINTS

QUESTION: What is the clinical efficacy of the vendor-provided HMC algorithm NeuroFocus for the uMI Panorama PET/CT system, and what is the prevalence of HM in clinical ^{18}F-FDG studies?

PERTINENT FINDINGS: In short-duration (3-min) clinical brain ^{18}F-FDG studies, approximately 12% of patients experienced substantial HM that necessitated the use of HMC. NeuroFocus effectively corrected for HM, and its accuracy was deemed adequate for clinical applications.

IMPLICATIONS FOR PATIENT CARE: NeuroFocus has the potential to enhance the quality of brain PET images. It can reduce the clinical necessity for rescanning patients due to HM, thereby improving the patient experience and streamlining the diagnostic process.

REFERENCES

1. Li G, Ma W, Li X, et al. Performance evaluation of the uMI Panorama PET/CT system in accordance with the National Electrical Manufacturers Association NU 2-2018 standard. *J Nucl Med.* 2024;65:652–658.

2. Polycarpou I, Soultanidis G, Tsoumpas C. Synergistic motion compensation strategies for positron emission tomography when acquired simultaneously with magnetic resonance imaging. *Philos Trans A Math Phys Eng Sci.* 2021;379:20200207.
3. Rahmim A, Dinelle K, Cheng JC, et al. Accurate event-driven motion compensation in high-resolution PET incorporating scattered and random events. *IEEE Trans Med Imaging.* 2008;27:1018–1033.
4. Picard Y, Thompson CJ. Motion correction of PET images using multiple acquisition frames. *IEEE Trans Med Imaging.* 1997;16:137–144.
5. Montgomery AJ, Thielemans K, Mehta MA, Turkheimer F, Mustafovic S, Grasby PM. Correction of head movement on PET studies: comparison of methods. *J Nucl Med.* 2006;47:1936–1944.
6. Herzog H, Tellmann L, Fulton R, et al. Motion artifact reduction on parametric PET images of neuroreceptor binding. *J Nucl Med.* 2005;46:1059–1065.
7. Fulton RR, Meikle SR, Eberl S, Pfeiffer J, Constable C, Fulham MJ. Correction for head movements in positron emission tomography using an optical motion tracking system. In: *2000 IEEE Nuclear Science Symposium. Conference Record (Cat. No.00CH37149)*. IEEE. 2000;3:17/58–17/62.
8. Costes N, Dagher A, Larcher K, Evans AC, Collins DL, Reilhac A. Motion correction of multi-frame PET data in neuroreceptor mapping: simulation based validation. *Neuroimage.* 2009;47:1496–1505.
9. Bloomfield PM, Spinks TJ, Reed J, et al. The design and implementation of a motion correction scheme for neurological PET. *Phys Med Biol.* 2003;48:959–978.
10. Carson RE, Barker WC, Liow JS, Johnson CA. Design of a motion-compensation OSEM list-mode algorithm for resolution-recovery reconstruction for the HRRT. In: *2003 IEEE Nuclear Science Symposium.* IEEE; 2004:3281–3285.
11. Thielemans K, Schleyer PJ, Dunn JT, Marsden PK, Manjeshwar RM. Using PCA to detect head motion from pet list mode data. In: *2013 IEEE Nuclear Science Symposium and Medical Imaging Conference*. IEEE; 2013:1–5.
12. Schleyer PJ, Dunn JT, Reeves S, Brownings S, Marsden PK, Thielemans K. Detecting and estimating head motion in brain PET acquisitions using raw time-of-flight PET data. *Phys Med Biol.* 2015;60:6441–6458.
13. Lu Y, Naganawa M, Toyonaga T, et al. Data-driven motion detection and event-by-event correction for brain PET: comparison with Vicra. *J Nucl Med.* 2020;61:1397–1403.
14. Lu Y, Gallezot JD, Naganawa M, et al. Data-driven voluntary body motion detection and non-rigid event-by-event correction for static and dynamic PET. *Phys Med Biol.* 2019;64:065002.
15. Revilla EM, Gallezot JD, Naganawa M, et al. Adaptive data-driven motion detection and optimized correction for brain PET. *Neuroimage.* 2022;252:119031.
16. Fischl B, van der Kouwe A, Destrieux C, et al. Automatically parcellating the human cerebral cortex. *Cereb Cortex.* 2004;14:11–22.
17. Fischl B, Salat DH, Busa E, et al. Whole brain segmentation: automated labeling of neuroanatomical structures in the human brain. *Neuron.* 2002;33:341–355.
18. Tzourio-Mazoyer N, Landeau B, Papathanassiou D, et al. Automated anatomical labeling of activations in SPM using a macroscopic anatomical parcellation of the MNI MRI single-subject brain. *Neuroimage.* 2002;15:273–289.
19. Guedj E, Varrone A, Boellaard R, et al. EANM procedure guidelines for brain PET imaging using [^{18}F]FDG, version 3. *Eur J Nucl Med Mol Imaging.* 2022;49:632–651.
20. Spangler-Bickell MG, Khalighi MM, Hoo C, et al. Rigid motion correction for brain PET/MR imaging using optical tracking. *IEEE Trans Radiat Plasma Med Sci.* 2019;3:498–503.
21. Zeng T, Lu Y, Jiang W, et al. Markerless head motion tracking and event-by-event correction in brain PET. *Phys Med Biol.* 2023;68:1397–1403.
22. Olesen OV, Sullivan JM, Mulnix T, et al. List-mode PET motion correction using markerless head tracking: proof-of-concept with scans of human subject. *IEEE Trans Med Imaging.* 2013;32:200–209.
23. Kyme AZ, Se S, Meikle SR, Fulton RR. Markerless motion estimation for motion-compensated clinical brain imaging. *Phys Med Biol.* 2018;63:105018.
24. Iwao Y, Akamatsu G, Tashima H, Takahashi M, Yamaya T. Brain PET motion correction using 3D face-shape model: the first clinical study. *Ann Nucl Med.* 2022;36:904–912.
25. Zeng T, Zhang J, Revilla E, et al. Supervised deep learning for head motion correction in PET. In: *Medical Imaging Computing and Computer Assisted Intervention–MICCAI 2022.* Springer; 2022:194–203.
26. Shiyam Sundar LK, Iommi D, Muzik O, et al. Conditional generative adversarial networks aided motion correction of dynamic ^{18}F-FDG PET brain studies. *J Nucl Med.* 2021;62:871–879.
27. Reimers E, Cheng J-C, Sossi V. Deep-learning-aided intraframe motion correction for low-count dynamic brain PET. In: *IEEE Transactions on Radiation and Plasma Medical Sciences*. IEEE; 2024:53–63.
28. Rezaei A, Spangler-Bickell M, Schramm G, Van Laere K, Nuyts J, Defrise M. Rigid motion tracking using moments of inertia in TOF-PET brain studies. *Phys Med Biol.* 2021;66:184001.

Performance Characteristics of the NeuroEXPLORER, a Next-Generation Human Brain PET/CT Imager

Hongdi Li[1], Ramsey D. Badawi[2], Simon R. Cherry[2], Kathryn Fontaine[3], Liuchun He[4], Shannan Henry[3], Ansel T. Hillmer[3], Lingzhi Hu[1], Nikkita Khattar[3], Edwin K. Leung[1,2], Tiantian Li[1,2], Yusheng Li[1], Chi Liu[3], Peng Liu[4], Zhenrui Lu[4], Stanislaw Majewski[2], David Matuskey[3], Evan D. Morris[3], Tim Mulnix[3], Negar Omidvari[2], Suranjana Samanta[1], Aaron Selfridge[1,2], Xishan Sun[1], Takuya Toyonaga[3], Tommaso Volpi[3], Tianyi Zeng[3], Terry Jones[2], Jinyi Qi[2], and Richard E. Carson[3]

[1]United Imaging Healthcare North America, Houston, Texas; [2]University of California, Davis, Davis, California; [3]Yale University, New Haven, Connecticut; and [4]United Imaging Healthcare, Shanghai, China

The collaboration of Yale, the University of California, Davis, and United Imaging Healthcare has successfully developed the NeuroEXPLORER, a dedicated human brain PET imager with high spatial resolution, high sensitivity, and a built-in 3-dimensional camera for markerless continuous motion tracking. It has high depth-of-interaction and time-of-flight resolutions, along with a 52.4-cm transverse field of view (FOV) and an extended axial FOV (49.5 cm) to enhance sensitivity. Here, we present the physical characterization, performance evaluation, and first human images of the NeuroEXPLORER. **Methods:** Measurements of spatial resolution, sensitivity, count rate performance, energy and timing resolution, and image quality were performed adhering to the National Electrical Manufacturers Association (NEMA) NU 2-2018 standard. The system's performance was demonstrated through imaging studies of the Hoffman 3-dimensional brain phantom and the mini-Derenzo phantom. Initial ^{18}F-FDG images from a healthy volunteer are presented. **Results:** With filtered backprojection reconstruction, the radial and tangential spatial resolutions (full width at half maximum) averaged 1.64, 2.06, and 2.51 mm, with axial resolutions of 2.73, 2.89, and 2.93 mm for radial offsets of 1, 10, and 20 cm, respectively. The average time-of-flight resolution was 236 ps, and the energy resolution was 10.5%. NEMA sensitivities were 46.0 and 47.6 kcps/MBq at the center and 10-cm offset, respectively. A sensitivity of 11.8% was achieved at the FOV center. The peak noise-equivalent count rate was 1.31 Mcps at 58.0 kBq/mL, and the scatter fraction at 5.3 kBq/mL was 36.5%. The maximum count rate error at the peak noise-equivalent count rate was less than 5%. At 3 iterations, the NEMA image-quality contrast recovery coefficients varied from 74.5% (10-mm sphere) to 92.6% (37-mm sphere), and background variability ranged from 3.1% to 1.4% at a contrast of 4.0:1. An example human brain ^{18}F-FDG image exhibited very high resolution, capturing intricate details in the cortex and subcortical structures. **Conclusion:** The NeuroEXPLORER offers high sensitivity and high spatial resolution. With its long axial length, it also enables high-quality spinal cord imaging and image-derived input functions from the carotid arteries. These performance enhancements will substantially broaden the range of human brain PET paradigms, protocols, and thereby clinical research applications.

Key Words: brain PET; NEMA; NeuroEXPLORER; DOI; high resolution

J Nucl Med 2024; 65:1320–1326
DOI: 10.2967/jnumed.124.267767

The use of brain PET in research has spanned more than 5 decades. PET has been shown to be a valuable tool for assessing changes in flow, metabolism, and receptor occupancy resulting from pharmacologic or cognitive stimulation. This accomplishment is made possible through the integration of PET imagers, quantitative reconstruction techniques, kinetic modeling, and targeted radiotracers, collectively enabling a broad range of quantitative approaches for studying pharmacologic and physiologic aspects of the brain (*1*). This powerful modality can also address basic neuroscience questions in humans and assess the brain pharmacokinetics of novel drugs. Subsequently, the same tools are applied clinically, for example, to diagnose and stage neurodegenerative conditions such as Parkinson and Alzheimer diseases (*2,3*) and directly monitor the effects of drugs (*4*).

Nonetheless, dynamic assessment of neurochemical-specific brain function remains challenging. Accurate quantification demands high-sensitivity imaging across the entire brain, to define and quantify important areas such as subnuclei within the thalamus and amygdala, hippocampal subfields, and midbrain nuclei (e.g., superior and inferior colliculi). Achieving ultrahigh resolution is also crucial to enhance the quantification of small brain structures by minimizing partial-volume effects (*5*).

For kinetic modeling, having precise measurements of the arterial input function is crucial for accurate quantification. High-sensitivity and high-resolution imaging offers the potential for obtaining image-derived input functions from the carotid arteries, reducing or eliminating the necessity for arterial sampling (*6*).

Existing state-of-the-art commercial PET imaging systems, including the 25-y-old High Resolution Research Tomograph (Siemens) (*7*), do not adequately meet this challenge. For the High Resolution Research Tomograph, the limited sensitivity and lack of time-of-flight (TOF) capability produce insufficient statistical precision for measurements, especially in small regions. In the last decade, there has been renewed interest in dedicated brain PET systems (*8*). Systems developed in both commercial and academic settings are demonstrating substantially improved performance compared with clinical whole-body PET systems (*9–17*).

Received Mar. 19, 2024; revision accepted May 13, 2024.

For correspondence or reprints, contact Richard E. Carson (richard.carson@yale.edu).

Despite this progress, these systems must demonstrate whether they meet the goals of comprehensively capturing the wide dynamic range of brain function with both high temporal and high spatial precision.

In 2019, the EXPLORER consortium developed a total-body PET scanner with a long axial field of view (AFOV) of almost 2 m, boosting sensitivity by up to 40 times (*18,19*). Studies on this system clearly demonstrated that high sensitivity plays a pivotal role in obtaining low-noise, high-resolution images at the temporal resolution desired for dynamic imaging and kinetic modeling (*20,21*).

Subsequently, the NeuroEXPLORER (NX) was developed collaboratively by Yale, the University of California, Davis, and United Imaging. The NX incorporates a long-AFOV concept with a 49.5-cm axial length and innovative high-resolution PET detectors featuring TOF and depth-of-interaction (DOI) encoding technologies to yield high sensitivity and high spatial resolution across the entire head. Including the impact of TOF, the NX was designed to produce an order-of-magnitude higher effective sensitivity than is possible with the High Resolution Research Tomograph to yield significantly improved image quality. The objective of this study was to evaluate the NX system's physical performance and quantitative accuracy following the National Electrical Manufacturers Association (NEMA) NU 2-2018 standard and to provide an initial demonstration of the system's capabilities with phantom and human images.

MATERIALS AND METHODS

System Parameters

The NX combines an 80-slice CT scanner (United Imaging uCT 550) with a dedicated brain PET scanner as shown in Figure 1. The CT scanner, capable of performing helical acquisitions with a minimum slice thickness of 0.5 mm and a minimum rotation time of 0.5 s, can be used in a low-dose mode for PET attenuation correction. There is an 80-cm gap between the CT and PET components, streamlining patient preparation, tracer injection, blood sampling, and other clinical procedures that require easy access to the subject.

The NX PET consists of 20 detector modules (each containing 5 or 6 blocks aligned axially) forming a cylindric detector ring with a diameter and AFOV of 52.4 and 49.5 cm, respectively. A smaller ring diameter was not used because of patient comfort concerns, especially for long dynamic scans. In addition, the larger bore may facilitate pediatric imaging. To minimize parallax errors in a compact detector ring, a depth-encoding detector design is necessary. The NX DOI detectors (Fig. 1) incorporate a U-shaped light-sharing detector array design with single-ended readout by silicon photomultipliers (SiPMs). Every U-shaped element comprises 2 lutetium-yttrium oxyorthosilicate crystals measuring 1.56 × 3.07 × 20.0 mm, and a microblock is created by combining 4 U-shaped elements. This microblock is then read out by a 2 × 2 array of 3-mm SiPMs. DOI is read out in 8 bins, determined by the proportion of light detected by the 2 axial SiPMs (Fig. 1). A DOI resolution of less than 4 mm was determined on the benchtop from coincidence data acquired while a point source was stepped along the depth direction of the detector (*22*). Overall, the detector delivers high-spatial and -energy resolution and very good TOF capability. Using individual-event DOI and energy information, we detect and recover intercrystal scatter events that occur between adjacent microblocks (*23*).

FIGURE 1. NX system. (Left) Overview of PET/CT with CT in front. (Center) NX PET detector ring (before removal of shoulder cutouts). (Right) U-shaped light-sharing detector array design providing DOI information.

An NX detector block consists of 12 × 12 microblocks. In total, the NX has 131,328 crystals read out by 65,664 SiPMs organized into 114 blocks. To enhance signal quality and reduce dead-time effects, we used a custom-designed 32-channel application-specific integrated circuit capable of precise time and amplitude measurements. The front-end electronics, consisting of 2,052 application-specific integrated circuits and 248 field-programmable gate arrays, handle real-time event localization and intercrystal scatter correction while maintaining low dead time.

To optimize detection sensitivity, we created a partial sixth ring by eliminating 3 blocks on both sides of the ring. This adaptation allows for different shoulder sizes, maintaining the brain at the scanner's central position for optimal sensitivity in the primary region of interest. It also improves sensitivity for imaging the carotid arteries. Furthermore, an integrated markerless 3-dimensional camera allows real-time motion tracking during imaging (*24*).

The console reconstruction is a 3-dimensional ordered-subset expectation-maximization (OSEM) algorithm including TOF, DOI, and point spread function (PSF) modeling. Data from the full axial acceptance angle are included. The console reconstruction incorporates DOI rebinning, which uses the DOI data to reassign the endpoints of the lines of response (LORs) to the front surface of appropriate nearby detectors. This facilitates rapid reconstruction and ensures smooth compatibility with established commercial reconstruction software (*25*).

NEMA NU 2-2018 Performance Evaluation

Spatial Resolution. We measured spatial resolution at 6 different locations using a 0.25-mm ^{22}Na point source (370 kBq, 10 μCi) embedded in a solid disk. The source was positioned at 2 axial positions: the axial center of the system ($^1\!/_2$ AFOV) and about 6 cm from the end of the tomograph ($^1\!/_8$ AFOV). Within each transaxial plane, resolution measurements were performed at 1-, 10-, and 20-cm radial offsets. The list-mode data (energy window of 430–800 keV) containing LORs with oblique angles less than 3.7° were adjusted by DOI rebinning and transformed into 2-dimensional sinograms using Fourier rebinning (*26*). The data were then reconstructed using a 2-dimensional filtered backprojection algorithm without attenuation correction, scatter correction, or postsmoothing, with a voxel size of 0.5 × 0.5 × 0.5 mm; the TOF information was not used. The axial, radial, and tangential resolutions were evaluated according to the NEMA NU 2-2018 standard.

Sensitivity. The sensitivity measurement was performed using a NEMA PET sensitivity phantom consisting of 5 concentric aluminum sleeves, each 70 cm in length. A 70-cm-long polyethylene tube filled with a solution of 13 MBq (0.35 mCi) of ^{18}F was inserted into the aluminum sleeves and positioned at the center of the transaxial field of view (FOV). Five 300-s acquisitions were conducted, successively removing the outermost sleeve to extrapolate attenuation-free sensitivity. The collected list-mode data were binned into sinograms using single-slice rebinning to estimate the total sensitivity and axial slice sensitivity. The entire process was replicated with the line source positioned 10 cm off-center within the transaxial FOV.

Count Rate Performance. Following the NEMA NU 2-2018 standard, count rate performance was evaluated using a scatter phantom consisting of a 70-cm-long polyethylene

TABLE 1
Spatial Resolution of ^{22}Na Point Source Measured with Filtered Backprojection

		Full width at half maximum (mm)		
Axial position	Radial off-center position (cm)	Radial	Tangential	Axial
½ AFOV	1	1.63	1.68	2.55
	10	2.10	2.06	2.97
	20	2.17	2.87	2.82
⅛ AFOV	1	1.76	1.47	2.91
	10	1.99	2.08	2.80
	20	2.20	2.78	3.05

cylinder with a 20-cm diameter. The line source was initially loaded with 1.54 GBq (41.6 mCi) of ^{18}F-FDG. In total, 34 acquisition frames were acquired with increasing durations as the activity decayed. Random estimation was obtained from the delayed coincidence channel. The scatter fraction was determined in accordance with the NEMA standard, and Monte Carlo scatter simulation was used in the image reconstruction for evaluation of accuracy (relative count error). Dead-time correction was based on a nonparalyzable model. System count rates, including trues, randoms, scatters, total counts, ideal trues, and the noise-equivalent count rate, were plotted alongside their corresponding activity concentrations. Additionally, a plot illustrating the scatter fraction in relation to activity concentration was generated. The ideal trues count rate was estimated from a linear fit to the trues rate at low activities when dead-time effects are negligible; count loss due to dead time was calculated by comparing measured and ideal trues count rates.

Energy and Timing Resolution. The data obtained during the count rate performance measurement were used to assess the system timing resolution and energy resolution (*27*). For source position determination, the acquisition data, at an activity concentration just below the peak noise-equivalent count rate, were reconstructed using non-TOF OSEM with all corrections applied. Only coincidences occurring within the ±20-mm region of interest centered on the line source were used to obtain the timing histogram. For each coincidence dataset, the time error was computed by measuring the difference between the actual TOF data and its expected TOF offset based on the point closest to the line source on the corresponding LOR. Scatter and random coincidences were subtracted using the tails of the TOF histograms. For energy resolution, crystal-level energy spectra with a 1-keV energy bin width were combined into a single spectrum. The full width at half maximum of energy resolution was determined by the linear interpolation between the adjacent pixels at half the maximum value. This value was determined over all count rates.

Image Quality and Accuracy of Corrections. A NEMA NU 2 image-quality phantom was used to evaluate image quality. At the start of image acquisition, the background activity concentration of ^{18}F-FDG was 5.3 kBq/mL. Six spheres with diameters of 10, 13, 17, 22, 28, and 37 mm were filled with the ^{18}F-FDG solution with an activity concentration ratio of 4.0:1 relative to the background. An adjacent scatter phantom (used for count rate performance measurement) was placed axially to the NEMA image-quality phantom; the line source activity in the scatter phantom was 116 MBq (3.14 mCi), the duration of the scan was 15 min, and 3 sequential measurements were acquired. Images were reconstructed using the standard TOF-DOI-PSF OSEM algorithm with all corrections applied. Mean, minimum, and maximum results are shown at multiple iterations with 10 subsets (voxel size, 1.8 × 1.8 × 1.72 mm).

Phantom Studies

A 3-dimensional Hoffman brain phantom was filled with 30 MBq (0.81 mCi) of ^{18}F-FDG, placed at the center of the FOV, and scanned for 30 min. A mini-Derenzo resolution phantom was used to further evaluate the PET resolution performance. This phantom contained rods of various diameters (1.2, 1.6, 2.4, 3.2, 4.0, and 4.8 mm), and the center spacing between rods was twice the rod diameter. The phantom was filled with ^{18}F-FDG and imaged for 10 min at the center of the FOV (36.8 MBq, 0.99 mCi) and for 15 min at 85 mm off-center (26.5 MBq, 0.72 mCi), with the rod axes perpendicular to the transaxial plane. Both phantoms underwent image reconstruction using the console TOF-DOI-PSF OSEM algorithm with 7 iterations and 10 subsets. No postreconstruction filtering was applied, and the image voxel size was 0.4 × 0.4 × 0.6 mm. For the mini-Derenzo phantom, 2 additional reconstructions were performed with offline list-mode algorithms: one using no DOI information, and the other directly using DOI coordinates, that is, no DOI rebinning.

Human Study

A 58-y-old healthy male volunteer participated in a brain ^{18}F-FDG PET protocol approved by the Yale University Human Investigation Committee and the Yale Radiation Safety Committee. Written informed consent was obtained. The subject was administered 327 MBq (8.8 mCi) in a bolus–plus–continuous-infusion protocol. A CT scan was acquired for attenuation correction. Dynamic data were acquired in list mode for

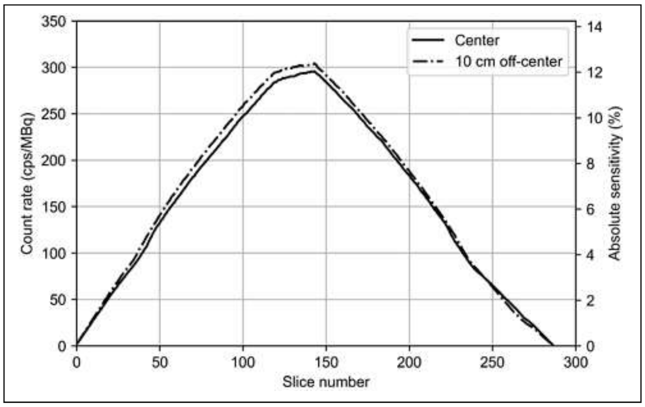

FIGURE 2. Slice sensitivity profiles along 49.5-cm AFOV measured with 70-cm line source positioned at transaxial center and 10 cm off-center. Data are shown for 287 slices calculated by single-slice rebinning. Count rates and absolute sensitivities are displayed on left and right vertical axes, respectively. Slice sensitivity was determined by normalizing slice count rate data from entire phantom by ratio of phantom length to slice thickness (1.725 mm).

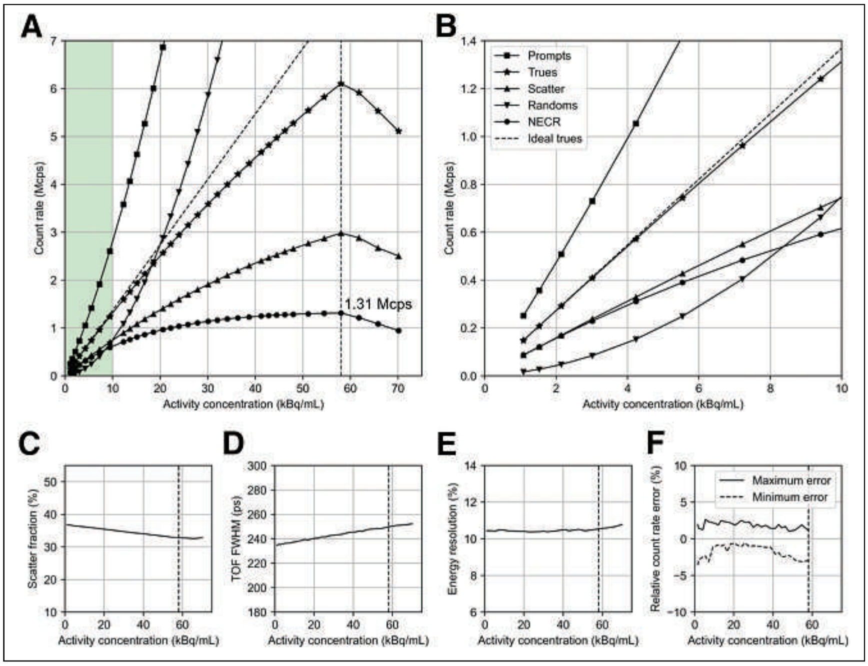

FIGURE 3. Count-rate performance of NX. (A) Prompts, trues, scatter, randoms, and noise-equivalent count rate. (B) Zoomed display of A at ∼0–10 kBq/mL, which corresponds to typical activity level for human brain imaging. (C) Scatter fraction. (D) TOF resolution. (E) Energy resolution. (F) Relative count rate error as function of activity concentration. Vertical dashed line denotes noise-equivalent count rate peak position at 58.0 kBq/mL, corresponding to 1,275 MBq (34.5 mCi). NECR = noise-equivalent count rate.

90 min. Reconstructed images contained 600 × 600 × 990 voxels with a voxel size of 0.5 × 0.5 × 0.5 mm. TOF-DOI-PSF OSEM was used with 7 iterations and 10 subsets and all corrections. A static ^{18}F-FDG PET image was generated by summing over 40- to 70-min data and registered to T1-weighted MR images using FSL (*28*) for anatomic localization. This choice of period was based on the camera data, which showed minimal subject motion during that time.

RESULTS

NEMA NU 2-2018 Performance Evaluation

Spatial Resolution. The transverse (averaged radial and tangential) spatial resolution using filtered backprojection was 1.64, 2.06, and 2.51 mm, and axial resolution was 2.73, 2.89, and 2.93 mm in full width at half maximum, with radial offsets of 1, 10, and 20 cm from the center, respectively (Table 1).

Sensitivity. The NEMA total-system sensitivities were 46.0 and 47.6 kcps/MBq at the center and at the 10-cm radial offset, respectively (Fig. 2). An absolute sensitivity of 11.8% was achieved at the center of the FOV.

Count Rate Performance. Figure 3 shows the count rate performance data for the NX. The peak noise-equivalent count rate was 1.31 Mcps at an activity concentration of 58.0 kBq/mL. Above this point, the count rate drops because of bandwidth limitations of the data acquisition hardware; note that this activity level is well above that

TABLE 2
Measured Contrast Recovery Coefficient and Background Variability for 3 and 7 Iterations of OSEM Reconstruction

	Sphere size						
Parameter	10 mm	13 mm	17 mm	22 mm	28 mm	37 mm	Lung residual error
Contrast recovery coefficient							
3-iteration OSEM							
Mean	74.5	82.1	82.6	86.1	89.4	92.6	1.7
Maximum	76.1	84.3	84.7	87.0	89.8	93.1	1.7
Minimum	72.6	80.3	81.5	85.0	88.9	91.6	1.7
7-iteration OSEM							
Mean	83.3	85.4	87.2	90.2	92.3	94.8	0.9
Maximum	85.6	87.9	90.3	91.7	92.9	95.5	0.9
Minimum	80.9	82.2	84.9	88.2	91.6	93.4	0.9
Background variability							
3-iteration OSEM							
Mean	3.1	2.4	1.9	1.6	1.4	1.3	1.4
Maximum	3.4	2.6	2.0	1.7	1.5	1.3	1.4
Minimum	2.6	2.1	1.8	1.5	1.4	1.3	1.4
7-iteration OSEM							
Mean	5.0	3.6	2.8	2.2	1.9	1.6	1.9
Maximum	5.4	3.9	3.0	2.4	2.0	1.7	1.9
Minimum	4.2	3.1	2.5	2.1	1.8	1.5	1.8

Results are reported as mean, minimum, and maximum percentages over 3 measurements.

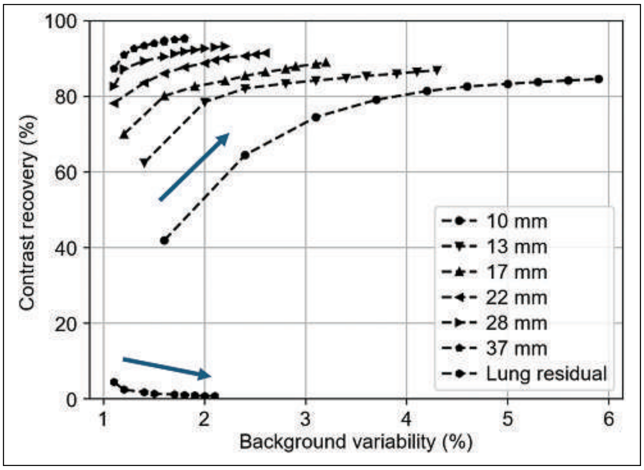

FIGURE 4. Contrast recovery coefficient measurements derived from image-quality phantom. OSEM results are shown for 1–10 iterations with 10 subsets; arrow denotes increasing iterations. Values are mean results from three 15-min acquisitions.

found in brain imaging. The average scatter fraction was 36.5% at 5.3 kBq/mL (Fig. 3). Count losses of 5.1% and 10.2% were noted at 12.3 and 23.9 kBq/mL, respectively, because of system dead time. The maximum count rate error was less than 5.0%.

Energy and Timing Resolution. The measured average system TOF resolution was 236 ps, and the energy resolution was 10.5% (full width at half maximum) at 5.3 kBq/mL. Both values were stable with count rate, with variations of 2.1% and 0.8% for TOF and energy resolution, respectively.

Image Quality and Accuracy of Correction. Table 2 summarizes the contrast recovery coefficient, background variability, and residual error in the cold lung region for the 4.0:1 sphere-to-background ratio, based on 3 combined measurements of the image-quality phantom. The average contrast recovery coefficient varied from 74.5% (10-mm sphere) to 92.6% (37-mm sphere), and background variability varied from 3.1% to 1.4% at 3 iterations (10 subsets). Plotting the contrast recovery coefficient versus background variability for iterations 1–10 suggests that the contrast recovery coefficients reach convergence in most spheres at 8 iterations (Fig. 4).

Phantom Studies

Twelve transverse slices of the Hoffman phantom are shown in Figure 5. There is clear delineation of the fine structures in the phantom. This is most clearly portrayed when a central PET slice is compared with the matching CT slice, which depicts the accuracy of the border between gray and white matter structures.

Figure 6 shows the results of mini-Derenzo phantom images and the impact of DOI. The effects of uncorrected DOI are clearly seen by comparison of the central and offset images without DOI correction. Using the console reconstruction with DOI rebinning, PSF, and TOF, the 1.6-mm hot rods can be resolved using 7 or more iterations for both center and off-center cases. Comparing columns 1 and 2, the addition of DOI information produces the most notable improvement for the off-center phantom. To further assess DOI effects, list-mode reconstructions with 30 iterations were performed without DOI and with full DOI information. Increasing iterations further improved the images, and with DOI, the 1.2-mm rods were more clearly resolved. Overall, reconstructions using DOI information showed advantages at both a low and a high number of iterations compared with non-DOI results.

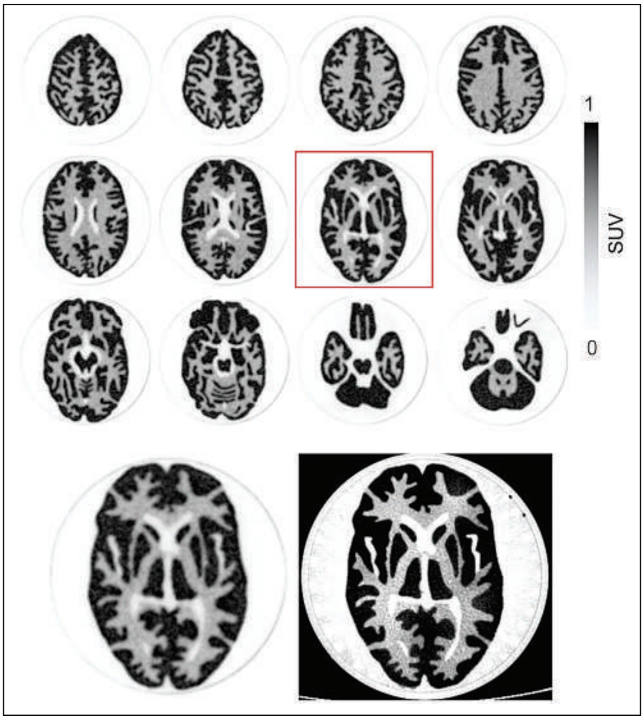

FIGURE 5. (Top) Reconstructed PET images of Hoffman 3-dimensional brain phantom. PET images were created with console reconstruction algorithm using 7 iterations and 10 subsets with voxel size of 0.4 × 0.4 × 0.6 mm. (Bottom) Matched slices of PET (highlighted slice from top) compared with CT image. PET images are displayed on SUV scale.

Human Study

Reconstructed human NX images are shown in Figure 7, demonstrating very high resolution in the cortex and subcortical structures. The improved visualization is clearly seen in marginal sulcus, posterior cingulate cortex, inferior colliculus, caudate, insular cortex, putamen, and hippocampus. The figure also depicts the full AFOV of the NX system, which provides improved capability for imaging the carotid arteries, head and neck tumors, and cervical spinal cord.

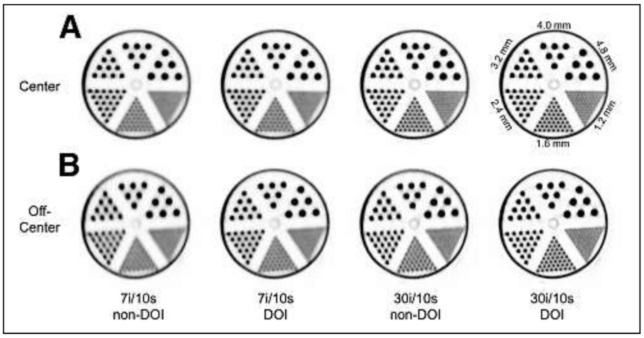

FIGURE 6. Image slices reconstructed from mini-Derenzo phantom, positioned at center (A) and 85 mm off-center (B) of transaxial plane, using TOF-PSF OSEM algorithm with voxel size of 0.4 × 0.4 × 0.6 mm. (Column 1) Seven iterations and 10 subsets (7i/10 s) with non-DOI offline reconstruction. (Column 2) Seven iterations and 10 subsets using DOI rebinning in console reconstruction. (Column 3) Thirty iterations and 10 subsets (30i/10 s) with non-DOI offline reconstruction. (Column 4) Thirty iterations and 10 subsets with full DOI offline list-mode reconstruction.

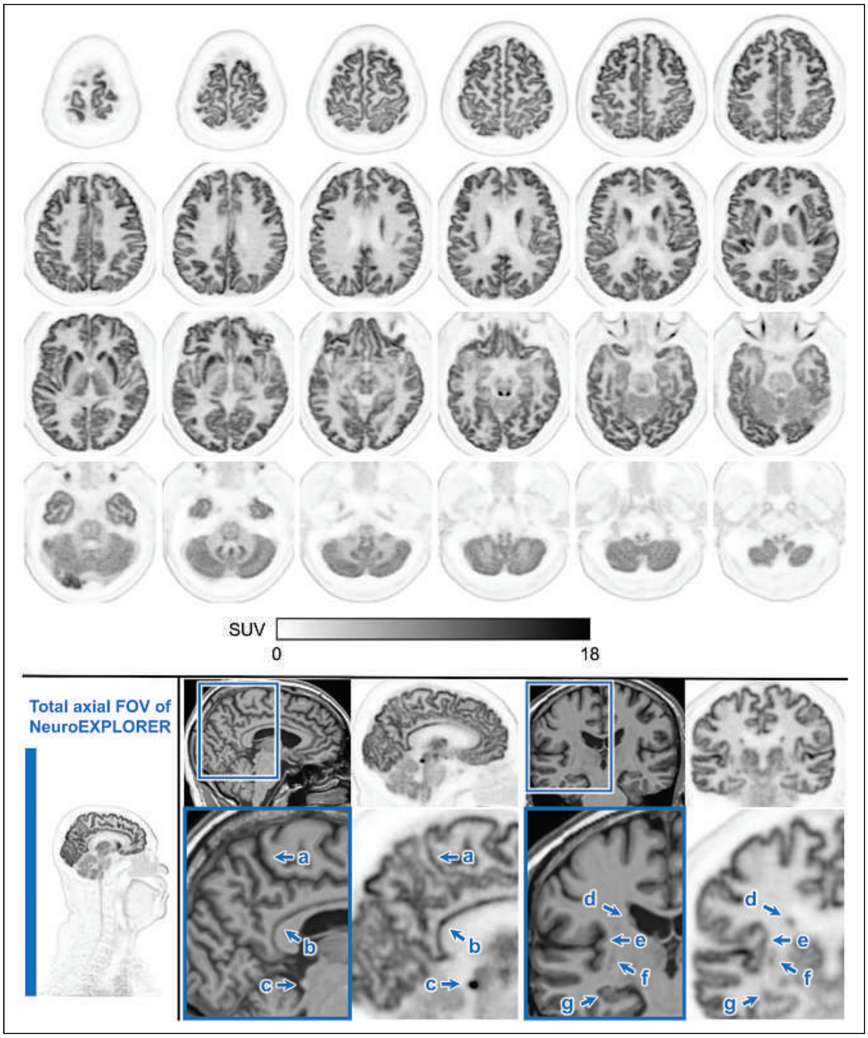

FIGURE 7. ^{18}F-FDG PET image (40–70 min after injection) on NX. (Top) Top-to-bottom axial slices showing excellent spatial resolution of NX, which provides clear delineation of cortical ribbon along with subcortical nuclei. (Bottom, far left) Sagittal image showing long AFOV of NX (49.5 cm), which allows inclusion of neck and upper chest structures. (Bottom right) Two pairs of T1-weighted MRI (left) and NX (right) image slices. Beneath are zoomed-in regions demonstrating NX's high spatial resolution for cortical ribbon structures and small brain nuclei, including marginal sulcus (a), posterior cingulate cortex (b), inferior colliculus (c), caudate (d), insular cortex (e), putamen (f), and hippocampus (g).

DISCUSSION

Here, we have presented the performance and first human images of the NX, a next-generation human brain PET/CT system. The design of this system was based on our long experience in brain PET, which showed that high resolution is critically important to measure activity in small brain nuclei and that high sensitivity may play an even greater role to provide sufficient statistics to reconstruct images that fully use the system's resolution capabilities.

The results for spatial resolution from point sources in air were shown with filtered backprojection. If the TOF-DOI-PSF OSEM reconstruction was applied, the transverse and axial spatial resolutions were substantially improved, with only minor degradation at off-center locations. Specifically, with the addition of a 5% warm background to the point source, the transverse and axial spatial resolutions at the center improved to 1.43 and 1.54 mm, respectively, at 20 iterations (10 subsets). However, we recognize that these OSEM values are likely to be better than what can be achieved in human studies because of the lack of sufficient background activity (*29*); these results therefore cannot be considered reliable. Nevertheless, considering the clear improvement in phantom image quality provided by OSEM using TOF and DOI (Figs. 5 and 6), it is important to recognize that filtered backprojection results do not provide an accurate measure of real-world system resolution. Ultimately, human brain image quality will depend on the choice of reconstruction parameters, to balance image resolution and voxel noise. Further work is required to characterize the spatial resolution of this system more meaningfully.

For a brain PET scanner with an extended axial length and wide acceptance angles, depth encoding plays a crucial role in reducing parallax errors, to provide nearly uniform spatial resolution across the entire FOV. In addition to precisely defining the LORs, DOI information enhances TOF accuracy by accounting for the variation in the pathlengths of light photons. Ignoring the DOI information resulted in a degradation of TOF resolution of about 99 ps. As demonstrated here, despite having smaller detectors and reduced light collection efficiency, after TOF compensation by the DOI, the NX achieves a TOF resolution of 236 ps, comparable to that of state-of-the-art clinical PET/CT systems with larger detectors.

By discretizing DOI into 8 bins per NX detector, the total number of DOI-based LORs increases 64-fold, which elevates spatial sampling, enhancing axial resolution, particularly for long-AFOV PET with large acceptance angles. This is clearly visualized with the improved image resolution in Figure 6.

Intercrystal scatter events result in inaccurate localization of annihilation photon interactions within detectors. Monte Carlo simulation studies indicate a higher proportion of such scattered events within each LOR within smaller detectors. Integrating DOI information and combining it with event energy can reduce intercrystal scatter events while restoring the original event energy and position information, potentially improving image resolution (*23*). Currently, NX intercrystal scatter localization is based on higher energy, and optimization using energy and DOI information is under way.

Unlike traditional PET, for which more activity leads to an increased scatter fraction due to event pileup, the NX shows a slight decrease in scatter fraction at high count rates, perhaps because of slightly insufficient cooling under high-count-rate and high-power-consumption conditions; this requires further investigation.

In high-resolution PET scanners, even minor patient movement can negatively impact quantification and produce motion artifacts. The NX is equipped with markerless motion-tracking hardware featuring a real-time stereovision camera with structured light to image the surface of the subject's head at 10–30 Hz, as well as a real-time data processing unit using an iterative-closest-point 3-dimensional point cloud registration algorithm (*24*). We are currently evaluating motion correction performance on the NX using the event-based motion correction capabilities of the MOLAR reconstruction platform (*30,31*). The vendor-provided console reconstruction does not currently use motion vectors for event-based image reconstruction; instead, frame-based postreconstruction methods are used. The console software also uses a DOI rebinning strategy to efficiently reconstruct all images, albeit at the cost of a slight reduction in image resolution. The incorporation of full list-mode DOI reconstruction is under way.

As demonstrated by the human images, the great sensitivity and spatial resolution of the NX provides a platform for imaging tasks previously considered difficult or impossible, such as accurate imaging of small subcortical regions with focal tracer uptake, low-density binding sites (e.g., cortical dopamine receptors), cervical spinal cord uptake, neurotransmitter dynamics, and carotid arteries for image-derived input functions.

CONCLUSION

The NX achieves very high spatial resolution and sensitivity, as shown by the NEMA NU-2 measurements and the images presented here. This performance is made possible by U-shaped DOI lutetium-yttrium oxyorthosilicate detectors combined with a single-ended SiPM-based application-specific integrated circuit readout. The system delivers a timing resolution of 236 ps. In view of these design and performance features, the NX introduces exciting possibilities for human brain PET protocols and clinical research applications, pushing the boundaries of what can be achieved in neuroimaging.

DISCLOSURE

This work was supported by NIH BRAIN Initiative grant U01EB029811. The University of California, Davis, has a research agreement and a sales-based revenue-sharing agreement with United Imaging Healthcare. No other potential conflict of interest relevant to this article was reported.

KEY POINTS

QUESTION: What is the performance of the next-generation dedicated brain PET imager—the NX—according to the NEMA NU 2-2018 standard?

PERTINENT FINDINGS: The NX provides a spatial resolution below 2 mm, a sensitivity of 46 cps/kBq, and a timing resolution of 236 ps and includes a built-in camera for real-time motion correction.

IMPLICATIONS FOR PATIENT CARE: The NX allows for operation at high resolutions or low doses, with the potential to substantially improve quantification and to allow for early detection and treatment monitoring of neurodegenerative and neuropsychiatric disorders.

REFERENCES

1. Hooker JM, Carson RE. Human positron emission tomography neuroimaging. *Annu Rev Biomed Eng.* 2019;21:551–581.
2. Young PNE, Estarellas M, Coomans E, et al. Imaging biomarkers in neurodegeneration: current and future practices. *Alzheimers Res Ther.* 2020;12:49.
3. Berti V, Pupi A, Mosconi L. PET/CT in diagnosis of dementia. *Ann N Y Acad Sci.* 2011;1228:81–92.
4. van Dyck CH, Swanson CJ, Aisen P, et al. Lecanemab in early Alzheimer's disease. *N Engl J Med.* 2023;388:9–21.
5. Hoffman EJ, Huang SC, Phelps ME. Quantitation in positron emission computed tomography: 1. Effect of object size. *J Comput Assist Tomogr.* 1979;3:299–308.
6. Volpi T, Maccioni L, Colpo M, et al. An update on the use of image-derived input functions for human PET studies: new hopes or old illusions? *EJNMMI Res.* 2023;13:97.
7. de Jong HW, van Velden FH, Kloet RW, Buijs FL, Boellaard R, Lammertsma AA. Performance evaluation of the ECAT HRRT: an LSO-LYSO double layer high resolution, high sensitivity scanner. *Phys Med Biol.* 2007;52:1505–1526.
8. Catana C. Development of dedicated brain PET imaging devices: recent advances and future perspectives. *J Nucl Med.* 2019;60:1044–1052.
9. Grogg KS, Toole T, Ouyang J, et al. National Electrical Manufacturers Association and clinical evaluation of a novel brain PET/CT scanner. *J Nucl Med.* 2016;57:646–652.
10. Watanabe M, Saito A, Isobe T, et al. Performance evaluation of a high-resolution brain PET scanner using four-layer MPPC DOI detectors. *Phys Med Biol.* 2017;62:7148–7166.
11. Gaudin É, Toussaint M, Thibaudeau C, Paille M, Fontaine R, Lecomte R. Performance simulation of an ultra-high resolution brain PET scanner using 1.2-mm pixel detectors. *IEEE Trans Radiat Plasma Med Sci.* 2019;3:334–342.
12. Moliner L, Rodriguez-Alvarez MJ, Catret JV, Gonzalez A, Ilisie V, Benlloch JM. NEMA performance evaluation of CareMiBrain dedicated brain PET and comparison with the whole-body and dedicated brain PET systems. *Sci Rep.* 2019;9:15484.
13. Akamatsu G, Takahashi M, Tashima H, et al. Performance evaluation of VRAIN: a brain-dedicated PET with a hemispherical detector arrangement. *Phys Med Biol.* 2022;67.
14. Morimoto-Ishikawa D, Hanaoka K, Watanabe S, et al. Evaluation of the performance of a high-resolution time-of-flight PET system dedicated to the head and breast according to NEMA NU 2-2012 standard. *EJNMMI Phys.* 2022;9:88.
15. Zeng X, Wang Z, Tan W, et al. A conformal TOF-DOI Prism-PET prototype scanner for high-resolution quantitative neuroimaging. *Med Phys.* January 18, 2023 [Epub ahead of print].
16. Fang L, Zhang B, Li B, et al. Development and evaluation of a new high-TOF-resolution all-digital brain PET system. *Phys Med Biol.* 2024;69.
17. Kuang Z, Sang Z, Ren N, et al. Development and performance of SIAT bPET: a high-resolution and high-sensitivity MR-compatible brain PET scanner using dual-ended readout detectors. *Eur J Nucl Med Mol Imaging.* 2024;51:346–357.
18. Badawi RD, Shi H, Hu P, et al. First human imaging studies with the EXPLORER total-body PET scanner. *J Nucl Med.* 2019;60:299–303.
19. Spencer BA, Berg E, Schmall JP, et al. Performance evaluation of the uEXPLORER total-body PET/CT scanner based on NEMA NU 2-2018 with additional tests to characterize PET scanners with a long axial field of view. *J Nucl Med.* 2021;62:861–870.
20. Wang Y, Nardo L, Spencer BA, et al. Total-body multiparametric PET quantification of ^{18}F-FDG delivery and metabolism in the study of coronavirus disease 2019 recovery. *J Nucl Med.* 2023;64:1821–1830.
21. Wang Y, Spencer BA, Schmall J, et al. High-temporal-resolution lung kinetic modeling using total-body dynamic PET with time-delay and dispersion corrections. *J Nucl Med.* 2023;64:1154–1161.
22. Selfridge A, Schmall J, Li H. Detector design and characterization for the NeuroEXPLORER brain imager. Paper presented at: 2021 Virtual IEEE Nuclear Science Symposium and Medical Imaging Conference; October 16–23, 2021.
23. Samanta S, Sajedi S, Hu L, Li H. Inter-crystal scatter processing in NeuroEXPLORER brain imager. IEEE Xplore website. https://ieeexplore.ieee.org/document/10399134. Published January 26, 2024. Accessed May 21, 2024.
24. Zeng T, Lu Y, Jiang W, et al. Markerless head motion tracking and event-by-event correction in brain PET. *Phys Med Biol.* 2023;68:245019.
25. Feng T, He L, Selfridge A, Li H. Depth-of-interaction reconstruction in NeuroEXPLORER. IEEE Xplore website. https://ieeexplore.ieee.org/document/9875716. Published September 9, 2022. Accessed May 21, 2024.
26. Defrise M, Kinahan PE, Townsend DW, Michel C, Sibomana M, Newport DF. Exact and approximate rebinning algorithms for 3-D PET data. *IEEE Trans Med Imaging.* 1997;16:145–158.
27. Bharkhada D, Rothfuss H, Conti M. A new method to calculate energy resolution based upon NEC phantom. IEEE Xplore website. https://doi.org/10.1109/NSSMIC.2017.8533007. Published November 15, 2018. Accessed May 21, 2024.
28. Jenkinson M, Beckmann CF, Behrens TE, Woolrich MW, Smith SM. FSL. *Neuroimage.* 2012;62:782–790.
29. Gong K, Cherry SR, Qi J. On the assessment of spatial resolution of PET systems with iterative image reconstruction. *Phys Med Biol.* 2016;61:N193–N202.
30. Jin X, Mulnix T, Sandiego CM, Carson RE. Evaluation of frame-based and event-by-event motion-correction methods for awake monkey brain PET imaging. *J Nucl Med.* 2014;55:287–293.
31. Jin X, Chan C, Mulnix T, et al. List-mode reconstruction for the Biograph mCT with physics modeling and event-by-event motion correction. *Phys Med Biol.* 2013;58:5567–5591.

Brain Metabolic Correlates of the Off-Target Effects of Enzalutamide on the Central Nervous System of Patients with Advanced Prostate Cancer

Matteo Bauckneht[1], Giuseppe Fornarini[1], Tania Di Raimondo[1], Matteo Pardini[1], Maria Isabella Donegani[1], Giuseppe Luigi Banna[2], Massimo Di Maio[3], and Silvia Morbelli[3]

[1]IRCCS Ospedale Policlinico San Martino, Genova, Italy; [2]Portsmouth Hospitals University NHS Trust, University of Portsmouth, Portsmouth, United Kingdom; and [3]AOU Città della Salute e della Scienza di Torino, University of Turin, Turin, Italy

The management of prostate cancer increasingly relies on androgen axis–targeted therapies, such as enzalutamide, which is now administered progressively earlier and for longer durations (*1*). Enzalutamide increases the risk of fatigue, falls, dizziness, headache, and mild cognitive impairment (*2,3*). These off-target effects seem to be associated with enzalutamide's pharmacodynamics and ability to penetrate the blood–brain barrier. [^{18}F]FDG PET can capture synaptic function or dysfunction in neurocognitive disorders.

We compared brain metabolism in a cohort of metastatic castration-resistant prostate cancer patients, some treated with enzalutamide and others not, all undergoing [^{18}F]FDG PET. The institutional review board approved this retrospective study (Ethics Committee, Liguria, approval 590/2020), and the requirement to obtain informed consent was waived. Patients had preserved daily living activities and no history of neuropsychiatric diseases. Whole-brain voxelwise group analysis (SPM12 software) was used to identify relative hypometabolism compared with 48 age-matched controls (familywise error–corrected $P < 0.05$; nuisance variables: age, previous androgen deprivation therapy duration, previous abiraterone or taxane-based chemotherapy).

Of 68 patients, 39 had previously received enzalutamide. Aside from the duration of previous androgen deprivation therapy, the clinical characteristics of the 2 subgroups were balanced (Supplemental Table 1; supplemental materials are available at http://jnm.snmjournals.org). Enzalutamide treatment was associated with hypometabolism in the left dorsolateral-prefrontal and front-insular cortex ($P < 0.005$; Fig. 1), whereas enzalutamide-naïve patients did not show significant regions of hypometabolism. The topography of these findings corresponds to cortical correlates of fatigue and memory/executive dysfunction (*2,3*). These findings align with the only imaging study with arterial spin-labeling MRI showing reduced blood flow in the prefrontal cortex in patients receiving enzalutamide (*4*). Our finding linking prefrontal cortex metabolism to enzalutamide suggests further investigation of [^{18}F]FDG PET for symptom objectification or biomarker validation.

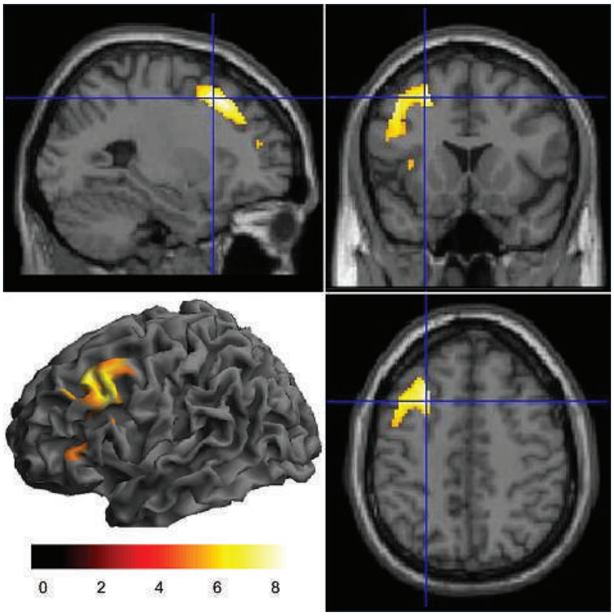

FIGURE 1. Hypometabolism in patients treated with enzalutamide compared with controls. Color bar indicates *z* scores for significant voxels. Left in the image is left in the patient.

DISCLOSURE

No potential conflict of interest relevant to this article was reported.

REFERENCES

1. Freedland SJ, de Almeida Luz M, De Giorgi U, et al. Improved outcomes with enzalutamide in biochemically recurrent prostate cancer. *N Engl J Med.* 2023;389:1453–1465.
2. Thiery-Vuillemin A, Poulsen MH, Lagneau E, et al. Impact of abiraterone acetate plus prednisone or enzalutamide on patient-reported outcomes in patients with metastatic castration-resistant prostate cancer: final 12-mo analysis from the observational AQUARiUS study. *Eur Urol.* 2020;77:380–387.
3. Marandino L, Vignani F, Buttigliero C, et al. Evaluation of cognitive function in trials testing new-generation hormonal therapy in patients with prostate cancer: a systematic review. *Cancers (Basel).* 2020;12:2568.
4. Williams SCR, Mazibuko N, O'Daly O, et al. Comparison of cerebral blood flow in regions relevant to cognition after enzalutamide, darolutamide, and placebo in healthy volunteers: a randomized crossover trial. *Target Oncol.* 2023;18:403–413.

Received Jan. 26, 2024; revision accepted Mar. 15, 2024.

For correspondence or reprints, contact Matteo Bauckneht (matteo.bauckneht@unige.it).

DOI: 10.2967/jnumed.124.267526

BRAIN METABOLISM EFFECTS OF ENZALUTAMIDE • Bauckneht et al. 1327

[^{68}Ga]Ga-FAPI-46 False-Positive Uptake After Chemotherapy in Nonseminomatous Germ Cell Tumor Metastatic Lesions

Vinicius Ludwig[1], Peter George Maliha[1–3], John Shen[4,5], David Tonnelet[6], Steve Raman[7], Mark S. Litwin[5], and Jeremie Calais[1]

[1]Ahmanson Translational Theranostics Division, Department of Molecular and Medical Pharmacology, David Geffen School of Medicine, UCLA, Los Angeles, California; [2]Nuclear Medicine, Centre Hospitalier de l'Université de Montréal Centre de Recherche, Université de Montréal, Montréal, Québec, Canada; [3]Nuclear Medicine Department, Centre Hospitalier de l'Université de Montréal, Montréal, Québec, Canada; [4]Department of Hematology/Oncology, UCLA, Los Angeles, California; [5]Department of Urology, David Geffen School of Medicine, UCLA, Los Angeles, California; [6]Department of Nuclear Medicine, Henri Becquerel Cancer Center, and QuantIF–LITIS, University of Rouen, Rouen, France; and [7]Department of Radiology, UCLA, Los Angeles, California

A 38-y-old man with mixed, nonseminomatous germ cell carcinoma metastatic to the lung, liver, and retroperitoneal lymph nodes was treated with left orchiectomy and 4 cycles of cisplatin, etoposide, and ifosfamide. CT performed 3 d after the end of the last cycle showed significant improvement but persistent liver and retroperitoneal lesions. A liver lesion biopsy performed 1 mo after chemotherapy was negative for residual tumor (fibrosis, necrosis, and abundant hemosiderin-laden macrophages, consistent with treatment effect). An [^{18}F]FDG PET/CT scan performed 80 d after chemotherapy (Fig. 1) demonstrated uptake in some of the residual liver lesions (SUV_{max}, 4.8–5.8), suggesting potential residual active disease, and there was moderate uptake in the retroperitoneal lymph nodes (SUV_{max}, 3.2). A PET/CT scan with a fibroblast activation protein (FAP) inhibitor (FAPI), [^{68}Ga]Ga-FAPI-46, was performed as part of an exploratory study, NCT04459273 (Fig. 1), 97 d after the last chemotherapy cycle. The liver lesions exhibited heterogeneous uptake (SUV_{max}, 2.6–4.9), and the retroperitoneal lymph nodes had moderate uptake (SUV_{max}, 3.2). Retroperitoneal lymphadenectomy, partial left lateral liver segmentectomy, and multiple wedge biopsies of liver lesions, performed 9 d after the [^{68}Ga]Ga-FAPI-46 PET scan, showed necrotic tumor nodules with variable stages of fibrosis and no viable germ cell tumor. Eighteen months after surgery, the patient did not show any signs of disease progression, and abdominal CT demonstrated a decrease in the size of the liver lesions.

FAP-targeted PET imaging is promising in malignancies associated with a high content of FAP-expressing cancer-associated fibroblasts. Some reports in the literature describe the potential use of [^{68}Ga]Ga-FAPI PET for therapy response assessment for a variety of cancers (*1–5*). However, FAP is also expressed by normal activated fibroblasts present in multiple fibroinflammatory conditions, remodeling processes, and wound healing. Nevertheless, posttreatment cancer cell apoptosis may not necessarily affect cancer-associated fibroblasts or decrease fibroblast activation. The ability of FAP tracer to assess therapy response is yet to be determined.

This case illustrates that postchemotherapy fibronecrotic tissue in nonseminomatous germ cell tumor can demonstrate [^{68}Ga]Ga-FAPI PET uptake and that caution is needed in the interpretation of posttherapy residual lesions.

DISCLOSURE

No potential conflict of interest relevant to this article was reported.

REFERENCES

1. Zhu Z, Cheng K, Yun Z, et al. [^{18}F] AlF-NOTA-FAPI-04 PET/CT can predict treatment response and survival in patients receiving chemotherapy for inoperable pancreatic ductal adenocarcinoma. *Eur J Nucl Med Mol Imaging.* 2023;50:3425–3438.
2. Zhao L, Chen S, Lin L, et al. [^{68}Ga]Ga-DOTA-FAPI-04 improves tumor staging and monitors early response to chemoradiotherapy in a patient with esophageal cancer. *Eur J Nucl Med Mol Imaging.* 2020;47:3188–3189.
3. Chen L, Zheng S, Chen L, et al. ^{68}Ga-labeled fibroblast activation protein inhibitor PET/CT for the early and late prediction of pathologic response to neoadjuvant chemotherapy in breast cancer patients: a prospective study. *J Nucl Med.* 2023;64:1899–1905.
4. Miao Y, Feng R, Yu T, et al. Value of ^{68}Ga-FAPI-04 and ^{18}F-FDG PET/CT in early prediction of pathologic response to neoadjuvant chemotherapy in locally advanced gastric cancer. *J Nucl Med.* 2024;65:213–220.
5. Hotta M, Rieger AC, Jafarvand MG, et al. Non-oncologic incidental uptake on FAPI PET/CT imaging. *Br J Radiol.* 2023;96:20220463.

Received Feb. 14, 2024; revision accepted Mar. 25, 2024.

For correspondence or reprints, contact Jeremie Calais (jcalais@mednet.ucla.edu).

DOI: 10.2967/jnumed.124.267609

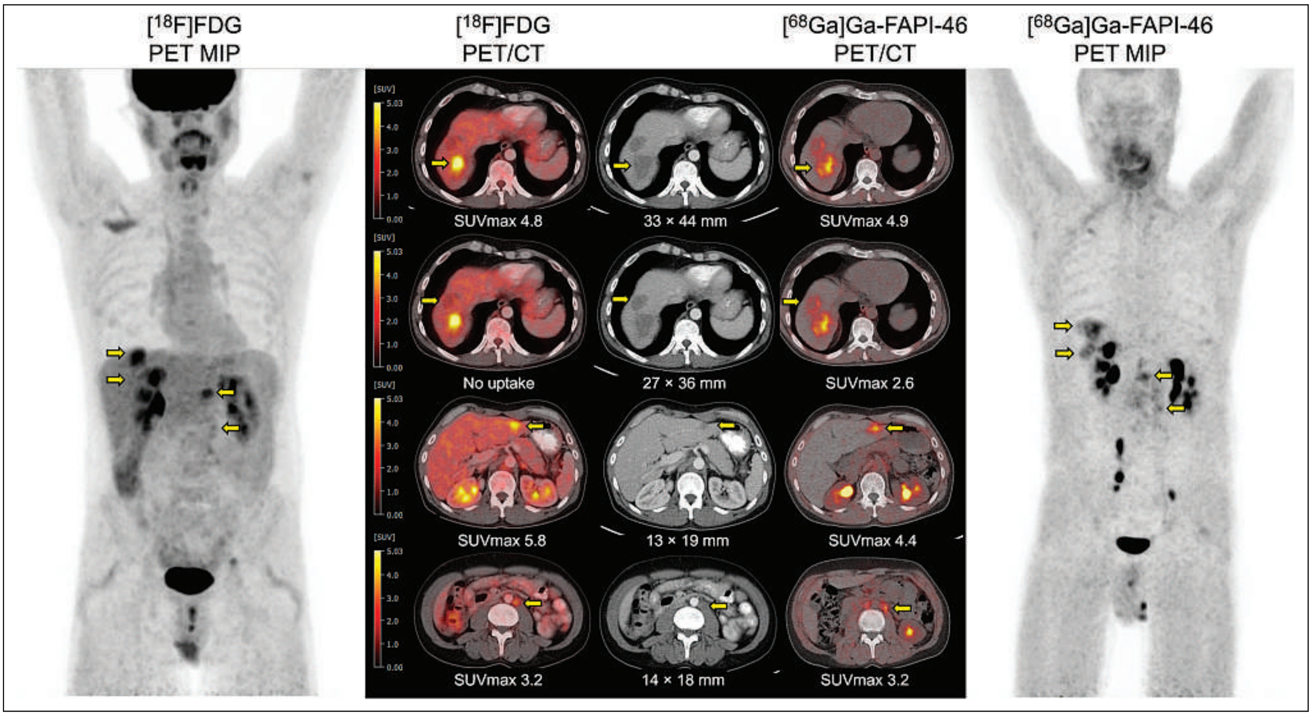

FIGURE 1. [^{18}F]FDG PET and [^{68}Ga]Ga-FAPI-46 PET maximum-intensity projections showing liver lesions and retroperitoneal lymph nodes (arrows). Hypoenhancing liver lesions in segments VII and III measuring 35 × 47 mm and 13 × 19 mm had increased [^{68}Ga]Ga-FAPI-46 uptake (SUV$_{max}$, 4.9 and 4.4) and [^{18}F]FDG uptake (SUV$_{max}$, 4.8 and 5.8). Segment VIII lesion measuring 27 × 36 mm had mild peripheral rim of [^{68}Ga]Ga-FAPI-46 uptake (SUV$_{max}$, 2.6) and no [^{18}F]FDG uptake. Residual retroperitoneal lymph node measuring 14 × 18 mm presented moderate [^{68}Ga]Ga-FAPI-46 uptake (SUV$_{max}$, 3.2) and [^{18}F]FDG uptake (SUV$_{max}$, 3.2).

FALSE-POSITIVE FAPI PET AFTER THERAPY • Ludwig et al. 1329

Nuclear Pharmacy Training in the Era of Theranostics: Toward Meeting the Needs of Nuclear Medicine Patients for Comprehensive Pharmaceutical Care

TO THE EDITOR: Novel radiopharmaceutical therapies against cancer are revolutionizing cancer care, and many more are in the pipeline. Although such therapies are currently approved for use as monotherapies in later stages of the disease, clinical trials are under way investigating radiopharmaceutical therapies earlier or in combination with other treatments such as classic and targeted chemotherapies, immunotherapy, and hormonotherapy, increasing the complexity of regimens and clinical follow-up (*1,2*). Although calling for an even closer collaboration between the nuclear medicine and oncology teams, this also prompts the need for increased participation by pharmacists with expertise in radiopharmaceuticals in the care of theranostic patients.

Historically, because most nuclear medicine activities have been oriented toward diagnostics, the pharmacist's participation in the clinical management of nuclear medicine patients has been limited. Besides, the nuclear pharmacist (formerly known as the radiopharmacist) has been focused primarily on activities related to radiopharmaceutical services, such as implementing and supervising local radiopharmaceutical production and dispensing (*3,4*). Over the last 3 decades, however, the Canadian supply of radiopharmaceuticals has shifted toward kit-based radiolabeling, typically performed by nuclear medicine technologists or provided by licensed facilities. In parallel, Canadian undergraduate pharmacy programs (PharmD) evolved toward clinical pharmacy and pharmaceutical care-oriented training, and nuclear pharmacy subspecialty programs are no longer offered. Paradoxically, as theranostics are becoming a new pillar in the anticancer arsenal, most Canadian-trained nuclear pharmacists are retiring without successors, creating a knowledge void at a time when their expertise would be most valuable. Furthermore, the exponential rise of radiopharmaceutical therapy creates a unique opportunity for the nuclear pharmacist to get increasingly involved in clinical care (*5*). Unfortunately, in the Canadian setting, this opportunity appears to be lost. A new approach to nuclear pharmacy training was thus needed.

In 2022, the Faculty of Pharmacy at Université Laval (Quebec City, Canada) launched a nuclear pharmacy training curriculum leading to a professional graduate diploma in specialized pharmaceutical care (*6*), offered in partnership with the CHU de Québec–Université Laval Hospital Center—a designated SNMMI Comprehensive Radiopharmaceutical Therapy Center of Excellence—and international collaborators. Université Laval's Faculty of Pharmacy and Department of Physics, Physics Engineering, and Optics, and CHU de Québec–Université Laval's Department of Pharmacy, Division of Nuclear Medicine, as well as Division of Medical Physics and Radiation Protection, teamed to develop a training curriculum for hospital pharmacists that is aligned with the emerging needs driven by theranostics. The completion of an accredited Canadian pharmacy residency (recognized PGY-1 residency program by the Board of Pharmacy Specialties in the United States), like the master's degree in advanced pharmacotherapy in Quebec (totaling 60 credits [2,700 h]) (*7*), and additional work experience in oncology are prerequisites for this new professional postgraduate diploma (30 credits [1,350 h]) in the specialty of nuclear pharmacy. It includes academic courses covering basic radiopharmacy sciences and radioprotection and an internship that includes rotations in both nuclear medicine clinics and radiopharmaceutical production, as well as an introduction to regulatory and quality assurance aspects thereof. In particular, building on the strong clinical background of the candidates, the clinical rotations in nuclear medicine aim to enable full participation of the nuclear pharmacy trainee in the interdisciplinary management of theranostic patients by providing comprehensive pharmaceutical care that includes radiopharmaceutical therapy. Combined with internships in facilities producing and dispensing radiopharmaceuticals, trainees will acquire the knowledge enabling them to take part in all stages of the theranostic agent circuit and ensure safe use in health care establishments. An oncology pharmacist (PharmD, MSc) is already engaged in the program.

The proposed training curriculum is in line with our vision in which the field of nuclear pharmacy represents a continuum spanning from the activities surrounding radiopharmaceutical services to the pharmaceutical care and counseling of patients treated with theranostics, that is, predominantly in oncology. The nuclear pharmacist will remain a pillar of the management of the entire process for the safe servicing and use of radiopharmaceuticals in health care establishments (including preparation, dispensing, distribution, administration, disposal, product traceability and quality control, radiation safety, etc.). In addition, the training curriculum will emphasize the clinical dimension of nuclear pharmacy, increasing patient support and hopefully filling an emerging clinical need. The clinical activities of the nuclear pharmacist will be structured around the optimization and safety of radioactive and nonradioactive therapies, in collaboration with the local nuclear medicine team. To the traditional clinical activities of the pharmacist in oncology are added those specific to treatments involving radiopharmaceuticals. The nuclear pharmacist providing pharmaceutical care will ensure that patients receive the right treatment at the right time and with the right activity, dose, and manner; identify and solve pharmacotherapeutic problems; provide pharmaceutical advice to patients and care teams (regarding radiopharmaceuticals, other anticancer and supportive drugs, and other pharmacotherapies); and monitor and manage adverse effects. These roles will both overlap and complement those of the nuclear medicine physician. To become this novel model of the nuclear pharmacist, the candidate needs to have a solid knowledge foundation on pharmaceutical care in oncology and, moreover, to master the basic sciences, radiation safety, and clinical aspects of radiopharmaceuticals. In so doing, the candidate might become eligible for an international nuclear pharmacy specialty certification (as no such certification is currently available in Canada).

The rapid growth of radiopharmaceutical therapy is opening new opportunities—requiring skills and knowledge in both nuclear and clinical pharmacy—for nuclear pharmacists to participate in the clinical management of nuclear medicine patients. To concretize this vision in the current Canadian setting, we developed a

---

nuclear pharmacy training program for clinical pharmacists that we believe will ultimately lead to improved health care offered in synergy with nuclear medicine and oncology, while broadening the scope of nuclear pharmacy in the era of theranostics.

DISCLOSURE

Isabelle Laverdière and Jean-Mathieu Beauregard are clinical research scholars from the Fonds de recherche du Québec–Santé. Jean-Mathieu Beauregard is consultant/advisor for Novartis and ITM and an investigator for Novartis and POINT Biopharma. No other potential conflict of interest relevant to this article was reported.

REFERENCES

1. Inderjeeth AJ, Iravani A, Subramaniam S, Conduit C, Sandhu S. Novel radionuclide therapy combinations in prostate cancer. *Ther Adv Med Oncol.* 2023;15: 17588359231187202.
2. Adant S, Shah GM, Beauregard JM. Combination treatments to enhance peptide receptor radionuclide therapy of neuroendocrine tumours. *Eur J Nucl Med Mol Imaging.* 2020;47:907–921.
3. Ponto JA, Hung JC. Nuclear pharmacy, part II: nuclear pharmacy practice today. *J Nucl Med Technol.* 2000;28:76–81.
4. Nuclear pharmacy specialty certification (BCNP). Board of Pharmacy Specialties website. https://bpsweb.org/nuclear-pharmacy/. Accessed June 13, 2024.
5. Augustine SC, Norenberg JP, Colcher DM, et al. An opportunity for pharmaceutical care in a specialty practice. *J Am Pharm Assoc (Wash).* 2002;42:93–100.
6. Diplôme professionnel de troisième cycle en soins pharmaceutiques spécialisés. Université Laval website. https://www.pha.ulaval.ca/etudes/programmes/diplome-professionnel-de-troisieme-cycle-en-soins-pharmaceutiques-specialises. Accessed June 13, 2024.
7. Accredited & accreditation pending programs. Canadian Society of Hospital Pharmacists website. https://cshp-scph.ca/year-1-programs. Accessed June 13, 2024.

Isabelle Laverdière*
Gilbert Matte
Martin Darveau
Jean-Mathieu Beauregard*
**CHU de Québec-Université Laval*
Quebec City, Canada
E-mail: isabelle.laverdiere@crchudequebec.ulaval.ca or jean-mathieu.beauregard@crchudequebec.ulaval.ca

---

DOI: 10.2967/jnumed.124.267603

LNCYT · 蓝纳成

GLOBAL LEADER IN RADIOTHERANOSTICS

YANTAI LANNACHENG BIOTECHNOLOGY CO., LTD.

Yantai Lannacheng Biotechnology Co., Ltd. was founded in 2021. As a wholly owned subsidiary of Yantai Dongcheng Pharmaceutical Group (Dongcheng), LNC is dedicated to develop and commercialize first-in-class radioligand theranostics, and is committed to becoming a global leader in radiopharmaceutical innovation. LNC has established its comprehensive industry chain covering early development, radiolabeling, and clinical studies.

LNC TOP PRODUCTS

^{177}Lu-LNC1004

^{177}Lu-LNC1004 is a first-in-class radionuclide therapeutic drug and is being used to treat patients with advanced FAP-positive solid tumor.

IP Advantages:

- High binding affinity and FAP targeting specificity
- Prolonged circulation half-life
- Increased tumor uptake and retention
- Favorable PK and efficacious FAP-positive tumor therapy effect

^{177}Lu-LNC1011

^{177}Lu-LNC1011 Injection is a long-acting PSMA targeting radiopharmaceutical, used to treat patients with prostate specific membrane antigen (PSMA)-positive metastatic castration-resistant prostate cancer (mCRPC)

IP Advantages:

- Rapid tumor uptake
- Prolonged blood half-life and tumor uptake/retention
- Visible lesion uptake with good contrast
- Good tumor to background ratio

^{18}F/^{68}Ga-LNC1007

^{18}F/^{68}Ga-LNC1007 Injection is being developed as a dual-targeting PET radiotracer. It is designed for FAP and integrin αvβ3 dual-targeted imaging in adult patients with solid tumor.

IP Advantages:

- Higher tumor uptake
- Good tumor to background ratio
- Better than FAPI and RGD counterparts

https://www.dc-lnc.com cczhi@dcb-group.com

FULL-LIFE
TECHNOLOGIES

Unleashing the power of half-life to bring
a full-life to cancer patients across the world

Full-Life Technologies Limited is a fully integrated global radiotherapeutics company with operations in Belgium, Germany, and China. We seek to own the entire value chain for radiopharmaceutical research & development, production & commercialization in order to deliver clinical impact for patients.

UniRDC™ Discovery Platform

Optimization of RDC biodistribution profiles

Radioisotope Production & Logistics

In-house GMP manufacturing facilities with global logistics capability

Clinical Development Capability

Established global clinical development platform with experienced team

www.full-life.com


VERITON-CT
SPECTRUM


SPECTRUM
D-SPECT
VISTA

8/24

The Journal of Nuclear Medicine

August 2024 ▪ Vol. 65 ▪ **Pages** 1163–1331